Advancing Transport Decarbonisation: Aerodynamic Optimisation of Flywheel Energy Storage for Low-Carbon Powertrains

Mahmoud Mohamed Hassan Eltaweel

Submitted to the University of Hertfordshire in partial fulfilment of the requirement of the degree of Doctor of Philosophy

School of Physics, Engineering and Computer Science

July 2024

Declaration of Originality

I declare that the work in this dissertation was carried out in accordance with the requirements of the University's Regulations and Code of Practice for Research Degree Programmes and that it has not been submitted for any other academic award. Except where indicated by the specific reference in the text, the work is the candidate's work. Any views expressed in the dissertation are those of the author.

Parts of the work outlined in Chapters 3, 4, 5 and 6 are published in the following journal articles:

- Eltaweel, M. and Herfatmanesh, M.R., 2024. Enhancing vehicular performance with flywheel energy storage systems: Emerging technologies and applications. Journal of Energy Storage, 103, p.114386.
- Eltaweel, M. and Herfatmanesh, M.R., 2024. Optimising Flywheel Energy Storage Systems: The Critical Role of Taylor–Couette Flow in Reducing Windage Losses and Enhancing Heat Transfer. Energies, 17(17), p.4466.
- Motaman, S., Eltaweel, M., Herfatmanesh, M.R., Knichel, T. and Deakin, A., 2023. Numerical analysis of a flywheel energy storage system for low carbon powertrain applications. Journal of Energy Storage, 61, p.106808.
- Eltaweel, M. and Herfatmanesh, M.R., 2023. Analysis of Standby Power in an Enclosed High-Speed Flywheel Energy Storage System Using the CFD-ANOVA Approach (No. 2023-32-0069). SAE Technical Paper.
- Eltaweel, M. and Herfatmanesh, M.R., 2023, June. Numerical Investigation of Windage Loss and Heat Transfer in a High-Speed Flywheel Energy Storage System With Slit Wall. In Turbo Expo: Power for Land, Sea, and Air (Vol. 86991, p. V006T09A013). American Society of Mechanical Engineers.
- Eltaweel, M., Kalyvas, C., Chen, Y. and Herfatmanesh, M.R., 2022, September. Development of a CFD Model for the Estimation of Windage Losses Inside the Narrow Air Gap of an Enclosed High-Speed Flywheel. In International Conference on Energy and Sustainable Futures (pp. 157-167). Cham: Springer Nature Switzerland.

Parts of the work presented in Chapters 4, 5, 6 and 7 are submitted for publication in the following journal articles:

- Eltaweel, M., Mostafa, N., Kalyvas, C., Chen, Y. and Herfatmanesh, M.R., 2024, Optimising Flywheel Energy Storage Systems for Enhanced Windage Loss Reduction and Heat Transfer: A Computational Fluid Dynamics and ANOVA-Based Approach. (Article submitted to Journal of Energy Reports).
- Eltaweel, M. and Herfatmanesh, M.R., 2024, Optimisation of Flywheel Energy Storage System through Advanced Slit Wall Design. (Article submitted to Journal of Energy Storage).
- Eltaweel, M. and Herfatmanesh, M.R., 2024, Optimising Flywheel Energy Storage Systems for Fuel Reduction in Hybrid Vehicle: A CFD-MATLAB/Simulink-Based Investigation. (Article submitted to Journal of Energy Storage).

Mahmoud Eltaweel

Abstract

Given the pressing need to reduce carbon emissions and the significant role of the transportation sector in global carbon dioxide output, Flywheel Energy Storage Systems (FESS) offer excellent energy recovery potential to significantly improve energy efficiency and reduce emissions in low-carbon powertrains. However, a gap exists between theoretical potential and practical application, as current FESS technologies have not been fully optimised for aerodynamic efficiency, limiting their adoption in real-world applications. Enhancing FESS to operate at optimal aerodynamic efficiency promises greater energy storage and retrieval efficiencies for vehicles and enables a broader range of applications in the search for transport decarbonisation. This thesis introduces a new concept for the aerodynamic optimisation of FESS, utilising an integrated approach of Computational Fluid Dynamics (CFD) and Design of Experiments (DoE) analysis. This concept is explored through analytical models and CFD simulations tailored to the unique characteristics of FESS. The implementation of this optimised FESS demonstrates, through various design modifications and operational conditions, an ability to significantly reduce standby losses and enhance overall energy efficiency, with potential applications extending to medium-duration storage solutions. A comprehensive evaluation of current FESS technologies highlighted barriers to achieving optimal aerodynamic efficiency. To overcome these challenges, the thesis proposes a refined FESS design that incorporates adjustments to airgap size, radial and axial radius ratios, and enhanced surface roughness. Notably, the integration of reversed trapezoidal slit shapes, operating at reduced pressure levels of 200 mbar and using helium as the gas medium, led to significant enhancements, reducing windage losses by 88% and increasing the Nusselt number by up to 18%, indicative of improved heat transfer efficiency. These aerodynamic enhancements were validated by a substantial 580% increase in standby time in the optimised model, demonstrating the effectiveness of the design modifications. Vehicle simulations using MATLAB/Simulink, specifically for the Vauxhall Corsa model, revealed that the initial integration of the baseline FESS model into a Hybrid Electric Vehicle (HEV) resulted in a 13% reduction in fuel consumption and a 10% decrease in carbon dioxide emissions, demonstrating FESS's benefits for vehicle efficiency. Further refinements in the FESS integration, particularly in the most optimised Model, resulted in an 18% reduction in fuel consumption and a 15% decrease in carbon dioxide emissions across various Worldwide Harmonised Light Vehicle Test Procedure (WLTP) classes. The FESS transformation from a short-duration to a medium-to-short-duration storage solution broadens its application spectrum, accommodating both short and extended vehicular journeys. These findings signify a considerable advancement towards closing the gap between the current capabilities and the theoretical potential of FESS in contributing to the decarbonisation of the transportation sector, paving the way for future developments in low-carbon vehicle technologies.

Acknowledgments

I would like to express my sincere gratitude to my main supervisor, Associate Professor Mohammad Reza Herfatmanesh, for his invaluable guidance, support, and encouragement throughout my PhD journey. His expertise and dedication have been instrumental in shaping my research and helping me overcome numerous challenges.

I am also deeply thankful to my second supervisor, Professor Yong Chen, and my third supervisor, Dr. Christos Kalyvas, for their insightful advice, continuous support, and constructive feedback. Their contributions have significantly enriched my work and broadened my academic perspective.

I would like to extend my appreciation to the University Alliance Doctoral Training Alliance (DTA) for their support and for providing the funding for my research through the Horizon 2020 Marie Skłodowska-Curie PhD Fellowship programme. This opportunity has been pivotal in advancing my academic and professional career. Furthermore, I would like to acknowledge the University of Hertfordshire for providing the excellent facilities, especially the High-Performance Computing facilities, which have been crucial for my research.

Aya, my wife, Thank you for bearing with me and continuing to endure my flaws, mistakes, and shortcomings. Thank you for accepting to live with me despite my flaws. Thank you for being a support and a refuge for me, enabling me to carry out my work.

I am deeply grateful to my parents, Mohamed and Doaa, for always prioritising my education and for their patience and support throughout my academic journeys. Without your love, I would not have had the energy and motivation to continue. I am grateful to my sister and brothers, Marwa, Mostafa, and Moez, for always believing in and supporting me.

I'm also grateful to my colleagues, Aamir, Hamza, Kumar, and Surya, for their friendship and support, which have made this journey more fun and memorable. Thank you all for your invaluable contributions to my PhD journey.

Nomenclature

Latin symbols

A	Area	K_n	Knudsen number
A_s	Cylinder surface area	K_s^+	Dimensionless roughness height
B	Slit base length	K_s	Roughness height
C	Slit height	K_w	Weighting factor
C_D	Drag coefficient	l	Rotor length
C_l	Dynamic load rating	L_{10}	Rating life
C_m	Disc torque coefficient	L_{10h}	Operational hours rating life
C_s	Static load rating	L_i	Characteristic length of flow field
C_w	Cylinder skin friction coefficient	M	Molecular weight
C_μ	Turbulence model constant	m	Mass
D	Desirability	Ma	Mach number
$\frac{DV}{Dt}$	Fluid particle acceleration	M_c	Cylinder moment
D_h	Hydraulic diameter	M_D	Disc moment
D_i	Diameter	n	number of slits
D_p	Diameter of the pitch circle	n_d	Number of measured responses
E	Kinetic energy	n_l	Rotational speed of a ball bearing
$e_{k,m}$	Specific energy	n_s	Bearing speed
$e_{k,v}$	Energy density	Nu	Nusselt number
F	Force	P	Pressure
F_a	Axial bearing load	P_1	Initial pressure
F_b	Applied load	P_2	Required pressure
F_g	Geometrical factor	$P_{bearing}$	Bearing losses
f_L	Factor dependent on bearing design	P_{in}	Initial power stored
f_o	Factor dependent on bearing type	P_l	Equivalent dynamic load
F_r	Radial bearing load	P_{out}	Available output power
F_s	Static equivalent load	Pr	Prandtl number
g	Gravity	$P_{W,C}$	Windage loss for concentric rotating cylinder
g	Airgap width	$P_{W,D}$	Windage loss for two-disc surface
H	Angular momentum	$P_{windage}$	Windage losses
h	Convective heat transfer	Q_{Con}	Heat transfer by conduction
HE	Half-ellipse	Q_{Conv}	Heat transfer by convection
h_r	Rotor height	Q_{rad}	Heat transfer by radiation
I	Moment of inertia	QL	Quality loss function
K	Shape factor	Q_t	Total heat transfer
k	Turbulent kinetic energy	R	Universal gas constant
k_{cr}	Axial wave number	R^2	Coefficient of Determination

r_i	Inner radius of the hollow cylinder
r_o	Outer radius of the hollow cylinder
r_s	Shaft radius
r_{sd}	Radius of the solid cylinder
Ra	Rayleigh number
RC	Rectangle
Re	Reynolds number
RT	Reversed trapezoid
R_T	Total thermal resistance
R_{th}	Thermal resistance
r_x	Specific location of interest
Re_t	Tip Reynolds number
Re_w	Working fluid Reynolds number
S	Pumping rate
T	Temperature
t	Time
T_a	Taylor number
T_A	Ambient temperature
T_{ap}	Torque applied on a flywheel
Ta_m	Modified Taylor number
T_B	Rolling bearing torque
T_h	Housing temperature
T_L	Load-dependent rolling bearing torque
T_r	Reaction torque from the flywheel
T_v	Speed-dependent rolling bearing torque
TR	Trapezoid
u	Velocity of specified radius
u^*	Friction velocity
u_o	Rotating cylinder surface speed
$\bar{u}$	Mean velocity parallel to the wall
V	Volume
$\mathbf{v}$	Velocity vector
V_e	Actual performance
V_t	Desired performance
w	Slit Top length
$\mathcal{X}$	Radial load factors of a ball bearing
X_s	Static radial load factor
y	Normal distance to the wall
Y	Observed response
$\mathcal{Y}$	Axial load factors of a ball bearing
Y_m	Mean of observed responses
Y_s	Static axial load factor

Greek symbols

β	Thermal expansion coefficient
Γ	Aspect ratio
γ	Specific heat ratio
ΔT	Temperature difference
ε	Emissivity
θ	Angle
$\mathcal{K}$	Boltzmann constant
κ	Ratio of specific heats
η	Radius ratio
η^*	Interaction term
η^o	Estimated S/N ratio
η^m	Average of the total mean S/N ratio
η^t	Estimated S/N ratio for the factor while including the interaction effect
λ	Thermal conductivity
$\lambda(t)$	Flywheel state of charge
λ_{cr}	Critical wavelength of the Taylor vortices
μ	Dynamic viscosity
ν	Speed
ρ	Density
τ	Shear stress
τ_{turb}	Reynolds stress tensor
τ_w	Wall shear stress
τ_{xy}	Shear stress
v	Kinematic viscosity
v_o	Kinematic viscosity of lubricant
ν_p	Poisson's ratio
σ^2	Variance
σ_θ	Hoop stress
σ_r	Radial stress
σ_s	Stefan-Boltzmann constant
σ_t	Tangential momentum coefficient
ϑ	Molecular mean free path
Φ	Heat from conversion of mechanical energy
ω	Angular velocity
$\omega(t)$	Flywheel's instantaneous angular velocity
ω_{max}	Maximum permissible angular velocities
ω_{min}	Minimum permissible angular velocities
Ω	Precession rate

Abbreviations

ABS	Anti-lock Braking System	FIA	Fédération Internationale de l'Automobile
AC	Alternating Current	FVM	Finite Volume Method
AFD	Analytical Fluid Dynamics	FWB	Flywheel Battery
ANOVA	Analysis of Variance	GHG	Greenhouse Gas
B/C	Base Length-to-Height Ratio	GTR	Global Technical Regulation
BEVs	Battery Electric Vehicles	GVEA	Golden Valley Electric Association
BLDCM	Brushless Direct Current Machine	HC	Hydrocarbons
BM	Bearingless Machines	He	Helium
CAE	Computer Aided Engineering	HEV	Hybrid Electric Vehicle
CAF	Construcciones y Auxiliar de Ferrocarriles	HM	Homopolar Machines
CAV	Connected and Autonomous Vehicle	ICE	Internal Combustion Engine
CCM	Capacitor Charging Method	IM	Induction Machine
CFD	Computational Fluid Dynamics	IVT	Infinitely Variable Transmission
CO2	Carbon Dioxide	JET	Joint European Torus
COVID	Coronavirus Disease	KE	Kinetic Energy
CVT	Continuously Variable Transmission	KERS	Kinetic Energy Recovery System
DC	Direct Current	LES	Large Eddy Simulation
DNS	Direct Numerical Simulation	LLC	Limited Liability Company
DoE	Design of Experiments	LLP	Limited Liability Partnership
DOF	Degrees of Freedom	LTB	Larger-The-Better
DVLA	Driver and Vehicle Licensing Agency	MATLAB	Matrix Laboratory
EFD	Experimental Fluid Dynamics	MG	Motor-Generator
EMALS	Electromagnetic Aircraft Launch System	MIMO	Multiple Input Multiple Output
ER	Energy Recovery	MRF	Moving Reference Frame
ERS	Energy Recovery System	MWV	Modulated Wavy Vortices
ESS	Energy Storage System	N	Nitrogen
EV	Electric Vehicle	NASA	National Aeronautics and Space Administration
FCEV	Fuel Cell Electric Vehicle	NEDC	New European Driving Cycle
FDM	Finite Difference Method	NOx	Nitrogen Oxides
FEM	Finite Element Method	NTB	Nominal-The-Better
FESS	Flywheel Energy Storage Systems	OA	Orthogonal Array
BEVs	Battery Electric Vehicles	OEM	Original Equipment Manufacturer
BLDCM	Brushless Direct Current Machine	PGS	Planetary Gear Set
FESS	Flywheel Energy Storage Systems	PI	Proportional-Integral

PID	Proportional-Integral-Derivative
PMR	Power-to-Mass Ratio
PMSM	Permanent Magnet Synchronous Machine
QUICK	Quadratic Upstream Interpolation for Convective Kinematics
RANS	Reynolds-Averaged Navier-Stokes
RB	Regenerative Braking
RR	Radius Ratio
RSA	Regenerative Shock Absorber
RSM	Response Surface Methodology
RSM	Reynolds Stress Model
RTG	Rubber-Tyred Gantry crane
S/N	Signal-to-Noise Ratio
SIMPLE	Semi-Implicit Method for Pressure-Linked Equations
SOC	State of Charge
SRM	Switched Reluctance Machine
SRM	Switched Reluctance Machine
SST	Shear Stress Transport
STB	Smaller-The-Better
SUV	Sport Utility Vehicle
TERS	Thermal Energy Recovery Systems
TTV	Turbulent Taylor Vortices
TUR	Featureless turbulent flow
TVF	Taylor Vortex Flow
UK	United Kingdom
UNECE	United Nations Economic Commission for Europe
UPS	Uninterruptible Power Supply
US	United States
VRM	Variable Reluctance Machines
WLTP	Worldwide Harmonised Light Vehicle Test Procedure
WLTP	Worldwide Harmonised Light Vehicle Test Procedure
WVF	Wavy Vortex Flow
ZEV	Zero Emission Vehicle

Contents

Declaration of Originality II
Abstract III
Acknowledgments IV
Nomenclature V
List of Figures XIV
List of Tables XVIII
Chapter 1. Introduction 1
1.1. Motivation 1
1.2. Background 2
1.3. Creating Low-Carbon Vehicles 6
1.4. Objectives 8
1.5. Research Questions 8
1.6. Contributions to Knowledge 9
1.7. Scope And Limitations 10
1.8. Thesis Structure 11
Chapter 2. Literature Review 13
2.1. Energy Recovery Systems 13
2.1.1. Energy Recovery from Exhaust Gases 14
2.1.2. Energy Recovery from Vertical Oscillations 14
2.1.3. Energy Recovery from Vehicle Inertia 15
2.2. Storage Devices 16
2.2.1. Electric Storage 20
2.2.2. Alternator-Control Storage 22
2.2.3. Ultracapacitors Storage 22
2.2.4. Pneumatic/Hydraulic Storage 22
2.2.5. Elastomers And Spring Storage 23
2.2.6. Flywheel Storage 23
2.3. FESS Applications 27
2.3.1. Transportation 27
2.3.2. Mobile Applications 31
2.3.3. Grid-Connected Power Management 32
2.3.4. Industrial and Commercial Power Management 33
2.3.5. Pulsed Power 33
2.3.6. Uninterruptible Power Supplies 34
2.4. FESS-Based Powertrain for Vehicles 35
2.4.1. FESS ICE-Based Powertrain 35
2.5. FESS HEV Powertrain 37
2.5.1. FESS Electric Powertrains 38
2.6. FESS Components 39

2.6.1. Bearings 39
2.6.2. Control 41
2.6.3. Housing 44
2.6.4. Transmission 44
2.6.5. Rotor Design 49
2.7. Limitations of FESS 50
2.7.1. Safety 50
2.7.2. Gyroscopic Moment Effect 53
2.8. Optimisation of FESS Standby Losses 56
2.8.1. Airgap size 56
2.8.2. Working Pressure 58
2.8.3. Rotor Material 59
2.8.4. Slit Wall Design 59
2.8.5. Knowledge Gap 62
2.9. Summary 64
Chapter 3. Methodology 65
3.1. Research Design 65
3.2. Methodology 67
3.3. Design of Experiment 69
3.4. Computational Fluid Dynamics 71
3.4.1. Governing Equations 72
3.4.2. Turbulence Modelling 76
3.4.3. Turbulent Boundary Layer 76
3.4.4. Discretisation Method 78
3.4.5. Numerical Scheme 80
3.4.6. Convergence 81
3.4.7. Modelling Rotating Systems 82
3.4.8. CFD Modelling of Rotary Systems 82
3.4.9. CFD Simulation for Vacuum Environment 84
3.4.10. CFD Model Validation 84
3.5. FESS Loss Calculations 93
3.5.1. Bearing Selection for FESSs 93
3.5.2. Aerodynamic Losses 97
3.5.3. Thermal Analysis 105
3.6. Rotor Design Criteria 109
3.6.1. FESS Rotor Design 110
3.6.2. Rotor Material 114
3.6.3. Maximum Outer Radius 116
3.6.4. Rotor Length 117
3.6.5. Hub Design 117
3.6.6. Optimal Design 118
3.7. Summary 121
Chapter 4. FESS Aerodynamic Performance Characteristics 123
4.1. Pre-Processing 123
4.1.1. Mesh Independence Analysis 125
4.2. Solver 128
4.3. Post-Processing 129
4.3.1. Flow Field of the FESS 129

4.3.2. Characterisation of Windage Losses and Heat Transfer 142
4.4. Summary 149
Chapter 5. Optimisation of FESS Geometric and Operating Conditions 151
5.1. Optimisation of Airgap and Roughness 151
5.1.1. Responses Selection 152
5.1.2. Factors Selection 152
5.1.3. Analysis Setup 154
5.1.4. Responses 155
5.1.5. Nusselt Number Response 158
5.1.6. Windage Losses Response 163
5.1.7. Influence of Surface Roughness 168
5.1.8. Optimisation 175
5.2. Optimisation of Airgap and Partial Vacuum Pressure 177
5.2.1. Responses Selection 177
5.2.2. Factors Selection 178
5.2.3. Responses 180
5.2.4. Optimisation 185
5.3. Optimisation of Airgap Size and Medium Gas 187
5.3.1. Taguchi Method 188
5.3.2. The Optimised Design 203
5.4. Summary 204
Chapter 6. The Effect of Casing Design on FESS Aerodynamic Performance 206
6.1. Introduction of Slit Walls in FESS Casing 206
6.1.1. Boundary Conditions 207
6.1.2. Influence of Slit Walls on Windage Losses 210
6.1.3. Influence of Slit Walls on Heat Transfer 214
6.1.4. Flow Characteristics 219
6.1.5. Research Findings 221
6.2. RSM Application for Slit Walls Optimisation 222
6.2.1. Responses Selection 222
6.2.2. Factors Selection 223
6.2.3. Responses 225
6.2.4. Fluid Flow Characteristics 228
6.2.5. Windage Losses Response 230
6.2.6. Heat Transfer Response 235
6.2.7. Optimisation 244
6.3. The Effect of Slits 245
6.4. Summary 245
Chapter 7. Contribution of FESS Aerodynamic Performance Optimisation on Transport Decarbonisation 247
7.1. The Optimised Designs of FESS for Vehicle Integration 247
7.2. Vehicle Simulation 249
7.3. Vehicle Model Selection 250
7.3.1. Hybrid Vehicle Model 251
7.3.2. Driving Cycle 253
7.4. Integration of FESS into the Hybrid Vehicle Model 255
7.4.1. Powertrain Structure 255

7.4.2. Operating Modes 255
7.4.3. FESS Modelling 258
7.4.4. FESS Mechanical Losses 259
7.4.5. Rule-Based Control Strategy 259
7.5. FESS Impact on Vehicle Performance 260
7.5.1. Model Verification 260
7.5.2. Analysis of The FESS Models 261
7.6. Summary 265
Chapter 8. Conclusion and Future Work 266
8.1. Research Questions 267
8.1.1. How do energy recovery systems enhance transportation energy efficiency and emissions reduction? 267
8.1.2. How do CFD and DoE enhance FESS optimisation precision and reliability for low-carbon solutions? 267
8.1.3. How do FESS design parameters impact its windage losses and heat transfer, and what are the optimal conditions for energy efficiency and thermal management? 268
8.1.4. How do geometric and operating conditions in FESS affect its aerodynamic performance, and what configurations yield maximum energy storage efficiency with minimal losses? 268
8.1.5. How do slit walls in FESS casing affect aerodynamic efficiency and what are the optimal characteristics for system efficiency? 269
8.1.6. How does integrating optimised FESS into light-duty vehicles affect fuel efficiency and emissions reduction? 270
8.2. Contributions to Knowledge 270
8.3. Implications for Practice 271
8.4. Limitations of the Study 272
8.5. Recommendations for Future Work 272
8.6. Concluding Remarks 273
References 274
Appendix A 295
Appendix B 296
Appendix C 298

List of Figures

Fig. 1-1 Distance travelled by different passenger transport mode, in billion passenger kilometres [9] 2
Fig. 1-2 UK's 2020 roadmap for propulsion technologies in light-duty vehicles [18] 5
Fig. 2-1 The categorisation of energy recovery systems for automotive applications [1] 13
Fig. 2-2 Comparison of different energy storage systems based on: (a) power and energy densities (b) specific power and specific energy [12] 18
Fig. 2-3 The system configuration used by Eindhoven University [112] 36
Fig. 2-4 Imperial College concepts for brake-only and CVT-brake hybrid systems [111] 36
Fig. 2-5 Hybrid electric powertrain with flywheel acting as an energy storage [114] 37
Fig. 2-6 ETH-III powertrain schematic for hybrid powertrain with flywheel [115] 37
Fig. 2-7 Schematic of the flywheel battery components [86] 38
Fig. 2-8 Three different MG and FESS configurations [170] 49
Fig. 2-9 The angle between the precession rate and angular momentum vectors [179] 54
Fig. 2-10 vehicle manoeuvres and the corresponding reaction torque [180] 55
Fig. 2-11 The schematic diagram of counter-rotating flywheels [182] 55
Fig. 2-12 Analysis of the keywords "Flywheel energy storage" from the Web of Science in VOS viewer. The search yielded 2241 papers as of May 2024. (a) The recurring topics are design, optimisation, control, power, etc. Losses are not a recurring topic. (b) The time distribution shows that composite flywheel and vibration control are among the oldest topics, whereas design and optimisation are among the newest 62
Fig. 3-1 Research framework 68
Fig. 3-2 Near wall boundary layer regions [293] 77
Fig. 3-3 Wall treatment methods [296] 77
Fig. 3-4 Experimental flywheel system, (a) the Setup with motor, safety casing, and containment, (b) the schematic diagram of the flywheel tested 85
Fig. 3-5 Simplified FESS geometry with periodic region and symmetry plane 86
Fig. 3-6 Mesh independence test 87
Fig. 3-7 FESS with tetrahedral and hexahedral mesh 87
Fig. 3-8 Carbon fibre temperature vs flywheel speed predictions with different turbulence models 89
Fig. 3-9 3D model of the FESS geometry with solid rotor 90
Fig. 3-10 Validation of numerical predictions of seal and bearing losses as a function of flywheel speed against experimental data at different working pressures 90
Fig. 3-11 Validation of rotor skin friction coefficient vs Taylor number against Donnelly and Simon's experimental data [314] 92
Fig. 3-12 Validation of average velocity profile within the airgap against the experimental results reported by Hosain et al. [222], H. Reichardt [316] 92
Fig. 3-13 Validation of radial velocity distribution in the R-Z plane against the experimental results reported by Liu et al. [267] 93
Fig. 3-14 Taylor vortices within the annulus of a concentric cylinder [339], [340] 102
Fig. 3-15 The flow regime map within the annulus of concentric cylinders with radius ratio of 0.833 [341] 103
Fig. 3-16 Different flow configurations in FESSs [342] 103
Fig. 3-17 The thermal resistance of the studied FESS 106
Fig. 3-18 The thermal resistance circuit of the studied FESS 109
Fig. 3-19 FESS design requirements analysis flowchart 110
Fig. 3-20 Flywheel rotor shape optimisation [359] 114
Fig. 3-21 Different flywheel hub designs [76] 118
Fig. 3-22 A comparison between the cost and kinetic energy storage capacity of various flywheel rotor materials 120
Fig. 3-23 A comparison between the mass and kinetic energy storage capacity of various flywheel rotor materials 120
Fig. 4-1 Numerical domain, (a) FESS geometry in 3D, (b) the simplified geometry with periodic and symmetry regions 124
Fig. 4-2 The Nusselt number and skin friction coefficient values obtained for five tested meshes at different radius ratio values; (a) $\eta = 0.99$, (b) $\eta = 0.98$, (c) $\eta = 0.97$, (d) $\eta = 0.96$, and (e) $\eta = 0.95$ 127
Fig. 4-3 The mesh employed for the system 128

Fig. 4-4 Air velocity distribution within the airgap of a FESS with a radius ratio of 0.99 at different rotational speeds; (a) 200 rad/s, (b) 800 rad/s, (c) 1600 rad/s, and (d) 2400 rad/s.....130
Fig. 4-5 Velocity vector plot within the airgap of a FESS with a radius ratio of 0.99 at different rotational speeds; (a) 200 rad/s, (b) 800 rad/s, (c) 1600 rad/s, and (d) 2400 rad/s.....130
Fig. 4-6 Linear velocity as a function of distance at the midpoint of the FESS airgap within a radius ratio of 0.99 130
Fig. 4-7 The observed number of Taylor cells vs computed Taylor cell number as a function of Taylor number at radius ratio of 0.975.....131
Fig. 4-8 Velocity vector plot within the airgap of a FESS operating at 1600 rad/s at different radius ratios; (a) 0.99, (b) 0.98, (c) 0.97, and (d) 0.96.....132
Fig. 4-9 Air velocity distribution within the airgap of a FESS operating at 1600 rad/s at different radius ratios; (a) 0.99, (b) 0.98, (c) 0.97, and (d) 0.96.....132
Fig. 4-10 Temperature distribution within the airgap of a FESS operating at 1600 rad/s at different radius ratios; (a) 0.99, (b) 0.98, (c) 0.97, and (d) 0.96.....133
Fig. 4-11 Enlarged velocity vectors within the airgap of a FESS operating at 1600 rad/s with the radius ratio of 0.96.....134
Fig. 4-12 Contour plot illustrating the examined section of axial velocity in the Z-Y plane within the airgap of a FESS operating at 1600 rad/s with a radius ratio of 0.96 134
Fig. 4-13 Contour plot of axial velocity in the Z-Y plane within the airgap of a FESS operating at 1600 rad/s at different radius ratios; (a) 0.96, (b) 0.97, (c) 0.98, and (d) 0.99.....135
Fig. 4-14 Contour plot of radial velocity in the Z-Y plane within the airgap of a FESS operating at 1600 rad/s at different radius ratios; (a) 0.96, (b) 0.97, (c) 0.98, and (d) 0.99.....135
Fig. 4-15 Contour plot of tangential velocity in the Z-Y plane within the airgap of a FESS operating at 1600 rad/s at different radius ratios; (a) 0.96, (b) 0.97, (c) 0.98, and (d) 0.99.....137
Fig. 4-16 Air velocity distribution within the airgap of a FESS with radius ratio of 0.98 at different rotational speeds; (a) 200 rad/s, (b) 800 rad/s, (c) 1600 rad/s, and (d) 2400 rad/s.....139
Fig. 4-17 Air velocity distribution within the airgap of a FESS with radius ratio of 0.97 at different rotational speeds; (a) 200 rad/s, (b) 800 rad/s, (c) 1600 rad/s, and (d) 2400 rad/s.....139
Fig. 4-18 Air velocity distribution within the airgap of a FESS with radius ratio of 0.96 at different rotational speeds; (a) 200 rad/s, (b) 800 rad/s, (c) 1600 rad/s, and (d) 2400 rad/s.....140
Fig. 4-19 Velocity vector plot within the airgap of a FESS with radius ratio of 0.98 at different rotational speeds; (a) 200 rad/s, (b) 800 rad/s, (c) 1600 rad/s, and (d) 2400 rad/s.....140
Fig. 4-20 Velocity vector plot within the airgap of a FESS with radius ratio of 0.97 at different rotational speeds; (a) 200 rad/s, (b) 800 rad/s, (c) 1600 rad/s, and (d) 2400 rad/s.....140
Fig. 4-21 Velocity vector plot within the airgap of a FESS with radius ratio of 0.96 at different rotational speeds; (a) 200 rad/s, (b) 800 rad/s, (c) 1600 rad/s, and (d) 2400 rad/s.....141
Fig. 4-22 Linear velocity as a function of distance at the midpoint of the FESS airgap within a radius ratio of 0.98 operating at different operational speeds.....141
Fig. 4-23 Linear velocity as a function of distance at the midpoint of the FESS airgap within a radius ratio of 0.97 operating at different operational speeds.....142
Fig. 4-24 Linear velocity as a function of distance at the midpoint of the FESS airgap within a radius ratio of 0.96 operating at different operational speeds.....142
Fig. 4-25 Skin friction coefficient vs Taylor number for different radius ratios.....143
Fig. 4-26 Taylor number vs rotational speed for different radius ratios 143
Fig. 4-27 Skin friction coefficient vs the rotational speed for different radius ratios 144
Fig. 4-28 Rotor temperature vs rotational speed for different radius ratios.....145
Fig. 4-29 Windage losses vs rotational speed for different radius ratios 146
Fig. 4-30 Reynolds number vs rotational speed for different radius ratios.....146
Fig. 4-31 Taylor number vs Reynolds number for different radius ratios 147
Fig. 4-32 Windage losses vs Taylor Number for different radius ratios.....148
Fig. 4-33 Nusselt number vs rotational speed for different radius ratios.....149
Fig. 4-34 Nusselt number vs Taylor number for different radius ratios 149
Fig. 5-1 The FESS's simplified geometry in the Z-Y plane.....153
Fig. 5-2 3D plot of Nusselt number as a function of radial and axial radius ratios at different rotational speeds: (a) 800 rad/s, (b) 1600 rad/s, (c) 2400 rad/s.....159
Fig. 5-3 3D plot of Nusselt number as a function of rotor and housing surface roughness at different rotational speeds: (a) 800 rad/s, (b) 1600 rad/s, (c) 2400 rad/s.....160

Fig. 5-4 Air velocity distribution within the airgap at 1600 rad/s for radial and axial radius ratios of 0.98 at different rotor surface roughness heights: (a) Ks=0, (b) Ks=5e-7 m, (c) Ks=5e-6 m, (d) Ks=5e-5 m 161
Fig. 5-5 3D plot of Nusselt number as a function of radial radius ratio and rotational velocity at different axial radius ratios: (a) 0.99, (b) 0.98, (c) 0.97, (d) 0.96 162
Fig. 5-6 Main effects plot for mean Nusselt number for the studied five factors 163
Fig. 5-7 3D plot of windage losses as a function of radial and axial radius ratios at different rotational speeds: (a) 800 rad/s, (b) 1600 rad/s, (c) 2400 rad/s 164
Fig. 5-8 3D plot of rotor skin friction coefficient as a function of radial and axial radius ratios at different rotational speeds: (a) 800 rad/s, (b) 1600 rad/s, (c) 2400 rad/s 165
Fig. 5-9 3D plot of disc torque coefficient as a function of radial and axial radius ratios at different rotational speeds: (a) 800 rad/s, (b) 1600 rad/s, (c) 2400 rad/s 166
Fig. 5-10 3D plot of windage losses as a function of rotational velocity and (a) radial radius ratio, (b) axial radius ratio 167
Fig. 5-11 Main effects plot for mean windage losses for the studied five factors 167
Fig. 5-12 3D plot of windage losses as a function of rotor and housing surface roughness with the radial and axial radius ratios of 0.99 at different rotational speeds: (a) 800 rad/s, (b) 1600 rad/s, (c) 2400 rad/s 169
Fig. 5-13 3D plot of windage losses as a function of rotor and housing surface roughness with the radial and axial radius ratios of 0.98 at different rotational speeds: (a) 800 rad/s, (b) 1600 rad/s, (c) 2400 rad/s 170
Fig. 5-14 3D plot of windage losses as a function of rotor and housing surface roughness with radial and axial radius ratios of 0.97 at different rotational speeds: (a) 800 rad/s, (b) 1600 rad/s, (c) 2400 rad/s.....171
Fig. 5-15 3D plot of windage losses as a function of rotor and housing surface roughness with radial and axial radius ratios of 0.96 at different rotational speeds: (a) 800 rad/s, (b) 1600 rad/s, (c) 2400 rad/s.....172
Fig. 5-16 3D plot of rotor skin friction coefficient as a function of rotor and housing surface roughness at a rotational speed of 2400 rad/s with the axial radius ratio of 0.96 and radial radius ratios of: (a) 0.96, (b) 0.97, (c) 0.98, (d) 0.99 173
Fig. 5-17 3D plot of rotor skin friction coefficient as a function of rotor and housing surface roughness at the radial and axial radius ratios of 0.96 at different rotational speeds: (a) 800 rad/s, (b) 1600 rad/s, (c) 2400 rad/s.....174
Fig. 5-18 3D plot of disc torque coefficient as a function of rotor and housing surface roughness at the radial and axial radius ratios of 0.99 at different rotational speeds: (a) 800 rad/s, (b) 1600 rad/s, (c) 2400 rad/s.....175
Fig. 5-19 The windage losses with respect to rotational velocity for the 25 ANOVA runs 183
Fig. 5-20 3D plot for windage losses between radius ratio and pressure level 184
Fig. 5-21 3D plot for Nusselt number between radius ratio and pressure level 184
Fig. 5-22 3D plot for standby power between radius ratio and pressure level.....185
Fig. 5-23 The desirability contours for the three studied responses when only standby power is selected for optimisation 186
Fig. 5-24 The desirability contours for the three studied responses when standby power and Nusselt number are selected for optimisation 187
Fig. 5-25 Block diagram of the process optimisation. 188
Fig. 5-26 The windage losses with respect to rotational velocity for the 16 Taguchi runs.....192
Fig. 5-27 The mean S/N ratio for windage losses for the four studied parameters.....195
Fig. 5-28 The mean S/N ratio for Nusselt number for the four studied parameters.....195
Fig. 5-29 Interaction plot (ANOVA) between the studied four factors and the mean S/N ratio for windage loss response 197
Fig. 5-30 Interaction plot (ANOVA) between the studied four factors and the mean S/N ratio for Nusselt number response 197
Fig. 5-31 The relationship between the windage losses and the radial airgap for the studied gases and pressures 199
Fig. 5-32 3D plot for windage losses between radial radius ratio and pressure level for gas mediums: (a) Air, (b) Carbon Dioxide, (c) Helium, and (d) Nitrogen 199
Fig. 5-33 The relationship between Nusselt number and the radial airgap for the studied gases and pressures 201
Fig. 5-34 3D plot for Nusselt number between radial radius ratio and pressure level for gas mediums: (a) Air, (b) Carbon Dioxide, (c) Helium, and (d) Nitrogen 201
Fig. 5-35 The windage losses with respect to rotational velocity for optimised cases 204

Fig. 6-1 Simplified geometry of FESS with periodic regions and symmetry plane 207
Fig. 6-2 Different slit cross sections, (a) triangle, (b) trapezoid, (c) rectangle, and (d) half ellipse 208
Fig. 6-3 Variation of Nusselt Number and skin friction coefficient with the number of mesh elements for, (a) no slit walls, (b) 24 triangle slits, (c) 24 trapezoid slits, (d) 24 rectangle slits and (e) 24 half-ellipse slits 209
Fig. 6-4 The quadrilateral mesh used to model the FESS.....210
Fig. 6-5 Relationship between windage loss and rotational speed for the triangle slit wall geometry 211
Fig. 6-6 Relationship between windage loss and rotational speed for the trapezoid slit wall geometry.....212
Fig. 6-7 Relationship between windage loss and rotational speed for the rectangle slit wall geometry.....213
Fig. 6-8 Relationship between windage loss and rotational speed for the half-ellipse slit wall geometry..213
Fig. 6-9 Relationship between Nusselt number and rotational speed for the triangle slit wall geometry...215
Fig. 6-10 Relationship between Nusselt number and rotational speed for the trapezoid slit wall geometry 216
Fig. 6-11 Relationship between Nusselt number and rotational speed for the rectangle slit wall geometry 217
Fig. 6-12 Relationship between Nusselt number and rotational speed for the half-ellipse slit wall geometry 217
Fig. 6-13 Comparison of Taylor number and rotational velocity across all analysed slit wall geometries 218
Fig. 6-14 Velocity contour of the FESS with no slit walls at the rotational velocity of (a) 800 rad/s, (b) 1200 rad/s, (c) 1600 rad/s, (d) 2000 rad/s, and (e)2400 rad/s 220
Fig. 6-15 Velocity contour of studied slit wall geometries in Y-Z plane at the rotational velocity of 1600 rad/s (a) no slit wall, (b) triangle, (c) trapezoid, (d) rectangle, and (e) half-ellipse 220
Fig. 6-16 The streamlines distribution at the slit region in the X-Y plane at the rotational velocity of 1600 rad/s (a) triangle, (b) trapezoid, (c) rectangle, and (d) half-ellipse 221
Fig. 6-17 Velocity contour of studied slit wall geometries in X-Y plane at the rotational velocity of 1600 rad/s (a) triangle, (b) trapezoid, (c) rectangle, and (d) half-ellipse 221
Fig. 6-18 The geometries for the slit designs, (a) different slit cross sections, (b) different slit orientation and direction. 224
Fig. 6-19 Velocity contour of the FESS with no slits under 1 bar pressure at the rotational velocity of (a) 800 rad/s, (b) 1200 rad/s, (c) 1600 rad/s, (d) 2000 rad/s, and (e)2400 rad/s.....228
Fig. 6-20 Velocity contour of the FESS in Y-Z plane for rectangle shape under 1 bar pressure and rotational velocity of 1600 rad/s as a function of factors D and E where: (a) radial/grooved, (b) radial/inserted, (c) axial/grooved, and (d) axial/inserted 229
Fig. 6-21 The streamlines distribution of the FESS in X-Y plane for rectangle shape under 1 bar pressure and rotational velocity of 1600 rad/s as a function of factors D and E where: (a) radial/grooved, (b) radial/inserted, (c) axial/grooved, and (d) axial/inserted 230
Fig. 6-22 3D plot of windage losses for a rectangle shape as a function of factors D and E where: (a) radial/grooved, (b) radial/inserted, (c) axial/grooved, and (d) axial/inserted.....231
Fig. 6-23 3D plot of windage losses for a trapezoid shape as a function of factors D and E where: (a) radial/grooved, (b) radial/inserted, (c) axial/grooved, and (d) axial/inserted.....232
Fig. 6-24 3D plot of windage losses for a reversed trapezoid shape as a function of factors D and E where: (a) radial/grooved, (b) radial/inserted, (c) axial/grooved, and (d) axial/inserted 233
Fig. 6-25 3D plot of windage losses for a half-ellipse shape as a function of factors D and E where: (a) radial/grooved, (b) radial/inserted, (c) axial/grooved, and (d) axial/inserted.....234
Fig. 6-26 3D plot of Nusselt number for a rectangle shape as a function of factors D and E where: (a) radial/grooved, (b) radial/inserted, (c) axial/grooved, and (d) axial/inserted.....236
Fig. 6-27 3D plot of Nusselt number for a trapezoid shape as a function of factors D and E where: (a) radial/grooved, (b) radial/inserted, (c) axial/grooved, and (d) axial/inserted.....237
Fig. 6-28 3D plot of Nusselt number for a reversed-trapezoid shape as a function of factors D and E where: (a) radial/grooved, (b) radial/inserted, (c) axial/grooved, and (d) axial/inserted 238
Fig. 6-29 The streamlines distribution of the FESS in X-Y plane for reversed trapezoid axial/inserted configuration under 1 bar pressure and rotational velocity of 1600 rad/s as a function of B/C ratio where: (a) 0.5, (b) 1, and (c) 1.5 239
Fig. 6-30 Velocity contour of the FESS in Y-Z plane for reversed trapezoid shape under 1 bar pressure and rotational velocity of 1600 rad/s as a function of B/C ratio where: (a) 0.5, (b) 1, and (c) 1.5.....239
Fig. 6-31 3D plot of Nusselt number for a half-ellipse shape as a function of factors D and E where: (a) radial/grooved, (b) radial/inserted, (c) axial/grooved, and (d) axial/inserted.....240

Fig. 6-32 The streamlines distribution of the FESS in the X-Y plane for the axial/grooved configuration under 1 bar pressure and rotational velocity of 1600 rad/s for: (a) rectangle, (b) trapezoid, (c) reversed trapezoid, and (d) half-ellipse 241
Fig. 6-33 Velocity contour of the FESS in X-Y plane for the axial/grooved configuration under 1 bar pressure and rotational velocity of 1600 rad/s for: (a) rectangle, (b) trapezoid, (c) reversed trapezoid, and (d) half-ellipse....241
Fig. 6-34 Velocity contour of the FESS in Y-Z plane for half-ellipse shape under 1 bar pressure and rotational velocity of 1600 rad/s as a function of factors D and E where: (a) radial/grooved, (b) radial/inserted, (c) axial/grooved, and (d) axial/inserted 242
Fig. 6-35 Velocity contour of the FESS in Y-Z plane for the radial/grooved configuration under 1 bar pressure and rotational velocity of 1600 rad/s for: (a) rectangle, (b) trapezoid, (c) reversed trapezoid, and (d) half-ellipse....243
Fig. 6-36 Velocity contour of the slit in Y-Z plane for the radial/grooved configuration under 1 bar pressure and rotational velocity of 1600 rad/s for: (a) rectangle, (b) trapezoid, (c) reversed trapezoid, and (d) half-ellipse....243
Fig. 7-1 The FESS's state of charge over time for the base model and the four optimised models....249
Fig. 7-2 Schematic diagram of the HEV main blocks 251
Fig. 7-3 Detailed MATLAB/Simulink open-source hybrid vehicle series-parallel model [416]....252
Fig. 7-4 The driving cycles of the WLTP test classes [422]....254
Fig. 7-5 Schematic diagram of the integrated hybrid vehicle main blocks....255
Fig. 7-6 (a) Parallel Regenerative braking strategy, (b) Series Regenerative braking strategy [425]....257
Fig. 7-7 Detailed MATLAB/Simulink open-source hybrid vehicle series-parallel model with FESS 260
Fig. 7-8 Percentage reduction in fuel consumption for an HEV equipped with various FESS models across three WLTP driving cycle classes....263

List of Tables

Table 2-1 Technical specifications of different energy storage technologies....19
Table 2-2 Techno-economical characteristics of different energy storage technologies 20
Table 2-3 Battery technologies [47] [48]....21
Table 2-4 Comparison between the hybrid electric and Flybrid systems [63]....25
Table 2-5 Comparison between Li-ion battery and flywheel systems for vehicular applications [64]....25
Table 2-6 Different commercial flywheel systems [85] 29
Table 2-7 Comparison of different FESS control systems....43
Table 2-8 Comparison of electric machines used with a FESS [168] [169]....48
Table 2-9 Flywheel failure modes, reasons, and their consequences [174], [175] 52
Table 2-10 The flywheel orientation and their reaction torque sense [177] 54
Table 3-1 The advantages of using CFD for FESS optimisation....66
Table 3-2 Comparison of suitable bearings for FESSs....95
Table 3-3 Shape factor for several flywheel designs [101]....113
Table 3-4 The characteristics of various flywheel rotor materials [109] [110] [94]....115
Table 3-5 Flywheel rotor material ranking 121
Table 3-6 Optimal rotor design values and parameters 121
Table 4-1 Studied FESS geometries 124
Table 4-2 Mesh independence test parameters 126
Table 5-1 Examined FESS factors and levels....154
Table 5-2 ANOVA for response surface quadratic model for Nusselt number....156
Table 5-3 ANOVA for response surface quadratic model for windage losses 156
Table 5-4 The fit statistics pertaining to the responses obtained 158
Table 5-5 The desirability levels for the suggested solutions....176
Table 5-6 The factors studied with different levels 178
Table 5-7 The simulation cases for the ANOVA analysis....179
Table 5-8 ANOVA for response surface quadratic model for windage losses 180
Table 5-9 ANOVA for response surface quadratic model for Nusselt number....180
Table 5-10 ANOVA for response surface quadratic model for standby power....181

Table 5-11 The fit statistics for the obtained responses....182
Table 5-12 The factors studied with different levels....190
Table 5-13 L_{16} Orthogonal array (OA)....191
Table 5-14 L_{16} Orthogonal array (OA) with the S/N ratios....193
Table 5-15 The optimised designs for windage losses as a response....204
Table 6-1 Slit walls geometrical parameters....208
Table 6-2 Slit walls geometrical parameters....224
Table 6-3 The continuous factors and their levels....224
Table 6-4 The categorical factors and their levels....225
Table 6-5 Analysis of variance for windage losses....226
Table 6-6 Analysis of variance for Nusselt number....227
Table 6-7 The fit statistics for the studied responses....228
Table 7-1 The comparison of the baseline and final optimised models....248
Table 7-2 Model parameters of 2024 Vauxhall Corsa [6][411], [415]....251
Table 7-3 WLTP vehicle categories [422]....254
Table 7-4 WLTP driving cycles data [422]....254
Table 7-5 FESS physical system parameters....258
Table 7-6 the mathematical expression for windage losses for the five studied models....259
Table 7-7 Fuel consumption values for simulation and reference values based on the driving cycle....261
Table 7-8 Fuel consumption and CO_2 emission values for HEV without and with FESS for the five examined models based on the driving cycle....264

Chapter 1. Introduction

1.1. Motivation

The urgency to decrease emissions has never been more critical. The current path of greenhouse gas emissions is causing unprecedented shifts in the climate, which could have severe and irreversible consequences for ecosystems, economies, and communities [1]. The levels of carbon dioxide, a major greenhouse gas released by human activities, have reached unprecedented levels, leading to global warming and a wide range of climate disruptions [2]. Urgent and ongoing efforts to reduce emissions are crucial to address the severe consequences of climate change, safeguarding a stable and thriving planet for future generations. At this critical moment, the shift towards low-emission technologies and sustainable practices is crucial for both the environment and the well-being of humankind [3]. The road transport sector is a major contributor to global carbon dioxide emissions, accounting for approximately 25% of the total emissions [4]. Manufacturers and researchers are increasingly motivated to improve energy production efficiency due to stricter regulations on carbon emissions and a growing awareness of the limited availability of fossil fuel resources. The necessity to maximise energy efficiency is crucial for the shift towards a more sustainable and low-carbon future [5].

Transportation is a significant consumer of energy, with vehicles playing a significant role. Despite technological and efficiency improvements, there is currently no indication of a sudden change in this pattern. The demand for vehicles remains strong due to factors such as affordable prices, reduced maintenance expenses, and improved living conditions [6]. Vehicular emissions are divided into two distinct categories: toxic pollutants and carbon dioxide emissions. The main contaminants emitted by vehicles commonly include Hydrocarbons (HC), Nitrogen Oxides (NOx), Carbon Monoxide (CO), Particulate Matter (PM), and Sulphates. Each of these pollutants has significant environmental and health implications, contributing to air quality degradation, respiratory issues, and climate change. Hydrocarbons and nitrogen oxides are particularly involved in the formation of ground-level ozone, which leads to smog, while particulate matter can cause severe respiratory and cardiovascular diseases [7]. These have been greatly reduced by improving engine designs and incorporating exhaust after-treatment technologies such as catalytic converters. However, the overall quantity of pollutants being discharged into the atmosphere continues to increase. Carbon dioxide emissions are associated with fuel consumption due to the limitations of the combustion process, which means that there is a minimum level of emissions that can be attained using existing technologies [8].

In 2021, the total number of passenger kilometres travelled in the United Kingdom (UK) amounted to 645 billion, out of which cars, vans, and taxis contributed to 88% of the total passenger kilometres travelled in Great Britain. While buses and coaches made a modest contribution of only 3%, rail

accounted for a more substantial 7%, while other modes of transport constituted a mere 2% [9]. Fig. 1-1 displays the data concerning the distance covered by different modes of passenger transport in the UK, measured in billions of passenger kilometres, from 1952 to 2021. It is evident that the use of cars, vans, and taxis has dramatically increased over the last decades, indicating a significant shift in the preferred modes of transport. In the year 2020, there has been a significant decrease in travel, primarily due to the COVID-19 pandemic travel restrictions [9].

Although fuel consumption for road transport has remained steady in recent years, it remains the primary sector for fuel usage, especially for passenger vehicles. Fuel efficiency is significantly reduced with urban driving, where the driving cycle involves continuous acceleration and deceleration [10]. Continued research into vehicle propulsion systems is crucial in addressing the pressing issues of fuel consumption and emissions. This need is particularly urgent given the limited availability of fossil fuel reserves [5].

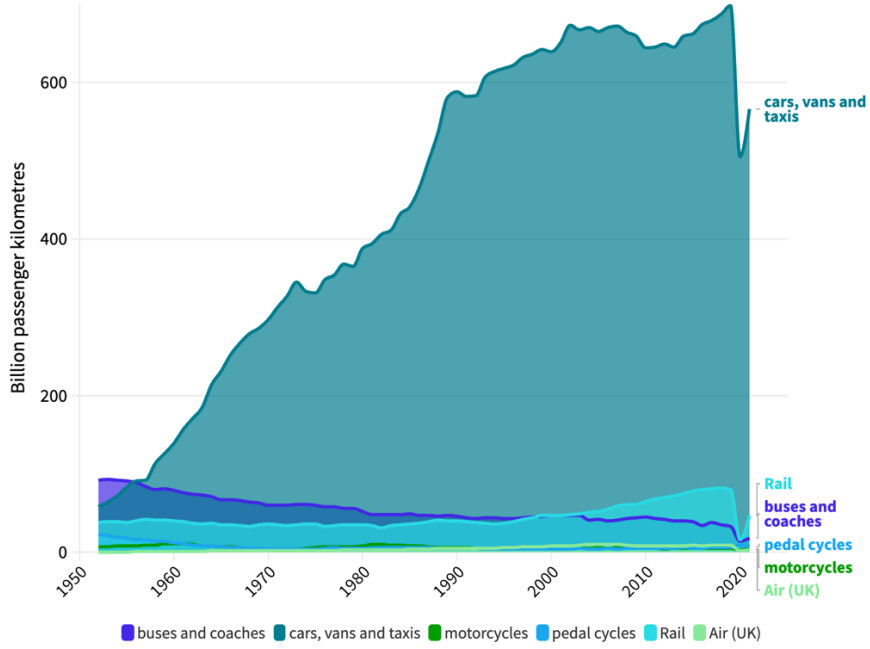

Fig. 1-1 Distance travelled by different passenger transport mode, in billion passenger kilometres [9]

1.2. Background

The domestic Greenhouse Gas (GHG) emissions from the transportation sector have remained relatively stable over the past three decades, while emissions from other sectors have decreased. The improvement in engine efficiency has been offset by the increase in the number of journeys made. Similarly, the rise in electric and hybrid vehicles has been counterbalanced by the increase in the number of diesel and petrol SUVs on the road. Cars and taxis account for 55.4% of the United Kingdom's emissions from domestic transport, amounting to 67.7 $MtCO_2$ [11]. The primary objective of the UK government is to achieve transport decarbonisation through zero tailpipe emissions [12].

However, it can be argued that this objective may provide a limited viewpoint on the wider environmental issues linked to transportation. Although zero tailpipe emissions do decrease local pollutant levels, it is important to recognise that this does not necessarily imply that electric vehicles are completely environmentally neutral. This is because the carbon footprint associated with generating the electricity required to power these vehicles must be considered. In areas where the energy grid is heavily dependent on fossil fuels, the transition to electric vehicles may not result in the desired overall decrease in GHG emissions [13].

Hence, the process of decarbonizing the transportation sector encompasses more than simply shifting to electric vehicles [14]. A comprehensive strategy is needed, encompassing the establishment of a low-carbon energy network, enhancements in the energy efficiency of all transportation methods, and funding for zero-carbon fuels that can be used to curtail the emissions from the existing fossil fuel powered vehicles and for applications where electrification remains unattractive such as mining and off-road machinery [15]. In the near to intermediate future, a practical approach would entail decreasing emissions from current vehicles, a significant portion of which will continue to be utilised for the next two to three decades. In essence, the primary objective is to reduce overall emissions rather than simply shifting the origin of these emissions. Instead of completely replacing the existing vehicle fleet with new electric vehicles, which could unintentionally increase total emissions due to energy intensive manufacturing processes and the potential GHG emissions associated with electricity production, it is recommended to adopt measures that reduce the emissions from the vehicles already in use. This approach not only conserves the stored energy and materials of the current vehicles, but also avoids the significant emissions linked to the manufacturing of new vehicles, which may only reduce tailpipe emissions. Policy and innovation should prioritise improving the environmental performance of the transport sector in a comprehensive and sustainable manner [16]. In alignment with the focus on achieving net zero goals, government agencies and manufacturers are employing roadmaps to pinpoint crucial domains for the advancement of new technologies. These roadmaps facilitate the identification of opportunities for innovation within the current transportation infrastructure. This strategy guarantees that actions to decrease emissions are prompt and incremental, utilising current resources while preparing for future advancements in technology [17].

The most recent propulsion technology forecast for the global automotive industry was outlined in a roadmap released by the Automotive Council UK in 2020 [18]. This document outlines the anticipated mass market trends in vehicle propulsion technologies. It categorically acknowledges that light-duty vehicles are the predominant source of emissions within the transport sector and divides these into three distinct classifications [18]:

1. Urban Mobility: Characterised by low power requirements, this category predominantly encompasses compact passenger cars designed for city use and short-distance travel.

2. Long Range Mobility: Encompassing medium-powered vehicles, this classification typically includes passenger cars and vans with a gross vehicle weight of less than 3.5 tonnes, suitable for extended travel distances.
3. High Power and Performance: This final category comprises vehicles requiring high power outputs, such as SUVs/pickups and high-performance vehicles, designed for advanced capabilities and high speeds.

Each segment presents a unique set of challenges and opportunities for emissions reduction and technological advancement as shown in Fig. 1-2. During the period from 2020 to 2035, the roadmap projects significant strides in the three vehicular categories, each moving towards net-zero emissions.

Urban mobility primarily targets the reduction of tailpipe emissions by prioritising Internal Combustion Engine (ICE) and hybrid vehicles that adhere to emissions standards and demonstrate high efficiency at low speeds. During the last decade, Battery Electric Vehicles (BEVs) have gained significant traction and popularity in the automotive sector. Efforts are being made to lower their costs, improve energy density, and incorporate flexible charging options, such as Vehicle-to-Grid (V2G) systems. Anticipated advancements in low-voltage systems for city-specific applications are expected to drive the shift towards urban vehicles that are customised for inner city driving [18]. On the other hand, long-range mobility concentrates on improving the efficiency of ICE and hybrid vehicles for sustained highway driving, alongside the development of BEVs optimised for longer ranges. Fuel Cell Electric Vehicles (FCEVs) are anticipated to become competitive with BEVs, particularly through improved range parity with ICE vehicles and the introduction of fast charging and 800V battery systems [18]. Finally, high power and performance vehicles saw a push towards augmenting ICE performance initially, with a gradual shift towards high-performance BEVs incorporating advanced battery chemistries, lightweight design, and ultra-fast charging capabilities. In parallel, FCEVs are expected to achieve mainstream performance levels suitable for SUVs, pickups, sports, and luxury segments [18].

Across all categories, a harmonised transition to propulsion technologies that are cost-competitive with ICE, particularly BEVs and FCEVs, is a clear trend. Policy, environmental, social, and economic factors play a critical role in shaping this transition, including tightening CO2 emission targets, zero emission vehicle (ZEV) mandates, and increasingly stringent environmental legislation focusing on holistic lifecycle assessments [18]. Engineering and technological enablers will also be instrumental in achieving these goals, with the roadmap highlighting cross-OEM scalable EV platforms, the integration of Connected and Autonomous Vehicles (CAVs), and digitally enhanced supply chains as key areas of focus. By 2035, the roadmap envisages a transformed light-duty vehicle sector that is significantly more efficient, integrated, and compliant with net-zero emission targets, reflecting the UK's commitment to combating climate change and reducing its transportation sector's carbon footprint [18].

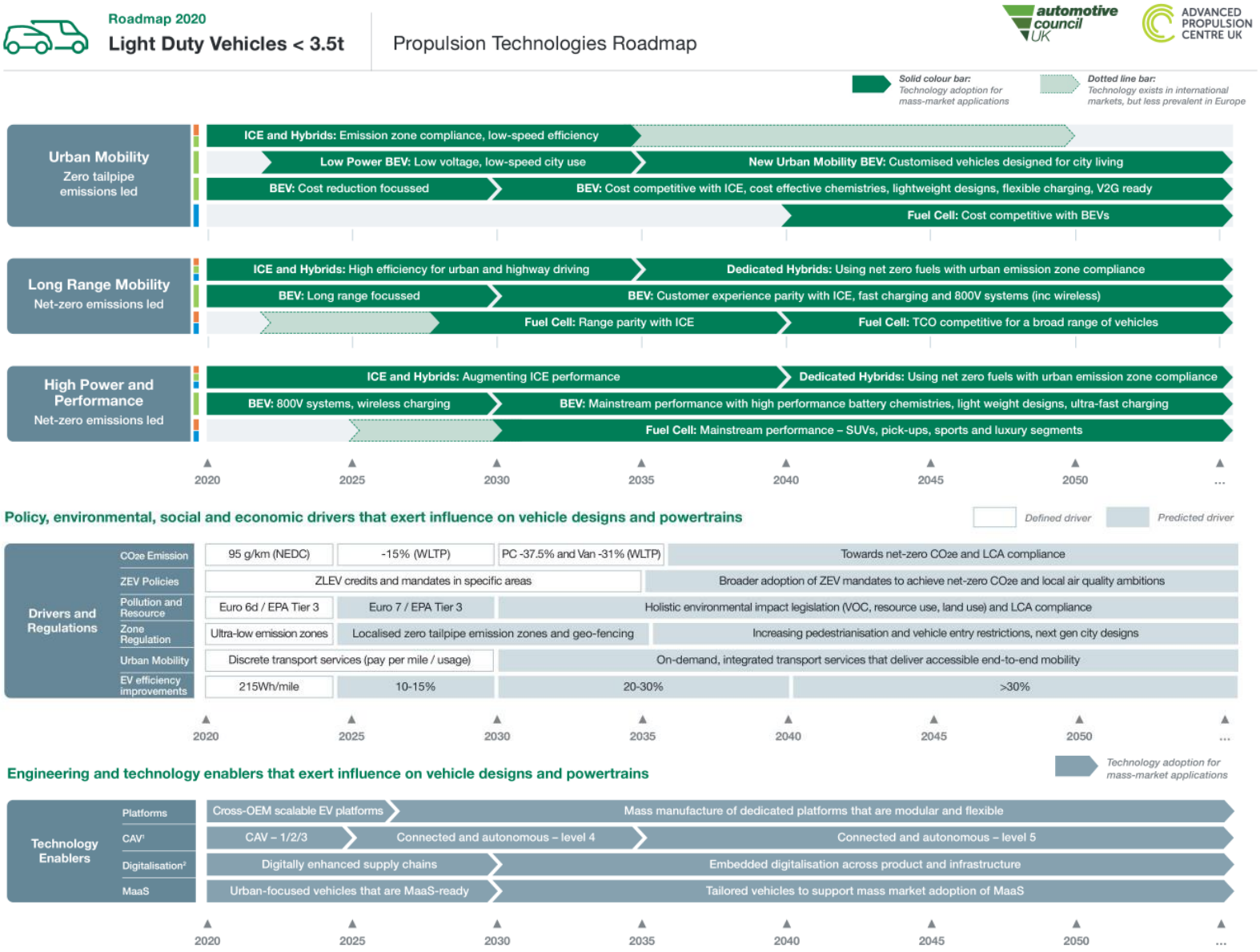

Fig. 1-2 UK's 2020 roadmap for propulsion technologies in light-duty vehicles [18]

1.3. Creating Low-Carbon Vehicles

A vehicle with reduced carbon emissions can be achieved by several approaches. The use of technological advancement in vehicle manufacturing can decrease the energy losses associated with vehicle movement on the highway and in urban driving [19]. Energy-efficient automotive technology concentrates on three key areas:

- Aerodynamic Drag Reduction: Optimising vehicle designs to reduce aerodynamic drag, thus improving fuel efficiency [20].
- Rolling Resistance Improvement: Researching tyre technologies utilising sophisticated materials to minimise energy dissipation during tyre rotation, thereby enhancing fuel efficiency [19].
- Weight Reduction: Utilising lightweight materials such as high-strength steel, aluminium, and carbon fibre to decrease the weight of the vehicle, thereby reducing the amount of energy required for acceleration thus enhancing the overall efficiency [21].

These strategies are crucial for advancing vehicle design to achieve lower fuel consumption and emissions. Improved design technology is expected to contribute to a decrease of approximately 10% in overall carbon emissions, aligning with long-term goals of reducing carbon footprint in the automotive industry [19]. Powertrain technology has the capability to accomplish the remaining 90% of the specified goal. Powertrain technology covers all characteristics of the vehicle's propulsion scheme. These technologies include the following [22]:

- Advanced clean diesel ICEs
- Battery electric powertrain systems
- Fuel cell systems
- Hybrid powertrain systems
- Hydrogen-powered ICEs
- ICEs using refined gasoline formulations

Selecting the appropriate powertrain technology necessitates careful consideration of several factors to meet carbon reduction targets effectively [22]. First, consumer accessibility is critical, and the overall cost depends on the usage of customers. A low-speed urban user has an entirely different profile than a high-speed driving profile, with significant energy consumption issues linked to overall vehicle life [23]. Secondly, a comprehensive end-of-life assessment is crucial, factoring in the public resources involved in the recycling, repurposing, and manufacturing processes associated with vehicle production. Considerations extend to subsequent stages of a vehicle's life, such as the necessity to replace an electric vehicle's battery approximately a decade after its initial deployment, thus addressing the cumulative costs and resource implications [24].

Maintenance strategies also play a crucial role, with an emphasis on systems that confer longevity and reduce wear, such as energy recovery systems in hybrid vehicles. While most advancements essential for achieving low carbon objectives are expected to arise from within powertrain technology, it is equally important to educate consumers to make informed decisions that align with their driving needs. Significant driver training and changes in infrastructure are also necessary to guarantee that these technologies will be fully beneficial [25]. On the other hand, congestion is an additional factor that impacts fuel efficiency. A vehicle that is stationary in a traffic jam with an ICE emits a significant amount of carbon dioxide per kilometre. The stationary vehicle can generate energy that can be stored and subsequently utilised while driving to enhance performance [26].

The waste energy generated by vehicles can be utilised to improve the efficiency of the system. Energy Recovery Systems (ERSs) are used to retrieve the energy that would otherwise have been lost. These systems collect and store the unused energy, allowing it to be used later, which decreases the need for external energy sources or fuel. The deliberate utilisation of ERSs across various powertrain technologies greatly enhances the overall efficiency of the vehicle. ERSs play a crucial role in improving the energy efficiency of vehicles and are also instrumental in tackling concerns surrounding GHG emissions and the adverse effects of global warming. These solutions are crucial and can be implemented in the near to medium future. They help reduce the negative effects of the automotive industry on the environment by lowering carbon emissions and supporting the goals of sustainable transportation [27]. Research and innovation related to energy recovery (ER) have been ongoing since the 1970s [27]. Nevertheless, the automotive industry historically prioritised conventional areas of improvement, such as engine efficiency and aerodynamics, to enhance the fuel efficiency of vehicles. However, automotive manufacturers have recently recognised that ERSs offer a cost-effective solution. As a result, they are now fully exploring the potential benefits of these systems [27].

ERSs are currently present in certain vehicle models, regardless of the powertrain type. ERSs have already been incorporated into ICE vehicles by BMW and Renault [28] [29]. However, Hybrid Electric Vehicles (HEVs) such as the Toyota Prius and BEVs such as the Nissan Leaf already incorporate kinetic energy recovery systems (KERSs) in their vehicles [30]. Amidst an automotive sector that prioritises efficiency improvements, the growing prevalence of new vehicles equipped with ERSs underscores the advantages derived from these systems in terms of fuel economy.

1.4. Objectives

This research work presents an investigation into the application of Flywheel Energy Storage Systems (FESS) as an energy recovery system, focusing on its potential for emissions reduction and fuel efficiency enhancement in light-duty vehicles. FESS offers a robust, efficient, and eco-friendly energy recovery and storage solution. It facilitates the development of energy-efficient vehicles by avoiding the need for conventional battery energy storage systems, which may contain hazardous materials that pose recycling challenges and adverse environmental impact at the end of their lifetime. The potential for FESS technology to improve the fuel economy of light-duty passenger vehicles by up to 18% is explored, with a particular emphasis on the resultant reduction in CO_2 emissions. Such advancements could significantly contribute to achieving the UK government's CO_2 reduction targets. The core aim of this research is to formulate an optimised aerodynamic design for a FESS, with the view to maximise energy recovery while minimising losses. Employing commercial Computational Fluid Dynamics (CFD) software, Ansys Fluent, the study assess the aerodynamic performance of FESS under various operating conditions. The investigation seeks to establish a direct correlation between the FESS's aerodynamic losses and its operating conditions, as well as its geometric configuration. Through this exploration, the research intends to contribute to the development of a low-carbon powertrain architecture that incorporates FESS, positioning it as a sustainable alternative energy recovery and storage system within the automotive sector.

1.5. Research Questions

The primary objective of enhancing the FESS is to transform it from a short-time storage solution to a short to medium-term storage solution, thereby extending its utility and efficiency to improve energy efficiency and lessen emissions in vehicles, playing a substantial role in promoting the progress of transport decarbonisation. To accomplish this, the following research questions arise:

- How does the urgent need for emissions reduction highlight the need for innovative energy recovery solutions in transport decarbonisation?
- How do energy recovery systems, especially FESS, enhance transportation energy efficiency and emissions reduction, and what advancements indicate their potential?
- How do CFD and Design of Experiments enhance FESS optimisation precision and reliability for low-carbon solutions?
- How do FESS design parameters impact its windage losses and heat transfer, and what are the optimal conditions for energy efficiency and thermal management?

- How do geometric and operating condition modifications in FESS affect its aerodynamic performance, and what configurations yield maximum energy storage efficiency with minimal losses?
- How do slit wall introductions in FESS casing, regarding shape, orientation, and configuration, affect aerodynamic efficiency and what are the optimal characteristics for system efficiency?
- How does integrating optimised FESS into light-duty vehicles affect fuel efficiency and emissions reduction?

Each chapter in this thesis is intended to address specific research question, revealing the complexities of optimising FESS for transport decarbonisation. As one progresses through each chapter, the answers to the research questions become clearer, providing valuable insights into the role of FESS in reducing the environmental impact of the transport sector.

1.6. Contributions to Knowledge

The primary contributions of this research, with regard to the research questions, can be summarised as follows:

- This study underscores the critical need for innovative energy recovery solutions in the context of global emissions reduction efforts, specifically focusing on the transportation sector's significant role in carbon dioxide emissions. By exploring the efficiency of FESS in this domain, the research contributes to understanding how such technologies can be pivotal in transport decarbonisation.
- Through a detailed examination of existing energy recovery systems, this work highlights the unique contributions of FESS to enhancing energy efficiency and reducing emissions within the transportation sector. The identification of technological advancements and applications of FESS marks a significant contribution to the discourse on low-carbon mobility solutions.
- The integration of CFD and Design of Experiments for FESS optimisation represents a novel approach to improving the precision and reliability of simulations. This methodology enhances the understanding of how to optimise aerodynamic performance to reduce standby losses, which refer to energy dissipated when the system is idle but still operational, thereby contributing to the development of more effective low-carbon solutions.
- This research provides insights into how specific design parameters, such as airgap size and rotational velocity, influence aerodynamic efficiency, windage losses, and heat transfer in FESS. The determination of optimal conditions for energy efficiency and thermal management effectiveness offers valuable guidance for future FESS design and application.

- By examining modifications in the geometric design parameters and operating conditions of FESS, this work contributes knowledge on how such changes impact aerodynamic efficiency. The identification of optimal configurations for maximising energy storage efficiency while minimising energy losses offers a roadmap for enhancing FESS technology.
- The exploration of the effects of introducing slit walls into FESS casing, in terms of shape, orientation, and configuration, adds to the understanding of aerodynamic efficiency improvements. This research identifies the optimal slit wall characteristics that maximise system efficiency and operational effectiveness, providing a novel contribution to FESS design.
- Finally, the study of optimised FESS integration into vehicles and its impact on vehicle performance across WLTP classes offers significant contributions. This research reveals how FESS advancements in windage loss reduction and operational parameters can lead to substantial improvements in fuel efficiency and emissions reduction, advancing the goal of transport decarbonisation.

1.7. Scope And Limitations

The investigation into FESS for use in light-duty vehicles as an energy recovery system is delineated with specific scope and limitations as follows:

Within the scope of the study, the theoretical framework establishes a foundation by reviewing the array of available energy storage technologies and identifying the most viable options for light-duty vehicles. This review covers the operational principles, energy recovery processes, and storage mechanisms, providing context for flywheel technology within the broader landscape of energy storage solutions. To create a track for this research, a thorough analysis of the literature on FESS is conducted to determine their main characteristics and applications, identifying gaps in the current knowledge.

The mathematical and modelling techniques employed involve a detailed analysis of FESS, including the development of a high-speed flywheel model suitable for this research. This model encompasses considerations of integration selection, control techniques, bearing loss analysis, and rotor and containment design. To ensure the model's prediction accuracy which is validated by experimental data.

In terms of design and engineering, the presented research work articulates the criteria for the FESS design, with a focus on material selection, structural integrity, and energy density. CFD modelling plays a pivotal role in this process, with the selection and optimisation of appropriate CFD models for system simulation, supported by mesh independence testing and CFD model validation.

Aerodynamic performance is examined through CFD simulations under various operating conditions and geometrical configurations, aiming to optimise the system for minimal self-discharge. Additionally,

strategic analysis of flywheel operation seeks to determine the optimal configuration for improved efficiency and reliability. The research extends to the simulation of the FESS in MATLAB/Simulink, utilising the WLTP driving cycle to assess the potential for fuel savings and emission reductions when integrated into light-duty vehicles.

Addressing the limitations of the study, it is acknowledged that the reference vehicle type is limited to light-duty vehicles, which, despite being a significant source of emissions, presents a scope that does not encompass heavier vehicles or stationary applications. The FESS experimental testing was conducted in a laboratory environment, and while attempts were made to mirror real-life conditions, they may not capture the full complexity of on-road usage.

Material analysis of the flywheel is theoretical due to the practical limitations of conducting experimental tests, given the restricted access to facilities and budget constraints. The system simulation deliberately simplifies the design by excluding the shaft to manage the complexity of the model, a decision justified by the acceptable error margins in the resulting data compared to experimental findings.

Finally, the study concentrates on FESS as an isolated solution, without exploring its integration with other hybrid technologies or energy recovery systems that could be employed in light-duty vehicles.

1.8. Thesis Structure

This thesis is comprised of eight chapters, along with references and appendices. The chapters are summarised as follows:

Chapter 1: Introduction – This chapter lays the foundation, articulating the motivation behind the research, providing the necessary background information, and delineating the aims, objectives, and research questions. It also outlines the scope and limitations of the study and gives a structural overview of the thesis.

Chapter 2: Literature Review – This chapter delves into various energy harvesting techniques, storage devices, and specifically the FESS. This chapter discusses FESS applications, with a focus on vehicle use, evaluating components, performance, advantages, disadvantages, and the challenges faced. It concludes with a review of previous aerodynamic optimisation strategies in FESS and identifies gaps in the existing knowledge base.

Chapter 3: Methodology – This chapter describes the research design and the computational tools and equations used, particularly Computational Fluid Dynamics (CFD), for modelling FESS applications. It includes the validation of the CFD model with experimental data. Flywheel loss calculations are explored in detail, covering bearing and windage losses and thermal analysis. Design criteria for FESS, including material selection, storage capacity, and rotor design, are specified, and their implications on operating conditions and driving cycles are considered.

Chapter 4: FESS Performance Characteristics – This chapter analyses the impact of windage losses, heat generation, and the effects of housing and flywheel surface temperatures. The simulations demonstrate the development of turbulent Taylor vortices and investigate how atmospheric and partial vacuum conditions affect the performance of FESS. It also analyses the energy conversion efficiencies at various operating pressures.

Chapter 5: Optimisation of FESS Geometric and Operating Conditions – This chapter applies statistical methods such as ANOVA to study design parameters, explore the effects of airgaps, surface roughness, and internal pressure levels, and seeks to optimise FESS design for reduced losses and enhanced performance. This chapter also discusses strategies to mitigate standby losses.

Chapter 6: The Effect of Casing Design in FESS Performance – This chapter considers the introduction of slit walls in the FESS casing and the computational analysis of their effects on flow field distributions, windage losses, and heat transfer. It applies Response Surface Methodology (RSM) for FESS performance optimisation and assesses the impact of slit wall geometry on system efficacy.

Chapter 7: Contribution of FESS to Transport Decarbonisation – This chapter investigates the integration of FESS in vehicles using the MATLAB/Simulink simulation tool. It investigates the impact of incorporating the FESS's optimised cases and compares various scenarios for emissions reduction, fuel savings, and performance improvements.

Chapter 8: Conclusion and Recommendation for Future Work – This chapter offers an executive summary and draws conclusions from the research conducted. It also proposes recommendations for future work, suggesting avenues for continued exploration and development in this field.

Chapter 2. Literature Review

2.1. Energy Recovery Systems

An Energy Recovery System (ERS) is designed to make the most of an abandoned energy source and achieve a high ratio of energy recovery. The system should facilitate the ongoing extraction of energy and provide a significant improvement in efficiency under all driving conditions. An ideal ERS is anticipated to efficiently capture and store all retrievable energy with minimal losses during charge and discharge cycles [27]. Furthermore, an efficient ERS should integrate seamlessly into a vehicle's architecture without imposing significant additional weight or space demands. It should utilise existing vehicle components to the greatest extent feasible, ensuring that any necessary new parts are cost-effective, sustainable in terms of their life cycle (recyclable and non-toxic), and involve low embodied energy in their production. The system should be easy to retrofit, avoiding the need for extensive alterations to the existing vehicle framework [27]. ERSs are initially categorised based on the energy source that can be recovered, exhaust gas energy, energy from the vertical oscillations of the vehicle body, and kinetic energy from the vehicle inertia. After the initial classification, systems are further categorised based on the type of energy they recover, the storage mechanisms they use, and the specific technologies they employ. Fig. 2-1 displays the categorisation of the ERS for automotive applications.

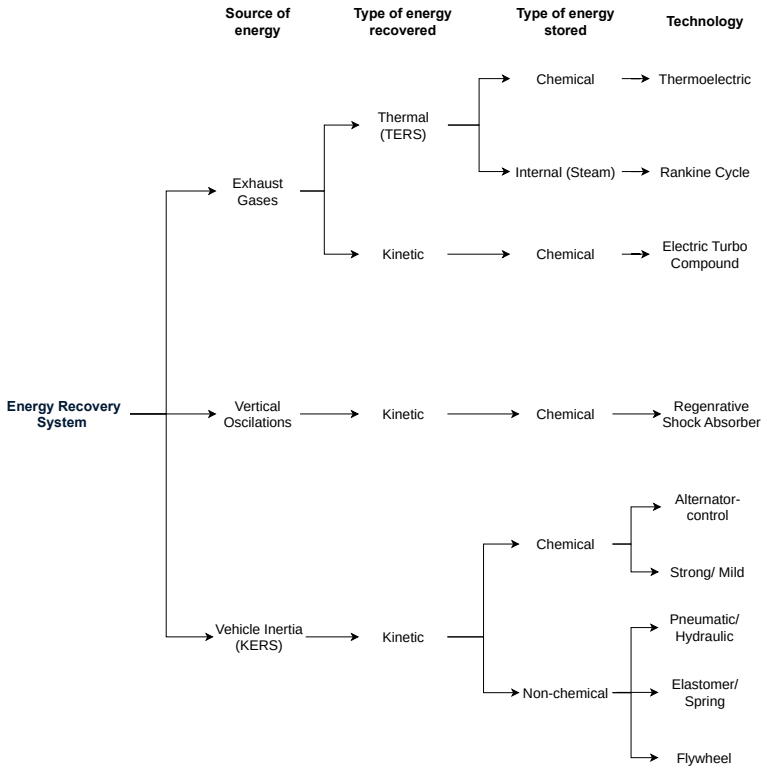

Fig. 2-1 The categorisation of energy recovery systems for automotive applications [27]

2.1.1. Energy Recovery from Exhaust Gases

During engine operation, ICEs emit exhaust gases at high temperatures and velocities, which provide a consistent energy source that can be utilised by ERSs. These systems are specifically designed to recover energy that would otherwise be wasted, with a specific emphasis on recovering thermal energy or kinetic energy. Approximately two-thirds of the energy derived from fuel in ICEs is released as heat. Thermal Energy Recovery Systems (TERSs) are designed to harvest the thermal energy and store it for later use [31]. There are two principal technologies employed in TERSs:

Thermoelectric Generators: These systems utilise a thermoelectric generator module to convert the waste heat from the exhaust gases into electricity, effectively transforming thermal gradients directly into electrical energy [32].

Rankine Cycle Systems: These systems adopt the Rankine cycle to transform the thermal energy from the exhaust into mechanical energy by heating a working fluid until it vaporises. The generated steam is then employed to drive a turbine. The mechanical energy produced can either be utilised to generate electricity or as direct power within the powertrain [33].

In addition to thermal energy recovery, the Kinetic Energy (KE) inherent in the exhaust gases can also be recuperated. Turbo generator systems, commonly known as electric turbo compound, can capture this kinetic energy. These systems utilise a turbine generator to convert the energy from high-velocity gases into electrical power [34].

Thermoelectric systems offer continuous energy recovery, contributing to faster engine warm-up and allowing for a smaller exhaust system, albeit with a slight reduction in engine performance and without hybrid capabilities [32]. The Rankine cycle systems also provide constant energy recuperation and have the added benefit of hybrid capability, but they are complex and challenging to retrofit, with the limitation that energy cannot be stored indefinitely [33]. Electric turbo compounding is noted for its continuous recuperation and is relatively easy to install, offering moderate efficiency gains with minimal additional weight and space requirements; however, it lacks hybrid integration and requires additional cooling [34]. Considering the limited amount of energy that can be harnessed, energy recovery from exhaust gases may not be a viable solution for light-duty vehicles. This is especially true when considering the potential difficulties in retrofitting and the complexities involved. Moreover, upsizing the engine to enhance recovery would counteract the emissions reduction targets, presenting a contradiction to sustainability objectives.

2.1.2. Energy Recovery from Vertical Oscillations

Kinetic energy that arises from the vertical oscillations of a vehicle body during travel, such as that experienced over bumps, can be effectively harvested using regenerative shock absorbers (RSAs). These

devices are capable of converting KE into electrical energy, which can then either be directly utilised by the vehicle or stored within the battery. The observed enhancement in vehicle efficiency attributable to RSAs varies, with recorded improvements typically within the range of 2–10% [35]. The efficiency gains from this ERS solution are influenced by factors such as the type of vehicle and the nature of the road conditions; notably, heavier vehicles and more uneven surfaces may yield more substantial benefits. The RSA approach is well-suited for retrofitting across various vehicle types and offers noteworthy fuel saving potential [36]. Nonetheless, certain economic considerations may affect its appeal; for instance, the requirement to install multiple units (typically one per wheel) and the frequent replacement intervals could entail additional costs. Moreover, given the nature of the energy source, RSAs may be more advantageous for off-road and heavy-duty applications compared to light-duty vehicles [35].

2.1.3. Energy Recovery from Vehicle Inertia

The primary source of energy recovery in these systems is the vehicle's inertia resulting from its speed. When deceleration is required, a force must be applied to counteract the vehicle's inertia. This is typically achieved by the braking system, which reduces the speed by converting the kinetic energy into heat due to friction [27]. However, it is feasible to recover a fraction of this kinetic energy and store it, particularly during the process of acceleration, thus decreasing the engine's load and subsequently reducing fuel consumption. Systems that recover energy based on vehicle inertia are known as Kinetic Energy Recovery Systems (KERS) [37]. As these systems recover the energy mainly during braking events, the process of energy recovery is known as Regenerative Braking (RB) [38]. KERS technology varies in terms of energy capture and storage capabilities. Nonetheless, all KERSs share a common benefit stemming from the considerable mass and velocity of light-duty vehicles which present a high potential for energy recovery due to their high momentum [37]. The usage of KERS has seen a significant rise in the past decade, driven by the growing interest in enhancing the efficiency of ICE vehicles and the advancements in hybrid and electric vehicle technologies. RB is a well-established technology in the transport sector, particularly in electric locomotives. RB can be a crucial component of electric vehicles as it addresses the requirements of reducing battery size, range extension, and improving performance [39]. The primary limitation of KERS, however, lies in the intermittent nature of energy recovery, which is constrained to the duration of braking events.

2.2. Storage Devices

Although RB maximises energy recovery in a vehicle, it requires a storage medium to store the captured energy. Some of the most cutting-edge technologies in the field include batteries, pneumatic/hydraulic storage, and flywheels. In addition, ongoing development in the field of supercapacitors has shown its potential as a future energy storage solution. Power density plays a crucial role in the effectiveness of KERS. Energy density is also considered when the same energy storage system serves as the main energy source for propulsion [40]. In most applications, the size of storage devices is crucial. Fig. 2-2 (a) presents a comparison of the power density and energy density of different energy storage technologies. As power and energy densities increase, the volume needed for energy storage decreases. The compact technologies ideal for applications with limited volume can be found in the top right corner of Fig. 2-2 (a), whereas the storage systems that require a larger volume are located in the bottom left corner [41].

Specific power and specific energy are valuable metrics that quantify the amount of power and energy in relation to weight. Fig. 2-2 (b) provides a comparison of the specific power and specific energy of various energy storage technologies [41].

The weight of the energy storage system depends on the specific power and specific energy required to obtain a certain amount of energy. As evident in Fig. 2-2 (a) the energy and power densities of most batteries, flywheels, and fuel cells are relatively low [40]. Supercapacitors and capacitors boast impressive power densities, yet their energy densities leave much to be desired. Due to their rapid response time, capacitors and supercapacitors exhibit high specific power but relatively low specific energy [42]. It is worth noting that fuel cells possess a remarkable specific energy to power ratio, although their specific power to energy ratio is relatively low. Located at the middle levels of specific power and specific energy, flywheels have a wide range of applications. Finally, Li-ion batteries are known for their impressive high specific energy and specific power [43].

It is acknowledged that no individual energy storage technology can meet the needs of all energy storage system applications. An extensive analysis of different energy storage technologies relevant to the automotive sector has been conducted in this research work. Response times ranging from milliseconds to seconds and discharge durations spanning from seconds to hours are crucial for transportation applications. These requirements can be met by utilising a variety of energy storage technologies, including fuel cells, capacitors, supercapacitors, flywheels, and Li-ion batteries. Tables 2-1 and 2-2 present the characteristics of various energy storage technologies that can be utilised in vehicular applications. Although each technology possesses distinct characteristics, flywheel technology has been identified as a promising technology due to its outstanding power and specific power capabilities, rapid response time, and exceptional cycle life. The aforementioned attributes make flywheels highly suitable for automotive

applications that require quick energy release and frequent cycling, providing a dependable and long-lasting energy storage solution. Although other technologies may have their own advantages, flywheels provide a compelling equilibrium of performance, efficiency, and longevity.

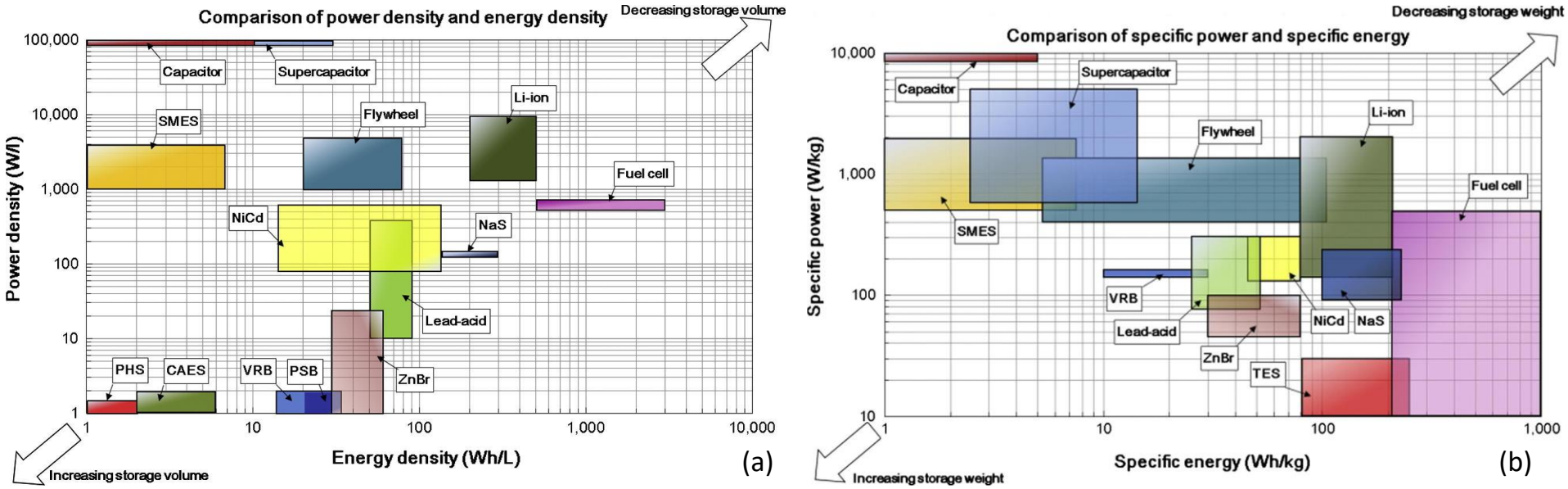

Fig. 2-2 Comparison of different energy storage systems based on: (a) power and energy densities (b) specific power and specific energy [41]

Table 2-1 Technical specifications of different energy storage technologies

Technology	Mechanism	Power density (W/L)	Energy density (Wh/L)	Specific power (W/kg)	Specific energy (Wh/kg)	Rated energy Capacity (MW h)	Power rating (MW)	Cycling time (cycles)	Discharge efficiency (%)	Response time	Cycle efficiency (%)	Daily self-discharge (%)	Lifetime (yr)
Flywheel	Mechanical	1000-2000 [44] 5000 [45]	20-80 [44]	400-1500 [44]	10-30 [44] 5-100 [46] 5-80 [47]	0.0052 [41] 0.75 [48] up to 5 [41]	<0.25 [44] 3.6 [41] 0.1-20 [41]	+20,000 [44] +21,000 [49]	90-93 [50]	<1 cycle [50] Seconds [41]	90-95 [44] 90 & 95 [48]	100 [44] >20% per hour [46]	15 [44] +15 [49] 20 [50]
Li-ion	Chemical	1500-10,000 [45]	200-500 [44] 200-400 [45] 150 [48]	150-315 [44] 300 [48] 500-2000 [46]	75-200 [44] 90 [48] 120-200 [51]	0.024 [52] 0.004-10 [41]	0-0.1 [44] 1-100 [41] 0.005-50 [41]	1000-10,000 [44] Up to 20,000 [53]	85 [50]	Milliseconds, <1/4 cycle [54]	90-97 [44] 75-90 [41]	0.1-0.3 [44] 1 & 5 [55]	5-15 [44] 14-16 [56]
Capacitor	Electrical	+100,000 [44]	2-10 [44] 0.05 [57]	100,000 [44] >3000-10^7 [57]	0.05-5 [44] <0.05 [57]	-	0-0.05 [44]	+50,000 [44]	75-90 [41]	Milliseconds, <1/4 cycle [54]	60-70 [44] +70 [58]	40 [44] 50 in 15 min [59]	5 [44] 1-10 [54]
Ultracapacitor	Electrical	+100,000 [44]	10-30 [44]	500-5000 [44] 10,000 [57]	2.5-15 [44] 0.05-15 [57]	0.0005 [48]	0-0.3 [44] +0.3 0.001-0.1 [48]	+100,000 [44] +50,000 [49]	95 [50] Up to 98 [41]	Milliseconds, <1/4 cycle [50]	90-97 [44] 84-95 [60]	20-40 [44] 5 [61] 10-20 [62]	10-30 [44] 10-12 [60]
Hydrogen Fuel cell	Chemical	+500 [44]	500-3000 [44]	+500 [44] 5-800 [57]	800-10,000 [44] 150-1500 [57]	0.312 [41]	<50 [44] <10 [45] 58.8 [41]	+1000 [44] +20,000 [63]	59 [44]	Seconds, <1/4 cycle [50]	20-50 [44] 32 [64] 45-66 [65]	Almost zero [44]	5-15 [44] 20 [66] +20 [63]

Table 2-2 Techno-economical characteristics of different energy storage technologies

Technology	Discharge time at power rating	Suitable storage duration	Energy capital cost ($/kWh)	Power capital cost ($/kW)	Operating and maintenance cost
Flywheel	Up to 8 s [44] 15s – 15 min [41]	Seconds to minutes [44] Short term (<1h) [67]	1000-5000 [44] 1000-14,000 [68]	250-350 [44]	0.004 $/kWh [48]
Li-ion	Minutes-hours [44] 1-8 h [69]	Minutes-days Short to med term [44]	600-2500 [44] 2770-3800 [41]	1200-4000 [44] 900-1300 [46] 1590 [41]	-
Capacitor	Milliseconds -1 h [44]	Seconds-hours [44] 5 h [58]	500-1000 [44]	200-400 [44]	13 $/kW/year [41] <0.05 $/kWh [58]
Ultracapacitor	Milliseconds -1 h [44] 1 min [69] 10 s [70]	Seconds-hours [44] <1 h [67]	300-2000 [44]	100-300 [44] 250-450 [70]	0.005 $/kWh [48] 0.6 $/kW/yr [50]
Hydrogen Fuel cell	Seconds-24 h [44]	Hours-months [44]	15 [50]	500 [50] 1500-3000 [71]	0.0019-0.0153 $/kW [71]

2.2.1. Electric Storage

Electric KERS convert a portion of the vehicle's kinetic energy into electrical energy through a Motor-Generator (MG), which is subsequently stored in batteries. These systems can be categorised into two principal types: strong/mild electric KERS and alternator-control based KERS. The MG not only assists the engine by providing additional torque but can also independently power the vehicle at low speeds [72]. However, the process of energy conversion (mechanical ⇌ electric ⇌ chemical) from the wheels to the battery and back introduces inefficiencies, diminishing the overall effectiveness of the system. Furthermore, factors such as the cost of battery storage systems, the increased complexity of the system, along the additional weight and space requirements, pose challenges for retrofitting these systems into existing vehicles. A 'mild' variant of electric KERS utilises smaller batteries and a less powerful MG, somewhat reducing these constraints. Two distinct configurations for mild KERS exist, providing varying levels of energy recovery and assistance to the vehicle's powertrain [73].

The utilisation of batteries as an energy storage medium presents a practical choice due to their widespread availability and the capability to maintain charge over extended periods, allowing energy to be retained for weeks or even months when the vehicle is not in use [74]. In the context of HEVs, battery selection is

principally determined by factors such as reliability, cost, and recyclability. Secondary considerations include low self-discharge rates and fast charging. Nevertheless, batteries do have limitations, including a relatively short lifespan and a rapid decline in efficiency over time. Challenges that affect battery performance encompass limited cycling durability, suboptimal functionality in cold conditions, and lower energy density compared to other energy storage solutions [75]. An overview of the fundamental battery technologies, their chemical compositions, and energy characteristics, along with their prominent challenges, is detailed in Tables 2-3. Among the array of battery technologies, three types are mainly considered for vehicular use: Nickel Metal Hydride, Lead Acid, and Lithium-Ion. Nickel Cadmium batteries, despite their once widespread use, have largely been phased out of mainstream applications due to their high raw material costs, difficulties in recycling, and toxic nature, relegating them to more specialised applications [76].

Table 2-3 Battery technologies [76] [77]

Type	Electrolyte	Positive electrode	Negative electrode	Nominal voltage	Cycles	Life (years)	Specific energy (Wh/Kg)	Specific power (W/kg)	Problems
Sodium Sulphur	Beta Alumina	S	Na	2	2500-40000	-	150-240	230	Safety, High Temperature, Low power
Lithium-Ion	PC/DMC	$LixCoO_2$	Li	4	3000	+5	80-180	200-1000	Safety, Life cycle, High cost
Zinc Bromine	$ZnBr_2$	Br complex	Zn	1.6	2000	-	65-85	90-110	Low power, Toxic, Bulky
Zinc Air	KOH	O_2	Zn	1.1	300	-	200	100	Low power, Life cycle, Bulky
Nickel Zinc	KOH	NiOOH	Zn	1.6	<500	-	70-100	170-260	Life cycle
Nickel Metal Hydride	KOH	NiOOH	H	1.2	300-600	2-5	60-80	200-300	High cost
Nickel Cadmium	KOH	NiOOH	Cd	1.2	1000-50000	10-15	30-60	80-150	Toxic, Maintenance, High cost
Nickel Iron	KOH	NiOOH	Fe	1.2	2000	20	50-60	80-150	Heavy, Maintenance
Lead Acid	H_2SO_4	PbO_2	Pb	2	250-1000	5	35-50	150-400	Heavy, High cost, Toxic

2.2.2. Alternator-Control Storage

An alternator-control KERS optimises the vehicle's alternator operation more efficiently than traditional mechanisms. Conventionally, the alternator's output is increased during braking phases to harness the vehicle's kinetic energy, thereby enhancing energy storage within the battery and supplying power to the vehicle's electrical systems [27]. Conversely, when the vehicle accelerates, the alternator's output is scaled back, allowing the electrical systems to draw power from the previously stored energy in the battery. The energy recaptured via this method is relatively low in comparison to other forms of KERS, resulting in more incremental improvements in efficiency. Nevertheless, the alternator-control system is highly beneficial to retrofitting. It does not necessitate substantial new components for installation, thereby maintaining a low complexity and cost profile, and minimal space requirements [73].

2.2.3. Ultracapacitors Storage

Ultracapacitors, functioning similarly to conventional capacitors over short durations, have the capacity to rapidly deliver and store electrical energy. The storage occurs within a polarised liquid layer that forms between the electrolyte and the electrode. While ultracapacitors excel in providing high currents and can be recharged more swiftly than batteries, they do not have the capability to hold substantial energy reserves, rendering them less effective for long-term energy storage [55]. The discharge rate of ultracapacitors is significantly greater than that of lithium-ion batteries, with a notable self-discharge rate that can result in a 10–20% loss of charge daily. Despite these limitations, ultracapacitors are advantageous in applications requiring quick energy deployment and recovery. This makes them particularly suitable for public transportation systems such as hybrid buses and trams [78].

2.2.4. Pneumatic/Hydraulic Storage

In this system, the vehicle's KE is conserved by elevating the pressure of a fluid. Pneumatic systems achieve this by compressing air and storing it in storage tanks, while hydraulic systems utilise a non-compressible fluid contained within accumulators. The energy is then reintroduced into the powertrain by reducing the fluid's pressure. These systems hold substantial promise for fuel savings, and their cost may be more competitive than that of electric-based systems [79]. However, the implementation of such a KERS does necessitate consideration of the additional space requirements and the increased mass due to the inclusion of storage tanks and accumulators. Consequently, this type of KERS is generally more applicable to heavy-duty vehicles rather than light-duty vehicles. Moreover, the integration of these systems may call for

significant modifications to the existing powertrain, which could complicate the process of retrofitting into current vehicle architectures [27].

2.2.5. Elastomers And Spring Storage

Spring and elastomer-based KERSs function by capturing energy during RB and storing it as potential elastic energy. This storage is accomplished through the elastic deformation of an elastomer or a metallic spring, which can return to its original shape to release the stored energy when required. To manage the energy transfer effectively, the inclusion of a Continuously Variable Transmission (CVT) may be necessary [27]. The operation of such a mechanical KERS is inherently efficient since it does not incur losses typically associated with energy conversion processes. Additionally, they have the advantage of being able to store energy for extended periods. However, one of the limitations of these systems is their substantial spatial requirement. The inclusion of a CVT also introduces additional complexity and contributes to the overall weight of the system, potentially impacting vehicle performance. Moreover, there seems to be no body of research exploring this technology in recent years [73].

2.2.6. Flywheel Storage

In this system, the KE of a vehicle is stored as rotational energy by increasing the angular velocity of a flywheel. A flywheel is a mechanical energy storage device that uses bearings to facilitate the free rotation of a rotor around an axle, thereby conserving KE through its motion. Provided that there is a mechanism for both the conservation and subsequent release of energy, the system has the flexibility for a range of applications. Traditional flywheel-based mechanical storage systems have been used for millennia, ranging from millstones to potter's wheels, which use kinetic energy to smooth out the supply of pulsed power. Historically, flywheels were substantial in size, with systems typically powered by a water mill, and the concept was notably refined with the advent of the steam engine in the 18th century, a principle that has continued into modern ICEs [80].

FESS is broadly categorised based on the flywheel speed: low-speed systems utilise metallic rotors, while high-speed systems employ rotors manufactured from advanced composite materials, such as carbon fibre [55]. Although high-speed composite flywheels can offer superior performance, they are generally more costly than traditional metallic flywheel systems [46].

Their adoption in automotive applications is on the rise due to their higher power capacity and energy density compared to ultracapacitors [81]. Some FESS can deliver specific power outputs of 5–10 kW/kg, which is significantly higher than the typical electrochemical batteries. Advanced FESS can attain specific

energies exceeding 100 Wh/kg, with some reaching up to 200 Wh/kg [82]. In comparison, the specific energy of lithium-ion batteries is above 100 Wh/kg, while commercial ultracapacitors have specific energies of around 6 Wh/kg [83]. While ultracapacitors could potentially demonstrate significantly greater specific power compared to lithium-ion batteries, thermal management is a major challenge for both ultracapacitors and lithium-ion batteries. This issue is considerably less problematic for flywheels [40].

The implementation of FESS can potentially reduce fuel consumption by 20–30%. However, due to standby losses, the energy recuperated cannot be stored indefinitely [84]. To further improve the efficiency of the system, FESS may require additional components such as a transmission, a high-speed rotor, a vacuum chamber, and magnetic bearings. These high-technology components can significantly increase both the cost and complexity of the system. Nonetheless, flywheel technology is often considered to be more cost-effective compared to equivalent electric KERS solutions [37].

The durability of a flywheel is often characterised by its capacity to sustain extensive charge and discharge cycles, commonly exceeding one million cycles. The resilience of its composite resin construction contributes to its wear resistance. Material fatigue, which results from repeated loading cycles, is less of a concern for flywheels as long as the charge/discharge rates remain below predefined levels [85].

Unlike batteries, the cycle life of flywheels is independent of the depth of discharge. High temperatures and discharge rates significantly affect battery performance, issues that are less critical for FESS. For instance, Tesla, a leading EV manufacturer, reports that its lithium-ion battery packs last between 300,000 and 500,000 miles, equating to approximately 1,500 cycles [86]. This indicates that a battery may require replacement once or twice during the lifespan of the vehicle. However, lithium-ion batteries present recycling challenges, raising environmental concerns [87]. Flywheels are considered to have a minimal environmental impact; they can be manufactured using non-toxic materials and are more readily recyclable compared to lithium-ion batteries, although recyclable, often face logistical hurdles in the recycling process due to the complexity of the materials involved [88]. Additionally, the Norwegian automobile federation has noted that cold weather can reduce an EV's range by up to 20%, a drawback that FESS can mitigate [89]. Moreover, flywheels exhibit less temperature sensitivity than batteries, maintaining performance across a range of temperatures without the capacity and power losses experienced by lithium-ion batteries [90].

The cost comparison between flywheels and batteries is complex due to the mass production of batteries, as opposed to low volume production of flywheels. Nevertheless, it is understood that raw material costs represent a significant proportion (60-70%) of the total cost in the large-scale manufacture of electrical machines. GKN Hybrid Power estimates the raw material cost for a standard ICE at approximately $685, while a low-power/low-energy flywheel (30 kW/111 Wh) is around $723 [91]. Flybrid has compared the

cost-effectiveness of their FESS against hybrid vehicle systems, with findings indicating advantages for FESS in aspects such as weight, volume, cost, and efficiency, as detailed in Table 2-4 [92].

Table 2-4 Comparison between the hybrid electric and Flybrid systems [92]

Parameter	**Hybrid Electric System**	**Flybrid System**
Cost per unit for production rate of 200,000 units	8,000 USD	2,000 USD
Volume	50 Litres	20 Litres
Weight	85 kg	35 kg
Round trip efficiency	34%	74%

Key attributes of flywheels, such as no performance degradation over time, extended cycle life, high power density, and simple state-of-charge assessment—referring to the ability to easily determine the stored energy level—render them an attractive option for energy storage applications. Table 2-5 provides a comparative analysis of lithium-ion batteries and flywheel systems for power buffering in city buses. Subsequent sections will elaborate on the various advantages offered by FESS.

Table 2-5 Comparison between Li-ion battery and flywheel systems for vehicular applications [93]

Type	**Li-ion battery system**	**Flywheel system**
Manufacturer	A123Systems	GKN
Energy capacity	26,400 Wh	456 Wh
Rated power	spe120 kW	120 kW
Specific power	500 W/kg	2200 W/kg
Specific energy	110 Wh/kg	8.3 Wh/kg
Cycle lifetime	$\sim 10^3$	$>10^6$
Weight	240 kg	55 kg

2.2.6.1. The Development of Flywheel Technology

The most historical record on flywheel technology, including automotive applications, is written by Genta [94]. One of the early integrations of flywheel technology was the Oerlikon Gyrobus, which operated in various European and African cities during the 1950s. However, it was eventually discontinued due to technical challenges. Early flywheel road vehicle applications, like Clerk's Gyreacta and Hydreacta in England in the 1960s, combined flywheels with ICE using complex gear sets. Gyreacta had stepped shifts

with speed loss; Hydreacta was smoother but less efficient. These complex and costly systems were pioneering for their time [95]. Rabenhorst's [96] introduction of the 'super-flywheel' concept in 1969 marked a significant milestone, featuring materials with high uniaxial tensile strength, capable of storing energy at 14 Wh/kg.

The 1970s witnessed heightened interest in flywheel technology spurred by U.S. government financing. Despite the initial enthusiasm, the focus on flywheel technology diminished with the stabilisation of oil prices by the late 1970s, leading to a reduction in research by the mid-1980s. However, the 1990s saw a resurgence in interest due to stricter global emissions regulations [97]. Notable advancements during this period included the electromechanical battery developed by the American Lawrence Livermore Laboratory [98] and research at Eindhoven University in the Netherlands [99]. The advent of hybrid vehicles in the late 1990s further strengthened the interest in flywheels, propelled by developments in high-speed MGs, durable magnetic bearings, and high-frequency power electronics.

The declaration by the Federation Internationale de l'Automobile (FIA) in 2006, focusing on the recovery and reuse of kinetic energy in Formula One (F1) racing cars, was a pivotal moment for flywheel technology. The 2009 F1 season saw the introduction of KERS, including flywheel-based systems. However, regulations at the time favoured battery-based systems due to power, energy, and packaging constraints. In F1, where budgets are extensive, the use of costly batteries was deemed a feasible solution, unlike road vehicles [97]. Currently, several vehicle manufacturers are exploring the development of flywheels for commercial vehicles to achieve cost-efficiency and performance benefits. It is anticipated that the production of flywheel-based motor vehicles will soon become a reality, signifying a promising future for this technology [97].

2.2.6.2. FESS Operating Principle

A flywheel functions by storing kinetic energy using a spinning mass. The energy stored is directly related to the rotor's moment of inertia and the square of its rotational speed, indicating that an increase in either parameter can enhance the energy storage capacity. High-speed operation places severe demands on the materials used in flywheel design [90]. Conventional flywheels are constructed from dense materials such as iron or steel and are limited to lower rotational speeds, typically up to 10,000 rpm. To achieve higher rotational speeds, ranging from 10,000 to 100,000 rpm, advanced composite materials have been developed. These innovative rotors, made from carbon fibre or glass fibre composites, are less dense than their metal counterparts, allowing them to store more energy at higher rotational speeds [41]. In most FESS, the rotor is cylindrical rather than disc-shaped, with its mass distributed as far from the rotation centre as possible. This configuration maximises the moment of inertia and thus the potential for energy storage. One of the

primary sources of energy loss in these systems is friction associated with the rotor [100]. Supporting the rotor as it spins is essential for its function. Mechanical bearings, while simple to use and well-understood, have high friction and wear rates, making them suitable for lower-speed applications. For high-speed flywheels, more sophisticated bearings are necessary. Magnetic bearings are the norm in high-performance systems, providing contact-free support to the rotor. These bearings are energised by electromagnets, which can be passive, bearing the load, or active, offering precise control of the rotor's motion [41].

2.3. FESS Applications

FESS applications can be distinguished based on their power capacity and discharge duration. Current advancements in flywheel technology have led to reduced costs and operational losses, with some systems capable of functioning efficiently for several hours. Furthermore, FESS are recognised for their extended lifecycle, rapid response times, and minimal thermal impact and sensitivity [101]. Primarily, FESS are deployed in vehicular and transportation sectors owing to their high power-to-mass ratio. Their adaptability and efficiency make them particularly suitable for applications where quick energy discharge and high power output are essential [85].

2.3.1. Transportation

2.3.1.1. Vehicles

FESS primarily serve as energy storage in hybrid and electric automobiles, providing assistance during uphill climbs or when abrupt acceleration is needed. ICEs are utilised in hybrid vehicles to supply constant power, enabling the vehicle to operate at the desired speed [102]. This approach is considered to increase engine life and reduce fuel consumption, thereby decreasing both air and noise pollution [103]. Flywheels are believed to be capable of regulating the varying power demands in electric vehicles, which utilise chemical battery storage systems. Therefore, FESS can stabilise the battery's charge-discharge cycles, thus prolonging its lifespan [104]. A proposed full-electric powertrain with a flywheel-based four-wheel-drive system demonstrated significant enhancements in overall performance and battery longevity.

Read et al. [105] conducted a study to optimise the flywheel design in hybrid vehicles, for energy recovery during braking and auxiliary power delivery during acceleration. Results indicated that for a particular vehicle, an optimal flywheel size and depth-of-charge is needed to maintain a balance between high transmission efficiency and low system mass.

FESSs have been utilised in F1 as a temporary energy storage device since the rules were revised in 2009. Flybrid Systems was amongst the primary suppliers of such innovative flywheel energy storage solution

for F1 race cars [106]. Flywheels in motorsport undergo several charge/discharge cycles per minute, thus standby losses are not a huge concern. Conventional driving schemes, on the other hand, necessitate a greater level of standby efficiency. On the New European Driving Cycle (NEDC), Flybrid Systems recorded an 18% savings for a 1.7-ton saloon car and a 35% savings for a 2.6-ton SUV [92]. The installed flywheel energy storage systems were designed to provide electricity by offloading a high-energy/low-power source. Flybrid Systems were purchased in 2014 by Torotrak PLC, which is a publicly traded company in London with a market capitalisation of $23 million dollars [85]. Flybrid was acquired by the PUNCH Group in 2018, gaining access to the engineering and manufacturing capabilities of PUNCH Powerglide and PUNCH Torino within the PUNCH Group [107].

On the other hand, from 2011 Jaguar's hybrid automobile Jaguar XF featured a mechanical flywheel technology designed by Flybrid Automotive. A Torotrak/Xtrac CVT gearbox transmits power to the driving wheels via the flywheel, which is made of composite material. The system weighs 65 kg and stores 120 Wh at 60,000 rpm. The highest power delivered by this technology was 60kW and the fuel savings were estimated to be around 20% [108]. In addition, Volvo is currently working on integrating FESS into its powertrain. The Flybrid Systems' FESS, installed in a Volvo S60, was similar to the one utilised by Jaguar, resulting in a 60 kW power boost and a 20% decrease in fuel consumption [109].

The Williams F1 team developed a technology similar to that of the Flybrid Systems, though it was not used in racing. However, it was used in the 2012 Le Mans 24 Hours when an Audi R18 E-Tron quattro became the first hybrid vehicle to win the event [109]. Their flywheel's magnetic section is composed of a magnetically loaded composite material, and the rotor operates in a partially depressurised environment to minimise peripheral drag losses while the bearings function at atmospheric pressure. This setup has a rated power of 150 kW and a storage capacity of 140 Wh [110].

Hua et al. [111] have researched the implementation of flywheels as secondary energy storage devices in hybrid vehicles. Meanwhile, the use of flywheel-based KERS in ICE-powered vehicles has gained significant traction in the realm of motorsport. The 2009 F1 racing season introduced regenerative braking systems. Flybrid Systems LLP developed a mechanical KERS with an adaptable CVT for both F1 and mainstream vehicular applications [112]. Boretti [113] engineered a flywheel-based KERS with an integrated CVT for small vehicles. Beyond automotive applications, KERS has potential use cases in other sectors such as off-highway applications. An overview of applications for flywheel energy storage from different commercial manufacturers is presented in Table 2-6.

Table 2-6 Different commercial flywheel systems [114]

	Amber Kinetics	**Gyroticity**	**PowerThru**	**Stornetic**	**Kinetic Traction Systems**	**Vycon**	**Rosseta T2**	**Beacon Power Gen 4**	**Temporal Power**	**Active Power**	**Piller Power Bridge**
Flywheel material	Steel	Laminated Steel	Fibre composite	Fibre composite	Fibre composite	Steel	Fibre composite	Fibre composite	Steel	Steel	Steel
Bearing system	NA	Mechanical & magnetic	Active magnetic	Active magnetic	Magnetic & hydrodynamic	Active magnetic	Rolling relieved magnetically	Rolling	NA	Rolling relieved magnetically	Rolling relieved magnetically
Max. RPM	10,000	20,000	52,000	45,000	37,800	36,000	25,000	16,000	11,500	7,700	3,300
Application	Micro-grid	Frequency stability, Railway	UPS	Railway, Grid	Railway, Micro-grid, UPS	Recuperation, UPS	Recuperation	Frequency stability	Voltage stability	UPS	UPS
Rated energy capacity (kWh)	32	0.069	0.63	4	1.5	0.83	4	25	50	0.9	4
Rated power (kW)	8	25	190	22	200	500	500	100	100-500	250	1,600

2.3.1.2. Buses

Buses operating in London have demonstrated potential energy consumption reductions of up to 45% when employing FESS such as the Flybrid system [92]. A cutting-edge flywheel, constructed from composite materials, utilising magnetic bearings, was installed on a bus at the University of Texas at Austin in the 1990s. This FESS boasted a capacity of 2 kWh and a continuous power output of 150 kW [115]. In 1996, a subsequent application featured in an Eindhoven city bus comprised of a compact 40 kW generator powered by liquified petroleum gas, integrated with FESS to harvest energy during braking, and manage peak power demand. This combination achieved up to 30% fuel savings and a remarkable 90% reduction in emissions [116].

In 2015, Transport for London announced the forthcoming deployment of 500 buses, each equipped with a 0.4 kWh flywheel system capable of accelerating a bus from 0 to 50 km/h by using the energy recovered during braking. These systems were projected to conserve between 20% and 25% of the energy typically supplied by diesel engines, translating into an annual saving of around 5,300 litres of fuel per bus. An added advantage is the flywheel's retrofit compatibility with existing buses, which facilitates hybridisation without incurring significant capital expenditure [117]. In 2023, London's bus fleet comprises 3,835 hybrid buses, 949 electric buses, and 20 hydrogen buses out of a total fleet of 8,643 buses. The widespread implementation of flywheel-equipped buses in London, however, has been deferred to a longer-term strategy [118]. The Flybus consortium has achieved a noteworthy milestone with the successful integration of prototype hardware into an Optare Solo Midibus. This Flybus system, which is anticipated to be significantly more cost-effective than the existing electric hybrid propulsion system, incorporates a Ricardo Kinergy flywheel for energy storage and a Torotrak CVT for power delivery [119].

Additionally, the GKN Hybrid Power flywheel is a flywheel battery (FWB) that uses a high-speed carbon rotor. The APC 'Gyrodrive' project, which ended in September 2017, aimed to develop, and test this technology for use in the hybrid bus market. Along with an operational fleet of 35 buses equipped with Gyrodrive technology in the UK [120].

2.3.1.3. Trains

The energy consumption of light rail transit trains can be reduced by 31% by energy recovery during braking, through the implementation of KERS such as FESS. The application of low-speed FESS is particularly beneficial for short-distance trains [101]. In the railway sector, FESS can be integrated by equipping diesel-electric locomotives with systems to store the kinetic energy that is usually lost. Additionally, enhancing the recuperation rate of DC systems, whether onboard or stationed at platforms, can also be an effective use of FESS [121].

The energy captured by one train during braking has the potential to power the acceleration of another. The Metro of Los Angeles exemplifies this application with the installation of a FESS at the Westlake/MacArthur Park Subway Station on the red line. Subsequent to the FESS installation, there has been an approximately 20% reduction in energy consumption, leading to annual energy and cost savings of 540 MWh and $99,000, respectively [122]. The FESS was constructed from steel with magnetic bearings and an operational speed of 20,000 rpm.

Further advancements have been made by the University of Texas at Austin, which developed a flywheel capable of storing 130 kWh at 15,000 rpm. The rotor, constructed from carbon fibre composites, was supported both axially and radially by active magnetic bearings, achieving a specific rotor energy density of 56 Wh/kg [123].

2.3.1.4.Trams

Several European cities have expressed interest in operating urban tram systems without the overhead cables traditionally used for electrical power supply. For short distances ranging from 0.8 km to 2 km within city centres, a short-term Energy Storage System (ESS) such as flywheels or ultracapacitors could be an optimal solution. In Zaragoza, Construcciones y Auxiliar de Ferrocarriles (CAF) has successfully implemented such a system [124]. Additionally, there has been an integration of a flywheel into the drivetrain of a tram in Karlsruhe. This tram, an eight-axle articulated model, originally constructed in 1959, has since been decommissioned. It featured three compartments with a total length of 27 metres. Alstom, as part of a European consortium, conducted trials of the Capacitor Charging Method (CCM) system. This system was integrated into a Citadis tram operating in Rotterdam, a city which sought a viable solution to traverse the Erasmus Bridge without reliance on a catenary system. These tests, conducted in 2005, confirmed the viability of the concept [125]. Subsequently, there has been an established collaboration with GKN to implement their advanced flywheel system [126].

2.3.2. Mobile Applications

Mobile applications of flywheel technology involve incorporating a flywheel system within a mobile framework. Goods handling encompasses the intermittent and repetitive exertion of power for the movement of loads. The peak power demands of transporting a load often surpass the average power requirements of the process, and traditionally, there has been no efficient method to reclaim energy during the lowering of loads. Flywheels are particularly well-suited to these scenarios due to their capacity for short, frequent loading times. One notable application is within Rubber-Tyred Gantry cranes (RTGs). Around 8,000 RTGs are in operation globally at container terminals. Unlike ship-to-shore cranes that are

grid-connected, RTGs have the flexibility to move around the terminal. Without energy storage, their operation tends to be inefficient, with high emissions due to the non-uniform load profile [127].

Since 2006, Calnetix has been producing flywheels for RTGs used in container handling. Typically, lifting a container for approximately 10 seconds requires about 240 kW of power. The FESS supplies the necessary power for the lift, allowing the generator set (Genset) to maintain a steady output. During the lowering of the hoist motors, the energy is regenerated back into the electric system, with the flywheels storing it for future lifting operations. Flywheel systems have been shown to reduce fuel consumption by 32–38% and nitrous oxide emissions by 26% in these applications [127]. The PUNCH Power 200 offers a quick power surge, enabling the reduction of the generator size or mains connection without sacrificing performance. Widespread implementation of FESS in goods handling sector can substantially decrease the carbon footprint of this industry [128].

2.3.3. Grid-Connected Power Management

Stationary grid-connected applications of FESS are available on the utility side of the electric grid. Two interconnected applications that utilise flywheels are frequency regulation and ramp management, which are necessary to address the variability of renewable energy sources [129].

An extensive electric grid synchronises generators with a near-constant frequency. This balance requires fine adjustment of the generator output to match the fluctuating load. If demand for electricity spikes faster than turbine generators can meet, generators may temporarily underperform. Desynchronisation of the grid due to load variations or sudden disconnect of a major power generation unit can cause power outages. Power plants can regulate frequency as auxiliary services to stabilise the grid. The operator can purchase frequency regulation services from a power plant in addition to electricity. This service requires a plant to rapidly scale its output in response to the grid operator's control signals, which may change very frequently, second-by-second. Because flywheels respond in milliseconds and cycle almost continuously, they are ideal for this task [130]. Integrating energy storage facilities into an existing substation facilitates interconnection. Beacon Power LLC led the way with flywheel-based frequency control, operating 20 MW facilities in Stephentown, New York, and Hazel Township, Pennsylvania. The Stephentown facility provides approximately 10% of the total frequency regulation required by the New York grid [130].

Frequency regulation reduces load and generation variability in large grids. Island and remote grids, which lack frequency regulatory markets, are especially unstable. The challenge is the increase in conventional generator output that often follows renewable energy integration. This 'ramping' can lead to high maintenance and operational costs. Renewable energy now accounts for 20–30% of power generation, but its variability makes grid management more difficult without adequate storage [131]. Some large islands

aim for over 40% wind penetration, making storage crucial [132]. Island grid operators are taking steps to address these issues. Duration, intensity, and frequency vary greatly between solar and wind energy. Solar energy variations occur gradually over a day, while wind patterns can change abruptly, with ±20% changes in under two minutes. Flywheels are particularly good at smoothing wind turbine electricity fluctuations due to their rapid response [133].

2.3.4. Industrial and Commercial Power Management

Calnetix and URENCO have used flywheels in transit systems to recover trackside energy [101]. FESS is installed at a transit station or substation to accelerate trains using regenerative braking. This allows longer and heavier trains to operate without increasing distribution line or transmission capacity. In systems without energy storage, a new substation is needed to reduce voltage drops or increase capacity. A transit station's FESS can support the same voltage as a new substation without power support and at a much lower cost. Flywheels are ideal for frequent charge-discharge cycles. Energy harvested from braking can reduce electrical consumption by up to 10% in 190 subway systems with 9,477 stations and 11,800 km of track, resulting in $90,000 savings per station annually [134]. Savings of up to $250,000 per station per year can be realised when the system is installed in areas with demand charges in the utility tariff structure.

The mining industry is also poised to benefit from FESS. Globally, open-pit mines employ electrically powered draglines for excavation. The load profile of a dragline is cyclical and highly variable, often resulting in the dissipation of regenerated electricity. Typical peak loads of 6 MW are observed during the hoisting phase, while the lowering phase can regenerate up to 3 MW. This process is repeated approximately every minute. For instance, At the Usibelli coal mine in Healy, Alaska, a 6 MW dragline operates fully on electricity supplied by the Golden Valley Electric Association (GVEA) network. The fluctuations in load were so substantial that they caused voltage flicker for other GVEA customers. Since 1982, the Usibelli mine has implemented a flywheel system to mitigate the effects of dragline load variations [135].

2.3.5. Pulsed Power

Pulsed power is characterised by the continuous accumulation of energy followed by its rapid discharge, releasing high-power pulses. Flywheels excel in these applications and are utilised in military, industrial driving, and research applications. A prime military application of flywheels is to serve as an energy source for Electromagnetic Aircraft Launch System (EMALS), intended to replace steam-powered catapults [136]. Traditional steam catapults, while effective, are bulky, heavy, and inefficient, consuming approximately 615 kg of steam from an aircraft carrier's nuclear reactor for each launch. The linear synchronous motor design of EMALS is expected to significantly reduce the amount of energy required to launch large aircraft.

The system is driven by high-inertia alternators, each featuring a dual-stator permanent magnet motor that generates an axial magnetic field. The rotor disk of the alternator fulfils a dual role, acting as the flywheel for energy storage as well as the magnetic field source for power generation. Between launches, the ship's electrical system steadily charges the alternator, bringing it to full charge within 45 seconds. During a launch event, the stored energy in the rotors is released in a pulse lasting 2 to 3 seconds. The EMALS rotors can store 121 MJ of extractable power at their maximum rotational speed of 6,400 rpm (106 Hz) when fully energised. The total energy reserve is substantially higher, given that the rotor speed only decreases by about 25% during a launch event, thus providing a significant amount of power while conserving the carrier's resources [137].

In research facilities, on the other hand, flywheels power the most powerful and largest tokamak, the Joint European Torus (JET) in Culham, UK. Free JET began in 1983. A single JET plasma pulse requires 1,000 MW with a typical day involving 22 tests. JET continuously loads two massive steel flywheels with grid power to power tests. The JET flywheels weigh 775 tonnes and are 9 m in diameter. Rotors rotate at 3.7 Hz at full speed, reaching 100 m/s at 225 rpm. Over 9 minutes, an 8.8 MW motor accelerates the wheels from half to full speed between shots. With 700 kWh of input energy, each twenty-second flywheel can produce 500 MW of power [44].

2.3.6. Uninterruptible Power Supplies

Flywheel systems are globally employed to provide temporary electrical backup. In scenarios where critical systems or networks must remain operational during power outages, flywheels are designed to supply the necessary power until diesel generators can be started and synchronised. Flywheels offer a competitive alternative to batteries, with the key benefits being an extended lifespan and the elimination of the need for frequent replacement of conventional batteries and the challenges associated with their recycling [138].

There are two main implementations of flywheel technology in Uninterruptible Power Supply (UPS) systems. Firstly, a standalone energy storage device known as a flywheel UPS, where the flywheel delivers electricity to a DC bus, and an inverter then converts this to AC power to drive the load. Here, the flywheel may either replace the traditional battery or complement it, typically providing several tens of seconds of discharge time [138]. Flywheel UPS rotors often operate in a vacuum or at low pressure, rotating around a vertical axis to reduce frictional losses. Another type, the rotary UPS, can also be termed as a power bridge, power platform, or diesel rotary power. A standard rotary system consists of a diesel generator, a kinetic energy storage device with a substantial moment of inertia (often an induction coupling), and a coaxial alternator, all mounted on a shared base frame. In the event of a power failure, the stored kinetic energy in the induction coupling drives the alternator to maintain the load while the generator initiates. The rotary

UPS configuration is typically substantial; even the smallest units have capacities of around 1 MW. Although rotary systems account for around 5% of the overall UPS market share, their prevalence increases with system size; they constitute about 35% of the market for systems larger than 2 MW. Furthermore, in Europe, approximately half of new UPS installations with a capacity exceeding 1 MW utilise rotary UPS technology [50].

2.4. FESS-Based Powertrain for Vehicles

Depending on the drivetrain system, type, structure, performance, and vehicle requirements, the FESS can be used in a vehicle in different ways. The design of the powertrain is essential to improving both the overall system performance and the energy management characteristics [90].

2.4.1. FESS ICE-Based Powertrain

Britain was the first to develop FESS with an integrated and differentiating planetary gear unit, using a complex mechanical transmission [95]. A similar powertrain was developed by the University of Wisconsin [139], and several others were developed by the Imperial College London [140] and the University of Eindhoven [141].

Such powertrains typically employ non-electric transmissions. Various configurations and operational modes are feasible, where the flywheel may be connected in either series or parallel. There has been at least one study investigating the use of a flywheel in a series configuration with two CVTs. Nonetheless, the parallel configuration, shown in Fig. 2-3, remains a more conventional approach, adopted by the University of Eindhoven [141]. In this setup, the flywheel operates in tandem with the ICE at speeds of up to 100 km/h, beyond which the ICE functions independently. The most efficient operating range for an ICE, particularly for charging the flywheel to its operational capacity, lies between 10 km/h and 55 km/h in a low-speed hybrid mode [142]. The flywheel is then used for driving the vehicle when the preferred flywheel speed is achieved so that the ICE is in the enabling mode. The ICE is always in operation between 55 and 100 km/h, with the flywheel acting as an auxiliary power source. The flywheel is furthermore switched off, and ICE drives the vehicle. The fuel economy is mainly enhanced by engine operation enhancement with a small contribution from regenerative braking [141].

The improvement of fuel economy can be achieved by the reduction of losses from the flywheel system. The hybrid flywheel drive system's enhanced prototype demonstrates the fuel economy in urban traffic by up to 35% [100]. A novel configuration from Imperial College London, shown in Fig. 2-4, adds a flywheel to the standard ICE powertrain with a mechanical drive. The primary role of the flywheel is to capture energy during regenerative braking, which would otherwise be dissipated as heat. During the braking

process, the flywheel stores the kinetic energy, which is then released when the vehicle accelerates. In this configuration, the engine is deactivated when the flywheel is working. It has been reported that the fuel economy of buses and cars can improve by up to 33% and 22%, respectively, compared to conventional powertrains [140].

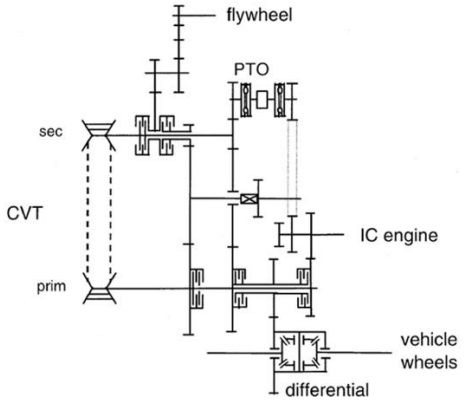

Fig. 2-3 The system configuration used by Eindhoven University [141]

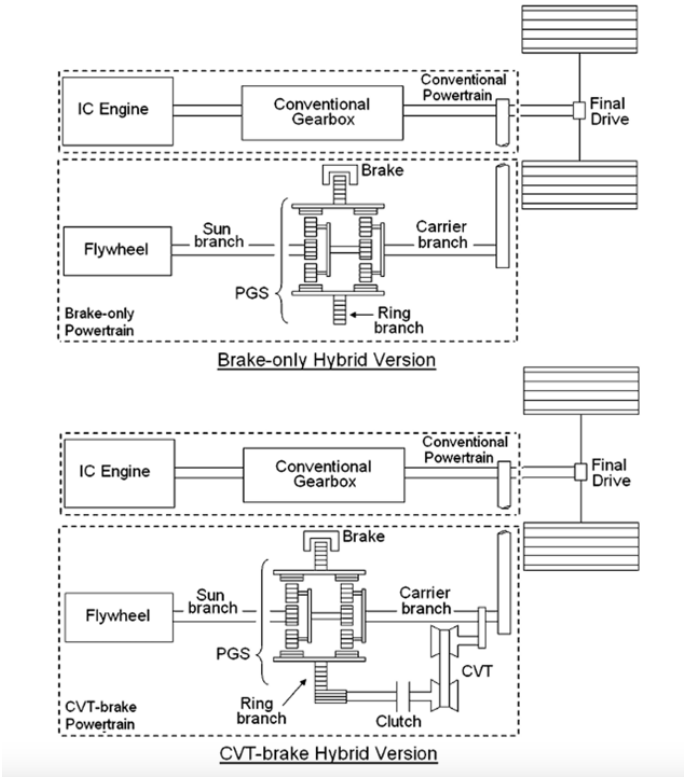

Fig. 2-4 Imperial College concepts for brake-only and CVT-brake hybrid systems [140]

2.5. FESS HEV Powertrain

The series configuration of hybrid electric vehicles is another common setup, as illustrated in Fig 2-5. In this arrangement, the ICE generates electrical energy that powers electric motors, with the flywheel acting as an energy storage medium. The University of Alberta, UT-Austin, and the University of Eindhoven have all developed FESS using a similar configuration [143]. This setup has been predominantly used in public transport systems, operating similarly to the battery-based series HEV powertrains. ETH Zurich developed a parallel hybrid powertrain known as the ETH-Hybrid III, the schematic of which is depicted in Fig. 2-6 [144]. This powertrain integrates a flywheel coupled with a CVT, batteries, an asynchronous electric machine, and an ICE. The presence of various components enables multiple operational modes, effectively combining the functions of battery charging and the strategy similar to that outlined by the University of Eindhoven. Despite its potential, the system was considered complex in both construction and control [99].

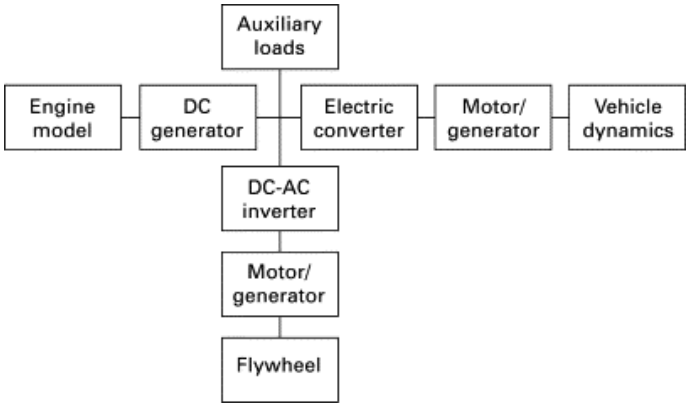

Fig. 2-5 Hybrid electric powertrain with flywheel acting as an energy storage [143]

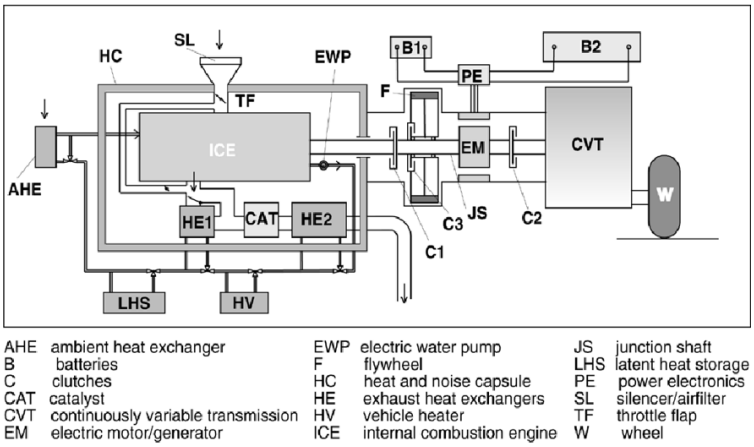

Fig. 2-6 ETH-III powertrain schematic for hybrid powertrain with flywheel [144]

2.5.1. FESS Electric Powertrains

One of the primary challenges of EVs is the limitations imposed by their battery storage systems. The cost of the vehicle and the limited range are factors that detract from their appeal. Employing a high-power storage device such as a flywheel to complement the 'state of charge' of batteries may mitigate some of these constraints. The battery would supply steady average power, while the flywheel would regulate power during deceleration and acceleration. This approach could extend the driving range and enhance battery longevity by alleviating the strain from power spikes, and concurrently reduce the cooling requirements of the battery system. Typically, flywheels are incorporated within a Flywheel Battery (FWB) system, a combination of a flywheel and a MG unit, often employing magnetic bearings, as depicted in Fig. 2-7 [115]. Recent studies by Lundin [145] involved using an FWB system with dual-voltage stages between the battery and the traction motor. The high-voltage section interfaces with the traction motor, while the battery connects to the low-voltage side. The FWB is capable of both charging and discharging the traction motor and battery at differentiated voltage and power levels, showing that partial charge/discharge cycles are significantly reduced, thereby diminishing the associated current and battery-resistive losses compared to systems without a flywheel.

Mechanical coupling of the flywheel and the EV drivetrain provides advantages in cost, and simplicity, and eliminates the need for energy conversion. Preliminary research funded by the US government in the 1970s examined this approach. However, at the time, EV performance was markedly inferior to conventional vehicles, and even with a flywheel, they did not offer a competitive edge [146]. Currently, research into this application continues at the City, University of London, examining the feasibility of the system considering the recent advancements in flywheel and EV technologies [147].

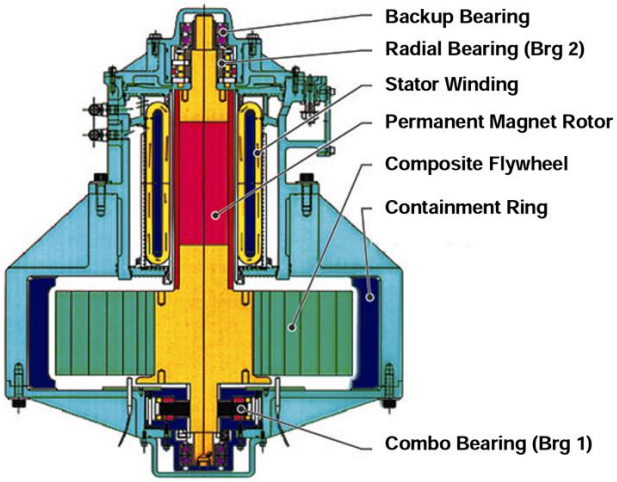

Fig. 2-7 Schematic of the flywheel battery components [115]

2.6. FESS Components

A flywheel is a mechanical device mounted on a shaft and supported by bearings. It can be paired with a MG for electrical energy transmission, which, in its simplest form, resembles a standard electrical machine. However, the required high operational speeds in FESS applications introduce unique engineering challenges that differentiate these systems from conventional flywheel applications [103]. Key aspects of FESS that require specialised consideration include the bearings, control systems, housing environment, transmission, and the flywheel. Each of these components and their associated engineering challenges will be thoroughly examined in the following sections.

2.6.1. Bearings

The design and selection of bearings are crucial for the operation of flywheels, where the chosen bearings must support not only the static rotor loads but also dynamic forces, which include shock and gyroscopic effects. It is essential for the bearings to have a considerable operational life expectancy. The primary selection criteria include durability, cost-effectiveness, minimal maintenance requirements between services, and low energy losses [148]. The available bearing types for FESS in vehicle applications will be further discussed in the following sections.

2.6.1.1. Hydrostatic And Hydrodynamic Bearings

Hydrostatic and hydrodynamic bearings employ a fluid film to separate the bearing surfaces. In hydrostatic bearings, the fluid is pressurised externally. Conversely, in hydrodynamic bearings, the fluid film is generated due to the motion of the bearing surfaces, trapping the fluid in a wedge-shaped space. Both types of bearings can operate at high speeds, absorbing significant levels of vibration, enduring substantial loads, and providing low operational torques [149].

2.6.1.2. Air Foil Bearings

Air foil bearings, initially designed for military and auxiliary power units, are suitable for environments where high temperatures and speeds render conventional bearings ineffective. These bearings do not require a lubrication system; instead, they use pressurised air to create a cavity between bearing surfaces. The design allows for a 'soft failure' mechanism, where in the event of a failure, the foils compress onto the shaft to limit damage, typically confining it to the foils and shaft surfaces [150].

2.6.1.3. Magnetic Bearings

Magnetic bearings are contactless, thus exhibiting minimal wear and low friction losses. They are suitable for use in low-pressure environments due to their lack of lubrication requirement. These bearings can be divided into different types based on their control systems [151].

Passive: utilising permanent magnets, passive magnetic bearings maintain stability as displacement increases the magnetic restoring force. However, they cannot withstand high forces and may need auxiliary bearings to support the load. They are cost-effective and exhibit low energy losses due to their independence from control systems, but their application is limited due to stability constraints in various suspension dimensions [151].

Active: unlike passive bearings, active magnetic bearings rely on electromagnets, which create attractive forces that are inherently unstable, requiring complex control systems to adjust the magnetic forces [152]. These systems need sensors to monitor rotor movement and control the electromagnetic strength to maintain rotor stability. While they provide precise suspension and high stiffness, they can be power-intensive and necessitate advanced, disruption-sensitive control strategies [153].

Superconducting Magnetic Bearings: Ideal for high-speed applications, these bearings offer frictionless operation, extended lifespan, and low energy loss at high speeds. Superconducting bearings operate at very low temperatures, requiring cryogenic cooling systems. Recent advances in cryogenic insulation technologies may help reduce the associated costs, though the requirements for cryogenic cooling and the high costs remain significant challenges [154].

2.6.1.4. Rolling Element Bearings

This type of bearing consists of an internal and an external ring that runs between rolling elements. The rolling elements are generally maintained against each other and separated equally by a cage. These bearings are available in various forms, with the main types being roller bearings and ball bearings. Their suitability for high-speed applications is contingent on the centrifugal forces exerted on the rolling elements and cages. It is important to note that while they can handle substantial loads, generally, a heavier load capacity correlates to a lower maximum speed due to material and lubrication constraints [155].

2.6.1.5. Bearing Selection

Selecting the most appropriate bearing for a FESS depends on the loads to which the bearings are subjected, including sudden impacts, such as hitting potholes, vibrations originating from the asphalt or irregular road surfaces, and stresses induced by vehicular manoeuvres such as cornering, accelerating, and decelerating. The most significant load is typically the shock resulting from abrupt road irregularities. Bischof et al. [156]

conducted numerical analyses on different orientations of a flywheel and discovered that the lowest total bearing loads were associated with a vertically oriented rotor spin axis. Isono et al. [157] reported the benefits of using high-temperature superconductors in applications such as FESS. However, relying exclusively on these may not be optimal, as they may not necessarily stabilise the rotor to the required level. Integrating active magnetic bearings with superconducting magnetic bearings could mitigate vibrations experienced by the rotor. Additionally, Murakami et al. [158] introduced a novel design where the flywheel rotor is supported by a passive magnetic bearing at the top for positional control, while a superconducting magnetic bearing at the bottom dampens vibrations. To facilitate the cooling requirements of a superconducting magnetic bearing, a cryocooler needs to be strategically installed. Flybrid opted for off-the-shelf rolling element bearings, having determined that the mechanical losses from these bearings do not significantly impact the performance of their FESS. This design choice simplified the system and reduced the overall cost [97].

2.6.2. Control

Despite the pursuit of ideal control solutions in engineering, many methods diverge from conventional optimal control strategies due to a lack of publicly available information on FESS control systems, since industrial entities often protect their intellectual property. Cross et al. [159] and Boretti [113] have not specified any control strategies but have provided descriptions that align with classic control approaches, including trial and error. Ghedamsi et al. [160] discussed the application of a PID control strategy used in wind generators, characterising it as a Multiple Inputs, Multiple Outputs (MIMO) control system. Furthermore, Ye et al. [161] referenced various energy recovery system strategies employed in the past, including neural network control, intelligent control, fuzzy control, and variable structural control. Cheng and Ye [162] also explored the use of genetic algorithm-based neural networks as a control technique alongside robust sliding mode control, H-infinity control, and fuzzy PID. Meanwhile, Hua et al. [111] introduced methods for constant power and constant torque control. Kirk [163] defined optimal control as the process of determining the control signals that cause a process to satisfy physical constraints and optimise a performance criterion, often related to energy or time, making it an appropriate choice for KERS applications seeking to maximise stored energy efficiency. Optimal control theory is commonly implemented through two independent methodologies: Pontryagin's Maximum Principle and Dynamic Programming, the latter being more frequently utilised due to the mathematical complexity of the former.
Cikanek et al. [164] have researched regenerative braking in hybrid electric vehicles, developing algorithms using MATRIXx software, with vehicle-based testing of the code. Inoue et al. [165] applied a variational method to devise an optimal torque controller, testing the strategy with the SimPowerSystems toolkit in

MATLAB/Simulink. Ye et al. [161] developed a strategy that integrates auxiliary and primary power sources of an EV to enhance performance by controlling regenerative current with an H2/H-infinity control strategy, improving performance by 6% and 3% for emergency and soft braking, respectively. Cao et al. [166] focused on improving the regenerative process without compromising the energy storage system, proposing a robust control solution for EVs. They highlighted the inherent robustness of the standard PID but acknowledged the need for enhanced operational effectiveness. The results indicated improved charging currents with the PI control.

Xiao et al. [167] analysed control systems for FESS, typically requiring two steps: accurate regulation of the rotor's rotational speed and axial movement, and a synchronisation controller to mitigate gyroscopic rotations due to external disturbances and model uncertainty. The case studies demonstrated that well-tuned control systems could stabilise an unsteady rotor and counteract gyroscopic effects, even at high speeds. Active magnetic bearings in particular benefit from closed-loop control systems to dampen system vibrations and adequately respond to sudden load changes. The rotor can exhibit two types of whirls, conical and translational. The conical whirl, influenced by gyroscopic forces, can significantly impact stability, while the translational whirl restricts radial motion to prevent rotation, a common industry practice. Synchronisation control has shown to be highly effective in managing nonlinear systems and rejecting disturbances within synchronous motion systems. Previously, the application of synchronisation control was confined to stable mechanical systems and was not easily adaptable to highly nonlinear and unstable systems, a constraint overcome by the advent of modern synchronisation control methods [167]. A detailed comparison of various control methods used in FESS, along with their respective advantages and disadvantages, is presented in Table 2-7.

Table 2-7 Comparison of different FESS control systems

Control Strategy	Advantages	Disadvantages	References
Proportional-integral (PI)	• Simplicity of implementation • Absence of steady-state error • Linearity	• Inadequate transient response • Inability to respond to non-linearity • Limited stability range	[168]
Proportional integral derivative (PID)	• Simplicity of implementation • Requires fewer resources • Has a good response to unmeasured interference	• Inability to perform operations with a longer deadtime • Inability to respond to non-linearity • Inability to respond to multiple variables	[169]
Feedback linearization (FL)	• Able to respond to a system's non-linearity • Able to transform original system models into simpler equivalent models • Able to transform non-linear systems into linear	• Inability to respond to all operating points due to a lack of robustness	[170]
Fuzzy logic control (FLC)	• Simplicity in computation. • Able to deal with non-linearity and uncertainty in the system. • Exceptional convergence speed. • Able to control one or more input/output systems.	• Difficult to design • Success is contingent upon the expert's knowledge and experience.	[171]
Field-oriented control (FOC)	• Accurate dynamic speed control. • Torque can be controlled at low speeds and frequencies. • Able to operate in all four quadrants.	• Has a short-term overload capability. • Accurate rotor positioning requires the use of a sensor	[172]
Artificial neural network (ANN)	• Able to tolerate failures • Able to store large amounts of data over the network • Able to function even when presented with incomplete information	• Success is contingent upon the expert's knowledge and experience. • Expensive • Limited to numerical data	[173]
Model predictive control (MPC)	• Responds with greater precision and accuracy • Optimal Controller • Possibility of controlling back-to-back multilevel converters	• Extensive computational time and expense • Requires the development of an accurate dynamic model	[174]
Direct torque control (DTC)	• Able to control flux and torque more rapidly • Less sensitive to parameter changes	• More noise in voltage and current signals • Higher Torque ripple and current distortion	[172]
Optimisation	• Irrespective of the ability of the user • The system's total cost can be minimised. • Able to determine the true optimal value of a response with fewer trials	• Must adhere to a set of rules for selecting the procedure's indices	[175]
V/f	• Requires a lower starting current • Allows the motor to operate in a relatively stable region • Assures that the output voltage is proportional to the frequency • Prevents magnetic saturation from deteriorating	• High installation cost • Unable to handle regenerating load	[176]

2.6.3. Housing

The flywheel housing fulfils three principal functions: it serves as the interface between the flywheel and the vehicle, ensures vacuum tightness to maintain the required working pressure, and provides a protective barrier to contain fragments in the event of premature rotor failure. The housing must be robust enough to serve as a containment, typically constructed from thick, high-strength steel or equivalent materials, capable of withstanding impact at high speed [35]. To meet the strict safety requirements in case of rotor failure, the housing design must prioritise the following requirements.

- Low Weight: The housing, often the heaviest component, must be designed to keep the system's overall specific energy high. The rotor alone contributes only a fraction of the total system weight.
- System Integration: The housing must include a suitable interface for attachment to the vehicle, which is generally more straightforward in commercial vehicles due to the larger space available for installation.
- High Stiffness and Damping: The housing should ideally improve the machine dynamics and acoustics by offering appropriate stiffness and damping characteristics.
- Cooling System Integration: Accommodations for the inclusion of an efficient cooling system for the electric MG and bearings are essential within the housing design.
- Cost Efficiency: Since structural steels are often chosen for their cost-effectiveness and ductility, the design must be optimised for ease of manufacture to prevent inflated process-related expenses.

FESS with high rotational speeds tend to operate in low-pressure environments with a range of vacuum levels from 100 to 10^4 Pa. One of the functions is to provide rotor failure safety protection. When the rotor fails, the containment should prevent the projectiles from bursting through the containment. However, it is rather complicated to predict the mechanism and behaviour of the bodies involved. An experimental study must be conducted to study the failure mechanism of flywheels [94]. An experiment was conducted to check and improve containment design by observing the impact behaviour [177]. There are some practical proposals for flywheel safety design considerations [178].

2.6.4. Transmission

The transmission is an integral component that connects the wheels and the energy storage system. It enables the transformation of kinetic energy from the wheels to the flywheel during braking, and conversely from the flywheel to the wheels during acceleration. The defining attributes of transmission for this application include high power density to ensure rapid operation during acceleration or deceleration, a high energy density for maximum energy storage, and high efficiency to minimise energy losses [179].

Lechner et al. [180] reviewed various transmission types within the automotive sector, concluding that they generally fall into two categories: Continuously Variable Transmissions (CVT) and geared transmissions. To incorporate a FESS in a conventional vehicle, the flywheel must seamlessly integrate with the vehicle's powertrain, accommodating continuous variations in speed as the vehicle accelerates or decelerates. The flywheel is required to absorb kinetic energy at different rotational speeds and release this energy back to the powertrain at the required speed. The optimal method of connecting a FESS to the vehicle's powertrain is through a CVT, which allows for bidirectional energy transfer with high efficiency. The CVT in a flywheel hybrid vehicle necessitates a broader ratio range, particularly when employing a high-speed flywheel with a low depth of discharge. Additional considerations for the CVT include cost-effectiveness, low weight, and ease of control [113]. Flywheel-based KERS transmissions can also be segmented into two subcategories: mechanical and electrical [160].

2.6.4.1. Mechanical Power Transfer

CVT is an ideal solution if the vehicle needs a transmission system to transform the recovered energy to kinetic energy with minimal losses. CVTs are recognised for their high efficiency; however, they are often limited by their torque capacity. Despite this limitation, CVTs hold significant potential as a future transmission system for KERS applications due to ongoing developments to enhance their torque-handling capabilities. The most prevalent CVT designs include the Toroidal, Pulley, and Hydrostatic models [179].

2.6.4.1.1. Hydrostatic transmission

Hydrostatic transmissions transfer power through fluid dynamics, regulated by a variable displacement pump that modulates the flow to the hydrostatic motor. This type of transmission comprises two hydraulic components: a variable displacement pump and a connected motor. Mechanical energy is converted into hydraulic pressure, which the motor can then reverse. Infinitely Variable Transmission (IVT) is achieved by adjusting the displacement of the pump, which eliminates the need for a starter clutch. While hydrostatic transmissions are relatively simple and adaptable, their large size and noise level generally make them more appropriate for heavy-duty applications rather than passenger vehicles [181].

2.6.4.1.2. Traction continuously variable transmission

Traction CVTs transmit torque through the frictional force between two surfaces, with the transmission ratio altered by varying the radius at the point of contact. These drives typically have a restricted ratio range and come in two main types: rolling traction drives and belt drives [181]. Rolling traction drives, such as toroidal transmissions, consist of two discs and two interposed rollers. By rotating the rollers,

the contact point and thus the gear ratio can be continuously varied. Torotrak is a leading manufacturer of such transmissions [182]. The Milner CVT, another rolling traction drive, employs spherical planetary rollers to transfer power between the discs and the carrier, with the ratio adjusted by axial displacement [183]. Belt drive CVTs utilise two pulleys with varying diameters linked by a belt, where the variable diameter pulleys result in different input/output ratios. Belts are typically made from rubber or steel, with rubber V-belt CVTs being the most common [184]. An improved version using steel blocks connected by steel ribbons was developed by Van Doorne [185], enhancing the capabilities of rubber belt drives. Another variation is the flat rubber strap design by Kumm Industries, which adjusts the transmission ratio by radially positioning the belt along guideways [186].

2.6.4.1.3. Mechanical transmission

The simplest form of mechanical CVT involves a clutch in series with a stepped gearbox. The gearbox operates with discrete ratios, and the clutch engages to achieve the desired ratio at each stage. Although power loss from clutch slip can be reduced using a gearbox with multiple ratios, the cost may be prohibitive. Read [187] proposed a method that combines a small gearbox with a multi-step gearbox to simulate a larger number of gears. Additionally, Beachley and Frank [181] suggested a design that allows a flywheel to connect to a hybrid drivetrain using a Planetary Gear Set (PGS). Typically, one element of the PGS is fixed while the others serve as inputs or outputs. If the PGS is utilised as a CVT, all three elements would be free to rotate, offering two degrees of freedom. The CVT function is accomplished by controlling the speed of any two elements, as PGS operates as a speed synchroniser [140].

2.6.4.1.4. Mechanical transmission topology

Mechanical hybrid powertrains that incorporate flywheels utilise purely mechanical means for power transmission. The CVT's ability to shift smoothly facilitates efficient charging and discharging of the flywheel without requiring energy conversion [188]. Mechanical components typically offer a cost advantage over their high-power electronic counterparts and, despite having a lower energy storage capacity, are generally sufficient for recuperating the majority of energy during braking [189]. The design of an effective mechanical hybrid powertrain involves meticulous consideration of the topology and the dimensions of the flywheel. The challenge in optimisation arises from the need to simultaneously address diverse objectives related to marketing and production, which can often conflict. Given the multitude of design parameters encompassing topology, component selection, flywheel size and mass, as well as powertrain benchmarks and operating conditions, it becomes a complex task to execute a comparative analysis. Moreover, as the control strategy is also tailored for each design iteration, the process of identifying the most effective powertrain configuration is inherently iterative.

2.6.4.2.Electric Power Transfer

In electric and hybrid vehicles, transmissions based on MG units are often employed to convert recovered kinetic energy into electrical energy, which can then be used to charge the battery pack. The MG is connected to the flywheel, enabling energy conversion. When the vehicle decelerates, ICE functions as a generator, extracting electrical energy to accelerate the flywheel and storing energy. Conversely, during discharge, the MG retrieves the energy stored in the flywheel [30]. There are several types of electric machines that can be paired to a FESS, including [190]:

2.6.4.2.1. Induction machines

Induction Machines (IMs) also referred to as asynchronous machines, typically have lower power and efficiency compared to permanent magnet motors. The absence of permanent magnetisation significantly mitigates idling losses. Although robust and mechanically simple, IMs do experience considerable losses within the rotor, which should be kept minimal to prevent overheating, especially when the flywheel is suspended in a vacuum on magnetic bearings. IMs are often chosen for their robustness, high torque capabilities, and cost-effectiveness. However, they are also subject to speed limitations, necessitate complex control systems, and have greater maintenance needs [191].

2.6.4.2.2. Permanent magnet synchronous machines

Permanent Magnet Synchronous Machines (PMSMs) are popular choices for FESS due to their high efficiency and low rotor losses, due to a permanent magnet-generated rotor flux. These machines are well-suited to high-speed applications and have high energy density and overall efficiency. Eddy current losses and camper hysteresis can be reduced using PMSMs. However, unlike an IM, PMSMs are more expensive, less robust, and temperature sensitive. PMSM issues include eddy current-based idle losses, low robustness, and high cost [192].

2.6.4.2.3. Brushless direct current machine

Brushless Direct Current Machines (BLDCMs) are a type of asynchronously controlled machine that uses permanent magnets and an inverter to regulate the current through the stator windings. They offer advantages such as compact build, mechanical robustness, broad operational speed range, high efficiency, and high power density [193].

2.6.4.2.4. Variable reluctance machine

Variable Reluctance Machines (VRMs) are beneficial for applications such as FESS due to their simplicity and low idle losses. They are resilient and capable of operating across a broad speed range,

even in harsh conditions with temperatures surpassing 400°C. VRMs can produce high torque but may present challenges in low-speed torque control, though at high speeds, control is easier compared to IMs [194].

2.6.4.2.5. Homopolar machine

Homopolar Machines (HMs), or AC homopolar synchronous machines, provide a robust rotor structure and low idling losses. They are known for their reliability, making them suitable for sustained high-speed operation [195].

2.6.4.2.6. Bearingless machine

Bearingless Machines (BMs) combine torque production and magnetic suspension in a single device. Compared to conventional magnetic bearings, BMs offer a more accessible structure, are compact, and can lead to cost reductions. They are appropriate for high-speed FESS applications, and there has been a range of BMs developed, including bearingless PMSMs, BLDCMs, IMs, reluctance machines, and Switched Reluctance Machines (SRMs) [196]. Table 2-8 provides a summary of the essential characteristics of various electric machines suitable for FESS.

Table 2-8 Comparison of electric machines used with a FESS [197] [198]

	Permanent Magnet Synchronous	**Variable Reluctance**	**Asynchronous**
Cost	High	Low	Low
Demagnetization	Yes	No	No
Maximum speed	Low	High	Medium
Torque ripple	Medium	High	Medium
Tensile strength	Low	Medium	Medium
Size	2.3 L/KW	2.6 L/KW	1.8 L/KW
Control	Trapezoidal: DSP. Sinusoidal: vector control.	Switched: DSP. Synchronous: vector control.	Vector control
Efficiency	95.2%	93%	93.4%
Spinning losses	Static flux, non-removable	Removable by annulling flux	Removable by annulling flux
Rotor losses	None	Iron	Iron and copper
Specific power	High	Medium	Medium
Power	Medium & low	Medium & low	High

2.6.4.2.7. Electrical transmission topology

The integration of a MG unit into a FESS can be realised through three distinct approaches: fully integrated, partially integrated, and non-integrated, as depicted in Fig. 2-8.

Fully Integrated Design: In this configuration, the flywheel and MG are combined, with the flywheel being part of the MG mass. This design maximises the power and energy densities of the system while maintaining compactness. However, due to the vacuum containment needed for high-speed operation, cooling becomes a challenge as heat can only be dissipated via radiation, necessitating an effective cooling system. High sealing is achieved in this configuration, with the unit requiring only electrical connections [115]. An example of a fully integrated design is the "hub less" configuration, where the MG and bearings are incorporated directly into the flywheel rim, eliminating the need for a central shaft.

Partially Integrated Design: In this configuration, the flywheel and MG share the same shaft and are housed together, which enhances the power density and energy storage capabilities of the system. Nevertheless, a vacuum environment is necessary to minimise windage losses, particularly for high-speed FESS applications, which bring additional thermal management requirements. An application of this design with active magnetic bearings has been utilised in the UT-CEM project in a hybrid bus [199].

Non-Integrated Configuration: In this setup, the flywheel is connected to the MG through a detachable link, offering considerable flexibility in terms of energy and power storage capabilities. It is the simplest and largest of the three configurations and eliminates the need for a complex cooling system due to the absence of the need for a vacuum environment [115].

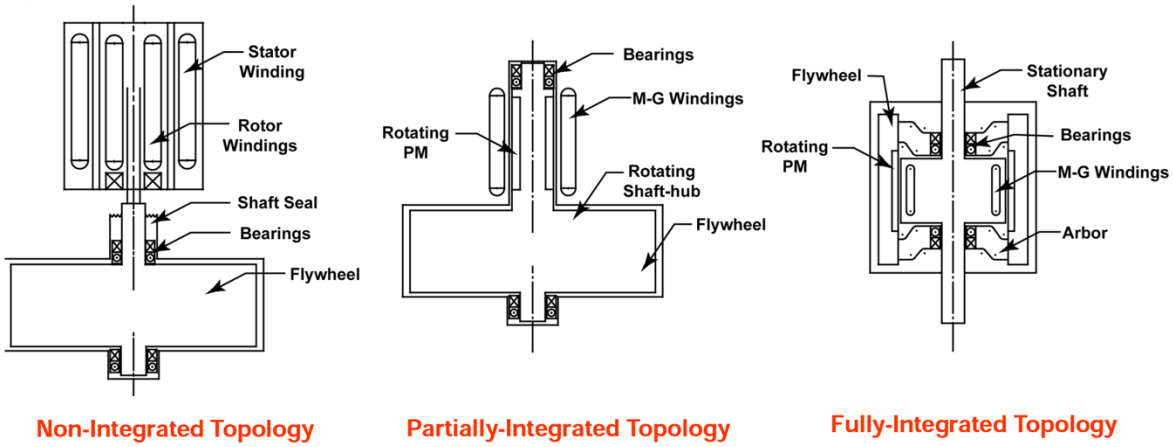

Fig. 2-8 Three different MG and FESS configurations [199]

2.6.5. Rotor Design

The efficacy of a FESS is significantly influenced by the careful selection of materials used and the optimisation of the flywheel geometry. The primary goal in flywheel design is to maximise specific energy storage, guided by the stress limits that the materials can withstand. Employing high-strength materials or composites allows for a reduction in mass while permitting higher rotational speeds, which

in turn, enhances the specific energy storage capacity [94]. Advanced composite materials, renowned for their directional strength and low density, facilitate the construction of rotors tailored for high-speed FESS applications. This advantage is particularly pronounced when using multi-rim composite rotors, where the number of rims, the material sequence, and the interference levels between rims, including their thicknesses, are strategically designed to boost energy capacity [200].

In contrast, metal flywheels, while simpler and less expensive to manufacture, generally operate at lower speeds. Although this limits their specific energy capacity, it reduces standby losses associated with components such as bearings and the electrical machine. These losses are proportional to speed, making metal flywheels more favourable in applications where low standby losses are required [194].

Considering the lifecycle, the cost-efficiency of energy storage technologies is crucial, with flywheels offering exceptional longevity. Although advanced composite flywheels may initially be less cost-competitive compared to battery storage solutions, they prove economical in medium to longer terms, with potential operational lifetimes extending over decades and cycle durability reaching 106 cycles, far exceeding that of conventional batteries [41].

Kale and Secanell [194] conducted an optimisation study on flywheel rotors manufactured from diverse metals and composites to ascertain the most suitable material based on system performance criteria. Their findings suggested that while composite rotors exhibited higher specific energy, metal rotors were more cost-effective in terms of energy storage. In situations where only tensile material failure was considered, composite rotors exhibited significantly lower specific energy than metallic counterparts, highlighting the critical role of material failure modes and other physical constraints. Further investigation into flywheel performance indicated that press-fitted, multi-rim composite rotors with strategically selected material combinations surpassed both single-rim composite and metal flywheels with respect to total and specific energy metrics.

Reviewing utility-scale flywheel storage solutions reveals a current production trend that balances the use of both composite and metal flywheels [194]. Composite materials enable high performance, but metal rotors remain appealing for their cost benefits and ease of manufacture. The impact of fatigue on various rotor types throughout their service life is a crucial consideration, as durability directly affects performance, making the choice of material a key determinant in the overall efficiency and utility of the FESS [194].

2.7. Limitations of FESS

2.7.1. Safety

Safety considerations are vital in the design and operation of flywheels, especially due to the potential hazards arising from premature system failure. Flywheels utilised for energy storage applications endure considerable centrifugal forces, particularly at rotational speeds approaching 10,000 rpm which is deemed relatively low. These forces increase proportional to angular velocity squared at speeds

ranging between 10,000 and 100,000 rpm. In the event of premature rotor failure, fragments could be ejected at high velocity. To mitigate such risks, flywheel housing is typically constructed of steel, with recommended thicknesses being doubled those used when operating within a low-pressure environment. Despite the infrequency of catastrophic failures, failure of high-speed flywheels made of composite materials is more common, while steel flywheels, which operate at lower speeds, tend to exhibit gradual failure, allowing for early detection before complete fracture [178].

In the United States, various safety-related research initiatives have been sponsored by organisations such as the Defence Advanced Research Projects Agency, the Metro Transit Authority of Houston (Texas), and NASA, which propose different strategies to enhance safety measures. A common approach to ensure safe operation involves setting the maximum operational speed well below the speed at which failure is anticipated [201]. Dynamic stress analysis and destructive spin tests are employed to ascertain the maximum permissible operational speed, with spin tests identifying the rate at which failure occurs. Stress variation analyses in relation to speed help establish the safety margin, and operational speeds are determined such that they remain well below the identified failure rate.

Another aspect of safety strategy involves safeguarding against material defects and cracks. Health monitoring sensors can be integrated within the flywheel system to monitor critical parameters, encompassing electronics, transmission, magnetic bearings, and the structural integrity of the flywheel system. These sensors, in conjunction with onboard computers, enable the system to execute an immediate shutdown in the event of a failure or when abnormal conditions are detected [202].

Effective containment solutions must balance the demands of low weight and cost while withstanding the forces of an impulsive flywheel rupture. An alternative strategy is to design the flywheel in such a way that mitigates the likelihood of catastrophic rotor failure modes. Currently, carbon fibre is the most widely used composite material in FESS due to its disintegration into fine particles upon failure, which, while creating high axial forces within the housing, behave more like a fluid and can reduce the impact of failure [203]. Table 2-9 lists potential failure triggers within a flywheel system along with their possible repercussions.

Hansen et al. [114] have explored the issue of FESS failure and proposed measures to mitigate it. Key design considerations for enhancing system safety include: implementing containment specifically tailored to the flywheel design, integrating instruments capable of early failure detection, designing for incremental failure that results in fewer, smaller fragments rather than the disintegration of the entire rotor, and allowing a larger margin between the operational stress levels and the material's ultimate strength, which can extend the lifespan of the system but may also increase its mass. The authors assert that the only viable automotive flywheel solution is one that guarantees containment without depending on devices or other measures under all anticipated conditions. Considering the need for cost-effective materials, the system and its parts may not undergo frequent checks, inspections, or monitoring. Therefore, the flywheel must not only be effectively contained; it should also be designed such that the angular deceleration rate of any fragments is sufficiently low to prevent the generation of dangerously

high torque levels that could compromise the housing. In the event of a crack reaching a critical size, metal-based flywheels typically fracture into three large pieces, requiring a robust housing capable of containing and absorbing the flywheel energy.

Table 2-9 Flywheel failure modes, reasons, and their consequences [203], [204]

Trigger	Reason	Initial Failure Mode	Consequences
Rotor shafts or housing break	Torsional or other stresses	Rotor imbalance, can fly off in the radial direction	▪ Projectiles bursting through the housing. ▪ Excessive noise. ▪ Excessive axial impulses penetrating the housing. ▪ Significant torsional loads on the housing. ▪ Large number of radial bending impulses on the housing.
Rotor cracks	circumferential stresses	Fragments break out, parts fly off in tangential and radial directions	▪ Projectiles bursting through the housing. ▪ Excessive noise. ▪ Excessive axial impulses penetrating the housing. ▪ Significant torsional loads on the housing. ▪ Large number of radial bending impulses on the housing.
Composite rotors form cracking or softening	Overheating	Fragments break out, parts fly off in tangential and radial directions	The rotor degrades into numerous small particles, resulting in an abrasive "pyro-plastic flow" and high hydrodynamic pressure, resulting in: 1. “Fluid” pressure cracks or deforms the housing. 2. "Fluid" flows along the housing, producing large impulses in the axial direction, lifting, or cracking the housing.

2.7.2. Gyroscopic Moment Effect

Gyroscopic effects can have detrimental impacts on vehicle handling and stability. A gyroscopic moment arises when the axis of a rotating flywheel is subject to rotation, and this axis is oriented perpendicularly to the rotor's axis of rotation. This situation leads to the generation of gyroscopic torque, influenced by the magnitude of torque, the angular velocity of the flywheel, and the rate at which the flywheel's axis is turning [205]. During vehicular manoeuvres such as cornering, or when traversing inclines or dips in the road, the vehicle can experience rotational forces around the cornering axis due to these gyroscopic interactions. McDonald [206] conducted comprehensive research into the issues posed by gyroscopic torque in vehicles equipped with flywheels, examining its influence on vehicle dynamics.

In the study of vehicle dynamics and the integration of FESS, the yaw angular velocity—rotation around the vehicle's vertical axis—is particularly significant. The orientation of the flywheel relative to the vehicle's axes can influence gyroscopic effects. When the flywheel's spin axis is transverse (perpendicular) to the vehicle's longitudinal axis, gyroscopic torques generated during yaw movements can affect the vehicle's roll behaviour. Mechanical transmission from the flywheel may be less suitable in scenarios where linear motion or motion along a different axis is preferred, due to the complexity and inefficiency of mechanically coupling motions across different axes. In such cases, electrical transmission methods offer more flexibility and efficiency.

Gyroscopic torque produced by the flywheel can resist roll motions, potentially improving vehicle stability by enhancing weight transfer characteristics during manoeuvres. However, according to McDonald's findings, the gyroscopic torques produced by the flywheel are typically insignificant compared to other forces and moments influencing vehicle dynamics. Dominant factors such as aerodynamic forces, tire interactions, and suspension characteristics have a more substantial impact on the vehicle's performance. Therefore, while gyroscopic effects exist, they generally have a minimal effect on the overall dynamics of the vehicle [206]. It is a question that needs attention, but it is not essential. As previously mentioned, it is of particular concern that the bearings can accept the subsequent loads to support the gyroscopic torque. Otaki [207] and McDonald [206] stated the fundamental equations of the gyro-dynamic forces. The flywheel's angular momentum is dependent on the flywheel's inertia and rotational speed. The angular momentum of a flywheel can be calculated by the following equation:

$$\mathbf{H} = \mathbf{J}\boldsymbol{\omega} \tag{2-1}$$

Where **J** is the flywheel inertia and **ω** is the flywheel rotational speed.

The most significant torque produced from a flywheel will be at the highest rotational speed since the flywheel inertia does not change. The torque applied on a flywheel can be calculated by the following expression:

$$\mathbf{T}_{\mathrm{ap}} = \frac{\mathrm{d}\mathbf{H}}{\mathrm{dt}} \tag{2-2}$$

The exerted reaction torque from the flywheel can be calculated by the following equation:

$$\mathbf{T}_r = -\mathbf{T}_{ap} = \frac{d\mathbf{H}}{dt} \quad (2\text{-}3)$$

When the vehicle manoeuvres, the rate of rotation on the flywheel is referred to as the precession rate (Ω). The precession rate affects the angular momentum, and the rate of change can be calculated by the following relationship:

$$\frac{d\mathbf{H}}{dt} = \mathbf{H} \times \boldsymbol{\Omega} \quad (2\text{-}4)$$

From Eq. 2-2 and 2-4 the reaction torque can be written as:

$$T_r = H\Omega \sin\theta \quad (2\text{-}5)$$

Where θ is the angle between the vectors shown in Fig. 2-9, the reaction torque is perpendicular to both the momentum and precession rate vectors.

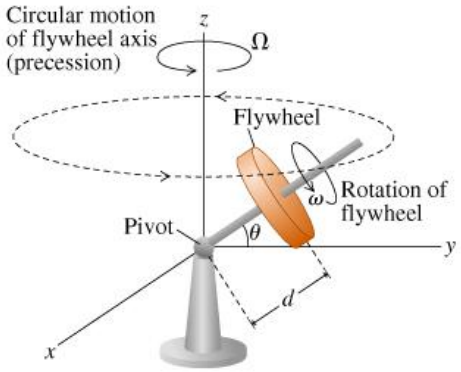

Fig. 2-9 The angle between the precession rate and angular momentum vectors [208]

The manoeuvres of the vehicle can be in three directions, with each having a different effect on the vehicle. Fig. 2-10 and Table 2-10 show the corresponding reaction torque to each direction.

Table 2-10 The flywheel orientation and their reaction torque sense [206]

Flywheel Orientation	**Effect on Pitch**	**Effect on Roll**	**Effect on Yaw**
Lateral (Side-to-Side Alignment)	No Effect	Increases Yaw	Decreases Roll
Longitudinal (Front-to-Back Alignment)	Decreases Yaw	No Effect	Increases Pitch
Vertical (Up-and-Down Alignment)	Increases Roll	Decreases Pitch	No Effect

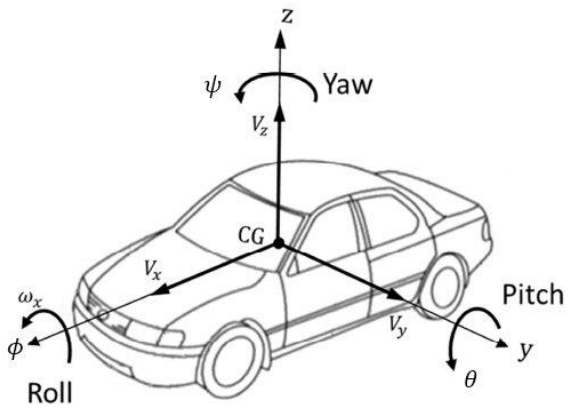

Fig. 2-10 vehicle manoeuvres and the corresponding reaction torque [209]

In conventional vehicles, the track width is typically narrower than the wheelbase, leading to a relatively small torque reaction to the vehicle pitch or yaw movements, with roll motions being insignificant under normal operating conditions. Research by Otaki [207] and McDonald [206] demonstrated that the gyroscopic reactions of flywheels within automobiles are relatively minor during regular driving. However, scenarios involving accidents must be thoroughly considered. Composite flywheels are often touted for their safety, since, upon failure, the material tends to shatter into dust-like particles, exerting pressure on the containment vessel more akin to a fluid than solid fragments. Simulating realistic catastrophic failures is a significant challenge in ensuring the safety of composite flywheels, as they are designed with high safety factors, making actual explosive failures at excessively high speeds unlikely. The methodology used in car crash analysis, which often involves dynamic finite element analysis corroborated by data from well-instrumented experiments, can be applied to the evaluation of flywheel containment in the event of a burst. It is crucial to establish standards that provide clear guidelines during the developmental phase to ensure that FESS used for automotive applications is safe [210].

The flywheel can be mounted on several gimbals to keep its axis of rotation fixed to the vehicle's motion. The mechanical transfer of power can be a fundamental design challenge with such an assembly. The two counter-rotating flywheels [211] are an alternative method for cancelling gyroscopic torques as shown in Fig. 2-11. In this configuration, the gyroscopic torque from each flywheel would counteract the gyroscopic torque produced by the other flywheel.

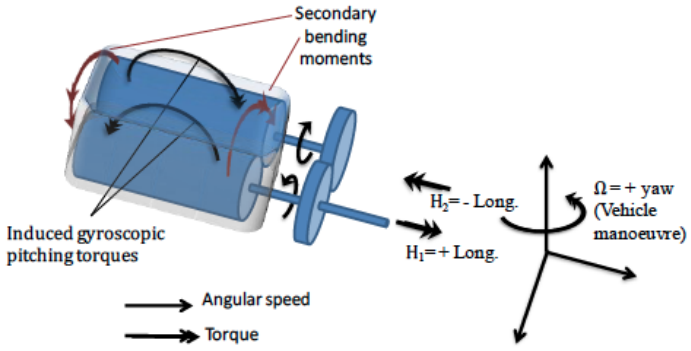

Fig. 2-11 The schematic diagram of counter-rotating flywheels [211]

2.8. Optimisation of FESS Standby Losses

The main drawback of FESS is the high mechanical losses, which originate from bearing and aerodynamic "windage" losses [101]. Bearing losses, which are influenced by the flywheel's mass and the choice of lubricant, tend to increase linearly as a function of flywheel speed. On the other hand, windage losses, which are due to friction between the rotor and the fluid within the housing, constitute a significant proportion of total losses, particularly in high-speed applications [212]. These losses not only contribute to increased self-discharge but also adversely affect the overall efficiency of FESS [84]. Windage losses result from the frictional interaction between the rotor and the fluid surrounding it, dissipating energy as heat. Mitigating these losses is essential for enhancing FESS performance [101]. With the high peripheral speeds, the frictional windage losses of a flywheel system become notably substantial. These losses occur due to both skin friction on the rotor's surface and the radial outward movement of air caused by the rotor's motion. This can lead to significant energy depletion and excessive heat generation, potentially causing the rotor to overheat [213]. Gurumurthy et al. [214] conducted experiments at atmospheric pressure and determined that mechanical losses, primarily from drag, were the major contributors to power losses in FESS, accounting for 72% of the total losses at high speeds.

Calculating windage loss is complex and is influenced by the skin friction coefficient, a parameter that is a function of the rotor radius ratio and Reynolds number [215]. For high-speed electric motors, several researchers have studied windage losses and presented methods to reduce them [216], such as those by Okada et al. [217], who demonstrated that shrouding the rotor could significantly decrease windage loss while preserving motor efficiency.

Computational Fluid Dynamics (CFD) has been utilised to model flow within the flywheel housing, aiming to develop ways to improve efficiency [215], [218]. Anderson [219] used commercial CFD software to analyse windage losses in high-speed motors, offering a method for designers to quickly assess the thermal impact of windage losses. Recent studies have combined CFD simulations with experimental data to advance the fundamental knowledge in this area [220], [221], [222], [223], [224]. Walton et al. [225] investigated the windage losses of a rotor supported by gas foil bearings, but they did not consider the fluid field's impact near the bearing journal. In the following section, the effects of various geometrical and operating conditions on FESS standby losses are discussed.

2.8.1. Airgap size

FESS optimisation involves careful consideration of various design parameters to minimise energy loss and enhance system performance. The intensity of the windage losses is a function of the flywheel rotational speed, airgap (annulus) size and operating pressure. The size of the airgap is an important factor when designing a FESS which is dependent on various parameters including flywheel speed and

expansion rate at high speeds. The rotation of an enclosed flywheel creates a complex flow within the FESS cavity, resulting in heat generation due to frictional losses. The flow characteristics are dependent on the flywheel speed, outer rim surface roughness, airgap size, and properties of the working fluid [226]. Couette and Taylor determined flow viscosity and flow stability in the annulus of two concentric cylinders, consequently, this type of flow is commonly referred to as Taylor-Couette flow. The stability of Taylor-Couette flow, which occurs between two concentric cylinders within the FESS, is a key factor in controlling windage losses. This type of flow is a well-studied phenomenon in fluid mechanics, particularly in applications such as FESS and electric motors, where both windage loss and heat transfer are critical considerations [222]. Previous studies have shown that by understanding and managing the parameters affecting the flow characteristics within the airgap, such as rotor speed and surface roughness, windage losses can be substantially reduced [227] [228].

In their pursuit of reducing windage losses, researchers such as Chirita [229] have explored design optimisations for flywheel components made from materials such as titanium alloys. Findings indicated that the flywheel outer diameter greatly impacts energy storage, more so than rim width and height. Similarly, Nakane [230] and Pfister [231] have proposed methods and models to lower windage losses in high-speed applications, reporting that certain configurations, such as the inclusion of rotor shrouds or adjusting the airgap size, can lead to improved torque and power efficiency.

The airgap size is a crucial design element, with small gaps defined by a gap-to-diameter ratio of less than 0.005 to 0.02 [225]. Larger airgaps have been extensively studied, particularly under atmospheric conditions, with findings highlighting the sensitivity of windage losses to airgap size [232]. Awad and Martin [233] investigated windage losses on both the disc and cylinder sides of pulse generator rotors. For the disc and cylinder sides, the skin friction coefficient is a function of the Taylor Number which is typically used to calculate the flow characteristics inside the annulus of concentric cylinders.

Windage losses are influenced by heat transfer within the FESS, and heat transfer within these systems is influenced significantly by Taylor-Couette flow. Gazley [234] was among the early researchers who examined the heat transfer in the annulus of concentric cylinders. Many researchers have studied heat transfer in the annulus of concentric cylinders both theoretically and experimentally. Becker and Kaye [235] studied heat transfer in concentric cylinder annuli without axial cross flow. Tachibana et al. [236] examined how airgap size affects electric motor heat generation and dissipation. In the annulus of high-speed electric motors, Howey et al. [237] examined how airgap size affects convective heat transfer of laminar and turbulent swirling air flows. The authors calculated surface convective heat transfer coefficients using non-dimensional parameters for the thermal modelling of radial-flux and axial-flux electrical machines.

2.8.2. Working Pressure

Research and development in the field of FESS have primarily concentrated on optimising the design of crucial components such as housing and rotors, given the substantial safety considerations involved due to the high rotational speeds these components endure [80]. Among these considerations, windage losses are significant, especially if the flywheel operates at atmospheric pressure [216]. To minimise such losses, FESS can operate at lower working pressures, medium to hard vacuum, to reduce aerodynamic losses due to drag [101]. However, this solution introduces increased system complexity and necessitates additional components such as vacuum pumps and cooling systems. The vacuum pump used in the system should use minimal energy so that it does not affect the overall efficiency of the system [178]. The power the vacuum pump uses to maintain the working pressure and the power needed to overcome drag is known as standby power. Standby power, along with the power needed to keep the flywheel rotor at a specific state of charge, is a crucial factor in determining the overall efficiency of the FESS [238], [239].

Establishing a medium to hard vacuum presents various challenges such as potential leaks, lubricant vaporisation at low pressures, and outgassing, where materials release trapped gases. These issues can lead to environmental contamination and a decline in the material's properties. Moreover, such an environment can lead to elevated flywheel temperatures due to diminished convective heat transfer, making it necessary to evaluate the trade-offs between reduced windage loss and the energy savings potential of the system [101]. A hermetically sealed flywheel containment can maintain a vacuum while minimising the need for continuous pump operation, thus preserving energy [240]. Asami et al. [238] have proposed a novel structure combining an aerodynamic step thrust bearing with a spiral-grooved viscous vacuum pump to reduce windage losses in high-speed motors.

Investigations by Liu et al. [241] into various vacuum levels show the impact on windage heating within a high-speed flywheel. An innovative approach to further reduce aerodynamic losses involves the use of a helium-air mixture, as studied by Suzuki et al. [242], who found that a 50% helium mixture could lower losses by 43%, with greater reductions at higher helium concentrations.

Analysis of mechanical and electrical losses, such as those by Skinner [243] on cylindrical composite rotor FESS, indicate that both flywheel speed and working pressure can influence mechanical losses. Similarly, Amiryar and Pullen [101] examined how different vacuum pressures and airgaps can affect windage and bearing losses, emphasising the significant role of design parameters on power losses. Complementing this, Anderson [219] used commercial CFD software to model windage loss in high-speed motors, providing valuable insights on mitigating thermal performance issues.

Ensuring a vacuum-tight seal is critical for maintaining the low-pressure environment within a FESS. Various seals, including mechanical, magnetic, and labyrinth seals, offer different advantages in terms of cost, reliability, and suitability for handling high-speed rotations [244] [215] [216]. The role of the

vacuum pump is also vital, with a variety of types available, each with specific benefits and suited for different vacuum levels and applications [218] [249].

FESSs often employ air or magnetic bearings to support the rotor, with each offering benefits in terms of friction reduction and operational longevity. While air bearings provide low-friction levitation with an extended lifespan, magnetic bearings are known for their high precision, though they come at a higher cost and complexity [250]. Integrating these bearings with the appropriate seals can help achieve the desired vacuum tightness and system durability [251].

2.8.3. Rotor Material

Metallic rotors represent a crucial subset of flywheel technology, using dense metals such as steel to store kinetic energy. Due to their robustness, metallic flywheels offer greater durability and cost-effectiveness compared to composite flywheels [227]. Their high density allows for a more compact energy storage solution, capable of storing substantial energy at lower rotational speeds. This inherent attribute means that metallic flywheels face lower centrifugal forces, which in turn simplifies the design requirements [100].

The relationship between the windage loss and the physical characteristics of flywheels is a critical consideration. Windage loss is heavily dependent on the flywheel diameter and velocity, scaling with the fifth power of diameter and the cube of velocity, as well as the 3/4 power of working pressure [242]. This principle dictates that for a given energy storage capacity, a composite flywheel, which typically operates at a higher peripheral speed than its metallic counterpart, requires a more substantial vacuum to mitigate losses.

The high-speed operation of flywheels, especially those made from composite materials, presents additional challenges. Increased rotational speeds can lead to significant frictional losses, which manifest as heat within the flywheel housing. For composite flywheels, which might include materials such as graphene composite rims, this heat can compromise the mechanical integrity of the material by softening the epoxy and reducing its tensile strength [252]. Similarly, the mechanical properties of a steel hub can be adversely affected by localised thermal stresses, leading to deformation, crack formation, and ultimately, the risk of premature failure [253]. Therefore, the implementation of a cooling system is imperative to manage the heat in these high-performance, non-vented systems, although this increases complexity and costs.

2.8.4. Slit Wall Design

The Taylor-Couette flow, which involves fluid motion between two rotating coaxial cylinders, has garnered significant attention from researchers due to its complex dynamics and applications in heat transfer enhancement [254]. The manipulation of cylinder surfaces through structures such as ribs and

slits has been a focal point of previous investigations to improve heat transfer efficiency [255]. Tsukahara et al. [256] examined how ribs on the rotor surface influence the frictional drag coefficient and pressure drag. They found that ribs increase pressure drag, but this is somewhat mitigated by the strong adverse pressure gradient caused by the Taylor vortices' in-flow motion. The overall resistance due to ribs is a factor of their orientation and spacing.

Investigations into heat transfer within grooved channels have shown varied results based on the groove designs. Karakas [257] reported on the heat transfer properties of the Taylor-Couette flow affected by longitudinal and oblique slits. Notably, slanting counterclockwise slits had better heat transfer capabilities compared to clockwise slits. Similarly, Hayase et al. [258] conducted numerical research on grooved channels within electric motors, reporting that inner grooved cylinders increase heat transfer more significantly than outer grooved cylinders.

Research by Gokul and Deepu [259] indicated that helical fins outperform longitudinal fins in terms of enhancing heat transfer and thermal performance due to the increased vorticity and turbulence intensity they induce. Tzeng et al. [260] demonstrated that the addition of axial ribs to rotating machines facilitates heat transfer, a finding that has practical implications for the design of high-speed rotating machinery. Kim et al. [261] explored the effects of airgap fans on the cooling of induction motors. They found significant improvements in heat transfer coefficients at the winding surface and airgap, leading to enhanced total winding cooling performance.

Liu et al. [262] provided a numerical analysis of turbulent Taylor-Couette flow within a slit model. Their results highlighted the relationship between velocity in the slit area and wall shear force, noting a contrasting behaviour in heat flux. Building upon this, Liu et al. [263] investigated the role of slit number and width on flow distribution and heat transfer in an annulus. Their findings suggested that the number and width of slits positively affect convection between the inner and outer walls, thus augmenting heat transfer. The study also revealed that the Reynolds number significantly influences the slit wall structure, affecting both flow field and heat transfer, with slit width playing a more pivotal role than the number of slits. In this research, Liu et al. [264] focused on the role of axial slit walls in Taylor-Couette flow, adjusting the rotating Reynolds number and applying a negative temperature gradient. Their comprehensive study, which tested six different models with up to 18 slits, found that these slits improved the Taylor vortex flow and minimised its azimuthal fluctuation. Significantly, the study concluded that more slits and higher Reynolds numbers facilitate better heat transfer and accelerate flow transition across both laminar and turbulent regimes.

Similarly, Sun et al. [254] employed large eddy simulations to assess the impact of slit structure on flow and heat transfer. By comparing slits of various shapes, including trapezoidal, rectangular, and elliptical, they determined that the elliptical model was superior. This shape not only prevented backflow but also maximised velocity-temperature interaction and energy utilisation, as evidenced by the lowest entropy generation and optimal field synergy angle. Sommerer and Lauriat [265] explored heat transfer in annular gaps with rectangular slits on the outer cylinder, underlining the significant influence of slit

quantity on heat transfer enhancement. Zhu et al. [266], through direct numerical simulation, found that V-shaped slits impacted the flow field structure only when the slit depth exceeded the boundary layer thickness. Liu et al. [267] compared the effects of different slit wall cross-sections; triangle, rectangle, and trapezium, on turbulent flow and heat transfer. The trapezoidal cross-section was particularly effective, promoting the merging of vortices within the annular and slit areas, thereby intensifying fluid mixing, which has implications for the design of rotating machinery. The geometry of grooves also plays a pivotal role, as studied by Bilen et al. [268], who examined how various groove geometries affect heat transfer and pressure drop. Lorenzini-Gutierrez et al. [269] and Liu et al. [270] further contributed to this area by investigating the benefits of curved flow deflectors and rounded axial grooves, respectively. The latter research work concluded that rounded grooves significantly reduce pressure loss compared to square grooves.

In a similar vein, Joo and Kim [271] sought to optimise the shape of grooved tubes, particularly focusing on natural convection in vertical orientations. The optimisation of tube shapes is vital for improving heat transfer efficiency in various applications. Tachibana and Fukui [236] examined the influence of grooves on the critical Taylor number, which determines the stability threshold of the onset of Taylor vortices. Their research demonstrated that grooved layouts can effectively delay the appearance of these vortices, raising the critical Taylor number substantially.

Eiamsa-ard and Promvonge [272] provided evidence that all groove shapes significantly elevate the heat transfer rate in comparison to a smooth channel. Nouri-Borujerdi and Nakhchi [273] studied fluid flow and heat transfer in grooved channels, discovering that grooves substantially increased the average Nusselt number and overall heat transfer efficiency. They noted the Taylor number as a pivotal factor for enhancing heat transfer, with the wall temperature exerting the least influence. Their study also considered the buoyancy effects within rotating grooved channels, which positively contributed to heat transfer coefficients. Furthermore, Nouri-Borujerdi and Nakhchi [274] employed the response surface methodology to fine-tune the design parameters of annular flow with an exterior slit cylinder and a revolving inner cylinder. Their work underscored the slit aspect ratio (b/c) as having a more pronounced effect on heat transfer enhancement than the number of slits (N), suggesting that optimal slit geometry can be identified to maximise heat transfer in Taylor-Couette flows.

Complementing these findings, Sun et al. [255] also utilised the response surface methodology to optimise the influence of slit number and width on Taylor-Couette flow. Their research highlighted that higher Reynolds numbers lead to increased heat transfer, mainly attributed to intensified jet flow and temperature gradients near the inner cylinder wall. The study concluded that while the slit width and Reynolds number are significant factors affecting heat transfer, the slit number and Prandtl number play a lesser role. They achieved a 12.42% improvement in heat transfer capacity at a Reynolds number of 4,652. The role of slit walls in the outer cylinder of rotating machinery is crucial for enhancing fluid mixing and achieving a uniform temperature distribution. Liu et al. [275] specifically examined the influence of the slit wall depth-to-width ratio on flow distribution and heat transfer. Their findings

indicated a strong correlation between the number of slits and heat transfer enhancement, providing insights into the structural design of rotating machines.

This collection of studies contributes to a better understanding of how changes to the physical geometry of the housing within the airgap can significantly advance heat transfer capabilities and reduce windage losses, a critical factor affecting FESS efficiency and performance.

2.8.5. Knowledge Gap

The review of existing literature reveals that a significant barrier to the widespread adoption of FESS is the need to limit standby losses. These losses are a critical factor in achieving an optimal FESS configuration and significantly affect the system efficiency. Despite numerous improvements in FESS design and optimisation, standby losses continue to pose a challenge, affecting the system's performance and the ability to conserve energy efficiently. Addressing this issue is vital for the integration of FESS in various sectors, including renewable energy storage, automotive, aerospace, and defence, all of which demand high-reliability and efficient energy storage solutions.

While research on FESS standby and operational losses has been conducted, a knowledge gap remains regarding effective loss reduction strategies. Exploring methods to minimise aerodynamic losses (windage losses), either through the application of low-friction designs or by minimising aerodynamic drag, could significantly enhance FESS efficiency. This is supported by the keyword analysis from the Web of Science search engine, which demonstrates a lack of focus on "losses" within the FESS field, as illustrated in Fig. 2-12. Most prior research has concentrated on FESS design, optimisation, control, and bearings. Although optimisation is a well-investigated topic, the statistical optimisation of FESS has not been studied.

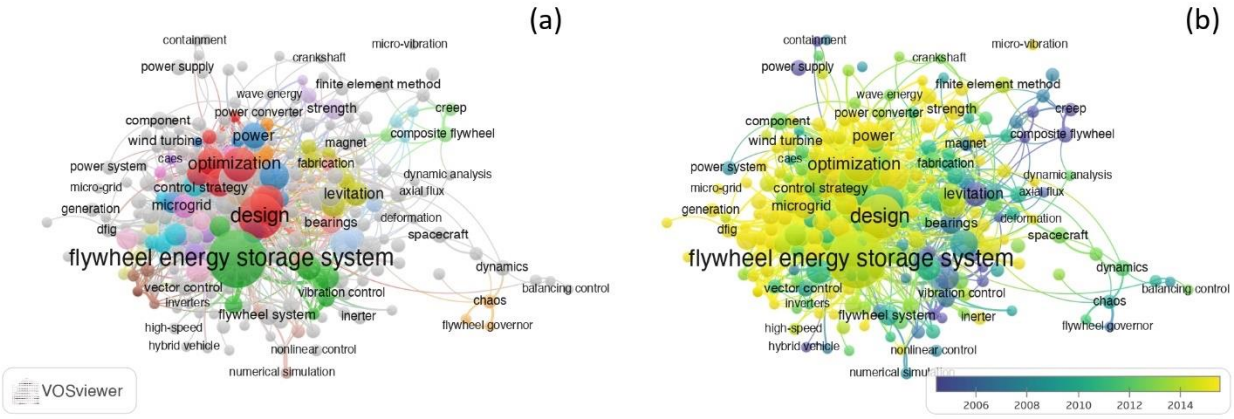

Fig. 2-12 Analysis of the keywords "Flywheel energy storage" from the Web of Science in VOS viewer. The search yielded 2241 papers as of May 2024. (a) The recurring topics are design, optimisation, control, power, etc. Losses are not a recurring topic. (b) The time distribution shows that composite flywheel and vibration control are among the oldest topics, whereas design and optimisation are among the newest

This study aims to fill the existing research gap regarding flow dynamics within FESS, especially under partial vacuum conditions. Previous CFD studies have predominantly focused on high-speed electric machines in atmospheric conditions, leaving a research gap in the thermal behaviour of FESS. Moreover, many CFD analyses have relied on overly simplistic models that consider only the airgap, neglecting the impact of the rotor and housing.

The literature has extensively explored the influence of the radial airgap between the flywheel and its housing; however, there is a lack of investigation into the effects of the axial airgap. Additionally, the surface roughness of the flywheel and housing and its impact on system performance has not been examined. This research delves into how design parameters such as airgap size, rotational speed, and surface roughness affect heat transfer and windage losses in FESS. It proposes a complete optimisation of these variables to enhance FESS efficiency. Analysis of Variance (ANOVA) is employed to determine the significance of these factors and their interplay, with the goal of identifying optimal design configurations.

While prior studies have acknowledged the benefits of employing a vacuum within FESS to reduce windage losses, the specific impact of vacuum pumps on standby power consumption has not been explored. This study also investigates optimal design parameters that minimise standby power in FESS, using ANOVA to assess the influence of airgap size and working pressure. CFD modelling provides an in-depth analysis of how these factors correlate with standby power requirements. Although previous research considered alternative gases to air for windage loss reduction, a comprehensive study investigating the effects of different working fluids is not available. This study introduces a novel strategy for FESS optimisation, leveraging a modified Taguchi method in conjunction with CFD simulations. It examines the synergistic effects of various parameters including radial and axial airgap sizes, rotational velocity, and working pressure using different gases to determine the optimal conditions for maximum FESS efficiency.

The integration of slit designs in the housing, known to boost heat transfer, is another area existing literature previously addressed. Although slit designs are acknowledged for their thermal management benefits, their specific role in optimising FESS performance remains uncharted territory. This study assesses the potential of incorporating slit walls within the FESS casing as a means to minimise windage losses. Various slit configurations, including rectangular and trapezoidal shapes, are examined to determine their effect on windage losses and heat transfer performance. The research evaluates five principal parameters through Response Surface Methodology (RSM): working pressure, slit geometry, base length-to-height ratio, and slit wall configuration and direction, employing numerical simulations to analyse the impact of these slit geometries on the flow field, heat transfer, and windage losses.

2.9. Summary

The literature review within this chapter began by exploring various energy recovery systems, emphasising the potential of flywheel-based KERS to enhance fuel efficiency and reduce emissions in vehicles. Despite the promise of such systems, their integration into mass-produced vehicles has been limited due to insufficient research on their optimisation for different vehicular applications.

The chapter proceeded to detail the applications of FESS across different sectors such as transportation, grid-connected power management, and industrial power management, demonstrating the versatility of the technology. It also delved into the specific use of FESS in different vehicle powertrains, including ICE-based and hybrid electric vehicles, as well as purely EVs.

A critical analysis of FESS components followed, covering bearings, control systems, housing, and transmission types. These components are essential for the FESS's functional integrity and directly influence its performance.

Subsequently, the chapter identified the main limitation of current FESS technology, standby losses, with a particular focus on windage losses. Various factors influencing these losses, such as airgap size, working pressure, and rotor material and design, were examined to assess their role.

The summary concludes by addressing the gap in the existing literature, particularly the lack of comprehensive studies on flow analysis within FESS. The chapter sets the stage for this research to bridge the gap by proposing a model that adjusts design parameters to optimise the FESS for various applications, with a focus on reducing standby losses through innovative design solutions.

Chapter 3. Methodology

3.1. Research Design

The two traditional approaches in the study of aerodynamics are the experimental and analytical methods. These are often referred to as Experimental Fluid Dynamics (EFD) and Analytical Fluid Dynamics (AFD). In EFD, a common approach involves constructing a prototype of the system being examined and situating it within a suitable testing facility equipped with suitable equipment to measure properties of interest such as temperature and pressure. The experimental method has its own set of advantages and disadvantages [276]. One of the major drawbacks of this approach is the significant amount of time and resources required. Moreover, potential flaws in the experimental setup or measurement techniques could arise such as equipment malfunction, calibration issues, and human error. Another critical issue is the accuracy of findings using scaled models; if the prototype is not properly scaled or the system performance is sensitive to size, it might fail to accurately represent the actual physical phenomenon. Having said that, the primary advantage of EFD is its ability to replicate the system characteristics under real operating conditions with high fidelity and minimal simplifications and/or approximation.

On the other hand, AFD involves attempting to solve the mathematical equations that govern the physical phenomenon under investigation. These analytical solutions represent the numerical solution to the governing equations. They can be derived through mathematical manipulations, provided that both the physics and the governing equations are relatively straightforward. AFD presents its own set of advantages and disadvantages [277]. Its primary advantage lies in its ability to yield precise solutions to the governing equations, thereby eliminating calculation errors. However, its major limitation is its applicability, it is only feasible for relatively simple systems. When faced with highly complex equations, there is no specific method available for solving them [278].

In addressing real-world industrial challenges, the experimental and analytical approaches often prove difficult due to constraints such as cost, time, or necessary simplifications. Consequently, within the engineering community, a "third approach," commonly referred to as "Computational Fluid Dynamics" (CFD), has gained prominence. CFD represents a methodology that can significantly reduce experimental costs and timelines while avoiding extensive approximation of governing equations. However, it is crucial to recognise that CFD is not a replacement for experimental or analytical methods. Instead, it is an approximation approach to real-world problems, potentially containing various errors, including discretisation errors, truncation errors, and algorithmic errors [279].

CFD model validation is essential to confirm the accuracy of the numerical results, either against experimental data, analytical data, or a combination of both. This validation step is especially vital during the preliminary design phase, where numerous initial designs are assessed. After narrowing down to a few designs, experiments can be conducted on these selected few to evaluate their

performance and confirm the CFD results. This approach noticeably reduces the cost and time involved in assessing all preliminary designs [280].

CFD is increasingly becoming a crucial tool in virtual engineering, as well as a significant research instrument in some physical sciences. As numerical solution methods and computer technologies advance, numerical modelling of complex geometries has become more feasible [281]. The benefits of employing CFD in the design optimisation of FESS, as opposed to relying solely on experimental testing, are listed in Table 3-1.

Table 3-1 The advantages of using CFD for FESS optimisation

Reduced development costs	▪ Traditional physical experiments for investigating the effects of various parameters can be very expensive. ▪ CFD simulations are relatively cost-effective, offering the flexibility to modify studied parameters without significant additional costs.
Rapid evaluation of design variations	▪ CFD simulations can be completed swiftly, making it ideal for time-sensitive projects. ▪ This rapid turnaround enables the integration of engineering data early in the design process, facilitating more informed decisions.
Comprehensive information	▪ Physical experiments are often limited in their data extraction capabilities, restricted to locations where gauges and sensors are placed. ▪ CFD allows for a thorough investigation of any location within the domain, providing detailed information about thermal and flow parameters.
Simulating various conditions	▪ Experimental testing of fluid flow within concentric cylinders, particularly at high rotational speeds, presents considerable challenges. ▪ CFD enables the exploration of diverse physical conditions, some of which may be difficult to replicate in an experimental setup.

This work will utilise the CFD approach to investigate the performance of FESS primarily due to its advantages over EFD and AFD methods. CFD offers a balanced approach, combining cost-effectiveness, speed, comprehensive data analysis, and the ability to simulate a wide range of

conditions. These factors make it a vital tool in the design and optimisation of FESS, complementing but reducing the reliance on traditional experimental and analytical methods.

3.2. Methodology

The methodology adopted for the FESS optimisation in the study is presented in Fig. 3-1. The process begins with the definition of objectives, where the main focus is on identifying metrics for assessing the aerodynamic performance. This foundational step sets the stage for the entire research, ensuring that the goals are clear and measurable. Following this, a thorough literature review is conducted to critically evaluate the previous studies, aiming to understand the current state of knowledge in the field. This step is crucial as it helps identify the influential factors that will guide the subsequent stages of the research, highlighting areas that this research intends to investigate further. Each step in the flowchart will be discussed in detail in this chapter.

The next step in the proposed methodology involves preliminary CFD analysis, conducting preliminary simulations to validate the CFD model against experimental data. The accuracy and reliability of the CFD model are vital, as they form the basis for the main CFD simulations. This validation step ensures that the simulations will provide meaningful and accurate information on the FESS system characteristics. The CFD simulation process entails several steps: pre-processing, which includes geometry and mesh generation; setting boundary conditions; selecting appropriate solver models; and solving the model. A key aspect of this process is the iterative nature of running simulations and checking if the solution has converged, otherwise necessary adjustments are made until the solution converges. Once the solution is converged, the methodology moves to post-processing. This involves extracting contours, vectors, residuals, and other relevant parameters of interest from the CFD results. The data extracted at this stage is critical for understanding the aerodynamic performance of the system and guides the optimisation strategy.

The Design of Experiments (DoE) is another significant phase. Here, the appropriate DoE method is chosen, and relevant factors and levels are selected for the simulations. This systematic approach is essential for exploring the design space comprehensively and efficiently. In the data analysis phase, statistical analysis of the results is conducted to identify the main effects and interactions between the factors. This analysis is pivotal in understanding how different variables influence the performance and efficiency of FESSs.

The final phase of the research is the optimisation stage, where optimum design parameters are determined and reported. This phase represents the conclusion of the study, integrating findings from all preceding stages to propose the most efficient design. Once the optimisation phase is completed, the resultant design undergoes a re-evaluation through the same steps to further enhance the aerodynamic performance of the system. Once the optimisation is deemed conclusive, when no further improvements are feasible, the data from this stage is adopted as the optimum design parameters. Each step in this

methodology is critical, contributing to a comprehensive understanding of the aerodynamic performance of FESSs. The structured approach ensures that the research is conducted in a systematic and scientifically rigorous manner, leading to findings that are both reliable and impactful in the field.

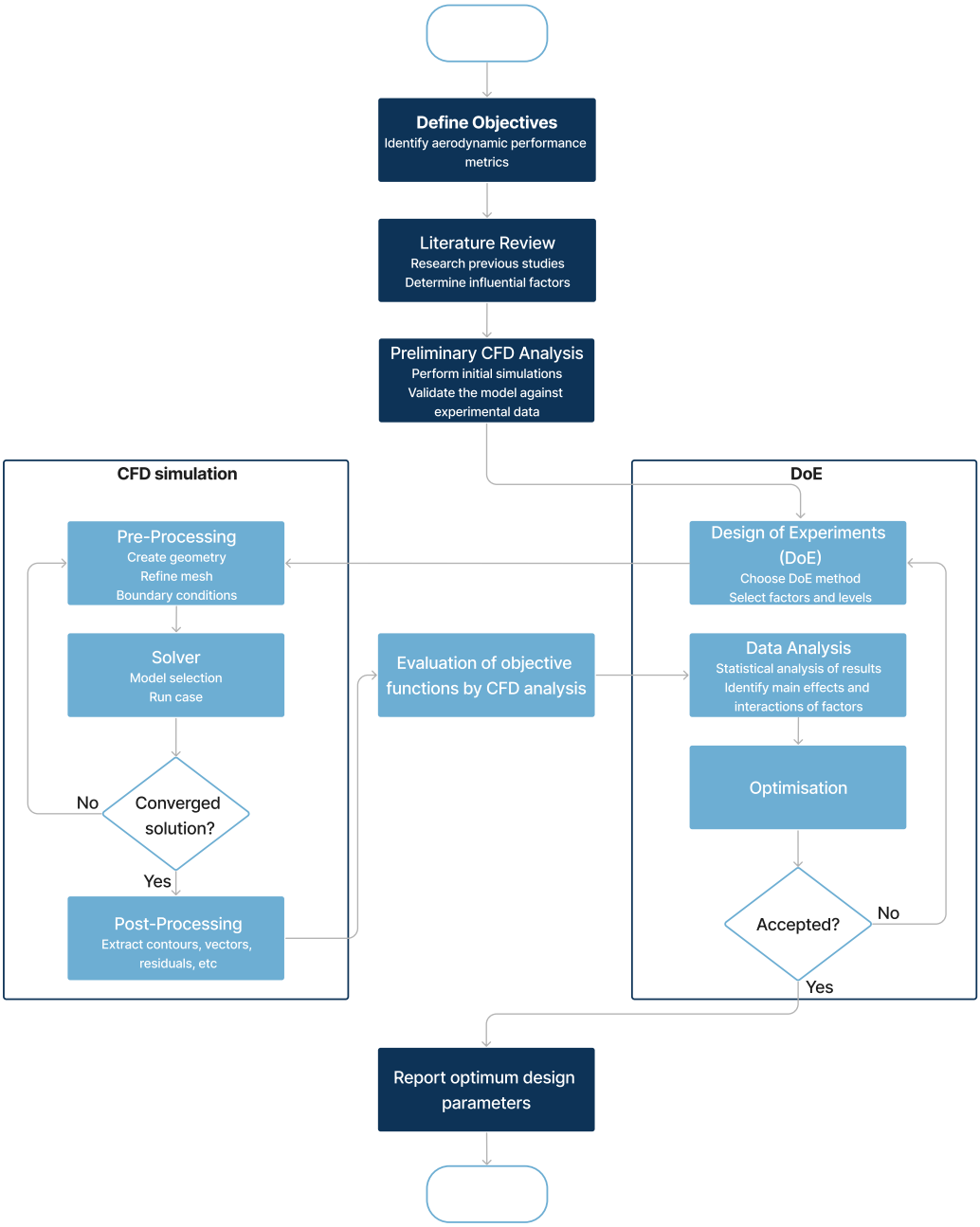

Fig. 3-1 Research framework

This chapter outlines the methodology employed in this research, beginning with the calculation of standby losses in FESSs, followed by an overview of the fluid flow governing equations. A critical aspect of this study involves detailed understanding of the parameters affecting fluid motion within the flywheel housing and how these parameters can be studied using CFD simulations. In this context, the work discusses and justifies the assumptions made and the methods used for CFD modelling of FESSs. This includes an in-depth examination of turbulence modelling to identify the most effective model for

the numerical simulation of Taylor-Couette flow. Following this, the work will present the process of validating the CFD model against experimental data. Finally, it will address the design criteria applicable to FESSs, detailing the considerations and parameters essential for the development of an efficient and reliable flywheel-based energy storage systems.

3.3. Design of Experiment

The integration of CFD simulation with the Design of Experiments (DoE) has gained considerable attention [282]. One significant advantage of combining CFD with DoE is the systematic understanding it provides about the interplay between design and operational variables, and their collective impact on the entire system [283]. This approach has been successfully implemented across various engineering disciplines. However, there is a notable gap in the literature regarding the incorporation of CFD and DoE for the analysis of FESSs. Additionally, efforts to apply CFD with DoE for multi-objective optimisation of FESSs are yet to be explored.

DoE is a structured method aimed at discerning the relationships between input and output variables to analyse factors influencing minimisation, maximisation, and trade-offs in a given problem. It is particularly effective in examining the influence of individual variables on the overall system response, enabling the collection of substantial information while minimising the number of simulations required. Typically, a set of design points is established for simulation evaluations [284]. In this framework, design variables are termed “factors” and the specific values assigned to them are known as “levels”. These factors have lower and upper bounds, forming a hypercube. Their numerical stability can be enhanced by scaling within the range of +1 to -1. Statistical methods such as regression analysis and Analysis of Variance (ANOVA) are then employed to determine the extent of the variables' influence on the response. DoE serves dual purposes; it can be used for screening design variables to assess their impact on a response parameter or as a means to identify an optimal starting point for a design optimisation algorithm [285]. The DoE methodology is applicable not only to physical processes but also to computer simulation models [286].

DoE is a statistical methodology that incorporates regression analysis and is applicable across a diverse array of scenarios. The commonly used design types include [287]:

- Comparison: This involves using one factor among several factors to compare against to determine the optimal choice.
- Variable Screening: This refers to employing two-level factorial designs to identify significant factors among a multitude of variables that influence the performance of a system, process, or product.
- Transfer Function Identification: This process involves determining the relationship between key input variables and the target output variable(s). This relationship is then used to further explore the performance of the system, process, or product using a transfer function.

- System Optimisation: The transfer function is employed to optimise the system by adjusting variables to their optimal settings, thereby enhancing system, process, or product performance.
- Robust Design: This approach focuses on minimising variation in a system, process, or product while accounting for underlying causes. It aims to make a system resistant to the effects of noise, including environmental and uncontrollable factors.

The following are a set of comprehensive and practical steps and guidelines for effectively planning and executing DoE [288]:

- State the Objective: Compile the objectives to be examined.
- Response Variable: Define the measurable outcome(s) of the simulation based on the objectives.
- Identify Factors and Levels: Select independent variables that could cause changes in the response variable.
- Determine The Design: Choose the type of design needed, such as a screening design for identifying significant factors, or a factor-response function for optimisation, and decide the number of test samples required.
- Conduct Simulations: Utilise a design matrix to plan and conduct simulations.
- Data Analysis: Employ statistical techniques, such as regression and ANOVA, to analyse data.
- Practical Implications and Suggestions: Include a visual depiction of the findings and verification of the results.

Following the principles of DoE, several statistical and optimisation methods are instrumental in analysing and interpreting simulation results in CFD. Among these methods, ANOVA, the Taguchi method, and Response Surface Methodology (RSM) are particularly noteworthy, each offering unique advantages and suited to different stages of the simulation and optimisation process [285].

ANOVA is a statistical technique used to determine the significance of different factors and their interactions on a response variable. By partitioning the total variation observed in the simulation data into components attributable to each factor and random error, ANOVA identifies which variables have a statistically significant effect on the outcome. In CFD simulations, ANOVA is particularly useful for screening design variables and simplifying models by focusing on the most influential factors. This allows researchers to allocate computational resources more efficiently and improve the reliability of the simulation results [286].

The Taguchi method is a robust design approach that employs orthogonal arrays to systematically plan experiments. This technique reduces the number of simulations required by strategically selecting combinations of factor levels, ensuring that essential information about main effects and interactions is captured efficiently. In the context of CFD simulations, the Taguchi method is advantageous during preliminary studies where the design space is extensive, and conducting a full factorial experiment is impractical due to resource constraints. By focusing on robustness against variability and optimising

multiple performance characteristics simultaneously, the Taguchi method enhances the reliability and efficiency of the design process [287].

RSM involves creating an approximate mathematical model that represents the relationship between input variables and the response. This model, often a polynomial equation, serves as a surrogate for the actual simulation model, allowing for exploration of the design space and identification of optimal conditions with fewer computational resources. In CFD simulations, RSM is utilised for developing predictive models of aerodynamic performance, facilitating a deeper understanding of complex relationships between variables. It is particularly useful when the objective is to optimise design parameters to maximise or minimise a response, such as reducing windage losses or enhancing energy efficiency [287].

The main differences among ANOVA, the Taguchi method, and RSM lie in their purposes and applications within the CFD simulation process. ANOVA is primarily used after experiments have been conducted to identify significant factors, making it ideal for factor screening and model simplification. The Taguchi method is employed during the experimental design phase to efficiently study a large number of variables with a limited number of simulations, emphasising robustness and efficiency. RSM, on the other hand, is best suited for detailed modelling and optimisation after significant factors have been identified, involving both the design and analysis of experiments to develop a predictive model [288].

3.4. Computational Fluid Dynamics

CFD codes are built upon numerical algorithms capable of solving fluid flow problems. Commercial CFD packages integrate user interfaces, allowing users to set/define problem parameters and retrieve specific data sets from results. This integration ensures easy access to solvers and enhances user efficiency [289]. CFD codes are typically composed of three primary components:

1. Pre-processing
2. Solver
3. Post-processing

The pre-processor consists of functions that assist users in defining flow parameters, converting these parameters into a format suitable for the solver. This stage involves various operations. The problem domain and geometry represent the study area and the geometrical configuration. Grid generation divides the domain into smaller, non-overlapping sub-domains. It also entails the determination of physical and chemical phenomena to be modelled, setting fluid characteristics and establishing appropriate boundary conditions for cells adjacent to or in contact with the domain boundary. The solution accuracy in CFD largely depends on the grid cell count, determined during pre-processing [289]. Generally, a higher cell count in the fluid flow domain translates to greater accuracy. The model accuracy and computational costs are directly related to the number of cells in the grid. Thus, the overall

accuracy of the model is primarily established during the pre-processing stage. Typically, half the time allocated to a CFD project is spent on defining the problem domain and generating a grid, aiming to achieve an optimal balance between accuracy and computational efficiency [290].

In the solver step, three primary numerical solution techniques are predominantly utilised: finite difference, finite element, and spectral methods [291]. The solver, a core component of CFD, typically employs a numerical algorithm that encompasses several operations:

1. Estimation of Unknown Flow Variables: This involves using simple functions to approximate unfamiliar flow variables.
2. Discretisation: This process substitutes the approximations into the governing flow equations, followed by mathematical manipulations to achieve discretisation.
3. Resolution of Algebraic Equations: Solving the resulting algebraic equations to find the flow variables.

The post-processor plays a crucial role in presenting the results to the user in a clear and comprehensible manner. Modern CFD software packages include a wide array of analytical tools to aid engineers with post-processing. These tools feature various functionalities, including geometry visualisation, creation of 2D and 3D surface plots, particle tracking, contour plots, and animations, as well as vector and streamline plots [292].

3.4.1. Governing Equations

The governing equations utilised in CFD codes are derived from the fundamental laws of fluid mechanics, namely the conservation of energy, momentum, and mass. These equations are presented in a differential form, having been derived by considering an infinitesimal fixed control volume. Due to their nature, as nonlinear partial differential equations, the differential analysis of fluid flow and heat transfer in FESSs can only be conducted numerically using a CFD code [293]. In a CFD study of a FESS, the domain is created and subsequently divided into computational cells and nodes. Following mesh generation, the governing equations are numerically discretised into a system of non-linear algebraic equations using the finite volume method. These equations are primarily used to compute the fluid density, velocity field, temperature field, pressure field, and internal energy of the system [294].

For thermal fluid analysis of a FESS, the governing equations are coupled. The temperature equation equates to the energy equation, while the density equation corresponds to the continuity equation. Variations in the density of the flow field, influenced by heat transfer, are dependent on temperature changes. In thermodynamics, the relationships between state variables in thermodynamic equilibrium are articulated through an equation of state. The fluid density is calculated using the ideal gas law given by the following expression [294]:

$$\rho = \frac{p}{RT} \tag{3-1}$$

Where *p* is the pressure, *T* is the temperature and *R* is the ideal gas constant. The equation of state serves as a pivotal link, connecting the energy equation with the continuity and momentum equations. To determine the resulting velocity field that follows the principle of mass conservation, a pressure-velocity coupling algorithm is employed. The resolution of the discrete linear system is achieved through an iterative method. Key elements such as the flow regime, boundary conditions, and fluid properties are accurately defined within the CFD solver. The simulation initiates with predetermined initial conditions and progresses until the solution converges [295].

3.4.1.1. Continuity Equation

The mass conservation equation, which is also referred to as continuity equations, presents the rate of change of mass in a fluid element which is given by the following relationship [294]:

$$\frac{\partial \rho}{\partial t} + \nabla . \rho \, \mathbf{v} = 0 \tag{3-2}$$

Where **v** is the velocity vector. The equation can be simplified for steady flow as [294]:

$$\nabla . \rho \, \mathbf{v} = 0 \tag{3-3}$$

The equation can be written in detailed form as follows [294]:

$$\frac{\partial \rho}{\partial t} + \frac{\partial (\rho u)}{\partial x} + \frac{\partial (\rho v)}{\partial y} + \frac{\partial (\rho w)}{\partial z} = 0 \tag{3-4}$$

3.4.1.2. Navier-Stokes Equation

The rate of change of momentum of a fluid particle, according to Newton's second law, is equal to the sum of the forces acting on the fluid particle. The Newton's second law is given by the following equation [293]:

$$Force = Mass \times Acceleration \tag{3-5}$$

In vector notation, the general momentum conservation equation is presented in the following form [294]:

$$\frac{D(\rho \mathbf{v})}{Dt} = -\nabla p + \nabla \cdot \tau_{ij} + \rho \boldsymbol{g} \tag{3-6}$$

Where ∇p is the pressure force, $\nabla \cdot \tau_{ij}$ is the viscous force, and $\rho \boldsymbol{g}$ is the gravitational force. Viscosity is caused by viscous stress components acting on the fluid element. The term *DV/Dt* refers to the fluid particle acceleration, which can be divided into local and convective acceleration, and describes the rate of change of the vector quantity when subjected to a space-and-time-dependent velocity field [294].

$$\frac{D\mathbf{v}}{Dt} = \frac{\partial \mathbf{v}}{\partial t} + u\frac{\partial \mathbf{v}}{\partial x} + v\frac{\partial \mathbf{v}}{\partial y} + w\frac{\partial \mathbf{v}}{\partial z} = \frac{\partial \mathbf{v}}{\partial t} + \mathbf{v} \cdot \nabla \mathbf{v} \tag{3-7}$$

Given that the fluid between the flywheel rotor and housing exhibits Newtonian behaviour, the equations outlined in this chapter focus on the linear relationship between the velocity gradient, which is perpendicular to the direction of shear, and the shear stress. For steady flow with constant viscosity the following equation applies [295]:

$$\mathbf{v} \cdot \nabla \rho\, \mathbf{v} = -\nabla \rho + \mu \nabla^2\, \mathbf{v} + \rho \boldsymbol{g} \quad (3\text{-}8)$$

For air, the gravitational term $\rho \boldsymbol{g}$ can be neglected. The momentum equation can be written in more detail based on the momentum direction, where the X-momentum, Y-momentum and Z-momentum can be calculated by the following relationships, respectively [294].

$$\frac{\partial(\rho u)}{\partial t} + \frac{\partial(\rho u^2)}{\partial x} + \frac{\partial(\rho uv)}{\partial y} + \frac{\partial(\rho uw)}{\partial z} = -\frac{\partial p}{\partial x} + \frac{1}{Re}\left[\frac{\partial \tau_{xx}}{\partial x} + \frac{\partial \tau_{xy}}{\partial y} + \frac{\partial \tau_{xz}}{\partial z}\right] \quad (3\text{-}9)$$

$$\frac{\partial(\rho v)}{\partial t} + \frac{\partial(\rho uv)}{\partial x} + \frac{\partial(\rho v^2)}{\partial y} + \frac{\partial(\rho vw)}{\partial z} = -\frac{\partial p}{\partial y} + \frac{1}{Re}\left[\frac{\partial \tau_{xy}}{\partial x} + \frac{\partial \tau_{yy}}{\partial y} + \frac{\partial \tau_{yz}}{\partial z}\right] \quad (3\text{-}10)$$

$$\frac{\partial(\rho w)}{\partial t} + \frac{\partial(\rho uw)}{\partial x} + \frac{\partial(\rho vw)}{\partial y} + \frac{\partial(\rho w^2)}{\partial z} = -\frac{\partial p}{\partial z} + \frac{1}{Re}\left[\frac{\partial \tau_{xz}}{\partial x} + \frac{\partial \tau_{yz}}{\partial y} + \frac{\partial \tau_{zz}}{\partial z}\right] \quad (3\text{-}11)$$

3.4.1.3. Energy Equation

The conservation of energy, as derived from the first law of thermodynamics, states that the rate of energy change in a fluid particle is equivalent to the sum of the net rate of work done on the particle and the net rate of heat added to it. For a compressible, viscous Newtonian flow, the corresponding energy equation is given by the following relationship [293]:

$$\frac{D(\rho C_p T)}{Dt} = \nabla \cdot (\lambda \nabla T) + \Phi \quad (3\text{-}12)$$

Where $\nabla \cdot (\lambda \nabla T)$ is the heat conduction through the fluid element boundaries, λ is the thermal conductivity, and Φ is the heat from conversion of mechanical energy which is given by the following equation [295]:

$$\Phi = \mu\left[2\left(\frac{\partial u}{\partial x}\right)^2 + 2\left(\frac{\partial v}{\partial y}\right)^2 + 2\left(\frac{\partial w}{\partial z}\right)^2 + \left(\frac{\partial v}{\partial x} + \frac{\partial u}{\partial y}\right)^2 + \left(\frac{\partial w}{\partial y} + \frac{\partial v}{\partial z}\right)^2 + \left(\frac{\partial u}{\partial z} + \frac{\partial w}{\partial x}\right)^2\right] \quad (3\text{-}13)$$

These equations are typically employed to solve laminar flows, however, in the case of FESSs, the flow between the rotor and the housing is turbulent. Therefore, the equations need to be adapted for turbulence modelling, a process known as Reynolds-Averaged Navier-Stokes (RANS) modelling [293].

3.4.1.4. Turbulent Flow

CFD simulations of turbulent flows present greater complexity compared to laminar flows, owing to the complicated features of turbulent flow fields. To determine whether a flow is turbulent or laminar, Reynolds number is used, which is the ratio of inertial forces to viscous forces. At higher Reynolds numbers, the dominance of inertial forces is sufficient to induce turbulent eddies, leading to a turbulent flow. Direct Numerical Simulation (DNS) is a method that fully resolves the unsteady turbulent eddies across all scales of the flow field, necessitating an extremely fine, fully three-dimensional mesh. Conversely, Large Eddy Simulation (LES) resolves only the large-scale turbulent eddies and requires fewer computational resources than DNS. However, both DNS and LES are not ideally suited for FESSs

analysis, considering their costs. This is due to their inherent complexities and the unnecessary solution accuracy and detail, which is not relevant for the modelling conducted, and the significant computational power they demand [294].

3.4.1.5. Reynolds-Averaged Navier-Stokes Equations

The Reynolds-Averaged Navier-Stokes (RANS) method is commonly employed in most product developments and research works, as it sufficiently captures the effects of turbulence on the mean flow, aiding in the characterisation of turbulent flow properties. This methodology involves applying a time-averaging operation to the Navier-Stokes equations, which incorporates instantaneous fluctuations. Consequently, the mean values are augmented with an additional term to represent these fluctuations in velocity, pressure, and temperature as shown below [294]:

$$u = \bar{u} + u'$$
$$v = \bar{v} + v'$$
$$w = \bar{w} + w'$$
$$p = \bar{p} + p'$$
$$T = \bar{T} + T'$$

The Reynolds stress tensor is an additional term which is given by the following relationship [295]:

$$\tau_{turb} = -\rho\overline{u_i' u_j'} = -\rho\begin{bmatrix} \overline{u'u'} & \overline{u'v'} & \overline{u'w'} \\ \overline{u'v'} & \overline{v'v'} & \overline{v'w'} \\ \overline{u'w'} & \overline{v'w'} & \overline{w'w'} \end{bmatrix} \quad (3\text{-}14)$$

The governing equations for turbulent flow motion by the average variable are [295]:

Continuity:

$$\nabla . \rho\bar{\mathbf{v}} = 0 \quad (3\text{-}15)$$

Momentum:

$$\bar{\mathbf{v}} \cdot \nabla\rho\bar{\mathbf{v}} = \rho\boldsymbol{g} - \nabla\bar{p} + \nabla \cdot \mu\left(\frac{\partial u_i}{\partial x_j} + \frac{\partial u_j}{\partial x_i}\right) - \rho\overline{u_i' u_j'} \quad (3\text{-}16)$$

Energy:

$$C_p\bar{\mathbf{v}} \cdot \nabla\rho\bar{T} = \nabla \cdot \left(\lambda\nabla\bar{T} - \rho C_p\overline{u_i' T'}\right) \quad (3\text{-}17)$$

In the RANS equations, the viscous force term of the momentum equation encompasses both the viscous stresses of the working fluid and the turbulent stresses, commonly referred to as Reynolds stresses. Due to the symmetric nature of the Reynolds stress tensor, the RANS approach involves six unknowns. Consequently, an equivalent number of equations is required to derive a solution. Similar to the momentum equation, turbulent eddy motion introduces an additional turbulent term into the energy equation. Eddy viscosity models, which rely on the Boussinesq approximation to correlate the Reynolds stresses with the mean rates of deformation, are utilised to solve for these stresses. To effectively compute turbulent flows using the RANS approach, various turbulence models have been developed. These models are categorised into algebraic, one or two equation models, or Reynolds stress models.

However, it is crucial to note that turbulence models are approximations of the actual phenomena and depend significantly on empirical constants [294].

3.4.2. Turbulence Modelling

The primary function of a turbulence model is to simulate turbulent flows. The field of turbulent modelling is focused on using mathematical equations to represent the increased mixing and diffusion caused by turbulent fluctuations on the mean flow, as well as the impact of turbulence on the mean flow properties. These models do not resolve all the relevant turbulent eddies, including the large-scale turbulent eddies that are accounted for in DNS and LES. Essentially, turbulence models predict the unknowns in the turbulent flow field and provide closure to the system of mean flow equations [293].
Among the various approaches, two-equation turbulence models are commonly used for turbulence modelling. Owing to their well-established nature and extensive validation, the k-epsilon and k-omega models are the predominant two-equation models in use. The Realizable k-epsilon model incorporates a model coefficient expressed as a function of mean flow and turbulence properties. On the other hand, the standard k-omega model is preferred over the standard k-epsilon model when dealing with flow problems that involve boundary layers under adverse pressure gradients. Additionally, the Shear Stress Transport (SST) k-omega model addresses the stream sensitivity issue of the standard k-omega free model, enhancing the stability of the model in both the free stream and viscous-affected regions [295].

3.4.3. Turbulent Boundary Layer

Turbulence models are generally not suitable for regions affected by viscosity. To address this, wall treatment models are employed. In the viscous-affected regions near solid walls, the flow field is predominantly influenced by shear due to the damping of turbulent velocity fluctuations perpendicular to the boundary and wall friction. This results in a complex flow structure characterised by rapid changes. The near-wall boundary layer is segmented into three distinct regions, as depicted in Fig 3-2. The wall velocity profiles are dimensionless and are represented by the following equations [293]:

$$u^+ = \frac{\bar{u}}{u^*} \tag{3-18}$$

$$y^+ = \frac{yu^*}{v} \tag{3-19}$$

$$u^* = \sqrt{\frac{\tau_w}{\rho}} \tag{3-20}$$

Where $\bar{u}$ is the mean velocity parallel to the wall, u^* is the friction velocity, y is the normal distance to the wall, and τ_w is the wall shear stress.

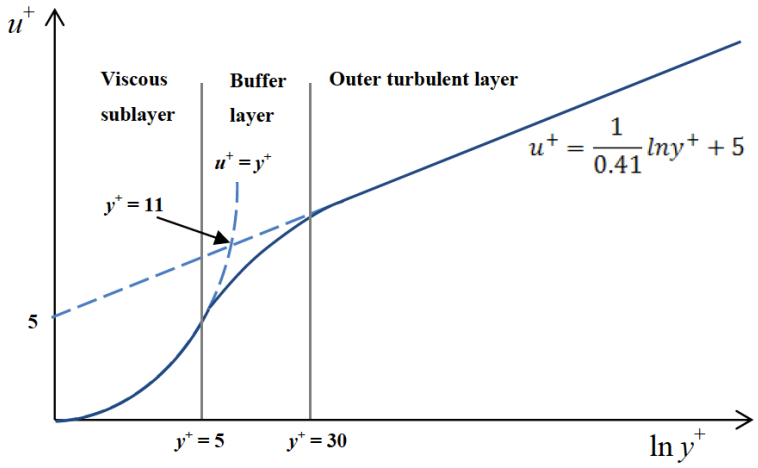

Fig. 3-2 Near wall boundary layer regions [293]

The first region, known as the viscous sublayer, is defined by $y^+ < 5$, where a linear relationship exists between y^+ and u^+ [295]:

$$y^+ = u^+ \tag{3-21}$$

The buffer layer, $5 < y^+ < 30$, acts as a transitional zone from laminar to turbulent flow and can be approximated by assuming $y^+ = 11$. The final region is the outer turbulent layer or log-law layer, $y^+ > 30$. This region is described by a logarithmic relationship shown below [295]:

$$u^+ = \frac{1}{0.41} \ln y^+ + 5 \tag{3-22}$$

There are two principal wall treatment models, as illustrated in Fig. 3-3. The first is the high y^+ wall treatment, and the second is the low y^+ wall treatment approach. The high y^+ wall treatment method does not resolve the buffer layer and viscous sublayer, instead employing wall laws to deduce the distributions of turbulence, temperature, velocity, and other scalar quantities based on wall distance. These values are then smoothly integrated with those from the log-law layer. In contrast, the low y^+ wall treatment approach, crucial for low-Reynolds number simulations, due to the dominance of fluid viscosity in the turbulent boundary layer, necessitates a more refined mesh resolution in the viscous-affected region and, as a result, requires greater computational resources than the wall function approach [295].

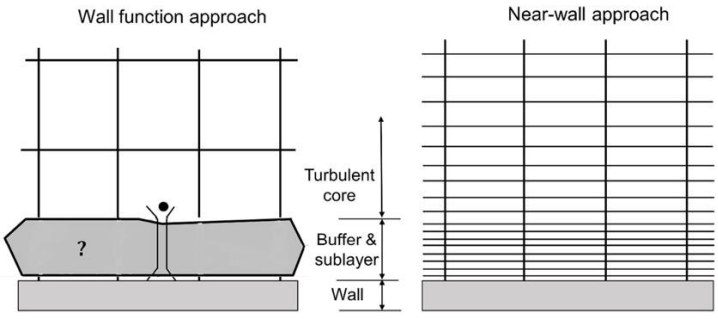

Fig. 3-3 Wall treatment methods [296]

3.4.4. Discretisation Method

The following section describes a series of steps integral to the numerical simulation of fluid flow problems. The principal objective of the discretisation method is to divide the problem domain into smaller sections, thereby representing the fluid domain within the predefined computational space. This entails defining a set of points where the solution to the governing equations is required. The secondary goal is to approximate the governing equations as a set of algebraic equations, which can then be resolved using computational methods [289].

The most prevalent discretisation techniques include the Finite Difference, Finite Element, and Finite Volume methods. While alternative approaches such as Spectral Element methods are available, the finite difference, finite element, and finite volume methods are the most common [289].

3.4.4.1. Finite Difference Method

The Finite Difference Method (FDM), the oldest among discretisation techniques, represents unknowns in flow problems using point samples at node points of a grid. Finite difference approximations are generated using truncated Taylor series expansions based on the point samples. The derivatives in the governing flow equations are replaced with finite differences, leading to an algebraic equation that reflects the flow characteristics at each grid point [297].

3.4.4.2. Finite Element Method

Finite Element Method (FEM) is predominantly utilised in structural engineering and fluid dynamics, especially in cases involving fluid-solid interactions. The FEM employs shape functions to discretise the spatial domain into a finite number of elements. A distinguishing feature of FEM is the multiplication of the equations by a weight function, followed by integration over the entire domain. The properties of the entire structure are deduced by analysing the properties of each individual element [297].

3.4.4.3. Finite Volume Method

Finite Volume Method (FVM) is regarded as a fundamental technique in CFD, which has been integrated into several commercial CFD software packages such as ANSYS Fluent and OpenFOAM [292], [298]. FVM involves spatial discretisation by dividing the fluid domain into a finite number of control volumes or cells, evaluated at their centroids to determine flow properties. The governing equations are numerically solved for each control volume. A key advantage of FVM, particularly compared to FEM, is its ability to conserve flow properties such as mass and momentum, at a discrete

level. The conservation principle in FVM is particularly effective for flows with abrupt changes and is thoroughly maintained within each individual cell volume. This ensures that conservation is achieved across the entire computational domain, irrespective of the number of control volumes involved. Following this principle, the integral equations of the flow are converted into a set of algebraic equations. These equations are then solved using an iterative method [297]. Due to the aforementioned advantages, FVM is used for the numerical analysis in this study using ANSYS Fluent software.

3.4.4.3.1. Spatial discretisation

For all CFD simulations utilising FVM, the computational domain is partitioned into a finite number of elements or cells. The cell serves as the control volume which divides the physical domain through the systematic arrangement of nodes, creating the mesh. The flow problem is resolved within the cell that is defined by the grid points or nodes. The cell-averaged flow state is established at these nodes, enabling the mathematical description of the flow by specifying the cell-averaged flow state at all spatial and temporal grid points. The precision and consistency of the numerical solution depends on the mesh quality. The ANSYS Fluent software has built-in features that assess mesh quality such as node point distribution, orthogonal quality smoothers, cell skewness, and cell aspect ratio [299].

The allocation of node points determines the extent to which shear layers, separated regions, shock waves, and boundary layers are accurately represented. Inadequate node density and uneven node distribution in crucial areas result in poor resolution, thereby reducing the accuracy of flow predictions. To achieve high-quality resolution in the boundary layer region of a laminar flow, the grid that is close to the wall must maintain an appropriate value for the non-dimensional wall distance y^+ [292].

Turbulent flows exhibit a higher sensitivity to mesh quality compared to laminar flows, primarily due to the interplay between the mean flow and turbulence. The required mesh resolution in the near-wall region is contingent upon the turbulence closure model employed.

Enhancing the smoothness of the computational mesh decreases the truncation error. To enhance the smoothness of the mesh, it is possible to refine the mesh by considering either the variation in cell volume or the gradient of cell volumes along the computational mesh lines [299].

Mesh orthogonal quality is a quantitative measure of how closely mesh elements adhere to an ideal 90-degree arrangement. Precision is essential as it directly affects the accuracy of the numerical solutions derived from the simulations. Ensuring a high level of orthogonal quality helps to minimise numerical diffusion. Numerical diffusion arises due to departure from orthogonality, resulting in the artificial diffusion of momentum, energy, and scalars, thereby potentially distorting outcomes. For accurate representation of physical phenomena, it is ideal for the angles between the face of a cell and the line connecting the centres of adjacent cells to be close to 90 degrees [292].

Cell skewness refers to the disparity in shape between a cell and an equilateral cell with the same volume. Cells with a high degree of skewness can reduce the accuracy of the solution and destabilise

the solution process. To ensure a high-quality unstructured mesh, it is necessary for the skewness to remain consistently below 0.98 [299].

The cell aspect ratio quantifies the degree of elongation or stretching of the cell. The term refers to the ratio of the greatest distance between the centroid of a cell and the centroid of a face, to the smallest distance between the nodes of the cell. It is generally recommended to refrain from using aspect ratios greater than 5:1 [299].

The selection of the mesh type is contingent upon the nature of the problem under investigation and the capabilities of the solver. A structured mesh is commonly limited to computational domains that are rectangular and consists of hexahedral elements. This mesh type is optimal for analysing rectangular shapes and straightforward cuboid geometries. Conversely, an unstructured mesh is generally characterised by non-uniform spacing between grid points, which are connected to create a tetrahedral mesh. This mesh variant is specifically intended for intricate geometries, as it allows for the placement of nodes within the computational domain based on the shape of the geometry. Multi-block structured mesh offers the advantages of reduced computational cost inherent in structured meshes, while providing the flexibility typically associated with unstructured mesh. In this mesh configuration, the computational domain is divided into distinct blocks that can be structurally meshed [299].

3.4.5. Numerical Scheme

In order to numerically solve the governing equations in each control volume, it is necessary to convert them into algebraic expressions. Discretisation refers to the process of converting these equations into solvable algebraic expressions. The FVM employed in ANSYS Fluent entails integrating the differential equations governing the flow across all control volumes within the domain. This integration yields a volume-averaged estimation of the flow state at each cell. The discretisation using the FVM entails replacing the terms in the integral equation that represent flow processes, such as convection, diffusion, and source terms, with piece-wise constant approximations. By applying the process described by Versteeg and Malalasekera [300], the integral equations can be transformed into a set of linear algebraic equations. The linear algebraic equations are solved iteratively across the control volumes to calculate the flow state until it reaches convergence. The accuracy of a converged solution relies on the physical models, grid resolution, and CFD model setup [292].

ANSYS Fluent offers two numerical solution techniques. The available solvers include a pressure-based solver, which utilises both segregated and coupled algorithms, and a density based solver [292]. Both methods involve obtaining the velocity field from the momentum equations. Both conservation of mass and momentum equations are solved using either method in their integral form. In addition, both methods employ a control-volume-based approach, and the discretisation process for both numerical methods is based on FVM. The two methods vary in their approach to linearise and solve the discretised equations [301]. The pressure-based solver can be formulated as either a segregated or coupled

algorithm. The pressure-based segregated solver has been utilised in this study. This solver linearises each discrete governing equation implicitly with respect to the conservative variable of that equation. In other words, the conservative variables in the governing flow equations are solved implicitly by sequentially considering all cells individually. This leads to a system of linear equations, where each equation corresponds to a cell within the domain. The pressure-based segregated solver is selected due to its computer memory efficiency, as it only requires the discretised equations to be stored one at a time. The pressure-based segregated solver necessitates approximately 1.5 to 2.0 times less computational memory compared to the density-based coupled solver [292].

3.4.6. Convergence

Convergence in fluid dynamics occurs when the system asymptotically approaches a limit. While an exact solution to an iterative problem might remain indefinable, the goal is to approximate the solution closely enough to meet a predetermined accuracy threshold. Convergence, therefore, is dependent on a predefined solution accuracy, which varies depending on the final precision level required. Convergence is achieved when all discrete conservation equations, such as those for momentum and energy within each cell, are fulfilled to a specified tolerance. Alternatively, it is deemed to have occurred when the solution stabilises and no longer changes with further iterations. Overall, the simulation ensures the conservation of mass, momentum, energy, and scalar quantities [292].

The evaluation of convergence in steady-state CFD analysis involves monitoring three specific criteria listed below.

Residual Values: Residuals are a critical metric for assessing convergence, as they measure the error in the solution. In CFD, the residual represents the local discrepancy of a conserved variable within each control volume. Each cell in the model will have its own residual value for every equation solved. A standard CFD simulation solves momentum, pressure, and turbulence equations iteratively, with the residuals plot displaying the disparity between consecutive solutions. These solutions are combined and standardised, allowing for a single value representation for each equation [297].

Addressing Disparities: Conservation implies that quantities described by conservation equations should remain constant throughout each iteration. Although solution imbalances will not reach absolute zero due to the translation of the physical system into a numerical representation, they must be minimal before deeming the solution converged. Initial targets for solution imbalances are typically less than 1%, with more precise convergence potentially required for highly sensitive analyses [297].

Monitoring Integrated Quantities: The calculation process in iterative solutions begins with initial estimations of various quantities, such as pressure, velocity, and temperature, which are updated in each iteration. In a converged steady-state solution, these quantities should stabilise at a predefined level. Monitoring integrated quantities such as force, drag, or average temperature can aid in determining when the analysis has reached this point [297].

3.4.7. Modelling Rotating Systems

In the context of simulating the rotor within a FESS, which rotates around its own axis, CFD offers two primary methodologies: The sliding mesh techniques and Moving Reference Frame (MRF) each offer a distinct approach to simulating rotary systems. The sliding mesh technique is a powerful method for modelling the motion of different components in a mechanical system. However, the sliding mesh technique is time-consuming due to its complexity and computational demands. It involves dynamically updating the mesh to simulate part movement, which necessitates extensive recalculations of fluid flow and interactions at each step. This process not only increases computational load, but it also requires finer meshes and smaller time steps for accuracy, which significantly increases simulation time [302].
The MRF approach, often referred to as the "frozen rotor" simulation, applies a rotating reference frame to the mesh area encompassing the rotor, termed as the rotating frame. The remainder of the mesh remains stationary. In this setup, the flow field observed by the stator is influenced by the relative position of the rotor, since the rotor is "frozen" (i.e. stationary) in space with respect to the stator. Consequently, different relative positions lead to varied solutions. This method provides an approximation of the time-averaged characteristics of the flow rather than time-resolved. In the MRF region, although there is no physical movement, the rotation of all walls within this region is considered to generate a constant grid flux. This technique is particularly suitable for steady-state analysis, capable of resolving key flow characteristics such as mass flow rate and pressure variations across rotating components. Furthermore, the MRF approach demands significantly fewer computational resources compared to the sliding mesh method, making it an optimal choice for research involving extensive simulations. Therefore, the MRF method is employed in this study to investigate fluid flow and heat transfer within the FESS [295].

3.4.8. CFD Modelling of Rotary Systems

This section reviews various literature methodologies employed in CFD modelling of applications similar to a FESS. A simplified representation of FESS is a concentric cylinder, with the inner cylinder rotating around its axis while the outer cylinder remains stationary. The induction motor is also referenced due to its structural resemblance to FESS.
Pawar et al. [226] explored Taylor-Couette flow using CFD, employing the k-epsilon model with no-slip boundary condition on both inner and outer walls. The rotational velocities studied ranged between 1 and 10 revolutions per second, with a convergence criterion of 10^{-5} for all equations. Hosain et al. [218] [221] [222] developed a CFD model for thermal analysis of rotating machines, capturing the complex Taylor-Couette flow and providing detailed insights into flow and heat transfer within the airgap. The turbulence model used was the Realizable k-epsilon model with enhanced wall treatment.

Romanazzi and Howey [303] investigated airgap convection in Switched Reluctance Machines (SRMs) which is a good alternative to the permanent magnet machines, employing the k-epsilon turbulence model and two-layer all y+ wall treatment for steady-state solutions. Adebayo and Rona [304] focused on the velocity distribution for wide gap Taylor-Couette flow using CFD. They evaluated two turbulence models for closing the RANS equations: the Realisable k-epsilon model and the Reynolds Stress Model (RSM). They reported that the Realisable k-epsilon model predicted stronger Taylor vortices and outperformed the standard k-epsilon model in scenarios involving rotation, boundary layers under strong adverse pressure gradients, separation, and recirculation.

Anderson et al. [219] used CFD to examine an electric motor thermal control system utilising air cooling which enters from the drive end and exiting from the non-drive end as the rotor dissipates heat. The SST k-omega turbulence model was chosen due to its suitability for narrow gap annulus and high swirl rotational flow applications. Nachouane et al. [215] investigated windage losses in a high-speed PMSM with a narrow airgap using CFD, employing the SST k-omega turbulence model in a steady-state configuration with velocity pressure coupling and the SIMPLE solution method, setting the convergence criteria at 10^{-4} for all equations except energy, which was set at 10^{-6}. Howey et al. [305] used experimental and CFD methods to investigate electrical machines, utilising the SST k-omega turbulence model and the MRF method for modelling rotation. Their study focused on a simple rotor-stator system with a flat rotor and stator. Lastly, Jungreuthmayer et al. [306] explored the conjugate heat transfer in a PMSM. The machine was modelled in three dimensions using the SST k-omega turbulence model with MRF and all y+ wall treatment.

Upon reviewing the existing literature relating to turbulence modelling of Taylor-Couette flow within concentric cylinders, it is evident that the Realisable k-epsilon and SST k-omega turbulence models are both suitable. These two-equation turbulence models are fundamentally based on Boussinesq's isotropic eddy viscosity assumption, which suggests that the Reynolds stress is proportional to the mean rate of deformation of the fluid element. However, for complex flows, including rotating flows and others with significant curvature effects, the validity of Boussinesq's assumption may be questionable. Nonetheless, it is important to recognise that no single turbulence model is universally acknowledged as superior for all types of flow problems. The selection of a turbulence model requires careful consideration of various factors, including the fluid flow physics, established practices for specific flow classes, desired accuracy levels, and available computational resources. In this study, the Realisable k-epsilon and SST k-omega turbulence models will be evaluated against experimental data to determine the more effective model. Within the realm of CFD, verification and validation are integral processes that collectively ensure the accuracy of numerical simulations. A mesh independence study will be conducted to verify the numerical accuracy of the solution. Concurrently, the validity of the simulations will be assessed by comparing them against experimental data.

3.4.9. CFD Simulation for Vacuum Environment

CFD simulation of a fluid is dependent on the Knudsen number, which determines whether the flow is continuous and thus subject to Navier-Stokes equations. If the Knudsen number is high, statistical mechanics should be used to model the system rather than continuum mechanics. A molecule's mean free path is comparable to the problem's length scale if the Knudsen number is near or greater than one, and the fluid mechanics continuum assumption no longer serves as a good approximation. Statistical methods should be used in these situations [238]. Continuum theory effectively describes the properties of gases at or near atmospheric pressure and in non-vacuum systems, based on the premise that gas properties are largely determined by molecular collisions [307]. Three fundamental gas laws govern this theory as shown below.

Ideal Gas Law: This law states that the density change in a perfect or ideal gas is proportional to changes in temperature and pressure.

Boyle's Law: This law postulates that, at constant temperature, the pressure of an ideal gas is inversely proportional to its volume.

Dalton's Law of Partial Pressures: This law asserts that the total pressure of a non-reacting gas mixture is the sum of the partial pressures of individual gases.

Advancements in vacuum pump technology has, shifted focus towards molecular considerations. In addition to intermolecular collisions, collisions with chamber walls becomes significant in defining gas properties. Consequently, the Kinetic Theory of Gases was developed, relevant not just at extremely low pressures (high vacuum) but across the entire pressure spectrum of industrial vacuums [239].

Gas flow in vacuum systems is governed by pressure. Above approximately 1 mbar, continuum flow dominates, characterised by frequent molecular collisions due to close proximity, thus governing the movement of molecules [308]. Conversely, at pressures below 0.001 mbar (high and ultra-high vacuum), molecular flow prevails. Here, gas molecules are widely spaced, resulting in infrequent intermolecular collisions. In this regime, molecules travel linearly until they hit a surface such as a container or cylinder wall. The mean free path length significantly exceeds the diameter of the container, allowing for unhindered molecular travel. In such cases, macroscopic continuum flow is not feasible [309]. For CFD simulations in partial vacuum environments, establishing that the flow remains within the continuum domain, based on the Knudsen number, is essential for model validity.

3.4.10. CFD Model Validation

The accuracy of CFD simulations plays a pivotal role in decision-making, particularly when it comes to design choices. The reliability of the results obtained from these simulations is essential for dependable decision-making [310]. Verification and validation are carried out to ensure that the model and simulation results are error-free. If there are acceptable levels of uncertainty and error, a claim is

considered credible. Verification and validation assessments are used to determine the levels of uncertainty and errors [311]. A validation assessment is carried out to determine the accuracy of a numerical model, primarily through comparing the numerical results against experimental data. This comparison is integral to examining the scientific validity of the models. Verification, on the other hand, involves analysing the accuracy of the conceptual model's programming and computational implementation. The aim of a verification assessment is to uncover any programming errors and to reduce the influence of cell size on the numerical results [312]. This section will discuss the experimental work that is integral to the validation of the CFD model.

3.4.10.1. Experimental Procedure

The experimental setup used for CFD model validation is depicted in Fig. 3-4 (a). This system features a flywheel, composed of a carbon fibre rim mounted on a five-spoked steel hub, which bears resemblance to the flywheel shown in Fig. 3-4 (b). For safety compliance in a laboratory setting, the flywheel assembly is encased within a stainless-steel containment. The flywheel is mechanically linked to an ABB induction motor (Model M3FT 180A 4), which boasts a rated power of 135 kW and a maximum speed of 6,500 rpm, enabling the flywheel to reach rotational speeds up to 40,000 rpm. The flywheel, designed and manufactured by PUNCH Flybrid, is intended for automotive applications [313]. The experimental rig was located at PUNCH Flybrid. The flywheel has a diameter of 0.26 m and a width of 0.13 m. The airgap between the flywheel and the housing is 0.00133 m, with the housing diameter measuring 0.32 meters. The experiment was conducted by Flybrid under atmospheric conditions, with rotational velocities ranging from 5,000 to 14,000 rpm.

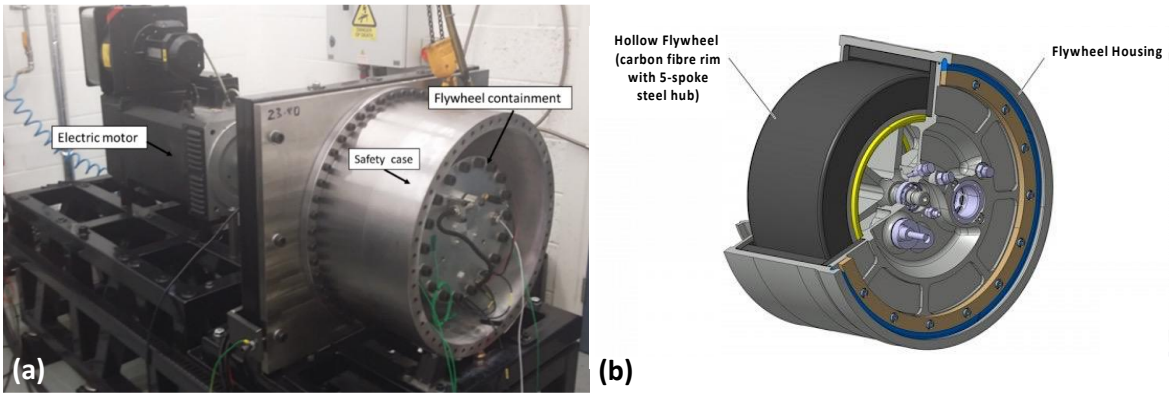

Fig. 3-4 Experimental flywheel system, (a) the Setup with motor, safety casing, and containment, (b) the schematic diagram of the flywheel tested

In the experimental setup, a closed oil circuit cooling system is implemented to maintain the shaft and bearings at optimal temperatures. Surface temperature measurements are conducted at various locations using five thermocouples. An infrared (IR) temperature sensor is employed to measure the surface

temperature of the flywheel's carbon fibre rim. The remaining four temperature sensors are dedicated to monitoring the temperatures of the flywheel housing, the oil inlet and outlet, and the ambient temperature. During the testing phase, the ambient temperature was maintained at 24°C.

The test procedure involved incrementally increasing the flywheel speed by 1,000 rpm and allowing the system temperature to stabilise at each new set point. Temperature stability was defined as a variation of less than 5% in the IR temperature data over a 60-second interval. Upon achieving this stabilisation criterion, temperature readings were recorded at each set point.

3.4.10.2. Model Definition and Mesh

The FESS geometry was modelled in 3D. Given the symmetrical nature of the flywheel, only half of the domain is considered in the simulations. This approach is adopted to reduce computational time and cost. To simplify the geometry further, the model is divided into 5-way sections, resulting in a 72° segment. This segmentation is based on the number of steel spokes present in the hub. The periodic and symmetry planes of the system are illustrated in Fig. 3-5. To ensure accurate representation of heat flux and temperature, coupled mapped mesh interfaces are created between the solid and fluid domains.

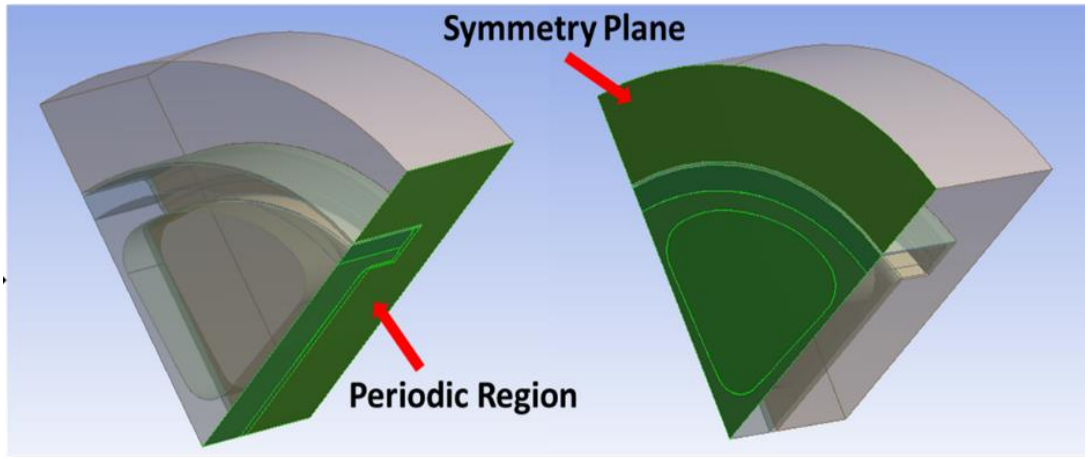

Fig. 3-5 Simplified FESS geometry with periodic region and symmetry plane

3.4.10.2.1. Verification

The verification of the numerical solution is a critical step in ensuring that the CFD model is setup correctly and the results are not mesh dependent. In qualitative CFD analysis, it is essential to employ a sufficient number of computational cells. For this purpose, three different mesh sizes were tested ranging from 0.14 mm to 0.16 mm in size in the fluid domain, and 1.5 mm to 2.5 mm in the solid domains. Fig. 3-6 illustrates the average temperature of the system components as a function of the mesh size. Notably, the temperature difference between mesh 2 and mesh 3 is found to be negligible. Further refinement of the mesh would result in increased computational time and cost without

significant improvements in the accuracy of the CFD model predictions. Consequently, mesh 2 was selected as the optimal mesh for this investigation. The complex geometry of the system required a combination of hexahedron and tetrahedron cells, as shown in Fig. 3-7.

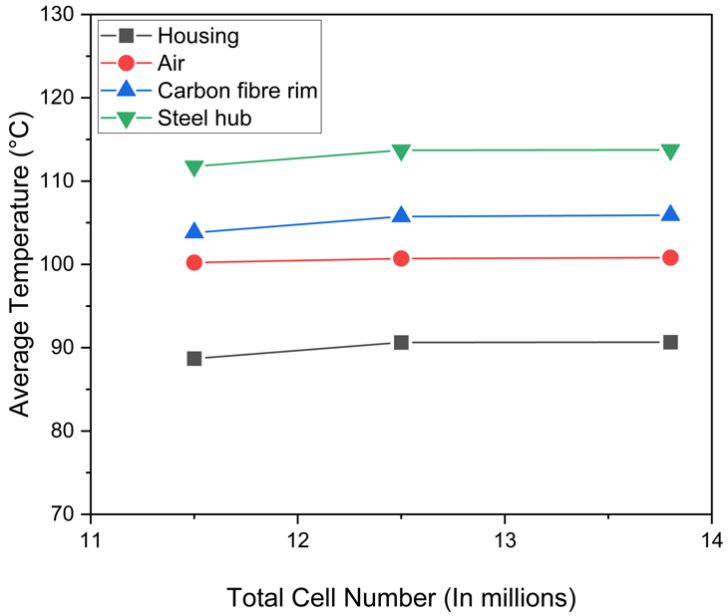

Fig. 3-6 Mesh independence test

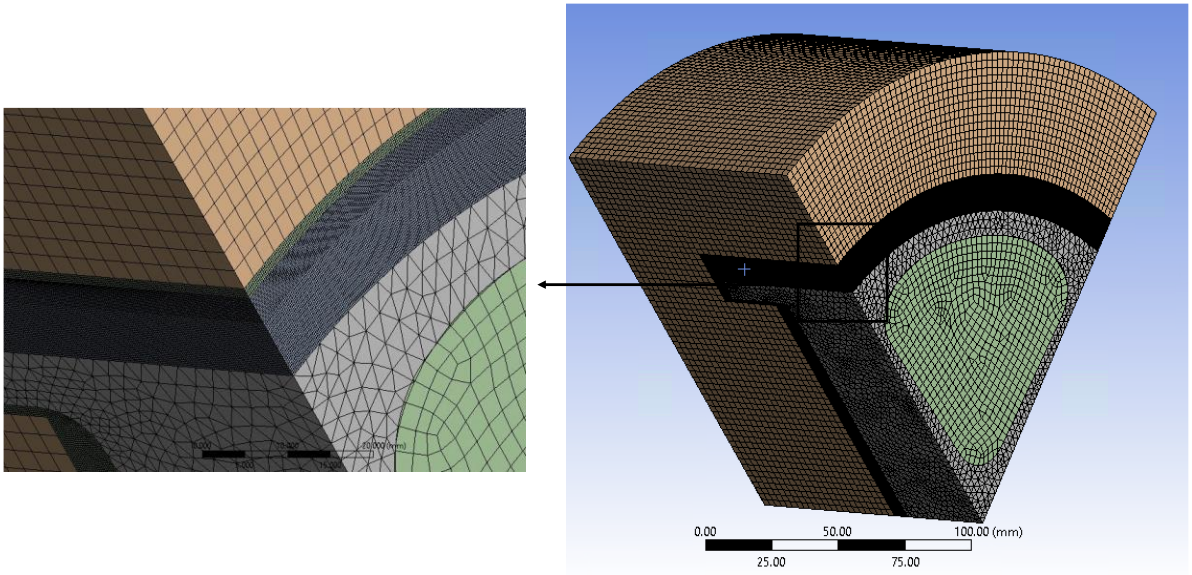

Fig. 3-7 FESS with tetrahedral and hexahedral mesh

3.4.10.2.2. Turbulent flow and energy modelling

CFD simulation was employed to analyse the steady-state operation of the machine, necessitating the use of steady-state models. The CFD runs were performed using the University of Hertfordshire SPECS Cluster. As previously mentioned, the time-averaged steady-state solutions for the rotor's relative

motion were modelled using a MRF approach. Due to the rotor's high peripheral Reynolds number, 1.02×10^6, a turbulence model was required for accurate simulation of the flow within the annulus of the FESS. To address this, RANS equations were solved using three different turbulence models: SST k-omega, Realizable k-epsilon, and the Reynolds Stress Equation Model (RSM). These models were then compared to evaluate their prediction accuracy. In this simulation, the influence of gravity was considered to be negligible. The gaseous medium within the FESS airgap, in this case air, was treated as an ideal gas. The viscosity of the air was determined using Sutherland's law, and both the thermal conductivity and specific heat capacity were assumed to be constant.

In the CFD model, specific boundary conditions were applied, reflecting the fact that the FESS can operate in a partial vacuum environment, and thus, the actual system is sealed for low-pressure operation. Consequently, there were no inlet or outlet flows considered in the model. The surfaces of both the rotor and the housing were assumed to be smooth with a no-slip condition. To replicate the thermal boundary conditions experienced by the FESS housing during the experiment, surface temperature of 24°C and heat transfer coefficients of 30 W/m².K were applied to all external FESS housing walls. Additionally, an initial temperature of 24°C was set for all system components.

Given the limitations of turbulence models in addressing the viscous-affected region of the boundary layer, wall treatment models were utilised to define the flow profiles in these areas. Details regarding near-wall flow velocities and distances were previously discussed in Section 3.4.3.. A wall cell $y_+ \leq 1$ was employed to generate a high-resolution boundary layer mesh, crucial for resolving the viscous sublayer.

The numerical discretisation of the governing equations was conducted using FVM. This approach involved solving a non-linear algebraic equation system for each cell. A second-order upwind discretisation scheme was adopted to simultaneously resolve equations based on the conservation of mass, momentum, energy, and turbulence parameters. To ensure convergence of the CFD solution for each run, iterations were meticulously converged in relation to each other. The convergence criteria for all residuals were set at 10^{-5}, except for energy, which was set at 10^{-7}. Several simulations were conducted to investigate the FESS performance under different rotational speeds and to identify the most suitable turbulence model for the remainder of the numerical work.

3.4.10.3. Validation

Experimental tests demonstrated that the temperature of the carbon fibre rim significantly influenced the air temperature within the airgap. The recorded experimental temperatures were compared to CFD model predictions using three different turbulence models. The validation exercise indicated that CFD predictions closely align with the experimental results using all three turbulence models. The Realisable k-epsilon model exhibited a 10.7% error in temperature rise predictions, while the SST k-omega model

showed a 10.6% error. Conversely, the RSM had an error of 10.4%, although with a 50% higher computational time compared to the other two-equation turbulence models.

Fig. 3-8 presents the average temperature of the carbon fibre rim from the experimental work alongside the numerical results from the three turbulence models at different rotational speeds. It was observed that at lower rotational speeds, the numerical results tend to underestimate the temperature, while at higher speeds, they overestimate it. This discrepancy between numerical and experimental results could be attributed to the simplified geometry used in the numerical analysis, where the cooling of the shaft and bearings was not considered. Additionally, the thermal mass of the safety containment, mounting brackets, and frame was omitted in the numerical models. Despite these simplifications, the discrepancies in all three numerical models fell within the predefined 15% uncertainty range.

Given these findings, the SST k-omega turbulence model with viscous heating was selected to model the highly turbulent flow within the flywheel airgap. This decision was based on its lower error percentage compared to the other two-equation model and a 50% reduction in computational time compared to the RSM model, while the difference in error between the two models was only less than 1%.

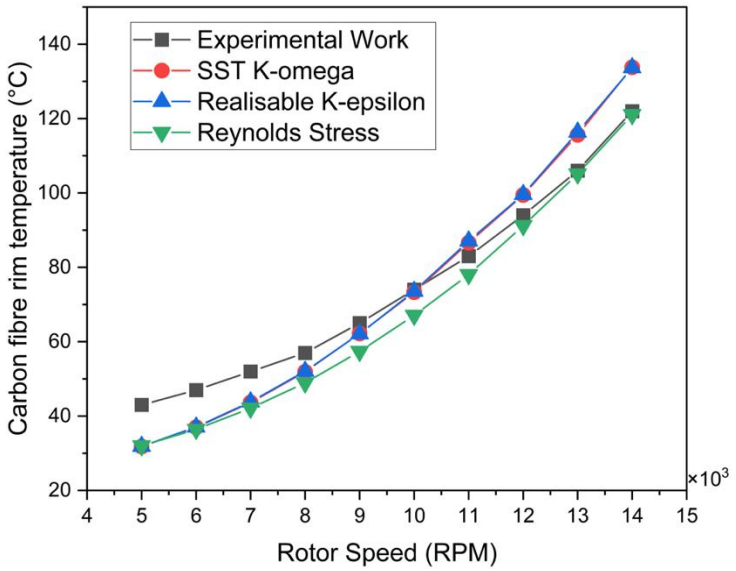

Fig. 3-8 Carbon fibre temperature vs flywheel speed predictions with different turbulence models

The initial step in validating the CFD model involved a composite flywheel comprising a carbon fibre rim and a steel hub. Additionally, a separate validation was conducted for a different FESS design, featuring a rotor made of high-strength steel, as depicted in Fig. 3-9. This validation aimed to compare the numerical results against experimental data collected for this FESS. The validation process followed the identical steps for pre-processing and solver models as the previous case.

The experimental procedure was carried out by PUNCH Flybrid and included a “coast down” test, where the flywheel was accelerated up to 23,000 rpm, and the losses were measured as it decelerated. The total drag losses on the flywheel, encompassing both windage and mechanical friction, were

determined by differentiating the measured speed and accounting for known losses from driveline components between the flywheel and the rig clutch. The friction from vacuum seals and flywheel bearings, excluding windage losses, is presented in Fig. 3-10. These values, derived from empirical data available to the company, were added to the numerical results for a comprehensive comparison between experimental and numerical coast down results.

As illustrated in Fig. 3-10, there is a noticeable discrepancy between the simulation results and the experimental data at each pressure level. On average, the simulation results are approximately 7% lower than the experimental findings. This variance could be attributed to the simplifications made in the CFD model, such as the exclusion of the shaft, bearing, and seals.

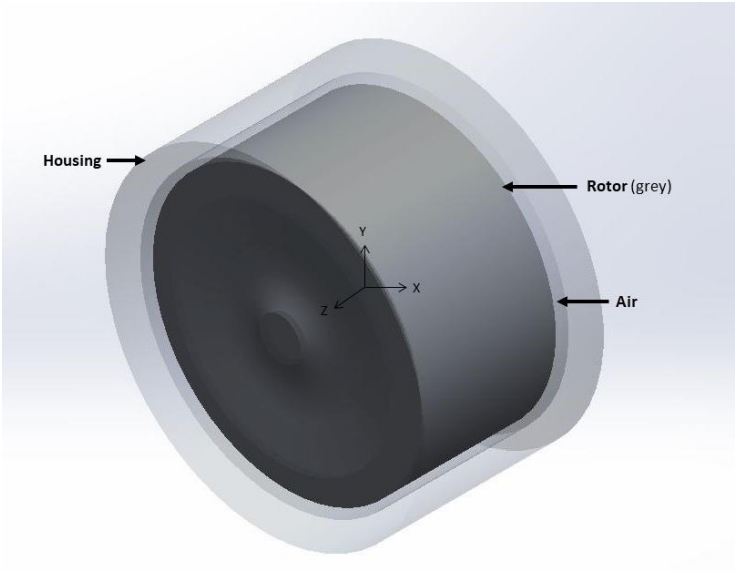

Fig. 3-9 3D model of the FESS geometry with solid rotor

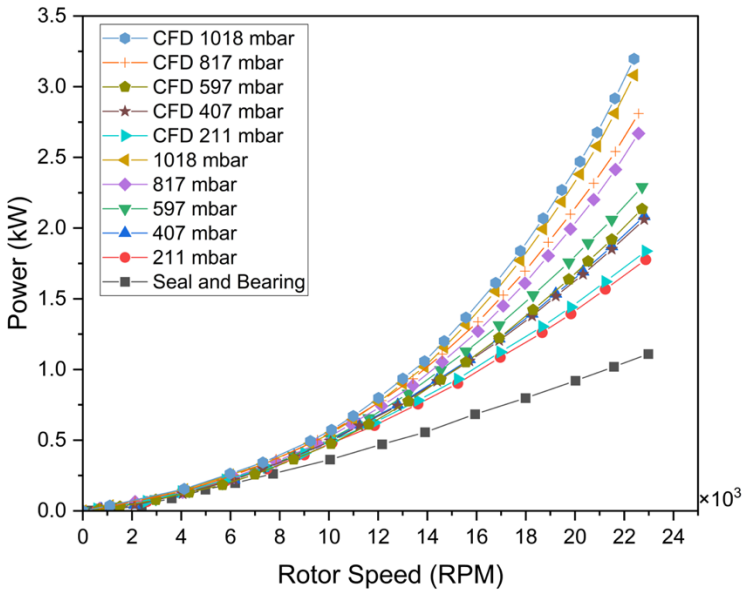

Fig. 3-10 Validation of numerical predictions of seal and bearing losses as a function of flywheel speed against experimental data at different working pressures

Although the CFD results were initially validated against specific experimental data, this process was somewhat limited by the scope of the data collected from the experimental test. To address this limitation, further validation was conducted using experimental data available in the literature on Taylor-Couette flow, where, for each of the three validations, a 3D model with the exact same dimensions was used to ensure accurate comparison with the experimental data.

The skin friction coefficient variation as a function of the Taylor number is compared with experimental data presented by Donnelly and Simon [314], [315]. Fig. 3-11 illustrates this relationship, identifying three distinct zones: the first zone is where the flow is laminar without vortices, the second zone is characterised by laminar flow with Taylor-Couette vortices (referred to as non-linear theory due to the non-linear distribution of skin friction coefficient), and the third zone represents turbulent flow. The Taylor numbers obtained numerically align well with those reported by Donnelly and Simon [315]. Additionally, the skin friction coefficients calculated by the CFD model match the results reported by Donnelly and Simon [315], accurately reproducing the flow characteristics in the first zone.

In Fig. 3-12, the simulated average velocity profile is compared to the experimental data from studies by Hosain et al. [222] and H. Reichardt [316]. The simulated values were scaled for consistency with the experimental results range. In this figure, the non-dimensional coordinates $X = -1$ and $X = 1$ represent the housing and rotor walls, respectively. At low Reynolds numbers, the velocity profile follows a linear pattern, whereas at high Reynolds numbers, a steeper gradient is observed near the walls due to viscous forces, with the average velocity occurring at the midpoint of the airgap. The simulated average velocity profile shows good agreement with the experimental profiles, corroborating patterns reported in previous studies [317], [318]. Fig. 3-13 presents the validation of the radial velocity distribution in the R-Z plane at the midsection of the FESS annulus, comparing the experimental work of Lie et al. [267] with the CFD results from this study. The agreement between the experimental and numerical radial velocity distributions further validates the CFD model.

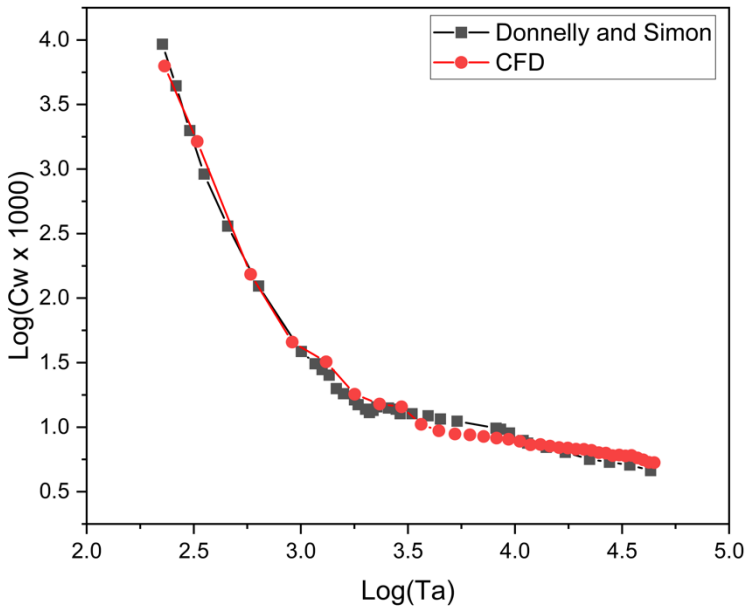

Fig. 3-11 Validation of rotor skin friction coefficient vs Taylor number against Donnelly and Simon's experimental data [314]

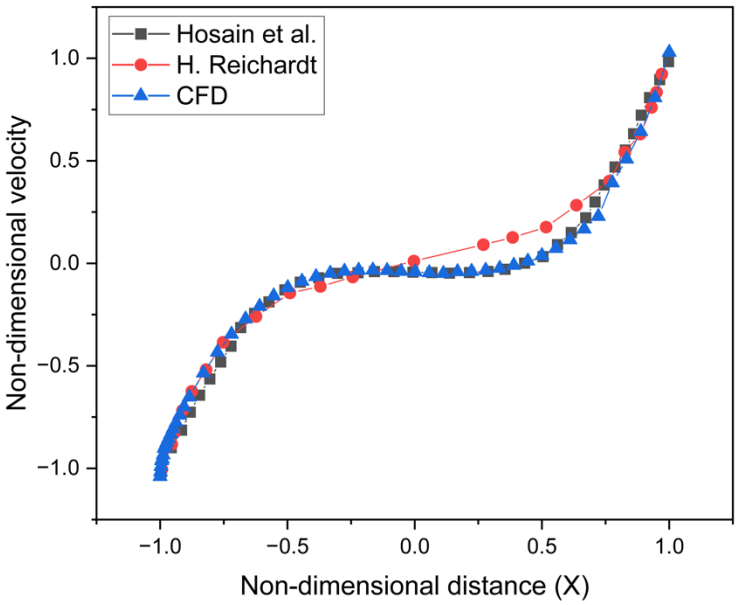

Fig. 3-12 Validation of average velocity profile within the airgap against the experimental results reported by Hosain et al. [222], H. Reichardt [316]

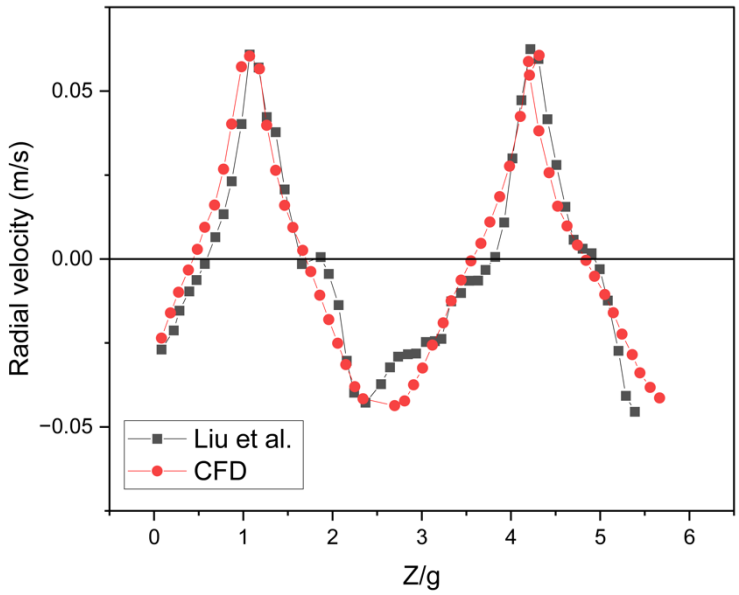

Fig. 3-13 Validation of radial velocity distribution in the R-Z plane against the experimental results reported by Liu et al. [267]

3.5. FESS Loss Calculations

The efficiency of a FESS plays a crucial role in its selection for applications such as transportation. The system efficiency is inversely proportional to its losses: higher system losses result in lower efficiency. The primary contributors to such losses in a FESS are mechanical, predominantly from aerodynamic and bearing friction losses. Although these losses are typically minimal in a well-designed FESS, their cumulative effect over time can lead to significant energy losses. This section will delve into the specifics of bearing and aerodynamic (windage) losses in FESSs, examining their implications on the overall efficiency of the system.

3.5.1. Bearing Selection for FESSs

The selection of an appropriate bearing for a FESS is a critical decision that must consider several factors such as cost, bearing volume, and compatibility with low-pressure operation. Airfoil bearings are not a viable option for FESSs due to their high costs. Additionally, sealing these bearings in a low-pressure system poses considerable challenges. The requirement of an external air supply for airfoil bearings further compounds the issue, as it would increase both the weight and cost of the system [319]. Hydrodynamic bearings, while another potential choice, are also unsuitable for FESSs. Their significant losses, high costs, and the necessity of an accompanying oil system (which adds weight and cost) render them impractical. The low pressure required by these bearings makes their integration into a vehicle's

oil system unfeasible. Moreover, sealing hydrodynamic bearings in a low-pressure environment presents considerable difficulties [319].

Passive magnetic bearings, despite gaining attention in recent years, are not capable of withstanding the loads encountered in a FESS, leading to the risk of premature failure. While the development of superconducting magnetic bearings holds promise for future applications in systems such as FESSs, they are not yet a practical solution. Active magnetic bearings emerge as a suitable choice for such systems; however, they require support for high-speed operation and consume significant power, which necessitates additional space due to their larger volume [319].

Rolling element bearings emerge as a suitable choice for applications such as FESSs, especially when equipped with grease lubrication to function effectively in low-pressure systems without the need for an accompanying oil supply. These bearings are simpler and more cost-effective compared to other types discussed. Considering the requirements for low loss, low cost, and high capacity, the selection of bearings for FESSs is largely limited to rolling element types. Despite the relatively small rotor weight and imbalance loads, rolling bearings must also accommodate gyroscopic effects and acceleration shocks. While magnetic bearings could be ideal for stationary applications, they would need to be substantially larger to handle these additional loads. An alternative approach involves positioning the FESS such that gyroscopic moments are not imparted to the rotor and casing [156].

A comparison of the two most suitable bearings for FESSs is presented in Table 3-2. Rolling bearings are advantageous due to their low loss moments, enabling them to withstand short-term loads or shocks that significantly exceed the constant design load, provided they offer sufficient fatigue life for regular operation. Angular contact bearings are typically the preferred choice, with options ranging from all-ceramic to steel balls at various accuracy levels, depending on cost considerations. Most manufacturers provide a loss correlation that includes a fixed loss moment and a speed-dependent loss moment component. It is important to note that over recent decades, technology in rolling element bearings has advanced significantly towards reduced loss moments and enhanced durability.

Rolling element bearings stand out as the most practical choice for FESSs due to their simplicity and effectiveness. They are ideal for the size requirements of FESSs, offering reliable performance without the need for complex power supply and control systems associated with magnetic bearings. Their design is less complex, which simplifies maintenance and replacement. Although they have moderate resistance to contamination and lower damping capabilities, they can be effectively sealed and lubricated to enhance their performance. With the ability to operate across a wide range of speeds and temperatures, rolling element bearings provide a robust and flexible solution that aligns well with the operational demands of FESSs.

Table 3-2 Comparison of suitable bearings for FESSs

	Rolling element bearings	Magnetic bearings
External support	Grease: None Oil: Oil supply	Power supply & control system
Bearing size	Small to medium	Large
Complexity	Simple	Complex
Resistance to contamination	Low to medium	High
Cleanliness	Low	High
Reliability	Medium to high	High
Damping	Low to medium	Control system to limit vibration
Speed	Low to high	Very high
Pressure	Lubricant limited	Virtually independent
Temperature	-20 to 150 ℃	-250 to 200℃

3.5.1.1. Bearing Lubrication

The choice of lubrication in rolling element bearings significantly influences their operating temperature, speed limits, and bearing losses. Oil lubrication is favoured for enabling high-speed operation due to its lower friction and superior cooling properties. However, this may necessitate more frequent maintenance, along with additional equipment for oil pumping. With oil lubrication, it is observed that power loss escalates as the rate of lubricant supply to the bearing increases. The cooling effect of the oil lubricant initially raises the operating temperature, which then decreases after reaching a certain level [320]. High-pressure oil feed systems offer effective temperature control, but their complexity adds to the overall cost of the system.

Alternatively, grease lubrication is advantageous in terms of maintenance and longevity, though it imposes a lower speed limit compared to oil lubrication. While the viscosity of the lubricant is a key factor in determining temperature range and power loss in bearings, it is not the sole determinant of loss estimation. Another critical aspect to consider is the working pressure. The lubricant selected must have a vapor pressure level compatible with the desired low-pressure conditions. As such, oil or grease lubrication is typically the preferred method for most bearing systems [320]. The selection of the lubricant also varies depending on the required vacuum pressure level. For environments with stricter vacuum limitations, silicon-based oils, which have lower lubricating properties, are necessary [156].

3.5.1.2. Bearing Losses

For FESSs, rolling element bearings such as ball bearings, have been chosen due to the advantages previously outlined. The total losses in a ball bearing primarily arise from shear and slip stress within

the bearing itself. Predicting the torque and power loss of a bearing analytically is challenging, largely due to the difficulty in accurately determining the relationship between the lubricant level in the bearing cavity and its application. It has been noted that increased lubricant volume tends to elevate bearing friction and consequently torque. Although some of this effect can be attributed to lubricant filling the bearing cavity, the exact relationship between lubricant supply to the cavity and its impact remains challenging to control and typically requires empirical determination [320].

Palmgren [321] developed an empirical approach for estimating bearing torque and power loss, which has been widely adopted in industry and by bearing manufacturers. The rolling bearing torque is proportional to both speed and load, and is given by the following expression:

$$T_B = T_L + T_v \tag{3-23}$$

Where T_v is the speed dependent load and T_L is the load-dependent component. The load-dependent component can be calculated through the following relationship:

$$T_L = F_b D_p f_L \tag{3-24}$$

Where F_b is the applied load on the bearing, D_p is the diameter of the pitch circle of the bearing in inches, and f_L is a factor dependent on the bearing design and can be calculated by the following equation:

$$f_L = z\left(\frac{F_s}{C_s}\right)^y \tag{3-25}$$

Where F_s is the static equivalent load, C_s is the static load rating, and *z* and *y* are load factors, which are detailed in Appendix A. The static equivalent load, assumed to result in a contact stress equal to the bearing's maximum stress under normal operation, given by the following equation:

$$F_s = max[(X_s F_r - Y_s F_a)\ ,\ F_r] \tag{3-26}$$

Where F_r and F_a are the radial and axial loads, respectively, while X_s and Y_s are static radial and axial load factors, respectively, whose values are mentioned in Appendix A. The load factor for the bearing can be determined using the following equation:

$$F_b = max[(0.9F_a - 0.1F_r)\ ,\ F_r] \tag{3-27}$$

The bearing torque speed component can be calculated through the following relationship:

$$T_v = \begin{cases} 1.42 \times 10^{-5} f_o (v_o n_s)^{\frac{2}{3}} {D_p}^3, & v_o n_s > 2000 \\ 2.3 \times 10^{-3} f_o {D_p}^3 \quad , & v_o n_s \leq 2000 \end{cases} \tag{3-28}$$

Where f_o is a factor dependent on the bearing type (Values provided in Appendix A), v_o is the kinematic viscosity of the lubricant, and n_s is the bearing speed in revolutions per minute (rpm).

3.5.1.3. Bearing Life

Bearing life refers to the duration for which a bearing can reliably perform its function. Due to the high number of cyclic stresses experienced, cracks may form either on or beneath the rolling surfaces. Surface cracks can lead to material breakage on the rolling surfaces, resulting in the formation of pits

in the rolling elements. Despite such failure modes, the bearing can often continue to operate safely for a period of time. Calculating fatigue life is a crucial aspect of bearing selection and design, especially in flywheel applications where minimal maintenance is desired and bearing failure could result in catastrophic consequences [320].

Several factors influence the lifespan of bearings, including errors in bearing design and selection, inadequate maintenance, and improper mounting. Beyond these practical considerations, the basic rating life provides a straightforward method for estimating bearing fatigue life. The basic rating life of a ball bearing, as a function of bearing load, can be calculated using the following formulas [320]:

$$L_{10} = \left(\frac{C_l}{P_l}\right)^3 \tag{3-29}$$

$$L_{10h} = \frac{10^6}{60 n_l} L_{10} \tag{3-30}$$

Where L_{10} represents the millions of revolutions rating life with a 90% reliability, L_{10h} is the operational hours rating life, C_l is the basic dynamic load rating, n_l is the rotational speed, and P_l is the equivalent dynamic load, which can be calculated by the following equation:

$$P_l = \mathcal{X} F_r + \mathcal{Y} F_a \tag{3-31}$$

Where $\mathcal{X}$ and $\mathcal{Y}$ are the radial and axial load factors, respectively (Values provided in Appendix A).

3.5.2. Aerodynamic Losses

Aerodynamic "windage" losses result from friction drag between the rotor and the fluid within the FESS airgap. Given the high peripheral speeds of flywheels, aerodynamic friction loss becomes substantial unless the working pressure is reduced. Running the rotor in air can lead not only to excessive energy loss but also potential overheating of the rotor [212]. While complete removal of air might appear as an attractive solution (i.e. Hard vacuum), achieving a very high vacuum can inadvertently lead to gas release, even in a hermetically sealed design without a shaft seal which makes leakage prevention a significant challenge. Additionally, the lubricant used for bearings can vaporise at low pressures if the bearings are not isolated from the vacuum. Implementing a shaft seal for a mechanical shaft power complicates the process of maintaining a high vacuum. One potential solution to mitigate leakage is to run a vacuum pump continuously, but this introduces extra cost and weight to the system [101].

Reducing windage losses is a crucial strategy for enhancing the efficiency of FESSs. To this end, many high-speed flywheels are placed in vacuum housings, effectively minimising windage losses thus improving system performance. However, this approach also makes the system more expensive and complex due to the addition of components such as vacuum chamber and pump. A significant challenge introduced by operating in a vacuum environment is the potential overheating of the flywheel. Since vacuum conditions preclude heat dissipation through convection, the system requires an alternative cooling mechanism [322].

A pragmatic approach involves identifying a balance between windage loss reduction and working pressure without incurring excessive energy loss. For pressures that are not exceedingly low, the losses can be approximated using continuum flow equations [322].

The work of Daily and Nece [323] is among the most comprehensive in covering windage in enclosed cylinders. In situations where hard vacuum is necessary, molecular flux becomes a consideration, and the application of differential equations is required. This regime is referred to as Knudsen flow. The transition from continuum to molecular flow occurs gradually.

Windage losses in a FESS arise from friction caused by intermolecular collisions between the flywheel surface and the fluid particles within the airgap. Although running FESSs in low-pressure environments reduce windage losses, it increases the temperature of the system components. Depending on the vacuum, three regimes for molecular flow can be established: free molecular flow, slip flow, and continuum flow [241]. The specific regime in play can be determined by the Knudsen number, calculated by the following equation:

$$K_n = \frac{\vartheta}{L_i} \tag{3-32}$$

Where ϑ represents the molecular mean free path and L_i is the characteristic length of the flow field. The molecular mean free path, the average distance travelled by gas molecules between collisions, can be determined for a gas in local thermodynamic equilibrium through the following expression [324]:

$$\vartheta = \frac{\mu}{\rho}\sqrt{\frac{\pi M}{2RT}} \tag{3-33}$$

Where μ is the dynamic viscosity, ρ is the density, M is the molecular weight, R is the universal gas constant, and T is the temperature of the working fluid. The mean free path for an air atmosphere is given by the following relationship:

$$\vartheta = \frac{(3.1\times10^{-5})T^2}{(T+110.4)P} \tag{3-34}$$

Where P is the working pressure in Pascals. The Knudsen number can also be expressed by the following relationship:

$$K_n = 1.26\sqrt{\gamma}\frac{Ma}{Re} \tag{3-35}$$

Where γ is the specific heat ratio, Ma is the Mach number, and Re is the Reynolds number. The value of the Knudsen number indicates the molecular flow regime [324].

- $K_n < 0.01$ Continuum flow
- $0.01 < K_n < 3$ Slip flow
- $K_n > 3$ Free molecule flow

The Knudsen number plays a pivotal role in categorising the flow into different regimes within a FESS. This number establishes the relationship between the airgap and the average molecular free path. The mean free path refers to the average distance a gas molecule travels between collisions. Depending on the degree of rarefaction, the flow in a FESS can be generally classified into several distinct regimes:

free molecule flow, slip flow, and continuum flow. Each regime corresponds to different density levels – "ordinary" for continuum flow, "relatively rarefied" for slip flow, and "highly rarefied" for free molecule flow [325].

Couette flow occurs in the annulus of coaxial cylinders where the inner cylinder rotates while the outer remains stationary, resulting in the steady relative motion of two parallel surfaces separated by a fluid. The flow regimes within this setup are influenced by various factors, including rotor speed, airgap size, temperature of the fluid, and working pressure. In the continuum flow regime, the behaviour of a Newtonian linear viscous fluid is governed by the Navier-Stokes's equations of momentum. These equations assume that the fluid's strain rates are linearly proportional to the viscous shear stresses, implying that the Knudsen number is negligible within the flow field. According to the Navier-Stokes's equations, there exists a zero-slip flow boundary condition between the solid and the fluid [325].

However, as air pressure decreases below the continuum flow limit, a rarefied gas stream occurs when the molecular mean free path is not small relative to the airgap. In this scenario, the fluid appears to slip over solid surfaces, leading to velocity and temperature discontinuities at the interfaces between the fluid and the boundaries. For a very rarefied free molecule flow, the mean free path is significantly larger than the airgap, and the flow field remains largely unaffected by the presence of the boundaries. In such cases, molecular-surface interactions are negligible, and flow phenomena are governed primarily by molecular collisions. Energy transfer and momentum in this regime are facilitated solely through direct encounters between the wall surfaces and the fluid molecules [325].

As the velocity of a fluid increases, so does the force exerted on an object moving through it. This force can be quantified using the following formula:

$$F = \frac{1}{2}\rho A C_D v^2 \tag{3-36}$$

Where ρ is the fluid density, A is the wetted area or cross-sectional area of the object, v is the relative velocity between the object and the fluid, and C_D is the drag coefficient which can be calculated by the following equation:

$$C_D = \frac{2\tau_{xy}}{\rho V^2} \tag{3-37}$$

Where τ_{xy} is the shear stress between two surfaces. The power required by the system to counteract the windage loss of a rotating cylinder is given by the following expression:

$$P_w = \tau_{xy} A_s r_o \omega \tag{3-38}$$

Where A_s is the cylinder surface area and r_o is the cylinder radius. If Beck's equation for shear stress is employed, the power can be written in the following form [326]:

$$P_w = \left(\frac{2\pi\rho h {r_o}^4}{M_a (2\pi\kappa)^{1/2} + Re}\right)\omega^3 \tag{3-39}$$

Where h is the flywheel height, κ is the ratio of specific heats, M_a is Mach number, and Re is Reynolds number. The Mach and Reynolds numbers can be calculated by the following equations:

$$M_a = \frac{v}{(2\pi\kappa)^{1/2}} \tag{3-40}$$

$$Re = \frac{\rho g v}{\mu} \tag{3-41}$$

Where g is the airgap size and μ is the viscosity of the working fluid.

Beck's equation [326] (referred to as Eq. 3-39), is applicable across all values of Knudsen numbers, making it a valuable tool for calculating drag losses in rarefied environments (i.e. FESS operating in hard vacuum). According to Lees [327], the results obtained using this equation show reasonable agreement with experimental data. Kuhlthau [328] notes that if the temperature difference between the housing and the rotor is disregarded, the experimental results align well with theoretical predictions.

For determining drag in cylindrical Couette flow of rarefied gases, Alofs and Springer [329] developed an expression for shear stress. This formulation integrates Kennard [330] and Bower and Talbot [331] equations for free molecular plane Couette flows, taking into account the tangential momentum accommodation coefficient when calculating shear stress. The shear stress can be calculated using the following equation:

$$\tau_{xy} = \frac{1}{2}\rho v \left(\frac{2RT}{\pi}\right)^{1/2} \left(\frac{r_i}{r_o}\right)^2 \left(\frac{\sigma_t}{2-\sigma_t}\right) \tag{3-42}$$

Where R is the universal gas constant, T is the temperature of the working fluid, r_i is the inner radius of the cylinder, r_o is the outer radius of the cylinder, and σ_t is the tangential momentum coefficient. The power equation can then be reformulated as:

$$P_w = \left(\frac{2\pi\rho h {r_i}^6}{M_a (2\pi\kappa {r_o}^4)^{1/2}}\right)\left(\frac{\sigma_t}{2-\sigma_t}\right)\omega^3 \tag{3-43}$$

This equation is valid for a broad range of Knudsen numbers, as evidenced by the experimental findings of Alofs [329]. For $K_n > 7$, an average of $\sigma_t = 0.972$ is found to be applicable for low gas densities in free molecular flow.

If windage losses occur at atmospheric pressure levels, a significant amount of energy can be wasted. The power required by the system to counteract the windage losses of a rotating cylinder is defined by the following expression [241]:

$$P_w = (M_D + M_c)\omega \tag{3-44}$$

Where M_D is the disc moment on the side part of the cylinder and M_c is the cylinder moment. These can be calculated using the following formulas [241]:

$$M_D = \rho\omega^2 {r_o}^5 C_m \tag{3-45}$$

$$M_c = \pi\rho\omega^2 {r_o}^4 h C_w \tag{3-46}$$

Where C_m is the disc torque coefficient, h is the axial length of the cylinder, and C_w is the cylinder skin friction coefficient, which can be calculated by the following expression [332]:

$$C_w = 0.0593 \times \left(\frac{2\pi\omega {r_o}^2 \rho}{\mu}\right)^{\frac{-1}{5}} \tag{3-47}$$

The skin friction coefficient can be calculated depending on the Reynolds number of the working fluid [333]:

$$C_w = \begin{cases} 10\frac{\left(\frac{g}{r_o}\right)^{0.3}}{{R_e}^1}, & R_e < 64 \\ 2\frac{\left(\frac{g}{r_o}\right)^{0.3}}{{R_e}^{0.6}}, & 64 < R_e < 500 \\ 1.03\frac{\left(\frac{g}{r_o}\right)^{0.3}}{{R_e}^{0.5}}, & 500 < R_e < 1\times10^4 \\ 0.065\frac{\left(\frac{g}{r_o}\right)^{0.3}}{{R_e}^{0.2}}, & R_e > 1\times10^4 \end{cases} \quad (3\text{-}48)$$

Bilgen and Boulos created a different correlation for skin friction coefficient as follows [215]:

$$C_w = \begin{cases} 0.515\frac{\left(\frac{g}{r_o}\right)^{0.3}}{{R_e}^{0.5}}, & 64 < R_e < 500 \\ 0.0325\frac{\left(\frac{g}{r_o}\right)^{0.3}}{{R_e}^{0.2}}, & R_e > 1\times10^4 \end{cases} \quad (3\text{-}49)$$

Where Reynolds number can be calculated by:

$$R_e = \frac{\omega r_o g \rho}{\mu} \quad (3\text{-}50)$$

Equation (3-45) can be redefined to consider the flywheel shaft, the disc moment on the side can be calculated by the following relationship [240]:

$$M_D = \rho\omega^2({r_o}^5 - {r_s}^5)C_m \quad (3\text{-}51)$$

Where r_s is the radius of the shaft. The Reynolds number at the tip is now a function of C_m which can be calculated by the following equation [334]:

$$Re_t = \frac{\omega r^2 \rho}{\mu} \quad (3\text{-}52)$$

The disc torque coefficient can be calculated by different correlations as shown below:

Von Karman Correlation [335]:

$$C_m = 0.073\,{Re_t}^{0.2} \qquad 5\times10^5 < Re_t < 2\times10^6 \quad (3\text{-}53)$$

Dorfman Correlation [336]:

$$C_m = 0.491 \times (\log_{10} Re_t)^{2.58} \qquad 1\times10^4 < Re_t < 1\times10^9 \quad (3\text{-}54)$$

Baylel and Owen Correlation [337]:

$$C_m = 0.0655 \times {Re_t}^{0.186} \qquad 1\times10^5 < Re_t < 1\times10^7 \quad (3\text{-}55)$$

Daily correlation [323]:

$$Cm = \frac{0.0102\left(\frac{g}{r_o}\right)^{\frac{1}{10}}}{Re_t^{\frac{1}{3}}} \quad (3\text{-}56)$$

The disc torque coefficient can also be calculated by the following relationship [240]:

$$Cm = \begin{cases} \frac{3.87}{Re_t^{\frac{1}{2}}}, & Re_t < 3\times10^5 \\ \frac{0.146}{Re_t^{\frac{1}{5}}}, & Re_t > 3\times10^5 \end{cases} \quad (3\text{-}57)$$

3.5.2.1. Airgap

The Reynolds number of the working fluid within the airgap can be calculated by the following equations:

$$Re_w = \frac{\rho \omega r_o (2g)}{\mu} \tag{3-58}$$

Where $(2g)$ is the hydraulic diameter of the annulus and g is the airgap size. The radius ratio between the rotor and the housing is determined by the following relationship:

$$\eta = \frac{r_o}{r_o + g} \tag{3-59}$$

Taylor [338] theoretically studied laminar flow between concentric cylinders and discovered an unstable flow structure characterised by complex toroidal vortices. This instability occurs when the angular velocity of the inner cylinder surpasses a certain value. In such scenarios, the centrifugal forces resulting from the rotation of a Couette flow dominate the viscous forces, leading to flow instability and the emergence of a secondary flow. Fig. 3-14 illustrates this secondary flow, manifesting as vortices that rotate in the opposite direction along the annulus. These steady alternate vortices, known as 'Taylor vortices', occur under specific flow conditions [338].

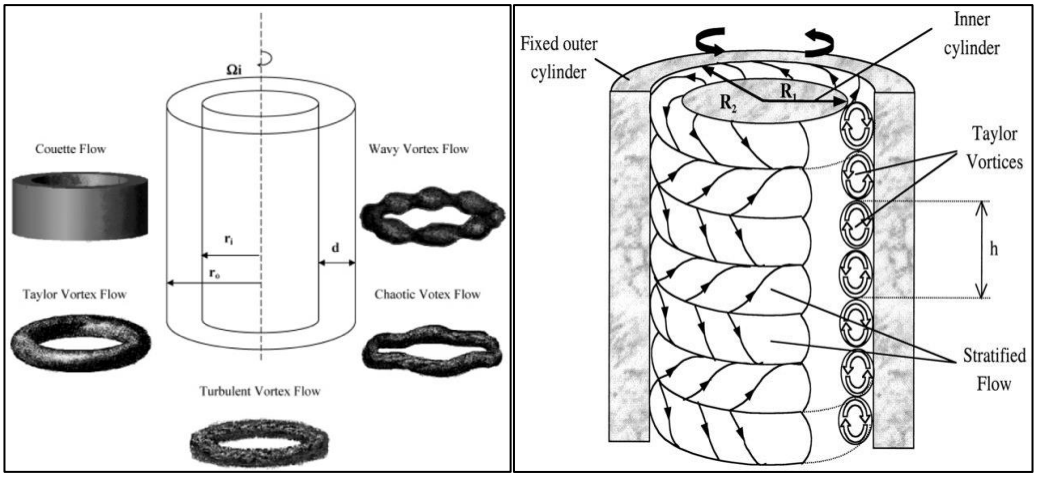

Fig. 3-14 Taylor vortices within the annulus of a concentric cylinder [339], [340]

Taylor vortex flow, a key phenomenon in fluid dynamics, is typically characterised by the Taylor number. This metric facilitates the classification of potential flow modes within the annulus of concentric cylinders. In the unstable regime of Taylor vortex flow, various complex spatial flow features such as spirals, modulated waves, and Taylor cells can be observed. The Taylor number enables the categorisation of the possible flows in a system with an inner rotating cylinder and an outer stationary cylinder as follows [341]:

- Couette flow (laminar flow)
- Taylor Vortex Flow (TVF)

- Wavy Vortex Flow (WVF)
- Modulated Wavy Vortices (MWV)
- Turbulent Taylor Vortices (TTV)
- Featureless turbulent flow (TUR)

A flow regime map as a function of inner and outer cylinder rotational speeds, was created by Rita Meyer and Max Planck [341], as depicted in Fig. 3-15. In the case of a FESS, where the outer cylinder is stationary (i.e. Outer Reynolds number of zero), different flow regimes are achieved at varying inner Reynolds numbers. Therefore, this work primarily focuses on the line where $Ro = Zero$ in the flow regime map.

In FESSs, the flow within the airgap can exhibit three distinct patterns: Taylor-Couette flow, occurring where the cylinder face meets the housing; Von Karman flow, existing between the discs and housing [342], and an "Intermediate Region" at the intersection of the two aforementioned flows, as illustrated in Fig. 3-16.

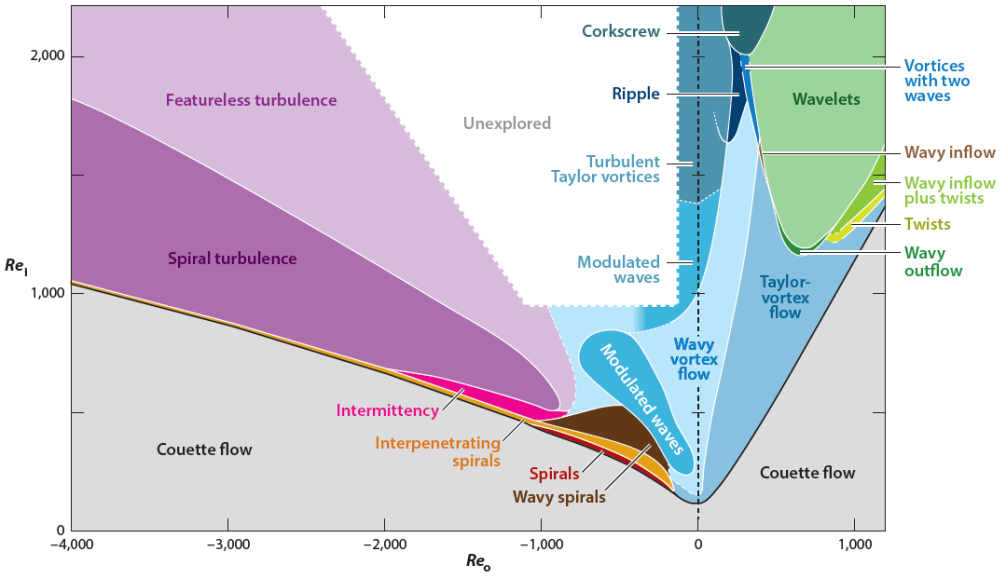

Fig. 3-15 The flow regime map within the annulus of concentric cylinders with radius ratio of 0.833 [341]

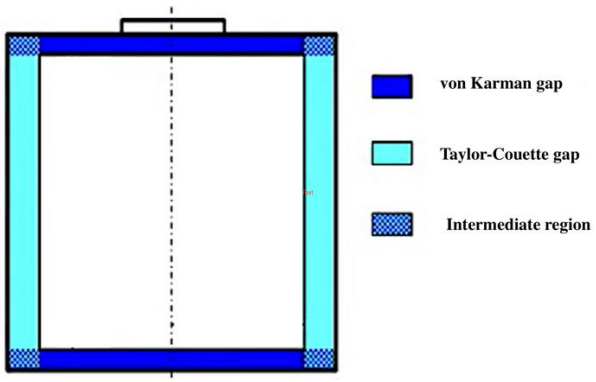

Fig. 3-16 Different flow configurations in FESSs [342]

In enclosed cylindrical systems, zero axial flow can disrupt the laminar flow between the cylinders at specific angular velocities, leading to the formation of circumferential Taylor vortices [343]. According to the classical criterion of rotational stability, Couette flow becomes unstable when there is an inner rotating cylinder with an outer cylinder at rest. The stability of the flow in scenarios where the airgap size is relatively small compared to the cylinder radius depends on the Taylor number. This critical number can be determined using one of the following two equations [344]:

$$T_a = \frac{\omega \times \left(\frac{2r_o+g}{2}\right)^{0.5} \times g^{1.5}}{\upsilon} \tag{3-60}$$

$$T_a = \frac{\omega \times r_o \times g}{\upsilon}\left(\frac{g}{r_o}\right)^{0.5} \tag{3-61}$$

Where r_o is the rotating cylinder radius (rotor) and g is the radial gap size. The flow regime can be identified based on the Taylor number as shown below:

$T_a < 41.3$	Laminar Couette flow
$41.3 < T_a < 400$	Laminar flow with Taylor vortices
$T_a > 400$	Turbulent flow

Under conditions where the Knudsen number is less than one, the Navier-Stokes equations are used to determine the wall shear stress. In this scenario, collisions between molecules can be neglected, and energy transfer and momentum result primarily from molecule-surface interactions [241]:

$$\tau = \frac{1}{2}\rho u_o \sqrt{\frac{2\mathcal{K}T}{\pi M}} = \frac{1}{2}\rho u_o \sqrt{\frac{2RT}{\pi}} \tag{3-62}$$

Where u_o is the rotating cylinder surface speed, $\mathcal{K}$ is the Boltzmann constant, *T* is the temperature of the working fluid, *M* is the molecular mass, and *R* is the gas constant. The power loss due to windage for a concentric rotating cylinder in free molecule flow is defined by the following expression [241]:

$$P_{W,C} = \tau A u_o = \left[\frac{1}{2}\rho u_o \sqrt{\frac{2RT}{\pi}}\right](2\pi aL)(u_o) \tag{3-63}$$

This can also be expressed using the ideal gas law:

$$P_{W,C} = \left[P\sqrt{\frac{2\pi}{RT}}\right] L\omega^2 a^3 \tag{3-64}$$

Where *P* is the gas pressure. The power loss on the two-disc surfaces due to windage drag is given by the following relationship:

$$P_{W,D} = 2\int \tau\, u\, dA = 2\int \frac{1}{2}\rho u \sqrt{\frac{2RT}{\pi}}(u)(2\pi r_o dr) \tag{3-65}$$

Where *u* represents the velocity of the specified radius on the disc. This equation can be rewritten as [241]:

$$P_{W,D} = \left(\frac{P}{2}\right)\left[\sqrt{\frac{2\pi}{RT}}\right]\omega^2 a^4 \tag{3-67}$$

As the Knudsen number increases, Couette flow transitions from the Navier-Stokes solution to a free-molecule solution [345]. The modified formula for shear stress in this regime is given by the following equation [241]:

$$\tau = \frac{1}{2}\rho u_o \sqrt{\frac{2RT}{\pi}}\left(\frac{2\lambda/L}{1+2\lambda/L}\right) \quad (3\text{-}68)$$

A roughing pump can achieve vacuum levels between 10 to 1 mbar. If the vacuum level is reduced to 1mbar compared to 10mbar at the highest surface tip speed, up to 90% of the windage losses can be eliminated, allowing for maximum energy storage. Although windage losses can be further reduced by employing a multistage vacuum system to reduce the working pressure below 1mbar, it increases the system cost and complexity significantly [346].

3.5.3. Thermal Analysis

To prevent changes in the material properties of a FESS rotor, such as dimensional expansions in critical areas and a decrease in tensile strength, it is crucial to maintain the temperature of the rotor and avoid overheating. These concerns underscore the need to minimise windage losses. Although windage losses are often considered a secondary issue due to their relatively small magnitude—typically less than 0.2% of the rated power—their reduction is significant for prolonging the energy storage duration of FESSs [101]. In this discussion, the rotor is modelled as a right circular cylinder. For simplicity, radiative transfer from the end discs of each cylinder is omitted. This simplification is justified as the rotor surface area is primarily circumferential, and the radiation view factor from the rotor perimeter to the housing disc ends is relatively small, rendering it insignificant. Heat transfer in a FESS occurs via conduction, convection, and radiation. Fig. 3-17 illustrates the thermal resistance of a typical FESS.

Under the assumption of a uniform temperature distribution across the rotor, the heat transfer components in a FESS are as follows:

- Conduction between the shaft and the rotor.
- Convection and radiation between the rotor and the housing within the airgap.
- Conduction within the case.
- Convection and radiation between the case and the surroundings.

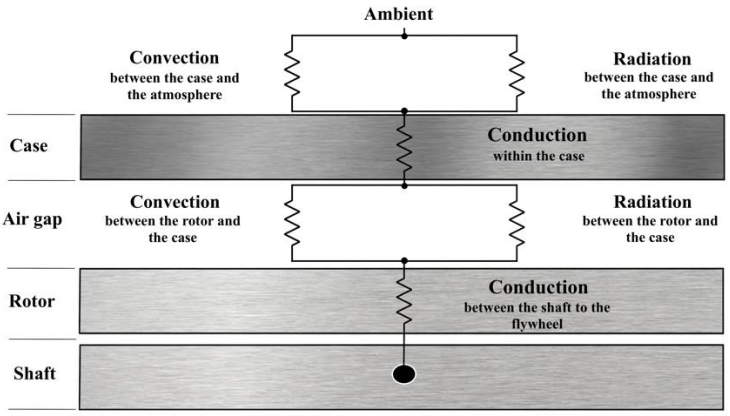

Fig. 3-17 The thermal resistance of the studied FESS

3.5.3.1.Conduction

Heat transfer from one body to another through direct contact is referred to as conduction. This mode of heat transfer is not only predominant in solids but can also occur within a single body. At the molecular level, conduction involves the transfer of energy through vibrations in the solid's atomic structure [347]. Fourier's law provides a mathematical framework to define the rate of heat transfer by conduction, which can be expressed by the following expression:

$$Q_{Con} = \frac{\Delta T}{R_{th}} \tag{3-69}$$

Where ΔT is the temperature difference over a defined distance and R_{th} is the thermal resistance. The thermal resistance specific to conduction can be calculated using the following formula [348]:

$$R_{th-con} = \frac{ln(^{r_2}/_{r_1})}{2\pi L\lambda} \tag{3-70}$$

Where r_1 and r_2 are the radii of the shaft and the rotor, respectively or between the housing outer and inner radii, respectively. L is the height of the body and λ is the thermal conductivity of the material.

3.5.3.2.Radiation

Heat transfer between two bodies through thermal radiation is facilitated by electromagnetic waves. This method of heat exchange is particularly useful in a vacuum environment, as it does not rely on any intervening medium, fluid or solid [349]. The heat output from thermal radiation can be calculated using the following equation:

$$Q_{rad} = \varepsilon A\sigma_s T^4 \tag{3-71}$$

Where ε is the emissivity of the body, A is the surface area of the body, σ_s is the Stefan-Boltzmann constant (valued at 5.6703× 10^{-8} $Wm^{-2}K^{-4}$), and T is the body temperature. The emissivity of the containment varies depending on the material used and coatings can alter this property. Radiation heat transfer between the housing and the surroundings can be calculated by the following equation [350]:

$$Q_{rad} = \varepsilon A \sigma_s \left({T_h}^4 - {T_A}^4 \right) \quad (3\text{-}72)$$

Where T_h is the housing temperature and T_A is the ambient temperature. The primary goal of this calculation is to determine the heat absorption of a flywheel rotor in vacuum, as radiation between surrounding surfaces is the sole means of heat dissipation in such an environment. However, in an atmospheric environment, the effect of radiation can be considered negligible [138]. The radiation emitted by the rotor in a system of two axisymmetric cylinders, where "1" refers to the rotor and "2" the housing, can be calculated by the following expression:

$$Q_{rad} = \frac{A_1 \sigma_s \left({T_1}^4 - {T_2}^4 \right)}{\frac{1}{\varepsilon_1} + \frac{A_1}{A_2}\left(\frac{1}{\varepsilon_2} - 1 \right)} = \frac{2\pi r_2 h \sigma_s \left({T_1}^4 - {T_2}^4 \right)}{\frac{1}{\varepsilon_1} + \frac{r_2}{r_2 + g}\left(\frac{1}{\varepsilon_2} - 1 \right)} \quad (3\text{-}73)$$

Where, A is the surface area, r is the radius, h is the rotor length, and g is the airgap. This formula applies specifically to cases involving an enclosed body [351].

3.5.3.3.Convection

Convection is the process of heat transfer either from one fluid to another or between a solid and a fluid. This mode of heat transfer involves the movement of fluid particles over a body and the circulation of bulk fluid. There are two primary types of convection: free convection and forced convection. Free convection is driven by temperature differences within the fluid, causing hotter, less dense parts of the fluid to rise and cooler, denser parts to sink which results in the bulk fluid flow. In contrast, forced convection occurs when an external force, such as a pump, propels the fluid movement. The heat transfer due to convection can be represented by the following equation [333]:

$$Q_{Conv} = \frac{\Delta T}{R_{th-conv}} \quad (3\text{-}74)$$

Where $R_{th-conv}$ represents the thermal resistance for convection, which is given by the following expression:

$$R_{th-conv} = \frac{1}{hA} \quad (3\text{-}75)$$

Where h is the local convection heat transfer coefficient. The efficiency of heat transfer by convection can be evaluated using the Nusselt number, a dimensionless quantity representing the ratio of convective to conductive heat transfer in the boundary layer between a solid surface and fluids. Nusselt number is given by the following expression [333]:

$$Nu = \frac{hD_i}{\lambda} \quad (3\text{-}76)$$

Where D_i is the diameter of the housing or rotor, and λ is the thermal conductivity of the material. Accurate calculation of the Nusselt number is crucial, as different conditions lead to varying correlations and values. For the convection between the FESS housing and the atmosphere, considered as natural convection, the Nusselt number can be calculated by the following equation [333]:

$$Nu = \left(0.6 + \frac{0.387 R_a^{\frac{1}{6}}}{\left[1+\left(\frac{0.559}{Pr}\right)^{\frac{9}{16}}\right]^{\frac{8}{27}}} \right)^2 \quad (3\text{-}77)$$

Where Pr is Prandtl number and Ra is Rayleigh number which can be calculated by the following relationship:

$$Ra = \frac{g*\beta*(T_C - T_A)*D^3}{v^2} \quad (3\text{-}78)$$

Where g is the gravity, β is the thermal expansion coefficient, and v is the Kinematic viscosity.

Taylor's work on heat transfer between smooth rotating cylinders addresses the effect of rotation. In this context, the influence of surface roughness is considered by increasing the coefficients derived by Taylor by approximately 10%, as suggested by Gazley [234]. This adjustment accounts for the impact of surface irregularities on heat transfer rate. The airgap is modelled as a smooth inner rotating cylinder surrounded by a stationary outer cylinder.

The convective heat transfer coefficient for the airgap can be calculated using the following formula [333]:

$$h = \frac{N_u k}{g} \quad (3\text{-}79)$$

The Nusselt number for the Taylor flow can be calculated using various correlations. The type of flow and the convective heat transfer coefficient in the annulus are determined using the Taylor number equation. Becker and Kaye [235] developed a correlation to calculate the Nusselt number based on the Taylor number as shown below:

$$Nu = \begin{cases} 2 & Ta_m < 1700 \\ 0.128 {Ta_m}^{0.367} & 1700 < Ta_m < 10^4 \\ 0.409 {Ta_m}^{0.241} & 10^4 < Ta_m < 10^7 \end{cases} \quad (3\text{-}80)$$

Where Ta_m is the modified Taylor number which can be calculated by the following equation:

$$Ta_m = \frac{Ta}{F_g} \quad (3\text{-}81)$$

Where F_g is the geometrical factor which is given by the following expression:

$$F_g = \frac{\pi^4 \left[\frac{2r_2 - 2.304g}{2r_2 - g}\right]}{1697\left[0.0056 + 0.0571\left(\frac{2r_2 - 2.304g}{2r_2 - g}\right)^2\right]\left[1 - \frac{g}{2r_2}\right]^2} \quad (3\text{-}82)$$

Gazley's correlation to calculate the Nusselt number based on the Taylor number is shown below [234]:

$$Nu = \begin{cases} 1.1 & Ta < 41 \\ 0.117 Ta^{0.63} Pr^{0.27} & 41 < Ta < 100 \\ 0.212 Ta^{0.5} Pr^{0.27} & 100 < Ta < \infty \end{cases} \quad (3\text{-}83)$$

3.5.3.4.Total Heat Transfer

The complete thermal resistance circuit of the studied FESS is illustrated in Fig. 3-18. This circuit encompasses all the thermal resistances within the system, with the exception of radiation, which is calculated separately due to the complexities involved in determining its thermal resistance. Each component within the FESS, from the shaft core to the ambient environment, has its own thermal resistance. To ascertain the total thermal resistance, the individual thermal resistances are summed. This cumulative thermal resistance is then used to calculate the total heat transfer within the FESS using the following equation:

$$Q_t = \frac{T_{Shaft} - T_{ambient}}{R_T} \tag{3-84}$$

Where R_T represents the total thermal resistance which is given by the following relationship:

$$R_T = \frac{\ln\frac{r_1}{r}}{2\pi L k_s} + \frac{\ln\frac{r_2}{r_1}}{2\pi L k_R} + \frac{1}{h_{airgap} A} + \frac{\ln\frac{r_4}{r_3}}{2\pi L k_H} + \frac{1}{h_{amb} A} \tag{3-85}$$

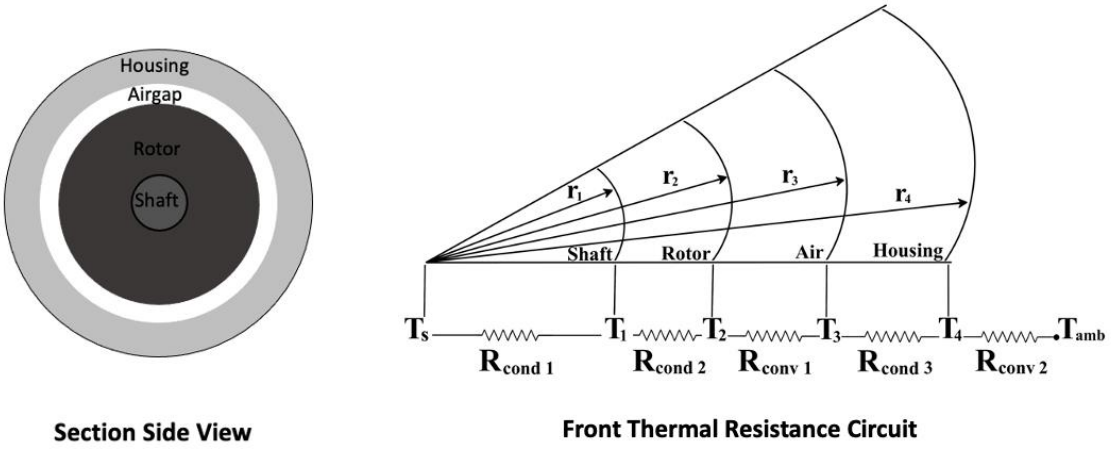

Fig. 3-18 The thermal resistance circuit of the studied FESS

3.6. Rotor Design Criteria

The design of a rotor capable of storing sufficient energy at high speeds while withstanding induced stresses is a pivotal aspect of a FESS design. This section describes the research and analytical processes that underpins the design of the flywheel rotor which is used as the base model in this work. Analytical methods are employed to explore various potential geometries for the flywheel. Fig. 3-19 illustrates the design process of a flywheel rotor and the factors that influence it. The design procedure encompasses several stages: requirements analysis, rotor type selection, initial design formulation, design optimisation, and performance evaluation.

To determine the geometric parameters of the flywheel, it is essential to consider a multitude of conditions and factors. These include the general configuration of the FESS, the amount of energy to

be stored, operational speed, material characteristics, moment of inertia, rotor dynamics, the mass of the flywheel rotor, and considerations for structural manufacturability. Each of these elements plays a significant role in shaping the final design, ensuring that the flywheel meets the desired performance criteria while adhering to engineering and material constraints.

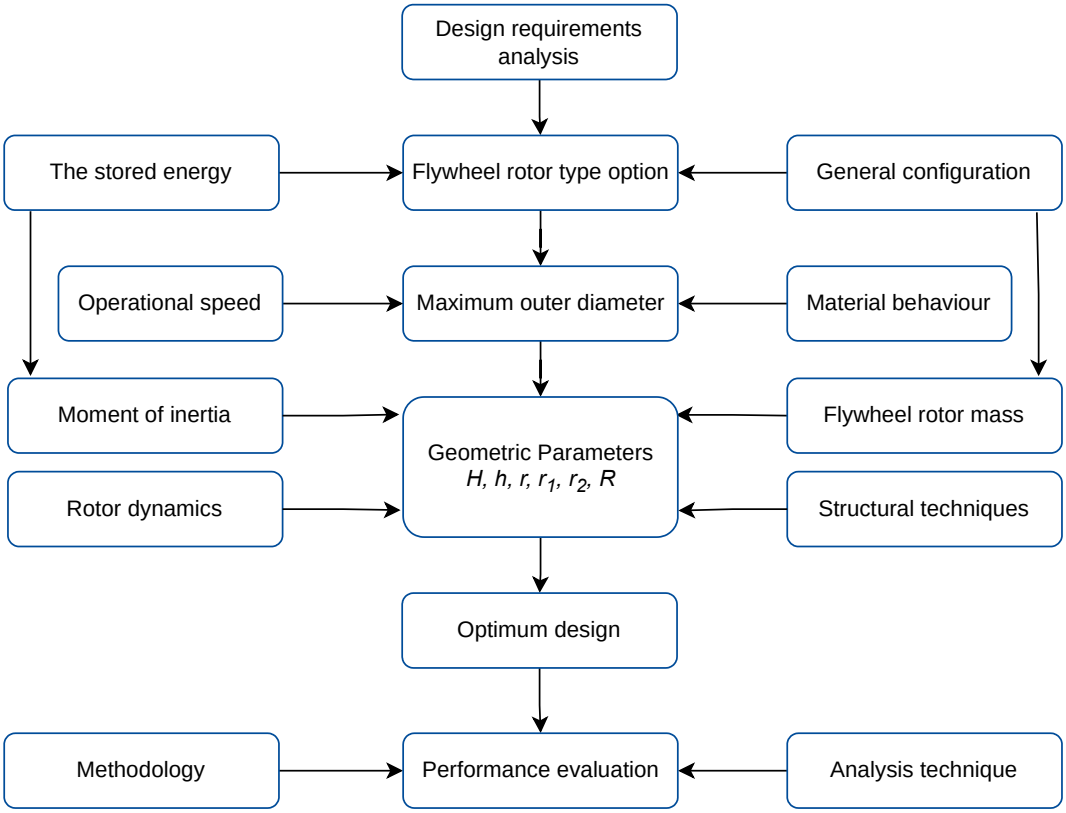

Fig. 3-19 FESS design requirements analysis flowchart

3.6.1. FESS Rotor Design

FESSs are broadly classified into two categories depending on the material used in their rotors. The first category includes FESSs with rotors made primarily of steel, characterised by a solid rotor. The second category consists of FESSs that feature a metallic hub, typically combined with a composite rim constructed from high-tech materials such as carbon fibre or graphite. Composite flywheels, while sharing the same geometrical shape and operational conditions as their steel counterparts, offer distinct advantages. Although steel is a common structural material, it is limited in application due to its lower operational speed ceiling of up to 10,000 rpm. In contrast, composite materials, being lighter than steel, are capable of withstanding higher rotational stresses. The primary drawback of composite materials is their high cost, which is anticipated to decrease in the future [352]. The kinetic energy stored in the rotor is a function of its moment of inertia and angular velocity, as expressed by the following equation:

$$E = \frac{1}{2} I \omega^2 \tag{3-86}$$

Where *I* is the moment of inertia and ω is the angular velocity of the rotor. It is important to note that the rotor structure may vary, ranging from hollow or solid cylinders to short disc or long drums. The moment of inertia for both hollow and solid cylindrical rotors can be determined using Eq. 3-87 and Eq. 3-88, respectively [346]:

$$I = \frac{1}{2}m({r_o}^2 - {r_i}^2) \tag{3-87}$$

$$I = \frac{1}{2}m{r_{sd}}^2 \tag{3-88}$$

Where *m* is the rotor mass and r_o and r_i are the outer and inner radii of the hollow cylinder, respectively, while r_{sd} is the radius of the solid cylinder. The mass and stresses affecting flywheel rotors, whether solid or hollow, are crucial factors to consider in their design. The mass of a rotor, whether solid or hollow, can be calculated using the following equations:

For solid cylinders:

$$m = \pi\rho h_r {r_{sd}}^2 \tag{3-89}$$

For hollow cylinders:

$$m = \pi\rho h_r({r_o}^2 - {r_i}^2) \tag{3-90}$$

Where ρ is the rotor density and h_r is the rotor height.

Tensile strength is a critical material property that indicates the maximum speed at which a FESS can safely operate without exceeding the material strength of the rotor. The maximum hoop stress experienced by the rotor can be calculated using the following formula [353]:

$$\sigma_{max} = \frac{F}{A} \tag{3-91}$$

Where *A* is the area affected by the hoop stress, and *F* is the force acting on both sides of the cylinder. In a rotating cylinder, whether solid or hollow, the rotor encounters three types of stress: longitudinal (or axial), radial, and hoop (or circumferential and tangential). The longitudinal stress is generally zero unless the cylinder is sufficiently long to experience longitudinal bending, or there is an axial force loading or pressure acting on it [354]. The radial and hoop stresses at a given location (r_x) in a solid cylindrical rotor can be calculated by Eq. 3-92 and Eq. 3-93, respectively [353]:

$$\sigma_r = \frac{(3+\nu_p)}{8}\rho\omega^2({r_o}^2 - {r_x}^2) \tag{3-92}$$

$$\sigma_\theta = \frac{\rho\omega^2}{8}\left[(3+\nu_p){r_o}^2 - (1+3\nu_p){r_x}^2\right] \tag{3-93}$$

Where σ_r is the radial stress, σ_θ is the hoop stress, ν_p is the Poisson's ratio, and r_x is the specific location of interest. The maximum stress occurs at the centre of the solid cylinder, which can be determined by setting $r_x = 0$ in Eq. 3-92 and 3-93. The maximum radial and hoop stresses are given by the following equations [355]:

$$\sigma_{r_{max}} = \frac{(3+\nu_p)}{8}\rho\omega^2{r_o}^2 \tag{3-94}$$

$$\sigma_{\theta_{max}} = \frac{\rho\omega^2}{8}\left[(3+\nu_p){r_o}^2\right] \tag{3-95}$$

In a hollow cylinder the radial and hoop stresses can be calculated by Eq. 3-96 and Eq. 3-97, respectively [355]:

$$\sigma_r = (3 + \nu_p)\frac{\rho\omega^2}{8}\left({r_i}^2 + {r_o}^2 - \frac{{r_i}^2{r_o}^2}{{r_x}^2} - {r_x}^2\right) \quad (3\text{-}96)$$

$$\sigma_\theta = \frac{\rho\omega^2}{8}\left[(3 + \nu_p)\left({r_i}^2 + {r_o}^2 + \frac{{r_i}^2{r_o}^2}{{r_x}^2}\right) - (1 + 3\nu_p){r_x}^2\right] \quad (3\text{-}97)$$

In the case of a hollow cylindrical rotor, the maximum stresses due to spin loads occur on the inner surface of the rotor. When $r_x = r_i$ (i.e. The inner radius), the maximum radial and hoop stresses can be calculated by the following equations:

$$\sigma_{r_{max}} = (3 + \nu_p)\frac{\rho\omega^2}{8}(r_o - r_i)^2 \quad (3\text{-}98)$$

$$\sigma_{\theta_{max}} = \frac{1}{4}\rho\omega^2\left((3 + \nu_p){r_o}^2 + (1 - \nu_p){r_i}^2\right) \quad (3\text{-}99)$$

At high tangential velocities, the mass at the outer surface of the cylinder exerts a pulling force on the inner material, leading to increased hoop stress towards the centre in solid rotors and at the inner radius for hollow cylinders. Radial stress tends to be more concentrated in the middle of the cylindrical shells. The Von Mises effective stress, derived from these two orthogonal stress components, is crucial for calculating the safety factor of the rotor. These stress equations also clarify why more complex flywheels feature thicker hubs, spokes, and outer rims. High tensile strength spokes are employed to manage the peak radial stress at the midsection, while additional composite material at the outer radius efficiently manages the high hoop stress.

This stress analysis also explains the motivation behind hybrid flywheels that combine steel hubs with composite rims, which can withstand extremely high loads along the fibre direction. However, the complexity and cost of manufacturing such hybrid flywheels are significant [356]. Steel is a favourable material for flywheels due to its density, strength, and commodity value, but its use is limited by its maximum rotational speed. The energy density and specific energy of the flywheel can be calculated using the following equations, respectively:

$$e_{k,v} = K\sigma_{max} \quad (3\text{-}100)$$

$$e_{k,m} = K\frac{\sigma_{max}}{\rho} \quad (3\text{-}101)$$

Where $e_{k,v}$ is the energy density and $e_{k,m}$ is the specific energy of the FESS. The "shape factor", denoted by *K*, is a crucial parameter in determining the speed limit and efficiency of a flywheel design. The Laval disc, characterised by its ability to maintain equal tangential and radial stress elements throughout, is assigned a shape factor of *K = 1*. The ideal shape of a flywheel varies depending on the material used. Isotropic materials, such as steel, exhibit equal strength in radial and tangential directions [103]. In contrast, fibre-reinforced composites, which are anisotropic, demonstrate superior strength in the longitudinal fibre direction due to their unidirectional tensile strength. As such, specific shapes are more suited to different types of materials, as outlined in Table 3-3 [94]. Thin (hollow, circular)

flywheels are particularly advantageous when using composite materials since this geometry leverages the high unidirectional strength of fibres [357]. Multiple studies [358] [129] [357] have identified the hollow cylindrical rotor as the optimum shape for a composite flywheel rotor.

Table 3-3 Shape factor for several flywheel designs [357]

Shape	Geometry	Shape factor (K)
Laval Disc	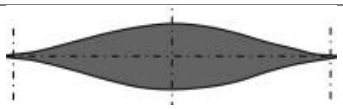	1.0
Real Laval Disc		0.70-0.90
Solid Disc	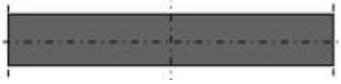	0.606
Thick Ring	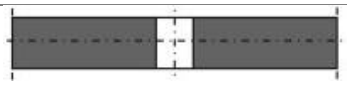	0.305
Thin Ring	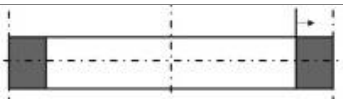	0.50
Laval Disc with rim	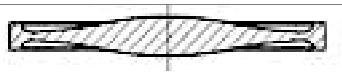	0.80-0.95
Conical Disc	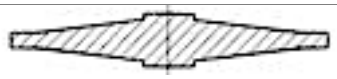	0.70-0.85
Disc with rim & centre hole		0.40-0.50

Singh and Chaudhary [359] explored the design of an optimal flywheel shape using nature-inspired optimisation algorithms. The optimisation process focused on maximising kinetic energy storage, considering factors such as the flywheel mass and Von Mises stress throughout the radial direction. The optimised flywheel shape, derived using the Jaya algorithm as depicted in Fig. 3-20, stores 36.55% more energy than the conventional design, without exceeding material stress limits during operation. However, it is important to note that this design, while theoretically effective, may be challenging and costly to manufacture due to its complex design.

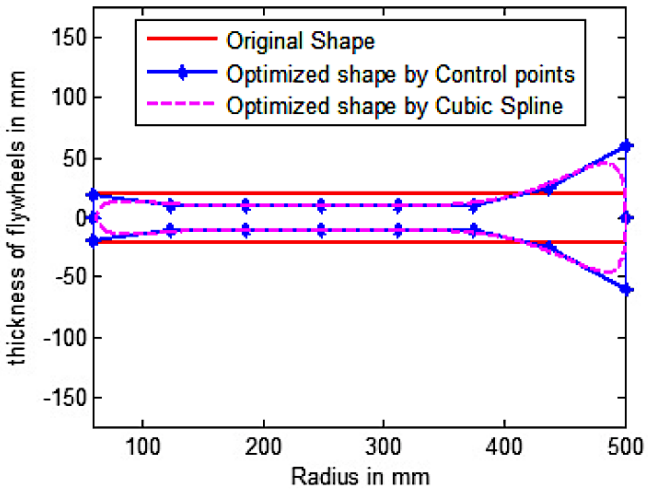

Fig. 3-20 Flywheel rotor shape optimisation [359]

3.6.2. Rotor Material

The choice of material for a flywheel rotor largely depends on the design requirements, subject to certain constraints. In scenarios where constraints are minimal, the pivotal feature to consider is the material's specific strength, defined as the ratio of its strength to its density. This ratio is directly proportional to the energy density of the material, making high-strength composite materials an optimal choice for flywheels [360]. Despite their high anisotropy, these materials may have limitations. For instance, if the materials are unidirectional and their weaker strength direction is perpendicular to the fibres, the use of high shape-factor designs may not be feasible. A shape factor value exceeding 0.5 typically indicates a bidirectional stress distribution [360].

Improving the strength in the weaker directions of composite materials through the use of suitable multidirectional composites can allow for higher shape factor values. Alternatives to composite materials include reinforced plastic materials with carbon, glass-fibre, or aramid fibres such as Kevlar, which offer comparable specific strength to uniaxial composite materials. The choice of material can also be influenced by cost considerations; for instance, fibreglass is the most economical option, while S-glass offers high specific strength but is limited by its lower Young's modulus and fatigue strength [91].

Materials with higher stiffness experience smaller displacements, reducing dynamic issues caused by asymmetric deformation, thus simplifying the challenges of connecting the shaft to the flywheel rim. Some rotor designs may require varying stiffness in different parts, which can be achieved by using distinct materials for each section of the rotor. However, the use of fibreglass is often constrained due to its low Young’s modulus [361].

Although a high-density material such as steel can store more energy than an equivalent low-density material at the same operational speed, low-density materials experience lower internal stresses thus

capable of operating at higher speeds. This capability allows the FESS to store the same amount of energy but with significantly lower system weight. Composite rotors are known for their benign failure modes, paralleling the technology used in lightweight, bulletproof vacuum chambers [362]. Table 3-4 presents a comparison of current materials with some emerging options, highlighting the future potential of FESSs.

Table 3-4 The characteristics of various flywheel rotor materials [85] [100] [352]

Material	**Ultimate Tensile Stress (MPa)**	**Density (kg/m^3)**	**Specific Energy (W/kg)**	**Cost (£/kg)**
Steel 4340	1520	7700	50	2.5
Aluminium 7075	572	2810	28	4
17-7 PH Stainless steel	1650	7800	29	4.7
Alloy steel 30CrNiMo8	1000	7760	36	6
Maraging steel 18Ni250	1860	8000	65	35.5
Titanium Ti-15V-3Cr-3Al-3Sn ST 790 °C	1380	4760	202	20
Advantix E-glass (glass fibre)	1400	2146	90	-
S-Glass	1470	1920	210	19.5
Kevlar	3800	1450	370	31
Vapour grown carbon nanofibers	2920	2000	202	-
Toray T1000G composite	3040	1800	234	80
Toray T1000G fibre	6370	1800	491	-
Carbon fibre reinforced composite material T700 +epoxy resin	2450	1550	439	51.5
T-700 graphite	7000	1780	545	-
Multi-walled carbon nanotubes (low end)	10,000	1750	793	-
Single wall carbon nanotube (low end)	50,000	1300	5,341	-
Multi-walled carbon Nanotubes (high end)	60,000	1750	4,761	-
Single wall carbon nanotube (high end)	500,000	1300	53,418	-

Table 3-4 presents the characteristics of various rotor materials used in FESSs. As the data indicates, materials with low density and high strength are the optimal choice for flywheel rotors. Composite materials, characterised by their high strength and low density, are particularly well-suited for this application. They enable flywheel rotors to achieve higher rotational speeds, resulting in flywheels with high-specific energy. As such, when designing flywheel rotors, composites are generally preferred over metals due to their superior performance characteristics. The theoretical specific energy of composite rotors is about five times greater than that of their metallic counterparts [91].

The concept of high-speed flywheels gained traction in the 1970s. A research approach to rotor design, advocating the use of composite materials over metals, was outlined in a Scientific American article by researchers at the Lawrence Livermore National Laboratory [360]. One advantage of composite materials is their failure mode; unlike metals, which can shatter into dangerous projectiles, composites typically develop cracks that gradually degrade, leading to a safer failure mode. For instance, carbon fibre flywheels are often designed with thin rims to minimise radial stresses caused by high centrifugal forces, which also helps with manufacturing. Utilising multiple thin rims to form a multi-ring structure enhances both safety and strength. Moreover, this configuration allows for higher rotational speeds [85]. Flybrid Systems LLP [159] conducted research on a filament-wound carbon composite flywheel, highlighting the potential for increased energy density and the ability to achieve rotational speeds of up to 64,000 rpm. It is also important to note that the stored energy in a flywheel depends on peripheral speeds; hence, a rotor with a smaller diameter at higher speeds may not store more energy than one with a larger diameter at lower speeds [91]. Flywheels designed for higher speeds tend to have larger but thinner rotor diameters, resembling a disc more than a drum. Therefore, the choice of speed does not significantly impact the overall form of the flywheel rotor mass package, but it does influence mechanical transmission requirements. For instance, if mechanical transmissions are involved, a higher-speed flywheel may necessitate a high-speed tailoring mechanism to reduce input speeds to the gearbox to a few thousand rpm or lower [346].

3.6.3. Maximum Outer Radius

This section focuses on determining the maximum outer radius of a flywheel rotor. The critical factor in this determination is the maximum hoop stress that the rotor, whether solid or hollow, can withstand. By selecting an appropriate safety factor and considering the maximum rotational speed permissible, the maximum outer radius can be calculated. The relationships used for calculating the maximum radius for solid and hollow rotors are as follows [363]:

For solid rotors:

$$r_{sd} < \sqrt{\frac{8\,\sigma_\theta}{\rho\omega^2(3+\nu)}} \tag{3-102}$$

For hollow rotors:

$$r_o < \sqrt{\frac{1}{(3+v)}\left[\frac{4\sigma_\theta}{\rho\omega^2} - (1-v){r_i}^2\right]} \quad (3\text{-}103)$$

For a flywheel with a metallic hub (i.e. Representing a hollow cylinder), the inner radius can be approximated as if it were a solid cylinder. There is a wide variety of possible combinations of rotor radii and thicknesses. While a higher mass contributes to greater energy density, larger radii necessitate more robust and heavier housing (i.e. Safety containment). Therefore, selecting an appropriate rotor radius is a key design consideration to optimise the overall system size and stored kinetic energy while withstanding hoop stresses.

3.6.4. Rotor Length

The optimal flywheel rotor length is fundamentally linked to its dynamic characteristics. A rotating body in a flywheel system can give rise to bending resonance modes, referred to as “criticals”, and affect the rigidity of the system. A highly rigid system can lead to substantial energy losses. Therefore, a sufficiently soft bearing system is often chosen to ensure that these criticals occur at lower speeds. This approach allows the critical effects to be transmitted during the run-up, after which the rotor rotates around its centre of mass, resulting in lower bearing forces and damping losses. Achieving this efficiency requires a well-balanced rotor with minimal centre shift. The rotor length has a significant influence on the system dynamics, particularly in terms of its effect on the rigidity of the conical body, which is contingent on the rigidity of the chosen bearing. To prevent issues of this mode within the operational speed range of the machine, the rotor length-to-diameter ratio should be significantly greater than 1:1. This consideration leads to a choice between a cylindrical or a disc rotor shape. Typically, the length is minimised to allow operation at maximum stress velocity, aiming to lower the rotor's speed [103].

In the context of hybrid powertrains, the size of the flywheel system has a direct impact on fuel consumption. Larger flywheels facilitate more efficient braking energy recovery, leading to lower fuel consumption. However, beyond a certain size, the drawbacks, including increased drag and a reduced dynamic speed range, begin to outweigh the benefits, resulting in increased fuel consumption. The relative payback period in hybrid powertrains is an essential metric, quantifying the fuel saving advantages relative to the capital investment in hybridisation and the service life of passenger vehicles [364].

3.6.5. Hub Design

Increasing the energy capacity of a flywheel at a fixed speed can be more efficiently achieved by enlarging the radius rather than the length of a conventional flywheel rotor. However, in vehicular

applications, augmenting the rotor length offers the advantage of a greater bearing span. This extended span effectively reduces bearing loads, particularly under gyroscopic couples, which are significant in dynamic vehicular environments. Traditional flywheel designs typically feature an energy storage ring attached to a symmetrical hub. Various hub designs, such as simple disc and spoked configurations, are depicted in Fig. 3-21. Precision in hub design becomes increasingly critical when operating at higher speeds to prevent issues with the rim. For instance, if a metal rim expands more than the hub during operation, a loss of contact can occur, leading to operational inefficiencies or mechanical failures. Conversely, if the rim expands less than the hub, it can result in elevated stress levels within the flywheel [76].

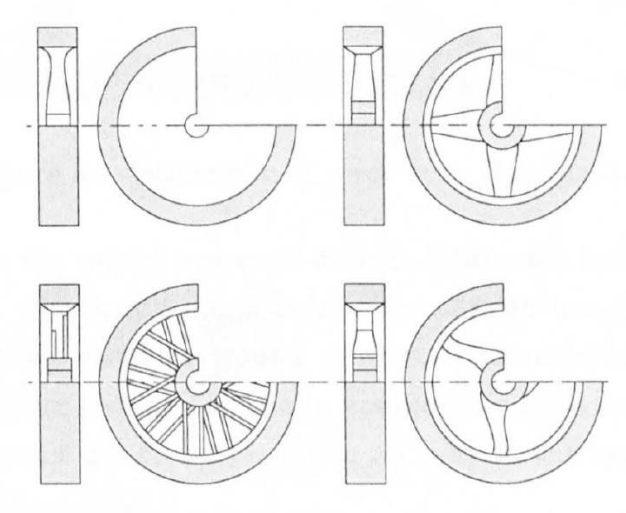

Fig. 3-21 Different flywheel hub designs [76]

3.6.6. Optimal Design

The implementation of FESSs in lightweight vehicles, particularly in passenger vehicles, necessitates a compact design to be viable for car manufacturers. Achieving a small-volume system requires the use of materials with high density, enabling sufficient mass within a compact space. To ensure a compact design, the rotor radius must be small, while the rotor length should ideally match its radius to minimise gyroscopic effects. The energy storage capacity of a FESS should exceed a minimum threshold to ensure effectiveness. Based on the comprehensive literature review conducted in Chapters 2 and 3, a set of design limitations has been established. These limitations are instrumental in streamlining the design process of a flywheel rotor, ensuring it meets the specified energy storage requirements. The predefined design constraints are as follows:

- Rotor Radius: The radius of the rotor must be less than 0.15 meters. This constraint ensures the compactness of the design, which is essential for integration into lightweight vehicles.

- Safety Factor: The rotor design should have a factor of safety greater than or equal to 2 at its highest operational speed. This consideration is critical for ensuring the reliability and safety of the FESS under extreme operational conditions.
- Energy Storage: The flywheel must be capable of storing more than 100 kJ of energy. This threshold is set to ensure that the flywheel contributes significantly to the vehicle's energy management system.
- Rotor Material Cost: The cost of rotor material should be less than £400. This limitation is placed to maintain the economic viability of the FESS, making it an attractive option for mass production.
- Rotor Mass: The rotor mass should be less than 60 kilograms. Keeping the rotor mass within this limit is crucial for maintaining the overall lightweight nature of the vehicle and for facilitating ease of integration.

The maximum allowable rotational velocity for a solid cylindrical rotor, with a safety factor of 2, can be calculated using the following formula:

$$\omega_{max} = \sqrt{\frac{4\sigma}{\rho {r_{sd}}^2 (3+\nu)}} \tag{3-104}$$

Where σ is the tensile strength of the rotor material. For a hollow cylindrical rotor, the maximum allowable rotational velocity is given by the following expression:

$$\omega_{max} = \sqrt{\frac{2\sigma}{\rho\left((3+\nu){r_o}^2 + (1-\nu){r_i}^2\right)}} \tag{3-105}$$

Considering these design limitations and the maximum allowable rotational speeds for both solid and hollow rotors, various values for rotor radii, materials for metal solid cylindrical rotors, and composite materials for hollow cylindrical rotors are evaluated. The corresponding rotor mass, material cost, and kinetic energy for each flywheel configuration are calculated, as detailed in Appendix B. Fig. 3-22 shows the kinetic energy storage capacity and rotor cost for different materials selected from Table 3-4. An analysis of the kinetic energy capabilities of various materials reveals that stainless steel and steel 4340 are among the top performers in terms of the highest kinetic energy storage achievable. This observation is further supported by the data presented in Fig. 3-23, which illustrates the relationship between the kinetic energy storage capacity and the flywheel rotor mass. A closer examination of this relationship, particularly focusing on the rotor mass in comparison to the kinetic energy it can store, indicates that stainless steel and steel 4340 exhibit very similar properties. Both materials not only achieve comparable levels of kinetic energy storage but also have closely related mass values.

The optimal rotor design involves selecting key parameters and assigning a value of significance to each parameter. The stored kinetic energy is deemed most significant, accounting for 50% of the consideration, followed by rotor material cost at 30%, and rotor mass at 20%. The preference order for materials, from most to least favoured, is presented in Table 3-5. The details of the optimum rotor design, which will be utilised in subsequent sections, are listed in Table 3-6.

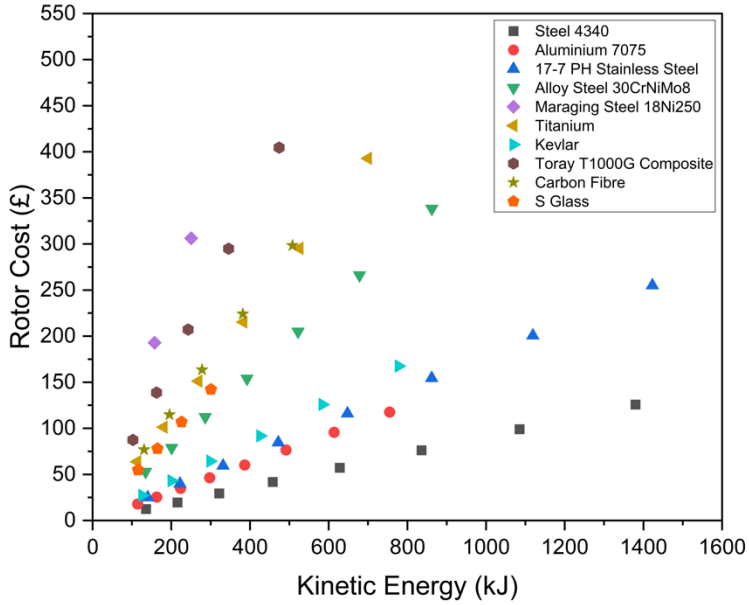

Fig. 3-22 A comparison between the cost and kinetic energy storage capacity of various flywheel rotor materials

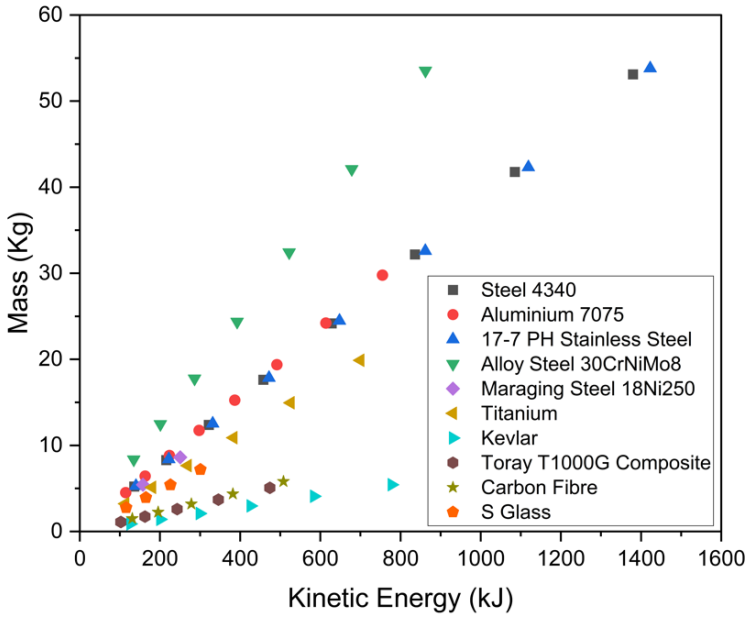

Fig. 3-23 A comparison between the mass and kinetic energy storage capacity of various flywheel rotor materials

Table 3-5 Flywheel rotor material ranking

Material	Favourability rate (1= highest)
Steel 4340	0.52626488
17-7 PH Stainless steel	0.52230114
Kevlar	0.44547621
Aluminium 7075	0.35015362
Alloy steel 30CrNiMo8	0.32077638
Toray T1000G composite	0.27288049
Titanium	0.26811973
Carbon fibre	0.24122487
S-Glass	0.19958894

Table 3-6 Optimal rotor design values and parameters

Parameter	Value
Material	Steel 4340
Design shape	Solid cylinder
Rotor radius	0.13 m
Rotor length	0.13 m
Rotor mass	53 kg
Max rotational speed	23,500 rpm
Rotor cost	£125
Safety factor	2
Kinetic energy	1380 kJ

3.7. Summary

The validation and verification of the numerical CFD model are integral steps in establishing confidence in the simulation data. Through the validation process, the SST k-omega turbulence model was identified as the most appropriate for investigating the FESS performance. This model is noted for its superior capability in predicting flow separation more accurately than most RANS models. Therefore, the SST k-omega model will be used for CFD modelling in subsequent sections. Additionally, verification will be performed for each new geometry introduced in the simulation to ensure results are mesh independent.

The efficiency of the FESS is a vital consideration for its application in vehicles. It is recognised that higher system losses correlate to lower overall system efficiency. The main sources of losses in a FESS

are aerodynamic and bearing friction losses. Even in well-engineered flywheel systems, these losses, while typically small, can accumulate significantly over time. This chapter has explored the characteristics of aerodynamic and bearing friction losses in FESSs. While bearing losses can only be reduced through the selection of an appropriate bearing system and lubrication, windage losses offer more opportunities for reduction. Modifications to the flywheel and housing can markedly decrease these losses. This study aims to investigate these modifications and their impact on the FESS efficiency, with further discussions on these aspects to follow in subsequent chapters. The results presented in this chapter on the composite rotor have been published in a journal paper [365].

In the context of rotor design for FESSs in vehicle applications, the selection of the size parameters and operating conditions was methodically executed. Rotor stress equations play a crucial role in this process, leading to the determination of a suitable operational speed. Various materials were evaluated for rotor optimisation, resulting in the selection of steel 4340 as the most suitable material. The chosen rotor, with a diameter of 0.260 m and a length of 0.13 m, balances the requirements of stress limits and energy storage capacity.

Chapter 4. FESS Aerodynamic Performance Characteristics

4.1. Pre-Processing

In preparation for the numerical analysis of the FESS performance, this section lays the groundwork for a comprehensive study of the factors influencing its aerodynamic performance. This investigation is pivotal to selecting appropriate parameters for subsequent analysis aimed at optimising the aerodynamic efficiency of the FESS. Conceptually, a FESS is structured as a concentric cylinder comprising a rotating inner cylinder and a stationary outer cylinder. The numerical estimation of windage losses, crucial for this study, is derived from the computation of the rotor skin friction coefficient.

Windage losses in a high-speed rotor are primarily due to viscous friction caused by the fluid in the FESS annulus. These losses are predominantly influenced by tangential fluid flow and Taylor-Couette flow, with key contributing factors being the airgap size, flywheel speed, and the thermo-physical properties of the working fluid. The assessment of windage losses typically involves analysing the flow between the rotor and the housing.

In this study, the airgap is defined using a dimensionless parameter known as the radius ratio (RR), denoted by $\eta = r_o/(r_o + g)$, where r_o is the rotor radius, and g is the gap width. Another critical parameter is the aspect ratio $\Gamma = L/g$, where L is the rotor length. The rotor radius and length have been set to 0.13 m, as detailed in Chapter 3. To align with the objective of the final FESS design being compact, the radius ratio is constrained to maintain a narrow airgap. Table 4-1 presents the values of the studied FESS geometries. As established earlier, the rotor's maximum rotational velocity is set at 2400 rad/s, with peripheral speeds tested ranging from 6.5 to 312 m/s.

Isothermal boundary conditions at an initial temperature of 24°C are applied to the rotor and housing walls. Fig. 4-1 depicts the FESS used in this investigation, with dimensions selected based on the geometrical analysis conducted in Chapter 3. Due to the symmetrical nature of the FESS geometry, the CFD domain is reduced to an 8-degree segment with a central symmetry plane, significantly reducing computational time, as illustrated in Fig. 4-1. Periodic boundary conditions are applied to the surfaces on either side of this 8-degree segment to accurately model the full computational domain.

Table 4-1 Studied FESS geometries

Design #	Gap g (mm)	Radius Ratio η	Aspect Ratio Γ
1	1.3	0.99	100
2	2.6	0.98	50
3	4.0	0.97	32.5
4	5.4	0.96	24
5	6.8	0.95	19

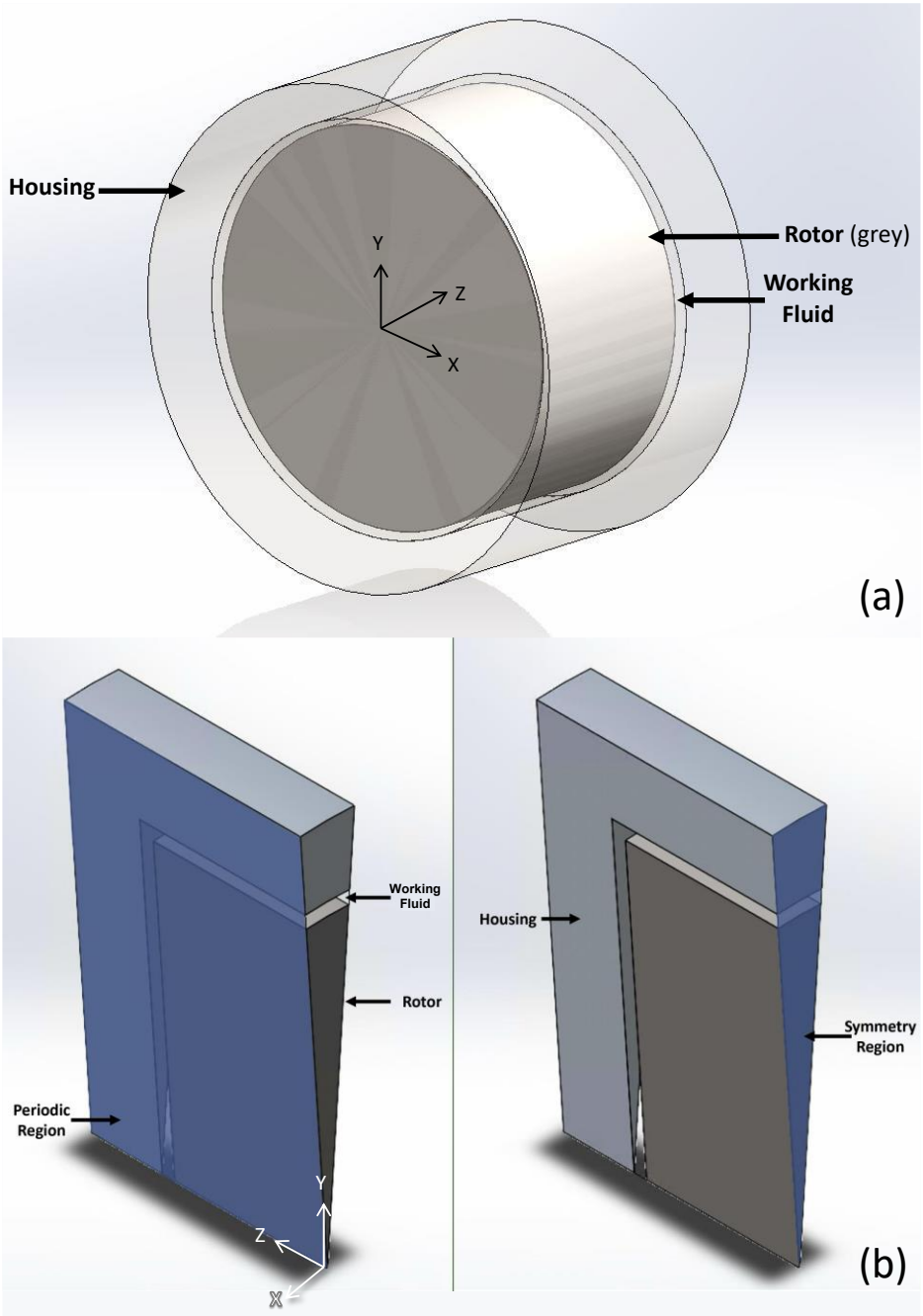

Fig. 4-1 Numerical domain, (a) FESS geometry in 3D, (b) the simplified geometry with periodic and symmetry regions

4.1.1. Mesh Independence Analysis

Mesh independence analysis constitutes a critical pre-processing step in numerical simulations, serving to enhance the accuracy and reliability of the results. The number of elements used in this investigation and the dimensions of each mesh component are detailed in Table 4-2. All airgap models employed in this study utilise a structured quadrilateral mesh. The primary aim of this process is to identify a mesh configuration that yields solutions independent of the mesh size. This objective was pursued by conducting a mesh independence test, focusing on the rotor skin friction coefficient and the Nusselt number as key parameters of interest, at the highest rotational speed of 2400 rad/s.

The relationship between the skin friction coefficient and the Nusselt number, and the number of mesh elements for the five radius ratios studied, is depicted in Fig. 4-2. Based on the outcomes of these tests, a mesh configuration comprising airgap element size of 0.125 mm and rotor and housing element size of 1.25 mm was selected. This configuration was chosen to optimise computational efficiency, as further increasing the mesh size showed negligible impact on the accuracy of the numerical results, indicating that the numerical predictions had become independent of the mesh size.

Selecting an appropriate mesh type and ensuring its quality are crucial in numerical studies to draw accurate and valid conclusions. In this research, high mesh quality was maintained by closely monitoring mesh metrics. By maintaining the mesh orthogonal quality above 0.8, the mesh cells align closely with the computational domain's coordinate directions, which is crucial for minimising numerical diffusion and improving the precision of gradient calculations. This level of orthogonality is particularly important when resolving complex flow patterns and thermal effects that are sensitive to the mesh's geometric fidelity. Furthermore, keeping the mesh skewness below 0.3 is a testament to the mesh's uniformity and balance, which plays a vital role in reducing errors in the simulation. Low skewness values indicate that the cells do not deviate significantly from the ideal shapes, which is essential for achieving accurate flux calculations between cells. The mesh orthogonal quality was kept above 0.9, and the mesh skewness was maintained below 0.15, ensuring the fidelity of the simulation results. Fig. 4-3 illustrates the mesh used in these simulations.

Table 4-2 Mesh independence test parameters

Mesh Number	Case	Element number	Gap	Rotor & Housing
			Element size (mm)	
1	0.99	908,028	0.2	2
2		1,340,936	0.175	1.75
3		1,867,804	0.15	1.5
4		2,889,173	0.125	1.25
5		4,672,452	0.1	1
1	0.98	1,180,415	0.2	2
2		1,729,824	0.175	1.75
3		2,535,730	0.15	1.5
4		3,952,091	0.125	1.25
5		6,890,190	0.1	1
1	0.97	1,479,895	0.2	2
2		2,220,412	0.175	1.75
3		3,270,519	0.15	1.5
4		5,222,153	0.125	1.25
5		9,358,620	0.1	1
1	0.96	1,821,634	0.2	2
2		2,686,524	0.175	1.75
3		4,033,366	0.15	1.5
4		6,642,483	0.125	1.25
5		11,915,970	0.1	1
1	0.95	2,136,892	0.2	2
2		3,092,805	0.175	1.75
3		4,745,840	0.15	1.5
4		7,777,068	0.125	1.25
5		14,561,976	0.1	1

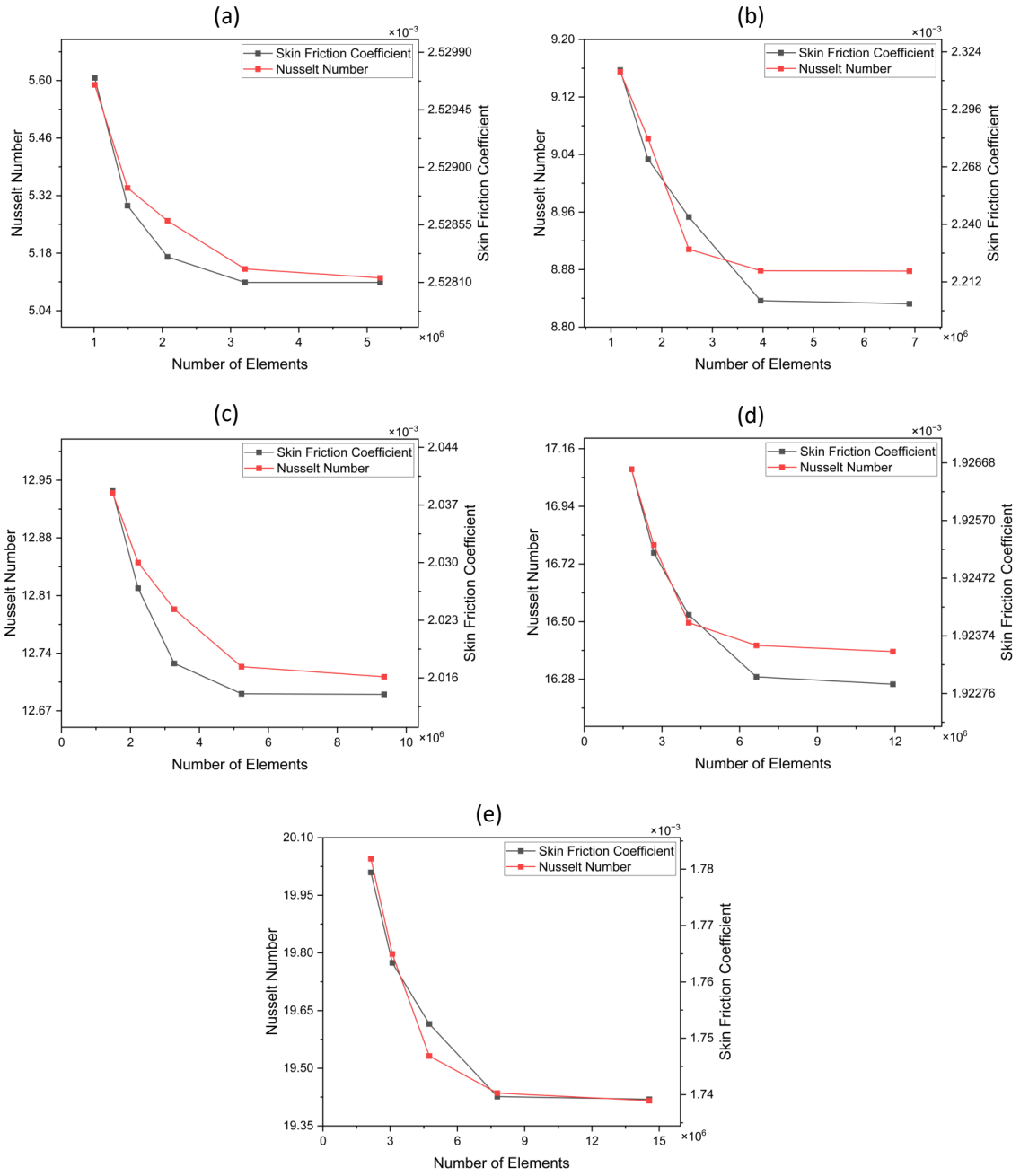

Fig. 4-2 The Nusselt number and skin friction coefficient values obtained for five tested meshes at different radius ratio values; (a) $\eta = 0.99$, (b) $\eta = 0.98$, (c) $\eta = 0.97$, (d) $\eta = 0.96$, and (e) $\eta = 0.95$

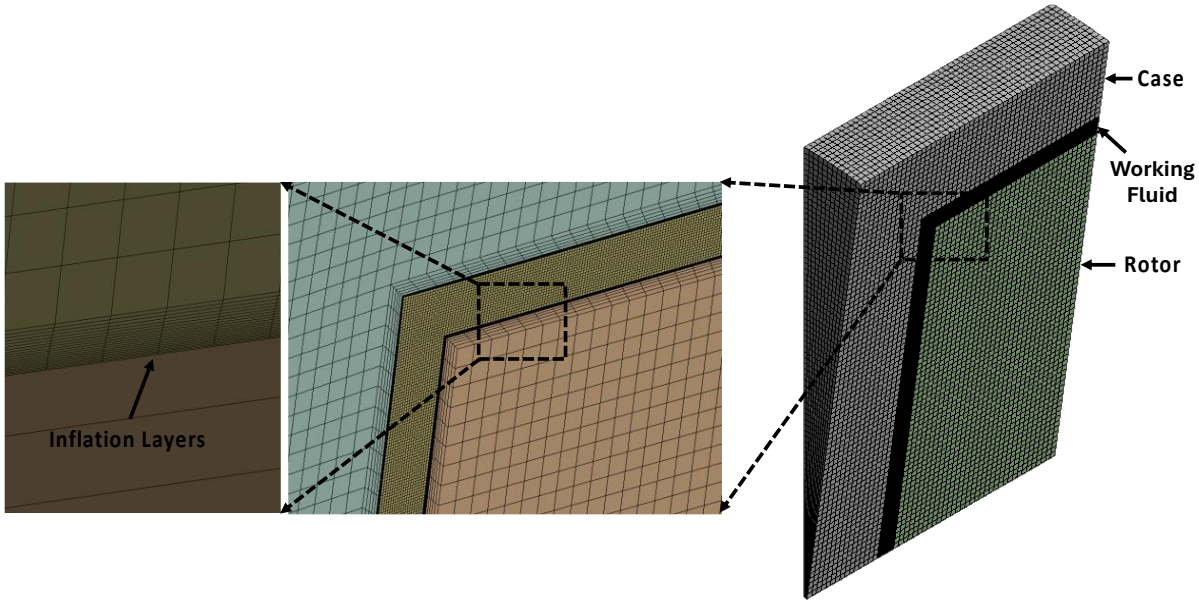

Fig. 4-3 The mesh employed for the system

4.2. Solver

The investigation of the steady-state operation of the simplified FESS was conducted using CFD. These simulations utilised steady-state models, with time-averaged steady-state solutions for the rotor's relative motion using MRF technique. Due to the rotor's high peripheral Reynolds number, calculated at 1.02×10^6, the use of a turbulence model was necessitated. The RANS equations were solved using the SST k-omega turbulence model, selected based on its effectiveness as demonstrated in numerical validations. For the numerical analysis, several assumptions were made to streamline the computation and focus on the key aspects of the system:

- Influence of gravity was disregarded.
- Air was modelled as an ideal gas.
- Thermal conductivity and specific heat were considered constant.
- The system was assumed to have no inlet or outlet.
- The thermal boundary condition of the housing was set with a free stream temperature of 24°C and heat transfer coefficients of 30 W/m²·K.
- All system components were initialised at a temperature of 24°C.

The CFD model employed in this study adheres to the following computational parameters and assumptions:

- Computations were performed using double precision for improved accuracy.
- A pressure-based solver was employed.
- The energy equation was incorporated into the solution process.
- A coupled solution method scheme was utilised.
- The pressure discretisation scheme maintained a second-order accuracy.

- The QUICK scheme was employed for the discretisation of various parameters, including density, momentum, turbulent kinetic energy, specific dissipation rate, and energy.

Wall treatment models were implemented to define flow profiles in the wall boundary layers, addressing the limitations of turbulence models in accounting for the viscous-affected region of the boundary layer. The wall cell $y_+ \leq 1$ was used to create a boundary layer mesh with a high resolution in order to resolve the viscous sublayer. The numerical discretisation of the governing equations was carried out using a FVM, solving a nonlinear algebraic equation system for each cell. To ensure the convergence of the CFD solution for each simulation run, iterations were carefully managed to achieve convergence with respect to successive iterations.

4.3. Post-Processing

4.3.1. Flow Field of the FESS

This study examines the influence of rotational speed on the air velocity distribution in the airgap of FESS with varying radius ratios. Rotational speeds of 200, 800, 1600, and 2400 rad/s were analysed. Fig. 4-4 illustrates the air velocity distribution within the airgap with the radius ratio of 0.99. The formation of Taylor-Couette flow within the airgap is responsible for the observed spike-shaped flow pattern. It is noted that air velocity near the housing approaches zero, while it reaches its peak near the rotor.

A critical Taylor number, indicative of flow instability, is reached at a rotational speed of 38 rad/s. Consequently, Taylor vortices form within the airgap at all the rotational speeds examined in this study. These vortices increase in intensity at higher rotational speeds. The simulations were conducted using both time-dependent and steady-state models to capture the dynamic behaviour and ensure comprehensive analysis of the flow patterns. The velocity vector plot showcasing the Taylor vortices at various studied rotational speeds is presented in Fig. 4-5. Within the airgap, Taylor vortices exhibit symmetry along the axial direction. As rotational speed increases, viscous forces are outweighed by inertial forces, leading to the formation of these vortices.

The size and compactness of Taylor vortices are influenced by the rotor speed. At higher speeds, the vortices appear more stretched, as illustrated in Fig. 4-6. This effect results from the fact that vortices traverse less distance within shorter time at higher speeds. The study demonstrates that Taylor vortex cells become progressively more compact as the rotational speed increases, a phenomenon primarily attributed to the reduced spatial travel of the vortices in a given timeframe.

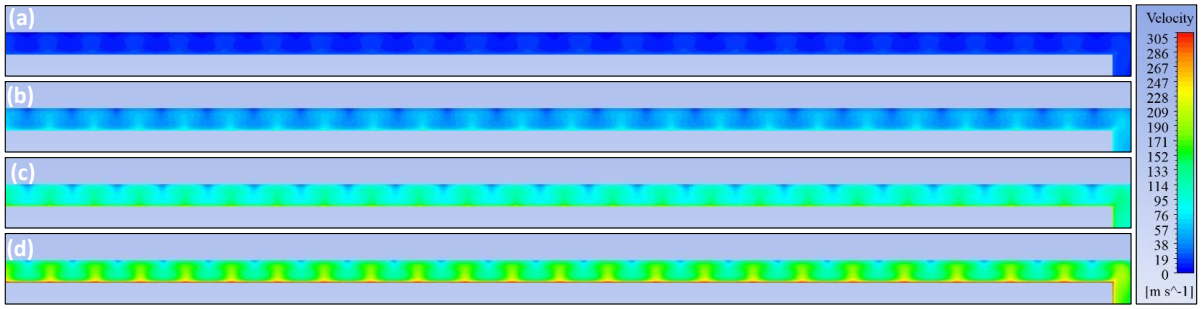

Fig. 4-4 Air velocity distribution within the airgap of a FESS with a radius ratio of 0.99 at different rotational speeds; (a) 200 rad/s, (b) 800 rad/s, (c) 1600 rad/s, and (d) 2400 rad/s

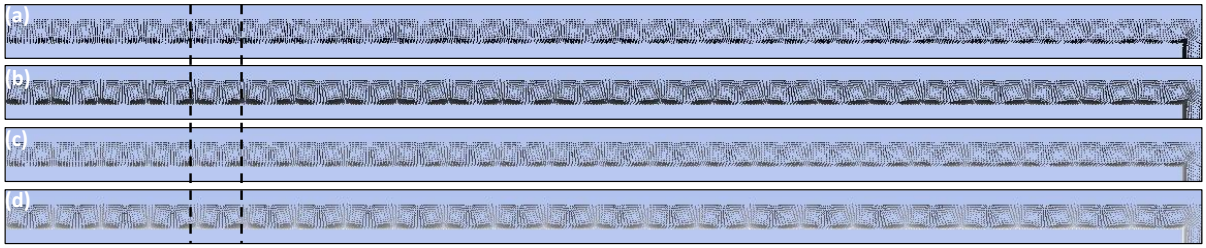

Fig. 4-5 Velocity vector plot within the airgap of a FESS with a radius ratio of 0.99 at different rotational speeds; (a) 200 rad/s, (b) 800 rad/s, (c) 1600 rad/s, and (d) 2400 rad/s

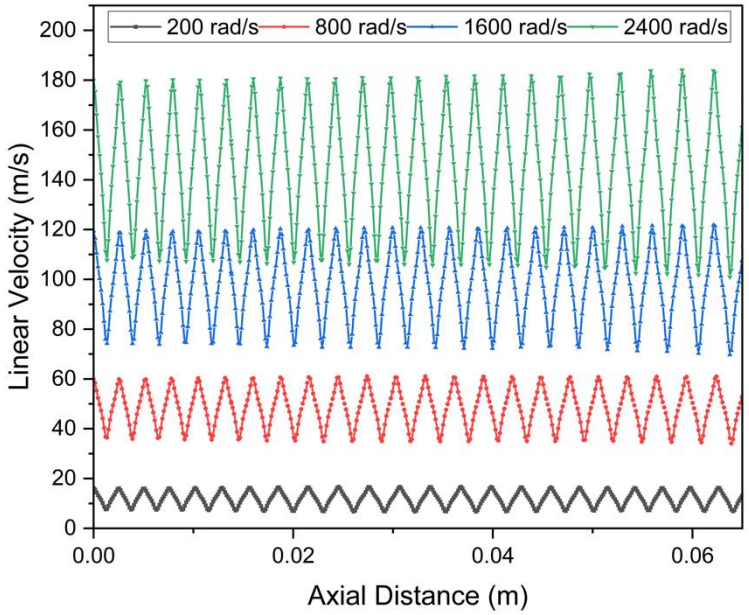

Fig. 4-6 Linear velocity as a function of distance at the midpoint of the FESS airgap within a radius ratio of 0.99

The variation in airgap size has a significant impact on the number of Taylor vortices formed, as the wavelength of these vortices is approximately equal to twice the size of the airgap. The critical wavelength of the Taylor vortices can be estimated using the following equation [366]:

$$\lambda_{cr} = \frac{2\pi g}{k_{cr}} \approx 2g \qquad (4\text{-}1)$$

Where k_{cr} represents the non-dimensional axial wave number at the onset of instability, which has a value of 3.12, and g is the airgap size. This relationship suggests that the height of a Taylor cell is nearly equal to the airgap size, resulting in a nearly square cell. However, it is important to note that this equation provides an approximation of the Taylor vortices wavelength and, while it offers a good representation of the number of Taylor vortices, it is not precise.

As the Taylor number increases, the discrepancy between the actual number of Taylor cells and the number calculated from this equation grows, as depicted in Fig. 4-7. This is due to the fact that the equation primarily considers the system in terms of airgap size, whereas, in reality, a higher Taylor number leads to an intensified formation of Taylor vortices. This increase in vortex formation consequently affects the number of Taylor cells, making the Taylor vortices more dominant, as illustrated in Fig. 4-7.

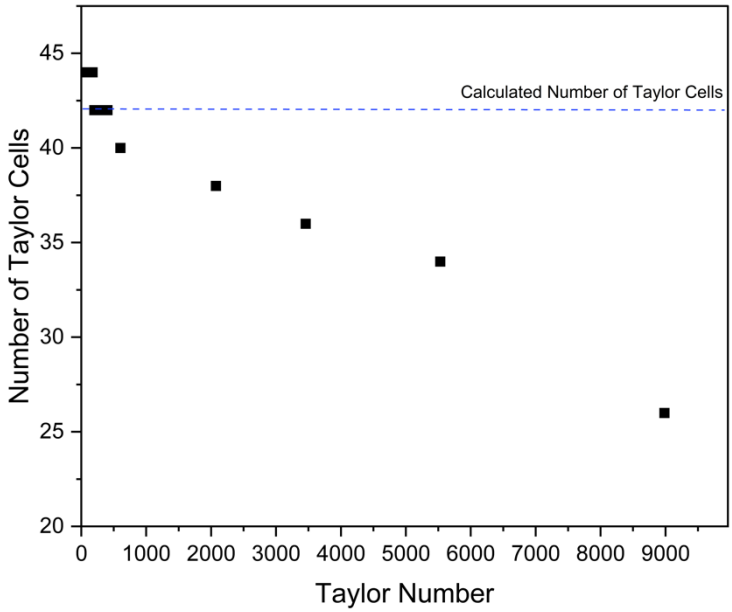

Fig. 4-7 The observed number of Taylor cells vs computed Taylor cell number as a function of Taylor number at radius ratio of 0.975

On the other hand, an increase in the airgap size results in a reduction in the number of Taylor vortices, as demonstrated in Fig. 4-8. This phenomenon becomes evident when maintaining a constant rotational speed; in this case as the airgap size increases, the number of Taylor vortices decreases. Further analysis reveals that the rotational velocity remains relatively consistent across various airgap sizes. This consistency is illustrated in Fig. 4-9, which shows that despite changes in the airgap size, the rotational velocity remains almost uniform.

The study reveals a direct correlation between the number of Taylor vortices and the temperature within the FESS, specifically the rotor, housing, and air. This relationship is illustrated in Fig. 4-10, where a decrease in the number of Taylor vortices corresponds to a reduction in temperature across these components. Notably, the highest temperature within the system was recorded in the smallest airgap

examined, while the lowest temperature in the housing was observed in the largest airgap size studied. The flow instability within the system manifests as counter-rotating toroidal vortices. This phenomenon is not only evident in the velocity contour plot but is similarly reflected in the temperature contour plot, underscoring the significant impact of Taylor vortices on air temperature distribution within the airgap. Consequently, it is observed that an increase in the number of Taylor vortices leads to a rise in the air temperature within the airgap.

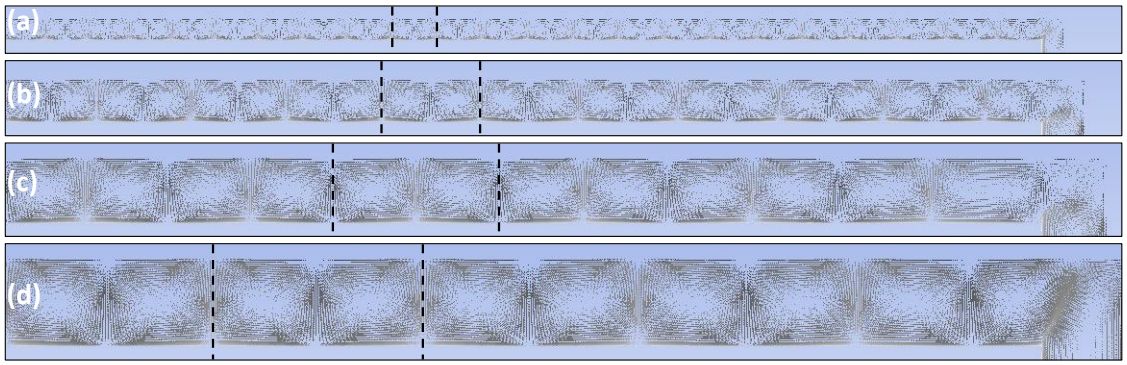

Fig. 4-8 Velocity vector plot within the airgap of a FESS operating at 1600 rad/s at different radius ratios; (a) 0.99, (b) 0.98, (c) 0.97, and (d) 0.96

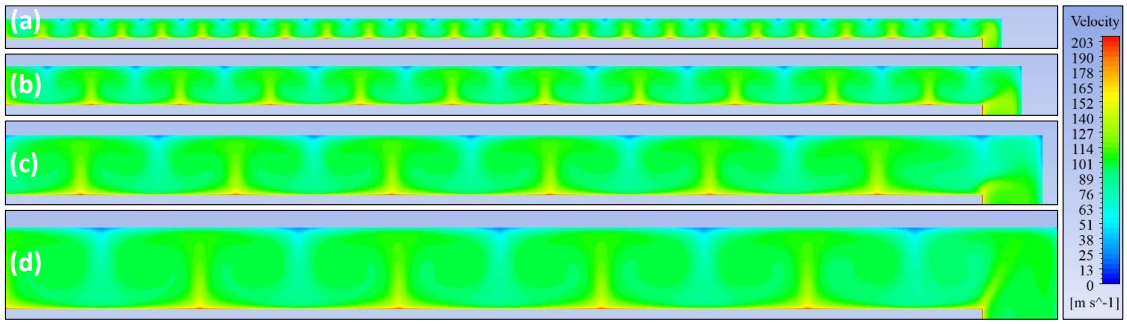

Fig. 4-9 Air velocity distribution within the airgap of a FESS operating at 1600 rad/s at different radius ratios; (a) 0.99, (b) 0.98, (c) 0.97, and (d) 0.96

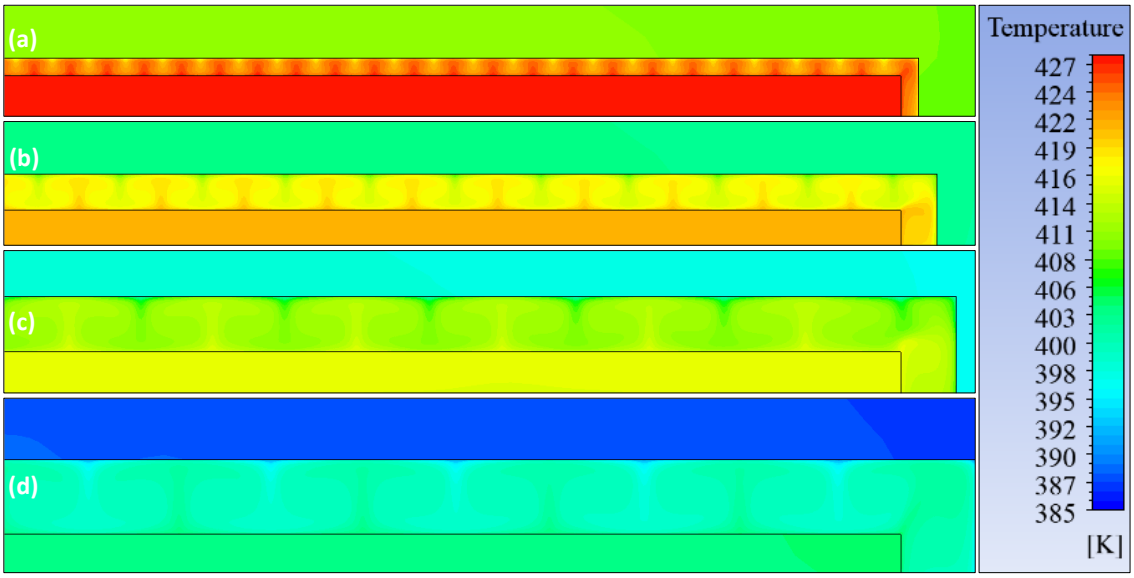

Fig. 4-10 Temperature distribution within the airgap of a FESS operating at 1600 rad/s at different radius ratios; (a) 0.99, (b) 0.98, (c) 0.97, and (d) 0.96

Due to the rotation of the inner cylinder, the fluid particles located near the rotor wall encounter an increased centrifugal force, causing them to exhibit a propensity to move outward. The vortices cause the fluid with significant tangential momentum near the rotor to move outward in a radial direction, specifically in the regions where the flow is moving away between two neighbouring pairs of vortices. In a symmetrical manner, fluid with low velocity is transported from the vicinity of the stationary housing towards the centre in the regions where two neighbouring vortices meet, as shown in Fig. 4-11. This process redistributes the rotational momentum of the fluid throughout the ring-shaped region. The subsequent redistribution of mass flow throughout the annulus impacts the velocity distribution of both the inward and outward flows. Therefore, the outward flow between the vortices is significantly more powerful than the inward flow.

An observed characteristic of the velocity vectors is the blending and transfer of momentum at the intersection of two neighbouring vortices. At this meeting point, there is substantial fluid mixture between neighbouring vortices. Each vortex contributes to the central mixing region of a vortex pair, located near the inner cylinder, and subsequently receives fluid from this mixing region, near the outer cylinder. A similar blending process takes place at the entrance area, where adjacent vortex pairs interact. Another notable observation regarding the velocity vectors is the movement of the vortex centres towards the outer cylinder. This phenomenon can be attributed to the flow regime being investigated at a high Reynolds number. At a high Reynolds number, the centrifugal force resulting from the rotation of the rotor exceeds the pressure gradient caused by the stationary housing wall. The disparity between these two forces results in the displacement of the vortex centre towards the outer cylinder wall.

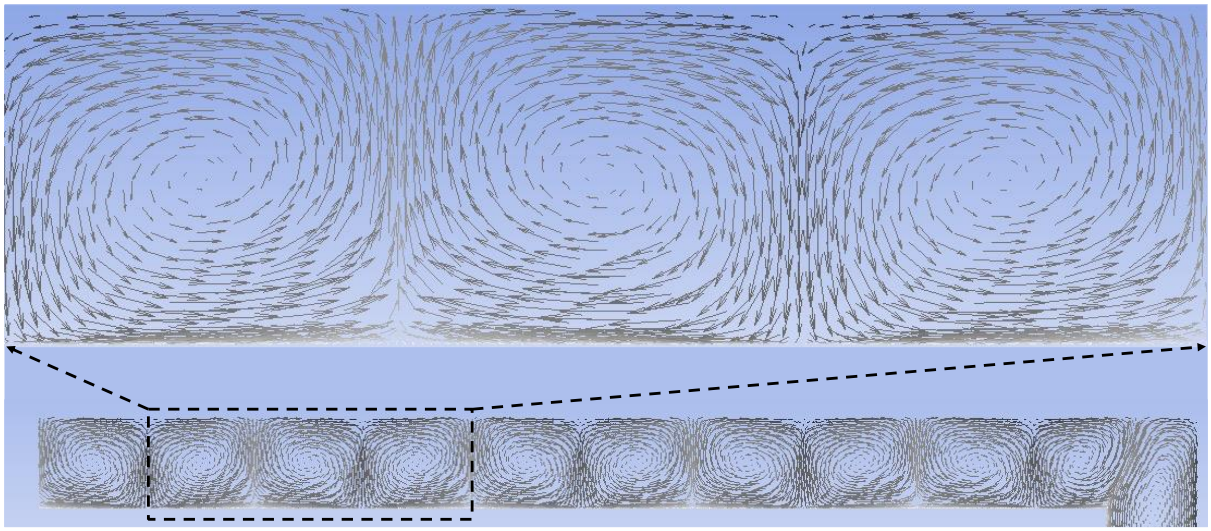

Fig. 4-11 Enlarged velocity vectors within the airgap of a FESS operating at 1600 rad/s with the radius ratio of 0.96

Fig. 4-12 presents a contour plot depicting the axial velocity in the Z-Y plane of the FESS for a RR of 0.96, at a rotational velocity of 1600 rad/s. This figure specifically highlights the radial airgap between the rotor and the housing, which is the primary area of interest for this study. The objective is to examine the influence of airgap size on the system performance, particularly at varying airgap sizes. To facilitate a clearer understanding of the effects, especially in scenarios where the airgap is relatively small, a more focused section of the airgap has been selected for detailed analysis. Approximately one-third of the airgap width will be used for this purpose. This strategic selection enables a more visible and precise observation of the velocity changes across different airgap sizes.

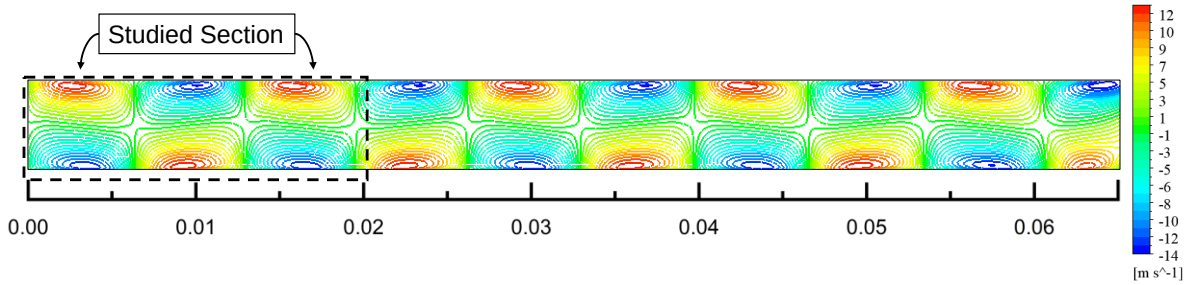

Fig. 4-12 Contour plot illustrating the examined section of axial velocity in the Z-Y plane within the airgap of a FESS operating at 1600 rad/s with a radius ratio of 0.96

Fig. 4-13 illustrates the development of a recurring pattern of maximum and minimum axial velocities within the annulus at the four examined RRs. The observed flow pattern is a consequence of the rotor operating at high speed, causing a transition from a stable Couette flow to a Taylor vortex flow. This transition is characterised by the formation of vortices that extend across the radial airgap. The velocity maxima and minima are caused by the rotational movement of the vortex and are positioned in a radial direction above and below each vortex core, as shown in Fig. 4-12. The zero contour lines in Fig. 4-13

represent the radial positions of the central core of the vortices shown in Fig. 4-12, which occur between the highest and lowest values. Fig. 4-13 illustrates that each Taylor vortex rotating in a clockwise direction causes maximum axial velocity below its central core near the rotor wall, and minimum axial velocity above its core near the housing wall on the Z-Y plane.

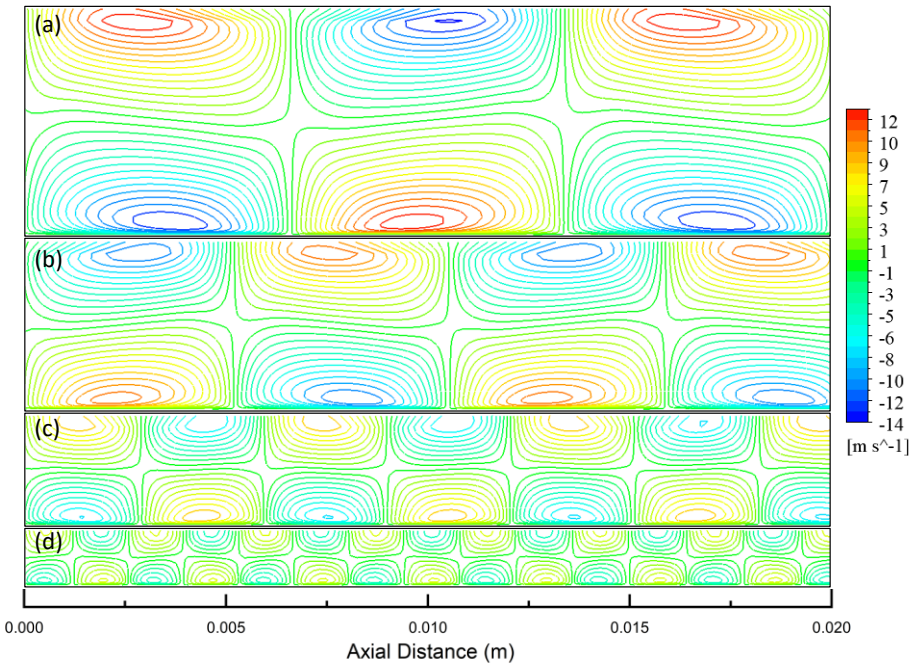

Fig. 4-13 Contour plot of axial velocity in the Z-Y plane within the airgap of a FESS operating at 1600 rad/s at different radius ratios; (a) 0.96, (b) 0.97, (c) 0.98, and (d) 0.99

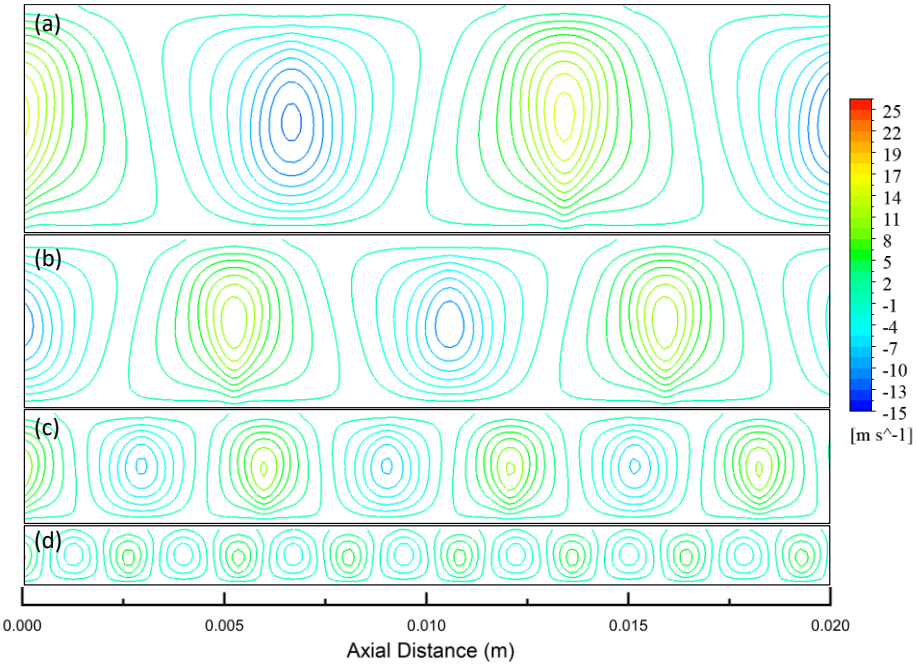

Fig. 4-14 Contour plot of radial velocity in the Z-Y plane within the airgap of a FESS operating at 1600 rad/s at different radius ratios; (a) 0.96, (b) 0.97, (c) 0.98, and (d) 0.99

The contour plots in Fig. 4-14 depict the radial velocity of the studied RR at a rotational velocity of 1600 rad/s. These plots reveal a recurring pattern of alternating minimum and maximum values of radial velocity along the axial direction. The radial flow occurs as a result of the difference between the centrifugal forces applied to the fluid caused by the rotor's rotation and the radial pressure gradients that restore equilibrium in the radial momentum of the flow. The amplitude of the alternating radial velocity maxima and minima is depicted at the centre of the corresponding concentric contours in Fig. 4-14.

The contour plot utilises a colour scheme where the red line represents positive values of radial velocity, while the blue line represents negative values of radial velocity. The contour displays the rotational direction of the Taylor vortices through positive and negative values. A red contour cluster followed by a blue contour cluster in the positive axial direction indicates the presence of an anti-clockwise vortex on the Z-Y plane. In the same manner, the presence of a blue contour cluster followed by a red contour cluster indicates the occurrence of a Taylor vortex rotating in a clockwise direction. The contour clusters in Fig. 4-14 display negative and positive values, which correspond to regions of inward flow and outward flow respectively. These regions occur at the meeting point of adjacent vortices.

The highest values of radial velocity are observed in the regions of outward flow along the radial direction, as depicted in Fig. 4-14, specifically at the location indicated in Fig. 4-12. The points of lowest radial velocity can be observed in the regions where the flow is directed inward. One specific location of interest is indicated in Fig. 4-12. The zero velocity contours correspond to the central positions of the vortices depicted in Fig. 4-14. The observed flow pattern, characterised by alternating axial and radial velocity maxima and minima, in Figs. 4-13 and 4-14, is consistent and qualitatively agrees with previous CFD research and experimental measurements conducted by Deshmukh et al. [339], Deng et al. [367] and Adebayo [368].

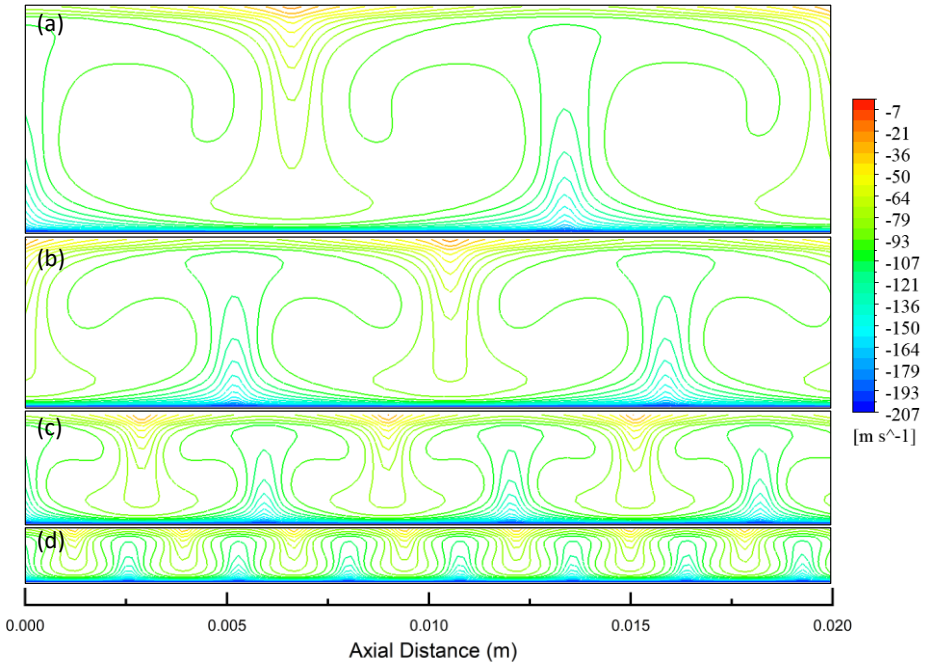

Fig. 4-15 Contour plot of tangential velocity in the Z-Y plane within the airgap of a FESS operating at 1600 rad/s at different radius ratios; (a) 0.96, (b) 0.97, (c) 0.98, and (d) 0.99

Fig. 4-15 displays the contour plots of the tangential velocity for the investigated RR at a rotational velocity of 1600 rad/s. The contour plots display a minimum tangential velocity adjacent to the rotor wall and a maximum tangential velocity adjacent to the housing wall. The magnitude of the minimum tangential velocity exceeds that of the maximum tangential velocity. Specifically, the tangential velocity is highest in the vicinity of the rotor, aligning with the rotational direction of the rotor. This outcome is anticipated due to the convective fluid motion caused by the rotation of the rotor, which aligns with the solid body and reaches its highest angular velocity at the surface of the rotor. The negative tangential velocity near the wall of the inner cylinder is a result of the rotor's direction of rotation, as indicated by the reference system in Fig. 4-1.

The tangential velocity of the fluid possesses two characteristics: magnitude, which refers to the absolute value of rotational speed, and direction. In this case, the rotor maintains a constant speed at its surface, and the direction of the rotor's motion is specified as clockwise. The alteration in the orientation of the tangential velocity vectors within the azimuthal plane results in a resultant centripetal force that is aimed towards the centre of the rotor. The red and blue colour codes on the contour plots represent the minimum and maximum negative values of tangential velocity, respectively.

In Fig. 4-15, the contours exhibit outward bulging in the regions were fluid flows radially outward. This is due to the transport of high tangential momentum fluid by the Taylor vortices from the vicinity of the rotor towards the stationary housing. The contours exhibit radial inward bulging in the regions where the flow is directed inward, as the Taylor vortices transport low momentum fluid from the stationary housing wall towards the rotor wall. The contour lines exhibit more pronounced curvature in the regions

where the flow moves away from the centre compared to the regions where the flow moves towards the centre. This is because the Taylor vortex centres are closer to the outward flow saddle planes, leading to a higher radial velocity in the outward flow regions caused by the Taylor vortices. This feature also demonstrates the magnitude of the induced velocity caused by the Taylor vortices in these regions.

Figs. 4-16 to 4-18 present the air velocity distribution within the airgap, each characterised by distinct radius ratios; 0.98, 0.97, and 0.96, respectively. A common observation across these figures is the spike-shaped flow pattern, a characteristic feature of the Taylor-Couette flow within the airgap. An aspect of these distributions is the change in air velocity contour colours with increasing rotational velocity. The colours transition from blue to yellow and red, visually representing the effect of the rotor velocity on the air velocity distribution within the airgap.

Adjacent to the housing, the air velocity is notably minimal, nearing zero, while it reaches its peak near the rotor. This pattern is consistent across the studied radius ratios. Additionally, an interesting phenomenon was observed, increase in the airgap size resulted in the reduction in the number of Taylor vortices. The reduction is quantitatively significant, as evidenced by the decrease in the number of vortices: from 22 vortices for RR of 0.98, to 14 for RR of 0.97, and down to 12 for RR of 0.96. This trend underscores the influence of airgap size on the formation and number of Taylor vortices within the FESS airgap.

The size of the airgap plays a pivotal role in determining the number of Taylor vortices. Each Taylor cell consists of a pair of Taylor vortices, which typically exhibit a quadrilateral shape. Consequently, an increase in the airgap size leads to larger Taylor vortices, resulting in the formation of fewer Taylor cells. Within the airgap, Taylor vortices exhibit a consistent symmetrical formation along the axial direction. This symmetry arises from the interplay of forces within the system. As the rotational velocity of the rotor increases, inertial forces begin to outweigh viscous forces, leading to the formation of Taylor vortices. This phenomenon is particularly pronounced at higher speeds. A notable characteristic of Taylor vortices is the variation in their size and compactness, which are influenced by the rotor speed. At higher rotational speeds, these vortices tend to stretch more compared to their appearance at lower speeds. This change in the physical structure of the vortices is depicted in Figs. 4-19 to 4-21. The figures illustrate how increasing speed stretches the vortices, altering their shape and spatial arrangement within the airgap.

Figs. 4-22 to 4-24 show the linear velocity within the airgap of the FESS at four rotational speeds: 200, 800, 1600, and 2400 rad/s. The data was collected from the centre of the airgap on the Y-Z plane. The rapid changes in the linear velocity are due to the Taylor vortices that form within the airgap. The wavelength of the Taylor vortices is equal to the distance between two adjacent spikes in Figs. 4-22 to 4-24. As the rotational velocity increases, so does the wavelength of the Taylor vortices. This is because the fluid has more inertia at higher rotational speeds, which allows the vortices to grow larger. The figures also show that the linear velocity distribution within the airgap is not symmetrical around the centre of the airgap. This is because the Taylor vortices are not symmetrical. The vortices are typically

stronger at the outer edge of the airgap than at the inner edge. This is because the fluid has more inertia at the outer edge.

The study compares the theoretical and simulated wavelengths of Taylor vortices (Taylor cells) across various radius ratios in a FESS. For a radius ratio of 0.99, the theoretical wavelength derived from Equation 4-1 is 2.6 mm, suggesting the presence of 100 Taylor cells. However, the simulation results yield a slightly larger wavelength of 2.8 mm, resulting in a lower cell count of 92. As the airgap size increases, a notable reduction in the number of Taylor cells is observed. For instance, with a radius ratio of 0.98, the theoretical calculation predicts 50 cells, whereas the simulation shows only 44 cells, each with a wavelength of 5.9 mm. This trend of fewer Taylor cells with larger airgap sizes is consistent for radius ratios of 0.97 and 0.96. Specifically, the simulation results for a 0.97 radius ratio show a wavelength of 8.1 mm with 32 cells, and for a 0.96 ratio, the wavelength extends to 10.8 mm, corresponding to only 24 cells.

This reduction in cell count with larger airgaps could be attributed to the limited space available for the formation of new Taylor cells. Importantly, the increase in airgap size and the corresponding decrease in the number of Taylor cells contribute to enhanced heat transfer between the rotor, housing, and air. This improved heat transfer efficiency results in lower temperatures for each of the above mentioned components, showcasing a critical aspect of the thermal management in FESS.

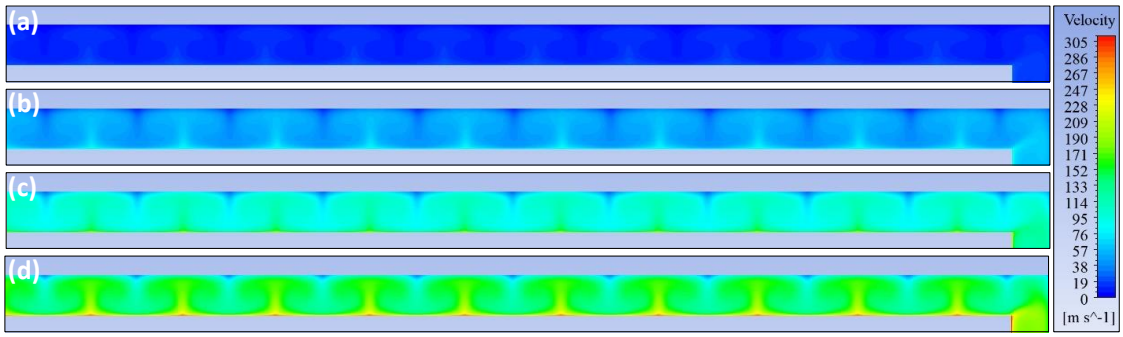

Fig. 4-16 Air velocity distribution within the airgap of a FESS with radius ratio of 0.98 at different rotational speeds; (a) 200 rad/s, (b) 800 rad/s, (c) 1600 rad/s, and (d) 2400 rad/s

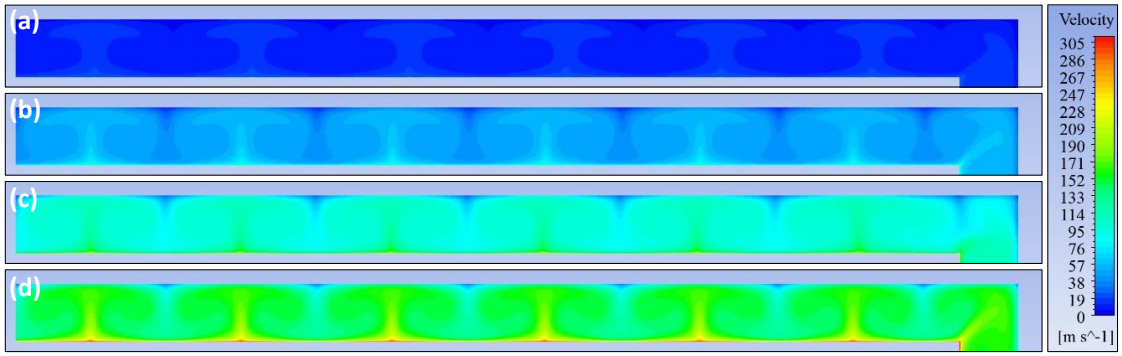

Fig. 4-17 Air velocity distribution within the airgap of a FESS with radius ratio of 0.97 at different rotational speeds; (a) 200 rad/s, (b) 800 rad/s, (c) 1600 rad/s, and (d) 2400 rad/s

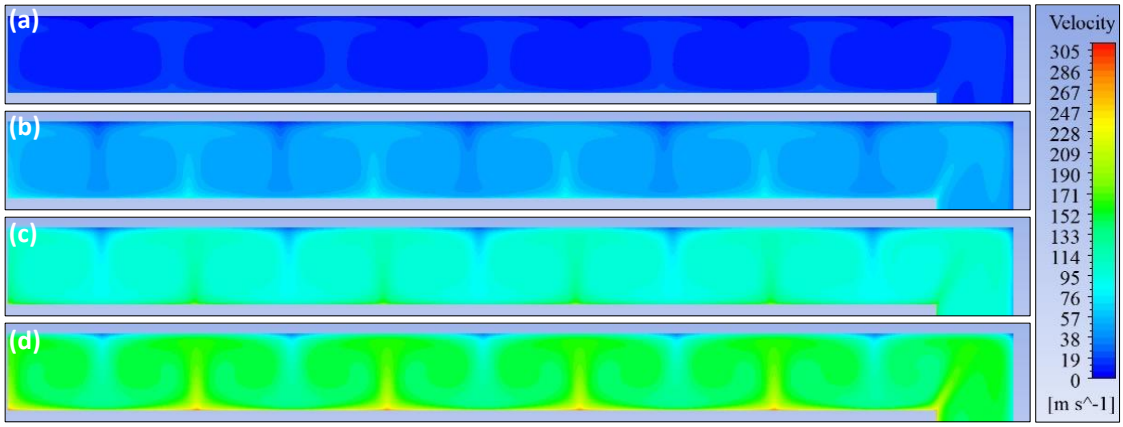

Fig. 4-18 Air velocity distribution within the airgap of a FESS with radius ratio of 0.96 at different rotational speeds; (a) 200 rad/s, (b) 800 rad/s, (c) 1600 rad/s, and (d) 2400 rad/s

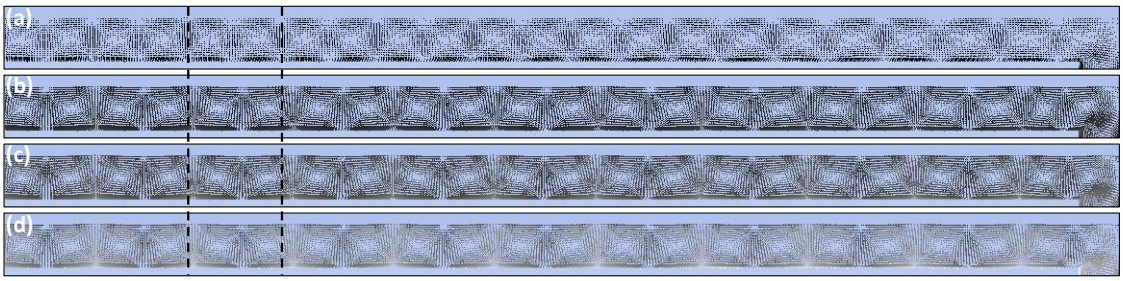

Fig. 4-19 Velocity vector plot within the airgap of a FESS with radius ratio of 0.98 at different rotational speeds; (a) 200 rad/s, (b) 800 rad/s, (c) 1600 rad/s, and (d) 2400 rad/s

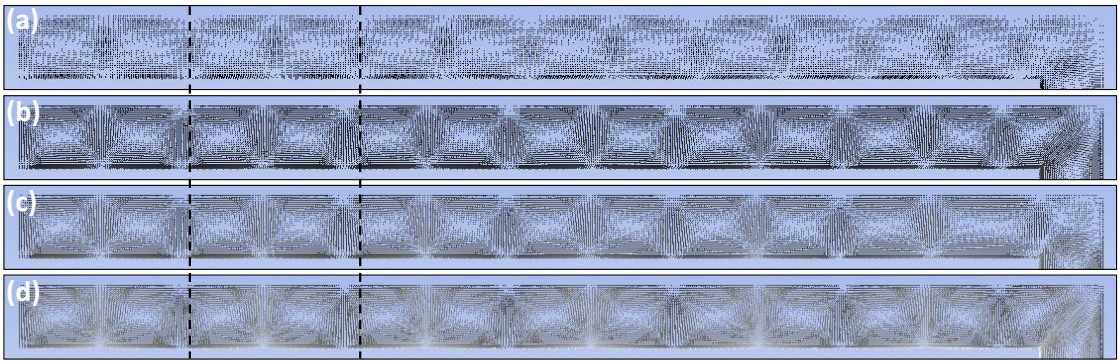

Fig. 4-20 Velocity vector plot within the airgap of a FESS with radius ratio of 0.97 at different rotational speeds; (a) 200 rad/s, (b) 800 rad/s, (c) 1600 rad/s, and (d) 2400 rad/s

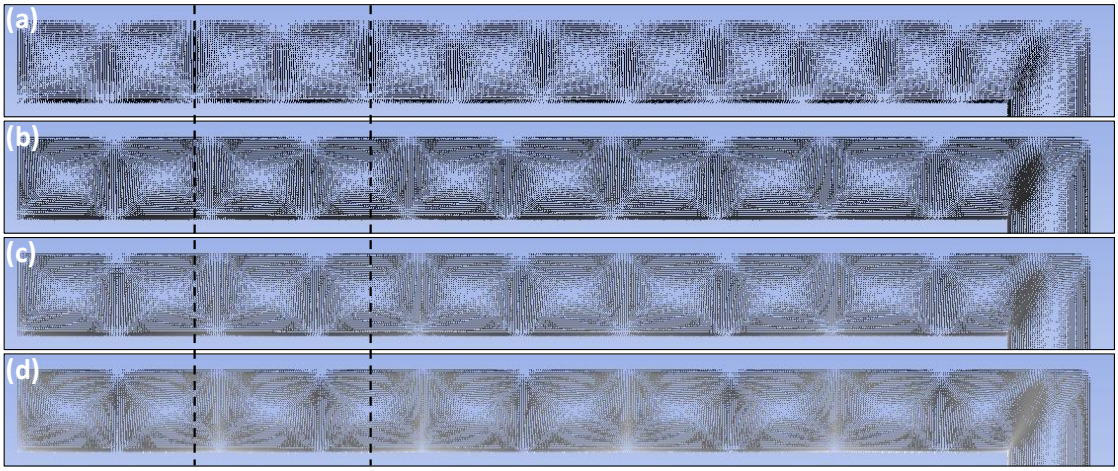

Fig. 4-21 Velocity vector plot within the airgap of a FESS with radius ratio of 0.96 at different rotational speeds; (a) 200 rad/s, (b) 800 rad/s, (c) 1600 rad/s, and (d) 2400 rad/s

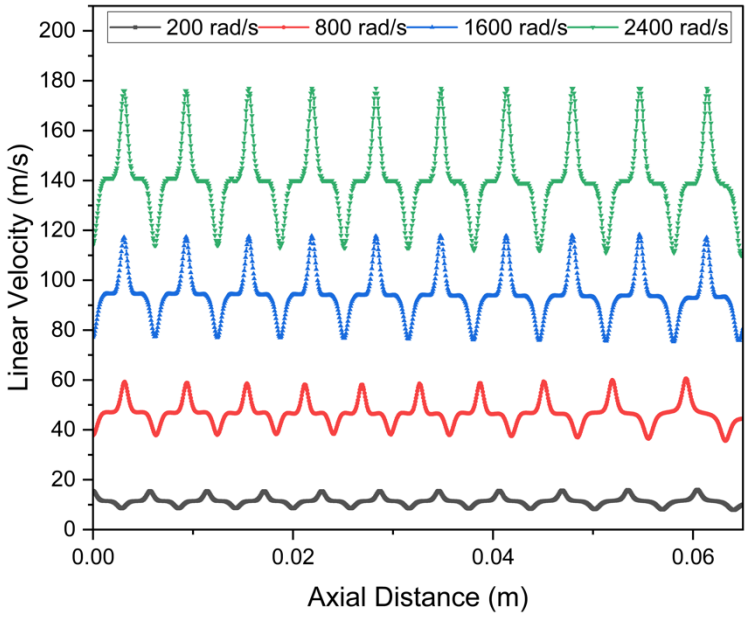

Fig. 4-22 Linear velocity as a function of distance at the midpoint of the FESS airgap within a radius ratio of 0.98 operating at different operational speeds

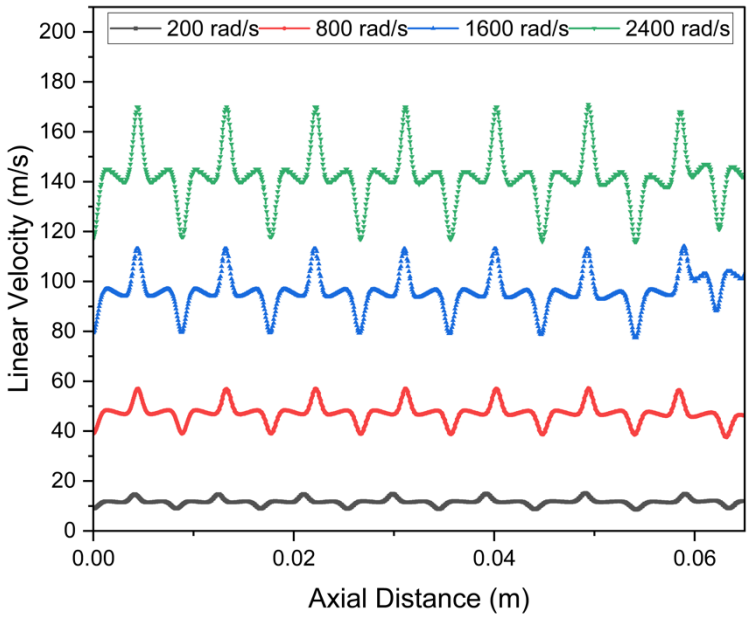

Fig. 4-23 Linear velocity as a function of distance at the midpoint of the FESS airgap within a radius ratio of 0.97 operating at different operational speeds

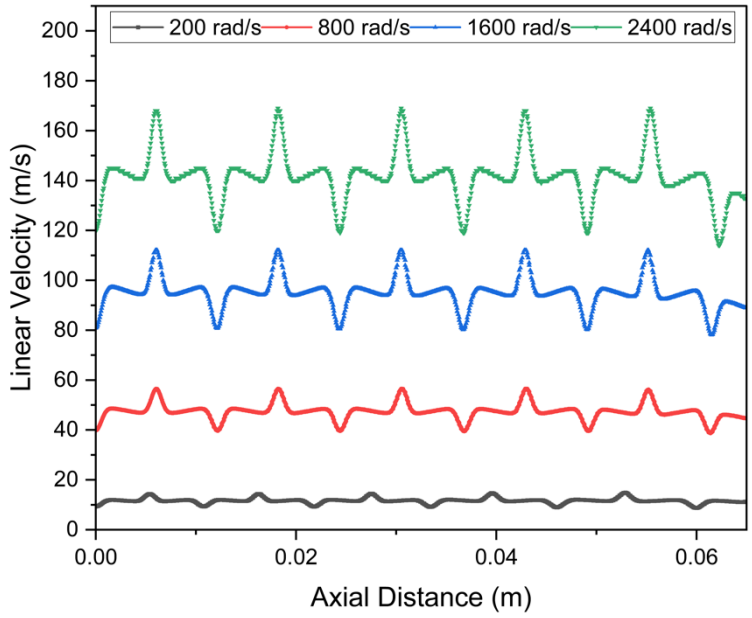

Fig. 4-24 Linear velocity as a function of distance at the midpoint of the FESS airgap within a radius ratio of 0.96 operating at different operational speeds

4.3.2. Characterisation of Windage Losses and Heat Transfer

The study analyses the effect of rotational speed on the rotor skin friction coefficient, considering five different radius ratios in a system where the outer cylinder (housing) remains stationary while the inner cylinder (rotor) rotates at an angular velocity of 2400 rad/s. The investigation reveals that the air velocity distribution within the airgap undergoes significant changes at different rotational speeds across all

radius ratios, as shown in Fig. 4-25. This change is attributed to the Taylor number surpassing the critical value of 41.3, leading to the formation of Taylor vortices. As Fig. 4-26 illustrates, Taylor number increases as the rotational velocity increases, thereby complicating the flow dynamics. A notable observation is the dramatic drop in the skin friction coefficient value beyond a Taylor number of 1700. Beyond this point, changes in the coefficient with respect to the Taylor number become minimal. This phenomenon is linked to the boundary layers becoming thinner and more dispersed, indicative of a transition to turbulent flow.

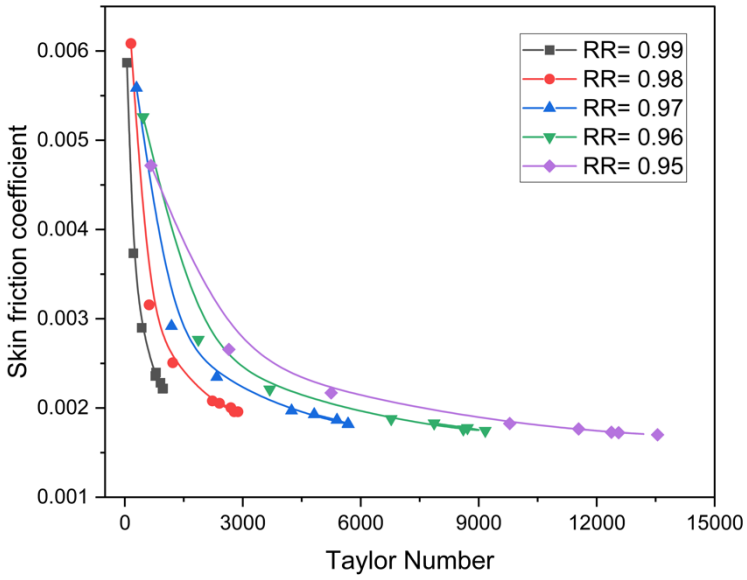

Fig. 4-25 Skin friction coefficient vs Taylor number for different radius ratios

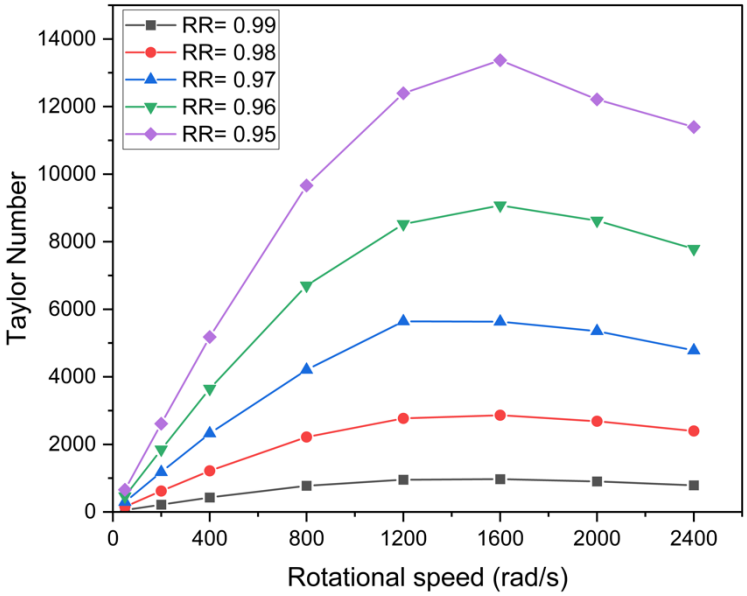

Fig. 4-26 Taylor number vs rotational speed for different radius ratios

Fig. 4-27 presents the variation of the rotor skin friction coefficient as a function of rotational speed for different radius ratios. For all radius ratios, the skin friction coefficient decreases sharply with an

increase in rotational speed up to a certain point, after which the decrease levels off. This trend suggests that as the flywheel spins faster, the relative impact of skin friction on its performance diminishes, possibly due to the onset of turbulent flow which reduces the relative effect of surface roughness. The curves suggest that the skin friction coefficient is also dependent on the radius ratio, with higher RR values starting off with higher skin friction coefficients at lower speeds. This could be due to the increased surface area in contact with the fluid at higher RR values, leading to greater initial resistance. Additionally, the skin friction coefficient is influenced by the fluid density, which is in turn affected by the temperature. Fig. 4-28 illustrates the correlation between rotor temperature in Kelvin (K) and rotational speed in radians per second (rad/s) for various RRs. There is a clear trend across all radius ratios showing that as the rotational speed increases, the rotor temperature also increases. This positive correlation suggests that higher speeds lead to greater frictional forces, thus generating more heat. At lower speeds, the increase in temperature is relatively moderate; however, the curve becomes steeper beyond a certain value for all RRs. This steeper rise indicates a nonlinear relationship, where temperature rise accelerates at higher speeds, due to the exponential increase in frictional heating. This increase in temperature has a significant impact on the rotor skin friction coefficient.

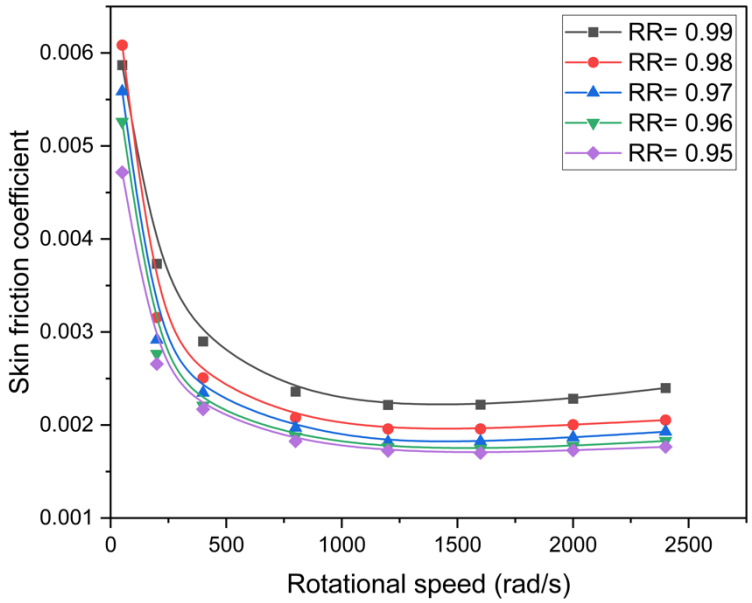

Fig. 4-27 Skin friction coefficient vs the rotational speed for different radius ratios

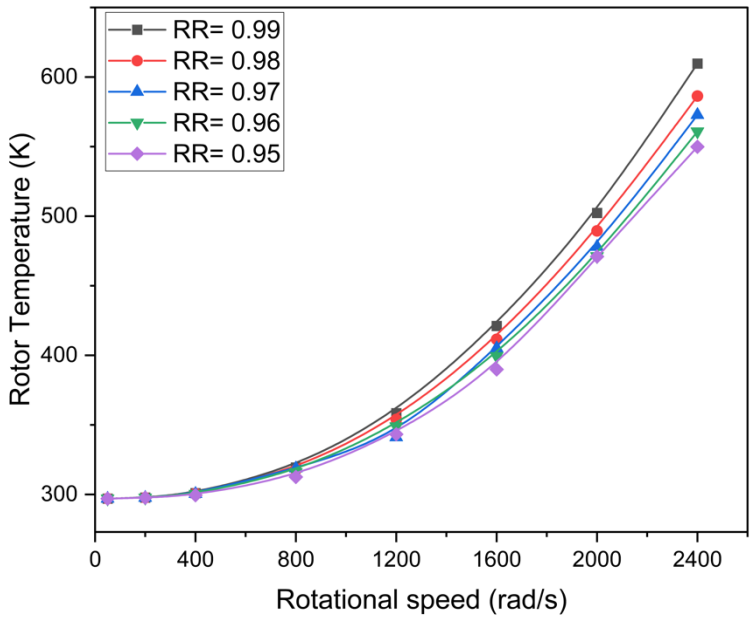

Fig. 4-28 Rotor temperature vs rotational speed for different radius ratios

Air friction is more significant in larger air gaps, this is due to the increasing rotor shear stress being exacerbated by the Taylor vortices. In fact, the critical Taylor number is reached in larger air gaps before the onset of these vortices in narrower air gaps, since the Taylor number is a function of the airgap size. The highest windage losses are achieved at the smallest airgap.

Fig. 4-29 shows the windage losses in Watts (W) as a function of rotational speed for various RRs. There is a pronounced increase in windage losses as the rotational speed increases for all RRs due to greater air resistance. At lower speeds, the windage losses for different RRs appear very similar, but as speed increases, slight divergences emerge. This indicates that the flywheel geometry affects windage losses, but its impact becomes more noticeable at higher speeds. Initially, the increase in windage losses is gradual, but beyond a certain speed threshold, the losses rise more sharply. This nonlinear increase is attributed to the transition from laminar to turbulent flow conditions, resulting in higher resistance thus greater windage losses.

Fig. 4-30 illustrates the Reynolds number as a function of rotational speed for FESS at various RRs. Reynolds number is a dimensionless quantity used in fluid mechanics to predict flow type in different fluid flow situations. For all radius ratios, as the rotational speed increases so does the Reynolds number, indicating a shift towards more turbulent flow conditions. This is a known fluid flow characteristic around rotating objects, were increased speed leads to increased turbulence. Each curve peaks at a certain rotational speed, suggesting an optimal speed at which the flow transitions from laminar to turbulent for each RR value. Beyond this speed, the Reynolds number decreases, which is due to the change in flow characteristics as the temperature of the air within the airgap rises with the increase in the rotational speed. This mainly attributed to the change in the kinematic viscosity of the air as the temperature changes which leads to the creation of a reverse parabolic shape. The peak Reynolds

number and the speed at which it occurs vary with the radius ratio. Higher RRs reach higher Reynolds numbers, implying that a larger airgap experiences more significant turbulent flow effects at a given speed.

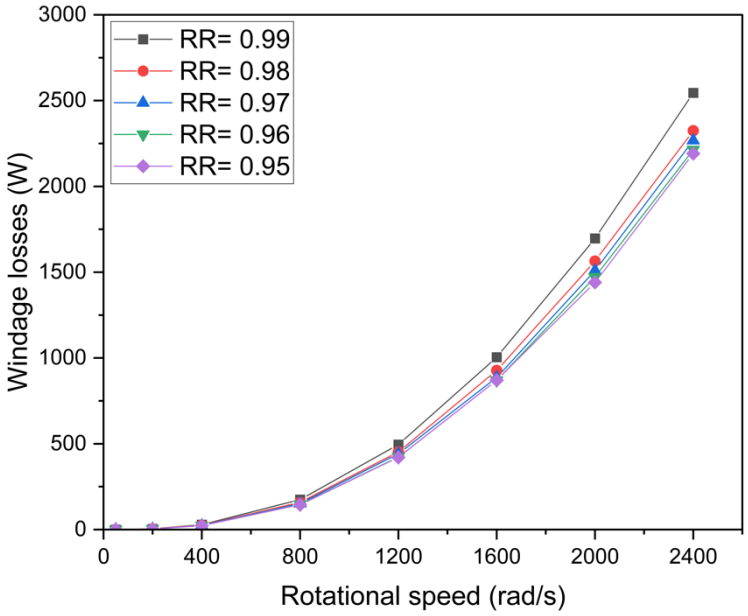

Fig. 4-29 Windage losses vs rotational speed for different radius ratios

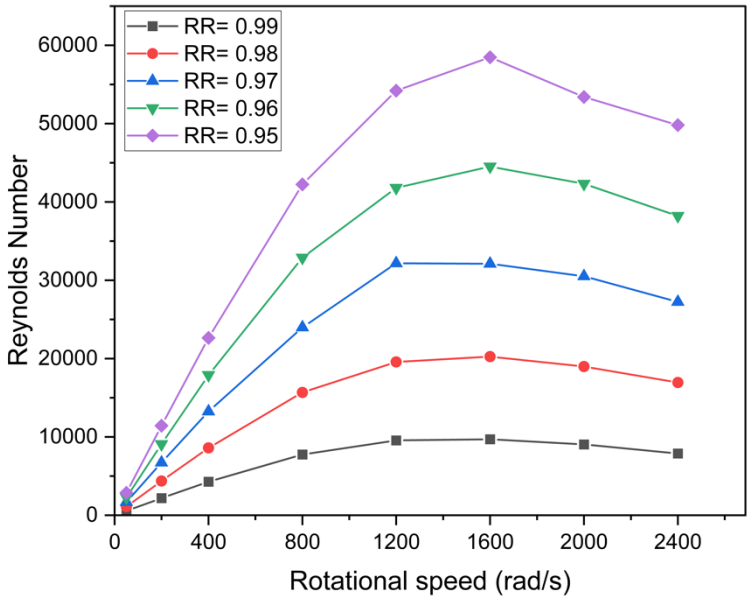

Fig. 4-30 Reynolds number vs rotational speed for different radius ratios

Fig. 4-31 shows the Taylor Number against the Reynolds Number across the studied RRs. The graph shows a direct relationship between these two critical dimensionless parameters, indicating how the rotational effects are captured by the Taylor Number and the inertial and viscous forces are represented by the Reynolds Number. There is a direct and almost linear correlation between the Taylor Number and the Reynolds Number for each RR, as the inertial forces become more significant relative to viscous forces (higher Reynolds Number), the impact of rotation on the flow (Taylor Number) also increases.

The graph displays different lines for each RR, indicating that the geometry of the flywheel affects how rotational effects scale with changes in the flow regime. Higher RRs show a steeper slope, which mean that a larger airgap amplifies the rotational effects more significantly at the same increase in inertial forces.

Fig. 4-32 presents the windage losses plotted against the Taylor number for the FESS with different RRs. The windage losses for all RRs initially increase with the Taylor number, indicating that as the flow becomes more influenced by rotational effects, the losses due to air resistance inside the FESS housing increase. Each RR displays a distinct relationship between the Taylor Number and windage losses, suggesting that the flywheel airgap size significantly impacts the aerodynamic performance of the system. Higher RRs appear to be associated with higher windage losses at lower Taylor numbers. The curves show that the windage losses increase to a peak before declining sharply. The peak represents a critical point where the fluid flow likely transitions from stable to unstable, marked by the formation of turbulent Taylor vortices.

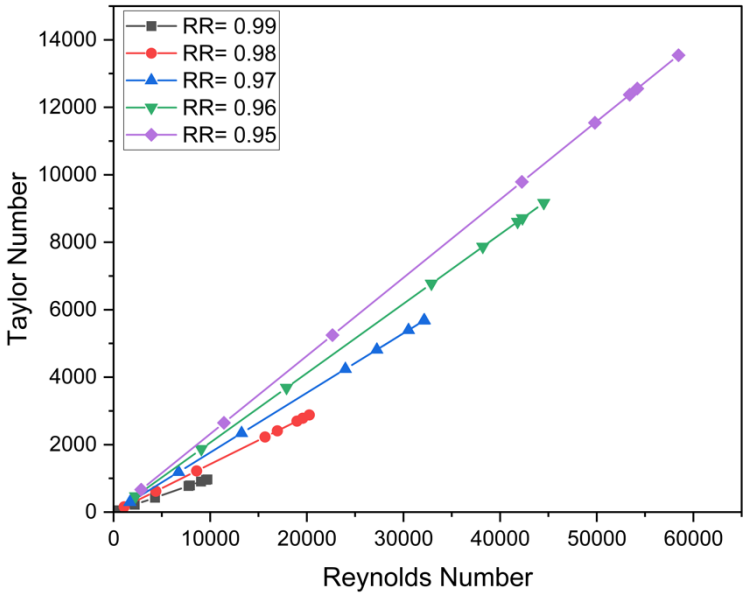

Fig. 4-31 Taylor number vs Reynolds number for different radius ratios

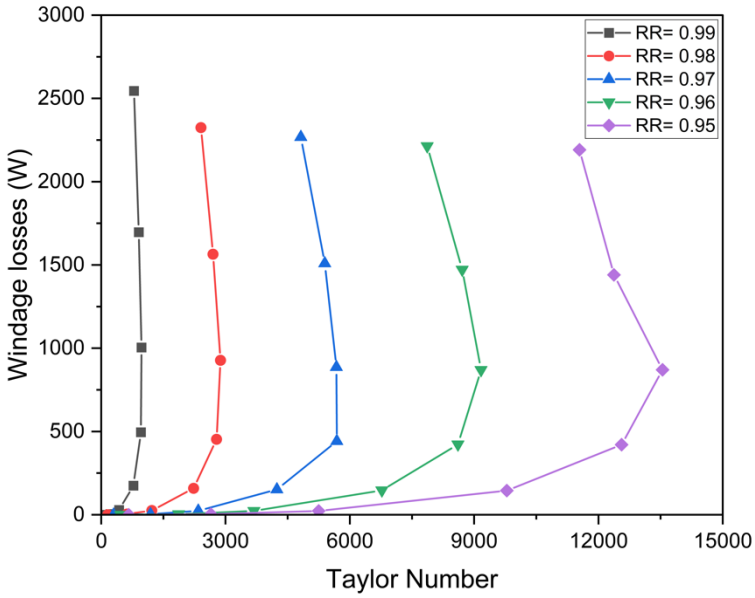

Fig. 4-32 Windage losses vs Taylor Number for different radius ratios

As for the Nusselt number response for the studied RRs, Fig. 4-33 presents the relationship between the Nusselt number and the rotational speed. The Nusselt number is a dimensionless parameter that describes the convective heat transfer relative to conductive heat transfer across a boundary. For all RRs, the Nusselt number initially increases with rotational speed, indicating enhanced convective heat transfer as the flywheel speed increases. This is because higher speeds increase fluid motion, thereby improving the heat transfer from the flywheel surface. Each curve peaks at a certain speed, which represents the point of maximum convective heat transfer efficiency for a given RR. Beyond this speed, the Nusselt number decreases. The graph shows that the peak Nusselt number and the speed at which it occurs vary with RR. Higher RRs reach higher Nusselt numbers at lower speeds, which is due to Taylor number value and the number of Taylor vortices. The trend implies that there is an optimal speed range for thermal management in FESS, where convective cooling is most effective. Operating beyond this range could lead to less efficient cooling, which must be considered when designing the system.

Nusselt number varies with the Taylor number for different RRs, as shown in Fig. 4-34. The trend shows that as the Taylor number increases, indicating more pronounced rotational effects, the Nusselt number also increases, meaning that stronger rotational flow provides better mixing between cold and hot surfaces. On the other hand, higher RRs tend to have higher Nusselt numbers, indicating that the flywheel airgap can significantly influence the convective heat transfer characteristics of the system. Unlike previous graphs where the Nusselt number peaks at certain speeds, here it shows a steady growth with the Taylor number.

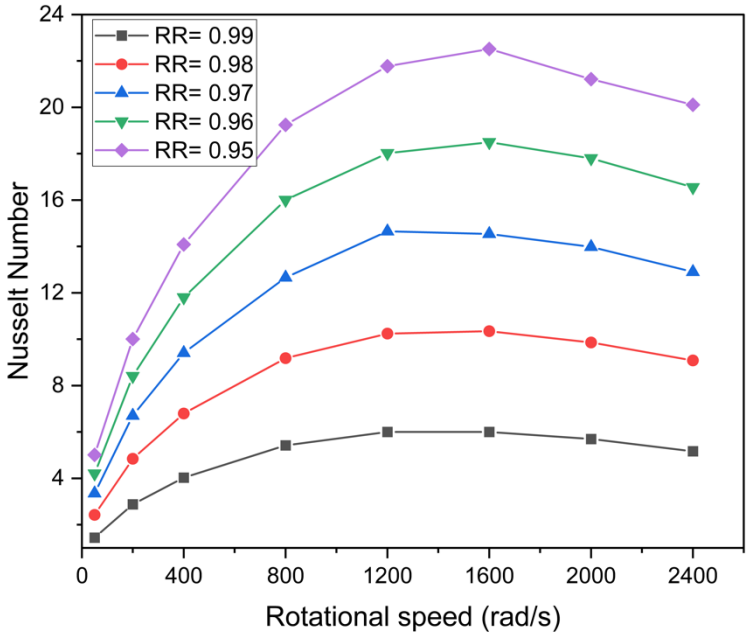

Fig. 4-33 Nusselt number vs rotational speed for different radius ratios

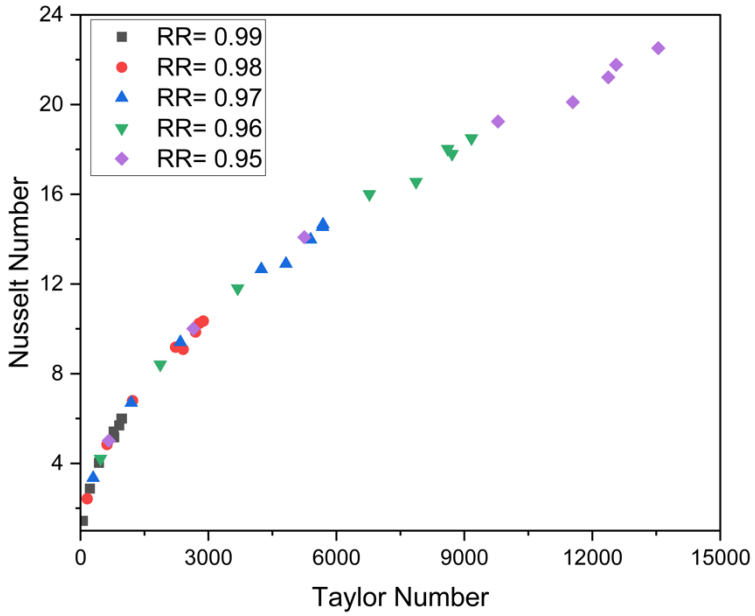

Fig. 4-34 Nusselt number vs Taylor number for different radius ratios

4.4. Summary

Chapter four focuses on various aspects of a FESS related to aerodynamics and thermal management. The chapter begins by setting the stage for a comprehensive numerical analysis of FESS. It details the structure of FESS, consisting of a rotating inner cylinder and a stationary outer cylinder, and the importance of assessing windage losses due to viscous friction. Several parameters such as rotor radius, aspect ratio, rotational velocity, and boundary conditions are established, with specific dimensions chosen based on the results presented in Chapter 3. Mesh independence analysis is conducted to ensure

the accuracy and reliability of CFD simulations, using structured quadrilateral mesh configuration. The study utilises steady-state models for the CFD simulations and employs the SST k-omega turbulence model. Assumptions made for simplifying the analysis include treating air as an ideal gas and ignoring the effects of gravity. The computational parameters include double precision computations and various discretisation schemes to ensure precise numerical results.

This section dives into the effects of rotational speed on air velocity distribution within the airgap of a FESS, particularly focusing on the formation of Taylor-Couette flow and its characteristics. It examines how the airgap size affects the number of Taylor vortices formed, their size, and compactness. The chapter also discusses the influence of these vortices on temperature distribution within the system, demonstrating how an increase in the number of Taylor vortices leads to a rise in the airgap temperature. The effects of rotational speed on the rotor skin friction coefficient and windage losses are also analysed. It is observed that as the flywheel spins faster, the impact of skin friction diminishes, likely due to the onset of turbulent flow. The study also finds a direct correlation between the number of Taylor vortices, rotor temperature, and windage losses, indicating that the geometry of the flywheel significantly impacts its aerodynamic performance. Additionally, the study explores the relationship between various dimensionless flow parameters such as Reynolds number, Taylor number, and Nusselt number, highlighting their roles in determining flow patterns and heat transfer efficiency in FESS. Overall, the chapter offers a detailed investigation into the aerodynamic and thermal characteristics of FESS, highlighting the importance of understanding and optimising these aspects for efficient energy storage. A portion of the numerical findings detailed in this chapter is published in reference [369].

Chapter 5. Optimisation of FESS Geometric and Operating Conditions

Chapter 5 delves into a thorough investigation of FESS optimisation. The foundational methodology used in Chapter 4 is crucial for the analyses carried out in this chapter. The pre-processing steps and solver configurations described in Chapter 4 have been directly implemented in the studies conducted in Chapter 5. This approach guarantees uniformity in the analytical framework, enabling a logical and comparable collection of outcomes. Chapter 4 provides a detailed explanation of the pre-processing steps, which include determining important parameters like the radius ratio and ensuring that the mesh is independent. These steps are crucial for accurately representing the aerodynamic performance of the FESS. Furthermore, the computational simulations in this chapter heavily rely on the solver steps, which involve utilising ANSYS Fluent for fluid and thermal analysis and implementing the SST k-omega turbulence model. The purpose of maintaining consistency in methodology is to strengthen the credibility of the findings and ensure that any discrepancies in results can be attributed to the specific variables being studied in Chapter 5, rather than differences in the analytical approach.

In the course of the investigation into the aerodynamic optimisation of FESS, a critical aspect is the establishment of a standard against which variations in performance can be measured. For this purpose, a base model design has been assigned, which is defined by a radius ratio of 0.99, serving as the standard for comparison. This base model serves a dual purpose. Firstly, it provides a reference point that embodies typical design parameters currently prevalent in FESS applications. Secondly, and more importantly, it acts as a control setup against which the impact of the studied parameters on the system's performance can be quantitatively assessed. The selection of a 0.99 radius ratio for the base model is based on its widespread use in current designs.

5.1. Optimisation of Airgap and Roughness

The optimisation of a FESS requires an understanding of how various design parameters interact and affect overall performance. Key parameters such as airgap size, operational speed, and surface roughness are pivotal in defining the system's efficiency. The primary objective of this section is to evaluate the influence of these parameters, both individually and collectively, on windage loss and heat transfer within a FESS. To achieve this, the study implements the Analysis of Variance (ANOVA) technique. ANOVA is instrumental in determining the most effective combinations of these parameters, providing insights into how each variable contributes to the system's performance. Specifically, the analysis focuses on exploring the interplay between airgap size and surface roughness, and their

combined impact on the FESS. By doing so, the study aims to identify strategies for reducing windage losses and enhancing heat transfer efficiency, thereby optimising the FESS's overall performance.
ANOVA is a robust statistical methodology employed to examine the relationships among multiple variables and to assess the individual and interactive effects of these variables on the outcomes. In the context of FESS, ANOVA plays a pivotal role in unravelling the significance of various geometrical and operational parameters of the system [370]. Specifically, ANOVA is utilised to determine the impact of these parameters on critical aspects such as minimising windage losses, maximising kinetic energy storage capacity, and optimising heat transfer performance. By applying ANOVA, this study aims to identify which factors most significantly influence the efficiency and effectiveness of the FESS. This analytical approach enables a comprehensive understanding of how different design, and operational elements interact and contribute to the overall performance of the FESS.

5.1.1. Responses Selection

The system responses are selected to demonstrate the response surface's local form by simulating the interaction and quadratic effects of the system parameters. They are also used to assess the system's strengths and weaknesses and determine the optimal system settings. Two responses are examined in this model: Nusselt number and Windage loss. The Nusselt number is the crucial factor in determining the convection heat transfer inside the airgap and how it is affected by the design parameters. The increase in the Nusselt number will improve the heat transfer by convection, reducing the rotor temperature and the need for an internal cooling device while allowing for higher rotational velocities, which could increase the kinetic energy storage capacity. In addition, the windage loss is a crucial factor in determining the frictional losses of a FESS which, is responsible for the self-discharge rate of the FESS.

5.1.2. Factors Selection

Several key factors play a crucial role in determining system performance. This study specifically focused on evaluating the effects of surface roughness of the rotor and housing, rotational velocity, and the dimensions of radial and axial airgaps, as depicted in Fig. 5-1. A primary consideration in this analysis is the overall size of the FESS, especially given its significance in diverse applications. To this end, four different airgap sizes were chosen to explore the effects of varying narrow airgap dimensions. Furthermore, the rotational velocity of the rotor is a critical parameter of the study. In this analysis, the rotor's rotational velocity has been fixed at 2400 rad/s [363]. The rate mentioned denotes the highest permissible speed for a cylindrical rotor made of solid steel, calculated with a safety factor of two. The aim is to provide a comprehensive understanding of how these key factors, individually and in combination, influence the efficiency and effectiveness of the FESS.

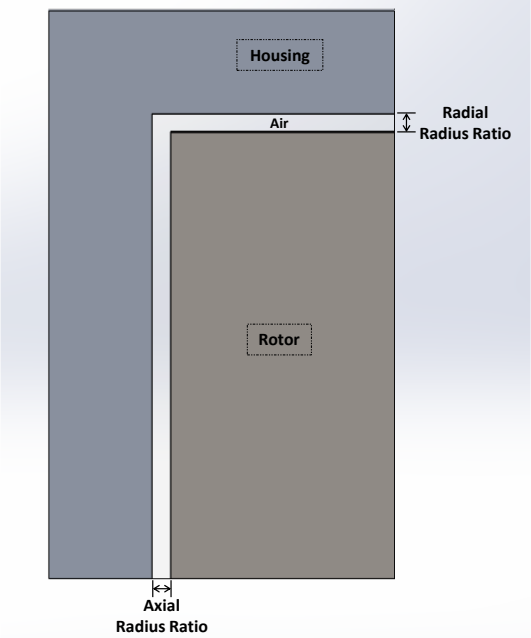

Fig. 5-1 The FESS's simplified geometry in the Z-Y plane

Surface roughness is the physical parameter used to characterise surface irregularities which impacts drag, heat and mass transfer on walls [371]. Despite its presence in heterogeneous structures such as the FESS rotor and housing, its effect on windage losses has rarely been discussed in the literature. Two parameters define surface roughness; the first is the roughness constant, a parameter that measures the uniformity of the roughness. Inputs can range from 0.5 to 1, where 0.5 indicates uniform wall roughness and 1 indicates strongly non-uniform roughness in terms of spacing and height. A value of 0.5 for the roughness constant was selected to ensure uniformity of wall roughness. The second parameter is the physical roughness height; its default value is zero, corresponding to a smooth wall. A dimensionless roughness height can be calculated by equation (5-1) [215].

$$K_s^+ = \frac{K_s C_\mu^{0.25} k^{0.5}}{\upsilon} \tag{5-1}$$

Where K_s is the roughness height, C_μ is the turbulence model constant, equal to 0.0845 and k is the turbulent kinetic energy. Depending on the value of K_s^+, the flow regime can be categorised into three regions as shown by case equation (5-2).

$$If \begin{cases} K_s^+ \leq 2.25 & Hydrodynamically\ smooth \\ 2.25 \leq K_s^+ \leq 90 & Transitional \\ K_s^+ > 90 & Fully\ rough \end{cases} \tag{5-2}$$

In the hydrodynamically smooth region, roughness effects can be ignored, but they become increasingly important in the transitional and fully rough regimes [215]. The dimensionless roughness height remained below 90 in all the tested cases in this study, indicating the flow regime to be either hydrodynamically smooth or transitional. The roughness values were chosen based on the selected

materials: steel 4340 for the rotor and Aluminium for the housing. Starting with a smooth surface ($K_s = zero$), another two roughness values were selected to be in the transitional region with K_s^+ greater than 2.25 [372] [373].

While the effect of rotor surface roughness has been previously studied by other researchers, to the best of the author's knowledge, the combined effect of rotor and housing surface roughness with the effect of the radius ratio has not been studied, which is the main contribution of this work. Although previous researchers have examined the impact of rotor surface roughness on heat transfer, there has been no investigation into the combined influence of rotor and housing surface roughness along with the radius ratio. This is the primary focus of this section, making it a novel contribution. In addition, the rotational speed is an essential factor to be considered to allow for different Taylor flows and study the effects of the selected parameters under different operating conditions. The factors studied in this investigation are listed in Table 5-1.

Table 5-1 Examined FESS factors and levels

	Factors				
	A	**B**	**C**	**D**	**E**
Levels	**Radial Radius Ratio**	**Axial Radius Ratio**	**Housing Surface Roughness (m)**	**Rotor Surface Roughness (m)**	**Rotational Speed (rad/s)**
1	0.99	0.99	0	0	200
2	0.98	0.98	5e-6	5e-7	800
3	0.97	0.97	5e-5	5e-6	1600
4	0.96	0.96	1e-4	5e-5	2400

5.1.3. Analysis Setup

The ANOVA model in this study utilised factorial analysis to determine the effects of the selected factors on responses at various levels [370]. This method allows for the variables to be ranked based on their influence on the objective function values [374] [375]. Therefore, parameters affecting the performance of FESS can be identified and optimised. Estimating the coefficients in a mathematical model, forecasting the response and determining the model's suitability are the main processes in the optimisation process. This study employs a factorial design that includes four levels for factors A, B, C, D, and E. This type of test is frequently used to determine the relative importance of system design factors and their interactions. For instance, the null hypothesis implies that the total mean of all treatments is equal, suggesting that no variation in treatment means exists. In comparison, the alternative hypothesis predicts that on average, at least one treatment will be significantly different. For

each treatment, the first four hypotheses show the null and alternative hypotheses. whereas for each treatment interaction, the last four hypotheses show the null and alternative hypotheses for each treatment.

5.1.4. Responses

The two selected responses were subjected to an analysis of variance, the results of the significant factors and their interactions are tabulated in Table 5-2 and Table 5-3 for the first response (Nusselt number) and the second response (windage loss), respectively. The F-values for each factor and their interactions were calculated to assess the significance of their impact on the response variables. The F-value is a ratio of the variance explained by a factor or interaction to the unexplained variance, known as the error term. A higher F-value indicates that the factor contributes more significantly to the variation in the response variable, suggesting that it has a substantial effect compared to random error. Corresponding P-values were computed at a 95% confidence level to determine the statistical significance of these factors and interactions. The P-value represents the probability of obtaining the observed results assuming that the null hypothesis is true—that is, assuming there is no effect of the factor on the response variable. A P-value less than 0.05 indicates that the factor's effect on the response is statistically significant and unlikely to have occurred by random chance.

The ANOVA for response surface quadratic models for Nusselt number and windage losses revealed that the models were significant, with F-values of 2431.14 and 87259.11, respectively. Model terms with P-values less than 0.05 are considered significant while model terms with values greater than 0.10 are considered insignificant. The responses shown in Table 5-2 and Table 5-3 are significant, the insignificant factors were removed to improve the model. In the analysis, several factors and interactions exhibited high F-values coupled with P-values less than 0.05, indicating that they have a statistically significant effect on the Nusselt number and windage losses. This signifies that variations in these factors lead to meaningful changes in the response variables. The statistical results from the ANOVA confirm that the developed models are robust and reliably predict the Nusselt number and windage losses within the studied range of variables. This validation through significant F-values and low P-values strengthens confidence in the models' ability to accurately capture the underlying physics and interactions affecting the system's performance.

Table 5-2 ANOVA for response surface quadratic model for Nusselt number

Source	Sum of Squares	df	Mean Square	F-value	p-value
A-Radial Radius Ratio	19.77	1	19.77	7241.96	< 0.0001
B-Axial Radius Ratio	42.27	1	42.27	15484.58	< 0.0001
C-Rotor Roughness	0.1836	1	0.1836	67.26	< 0.0001
D-Housing Roughness	0.0459	1	0.0459	16.82	< 0.0001
E-Rotational Velocity	11.72	1	11.72	4293.87	< 0.0001
AB	4.60	1	4.60	1686.89	< 0.0001
AC	0.0315	1	0.0315	11.53	0.0007
AE	0.6975	1	0.6975	255.53	< 0.0001
BC	0.0639	1	0.0639	23.39	< 0.0001
BD	0.0377	1	0.0377	13.81	0.0002
BE	0.0203	1	0.0203	7.45	0.0065
CD	0.0265	1	0.0265	9.73	0.0019
CE	0.4035	1	0.4035	147.80	< 0.0001
DE	0.0528	1	0.0528	19.33	< 0.0001
Residual	2.01	1008	0.0027		
Total	121.47	1023			

Table 5-3 ANOVA for response surface quadratic model for windage losses

Source	Sum of Squares	df	Mean Square	F-value	p-value
A-Radial Radius Ratio	0.6483	1	0.6483	945.78	< 0.0001
B-Axial Radius Ratio	0.0494	1	0.0494	72.06	< 0.0001
C-Rotor Roughness	1.59	1	1.59	2318.62	< 0.0001
D-Housing Roughness	0.8097	1	0.8097	1181.28	< 0.0001
E-Rotational Velocity	672.74	1	672.74	9.8×10^5	< 0.0001
AB	0.0035	1	0.0035	5.07	0.0246
AC	0.0255	1	0.0255	37.25	< 0.0001
AD	0.3429	1	0.3429	500.26	< 0.0001
AE	0.0327	1	0.0327	47.76	< 0.0001
BD	0.0029	1	0.0029	4.17	0.0414
CE	0.0189	1	0.0189	27.57	< 0.0001
DE	0.0100	1	0.0100	14.52	0.0002
Residual	0.5148	1008	0.0007		
Total	957.49	1023			

5.1.4.1. Model Adequacy

The statistical analysis presented in Table 5-4 focuses on the responses calculated from the mathematical model used to articulate the relationship between input variables and their corresponding dependent responses. Key findings from the statistical analysis include:

- Model Adequacy: Ensuring that the model accurately captures the underlying data patterns is crucial. The initial analysis revealed inadequacies in the model, prompting the necessity for a transformation to improve data normality. Specifically, a natural logarithm transformation was applied to both responses to rectify the lack of normality in the dataset [376]. This transformation was successful in enhancing the model's reliability, confirmed by improved data normality, homogeneity of variances, and randomness in the distribution of residuals.
- Coefficient of Determination (R^2): This metric measures how well the regression predictions approximate the real data points. For the models under consideration, the R^2 values exceed 0.98, indicating a close alignment of the regression line with the observed data. These high R^2 values suggest that the model explains a significant portion of the variability in the responses.
- Adjusted R^2: This value adjusts the R^2 for the number of predictors in the model, providing a more accurate assessment of the model's explanatory power. The adjusted R^2 values also surpass 0.98, signifying minimal variance left unexplained by the model. This indicates that both essential and non-essential parameters are appropriately accounted for, enhancing the model's reliability.
- Predicted R^2: This metric assesses the model's predictive capability by examining how well it forecasts new observations. The small disparity between the adjusted R^2 and predicted R^2 values (approximately 0.02) suggests a robust correlation and indicates that the model has good predictive power.
- Adequate Precision: This ratio measures the signal-to-noise ratio, with a value greater than 4 considered desirable. In this study, the adequate precision ratios are 219.724 for the first response and 768.567 for the second response. These high ratios confirm that the model captures a significant signal amidst the inherent data noise, demonstrating its capability to navigate the design space effectively.

These statistical parameters and tests confirm that the regression models are robust and reliable, exhibiting high predictive capability and low variability. This statistical robustness is crucial for making informed decisions based on the model's predictions and ensures that the model accurately reflects the underlying patterns in the data.

Table 5-4 The fit statistics pertaining to the responses obtained

First Response	**Std. Dev.**	0.0522	**R^2**	0.9834
	Mean	3.18	**Adjusted R^2**	0.9830
	C.V. %	1.64	**Predicted R^2**	0.9825
			Adequate Precision	219.7237
Second Response	**Std. Dev.**	0.0262	**R^2**	0.9995
	Mean	6.66	**Adjusted R^2**	0.9995
	C.V. %	0.3933	**Predicted R^2**	0.9994
			Adequate Precision	768.5666

5.1.5. Nusselt Number Response

The first response is the Nusselt number, an essential parameter for identifying the convective heat transfer between the rotor, air and housing. A higher Nusselt number indicates better convection, thus lower rotor and housing temperature within the safe range. Fig. 5-2 presents a 3D surface plot of the Nusselt number as it varies with radial and axial radius ratios. Each plot corresponds to a different rotational speed for the FESS being studied, which are (a) 800 rad/s, (b) 1600 rad/s, and (c) 2400 rad/s. From Fig. 5-2 (a), the surface plot suggests that as both the radial and axial radius ratios decrease, there is a slight increase in the Nusselt number, indicating an increase in convective heat transfer efficiency. While Fig. 5-2 (b), shows a more pronounced increase in the Nusselt number compared to Fig. 5-2 (a). This implies that as the rotational speed increases, so does the convective heat transfer, which is consistent with the theory that higher velocities enhance convective heat transfer. The gradient of the surface plot appears steeper than in Fig. 5-2 (a), indicating a more sensitive change in the Nusselt number with respect to changes in the radius ratios. Fig. 5-2 (c) represents the highest rotational speed at 2400 rad/s. As shown in Fig. 5-2, increasing the airgap size increases the Nusselt number at all rotational speeds. The highest Nusselt numbers were achieved at the radius ratio of 0.96 in the radial and axial directions and the rotational speed of 1600 rad/s. The Nusselt number is influenced by Taylor number, which increases as the rotational velocity increases until it reaches 1600 rad/s, at which point it begins to fall due to a reduction in the kinematic viscosity of air as the air temperature increases. Taylor vortices appear more frequently as the radial airgap increases, while Taylor cells are less rapidly affected by azimuth waves as the radial airgap reduces [377].

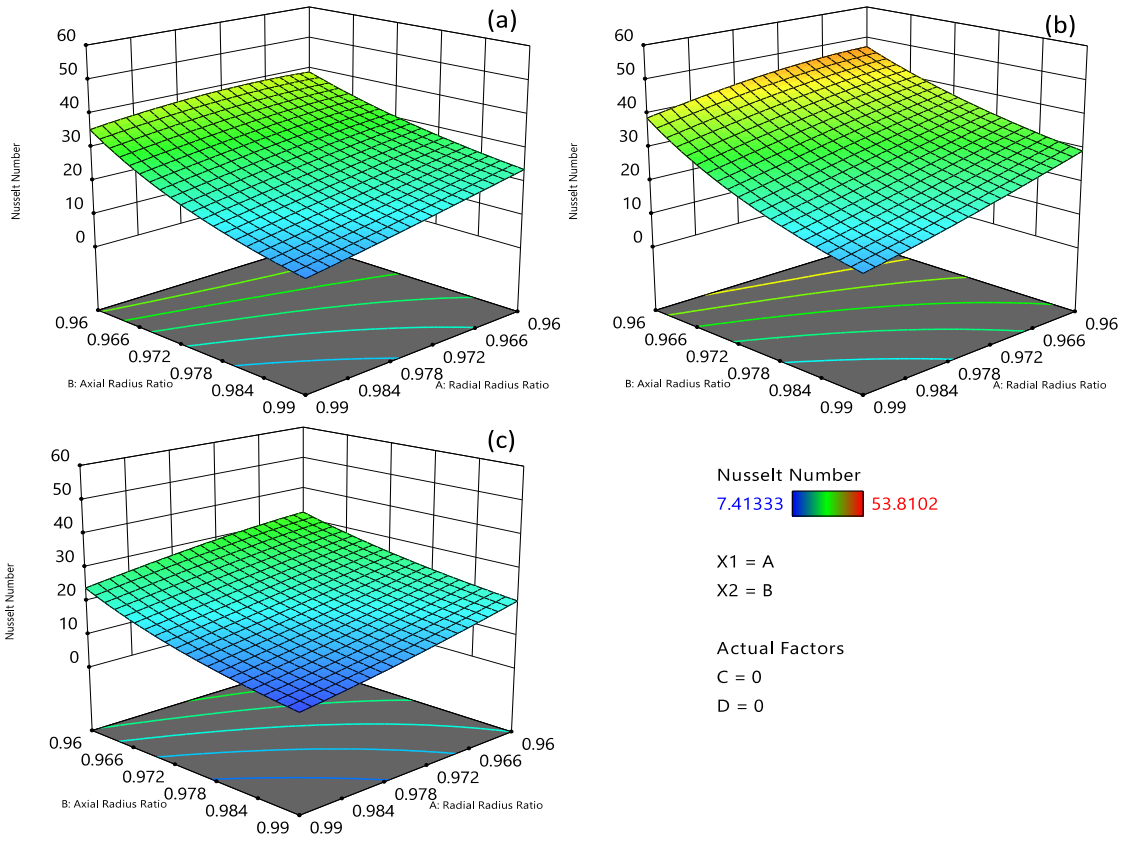

Fig. 5-2 3D plot of Nusselt number as a function of radial and axial radius ratios at different rotational speeds: (a) 800 rad/s, (b) 1600 rad/s, (c) 2400 rad/s

Fig. 5-3 presents 3D surface plots of the Nusselt number against the rotor and housing surface roughness at three different rotational speeds: (a) 800 rad/s, (b) 1600 rad/s, and (c) 2400 rad/s. As for Fig. 5-3 (a), the Nusselt number shows its dependency on the surface roughness of both the rotor and the housing. The plot indicates that the Nusselt number increases with surface roughness, but the increase is somewhat restrained, suggesting that surface roughness has a modest impact on heat transfer at this speed. Fig. 5-3 (b) shows that Nusselt number increases more significantly with surface roughness compared to the other two speeds, as evidenced by the steeper surface gradient. This indicates a strong correlation between surface roughness and convective heat transfer at 1600 rad/s, which could be attributed to the enhanced turbulence and consequent mixing induced by the rough surfaces. The increase in the rotor and housing surface roughness increases the Nusselt number for all the studied rotational velocities except 2400 rad/s, where the surface roughness did not affect the Nusselt number. The same trend was observed for the studied radius ratios. The Nusselt number of the roughened rotor and housing increases as Taylor number increases due to the increased turbulence intensity near walls. The flow regime is considered transitional between hydrodynamically smooth and fully rough when the dimensionless roughness height is between 2.25 and 90. In this case, the second and third roughness heights for the rotor and the housing are in the transitional regime.

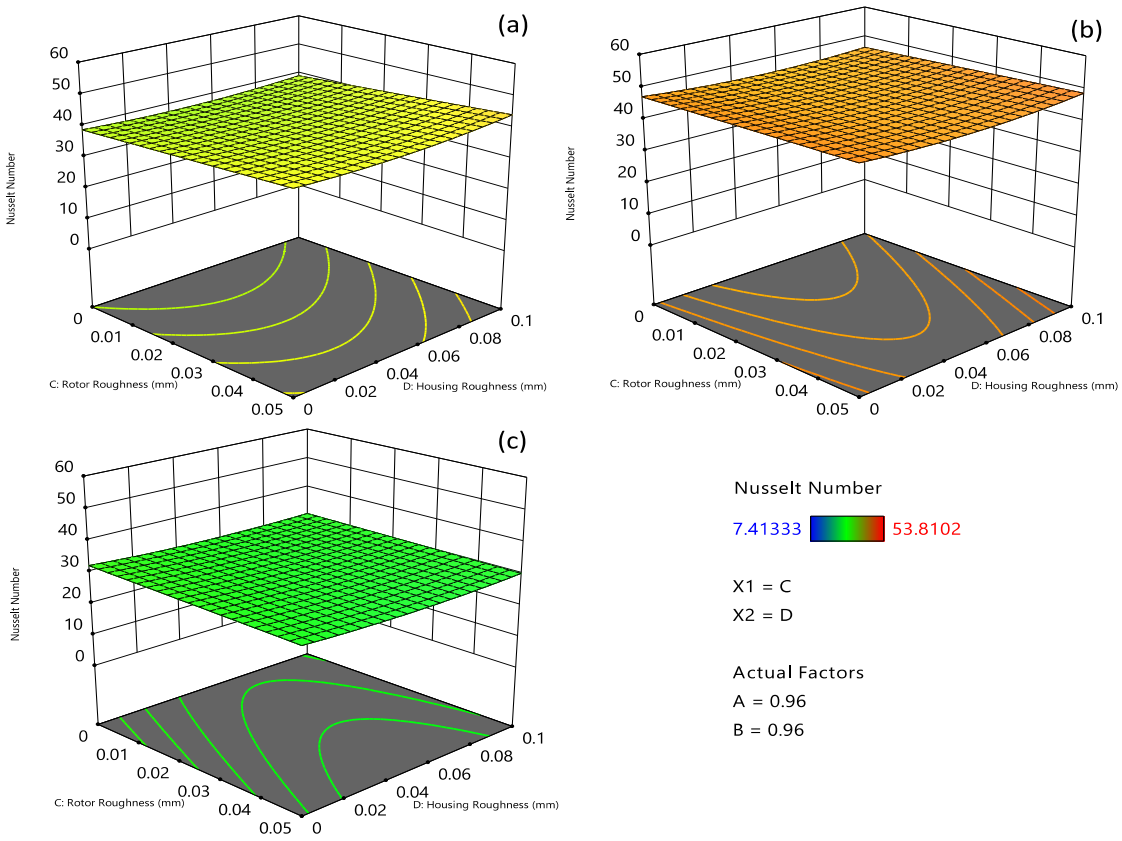

Fig. 5-3 3D plot of Nusselt number as a function of rotor and housing surface roughness at different rotational speeds: (a) 800 rad/s, (b) 1600 rad/s, (c) 2400 rad/s

Fig. 5-4(a) depicts the air velocity distribution within the airgap of the FESS with the radial and axial radius ratios of 0.98 at the rotational velocity of 1600 rad/s. The rotor surface roughness influences the shape of the Taylor vortices and the time at which they appear. The shear applied to a rough surface is more significant than a smooth surface due to the significant decelerating force exerted on the swirling flow by the rough surface. Consequently, the rotor has the highest and the housing the lowest temperature, thus there exists a temperature gradient between the rotor and housing surfaces. The spike-shaped flow shown in Fig. 5-4 is due to the presence of Taylor-Couette flow in the airgap. The air velocity near the housing is close to zero, while the maximum air velocity occurs near the rotor. The air molecules at high temperatures near the rotor are moved upwards towards the housing, causing the mixing temperature to rise. This finding is explained by an increase in centrifugal forces, which increases the speed of the vortices when they collide, as shown in Fig. 5-4 (b) and (c).

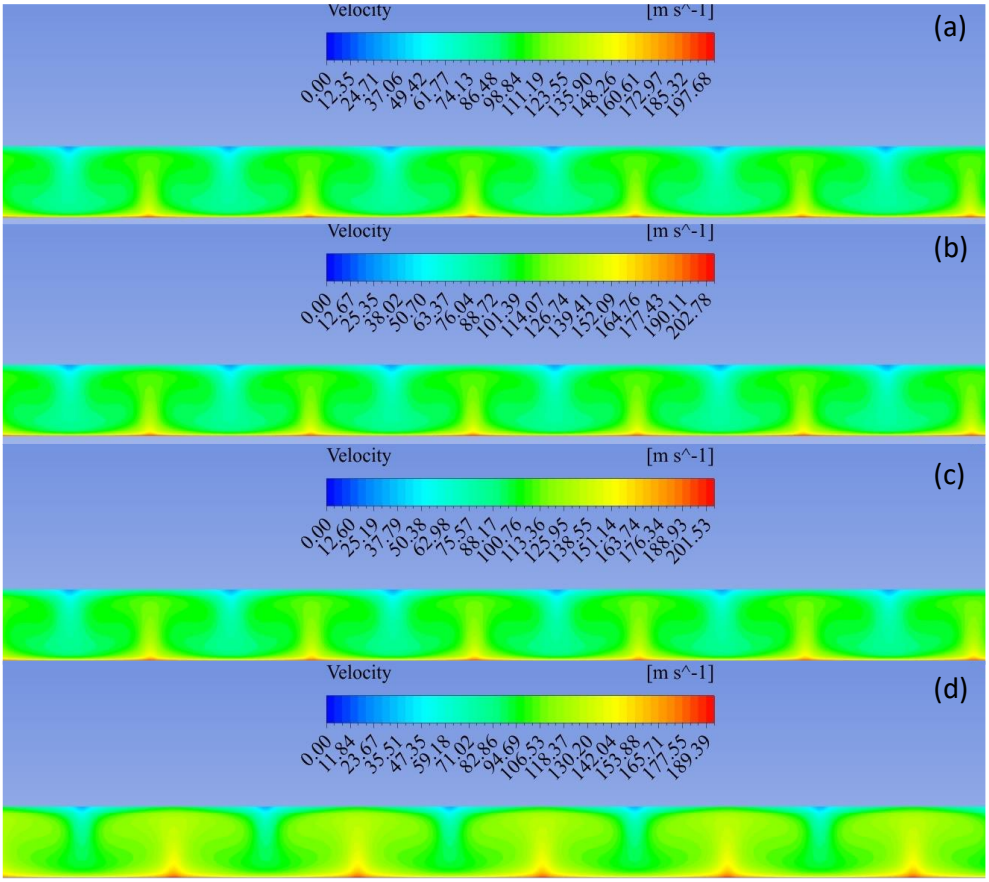

Fig. 5-4 Air velocity distribution within the airgap at 1600 rad/s for radial and axial radius ratios of 0.98 at different rotor surface roughness heights: (a) Ks=0, (b) Ks=5e-7 m, (c) Ks=5e-6 m, (d) Ks=5e-5 m

Fig. 5-5 showcase a series of 3D surface plots depicting the Nusselt number as a function of radial radius ratio and rotational velocity, differentiated by varying axial radius ratios. Fig. 5-5 (a) represents the Nusselt number for an axial radius ratio of 0.99. The surface plot suggests a moderate increase in the Nusselt number with the radial radius ratio. The Nusselt number for rotational velocity increases until it reaches 1600 rad/s, after which the values begin to decrease. While for the axial radius ratio of 0.98, the increase in the Nusselt number appears more pronounced than in the 0.99 axial radius ratio, indicating that a decrease in the axial radius ratio enhances the convective heat transfer. This is due to changes in the flow characteristics and the boundary layer development caused by the altered geometry. While an axial radius ratio of 0.97, shows a further increase in the Nusselt number. The trend observed indicates that as the axial radius ratio decreases, the impact of the radial radius ratio and the rotational velocity on the Nusselt number becomes more substantial, which suggests increased mixing between cold and hot surfaces. For an axial radius ratio of 0.96, exhibits the highest Nusselt numbers across the series. Fig. 5-5 (d) indicates the strongest relationship between the Nusselt number and the geometric and operational parameters, highlighting the sensitivity of heat transfer efficiency to these factors at this axial radius ratio.

The results demonstrated that increasing the rotational velocity improves the Nusselt number until the rotational velocity of 1600 rad/s at which point, the Nusselt number begins to drop drastically. Unfortunately, the effect of the axial radius ratio is typically ignored, even though it is significant in terms of the Nusselt number, which could lead to improved heat transfer rate, higher rotational velocities and increased kinetic energy storage capacity.

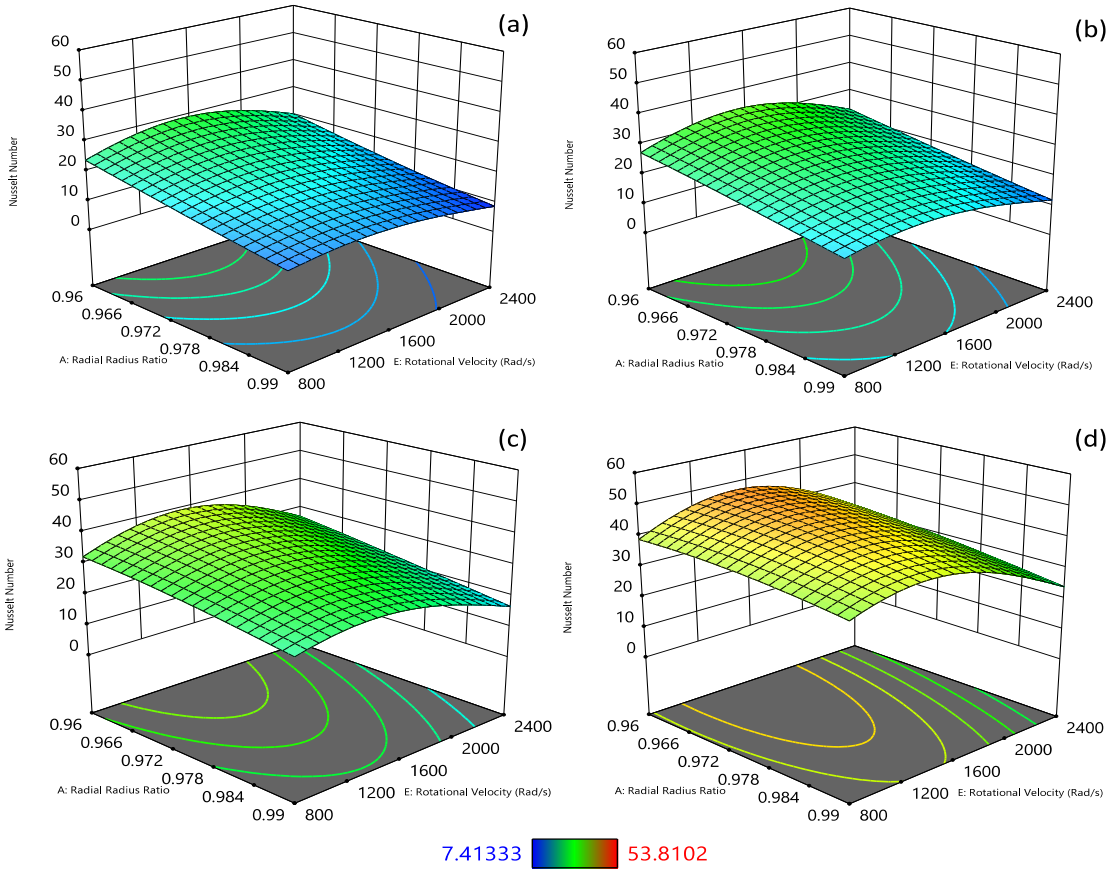

Fig. 5-5 3D plot of Nusselt number as a function of radial radius ratio and rotational velocity at different axial radius ratios: (a) 0.99, (b) 0.98, (c) 0.97, (d) 0.96

Fig. 5-6 presents a main effects plot that explains the influence of the five factors on the mean Nusselt number. It is visible from the plot that rotational velocity is a significant factor, with the Nusselt number increasing to a maximum at 1600 rad/s before the effect inverts, coinciding with a decline in the Reynolds number. Concerning the radius ratio, a rise in the airgap, both radially and axially, is correlated with an enhancement in the Nusselt number, although the effect of the axial radius ratio is found to be more pronounced. With regards to the surface roughness, an increase in rotor surface roughness is associated with an increased Nusselt number, while the impact of housing surface roughness exhibits a distinctively different trend.

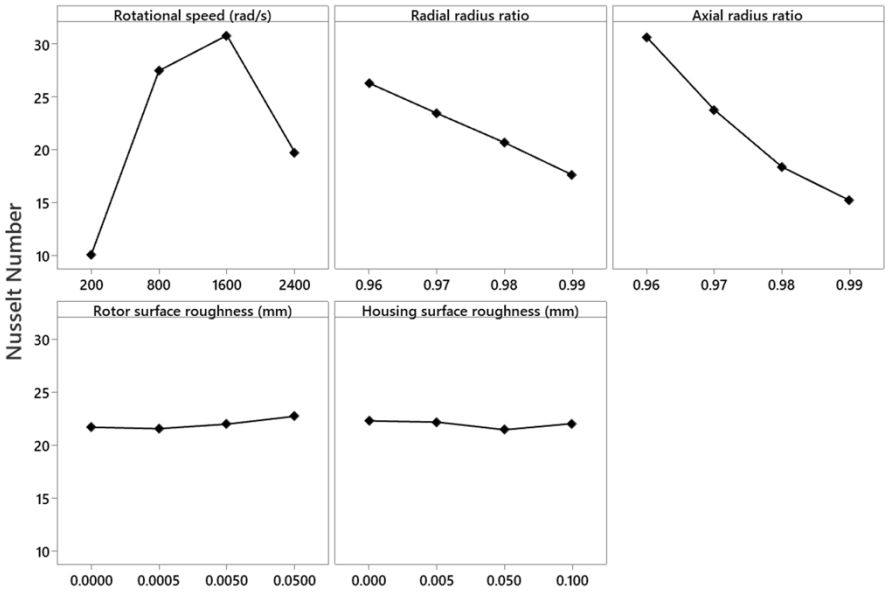

Fig. 5-6 Main effects plot for mean Nusselt number for the studied five factors

5.1.6. Windage Losses Response

Windage losses are due to viscous friction between the rotor and the air as the flywheel spins. The size of the airgap, surface roughness, rotational speed and thermo-physical properties of the confined fluid significantly affect the windage losses. The influence of the rotational speed on the windage losses is analysed for all different studied radius ratios. As previously mentioned, the maximum allowable angular velocity of the steel rotor was found to be 2400 rad/s. The air velocity distribution changes as the rotational speed increases since the Taylor number exceeds the critical value of 41.3, producing Taylor vortices. Fig. 5-7 illustrates the 3D surface plots of windage losses as they vary with radial and axial radius ratios at different rotational speeds. Fig. 5-7 (a) illustrates the windage losses occurring at a rotational speed of 800 rad/s. The plot demonstrates a decrease in windage losses achieved by reducing the ratios of radial and axial radii. However, at lower velocities, the losses due to windage are not substantial compared to the other speeds examined.

For windage losses at 1600 rad/s, as shown in Fig. 5-7 (b). Compared to Fig. 5-7 (a), the plot is higher, indicating increased windage losses at this speed. The impact of the radial and axial radius ratio is similar to the rotational velocity of 800 rad/s. Fig. 5-7 (c) corresponds to the highest rotational speed of 2400 rad/s. Here, the windage losses are considerably the highest, as shown by the elevated surface plot. The trend remains consistent with the previous plots, indicating that windage losses increase with rotational speed but the effect of the radial and axial radius ratio is more pronounced. Air friction is more significant in larger radius ratios compared to smaller radius ratios due to the higher shear stress produced by the Taylor vortices. The highest windage losses are achieved at the smallest airgap (i.e. highest radius ratios).

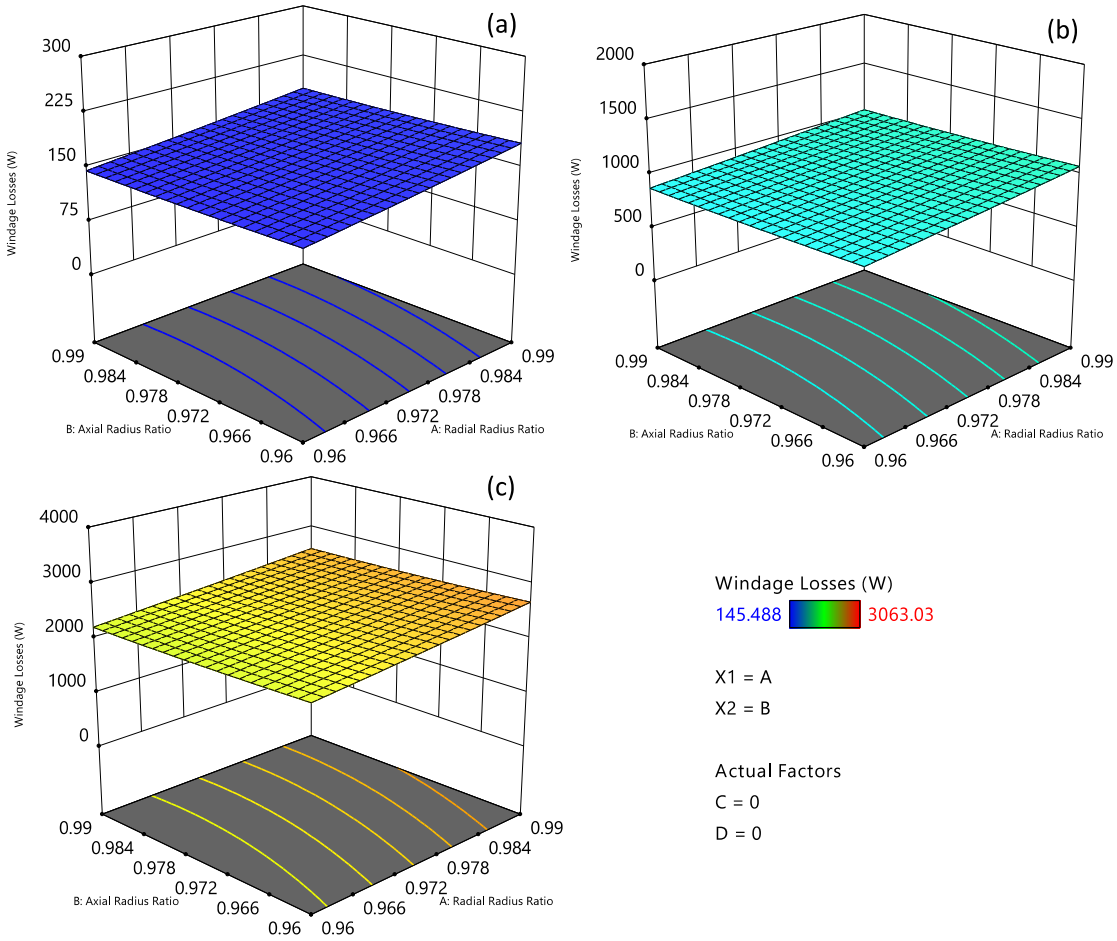

Fig. 5-7 3D plot of windage losses as a function of radial and axial radius ratios at different rotational speeds: (a) 800 rad/s, (b) 1600 rad/s, (c) 2400 rad/s

Fig. 5-8 displays 3D surface plots that represent the rotor skin friction coefficient in relation to radial and axial radius ratios at three different rotational speeds. Fig. 5-8 (a) shows the rotor skin friction coefficient at the rotational speed of 800 rad/s. The plot indicates a consistent decrease in the skin friction coefficient as the radial radius ratio decreases. However, the increase in the axial radius ratio has a less significant effect on reducing the skin friction coefficient. By increasing the rotational velocity to 1600 rad/s, the effect of the radial and axial radius ratio remained unchanged, but the values of the skin friction coefficient decreased significantly, as shown in Fig. 5-8 (b). At a rotational velocity of 2400 rad/s, the trend persists with a comparable surface, suggesting that reducing the radial radius ratio and increasing the axial radius ratio leads to a decrease in the rotor skin friction coefficient. However, this effect is more evident, as shown in Fig. 5-8 (c).

The radial radius ratio significantly affects the rotor skin friction coefficient. The higher the radial radius ratio (smaller airgap), the higher the rotor skin friction coefficient. The rotor skin friction coefficient is one of the most important factors influencing windage loss since approximately 70% of windage losses are due to frictional losses in the radial airgap while the remaining 30% originate from the losses in the axial airgap due to disc torque. It was observed that an increase in the axial radius ratio reduced the

rotor skin friction coefficient. The greater the axial distance between the rotor and the housing, the higher the heat transfer rate, resulting in lower surface temperatures.

Fig. 5-9 presents a sequence of 3D surface plots illustrating the variation of the disc torque coefficient as a function of radial and axial radius ratios at three distinct rotational speeds. The disc torque coefficient exhibits an inverse relationship with the radial and axial radius ratios, in contrast to the skin friction coefficient. An increase in the axial radius ratio and a decrease in the radial radius ratio results in a reduction of the disc torque coefficient. The minimum disc torque coefficient was obtained at a rotational velocity of 1600 rad/s, as depicted in Fig. 5-9 (b). Conversely, the impact of the radial radius ratio is more noticeable at a rotational velocity of 2400 rad/s, as illustrated in Fig. 5-9 (c). Although both radial and axial radius ratios affected the disc torque coefficient, increasing the radial radius ratio slightly increased the disc torque coefficient with the lowest value occurring at 1600 rad/s.

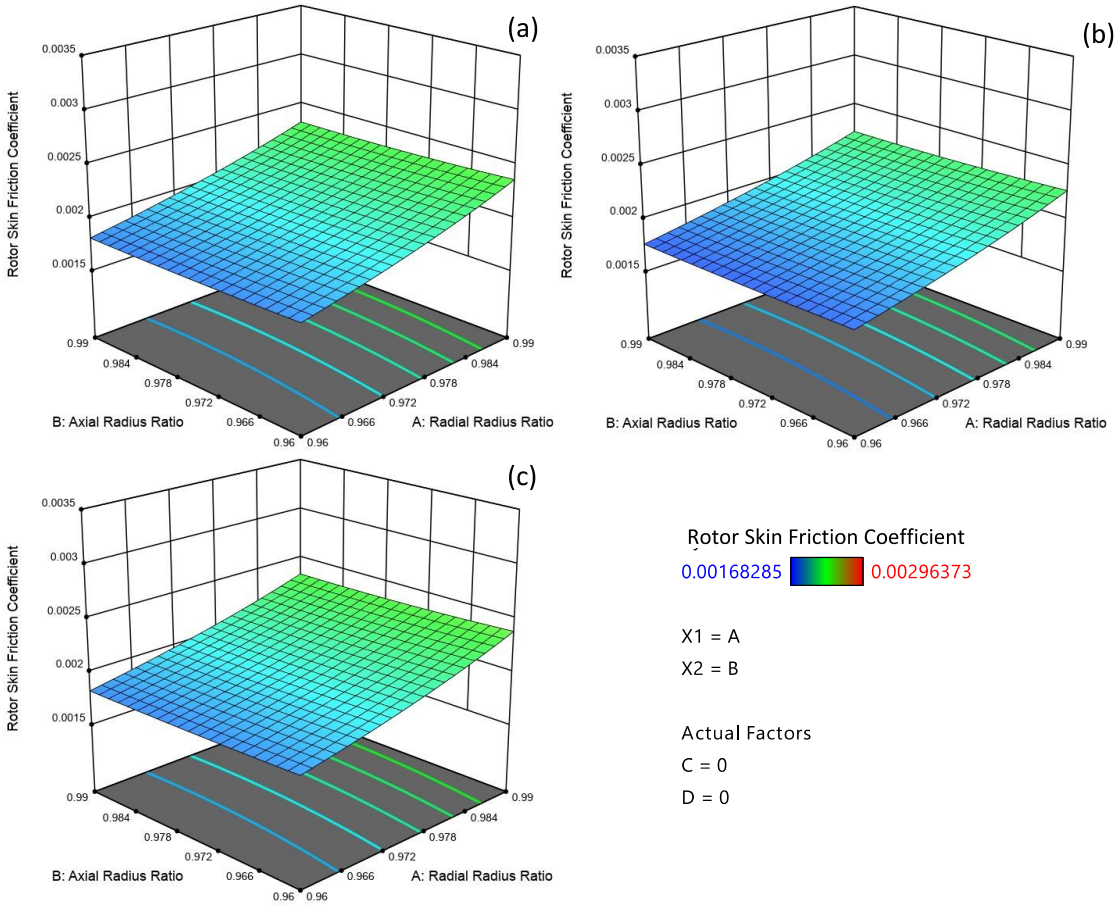

Fig. 5-8 3D plot of rotor skin friction coefficient as a function of radial and axial radius ratios at different rotational speeds: (a) 800 rad/s, (b) 1600 rad/s, (c) 2400 rad/s

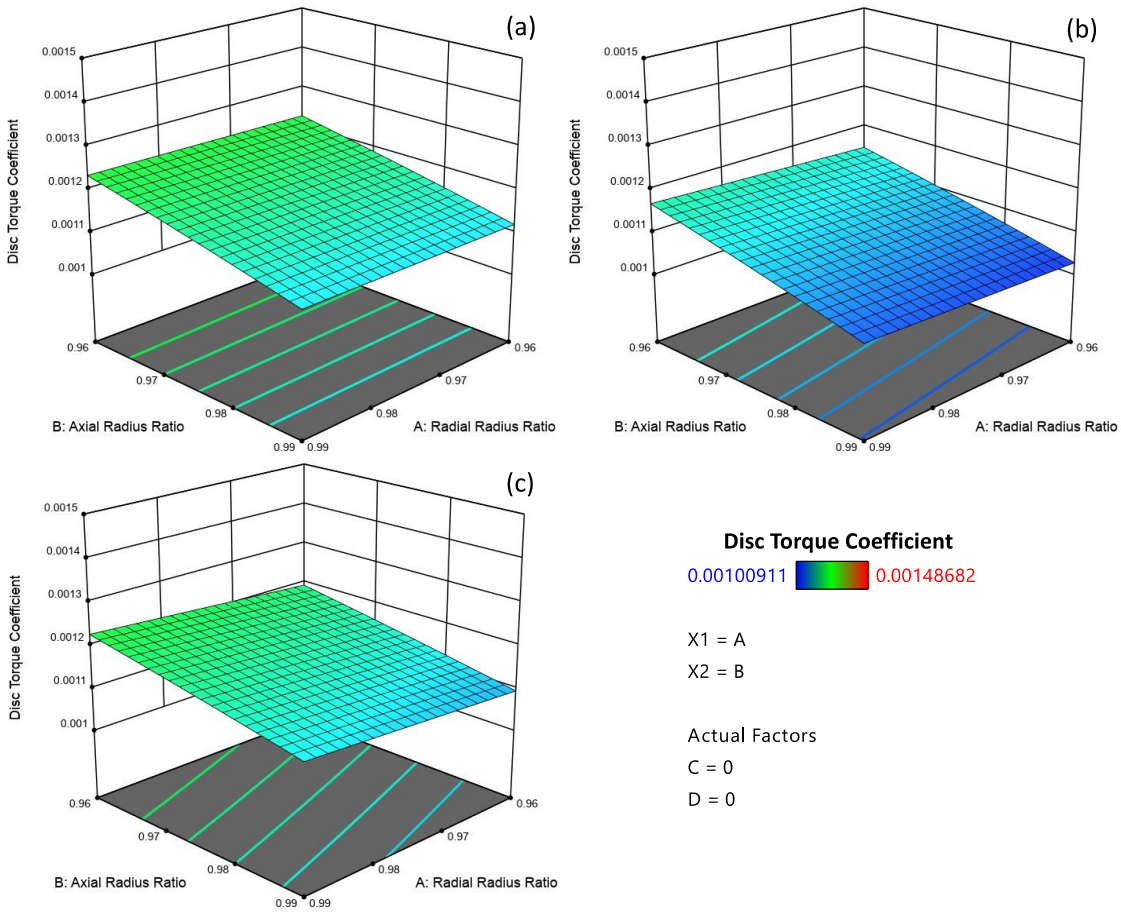

Fig. 5-9 3D plot of disc torque coefficient as a function of radial and axial radius ratios at different rotational speeds: (a) 800 rad/s, (b) 1600 rad/s, (c) 2400 rad/s

Fig. 5-10. Shows two 3D surface plots, each illustrating the variation of windage losses in relation to rotational velocity and one of two radius ratios: (a) radial radius ratio and (b) axial radius ratio. Fig 5-10 (a) visualises how windage losses change with rotational velocity and radial radius ratio. The plot shows a gradient that indicates an increase in windage losses with both an increase in rotational velocity and radial radius ratio. This trend suggests that higher speeds and bigger radial radius ratios lead to increased losses due to windage. On the other hand, Fig. 5-10 (b) depicts windage losses as a function of rotational velocity and axial radius ratio. Windage losses appear to increase with rotational velocity. However, increasing the axial radius ratio can reduce windage losses. The surface seems to show a gentle slope, which suggests a more modest impact of the axial radius ratio on windage losses compared to the radial radius ratio.

Windage losses increase exponentially as rotational velocity increases, irrespective of the radial or axial radius ratios. As previously stated, decreasing the radial radius ratio and increasing the axial radius ratio reduces windage losses. At the maximum rotational velocity, the axial radius ratio can reduce windage losses by approximately 4% for all the studied radial radius ratios. In comparison, the radial radius ratio

can reduce windage losses by 15%. However, the combination of a radial radius ratio of 0.99 and an axial radius ratio of 0.96 can reduce windage losses by approximately 19%.

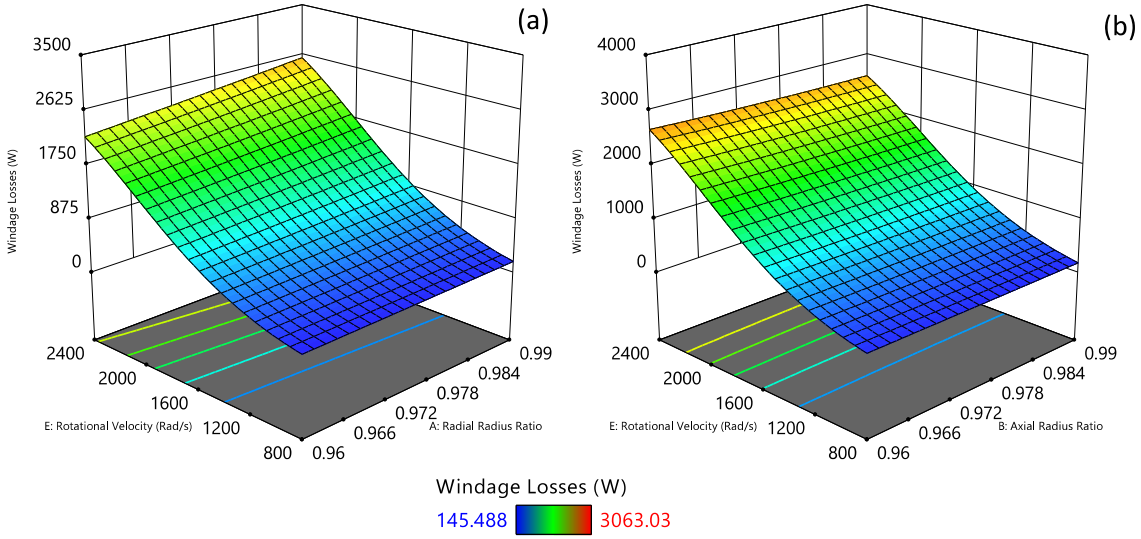

Fig. 5-10 3D plot of windage losses as a function of rotational velocity and (a) radial radius ratio, (b) axial radius ratio

Fig. 5-11 presents the main effects plot that explains the influence of five factors on the mean windage losses. The plots indicate that an increase in rotational velocity results in a substantial increase in windage losses. In contrast, a reduction in the radial radius ratio contributes to a decrease in windage losses, an effect that is inversely observed with the axial radius ratio where its reduction leads to increased losses. Furthermore, the complete removal of surface roughness is shown to contribute to a reduction in windage losses, irrespective of whether the surface roughness is on the rotor or the housing.

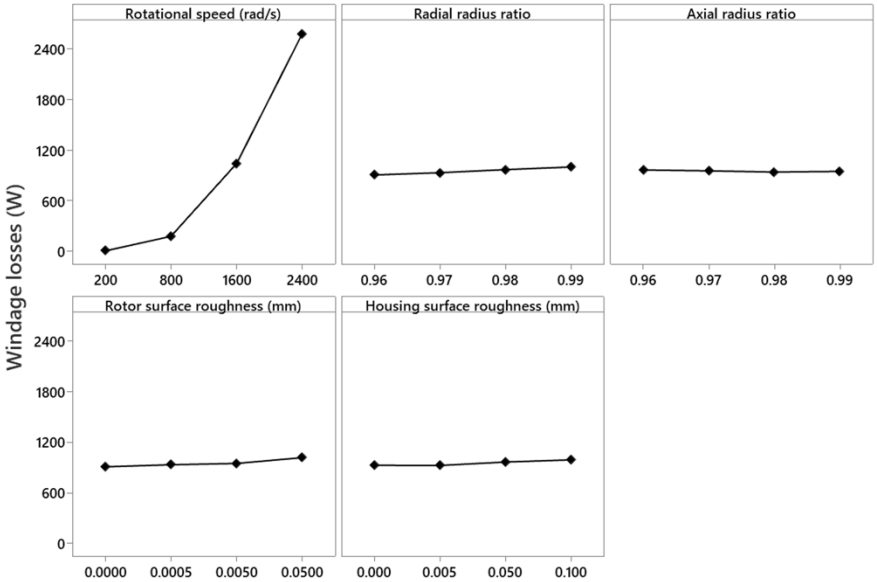

Fig. 5-11 Main effects plot for mean windage losses for the studied five factors

5.1.7. Influence of Surface Roughness

Turbulent flows within structures with rough walls can be found in both nature and industry. As the Reynolds number increases, the viscous length scales in the flow decrease, and eventually, every surface appears rough even if the roughness is very small on an absolute scale [378]. Fig. 5-12 - Fig. 5-15 depicts the effect of rotor and housing surface roughness on windage loss for the studied rotational velocities and radius ratios. The same trend is observed at each rotational velocity for all the studied radius ratios. The effect of housing surface roughness is small compared to the rotor surface roughness. At the maximum studied rotational velocity, regardless of the radius ratio, the difference between the lowest and highest studied housing surface roughness results in approximately a 3% increase in windage losses and a 2.7% increase in Nusselt number. The lowest windage losses were recorded with smooth surfaces on both the rotor and the housing, indicating that surface roughness has a negative impact on windage losses.

As shown in Fig. 5-12 - Fig. 5-15, the rotor surface roughness significantly impacts windage losses. Windage loss increases as the rotor roughness height increases until it reaches a peak value of 0.025 mm where it begins to decrease. The effect of rotor surface roughness on windage losses is almost constant regardless of the radius ratio, whereas the effect of housing surface roughness increases as the radius ratio decreases. With increasing rotor surface roughness, the velocity gradient close to the rotor decreases. The skin friction coefficient is a dimensionless factor, and as the Reynolds number increases, skin friction decreases until it becomes constant in the presence of surface roughness. The absolute value of skin friction is determined based on the characteristic roughness height [379]. Rotor surface roughness has a significant impact on the onset of Taylor vortices. The results suggest that the onset occurs at lower Reynolds numbers, while the onset of wavy Taylor vortices is more affected by the radius ratio. Additionally, it can be concluded that the radius ratio has a more significant impact on oscillation frequency in the wavy Taylor regime compared to surface roughness [380].

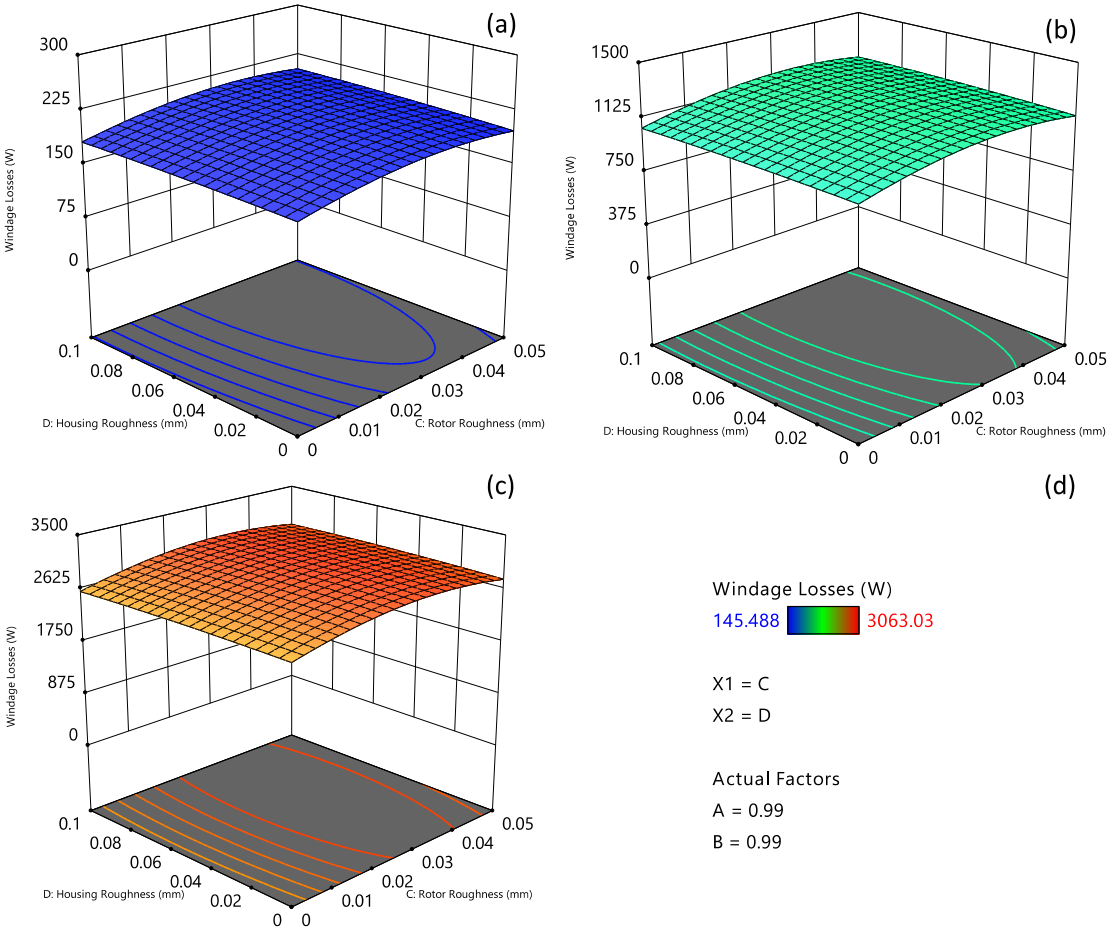

Fig. 5-12 3D plot of windage losses as a function of rotor and housing surface roughness with the radial and axial radius ratios of 0.99 at different rotational speeds: (a) 800 rad/s, (b) 1600 rad/s, (c) 2400 rad/s

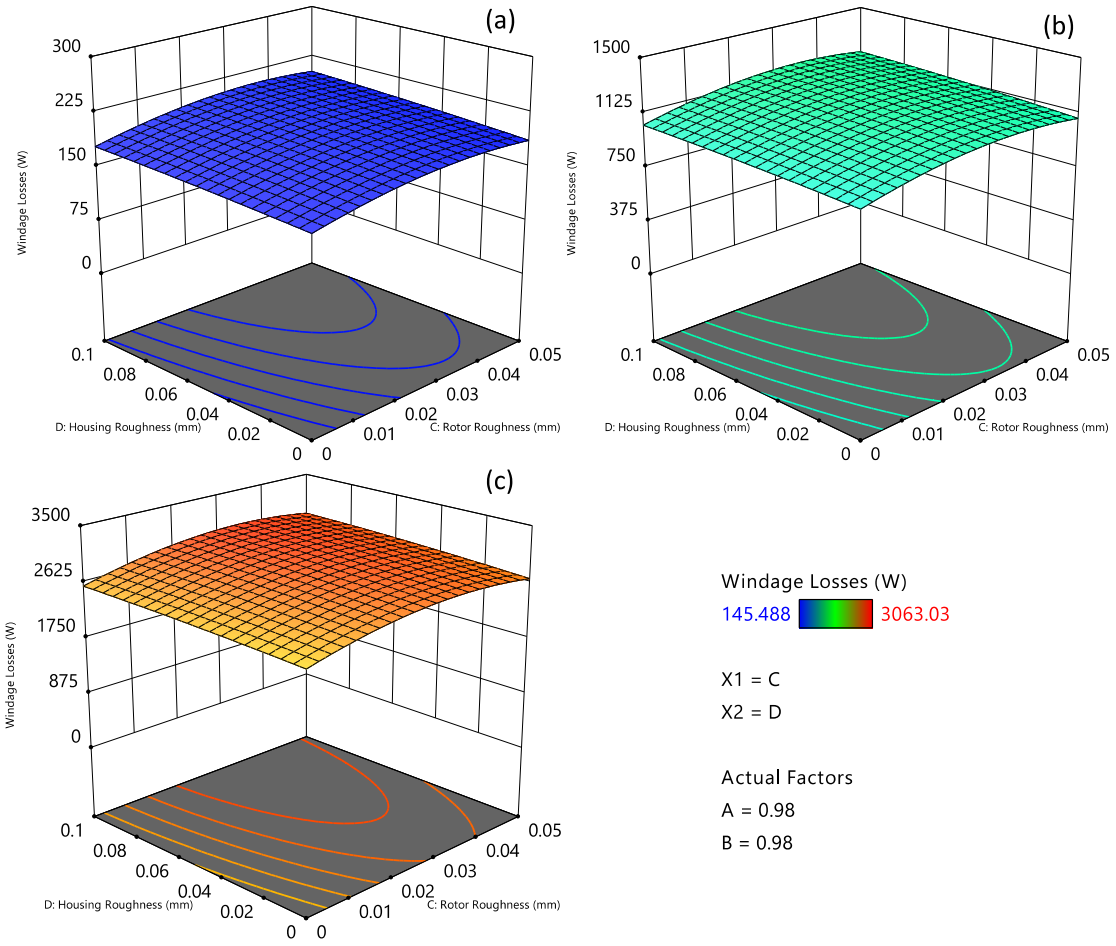

Fig. 5-13 3D plot of windage losses as a function of rotor and housing surface roughness with the radial and axial radius ratios of 0.98 at different rotational speeds: (a) 800 rad/s, (b) 1600 rad/s, (c) 2400 rad/s

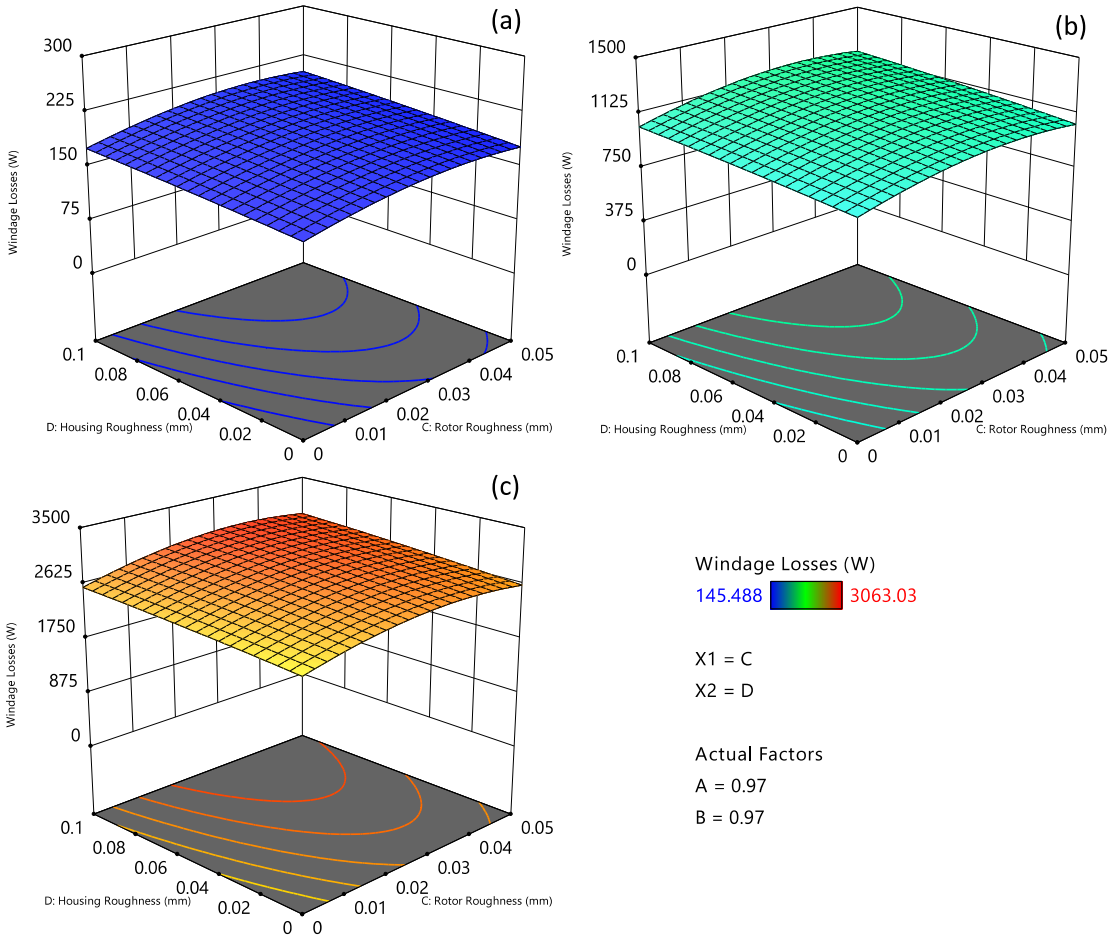

Fig. 5-14 3D plot of windage losses as a function of rotor and housing surface roughness with radial and axial radius ratios of 0.97 at different rotational speeds: (a) 800 rad/s, (b) 1600 rad/s, (c) 2400 rad/s

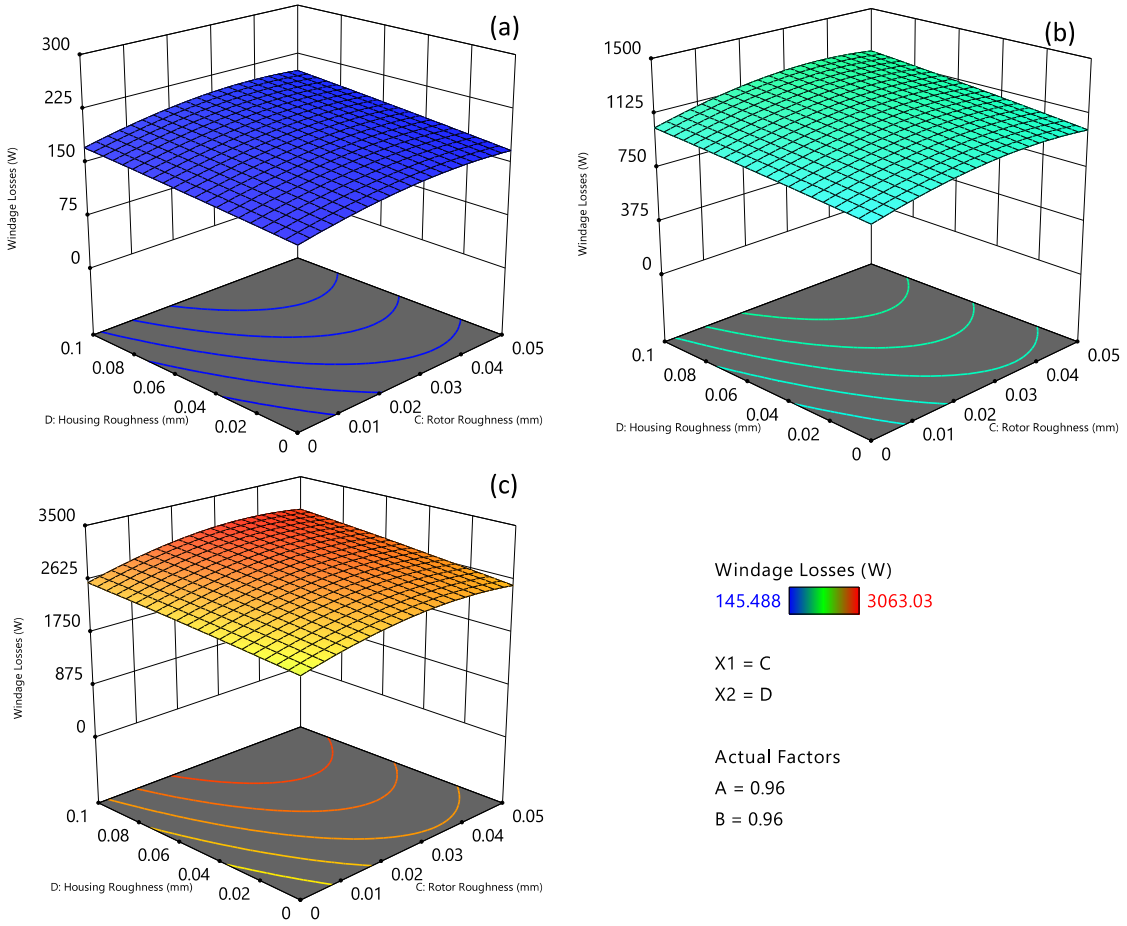

Fig. 5-15 3D plot of windage losses as a function of rotor and housing surface roughness with radial and axial radius ratios of 0.96 at different rotational speeds: (a) 800 rad/s, (b) 1600 rad/s, (c) 2400 rad/s

The effect of surface roughness on the rotor skin friction coefficient as a function of radial radius ratio at the maximum studied rotational velocity and a constant axial radius ratio of 0.96 is shown in Fig. 5-16. Compared to the effect of rotor surface roughness, the effect of housing surface roughness on the skin friction coefficient is minimal. The effect of housing surface roughness is further reduced as the radial radius ratio increases. The rotor roughness height of 0.035 mm produced the highest rotor skin friction coefficient for all the studied radial radius ratios. The critical Taylor number at which Taylor vortices appear is significantly higher for a rotor with higher surface roughness compared to a smooth surface. The increase in rotor surface roughness postpones the emergence of the first instabilities, where the roughness height directly relates to the observed delay. The fluid particle velocity will be reduced due to the friction between the flow and the rotor; therefore, it can be deduced that the surface roughness delays the formation of Taylor vortices. The surface roughness effect on Tayler cells is unnoticeable once they are present; instead, it results in flow disruption. Consequently, the transition from one flow regime to another occurs more quickly [381]. Fig. 5-17 depicts the effect of rotational velocity on the rotor skin friction coefficient. A similar trend is observed for the effect of rotor and housing surface

roughness on disc torque coefficient as shown in Fig. 5-18. As the roughness height increases, the drag coefficient and the Nusselt number increase. This is explained by regions of plume ejection caused by enhanced boundary layer detachment. As a result of the strong radial velocity component present in the plumes, they significantly contribute to the Reynolds stress term of the angular velocity flux [382].

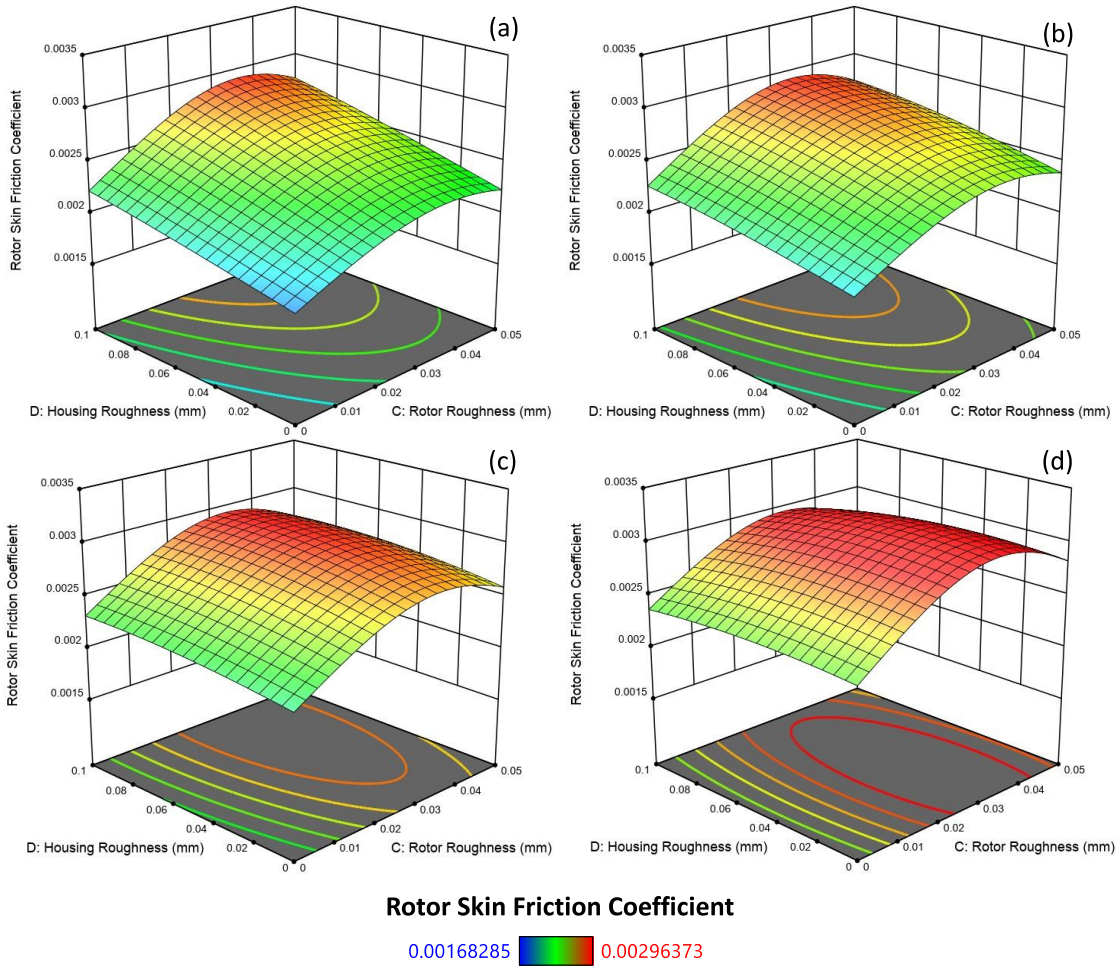

Fig. 5-16 3D plot of rotor skin friction coefficient as a function of rotor and housing surface roughness at a rotational speed of 2400 rad/s with the axial radius ratio of 0.96 and radial radius ratios of: (a) 0.96, (b) 0.97, (c) 0.98, (d) 0.99

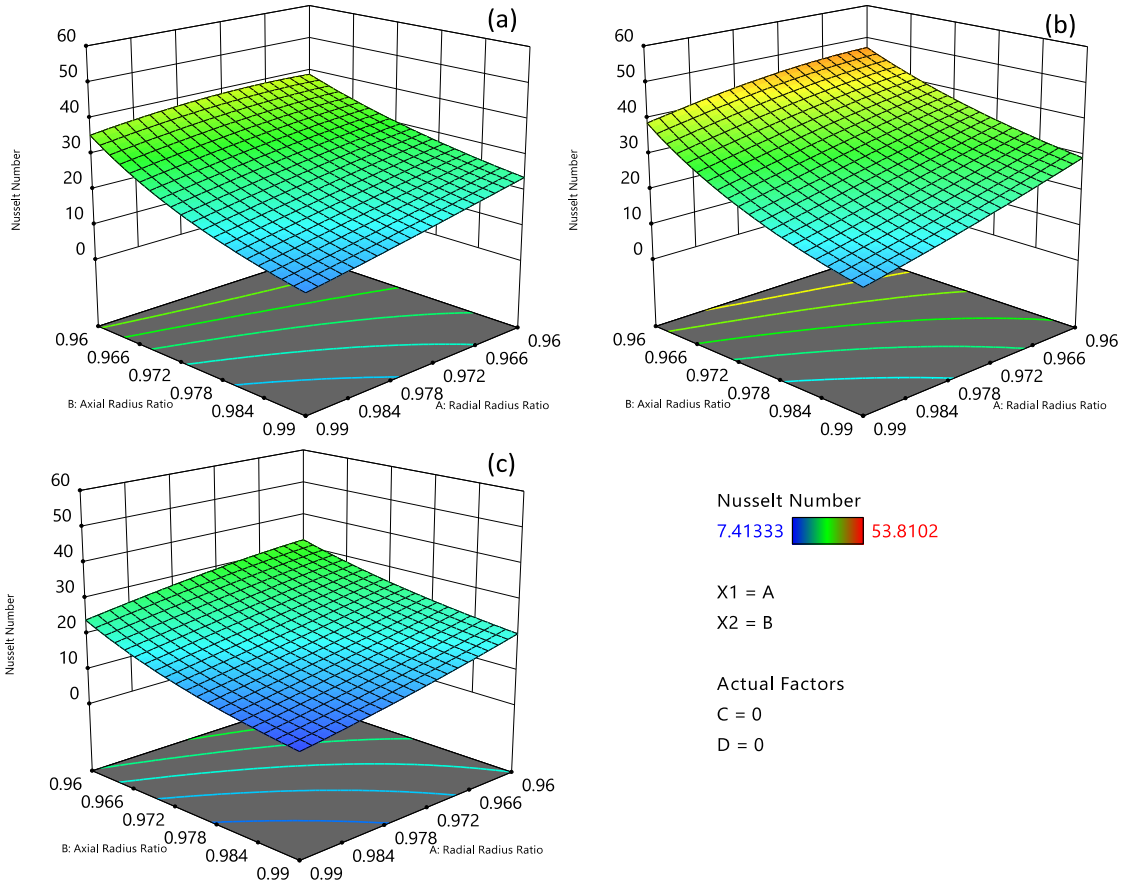

Fig. 5-17 3D plot of rotor skin friction coefficient as a function of rotor and housing surface roughness at the radial and axial radius ratios of 0.96 at different rotational speeds: (a) 800 rad/s, (b) 1600 rad/s, (c) 2400 rad/s.

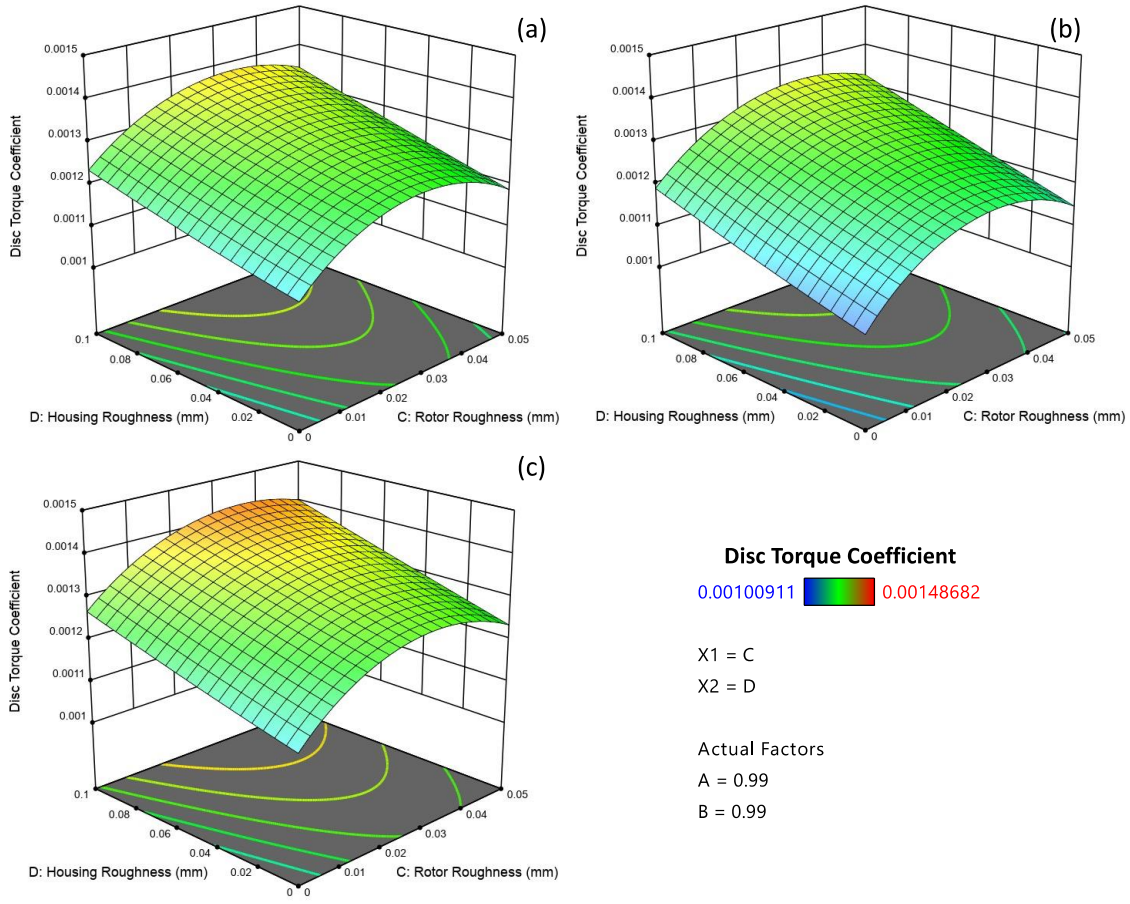

Fig. 5-18 3D plot of disc torque coefficient as a function of rotor and housing surface roughness at the radial and axial radius ratios of 0.99 at different rotational speeds: (a) 800 rad/s, (b) 1600 rad/s, (c) 2400 rad/s.

5.1.8. Optimisation

The term "desirability" is used by Myers and Montgomery [383] to describe the multiple-response method. The desirability function, *D(X)*, is an objective function used in this method. An ideal range for each response is denoted by d_i with zero to one representing the most and the least desirable range, respectively. It is the geometric mean of all the transformed responses that constitutes the simultaneous objective function as shown in equation (5-3).

$$D = (d_1 \cdot d_2 \cdot \dots d_{n_d})^{\frac{1}{n_d}} = \left(\prod_{i=1}^{n_d} d_i \right)^{\frac{1}{n_d}} \quad (5\text{-}3)$$

Where the number of measured responses is n_d. From zero outside the limits to one at the goal, desirability is an objective function. A point is found that maximises the desirability function by using numerical optimisation. Adjusting the weight or importance of a goal can change the goal's characteristics. A single desirability function is applied to a variety of responses and factors. Given the importance of each factor, the equation provided several solutions that could achieve the highest desirability, aiming at minimising the windage losses while maximising the Nusselt number. The

predicted windage losses and Nusselt number for the proposed solution were compared to CFD results for each case to confirm the validity of the predicted values. The numerical and predicted values are in good agreement, with a 2% difference for windage losses and a 4% difference for the Nusselt number. Table 5-5 lists several solutions suggested by the software with their corresponding desirability. The importance levels are selected based on the requirements; if reducing windage loss is the essential factor, the value will be five; if reducing windage loss is the least important, the value will be one. As previously stated, increasing the rotational velocity increases windage losses, but it also increases the amount of kinetic energy that can be stored, therefore the rotational velocity was selected to maximise the kinetic energy storage capacity. Solutions one and five could achieve this if the manufacturers decided that windage losses are the most important parameter and that the Nusselt number can be ignored due to the use of an active cooling system. Solutions three and four could be used if both parameters have the same importance levels.

Table 5-5 The desirability levels for the suggested solutions

#	Importance values	Radial Radius Ratio	Axial Radius Ratio	Rotor Roughness (m)	Housing Roughness (m)	Rotational Velocity (ω) (rad/s)	Predicted Windage Losses (WL) (Watt)	CFD Windage Losses (Watt)	Predicted Nusselt Number (Nu)	CFD Nusselt Number	Desirability
1	WL=5 Nu=1	0.96	0.962	6.7e-8	2.2e-5	1944	1478	1505	41.56	43.28	0.836
2	WL=1 Nu=5	0.96	0.96	7.5e-5	7.5e-6	2291	2098	2121	35.25	34.47	0.661
3	WL=3 Nu=3	0.96	0.96	1.4e-7	4.8e-7	2060	1695	1685	40.67	41.68	0.458
4	WL=5 Nu=5	0.96	0.96	4.6e-7	6.9e-7	1911	1423	1424	43.61	45.35	0.453
5	WL=5 Nu=1	0.96	0.97	1.9e-7	6.9e-7	2400*	2230	2259	26.80	26.26	0.371

* Maximum velocity is fixed to achieve the maximum storage capacity

The results showed that increasing the radial airgap size reduces windage losses and increases the Nusselt number while increasing the axial airgap size increases the windage losses and the Nusselt number. The number of Taylor cells decreases as the airgap size increases, resulting in improved heat transfer between the rotor, air and housing, thus lower windage losses. For all the studied radial radius ratios, the axial radius ratio could reduce the windage losses by approximately 4% at the maximum rotational velocity. In comparison, the radial radius ratio could reduce the windage losses by 15% and the rotor and housing surface roughness increase the windage losses while improving the Nusselt

number. At the maximum rotational velocity studied, regardless of the radius ratio, the housing surface roughness can increase the windage loss by approximately 3% and the Nusselt number by 2.7%.

5.2. Optimisation of Airgap and Partial Vacuum Pressure

Losses from aerodynamic drag contribute largely to total system losses. Losses are significant if the flywheel operates at atmospheric pressure. Reducing these losses is an efficient way of reducing system losses [216]. The flywheel can be mounted in a vacuum housing to reduce the aerodynamically induced drag loss. A vacuum housing can decrease air drag and reduce losses. However, it would increase the system's complexity and add auxiliary components to the system like the vacuum pump [242]. The vacuum pump used in the system should use a minimum amount of energy to be useful in the system and not consume the saved energy from creating a vacuum environment [178]. Creating a high vacuum for a FESS can be challenging, as it can still lead to gas creation and leakage. Lubricant for bearings also vaporises at low pressure in a vacuum. A solution is to run the vacuum pump continuously [101]. The power the vacuum pump uses to maintain the low-pressure environment and the power needed to overcome drag is known as standby power. Standby power, along with the power needed to keep the rotor at a specific state of charge, is a crucial factor in determining the overall efficiency of the FESS [238], [239]. Different types of pumps are available, and the selection depends on the system's specific requirements and desired vacuum level [247]. Mechanical pumps, such as rotary vane and piston pumps, are most widely used due to their affordability, compactness, ultimate high vacuum, and dust and particulate matter resistance. Cryogenic pumps can achieve higher vacuums but are more expensive and require specialised equipment, while molecular turbo pumps are highly efficient and expensive. Rotary vane and piston pumps are most suitable for low to medium vacuum applications [249].

This research focuses on identifying the most effective flywheel design parameters that minimise standby power in FESS. The ANOVA technique was used to investigate the impact of two crucial factors, namely the airgap size and the operating pressure, on standby power. The objective is to establish a correlation between these parameters and the energy efficiency of the system, thereby facilitating the development of improved FESS designs. ANOVA would aid in determining the significance of the studied FESS parameters and their effects on achieving optimal standby power.

5.2.1. Responses Selection

The choice of system responses in this study is crucial for demonstrating the behaviour of the response surface, as it relates to the interaction and effects of system parameters. These responses, specifically windage losses, the Nusselt number, and standby power, are integral for assessing the system's performance and constraints, and for pinpointing the most efficient system configurations. The primary

focus here is the standby power in the FESS. Standby power encompasses windage losses and the energy necessary to sustain a low-pressure environment via a vacuum pump. Minimising standby power is pivotal in decreasing the system's self-discharge rate. This reduction is particularly beneficial for prolonged storage durations and has wide-ranging applications.

5.2.2. Factors Selection

To effectively mitigate windage losses in FESS, a critical design consideration involves housing the flywheel rotor within a specialised, low-pressure enclosure, achieved using a vacuum pump. Windage losses, particularly in high-speed rotating machinery, are intensified by uncontrolled airflows within the annulus of the FESS, impacting the temperatures of both the rotor and the housing surface. To address this, increasing the airgap size is a common strategy, as it helps in temperature regulation. However, this approach presents a trade-off, as a larger airgap necessitates a higher power input for the vacuum pump to sustain the required low-pressure environment. Therefore, in designing an efficient FESS, optimising the airgap size and the rotor cavity pressure becomes imperative. The aim is to achieve an optimal balance between a minimal gap for efficiency and sufficient space to reduce thermal stresses. Furthermore, maintaining a low-pressure environment around the rotor cavity is essential to minimise windage losses. However, creating a complete vacuum is not practical, as it demands excessive energy from the vacuum pump and complicates maintenance processes. Instead, employing a partial vacuum offers a viable solution. It significantly lowers windage losses while being achievable with cost-effective and less complex vacuum systems like rotary vane pumps. This research investigated five varying rotor cavity pressures, ranging from standard atmospheric conditions down to 200 mbar. For the creation of these partial vacuum conditions, a DC rotary vane pump operating at 24 V was utilised [384]. The specific values for each level studied are detailed in Table 5-6. Table 5-7 displays the 25 simulation cases for the two factors under investigation, each at their designated levels.

Table 5-6 The factors studied with different levels

Levels	**Factors**	
	A: Radius Ratio (η)	**B: Rotor cavity pressure [mbar]**
1	0.99	1000
2	0.98	800
3	0.97	600
4	0.96	400
5	0.95	200

Table 5-7 The simulation cases for the ANOVA analysis

Simulation #	Radius ratio	Pressure (mbar)
1	0.99	1000
2	0.99	800
3	0.99	600
4	0.99	400
5	0.99	200
6	0.98	1000
7	0.98	800
8	0.98	600
9	0.98	400
10	0.98	200
11	0.97	1000
12	0.97	800
13	0.97	600
14	0.97	400
15	0.97	200
16	0.96	1000
17	0.96	800
18	0.96	600
19	0.96	400
20	0.96	200
21	0.95	1000
22	0.95	800
23	0.95	600
24	0.95	400
25	0.95	200

Factorial analysis via ANOVA is employed to assess the impact of two factors on various response levels. This approach facilitates the prioritisation of variables based on their influence on the values of the objective function. Such analysis is instrumental in optimising the FESS. It aids in identifying key parameters that influence performance and refining these parameters to attain the target standby power level. The core steps in optimisation involve estimating coefficients within a mathematical model, predicting the response, and evaluating the model's appropriateness.

5.2.3. Responses

The ANOVA conducted on the three key responses in this study – windage losses, Nusselt number, and standby power – revealed significant results, as indicated in Tables 5-8 to 5-10. The F-values obtained were 2327.37 for windage losses, 233.88 for the Nusselt number, and 1709.13 for standby power. These values suggest the statistical significance of the models, with a negligible probability (only 0.01%) that such high F-values could arise merely from random noise. In the context of model terms, P-values serve as indicators of significance. Terms with P-values less than 0.05 are considered statistically significant, implying a strong effect on the model's responses. Conversely, terms with P-values greater than 0.10 are deemed insignificant, suggesting a lack of substantial impact on the model. Accordingly, terms considered insignificant were removed from the model to enhance its predictive accuracy. The F-values for each factor and their interactions were calculated to assess the significance of their mean variation within the model. The results were tabulated, showing relevant P-values with a 95% confidence interval. This statistical approach ensures a high level of confidence in the model's predictions. These tables demonstrate that each factor under study has a P-value less than 0.05, confirming their significance. Such statistical findings affirm that the models developed in this study offer accurate predictions of standby power across various studied variables, thus providing a robust framework for understanding and optimising the performance of the FESS.

Table 5-8 ANOVA for response surface quadratic model for windage losses

Source	Sum of Squares	df	Mean Square	F-value	p-value
A-Airgap	3.747×10^5	1	3.747×10^5	938.40	< 0.0001
B-Pressure Level	4.627×10^5	1	4.627×10^5	1158.84	< 0.0001
AB	16754.13	1	16754.13	41.96	< 0.0001
Residual	7186.85	18	399.27		
Total	5.583×10^6	24			

Table 5-9 ANOVA for response surface quadratic model for Nusselt number

Source	Sum of Squares	df	Mean Square	F-value	p-value
A-Airgap	219.27	1	219.27	662.12	< 0.0001
B-Pressure Level	6.21	1	6.21	18.76	0.0008
AB	1.22	1	1.22	3.68	0.0772
Residual	4.31	13	0.3312		
Total	856.27	24			

Table 5-10 ANOVA for response surface quadratic model for standby power

Source	Sum of Squares	df	Mean Square	F-value	p-value
A-Airgap	1.563×10^{9}	1	1.563×10^{9}	304.01	< 0.0001
B-Pressure Level	3.201×10^{10}	1	3.201×10^{10}	6225.71	< 0.0001
AB	1.425×10^{9}	1	1.425×10^{9}	277.13	< 0.0001
Residual	1.028×10^{8}	20	5.142×10^{6}		
Total	3.525×10^{10}	24			

A mathematical model was employed to articulate the relationship between input variables and their corresponding dependent responses, specifically focusing on windage losses, Nusselt number, and standby power. Table 5-11 showcases the fit statistics for these responses calculated. A key metric in regression analysis is the coefficient of determination. In the models under consideration, the R^2 values are exceptionally high—0.9987 for windage losses, 0.9950 for the Nusselt number, and 0.9971 for standby power—indicating a close alignment of the regression lines with the observed data points.

To account for model complexity and the number of predictors, the adjusted R^2 values were utilised. These values, 0.9983 for windage losses, 0.9907 for the Nusselt number, and 0.9965 for standby power, also surpass 0.99, signifying minimal unexplained variance in the models. An important aspect of model validation involves examining the predicted R^2 to assess the models' proficiency in forecasting new observations. The close alignment between the adjusted and predicted R^2 values suggests robust predictive capabilities.

Another critical measure is the signal-to-noise ratio, evaluated through the metric of adequate precision. In this study, the adequate precision ratios exceed the desirable threshold of 4, confirming that the models capture significant signals amidst inherent data noise and can effectively navigate the design space.

The initial analysis revealed inadequacies in the standby power response, prompting the necessity for a power transformation (Box-Cox transformation) to improve data normality [376]. This transformation was successful; subsequent evaluations post-transformation confirmed improved data normality, variance homogeneity, and random distribution of residuals, thus enhancing the reliability and accuracy of the model fit.

Table 5-11 The fit statistics for the obtained responses

Windage Losses	**Std. Dev.**	19.98	**R^2**	0.9987
	Mean	1546.48	**Adjusted R^2**	0.9983
	C.V. %	1.29	**Predicted R^2**	0.9976
			Adequate Precision	155.7254
Nusselt Number	**Std. Dev.**	0.5755	**R^2**	0.9950
	Mean	13.31	**Adjusted R^2**	0.9907
	C.V. %	4.33	**Predicted R^2**	0.9827
			Adequate Precision	57.9136
Standby Power	**Std. Dev.**	2267.49	**R^2**	0.9971
	Mean	1.069×10^5	**Adjusted R^2**	0.9965
	C.V. %	2.12	**Predicted R^2**	0.9957
			Adequate Precision	132.0205

This study evaluates the FESS's standby power, which is the sum of windage losses, and the power required for maintaining a low-pressure environment. Decreasing standby power reduces the self-discharging rate of the system, making it well-suited for extended storage periods in various applications. The viscous friction between the rotor and the air in the gap during rotation generates windage losses. The size of the airgap and the thermophysical properties of the fluids involved influence the losses. In this system, the stationary outer cylinder acts as the housing, while the inner cylinder is the rotating rotor. As the rotational speed increases, the air velocity distribution changes due to the Taylor number exceeding the critical value of 41.3, creating the Taylor vortex.

Fig. 5-19 displays the windage losses in relation to the rotational velocity for 25 distinct cases. Each of the 25 cases demonstrates a consistent pattern in which windage losses increase as the rotational velocity increases. The anticipated rise in windage losses is a result of the quadratic relationship between speed and air resistance, wherein higher speeds lead to increased air resistance.

Fig. 5-20 illustrates a 3D surface plot showing how windage losses in a FESS are influenced by two variables: the radius ratio and the pressure within the FESS cavity. The plot demonstrates that as the radius ratio decreases, windage losses also decrease at all examined pressure levels. As the pressure in the FESS cavity decreases, the windage losses also decrease, but the decrease is much greater than the decrease in the radius ratio. Reduced pressure results in decreased air density within the cavity, leading to a decrease in air resistance and subsequently reducing windage losses. In order to minimise windage losses to the greatest extent, to decrease the number of Taylor vortices, the flywheel can be designed with a larger airgap between the rotor and the housing, resulting in a lower radius ratio. A reduced pressure within the FESS cavity would result in a decrease in air density and resistance against the rotating flywheel, thereby reducing windage losses. Increased airgaps result in decreased air friction,

resulting in reduced windage losses. This phenomenon occurs as a result of the heightened shear stress on the rotor in narrower spaces, which is further intensified by the presence of Taylor vortices. Taylor vortices appear more frequently as the airgap widens, while Taylor cells are less rapidly affected by azimuth waves as the airgap narrows [377].

Fig. 5-21 shows a 3D surface plot of the Nusselt number as a function of the radius ratio and the pressure within the FESS cavity. The Nusselt number, a dimensionless quantity, characterises the convective heat transfer relative to conductive heat transfer. As the radius ratio decreases, the Nusselt number increases. A lower radius ratio indicates a bigger airgap that enhances convective heat transfer. To maximise the Nusselt number, the design should therefore focus on decreasing the radius ratio, which potentially be achieved by increasing the airgap between the rotor and the housing. On the other hand, when pressure decreases, the Nusselt number also decreases. This is due to the reduced air density at lower pressures, which diminishes the convective heat transfer capabilities. To maximise the Nusselt number, it would be advisable to maintain a higher pressure within the FESS cavity as much as the design and operational constraints allow. In order to optimise the Nusselt number for effective thermal control in a FESS, the design should strive for a reduced radius ratio while simultaneously maintaining an elevated internal pressure. This method improves the transfer of heat through convection, which is advantageous for regulating the system's temperature.

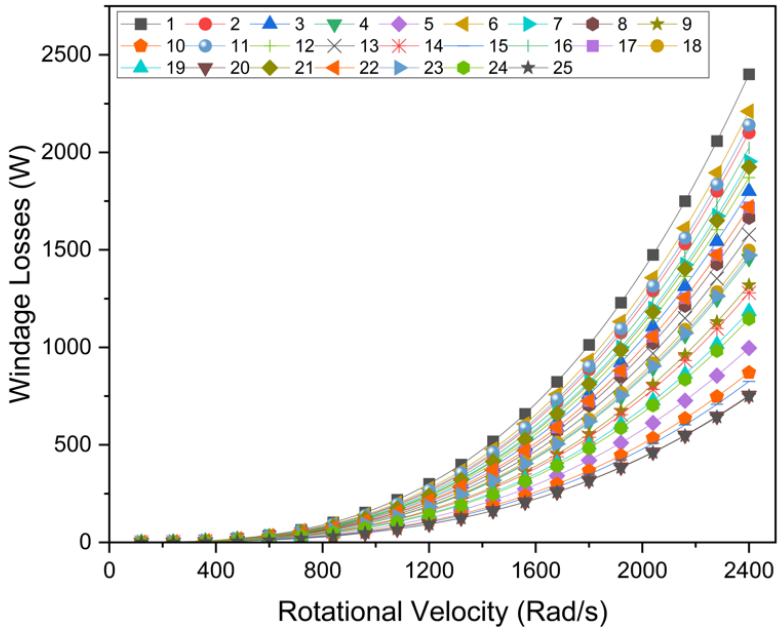

Fig. 5-19 The windage losses with respect to rotational velocity for the 25 ANOVA runs

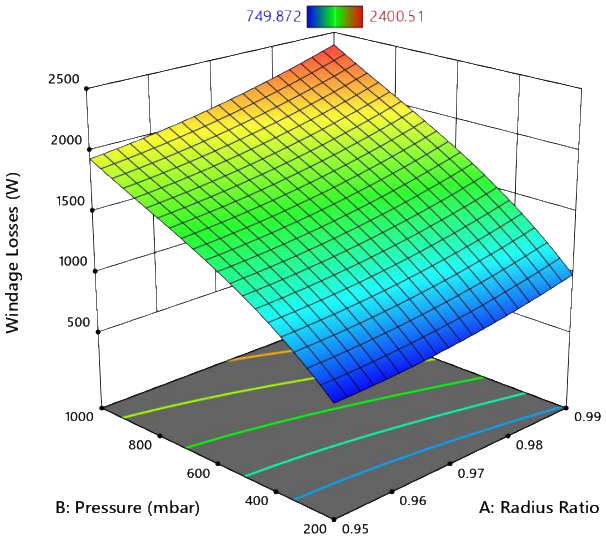

Fig. 5-20 3D plot for windage losses between radius ratio and pressure level

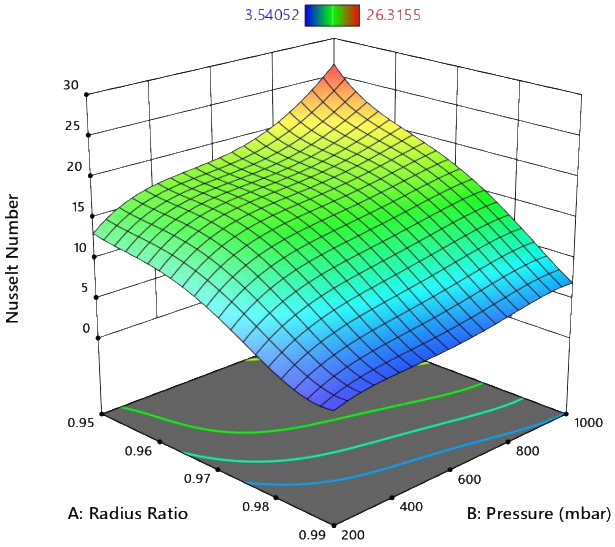

Fig. 5-21 3D plot for Nusselt number between radius ratio and pressure level

Multiple variables need to be taken into account when determining the power needed to operate a vacuum pump for reducing the pressure inside a FESS. Initially, it is essential to ascertain the preferred level of vacuum. For the second step, select a vacuum pump suitable for automotive applications, such as the Duo 3 DC, a Dual-stage, high-performance rotary vane pump with a pumping speed of 2.5 m^3/h (24 V DC, DN 16 ISO-KF) [384]. The third determinant is the specific seal and bearing employed to sustain the vacuum. Lastly, there is the amount of gas enclosed within the rotor cavity. The calculation of time the pump would run to achieve the required pressure level can be calculated using the following formula [385]:

$$t = \frac{V}{S} \times \ln \frac{P_1}{P_2} \tag{5-4}$$

Where V is the volume of the rotor's cavity, S is the pumping rate of the selected vacuum pump, P_1 is the initial pressure in the FESS, and P_2 is the required pressure. The power required to run the pump is 240 W [384]. However, due to the influence of the system's seal and bearing, the vacuum pump must control and maintain a consistent pressure level within the cavity. The study revealed that decreasing cavity pressure and increasing the size of the airgap successfully decreased windage losses. Nevertheless, it was noted that enlarging the airgap dimension led to a proportional rise in power consumption by the vacuum pump in order to attain the targeted pressure level.

Fig. 5-22 illustrates a 3D surface plot showing the relationship between standby power, pressure cavity, and the radius ratio. The standby power decreases as the pressure within the FESS cavity is reduced. This is because lower pressure reduces air density, resulting in lower windage losses. A reduction in the radius ratio leads to lower standby power, which aligns with the notion that a smaller radius ratio can decrease windage losses. However, at low-pressure levels, the vacuum pump must work harder to extract air to maintain a vacuum, thus consuming more power.

At a pressure level below 400 mbar, the relationship between standby power and radius ratio changes. The lowest radius ratio does not result in the lowest standby power. This is explained by an increase in the volume of gas within the cavity due to a larger airgap size implied by the lower radius ratio. Consequently, the vacuum pump must operate longer to achieve the required low pressure, thus increasing standby power.

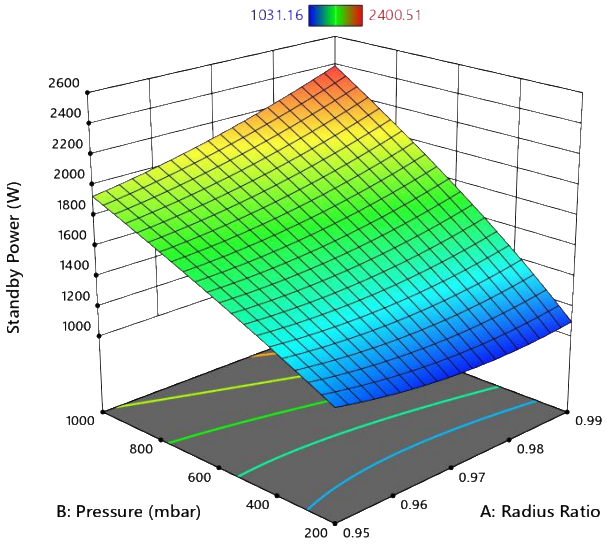

Fig. 5-22 3D plot for standby power between radius ratio and pressure level

5.2.4. Optimisation

A single desirability function is employed to assess a range of responses and factors in order to identify the most optimal solution with the highest level of desirability for system optimisation. The objective is to offer a solution that can attain optimal desirability by minimising standby power consumption. The proposed solution, after optimisation, achieves the minimum standby power when the pressure level is

set at 200 mbar and the radius ratio is 0.977. The desirability of this solution is 0.982, as shown in Fig. 5-23. The optimal solution, with equal emphasis on maximising the Nusselt number and minimising the standby power, was achieved at a pressure level of 313 mbar and a radius ratio of 0.95. The desirability of this solution was measured to be 0.714, as shown in Fig. 5-24.

In order to verify the accuracy and compatibility of the predicted values with the results obtained from CFD simulations, a CFD simulation is conducted to validate the predicted standby power for the proposed solution. The numerical and predicted values exhibit a high level of concordance, with a discrepancy of only 3%.

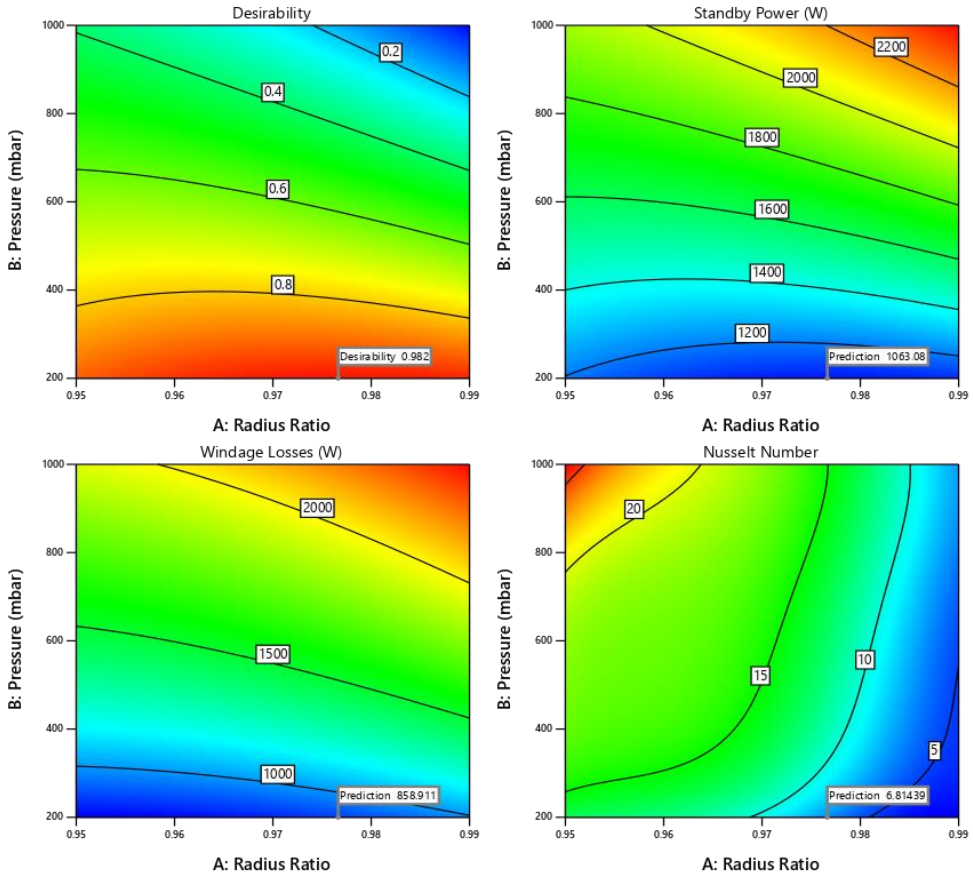

Fig. 5-23 The desirability contours for the three studied responses when only standby power is selected for optimisation

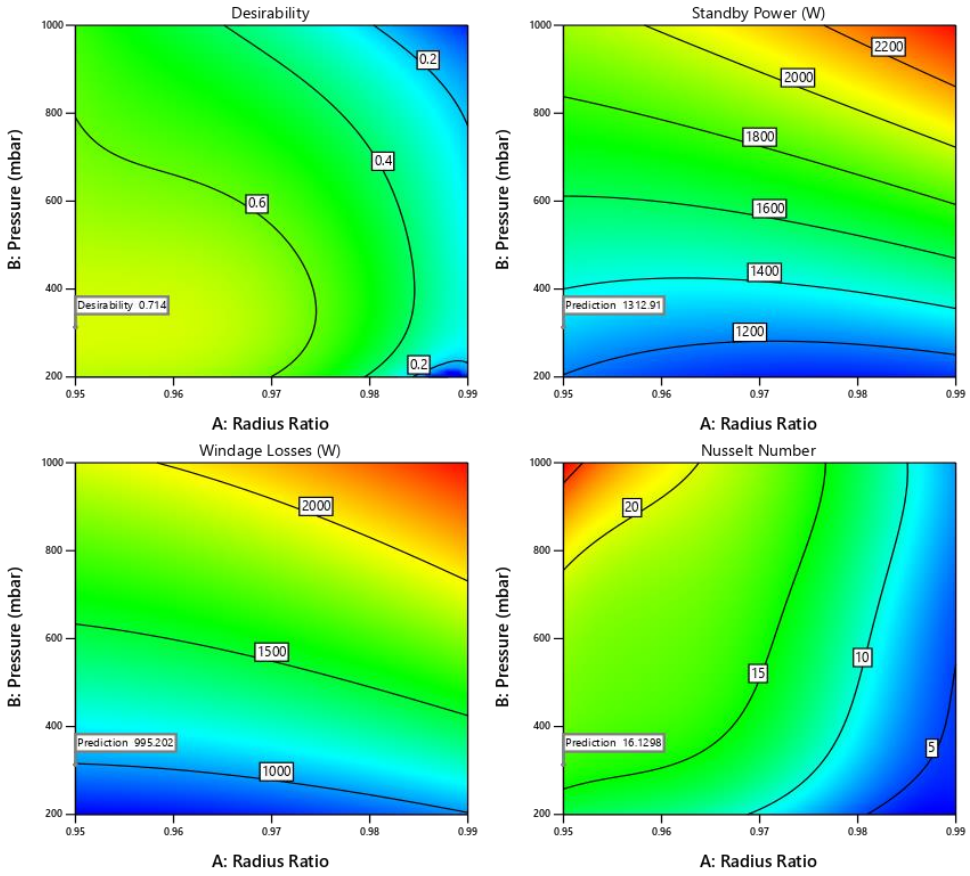

Fig. 5-24 The desirability contours for the three studied responses when standby power and Nusselt number are selected for optimisation

5.3. Optimisation of Airgap Size and Medium Gas

To operate the FESS in a vacuum or an alternative gas medium, an enhanced sealing mechanism is vital. This is necessary to maintain the chosen environment within the FESS, thereby eliminating the need for a vacuum pump or a storage tank for the gas medium to sustain a consistent level. To achieve this, a high-quality seal is essential, ensuring that the system can operate for extended periods in the same conditions. This seal, though more costly, enables the FESS to run efficiently with only regular maintenance checks needed to monitor the pressure level and gas medium. In this context, operating the flywheel in a vacuum setting without accounting for the energy consumption of the vacuum pump to achieve the desired vacuum level, a vacuum-tight seal becomes a crucial element for maintaining a low-pressure environment [244].

Mechanical, magnetic, and labyrinth seals are commonly used for this purpose. Mechanical seals comprise two metal surfaces held together by spring pressure to form a vacuum-tight seal. Magnetic seals are more expensive than mechanical seals but can handle high-speed rotation or vibration using magnetic force [246]. Labyrinth seals use grooves and ridges to form a barrier and are less expensive

but may be less reliable than other seals [245]. Before implementing a vacuum environment, it is crucial to evaluate the trade-off between windage loss and the potential energy savings offered by flywheels. The maintenance of a vacuum level within a FESS can be achieved by implementing a hermetically sealed flywheel containment and the intermittent utilisation of a low-cost pumping mechanism [238]. This approach reduces the requirement for a high vacuum level and mitigates the wear on the pump and the associated power loss resulting from the continuous operation of the pump [240]. Furthermore, a vacuum environment for FESS can increase flywheel temperatures due to reduced heat transfer via convection. As such, implementing a cooling device to remove heat may be necessary.

An alternative method to minimise aerodynamic drag loss involves utilising a combination of air and helium gas instead of operating the system at low pressure. An advantage is that the demand for the cooling system is reduced [242]. The study explores the combined effects of radial and axial airgap sizes, pressure level, and gas medium on FESS performance. Optimised factors are identified and tested using the mixed-level modified Taguchi approach, with the signal-to-noise (S/N) ratio mean analysing the impact of these factors on FESS performance. ANOVA is employed to evaluate the interaction between each factor.

5.3.1. Taguchi Method

The Taguchi method is vital for optimising the design of FESS because of its ability to handle complex systems with multiple factors. Furthermore, the Taguchi method employs a robust design, which seeks to reduce the impact of noise factors on system performance [386]. This is especially important in FESS design because these systems are frequently subjected to various operating conditions and environmental factors affecting their performance. Because of its ability to handle noise factors, identify optimal levels of control factors, and account for the specific costs or losses associated with different control factors, the Taguchi method is a powerful tool for optimising the design of FESS. Furthermore, the Taguchi method offers a low-cost and effective means of determining device-optimised geometry with the fewest possible experiments [387]. Seven steps make up the process of determining the ideal parameters [388], as shown in Fig. 5-25.

Fig. 5-25 Block diagram of the process optimisation.

Step 1: Determination of The Objective Function

As the optimisation objective, the Taguchi method measures the output volatility of the selected variables using a signal-to-noise (S/N) ratio [389]. The S/N ratio is used to quantify the relationship

between the signal (the desired response) and the noise (the unwanted variations) in the system. For example, the S/N ratio for each product category can be calculated using the Taguchi method as shown below [390]:

$$Larger - the - better: S/N_{LTB} = -10\log\frac{1}{n}\sum_{i=1}^{n}\frac{1}{(Y_i)^2} \quad (5\text{-}5)$$

$$Nominal - the - better: S/N_{NTB} = 10\log\frac{Y_m}{\sigma^2} \quad (5\text{-}6)$$

$$Smaller - the - better: S/N_{STB} = -10\log\frac{1}{n}\sum_{i=1}^{n}(Y_i)^2 \quad (5\text{-}7)$$

Where n is the number of observed responses, Y is the observed response, Y_m is the mean of the observed responses, and σ^2 is the variance. The S/N ratio can be used to evaluate the system's performance and determine the optimal levels of the control factors. Generally, the higher the S/N ratio, the better the system's performance. In addition to the S/N ratio, the Taguchi quality loss function method uses another equation to minimise the total loss to the system due to noise factors. The quality loss function equation is as follows [391]:

$$QL = K_w(V_e - V_t)^2 \quad (5\text{-}8)$$

Where K_w is the weighting factor, V_e is the actual performance of the system, and V_t is the desired performance of the system. The Taguchi Loss function method seeks to minimise the loss function's value by varying the control factors' levels. In addition, this method can consider the specific losses associated with different levels of the control factors, which makes it more potent than the traditional Taguchi method when the relationship between the control factors and the response variable is complex. Reducing windage losses will reduce the self-discharging rate of the FESS, meaning it could be helpful for a broader range of applications. Therefore, the goal is to minimise windage losses while maintaining the same kinetic energy by keeping the flywheel's size, shape, and weight. This can be achieved by changing the gap between the flywheel and the housing and choosing the appropriate pressure level within the system. The "smaller the better" model is used in this case because it is desired to minimise windage losses. This model is generally used when the goal is to minimise a specific variable or factor in the system. On the other hand, if the Nusselt number increases, it indicates that the FESS can effectively transfer heat from the rotor to the surrounding environment. This eliminates the requirement for a cooling system within the FESS, resulting in a reduction in the overall system's size and weight. In the case of the Nusselt number, the objective is to maximise it. Therefore, the “larger the better” model was selected as it is the way to achieve a higher Nusselt number.

Step 2: Selection of The Factors and Levels

The parameter design tests define an optimal set of parameter responses as generating a design while preserving adequate quality variation. By selecting the factor levels with the highest S/N ratio, it is possible to determine the ideal concentration of each factor. The Taguchi method aims to find the ideal mixture of controlling factors. A thorough literature review highlighted several factors that should be

considered for the FESS. The radial radius ratio between the rotor and the housing, the axial radius ratio between the rotor's side faces and the housing, the pressure environment, and the gas used within the airgap are all evaluated factors in this work.

The study employed four different airgap sizes to establish a gap size between the rotor and the housing. This section will examine the impact of larger airgaps, specifically focusing on radius ratios between 0.99 and 0.93. In contrast to the prior two sections, which examined the impacts of narrower airgaps, this section introduced a radius ratio of 0.93 to investigate the consequences of wider airgaps. The study used the maximum allowable rotational velocity to investigate the effect of windage losses on the maximum allowable kinetic energy storage.

A partial vacuum inside the flywheel housing can also reduce windage losses because there are fewer air molecules to create friction and drag [101]. Another method for reducing windage losses is to use a gas with a lower density than air, which has less friction and drag than air [242], [392]. Other gases that could be used in the system besides air include Helium (He), a non-toxic, non-flammable, and inert gas less dense than air, resulting in less friction and drag. In addition, Helium's low viscosity and thermal conductivity can reduce heat loss and energy dissipation [242]. Another gas that can be used to reduce windage losses is hydrogen (H). It is also less dense than air, which helps to reduce friction and drag. In addition, hydrogen has a high thermal conductivity, aiding heat and energy dissipation. However, hydrogen is highly flammable and explosive, which makes it dangerous to work with, meaning it will not be a good option for the FESS [393].

On the other hand, Carbon dioxide (CO_2) is a colourless, odourless gas that is non-toxic and non-flammable, making it safer to work with than hydrogen. Like hydrogen, CO_2 is less dense than air, which can reduce friction and drag. It also has a relatively high thermal conductivity, which can help dissipate heat and reduce energy dissipation [394]. Finally, Nitrogen (N) is a colourless, odourless, and tasteless gas that is non-toxic, inert, and non-flammable. Because it is less dense than air, it produces less friction and drag [395]. The factors mentioned above, and their levels are summarised in Table 5-12.

Table 5-12 The factors studied with different levels

Levels	**Factors**			
	A	**B**	**C**	**D**
	Radial Radius Ratio	**Axial Radius Ratio**	**Pressure level (mbar)**	**Gas**
1	0.99	0.99	1000	Air
2	0.97	0.97	750	CO_2
3	0.95	0.95	500	He
4	0.93	0.93	250	Ni

Step 3: Construction of an Appropriate Orthogonal Array (OA)

Instead of testing all possible models, the Taguchi approach only requires a certain number of experiments to test according to the orthogonal array (OA). The chosen optimisation approach typically requires a parameter matrix with a number of levels to analyse the parametric differences. Degrees of freedom (DOF) can be used to calculate the bare minimum of tests necessary for the Taguchi method [396]. The experimental design adjusts the OA to test four factors at four levels. L16 the possible OA for the total number of chosen parameters and levels and is constructed as shown in Table 5-13. As a result, 16 cases rather than 256 cases will be examined using the constructed orthogonal array.

Table 5-13 L_{16} Orthogonal array (OA)

No.	A: Radial Radius Ratio	B: Axial Radius Ratio	C: Pressure level (mbar)	D: Gas
Run 1	0.99	0.99	1000	Air
Run 2	0.99	0.97	750	CO_2
Run 3	0.99	0.95	500	He
Run 4	0.99	0.93	250	N
Run 5	0.97	0.99	750	He
Run 6	0.97	0.97	1000	N
Run 7	0.97	0.95	250	Air
Run 8	0.97	0.93	500	CO_2
Run 9	0.95	0.99	500	N
Run 10	0.95	0.97	250	H
Run 11	0.95	0.95	1000	CO_2
Run 12	0.95	0.93	750	Air
Run 13	0.93	0.99	250	CO_2
Run 14	0.93	0.97	500	Air
Run 15	0.93	0.95	750	N
Run 16	0.93	0.93	1000	He

Step 4: CFD Simulation

This section involves the development of 16 different models using SOLIDWORKS and their simulation using ANSYS Fluent 2022R1 software. The purpose is to ascertain the windage losses and Nusselt number of the FESS. The models are derived from the parameters specified in Table 5-14 and the constructed OA as shown in Table 5-13.

Fig. 5-26 illustrates the windage losses in correlation with the rotational velocity for 16 Taguchi runs. Each of the 16 cases exhibits a consistent correlation in which windage losses escalate with higher rotational velocity. The highest windage losses occurred in the second case, where CO_2 was used as the gas, despite the lower pressure level compared to air in the first case. The 10th run, using Helium as the gas medium at a pressure of 250 mbar, exhibited the least windage losses.

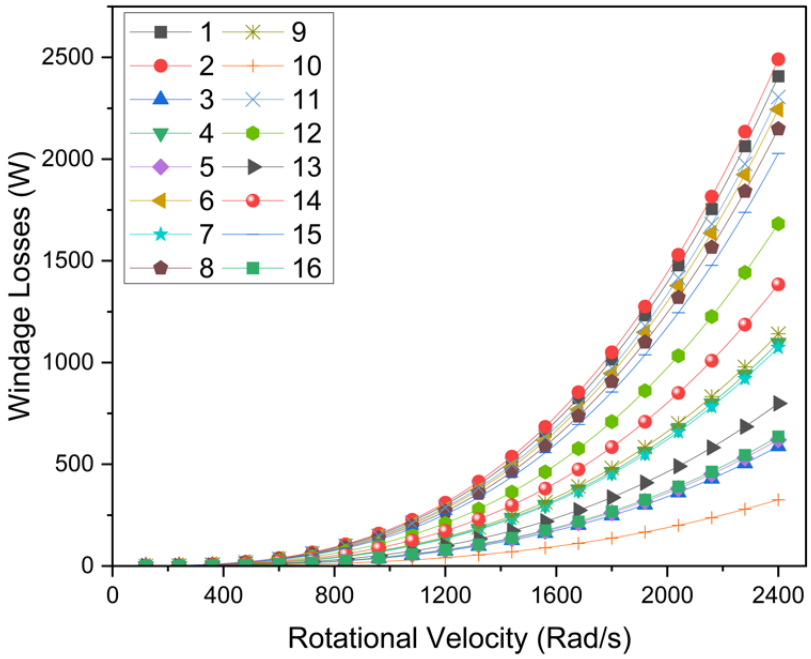

Fig. 5-26 The windage losses with respect to rotational velocity for the 16 Taguchi runs

Table 5-14 L_{16} Orthogonal array (OA) with the S/N ratios

No.	A: Radial Airgap (mm)	B: Axial Airgap (mm)	C: Pressure level (mbar)	D: Gas	S/N ratio Windage losses	S/N ratio Nusselt number
Run 1	0.99	0.99	1000	Air	-67.6304	12.5244
Run 2	0.99	0.97	750	CO_2	-67.9269	26.1108
Run 3	0.99	0.95	500	He	-55.3942	22.0272
Run 4	0.99	0.93	250	N	-60.8045	28.1217
Run 5	0.97	0.99	750	He	-55.8463	15.7515
Run 6	0.97	0.97	1000	N	-67.0227	33.1334
Run 7	0.97	0.95	250	Air	-60.6173	37.0642
Run 8	0.97	0.93	500	CO_2	-66.6434	42.5867
Run 9	0.95	0.99	500	N	-61.1526	30.1212
Run 10	0.95	0.97	250	He	-50.251	18.262
Run 11	0.95	0.95	1000	CO_2	-67.2559	40.1492
Run 12	0.95	0.93	750	Air	-64.5177	34.5244
Run 13	0.93	0.99	250	CO_2	-58.0496	24.1737
Run 14	0.93	0.97	500	Air	-62.826	32.2839
Run 15	0.93	0.95	750	N	-66.1393	43.4965
Run 16	0.93	0.93	1000	He	-56.0745	36.2848

Step 5: Analysing Taguchi's Results

Table 5-14 displays the calculated S/N ratios for 16 cases using the smaller-the-better model for windage losses and the larger-the-better model for Nusselt number. According to the model, the highest signal-to-noise ratio is achieved when the windage loss is minimised and the Nusselt number is maximised. Among the cases examined, Case 10 exhibits the most significant windage losses with a maximum S/N ratio of -50.25, while Case 15 demonstrates the highest Nusselt number with a maximum S/N ratio of 43.49.

The Taguchi method is utilised to determine the sequence of influence and the most favourable combination of selected parameters for the design. The utilised model for each response and Table 5-14 computes the average signal-to-noise ratios for parametric design.

Fig. 5-27 consists of four-line graphs, each plotting the mean S/N ratio against different variables in a FESS for windage losses response. The first graph shows a slight decrease in the mean S/N ratio as the radial radius ratio increases. This suggests that a smaller radial ratio is favourable for achieving a lower windage loss. The second graph illustrates an inverse correlation between the radius ratio and the S/N

ratio. Specifically, an increase in the axial radius ratio leads to an increase in the S/N ratio, resulting in a reduction of windage losses. The third graph displays a clear downward trend in the mean S/N ratio as the pressure within the FESS cavity increases. The fourth graph shows significant variability in the mean S/N ratio depending on the type of gas used in the FESS cavity. Air and Nitrogen show similar S/N ratios, which are the lowest among the gases. CO_2 has a slightly higher S/N ratio, while Helium stands out with a much higher mean S/N ratio before the trend reverses back down for Nitrogen. This implies that Helium dramatically improves its performance compared to the other gases, which is due to its lower density and resulting lower windage losses.

To determine the order of each factor's effect, a parameter (θ) is defined, which is the maximum and minimum response of each factor. The values for factors A, B, C, and D are 2.17, 1.68, 7.07, and 10.58, respectively. Factor D, the gas utilised in the system, is the predominant factor influencing the windage losses of the FESS among the four factors that were tested. In addition, factors A and B have a minor impact on windage losses.

Fig. 5-28 exhibits four-line graphs illustrating the correlation between the mean S/N ratio and four studied variables, specifically for the Nusselt number. The first graph demonstrates a significant decline in the mean S/N ratio as the radial radius ratio increases from 0.93 to 0.95. Subsequently, there is a slight increase in the ratio at 0.97, which is then followed by a sharp decrease at 0.99. The second graph shows a consistent decrease in the mean S/N ratio with an increase in the axial radius ratio. A lower axial ratio is associated with a higher Nusselt number. The axial radius ratio of 0.95 is a crucial point that corresponds to the highest S/N ratio achieved. In the third graph, the mean S/N ratio decreases with increasing pressure, indicating that lower pressure is associated with a lower Nusselt number.

The fourth graph presents a variable relationship between the mean S/N ratio and the type of gas. The S/N ratio is lowest with air, increases slightly with CO2, drops significantly with Helium, and then increases sharply with Nitrogen. This suggests that the type of gas has a complex effect on the system's performance, with Nitrogen showing the highest mean S/N ratio, which might indicate superior performance. In order to ascertain the impact of each factor, a parameter (θ) is established, representing the upper and lower bounds of the response for each factor. The values of factors A, B, C, and D are 11.86, 15.04, 4.85, and 10.64, respectively. Among the four factors that were tested, Factor B, which is the axial radius ratio, has the most significant influence on the Nusselt number of the FESS.

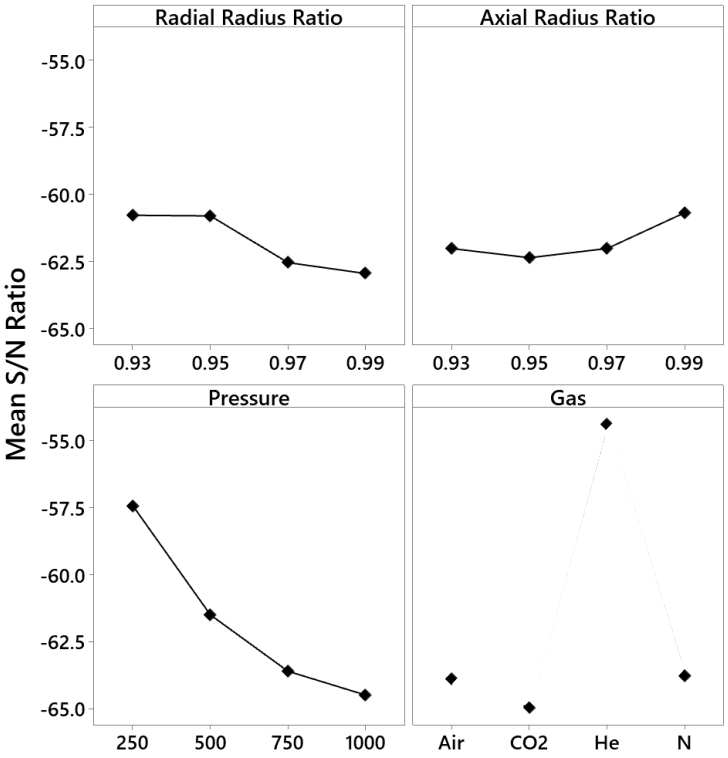

Fig. 5-27 The mean S/N ratio for windage losses for the four studied parameters

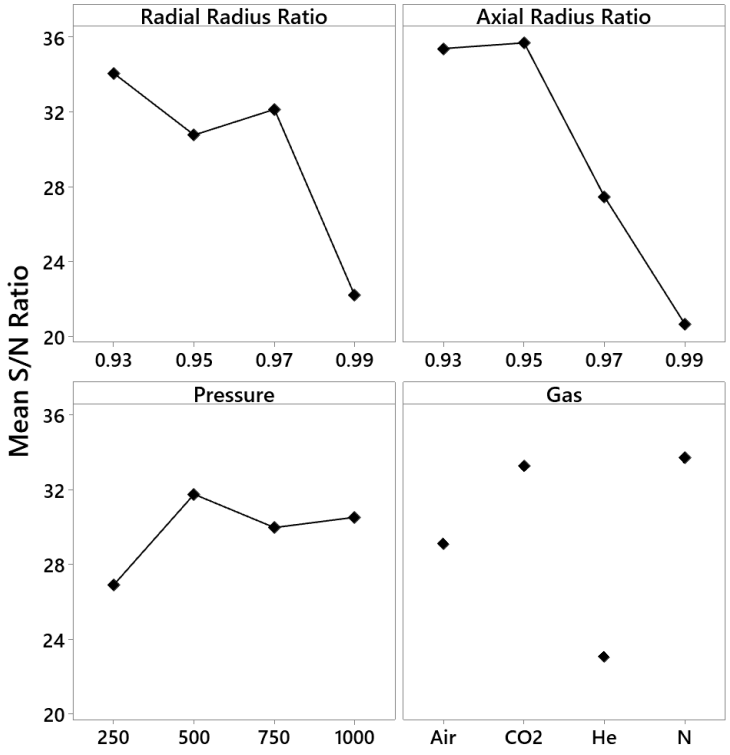

Fig. 5-28 The mean S/N ratio for Nusselt number for the four studied parameters

Step 6: Assessing The Interactions Between the Studied Parameters

A linear graph was created to easily examine the interaction information to determine the presence of any interactions between the selected factors. Parallelism of their effects can be observed without interaction between the two factors. In contrast, if there is non-parallelism between them, the two factors interact, which is a case of a synergistic interaction, also known as a weak interaction. If an anti-synergistic interaction occurs, the mutual effects of the factors must be regarded as an essential parameter influencing product quality. Interactions between the FESS parameters are critical in conducting meaningful experiments and analysing results [397]. To evaluate such interactions, the Analysis of Variance (ANOVA) technique can be used for S/N ratios. This method allows for the determination of data variability and analysis of mean differences in simulation quality instead of direct data analysis [398] [399]. In addition, ANOVA interaction plots can be used to visualise the relationship between factors [400].

In this study, the interaction of each two factors is calculated based on S/N ratios listed in Table 5-14 and plotted in Figs. 5-29 and 5-30. For the windage losses, the mean S/N ratio interaction graphs show that the radial and axial airgaps have the most significant impact on responses when interacting with other factors. The interaction effect occurs in all four-factor combinations, indicating that all two-factor interactions are either synergistic or anti-synergistic. Among these plots, the relationship between A, B and C demonstrates a typical pattern that can be considered an anti-synergistic interaction. The relationship between C and D demonstrates a typical pattern that can be considered a synergistic interaction.

Conversely, regarding the Nusselt number, Fig. 5-30 depicts the interaction between the mean S/N and the studied factors demonstrating that all factors under investigation have a noteworthy influence on the responses when they interact with other factors. The interaction effect is present in all combinations of four factors, suggesting that all two-factor interactions exhibit either synergy or anti-synergy. The ANOVA technique allows for reliable measures of interactions between the FESS parameters and should be considered in conducting meaningful simulations and analysing results.

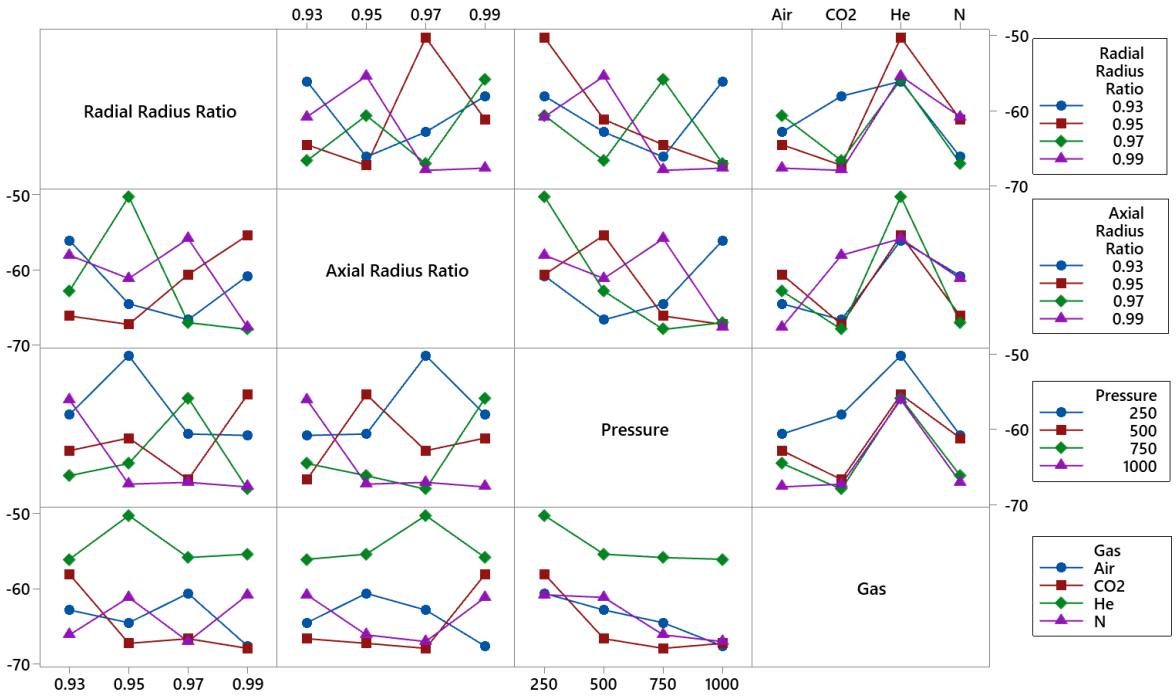

Fig. 5-29 Interaction plot (ANOVA) between the studied four factors and the mean S/N ratio for windage loss response

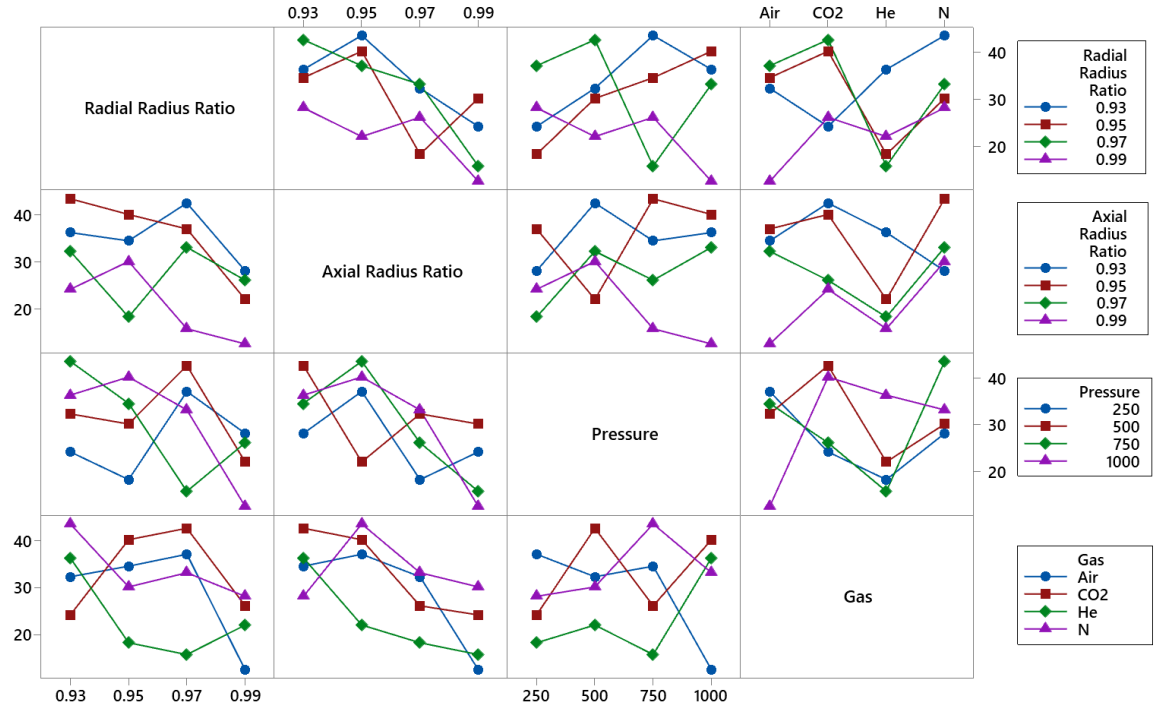

Fig. 5-30 Interaction plot (ANOVA) between the studied four factors and the mean S/N ratio for Nusselt number response

Fig. 5-31 presents the correlation between windage losses and radial radius ratio for the various gases and pressures examined in this study. The results demonstrate that Helium exhibits a consistent trend of decreasing windage losses with a decreasing radial radius ratio, and it has the lowest windage losses at all pressure levels when compared to the other gases studied. Both Air and Nitrogen exhibit similar windage losses across all tested pressures, although Air demonstrates slightly higher windage losses compared to Nitrogen at all examined pressures. On the other hand, Carbon dioxide experiences the highest value of windage losses compared to all other gases at all pressures that were studied. Notably, decreasing the pressure reduces windage losses for all the gases studied, with Helium demonstrating a gradual decrease and the remaining gases showing a more rapid decline.

Carbon dioxide is a denser gas than air and Nitrogen, which results in greater resistance and increased friction when it comes into contact with the rotating flywheel. As a result, the flywheel experiences higher windage losses when Carbon dioxide is used as the medium gas compared to air and Nitrogen. This effect is particularly noticeable at high pressures, where the density of Carbon dioxide is further increased, leading to even higher windage losses.

Fig. 5-32 presents four 3D surface plots representing windage losses as influenced by the radial radius ratio and the pressure level for different gas mediums at an axial radius ratio of 0.99. For the air as a gas medium, the windage losses increase both with an increase in the radial radius ratio and the pressure level. Similar to air, CO_2 shows an increase in windage losses with both higher radial radius ratios and pressure levels. Fig. 5-32 (c) exhibits a distinctively different pattern, with a significant reduction in windage losses across all radial radius ratios and pressure levels. Helium, being much lighter than air and CO2, results in lower windage losses due to its lower density, which reduces drag on the flywheel. The windage losses for nitrogen display an intermediate behaviour similar to air. The losses increase with both radial radius ratio and pressure, but the overall windage losses are lower than those in air and CO2, suggesting that nitrogen has a better performance than air and CO2 but not as good as helium.

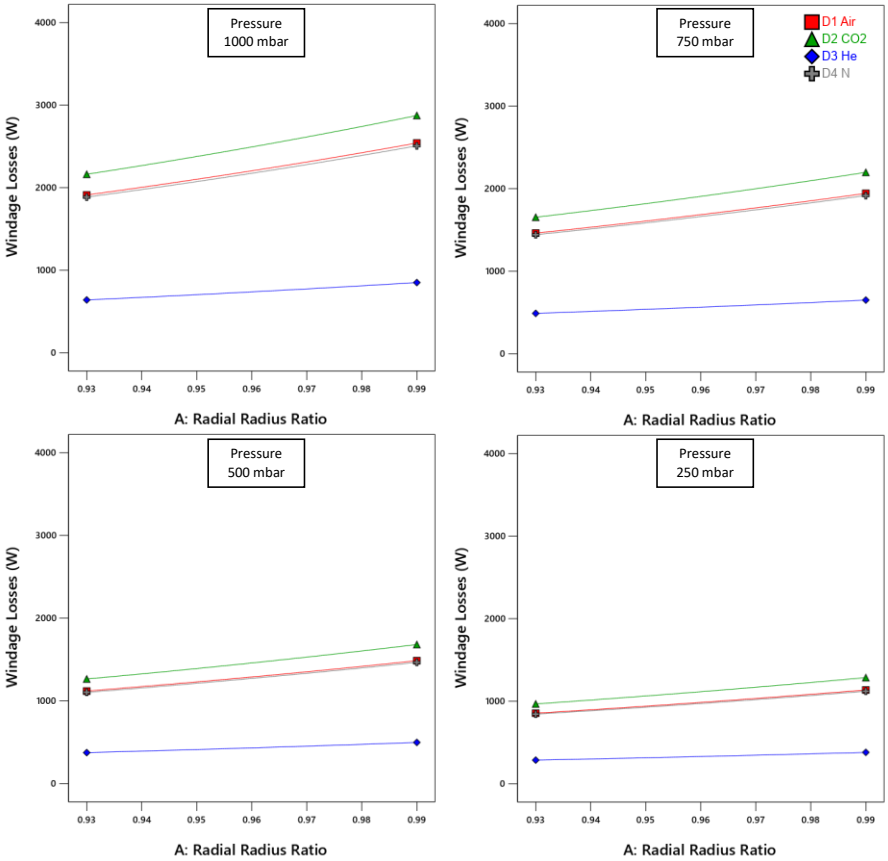

Fig. 5-31 The relationship between the windage losses and the radial airgap for the studied gases and pressures

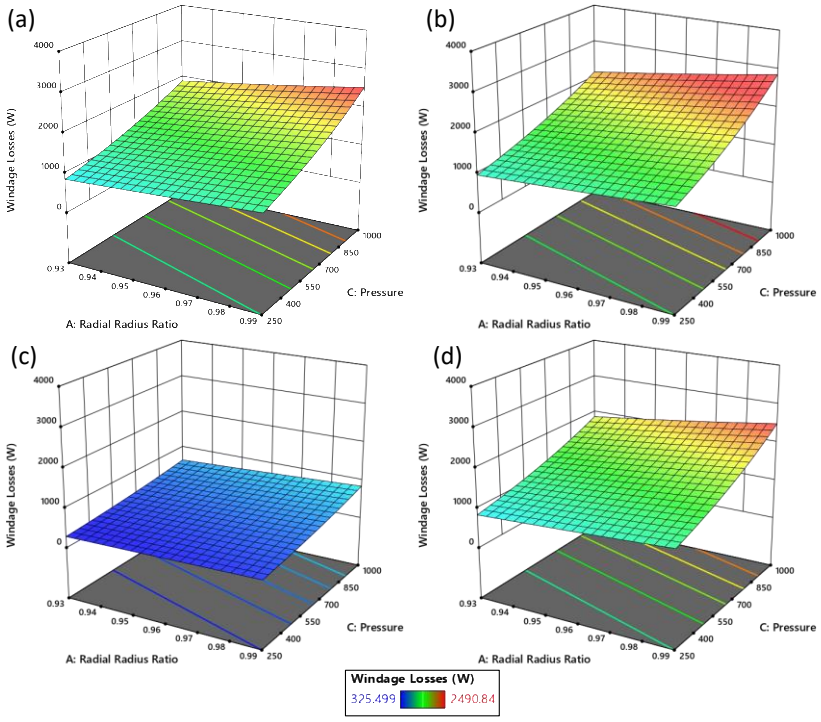

Fig. 5-32 3D plot for windage losses between radial radius ratio and pressure level for gas mediums: (a) Air, (b) Carbon Dioxide, (c) Helium, and (d) Nitrogen

Fig. 5-33 displays the relationship between the Nusselt number and the radial radius ratio for the studied gases at specific pressure levels. The Nusselt number decreases as the radial radius ratio increases. The reduction in pressure within the FESS cavity does decrease the Nusselt number for all studied gas mediums. Nitrogen achieves the highest Nusselt number among all pressure levels studied, while air closely approximates the Nusselt number values of Nitrogen. Helium achieved the lowest Nusselt number across all pressure levels studied. The response of carbon dioxide lies between that of air and helium. An increase in the radial radius ratio results in a decrease in the difference among the four gases that were studied.

Fig. 5-34 depicts the Nusselt number in relation to the radial radius ratio and pressure level for different gas mediums within FESS at an axial radius ratio of 0.95. For all gases, the plots suggest that the Nusselt number changes with variations in both the radial radius ratio and the pressure level. The Nusselt number appears to decrease as the radial radius ratio increases and as the pressure increases. This implies that for air, a bigger radial gap and higher pressure would enhance the convective heat transfer. Similar to air, the Nusselt number in CO_2 medium increases with an increase in both the radial gap and pressure. The surface plot for CO_2 shows a steeper and more pronounced change in the Nusselt number across the variables compared to air.

The surface plot for helium exhibits a marginal deviation, suggesting that variations in the radius ratio and pressure have no impact on the Nusselt number, unlike the other gases examined. The nitrogen plot shows a behaviour similar to air and CO_2 but with different rates of change due to nitrogen's specific thermal conductivity and viscosity properties.

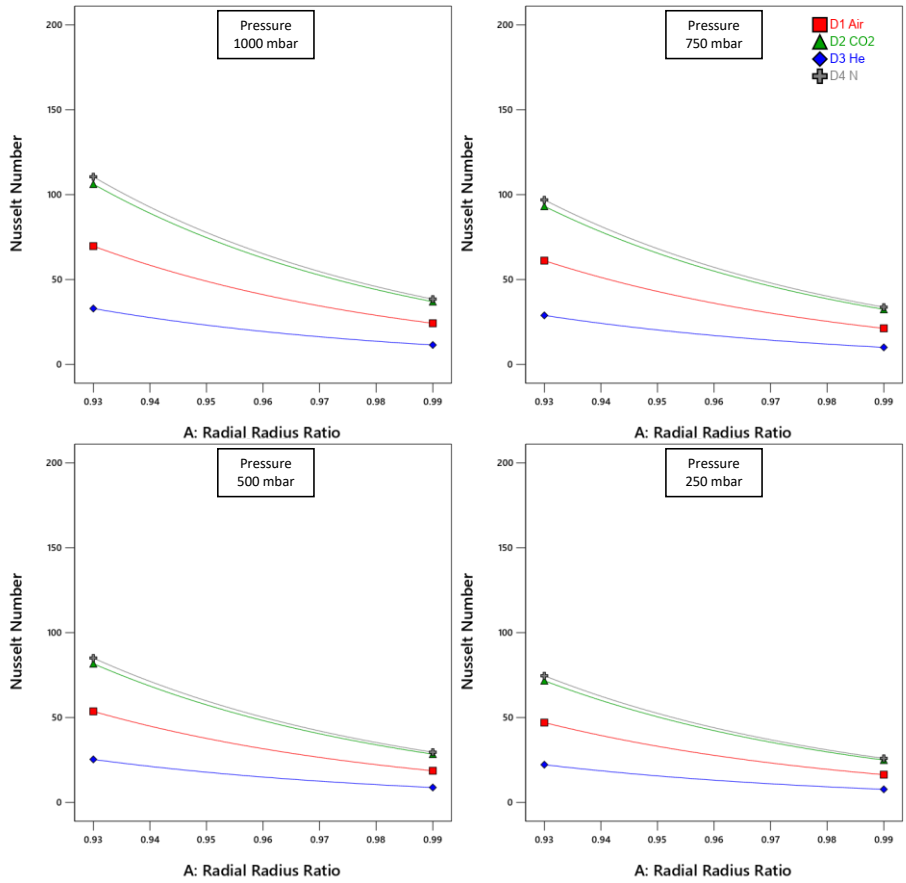

Fig. 5-33 The relationship between Nusselt number and the radial airgap for the studied gases and pressures

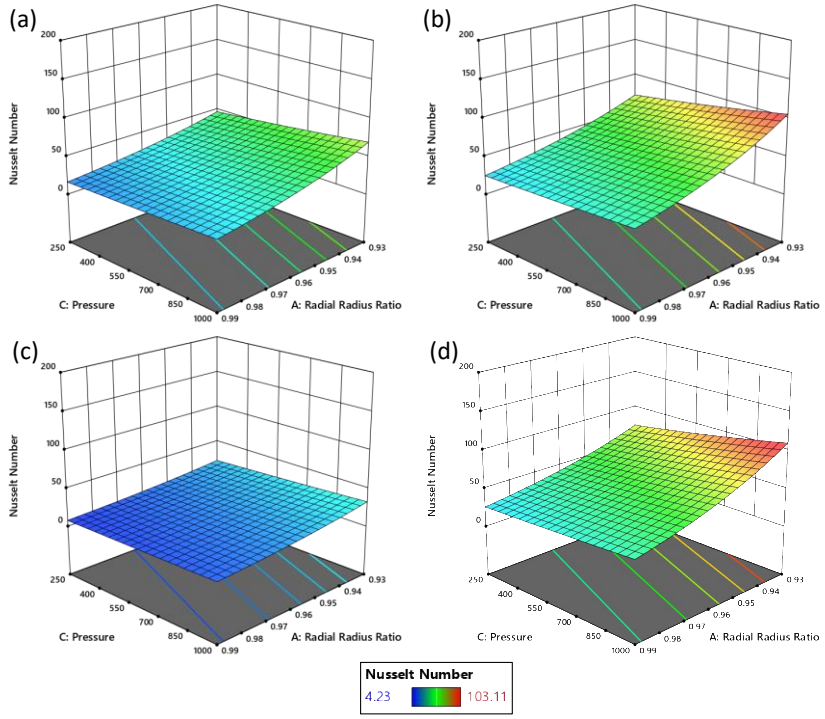

Fig. 5-34 3D plot for Nusselt number between radial radius ratio and pressure level for gas mediums: (a) Air, (b) Carbon Dioxide, (c) Helium, and (d) Nitrogen

Step 7: Superposition Model, Considering the Effects of Interaction

The superposition model can estimate all potential responses (S/N ratios) outside of an orthogonal array. Assuming a negligible amount of error, the superposition model for the four factors is defined as follows by Phadke [401]:

$$\eta^o(A_i, B_j, C_k, D_l) = \eta + (\eta_{A_i} - \eta) + \left(\eta_{B_j} - \eta\right) + (\eta_{C_k} - \eta) + (\eta_{D_l} - \eta) \quad (5\text{-}9)$$

Where η^o is the estimated S/N ratio, η is the average of the total mean S/N ratio, η_{A_i} is the S/N ratio for the factor A at level i, η_{B_j} is the S/N ratio for the factor B at level j, η_{C_k} is the S/N ratio for the factor C at level k, and η_{D_l} is the S/N ratio for the factor D at level l. To capture the effects of relationships between any two variables, the superposition equation should be updated to include the interaction of factors by including additional terms. As a result, the extra term of A and B is calculated as follows:

$$\eta^*(A_i, B_j) = \left(\eta_{A_iB_j} - \eta\right) - (\eta_{A_i} - \eta) - \left(\eta_{B_j} - \eta\right) \quad (5\text{-}10)$$

Where η^* is the interaction term, $\eta_{A_iB_j}$ is the average of the total mean S/N ratio between factors A and B. This approach can be used for all other interactions, so the modified superposition equation for calculating all possible cases (256 cases) can be written as follows:

$$\eta^t(A_i, B_j, C_k, D_l) = \eta + (\eta_{A_i} - \eta) + \left(\eta_{B_j} - \eta\right) + (\eta_{C_k} - \eta) + (\eta_{D_l} - \eta) + \left(\eta_{A_iB_j} - \eta\right) - (\eta_{A_i} - \eta) - \left(\eta_{B_j} - \eta\right) + (\eta_{A_iC_k} - \eta) - (\eta_{A_i} - \eta) - (\eta_{C_k} - \eta) + (\eta_{A_iD_l} - \eta) - (\eta_{A_i} - \eta) - (\eta_{D_l} - \eta) + \left(\eta_{B_jC_k} - \eta\right) - \left(\eta_{B_j} - \eta\right) - (\eta_{C_k} - \eta) + \left(\eta_{B_jD_l} - \eta\right) - \left(\eta_{B_j} - \eta\right) - (\eta_{D_l} - \eta) + (\eta_{C_kD_l} - \eta) - (\eta_{C_k} - \eta) - (\eta_{D_l} - \eta) \quad (5\text{-}11)$$

Where η^t is the estimated S/N ratio for the factor while including the interaction effect. The equation can be reduced to be as follows:

$$\eta^t(A_i, B_j, C_k, D_l) = 3\eta + \eta_{A_iB_j} + \eta_{A_iC_k} + \eta_{A_iD_l} + \eta_{B_jC_k} + \eta_{B_jD_l} + \eta_{C_kD_l} - 2\eta_{A_i} - 2\eta_{B_j} - 2\eta_{C_k} - 2\eta_{D_l} \quad (5\text{-}12)$$

Using the S/N ratio in Table 5-14 and a programme written in MATLAB was used to solve Eq. (5-12), the total number of S/N ratios for 256 cases is calculated. The results indicated that the highest achieved S/N ratio for windage losses was at run 143, where radial radius ratio is 0.95, axial radius ratio is 0.99, pressure is 250mbar, and Helium is the gas, which is considerably higher than the optimal case (case 10) with the combination of radial radius ratio of 0.95, axial radius ratio of 0.97, pressure of 250mbar and Helium as gas, calculated by the 16 cases in the Taguchi OA. The results showed that the highest S/N ratio for the Nusselt number was achieved at run 244. In this run, the radial radius ratio was 0.93, the axial radius ratio was 0.93, the pressure was 1000mbar, and Nitrogen was used as the gas. This value was higher than the optimal case (case 15) in which the radial radius ratio was 0.93, the axial radius ratio was 0.95, the pressure was 750mbar, and Nitrogen was used as the gas.

5.3.2. The Optimised Design

Utilising the superposition model, optimised systems were developed to minimise windage losses or maximise the Nusselt number. In order to attain the objective of identifying the design factors that would enhance both the windage losses and Nusselt number. A single desirability function was utilised to evaluate various responses and factors in order to determine the most optimal solution with the highest level of desirability for system optimisation. The solution that achieved the highest desirability of 1 was for a radial radius ratio of 0.933 with an axial radius ratio of 0.957 at a pressure level of 250mbar and Helium as gas. Given that windage losses are the sole factor that requires optimisation, Table 5-15 presents combinations of designs and their corresponding levels. The first case is the initial design operated under atmospheric pressure with air as the gas medium. The second case is similar to the first, except it was operated under 250mbar pressure. The third and fourth cases represent the optimised designs obtained from the OA analysis and superposition model. The remaining cases have the same levels as the superposition optimisation model for factors A and B but different approaches regarding factors C and D. The numerical simulation method is utilised to evaluate the performance of the new designs. The windage losses are calculated based on the data obtained from the CFD model.
The initial design has a total windage loss of 2407 W, while the modified initial design with a 250mbar pressure level has a lower total windage loss of 997 W, with a 59% reduction in windage losses only based on the pressure level. The optimised design based on the OA method has a further reduced total windage loss of 325 W. The optimised design based on the superposition method has an even lower total windage loss of 314 W. The superposition optimisation with atmospheric pressure and air as the gas medium has a higher total windage loss of 704 W. When air is used as the gas medium in the superposition optimisation, the total windage loss increases to 940 W. Finally, the superposition optimisation with both air and atmospheric pressure has the highest total windage loss of 2102 W. According to the results, the optimal choice for minimising windage losses is Helium as a gas medium, even when the pressure inside the cavity is maintained at atmospheric pressure. Notably, using Helium at atmospheric pressure results in significantly lower windage losses than using air at 250mbar pressure. The results suggest that the difference in windage loss reduction between the OA optimisation design and superposition optimisation is only 3.4%, and the selection between them depends on the airgap size. The study also finds that optimising the initial design using either approach significantly reduces windage losses, with an 86% reduction observed in the optimised system compared to the initial design. Furthermore, the study conducted a rundown test of the optimised designs and found that using Helium as a gas medium without reducing the pressure inside the system's cavity can lead to a 30% reduction in windage losses compared to the initial design running at a pressure of 250 mbar. Fig. 5-35 depicts the windage losses in the optimised designs during the rundown test.

Table 5-15 The optimised designs for windage losses as a response

Solution #	Run Name	A: Radial radius ratio	B: Axial radius ratio	C: Pressure	D: Gas	Total Windage losses (W)
S1	Baseline model	0.99	0.99	1000	Air	2407
S2	Baseline model (partial vacuum)	0.99	0.99	250	Air	997
S3	OA optimisation	0.95	0.97	250	He	325
S4	Superposition optimisation	0.95	0.99	250	He	314
S5	Superposition optimisation (atm pressure)	0.95	0.99	1000	He	704
S6	Superposition optimisation (air)	0.95	0.99	250	Air	940
S7	Superposition optimisation (air+atm pressure)	0.95	0.99	1000	Air	2102

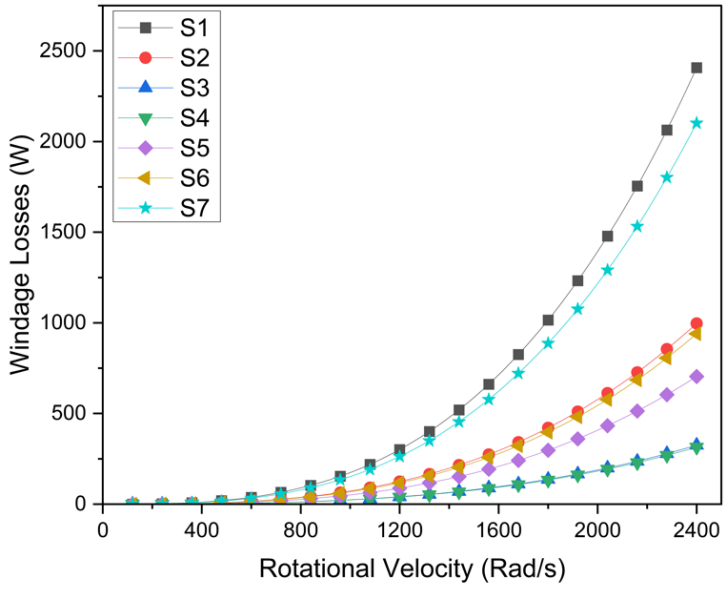

Fig. 5-35 The windage losses with respect to rotational velocity for optimised cases

5.4. Summary

A comprehensive analysis is conducted on the factors affecting FESS performance, with a focus on windage losses, the Nusselt number, and standby power. Initially, a detailed statistical analysis is

presented, showcasing the robustness and predictive capability of regression models for windage losses, Nusselt number, and standby power. The study then delves into the impact of standby power on FESS, particularly how its reduction can lower the self-discharging rate, thereby enhancing the system's suitability for extended storage periods. An exploration is made into how windage losses are influenced by operational parameters such as rotational velocity, radius ratio, and internal pressure level of the FESS cavity. A significant finding is that larger airgaps and reduced pressure substantially decrease windage losses. The dependence of the Nusselt number on radius ratio and internal pressure is also examined, providing critical insights for optimising thermal control in FESS. The power requirements for operating a vacuum pump in a FESS are thoroughly discussed, including a formula for calculating the necessary power. Optimisation techniques, including the Taguchi method and ANOVA, are employed to identify optimal solutions for minimising standby power and maximising the Nusselt number. A superposition model is developed to estimate potential responses and determine the most effective design solutions. The effects of different gases (Air, Helium, CO2, Nitrogen) on FESS performance are investigated, focusing on their impact on windage losses and the Nusselt number. The chapter concludes with an evaluation of various optimised designs, highlighting the superior performance achieved by using Helium as a gas medium in reducing windage losses and enhancing overall FESS efficiency. The findings provide valuable insights into optimising FESS, emphasizing the need for careful selection of operational parameters and gas mediums to improve efficiency and reduce losses. A portion of the numerical findings detailed in this chapter has been published in [402].

Chapter 6. The Effect of Casing Design on FESS Aerodynamic Performance

6.1. Introduction of Slit Walls in FESS Casing

Chapter 6 delves deeply into the optimisation of FESS, focusing particularly on the effects of incorporating slit walls within the housing. This chapter builds upon the foundational methodology established in Chapter 4, which is pivotal for the analyses conducted here. The pre-processing steps and solver configurations delineated in Chapter 4 have been applied in the studies carried out in Chapter 6. This consistent approach across chapters ensures a coherent and systematic analytical framework, facilitating a logical and directly comparable aggregation of results.

However, the introduction of slit walls in this chapter necessitates a modification of the pre-processing steps. These alterations are crucial as the slit walls influence the mesh configuration, thereby requiring additional mesh independence tests to ensure accuracy. The radius ratio chosen for this investigation, as deduced from the findings in Chapter 5, is 0.96 in both radial and axial directions. This ratio has been identified as optimal for achieving the dual objectives of minimising windage losses and enhancing heat transfer efficiency.

Moreover, the computational simulations in this chapter are heavily reliant on the solver steps, which involve the use of ANSYS Fluent for comprehensive fluid and thermal analysis. The application of the SST k-omega turbulence model is a critical component of these simulations. The purpose of maintaining consistency in methodology is to strengthen the credibility of the findings and ensure that any discrepancies in results can be attributed to the specific variables being studied in Chapter 6, rather than differences in the analytical approach.

This research is dedicated to a comprehensive exploration of how various slit wall shapes influence the flow field, windage losses, and heat transfer within FESS featuring a slit wall on the housing. The core objective of this study is to evaluate the impact of four distinct slit wall shapes on the FESS's performance. These shapes include triangular, trapezoidal, rectangular, and half-ellipse configurations. By examining these diverse geometries, the study aims to ascertain which slit wall shape optimises the FESS's efficiency. Each shape has unique characteristics that could potentially affect the flow dynamics and thermal behaviour inside the FESS.

The analysis of these shapes is not only intended to quantify their impacts on FESS performance but also to offer insights into the underlying mechanics driving these effects. This could involve examining how each shape alters the flow field within the FESS and its consequent effect on both windage losses and thermal management. The results of this study will be utilised to conduct further research on the impact of various shapes, configurations, and setups of slit walls. These findings will be employed in subsequent investigations for more comprehensive analysis.

6.1.1. Boundary Conditions

The radius ratio was chosen to be 0.96 based on the optimisation process conducted in Chapter 5. The number of slits (n) was selected to be 8, 16, and 24. Periodic conditions were applied to all periodic boundary surfaces since the FESS flow pattern permits the use of periodic regions [403]. The simulation was run on a 45°-slice from the FESS with a symmetry plane in the centre to reduce the computational resources and costs. Fig. 6-1 depicts the FESS geometry with no wall slits, which is used as the benchmark in this investigation. Fig. 6-2 depicts the slit wall cross sections for the four studied slit designs with varying numbers of slits. The size of the slit structure is chosen based on the geometrical values in Table 6-1 to maintain the heat transfer region of the various studied models to have the same surface area.

The hydraulic diameter of a concentric cylinder with slit walls on the outer cylinder can be calculated by [267]:

$$D_h = \frac{4 \times \text{Flow Area}}{\text{Wetted Perimeter}} \quad (6\text{-}1)$$

Where the flow area is the area through which the fluid flows. On the other hand, the wetted perimeter is the length of the walls in contact with the fluid and C is the height of the slit, B is the base length of the slit, w is the top length of the slit, and n is the number of the slit walls.

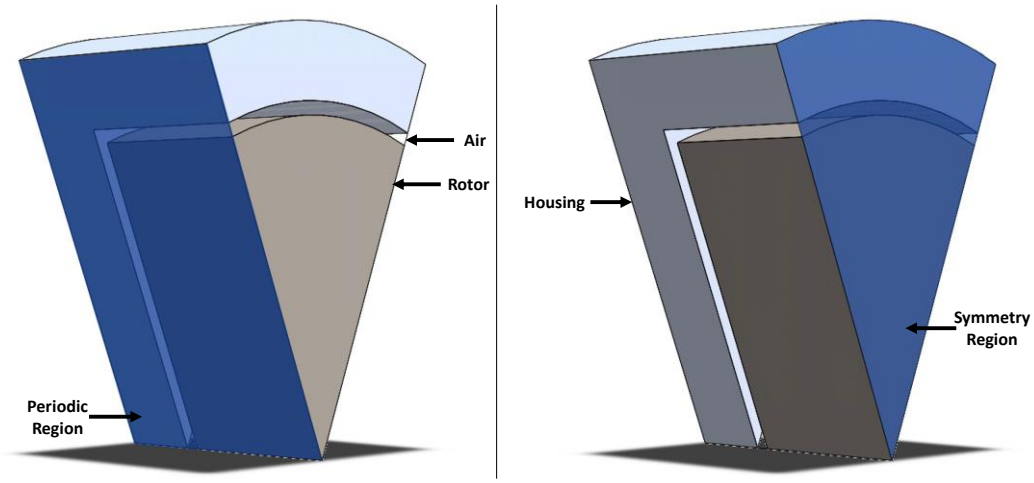

Fig. 6-1 Simplified geometry of FESS with periodic regions and symmetry plane

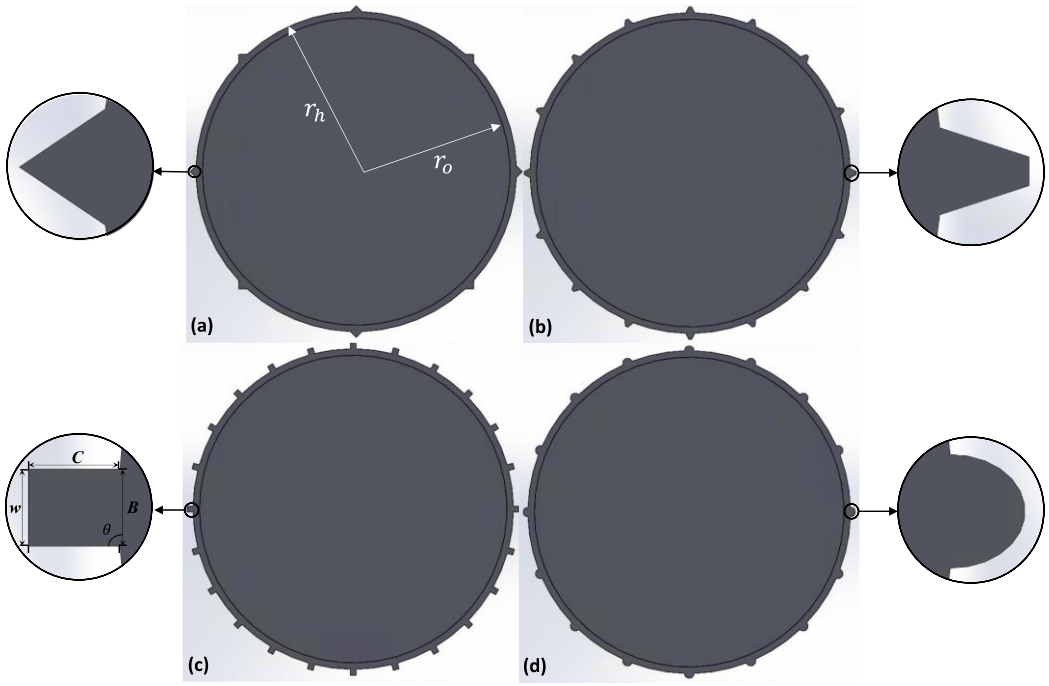

Fig. 6-2 Different slit cross sections, (a) triangle, (b) trapezoid, (c) rectangle, and (d) half ellipse

Table 6-1 Slit walls geometrical parameters

Model	Shape	Base length B (mm)	Height C (mm)	Top length w (mm)	Angle θ (°)
a	Triangle	10	5	0	60
b	Trapezoid	7.5	5	2.5	63
c	Rectangle	5	5	5	90
d	Half ellipse	8	4	NA	NA

Mesh independence analysis is an essential pre-processing step for ensuring the accuracy and reliability of numerical simulations. This study employed a structured quadrilateral mesh to model a system with rotor and housing mesh sizes of 1 to 2mm, respectively, and an airgap mesh size of 0.1 to 0.2mm. The objective was to identify the optimal mesh for the simulations by conducting a mesh independence test using the skin friction coefficient and the Nusselt number, as the parameters of interest, at the highest rotational speed of 2400 rad/s. To ensure the robustness of the results, several cases were tested, including the most complex mesh cases with the most slit walls for each geometry studied, as well as other cases, such as the base model. The skin friction coefficient values for the most severe mesh cases and the Nusselt number in relation to the number of mesh elements are depicted in Fig. 6-3. Based on the results of these tests, the third mesh configuration was chosen to save computational time and capacity. After that, the difference in the results is within an acceptable range and it can be observed that increasing the mesh size after that would only increase the computational time, not the results. It is important to carefully select an appropriate mesh type and quality in numerical investigations to draw

valid conclusions. Fig. 6-4 portrays the quadrilateral mesh used to model the FESS showcasing the inflation layers.

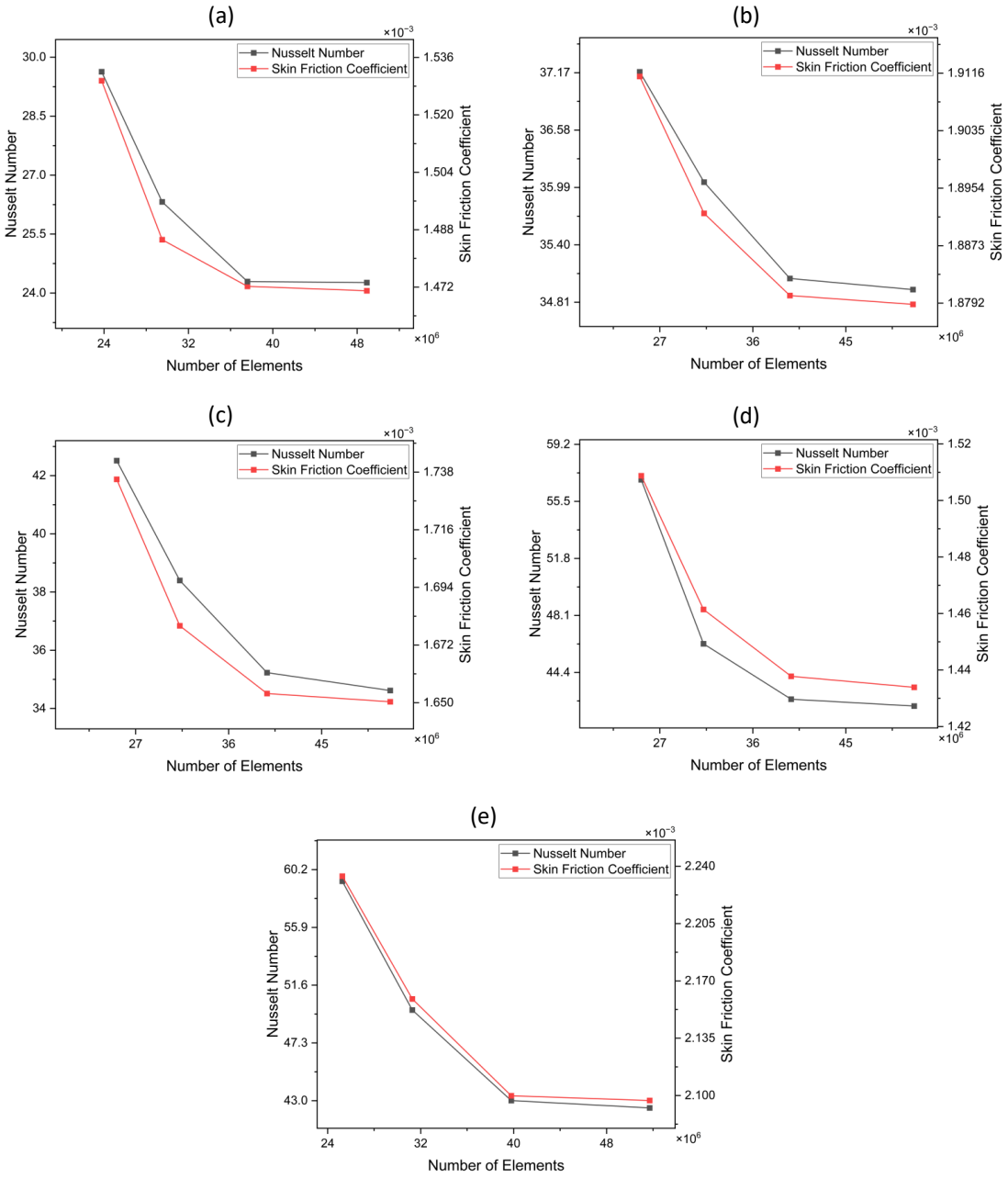

Fig. 6-3 Variation of Nusselt Number and skin friction coefficient with the number of mesh elements for, (a) no slit walls, (b) 24 triangle slits, (c) 24 trapezoid slits, (d) 24 rectangle slits and (e) 24 half-ellipse slits

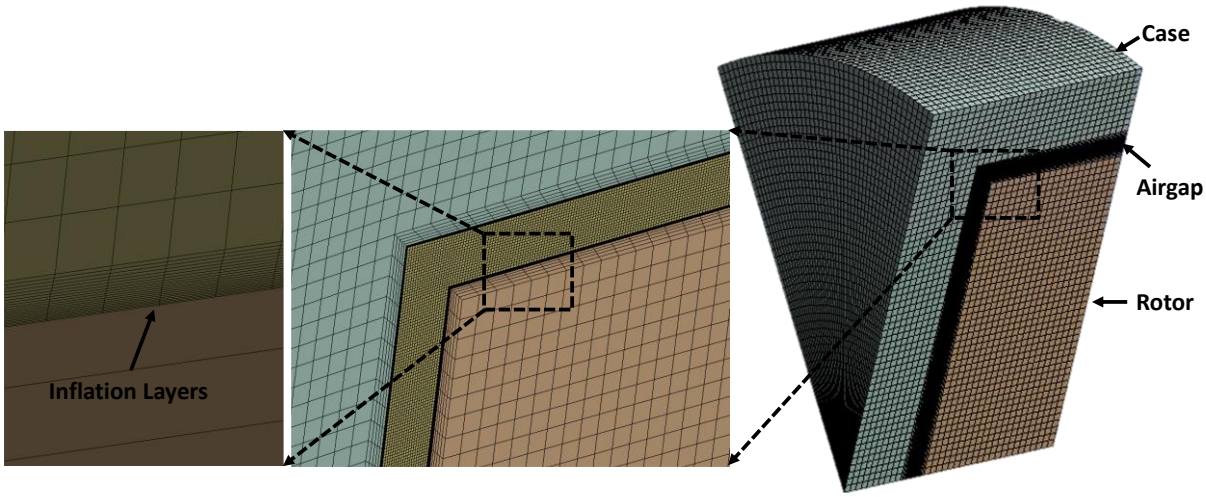

Fig. 6-4 The quadrilateral mesh used to model the FESS

6.1.2. Influence of Slit Walls on Windage Losses

Fig. 6-5 presents a bar chart that compares windage losses at various rotational speeds for different configurations of a triangular slit wall geometry. The chart categorises the data into four groups based on the presence and the number of slit walls. No slit wall configuration serves as a baseline. Windage losses increase substantially with rotational speed, which is expected as windage losses are known to increase with the square of rotational speed due to greater air resistance. Introducing 8 slit walls reduces windage losses across all speeds compared to the baseline, suggesting that the slits help reduce the air resistance affecting the flywheel. With 16 slit walls, windage losses are further reduced compared to both the baseline and the 8-slit wall configurations, indicating a continued benefit from increasing the number of slits. The configuration with 24 slit walls shows a mixed trend. At lower rotational speeds (800 and 1200 rad/s), the windage losses are similar to or slightly higher than the 16-slit wall case. However, at higher speeds (2000 and 2400 rad/s), the losses are lower than with 16 slits, suggesting a complex interaction between the number of slits and rotational speed. The use of triangular slit walls in a FESS was found to reduce windage loss by an average of 2% and a maximum of 4% compared to a system with no slit walls.

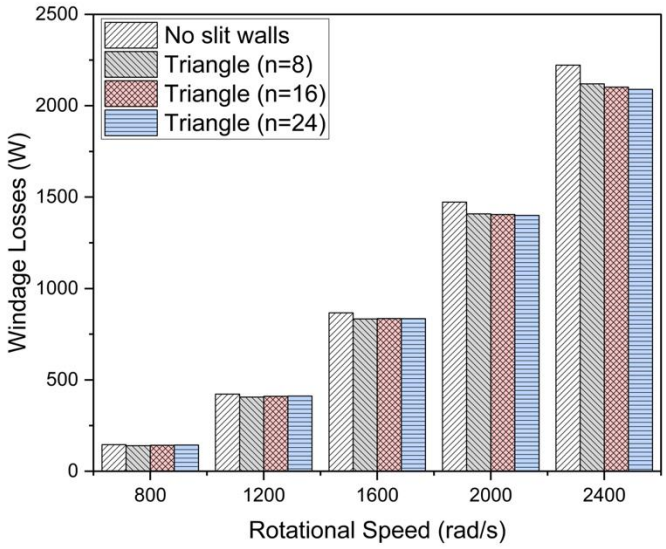

Fig. 6-5 Relationship between windage loss and rotational speed for the triangle slit wall geometry

Fig. 6-6 shows the bar chart that depicts windage losses in relation to rotational speed for different configurations of a flywheel with trapezoidal slit wall geometry. The configurations are categorised by the number of slit walls. The introduction of 8 trapezoidal slit walls results in reduced windage losses across all rotational speeds compared to the no-slit wall configuration. This suggests that the presence of slit walls can effectively reduce the air resistance impacting the flywheel. With 16 slit walls, there is a further reduction in windage losses across all speeds when compared to the 8-slit wall configurations, indicating that a greater number of slits can lead to more significant reductions in windage losses. The configuration with 24 slit walls shows that at lower rotational speeds (800 and 1200 rad/s), windage losses are comparable to the 16 slit wall configurations. However, at higher speeds (2000 and 2400 rad/s), the losses are reduced even further, indicating that the number of slit walls has a more pronounced impact at higher rotational speeds. For the trapezoidal slit wall geometry, an average windage loss reduction of 3% and a maximum reduction of 6% were observed. This indicates that the trapezoidal shape was more effective in reducing the windage loss than the triangle slit wall.

Fig. 6-7 illustrates the windage losses associated with a flywheel at different rotational speeds for various configurations of rectangular slit wall geometry. Including 8 rectangular slit walls reduces the windage losses across all rotational speeds when compared to the no-slit wall configuration. The 16-slit wall configuration shows further reduced windage losses across the rotational speeds, suggesting that an increase in the number of slit walls continues to benefit the reduction of windage losses. With 24 slit walls, the windage losses are decreasing even more for all the rotational velocities. However, at 2400 rad/s, the windage losses are similar to that seen with 16 slit walls.

The rectangular slit wall geometry was found to have an average windage loss reduction of 5% and a maximum reduction of 7.7%. These results suggest that the trapezoidal and rectangular slit wall

geometries effectively reduce the windage loss of a FESS. However, the half-ellipse slit wall geometry exhibited a more complex relationship.

Fig. 6-8 illustrates the windage losses at different rotational speeds for flywheel with varying quantities of half-ellipse slit wall geometries. Introducing 8 half-ellipse slit walls results in a slight decrease in windage losses at all rotational speeds when compared to the setup without slit walls. Using a configuration with 16 slit walls instead of 8 slit walls greatly decreases windage losses at all speeds. The configuration featuring the highest number of slit walls exhibits a rise in windage losses across all examined velocities. Although the windage loss was reduced by an average of 1.3% for 16 slit walls, the use of 24 slit walls increased windage losses compared to a system without any slit walls.

The base length of the slit walls would impact windage loss; a longer base length may pose a more significant obstruction to the flow of air, potentially leading to a reduction in windage loss. However, if the base length is too long, it may cause an increase in windage loss due to increased friction between the slit wall and the surrounding air. Similarly, a shorter base length may lead to a minor obstruction to the airflow, potentially resulting in lower windage loss. However, if the base length is too short, it may not effectively guide and control the airflow, leading to higher windage losses.

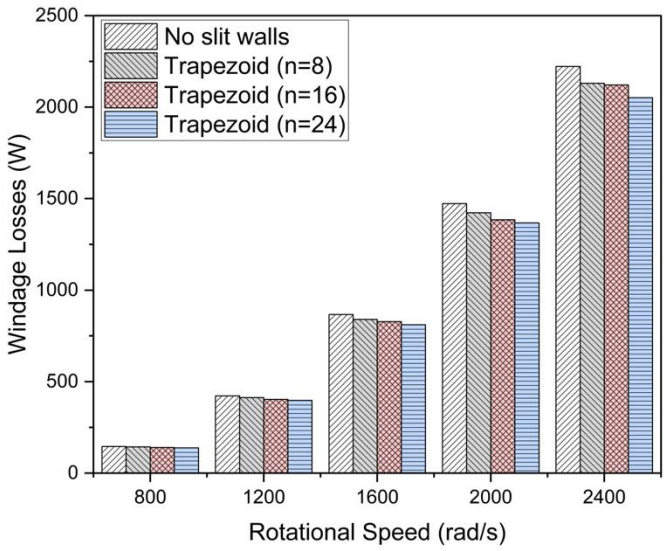

Fig. 6-6 Relationship between windage loss and rotational speed for the trapezoid slit wall geometry

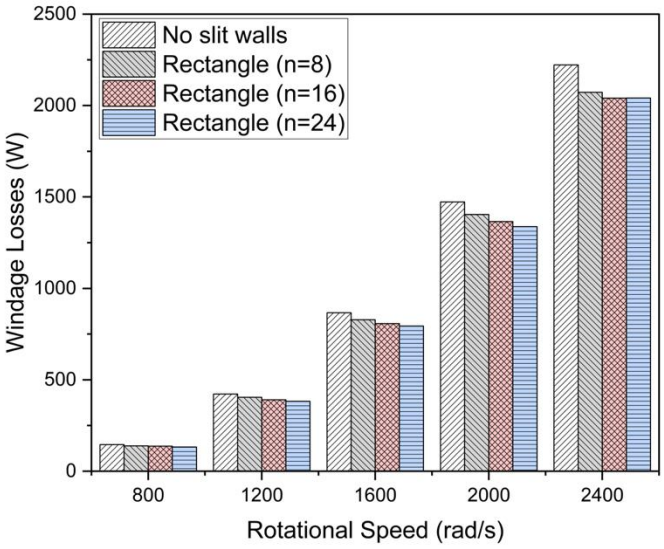

Fig. 6-7 Relationship between windage loss and rotational speed for the rectangle slit wall geometry

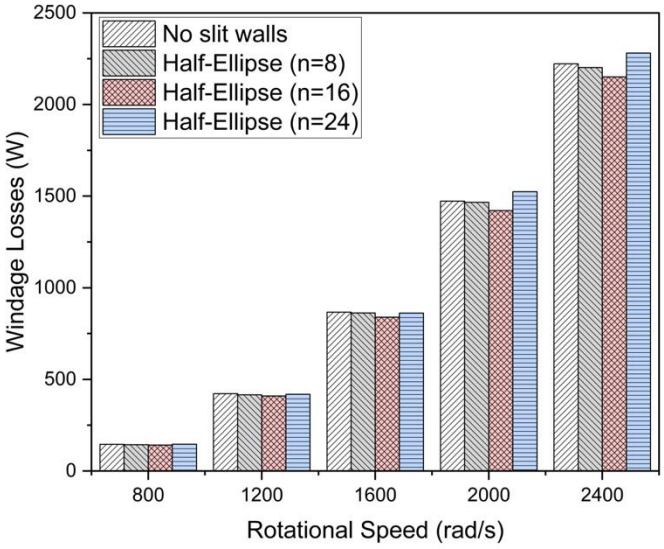

Fig. 6-8 Relationship between windage loss and rotational speed for the half-ellipse slit wall geometry

The strategic augmentation of slit walls has been identified as a potential way for mitigating windage losses. This approach hinges on the premise that altering the number of slit walls can significantly influence the flow field distribution and heat transfer dynamics within the system. By increasing the number of slit walls, the airflow around the flywheel is more effectively channelled, leading to a reduction in friction and consequently, windage loss. Empirical data have indicated that augmenting the number of slit walls tends to decrease windage losses across various geometries, such as triangles, rectangles, and trapezoids. However, this trend is not universal, as observed in the case of the half-ellipse geometry, where an increase in windage losses was recorded.

The unique outcome with the half-ellipse geometry can be attributed to the specific shape of the slit walls, which potentially redirects air particles towards the rotor. This redirection increases the skin

friction coefficient, thereby elevating windage losses. Notably, the half-ellipse slit wall geometry was associated with the highest windage losses, whereas the rectangular slit wall geometry demonstrated the lowest windage losses at peak rotational velocity. Meanwhile, the triangular and trapezoidal slit wall geometries exhibited intermediate levels of windage losses, with the trapezoidal configuration marginally surpassing the triangular in terms of loss.

In summary, the findings of this study illuminate the significant role played by slit wall geometry in influencing the windage losses of a FESS. While certain geometries like trapezoidal and rectangular slit walls effectively curtail windage losses, the half-ellipse configuration presents a more complex scenario. This investigation provides compelling evidence that the incorporation of slit walls in FESS design can be a pivotal factor in optimising windage loss.

6.1.3. Influence of Slit Walls on Heat Transfer

The configuration of slit walls within a FESS significantly impacts its heat transfer capabilities and the Nusselt number. Primarily, the shape and quantity of slit walls can influence the flow field distribution in the FESS. This, in turn, has impacts on heat transfer efficiency. For example, an increased count of slit walls could induce heightened turbulence within the air gap. This turbulence enhances mixing processes, thereby strengthening heat transfer effectiveness. Conversely, excessively large, or densely positioned slit walls might impede airflow, diminishing the heat transfer rate. Additionally, the specific geometry of the slit walls bears upon the convective heat transfer coefficient. This coefficient is pivotal in quantifying the rate of heat transfer between a solid surface and a fluid. Variations in slit wall geometry can lead to disparate convective heat transfer coefficients, thereby influencing the overall heat transfer rate in the FESS. Furthermore, the Nusselt number is related to the convective heat transfer coefficient, so changes in the convective heat transfer coefficient due to the presence of slit walls may also affect the Nusselt number.

Fig. 6-9 provided is a line graph that plots the Nusselt number against rotational speed with different numbers of triangular slit walls. The baseline configuration shows a behaviour where the Nusselt number increases with rotational speed, reaches a peak, and then decreases. This is due to the increase in Taylor number up to a point, after which the Taylor number starts to fall. As shown in Fig. 6-13. The introduction of 8 triangular slit walls raises the Nusselt number across all speeds compared to the no-slit wall configuration, indicating enhanced convective heat transfer. The peak Nusselt number for this configuration occurs at a similar speed to the no-slit wall case but at a higher value. With 16 triangular slit walls, the Nusselt number is further increased, especially at lower speeds, suggesting that the slits significantly improve convective heat transfer efficiency. The peak of the curve shifts slightly to the right, indicating that the maximum heat transfer rate is achieved at a slightly higher speed. The configuration with 24 slit walls shows the highest Nusselt numbers, particularly at the mid-range speeds. This suggests that having more slit walls continues to improve the convective heat transfer. However,

the peak is less pronounced, and the decline after the peak is more gradual, indicating a sustained transfer rate over a broader range of speeds. The Nusselt number increased as the number of slit walls increased. The average increase for 8, 16, and 24 slit walls, compared to no slit walls, is approximately 4.3%, 7.7%, and 8.4% respectively.

Fig. 6-10 shows the Nusselt number as a function of rotational speed with different numbers of trapezoidal slit walls. The introduction of 8 trapezoidal slit walls increases the Nusselt number across all rotational speeds compared to no slit walls, indicating enhanced heat transfer. With 16 slit walls, the peak Nusselt number is further increased, especially at the mid-range rotational speeds. This configuration appears to maintain higher heat transfer rates over a wider range of speeds compared to 8 slit walls. The housing with 24 trapezoidal slit walls exhibits the highest Nusselt numbers across almost all rotational speeds, demonstrating the most significant improvement in heat transfer. Nevertheless, the impact of the quantity of slits does not significantly affect the Nusselt number. The average increase for walls with 8, 16, and 24 slits, as compared to walls with no slits, is approximately 4.5%, 5.5%, and 5.0% respectively. Increasing the number of slit walls from 16 to 24 results in a decrease in the Nusselt number. Therefore, having 16 slit walls is the optimal choice for this case.

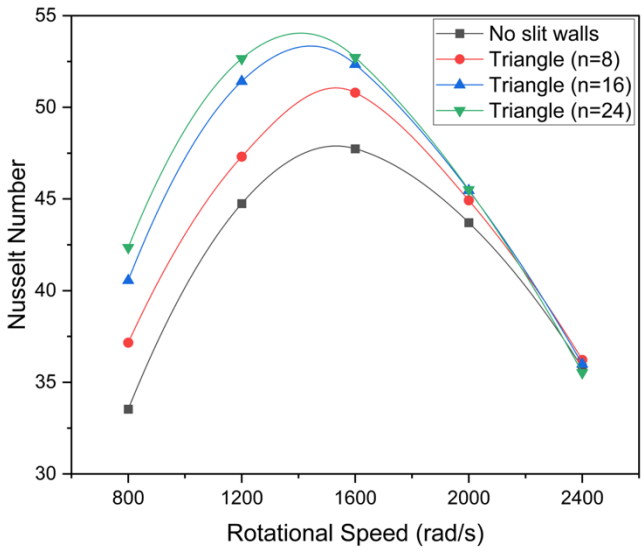

Fig. 6-9 Relationship between Nusselt number and rotational speed for the triangle slit wall geometry

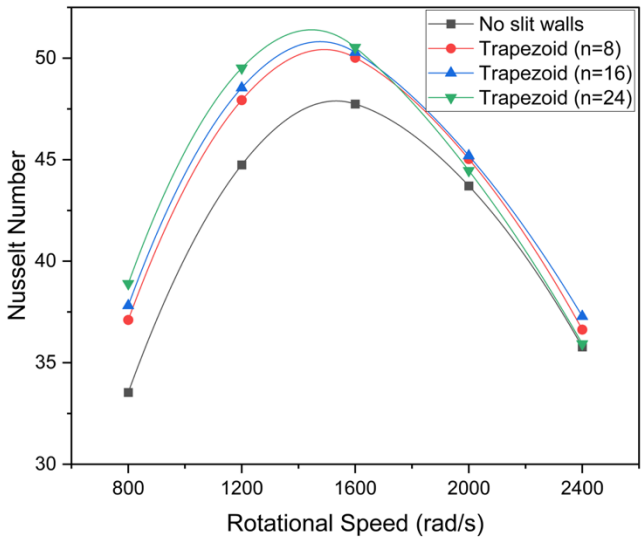

Fig. 6-10 Relationship between Nusselt number and rotational speed for the trapezoid slit wall geometry

Fig. 6-11 shows the Nusselt number as a function of rotational speed for flywheels with varying numbers of rectangular slit walls. Introducing 8 rectangular slit walls appears to enhance the heat transfer slightly, as indicated by the increased Nusselt number across all rotational speeds. A further increase in the number of slit walls to 16 shows the same Nusselt number. The peak of this line is roughly at the same rotational speed as for 8 slits. With the highest number of slit walls studied, the Nusselt number is elevated across the entire range of rotational speeds, reaching the highest peak among all configurations. This suggests that more slit walls contribute to a more effective convective heat transfer, although the descending part of the curve post-peak is similar to the other configurations. For the rectangular slit wall geometry, the Nusselt number showed a more complex trend, with the average increase for 8, 16, and 24 slit walls, compared to no slit walls, is approximately 0.2%, 0.2%, and 6.5% respectively.

Fig. 6-12 shows the Nusselt number against rotational speed featuring half-ellipse slit wall geometries with different slit quantities. Adding 8 half-ellipse slit walls results in an elevated Nusselt number across all rotational speeds compared to the baseline. The peak of the Nusselt number is higher, and it occurs at a similar rotational speed, indicating that the half-ellipse slits enhance convective heat transfer. With 16 slits, the Nusselt number is further increased, particularly at lower rotational speeds, suggesting that a greater number of slits improves heat transfer effectiveness. The peak Nusselt number is slightly higher than for the configuration with 8 slits, and the decline after the peak is less steep. The configuration with 24 half-ellipse slit walls shows an increase in Nusselt numbers across the range of rotational speeds, with the peak being like 8 slits configuration. In the case of the half-ellipse slit wall geometry, the average increase for 8, 16, and 24 slit walls, compared to no slit walls, is approximately 23.8%, 19.6%, and 23.7% respectively.

Shorter and narrower slit walls are expected to cause less airflow obstruction and potentially reduce turbulence, resulting in lower Nusselt numbers. Conversely, longer, and wider slit walls can impede the flow of air and cause increased turbulence, resulting in higher Nusselt numbers. The absence of sharp edges in the half-ellipse slit wall can lead to increased turbulence and more efficient fluid mixing, resulting in higher Nusselt numbers.

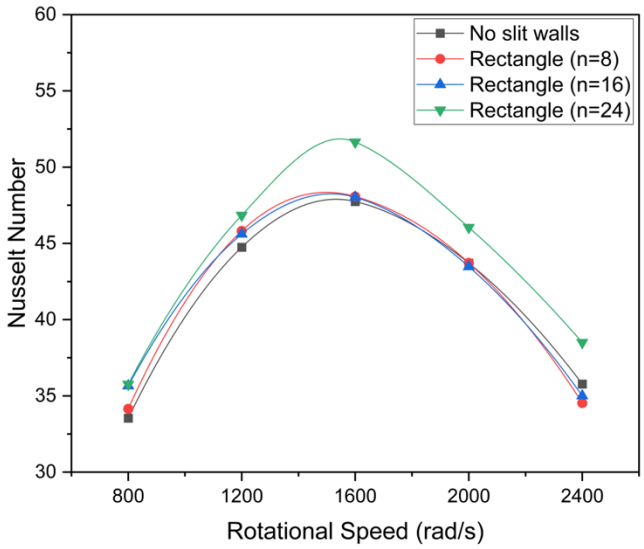

Fig. 6-11 Relationship between Nusselt number and rotational speed for the rectangle slit wall geometry

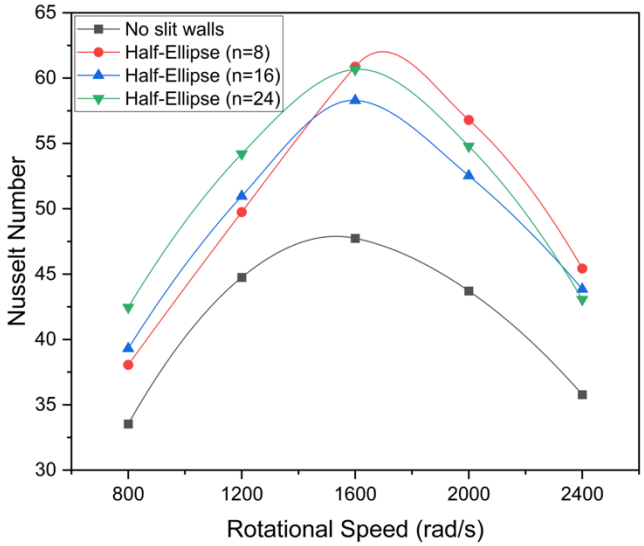

Fig. 6-12 Relationship between Nusselt number and rotational speed for the half-ellipse slit wall geometry

Fig. 6-13 depicts the relationship between the Taylor number and rotational speed for all the configurations that were investigated. The rise in the Nusselt number, followed by a decline after

reaching its maximum value at approximately 1600 rad/s, can be attributed to the correlation between the Taylor and Nusselt numbers. As the Tylor number increases, the Nusselt number also increases. The Taylor number exhibits a positive correlation with the rotational velocity, reaching its maximum value for each configuration at approximately 1600 rad/s, after which it begins to decline.

The shape and number of slit walls significantly impact the Nusselt number. The Nusselt number is higher for systems with more slit walls, indicating that the presence of the slit walls enhances heat transfer. This is especially evident for the triangle shape, where the Nusselt number increases as the number of slit walls increases. On the other hand, for the half-ellipse and the trapezoid shapes, the Nusselt number decreases as the number of slit walls increases, indicating that the presence of the slit walls may inhibit heat transfer in this case. The shape of the slit walls also appears to have a significant effect on the Nusselt number. For a given number of slit walls, the Nusselt number is generally the highest for the half-ellipse shape and the lowest for the rectangle shape. The triangle and trapezoid shapes have intermediate Nusselt numbers, with the triangle shape generally having higher Nusselt numbers than the trapezoid shape.

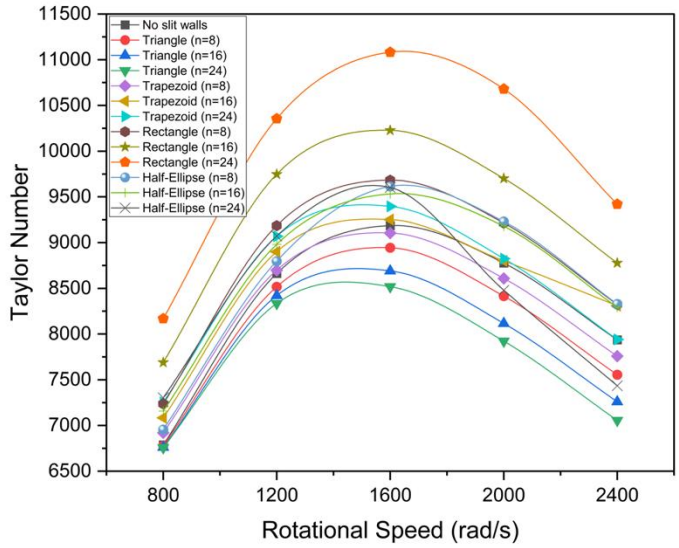

Fig. 6-13 Comparison of Taylor number and rotational velocity across all analysed slit wall geometries

The results of this study demonstrate that the number of slit walls can enhance heat transfer within the FESS. As the flywheel rotates, heat is generated due to the friction between the moving parts and the surrounding air. The generated heat needs to be efficiently dissipated to prevent the temperature of the flywheel from rising too high, which can lead to reduced performance and premature failure. By increasing the number of slit walls, the fluid within the air gap of a FESS can be more effectively mixed, leading to more efficient heat transfer. Increasing the number of slit walls in a FESS can help improve

the flow field distribution, reduce windage loss, and enhance heat transfer, leading to improved performance and longer lifespan.

6.1.4. Flow Characteristics

As the rotational velocity of a FESS increases, the Taylor-Couette vortices that form within the air gap become more pronounced. At low rotational velocities, the Taylor-Couette vortices are relatively weak and less pronounced, but as the velocity increases, vortices become more turbulent and intense, as shown in Fig. 6-14. This can have several effects on the overall performance of a FESS, including increased windage losses and reduced heat transfer rate. One of the primary ways that slit walls can affect the Taylor-Couette vortices is by disrupting the flow within the airgap. By introducing these barriers, the fluid within the air gap must navigate around the slit wall profile, which can alter the flow pattern and reduce the intensity of the vortices, as shown in Fig. 6-15.

As fluid flows through the annular gap, it undergoes collisions with the slit walls, resulting from the interplay of inertial forces and boundary layer separation, leading to the formation of small-scale vortex structures. This phenomenon is studied through the analysis of the streamlines of the four models in the slit region, as presented in Fig. 6-16. The resulting vortex structures are found to be located at the centre of the slit region for all four models. In the case of the trapezoid, half-ellipse, and rectangle models, the vortex at the centre induces a counter-rotating backflow on both sides of the wall corner. Conversely, the triangle model only exhibits backflow on the left side. Due to strong wall hysteresis, the backflow region is characterised by a relatively closed low-speed vortex that is not conducive to mass exchange with the mainstream in the slit, resulting in the formation of a thin boundary layer. Consequently, the backflow zone acts as a flow dead zone, inhibiting the heat transfer capability, which can be observed for both the triangle and rectangle models.

As shown in Fig. 6-17, it is apparent that the collision of the mainstream fluid with the wall on the left side of the slit generates a high-velocity region, which promotes mixing and heat exchange between the hot and cold fluids. The velocity of the fluid within the slit decreases gradually along the direction of rotation of the vortex, due to the viscous and friction forces of the wall. As a consequence, a low-velocity region is formed on the right wall of the slit, where the interfluid mixing effect is weakened, and a low-temperature zone emerges. Notably, the size of the high-velocity region is observed to be larger in the triangle and half-ellipse models compared to the trapezoid and rectangle models. This can be attributed to the unique geometrical features of these models, which result in a higher degree of fluid-wall interaction, leading to increased mixing and heat exchange between the fluids.

The number of Taylor vortices was lowest for the rectangle, highest for the half ellipse, and equal for the other two shapes. Increasing the number of vortices can lead to increased windage losses due to increased fluid friction. On the other hand, an increase in the number of vortices may also increase the heat transfer rate due to the enhanced fluid mixing and heat transfer between the fluid and the surface.

This can lead to improved performance of a FESS, including lower windage losses and enhanced heat transfer.

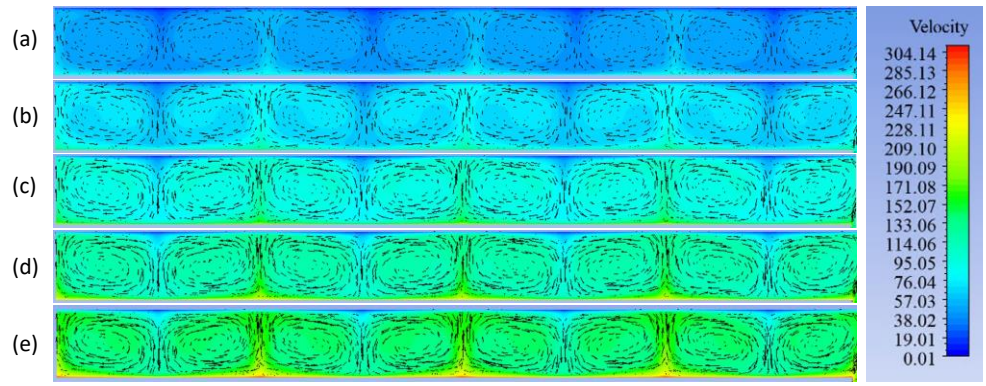

Fig. 6-14 Velocity contour of the FESS with no slit walls at the rotational velocity of (a) 800 rad/s, (b) 1200 rad/s, (c) 1600 rad/s, (d) 2000 rad/s, and (e)2400 rad/s

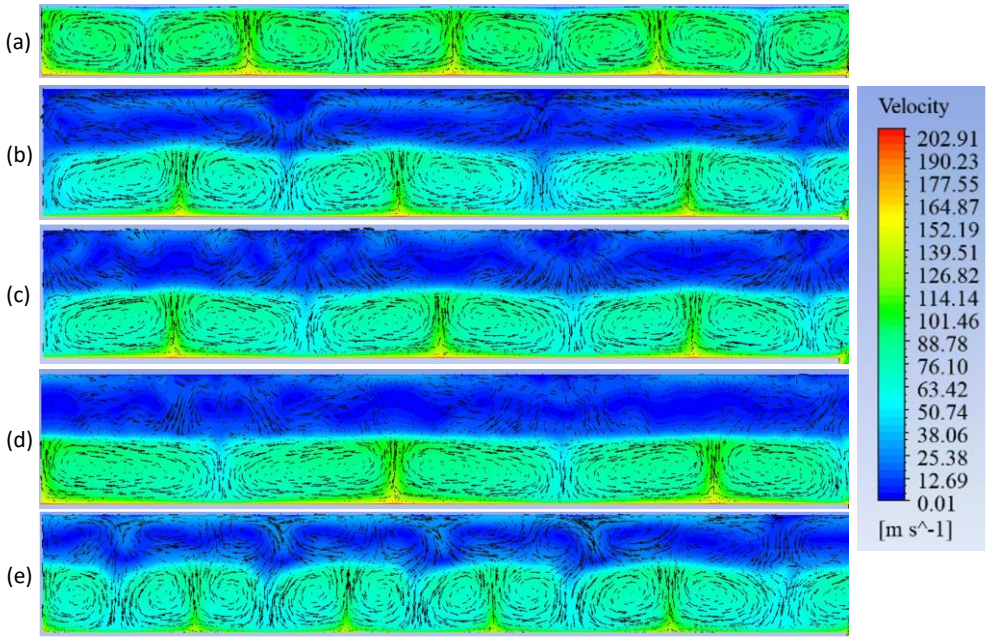

Fig. 6-15 Velocity contour of studied slit wall geometries in Y-Z plane at the rotational velocity of 1600 rad/s (a) no slit wall, (b) triangle, (c) trapezoid, (d) rectangle, and (e) half-ellipse

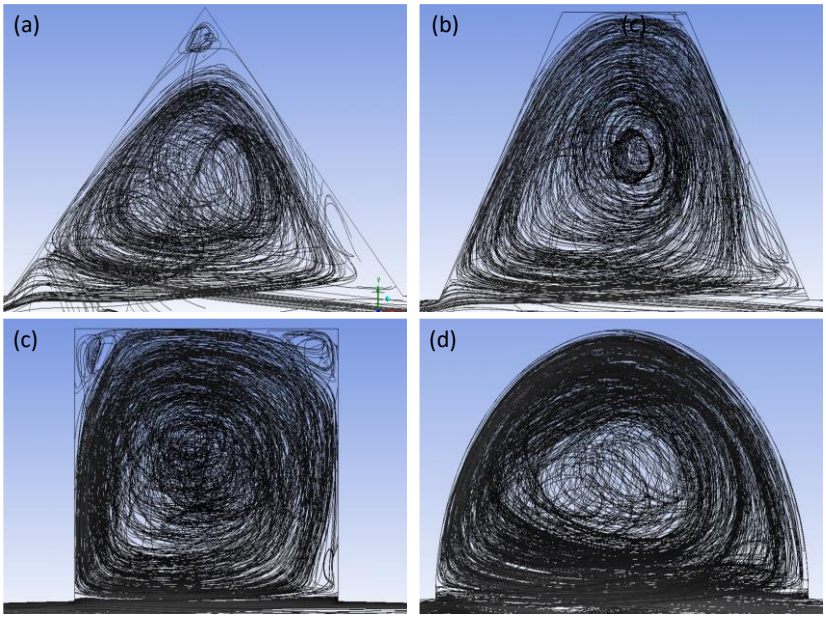

Fig. 6-16 The streamlines distribution at the slit region in the X-Y plane at the rotational velocity of 1600 rad/s (a) triangle, (b) trapezoid, (c) rectangle, and (d) half-ellipse

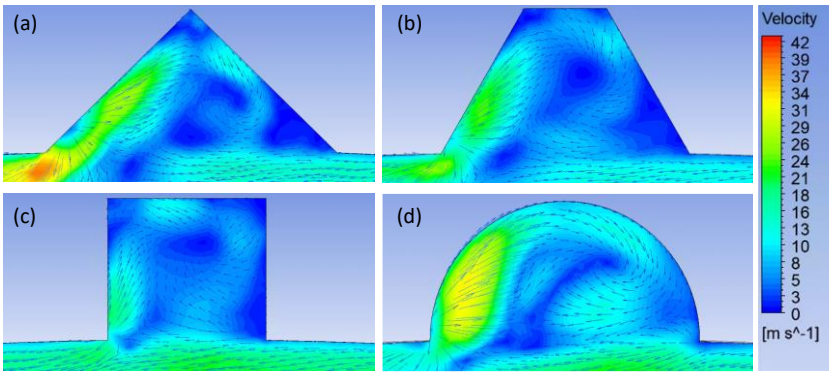

Fig. 6-17 Velocity contour of studied slit wall geometries in X-Y plane at the rotational velocity of 1600 rad/s (a) triangle, (b) trapezoid, (c) rectangle, and (d) half-ellipse

6.1.5. Research Findings

The study investigated the impact of varying quantities of slit walls (8, 16, and 24) and their geometric characteristics on the performance of FESS. The inclusion of slit walls, especially when they have the appropriate shape and quantity, can have a substantial effect on the efficiency of the system. According to the study's findings, the optimal number of slit walls is 16. This number effectively balances the reduction of windage losses and the enhancement of heat transfer. The research suggests that trapezoidal and rectangular slit walls are highly efficient in reducing windage losses. Among the two, the rectangular slit wall geometry exhibits the least windage losses when the rotational velocity is at its highest point. Nevertheless, the performance of the system is influenced by the intricate relationship with the half-ellipse slit wall geometry, which necessitates additional investigation. The distinctive configuration of the semi-elliptical slit walls has the potential to redirect air particles towards the rotor,

resulting in heightened skin friction and increased windage losses. The study's findings also indicate the need for additional research, specifically focusing on the trapezoidal, rectangular, and half-ellipse shapes, in order to gain a comprehensive understanding of their impact on improving FESS efficiency.

6.2. RSM Application for Slit Walls Optimisation

Following an initial assessment that establishes the influence of slit walls on FESS performance, the study progresses into a more comprehensive phase. This phase focuses on exploring the intricate interplay between the size, configuration, and geometry of slit walls and their consequent impact on the operational efficiency of FESS. This research undertakes an extensive examination of the effects of slit wall dimensions, configurations, and geometries on FESS. The investigation delves into a multi-dimensional parameter space, examining five pivotal factors: rotational velocity, internal pressure, slit geometry, base length-to-height ratio, and slit wall configuration. Employing Response Surface Methodology (RSM), the study encompasses a series of numerical simulations coupled with detailed data analysis. This methodology is instrumental in explaining the role of various slit geometries in shaping the flow field distribution, enhancing heat transfer, and minimising windage losses within the FESS.

RSM is a statistical technique for examining multifactorial studies using a small number of trials. It is especially useful in dealing with complex scenarios in which several independent variables influence a dependent response. Box-Behnken designs are essential in this context, generating higher-order response surfaces with fewer runs than standard factorial methods. The Box-Behnken design consists of a specific arrangement of twelve intermediate edge nodes and three central nodes that are tailored to fit a quadratic model. This design strategically places points on the mid-segments of the cubic design space's edges, as well as central points, to improve the statistical rigour of the analysis [404].

RSM stands out as a precise and efficient strategy for designing simulations, interpreting data, and refining system performance when it comes to optimising FESS performance within a parameter space. Its use is critical for gaining a thorough understanding of how slit wall geometry influences the formation and intensity of vortices in the slit regions, as well as the implications for flow field distribution, heat transfer, and windage losses. Thus, RSM is critical for determining optimal operational parameters, fostering increased efficiency and reliability in energy system outputs, and emphasising its significance in fluid dynamics and energy system optimisation.

6.2.1. Responses Selection

The system responses are chosen to demonstrate the local form of the response surface by simulating the interaction and effects of the system parameters. They are also used to evaluate the system's strengths and weaknesses, as well as to determine the best system settings. This model investigates two

responses: windage loss and Nusselt number. Nusselt number is critical for quantifying convective heat transfer within the airgap and determining its sensitivity to various design parameters. An increase in the Nusselt number improves convection-based heat transfer, which has the dual benefit of lowering rotor temperature and reducing reliance on internal cooling apparatuses. This thermal regulation allows for faster rotational speeds, potentially increasing the system's kinetic energy storage capacity. Concurrently, windage loss emerges as a determinant in quantifying the frictional losses within an FESS, having a direct influence on the system's self-discharge rate. The study aims to optimise the FESS's operational efficiency and energy conservation capabilities by analysing these parameters, highlighting critical areas for future research and development in energy storage systems.

6.2.2. Factors Selection

This study integrated slit walls into the FESS housing, focusing on enhancing the system's efficiency. The initial phase of the study assessed four distinct slit shapes: triangle, rectangle, trapezoid, and half-ellipse. Notably, the triangular shape was observed to generate substantial dead zones with stagnant flow, adversely affecting heat transfer performance. Conversely, the reversed trapezoid demonstrated promising results in directing airflow, leading to its selection as a replacement for the triangle shape in subsequent analyses.

The slit walls, featuring diverse cross-sectional geometries including rectangle, trapezoid, reversed trapezoid, and half-ellipse, are designed to optimise the FESS. The crucial aim is to strategically modify the internal structure of the housing to minimise windage losses while maximising heat transfer efficiency. To ensure uniformity and facilitate precise comparative evaluations, the slit wall area is maintained constant across all designs. Initial findings indicated that the most effective number of slit walls is 16. This quantity strikes an optimal balance, concurrently reducing windage losses and augmenting heat transfer. Therefore, this configuration, comprising 16 slit walls, is adopted across all designs in this comprehensive study.

The study investigated a range of parameters, thoroughly investigating the impact of various elements on FESS performance. The rotor's rotational velocity, internal pressure, slit wall geometry, the base length-to-height ratio (B/C) of the slits, slit direction, and slit wall configuration are all considered in this study. Fig. 6-18 presents cross-sectional views of the slit walls across four distinct slit configurations. To standardise the heat transfer area across the different models under examination, the dimensions of the slit structures are dictated by the geometric parameters detailed in Table 6-2, thereby maintaining the heat transfer region. Table 6-3 details the study's continuous factors and their respective levels, expressed in both actual and coded values. The upper and lower limits of the factors are encoded as +1 and -1, respectively, with 0 representing the intermediate level [404]. Table 6-4 and Fig. 6-18 show the categorical factors used in the analysis at the same time.

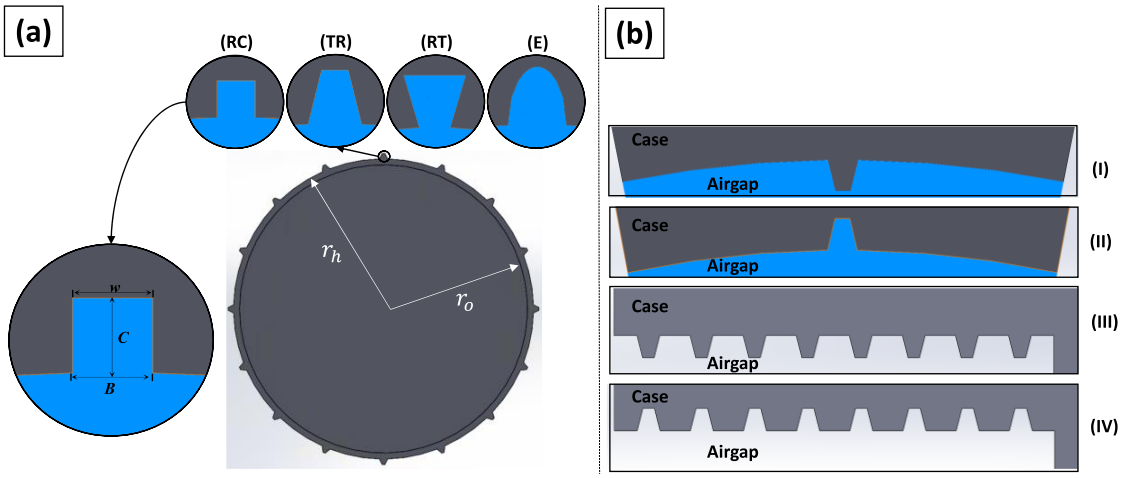

Fig. 6-18 The geometries for the slit designs, (a) different slit cross sections, (b) different slit orientation and direction.

Table 6-2 Slit walls geometrical parameters

Model	Shape	Base length B (mm)	Height C (mm)	Top length w (mm)	B/C
RC	Rectangle	2.24	4.47	2.24	0.5
		3.16	3.16	3.16	1
		3.87	2.58	3.87	1.5
TR	Trapezoid	2.58	5.16	1.29	0.5
		3.65	3.65	1.83	1
		4.47	2.98	2.24	1.5
RT	Reversed trapezoid	1.83	3.65	3.65	0.5
		2.58	2.58	5.16	1
		3.16	2.11	6.32	1.5
E	Half-ellipse	2.52	5.05	-	0.5
		3.57	3.57	-	1
		4.37	2.91	-	1.5

Table 6-3 The continuous factors and their levels

Parameters	**Levels**		
	Lower level (-1)	**Intermediate level (0)**	**Higher level (+1)**
A: Base Length-to-Height Ratio (B/C)	0.5	1	1.5
B: Rotational velocity (rad/s)	1200	1800	2400
C: Pressure (bar)	0.2	0.6	1

Table 6-4 The categorical factors and their levels

Parameters	Levels			
D: Modification direction	Radial	Axial		
E: Modification configuration	Grooved inside the case	Inserted into the case		
F: Modification shape	Rectangle (RC)	Trapezoid (TR)	Reversed trapezoid (RT)	Half-ellipse (E)

6.2.3. Responses

The windage loss and the Nusselt number were subjected to a thorough ANOVA in the study. Tables 6-5 and 6-6 show the results for windage loss and the Nusselt number, highlighting significant factors and their interactions. Both models were statistically significant, as evidenced by F-values of 3304.46 and 335.27 for windage losses and the Nusselt number, respectively. Model terms with P-values less than 0.05 were considered significant, while those with P-values greater than 0.10 were considered insignificant. As shown in Tables 6-5 and 6-6, certain responses were marked as significant, resulting in the exclusion of insignificant factors to improve the model's predictive precision. Furthermore, the F-values for individual factors and their interactions were computed to determine the significance of their mean square variations. Concurrently, relevant P-values were calculated using a 95% confidence interval. The statistical results validate the models' ability to predict windage losses and Nusselt numbers within the numerical variable range.

Table 6-5 Analysis of variance for windage losses

Source	Sum of Squares	df	Mean Square	F-value	p-value
A-B/C	0.0169	1	0.0169	16.95	< 0.0001
B-Rotational Velocity	90.20	1	90.20	90251.21	< 0.0001
C-Pressure	34.11	1	34.11	34126.84	< 0.0001
D-Direction	3.46	1	3.46	3463.11	< 0.0001
E-Design	4.76	1	4.76	4764.50	< 0.0001
F-Shape	0.1309	3	0.0436	43.67	< 0.0001
AD	0.0380	1	0.0380	38.06	< 0.0001
AE	0.0533	1	0.0533	53.31	< 0.0001
AF	0.0113	3	0.0038	3.77	0.0116
BC	0.0515	1	0.0515	51.50	< 0.0001
BD	0.0239	1	0.0239	23.88	< 0.0001
BE	0.0239	1	0.0239	23.87	< 0.0001
CD	0.0212	1	0.0212	21.16	< 0.0001
DE	2.11	1	2.11	2115.57	< 0.0001
DF	0.0127	3	0.0042	4.22	0.0064
EF	0.0327	3	0.0109	10.91	< 0.0001
Residual	0.1969	197	0.0010		
Total	138.90	239			

Table 6-6 Analysis of variance for Nusselt number

Source	Sum of Squares	df	Mean Square	F-value	p-value
A-B/C	0.0524	1	0.0524	201.56	< 0.0001
B-Rotational Velocity	0.3224	1	0.3224	1240.02	< 0.0001
C-Pressure	4.25	1	4.25	16345.26	< 0.0001
D-Direction	0.0047	1	0.0047	18.11	< 0.0001
E-Design	0.2312	1	0.2312	889.28	< 0.0001
F-Shape	0.0986	3	0.0329	126.37	< 0.0001
AC	0.0008	1	0.0008	3.16	0.0772
AD	0.0013	1	0.0013	4.86	0.0288
AE	0.0015	1	0.0015	5.60	0.0191
AF	0.0204	3	0.0068	26.20	< 0.0001
BC	0.1900	1	0.1900	730.84	< 0.0001
BD	0.0339	1	0.0339	130.25	< 0.0001
BE	0.0543	1	0.0543	209.00	< 0.0001
BF	0.0026	3	0.0009	3.29	0.0222
CD	0.0177	1	0.0177	67.96	< 0.0001
CE	0.0320	1	0.0320	123.19	< 0.0001
DE	0.4278	1	0.4278	1645.77	< 0.0001
DF	0.0287	3	0.0096	36.85	< 0.0001
EF	0.0159	3	0.0053	20.43	< 0.0001
Residual	0.0434	167	0.0003		
Total	6.32	239			

6.2.3.1. Model Adequacy

In regression analysis, the mathematical model serves to articulate the correlation between input variables and dependent responses. The fit statistics for the preliminary response, delineated in Table 6-7, exhibit a robust coefficient of determination (R^2) exceeding 0.98, signifying minimal discrepancy between the regression model and actual response data points. Furthermore, the adjusted R^2 values, refined to exclude unessential parameters, remain superior to 0.98, underscoring minimal data variability. The model's predictive ability for new observations is evaluated via the predicted R^2 value. A marginal deviation of 0.2 from the adjusted R^2 underscores a praiseworthy model correlation.

Table 6-7 The fit statistics for the studied responses

First Response	**Std. Dev.**	0.0316	**R^2**	0.9986
	Mean	6.63	**Adjusted R^2**	0.9983
	C.V. %	0.4771	**Predicted R^2**	0.9979
			Adequate Precision	247.264
Second Response	**Std. Dev.**	0.0161	**R^2**	0.9931
	Mean	1.58	**Adjusted R^2**	0.9902
	C.V. %	1.02	**Predicted R^2**	0.9833
			Adequate Precision	75.255

6.2.4. Fluid Flow Characteristics

As the rotational velocity of a FESS increases, the Taylor-Couette vortices that form within the air gap become more pronounced. These vortices arise due to the relative motion of the inner and outer cylinders of the FESS. Their formation is influenced by various factors, including air gap size, rotational velocity, and fluid properties within the air gap. At low rotational velocities, the Taylor-Couette vortices may be relatively weak and less pronounced; however, as the velocity increases, vortices become more turbulent and intense, as shown in Fig. 6-19. This has several effects on the overall performance of a FESS, including increased windage losses and reduced heat transfer rate. One of the primary ways that slit walls can affect the Taylor-Couette vortices is by disrupting the flow within the air gap. By introducing these barriers, the fluid within the air gap must navigate around the slit wall profile, which can alter the flow pattern and affect the intensity of the vortices, as shown in Fig. 6-20.

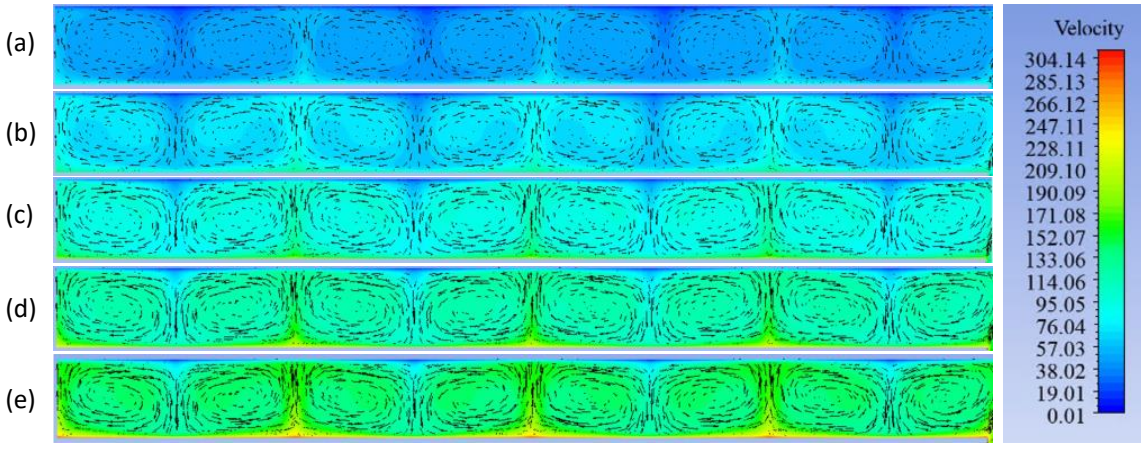

Fig. 6-19 Velocity contour of the FESS with no slits under 1 bar pressure at the rotational velocity of (a) 800 rad/s, (b) 1200 rad/s, (c) 1600 rad/s, (d) 2000 rad/s, and (e)2400 rad/s

During fluid flow through the annular gap, interactions with the boundary walls commence due to the combined effects of inertial forces and boundary layer separation. Such interactions consequently lead

to the formation of complex vortex formations. The shape and structure of these vortices are governed by parameters D and E. One of the primary factors affecting the occurrence of Taylor vortices is the airgap between the concentric cylinders. A diminished airgap is associated with a surge in the number of Taylor vortices, which in turn significantly impacts the skin friction coefficient, resulting in increased windage losses. Taylor vortices appear more frequently as the airgap increases, while Taylor cells are less rapidly affected by azimuth waves as the airgap reduces [377]. It is crucial to note that even though the airgap dimension is consistent across all examined configurations, configurations with inserted slits, as opposed to grooved ones, effectively present narrower airgaps. This encourages a higher occurrence of Taylor vortices. Among the configurations studied, the axial/grooved setup produces the fewest Taylor vortices. In contrast, the radial/inserted configuration exhibits the most, as illustrated in Fig. 6-20.

In the axial-inserted configuration, while the number of Taylor cells is not the highest, the slit disrupts the smooth flow of air. This deflection causes some air particles to be directed towards the rotor, leading to a significant rise in the skin friction coefficient, as depicted in Fig. 6-21. For the axial direction, a deviation in velocity streamlines can be observed when compared to the more direct radial direction. When the slit is grooved, air is channelled into the slit, resulting in minor toroidal vortices. These vortices have a marginal impact on redirecting air particles to the rotor. Conversely, with an inserted slit, a pronounced backflow effect is evident. The velocity streamlines are deflected upon encountering the slit, with a portion being directed towards the rotor. This phenomenon, in turn, contributes to an increased skin friction coefficient.

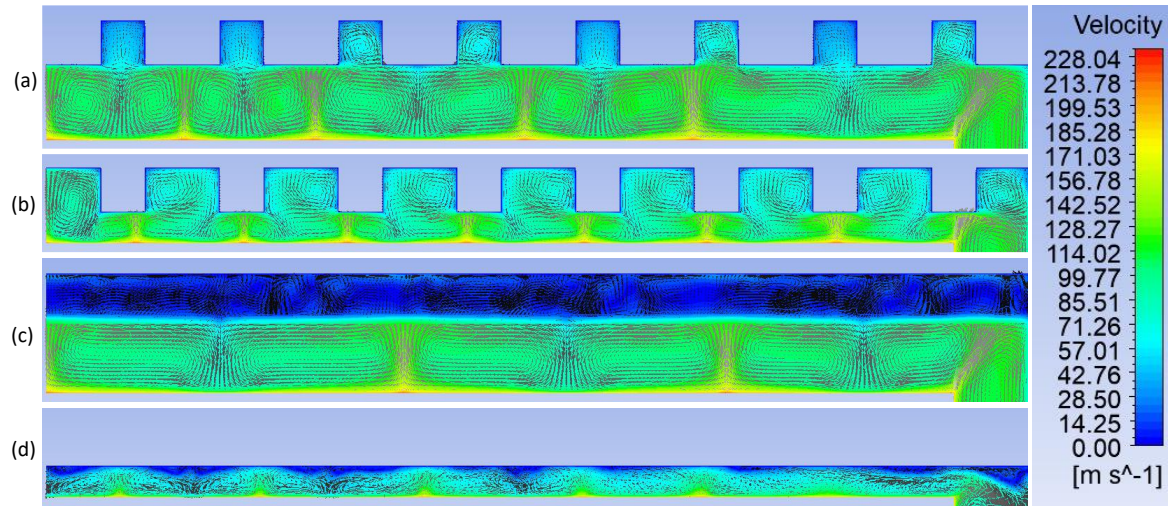

Fig. 6-20 Velocity contour of the FESS in Y-Z plane for rectangle shape under 1 bar pressure and rotational velocity of 1600 rad/s as a function of factors D and E where: (a) radial/grooved, (b) radial/inserted, (c) axial/grooved, and (d) axial/inserted

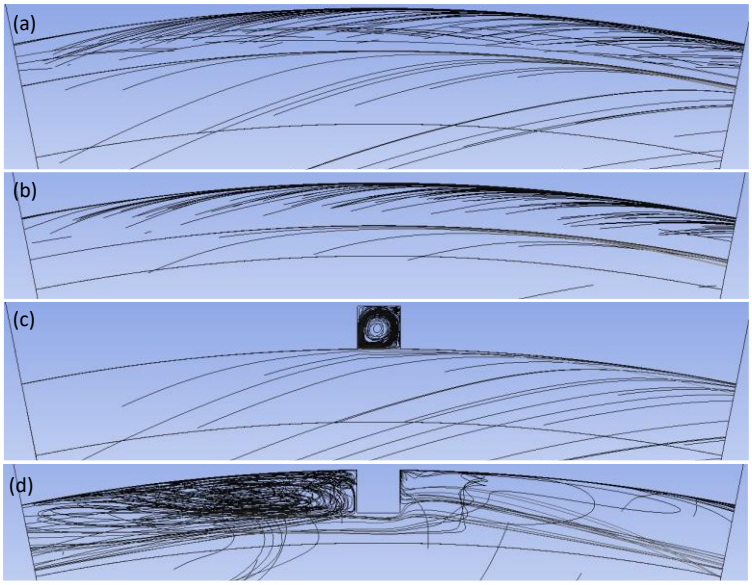

Fig. 6-21 The streamlines distribution of the FESS in X-Y plane for rectangle shape under 1 bar pressure and rotational velocity of 1600 rad/s as a function of factors D and E where: (a) radial/grooved, (b) radial/inserted, (c) axial/grooved, and (d) axial/inserted

6.2.5. Windage Losses Response

Windage losses arise from the viscous friction between the rotor and the surrounding fluid during the flywheel's rotation. Factors such as the rotational speed and the thermo-physical properties of the enclosed fluid play a significant role in determining these losses. An analysis has been conducted on the impact of rotational speed on windage losses across various examined scenarios. As the rotational speed escalates, there is an alteration in the air velocity distribution. This is attributed to the Taylor number surpassing its critical threshold of 41.3, resulting in the formation of Taylor vortices.

Fig 6-22 provides a comprehensive representation of windage losses corresponding to the rectangular slit shape, emphasising the interplay between the Base Length-to-Height Ratio (B/C) and the pressure within the cavity. A consistent decline in windage losses is observed with decreasing pressure, irrespective of the modification direction or configuration of the slit shape. Furthermore, an augmentation in the B/C ratio notably diminishes the windage losses, a trend particularly pronounced when the configuration adopts an inserted approach as opposed to a grooved one, as evidenced in Fig. 6-22 (b) and (d). However, the influence of increasing the B/C ratio is less prominent in a grooved configuration. Remarkably, the minimal windage losses were associated with an axial direction combined with a grooved configuration. In contrast, the maximal windage losses were linked to an axial direction paired with an inserted configuration.

In a radial direction, the air flows coherently with the Taylor vortices, leading to a reduced skin friction coefficient, as the number of Taylor vortices would be the significant contributor. This, in turn, results in a decreased rotor temperature and consequently lower windage losses. Conversely, the grooved

configuration promotes enhanced heat transfer, ensuring the rotor's temperature remains lower than in the inserted configuration. The inserted setup detrimentally impacts the skin friction coefficient, primarily due to the amplified Taylor vortices when employing this configuration. This amplification is influenced by the decreased airgap adjacent to the rotor. As the airgap diminishes, there's a notable rise in the number of Taylor vortices. Notably, the size of the Taylor cells closely matches the dimensions of the airgap.

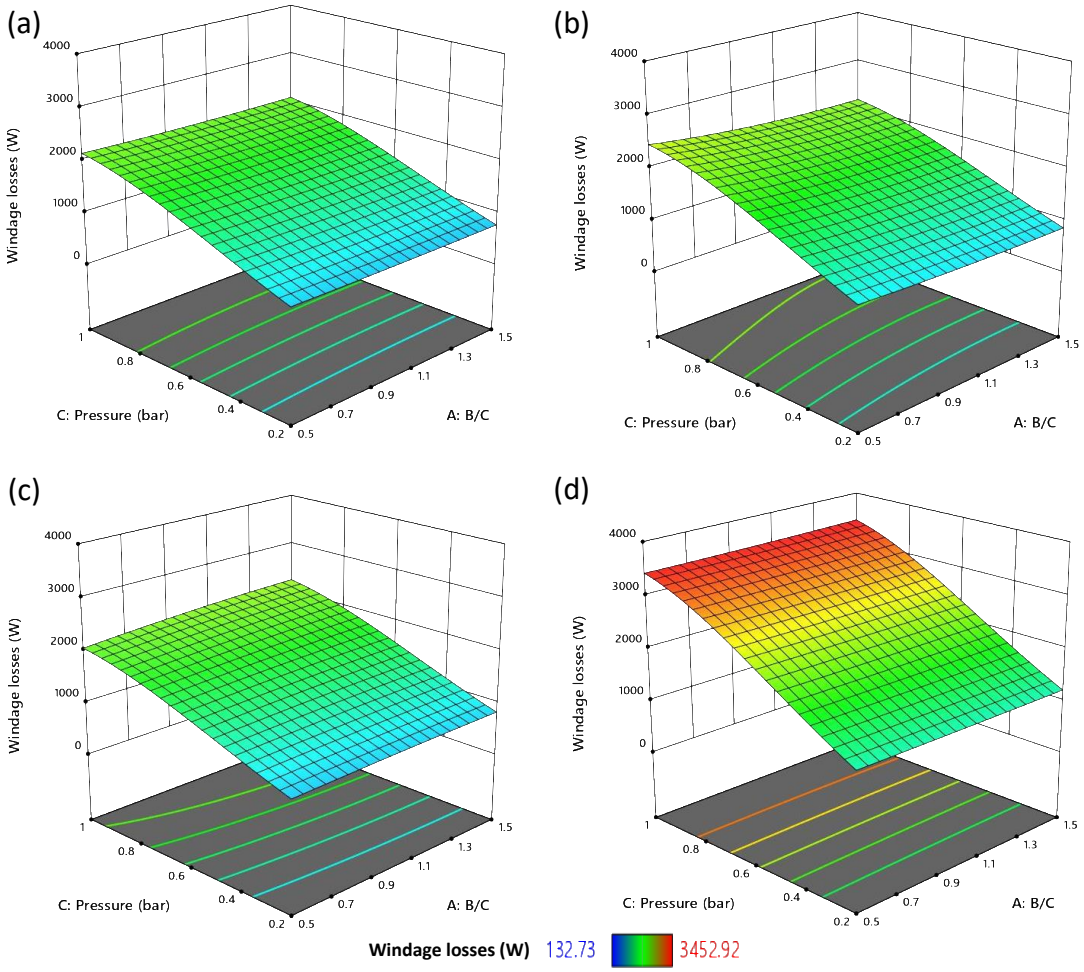

Fig. 6-22 3D plot of windage losses for a rectangle shape as a function of factors D and E where: (a) radial/grooved, (b) radial/inserted, (c) axial/grooved, and (d) axial/inserted

In the context of the trapezoid slit shape, Fig. 6-23 illustrates the windage losses, shedding light on the relationship between the B/C ratio and the cavity pressure. A uniform decrease in windage losses is seen as pressure drops. This reduction in pressure leads to fewer gas particles within the system, a trend observed regardless of the slit's modification direction or design. While elevating the B/C ratio leads to diminished windage losses, its impact is relatively subdued. Specifically, for the inserted configuration, optimal windage losses are observed when the B/C ratio is 1, as demonstrated in Fig. 6-23 (b) and (d). Notably, the least windage losses corresponded with an axial direction paired with a grooved slit design.

In stark contrast, the highest windage losses were attributed to an axial direction in conjunction with an inserted slit configuration.

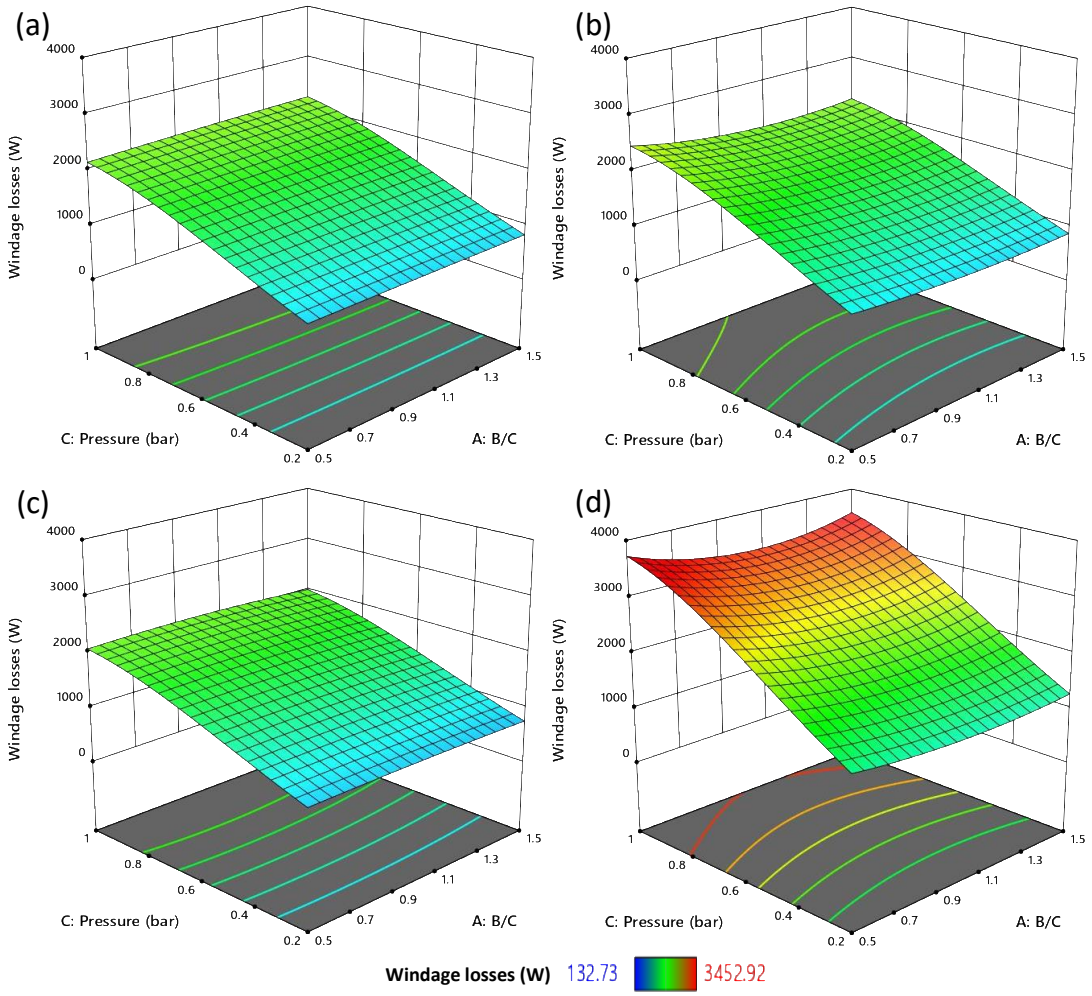

Fig. 6-23 3D plot of windage losses for a trapezoid shape as a function of factors D and E where: (a) radial/grooved, (b) radial/inserted, (c) axial/grooved, and (d) axial/inserted

For a reversed trapezoid slit shape, the impact of the B/C ratio mirrors that of the rectangle shape. An increase in the B/C ratio significantly reduces the windage losses, as shown in Fig. 6-24. This trend becomes especially marked when the slit employs an inserted design rather than a grooved one. At the maximum analysed pressure, the lowest windage losses were observed in the radial grooved configuration with a B/C ratio of 1. Conversely, at the same ratio and pressure, the axial inserted configuration recorded the highest windage losses.

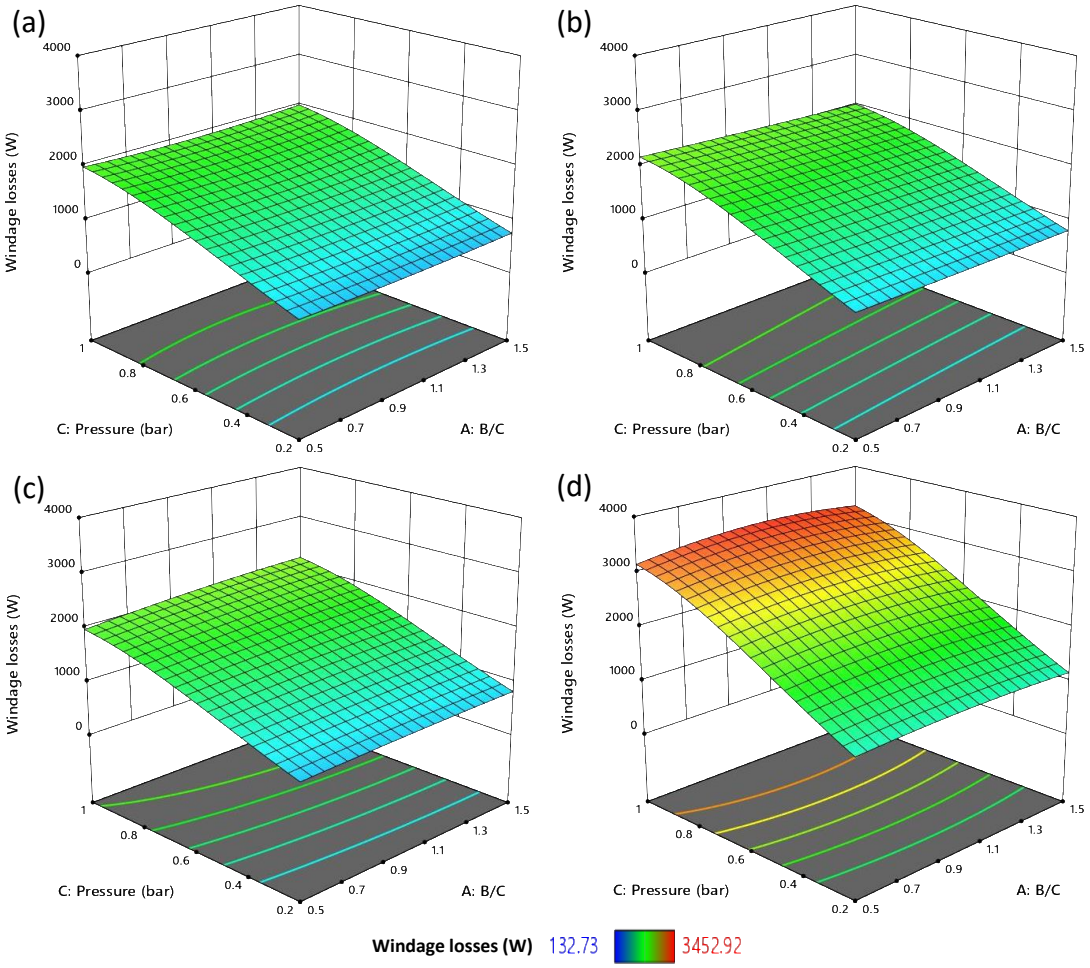

Fig. 6-24 3D plot of windage losses for a reversed trapezoid shape as a function of factors D and E where: (a) radial/grooved, (b) radial/inserted, (c) axial/grooved, and (d) axial/inserted

In Fig. 6-25, windage losses corresponding to the half-ellipse shape are presented. The data indicates a consistent pattern with the effects of decreasing cavity pressure. While the influence of escalating the B/C ratio echoes that of the trapezoid shape, the minimum windage losses are achieved with a ratio of 1 for the axial direction. In contrast, for the radial direction, a ratio of 1.5 records the highest windage losses. Across all examined shapes, the axial/inserted configuration consistently registers the peak windage losses for all evaluated pressures and B/C ratios. The other three configurations, however, exhibit comparable values in close proximity to one another.

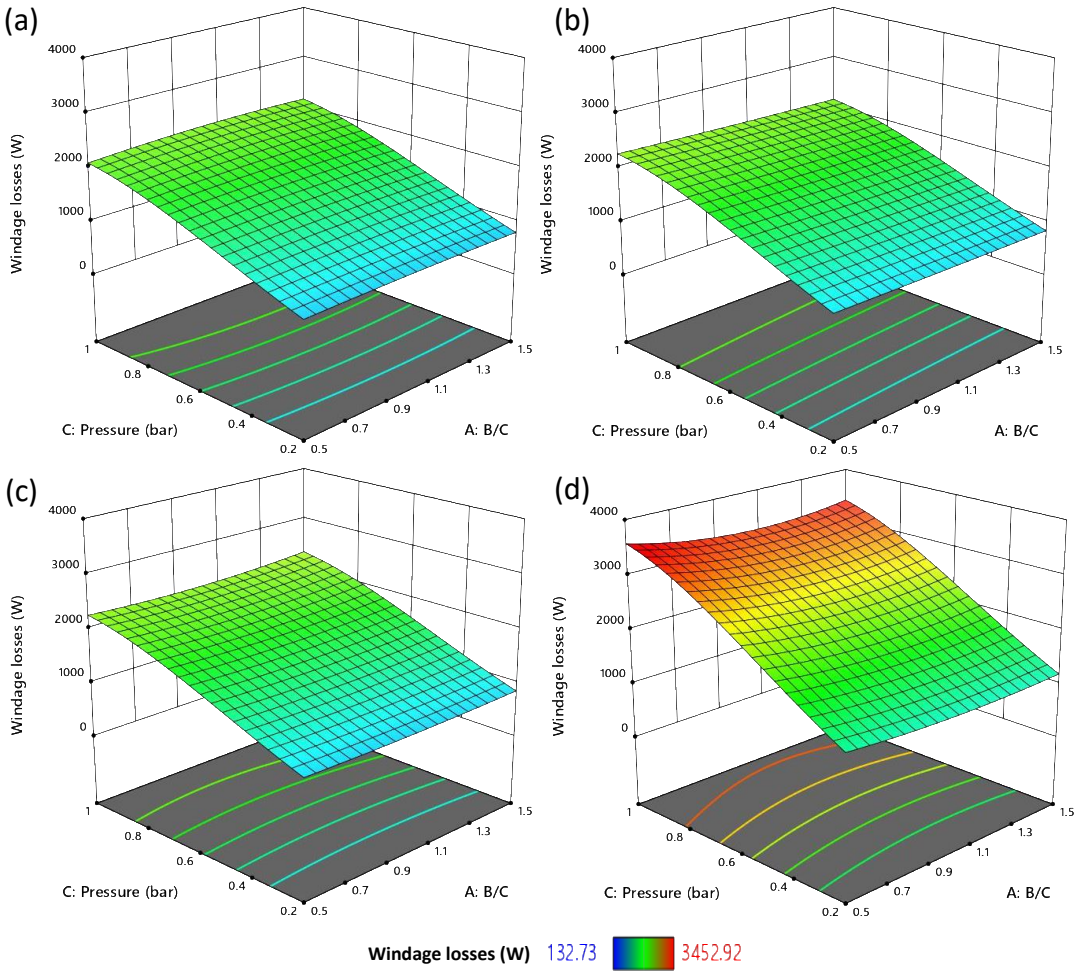

Fig. 6-25 3D plot of windage losses for a half-ellipse shape as a function of factors D and E where: (a) radial/grooved, (b) radial/inserted, (c) axial/grooved, and (d) axial/inserted

The aim to decrease windage losses has been addressed through the analysis of six factors. The investigation has revealed that aligning the base length of a slit with its height optimises its dimensions to effectively reduce aerodynamic drag. Concurrently, diminishing the rotational velocity emerges as a crucial parameter, directly diminishing windage losses by attenuating aerodynamic resistance. Minimising the pressure within the cavity also plays a vital role, substantially lowering the frictional forces acting upon the rotating elements. The strategic orientation of slits in the radial direction is identified to align with the natural flow, thereby minimising turbulence and subsequent energy losses. Additionally, the adoption of a grooved configuration contributes to a more streamlined flow and reduced surface friction. Finally, the study points to specific geometry such as reversed trapezoid as being superior in skin friction coefficient reduction, which in turn facilitates the reduction of windage losses.

6.2.6. Heat Transfer Response

The Nusselt number serves as a critical metric for quantifying the convective heat transfer among the rotor, the air, and the flywheel casing. A heightened Nusselt number suggests more efficient convection, which corresponds to reduced temperatures for both the rotor and the casing while remaining within safety parameters. As depicted in Figs. 6-26 to 6-29, an increase in the B/C ratio correlates with a rise in the Nusselt number across all rotational speeds. Optimal Nusselt numbers for each slit shape were observed in the axial grooved configuration, particularly in the rotational speed range of 1200 to 1600 rad/s. The relationship between the Nusselt and Reynolds numbers is evident, with the latter increasing with rotational speed up to 1600 rad/s. Beyond this speed, the Reynolds number declines, as a result of the decrease in air's kinematic viscosity as the temperature of the air continues to drop.

Fig. 6-26 delineates the Nusselt number trends for the rectangular slit shape, highlighting the interplay between the B/C ratio and the rotor's rotational velocity. An elevated B/C ratio enhances the Nusselt number for all configurations within the rectangular slit model, attributed to a wider base length of the slit, which redirects more airflow into the slit. This redirection facilitates improved mixing of the hot and cold air streams, driven by the presence of Taylor vortices. Taylor-Couette flow, characterised by a spike-shaped flow profile within the airgap, is integral to these dynamics. Here, air velocity is negligible near the casing and peaks near the rotor. Frictional heating between the rotor and air molecules raises the temperature of the air adjacent to the rotor, which is then conveyed upwards toward the casing, elevating the mixed air temperature. This process is intensified by centrifugal forces that increase the velocity of the vortices upon collision.

In the axial/inserted configuration, the Nusselt number is notably lower at all rotational velocities, pressures, and B/C ratios, a consequence of airflow disruption caused by redirected flow streamlines. This creates a high-pressure zone before the slit and a low-pressure zone after, as compared to other configurations (referenced in Fig. 6-21 and 6-29). Disruption from the inserted slit creates backflow, altering velocity streamlines and creating low-pressure zones that negatively impact heat transfer. In contrast, the radial direction aligns with Taylor vortices, and a grooved configuration fosters improved heat transfer, resulting in lower rotor temperatures and a higher Nusselt number, thereby enhancing convective heat transfer efficiency. When the slit is grooved, air is channelled into the slit, resulting in small toroidal vortices. These vortices have a good impact on remixing the hot and cold temperatures of the air.

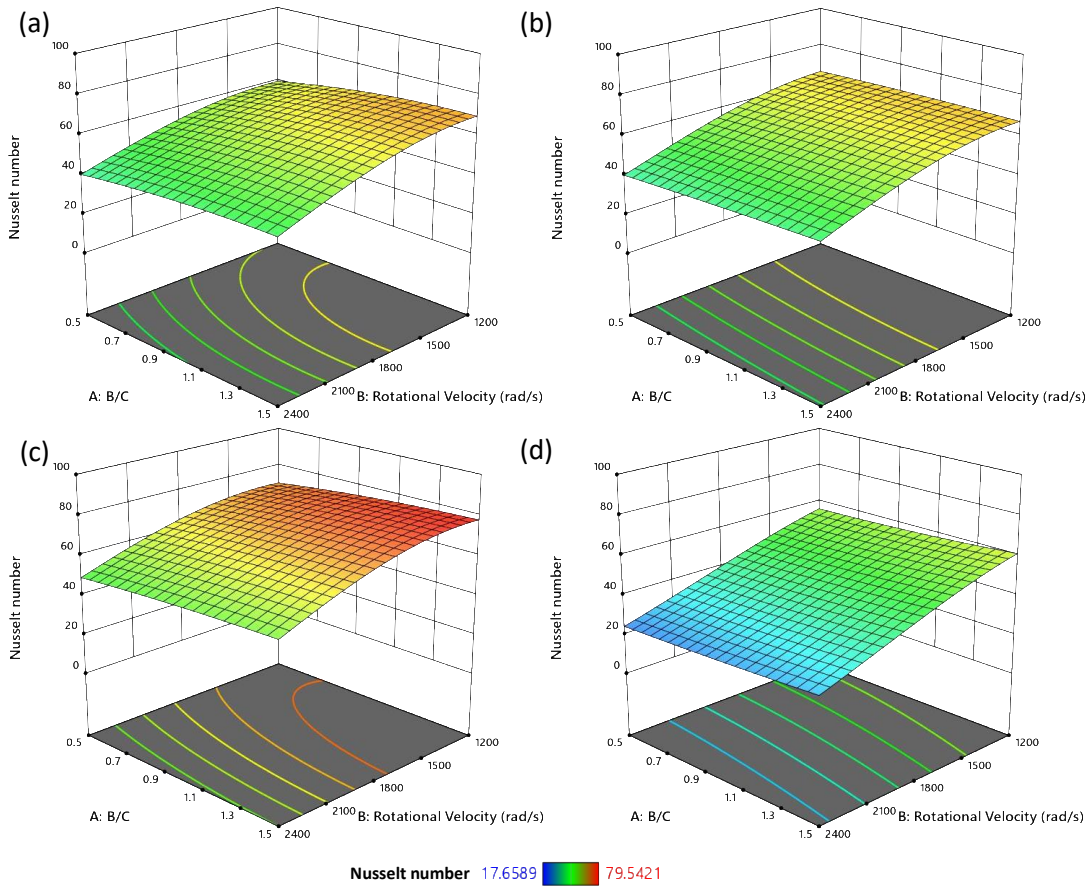

Fig. 6-26 3D plot of Nusselt number for a rectangle shape as a function of factors D and E where: (a) radial/grooved, (b) radial/inserted, (c) axial/grooved, and (d) axial/inserted

Regarding the trapezoid slit shape, the observed pattern is consistent with that of the rectangular slit shape, as illustrated in Fig. 6-27. Within the inserted configuration, there is a direct reduction in the Nusselt number with an increase in rotational velocity. Conversely, in the grooved configuration, the Nusselt number remains relatively stable within the rotational velocity range of 1200 to 1600 rad/s. Conversely, the reversed trapezoid shape demonstrates a lower overall Nusselt number compared to the rectangle and trapezoid shapes. The influence of the B/C ratio on the Nusselt number is less pronounced for the reversed trapezoid than for the previous shapes. Additionally, an increase in rotational velocity leads to a decrease in the Nusselt number across all configurations examined, a trend that is depicted in Fig. 6-28.

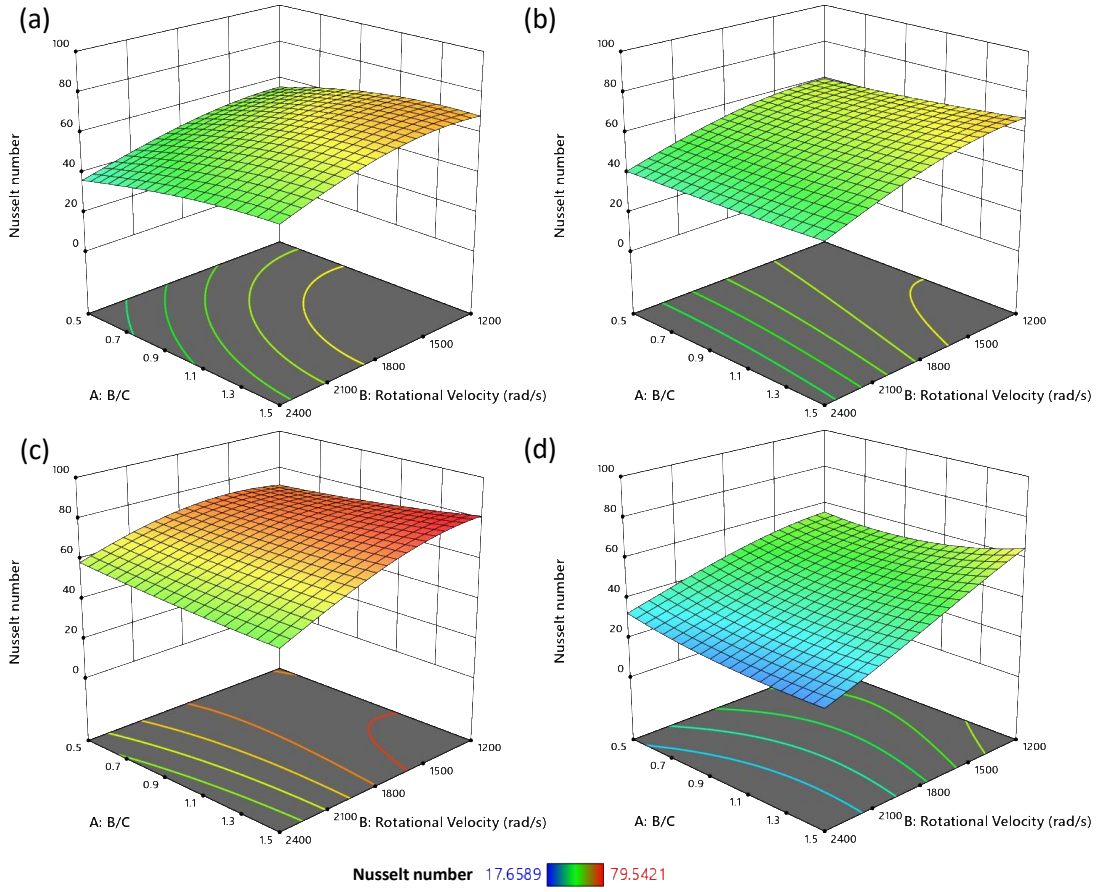

Fig. 6-27 3D plot of Nusselt number for a trapezoid shape as a function of factors D and E where: (a) radial/grooved, (b) radial/inserted, (c) axial/grooved, and (d) axial/inserted

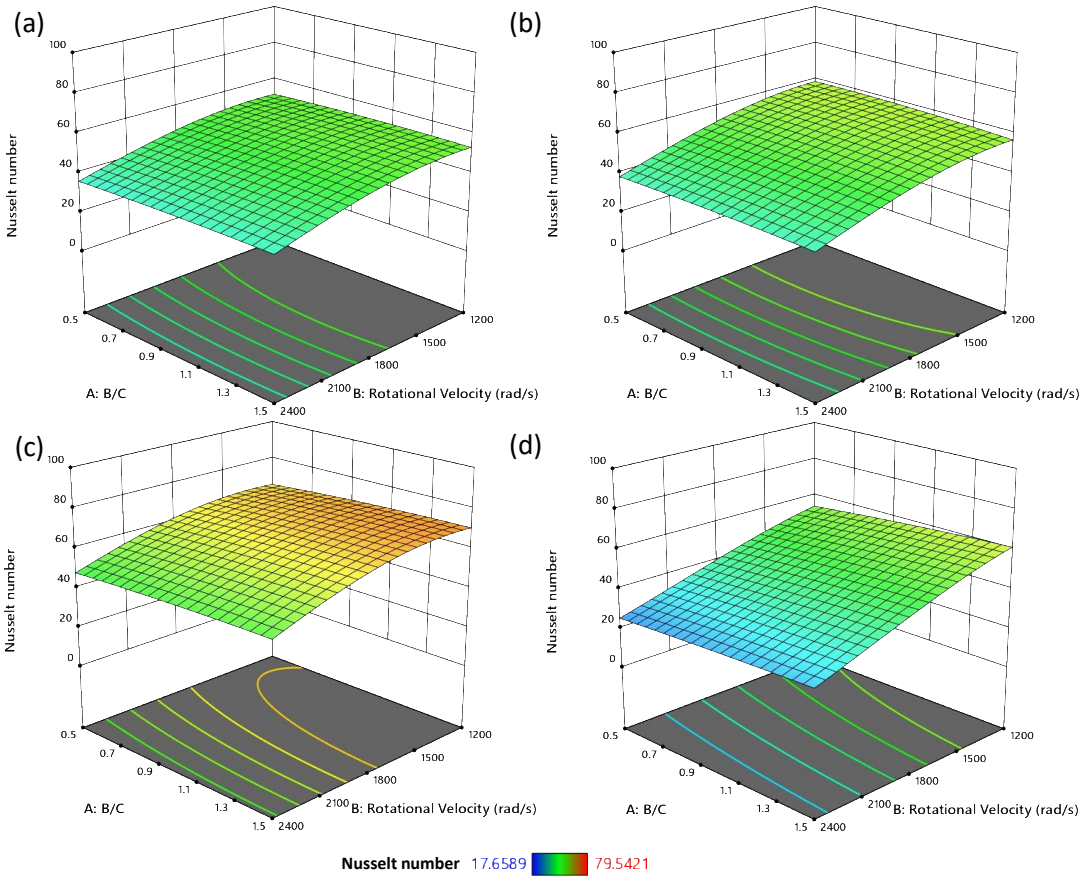

Fig. 6-28 3D plot of Nusselt number for a reversed-trapezoid shape as a function of factors D and E where: (a) radial/grooved, (b) radial/inserted, (c) axial/grooved, and (d) axial/inserted

With an increase in the B/C ratio, there is a marked alteration in the velocity streamlines of the air particles. At the highest B/C ratio under study, the airflow impacts the slit, redirecting the particles and consequently generating a high-pressure zone in front of the slit and a low-pressure zone behind it, as depicted in Fig. 6-29. When the B/C ratio is set at 0.5, the airflow remains in proximity to the rotor, a condition that is not conducive to the formation of Taylor vortices, as observed in Fig. 6-30 (a). The absence of Taylor vortices correlates with a significantly lower Nusselt number, indicating minimal thermal mixing between the rotor and the casing post-slit. However, as the B/C ratio is increased, the airflow streamlines are deflected towards the casing more rapidly, facilitating the development of Taylor vortices as illustrated in Fig. 6-30. The presence of these vortices, which are inherently undulating, leads to the emergence of several secondary vortices. These dynamics contribute to the complex flow pattern and the enhancement of convective heat transfer, as indicated by the variability in the Nusselt number.

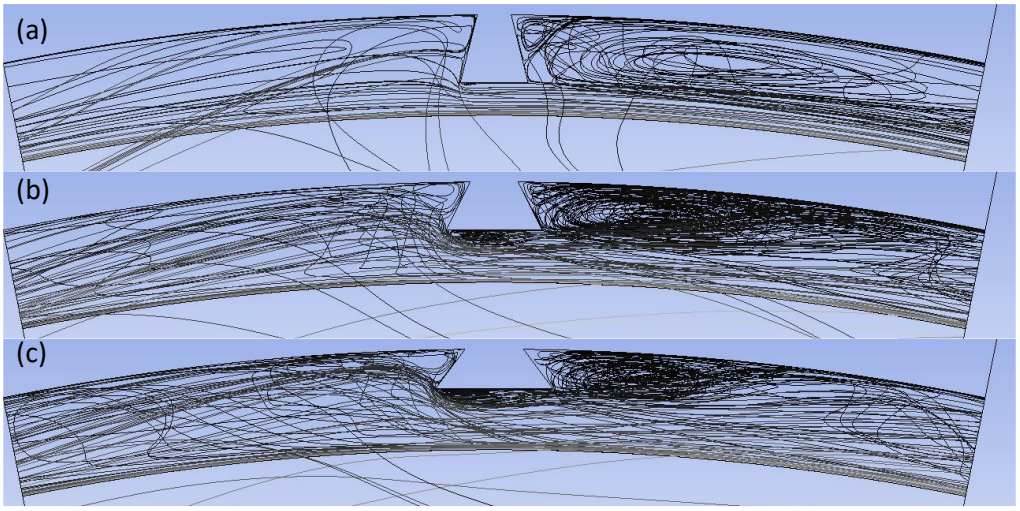

Fig. 6-29 The streamlines distribution of the FESS in X-Y plane for reversed trapezoid axial/inserted configuration under 1 bar pressure and rotational velocity of 1600 rad/s as a function of B/C ratio where: (a) 0.5, (b) 1, and (c) 1.5

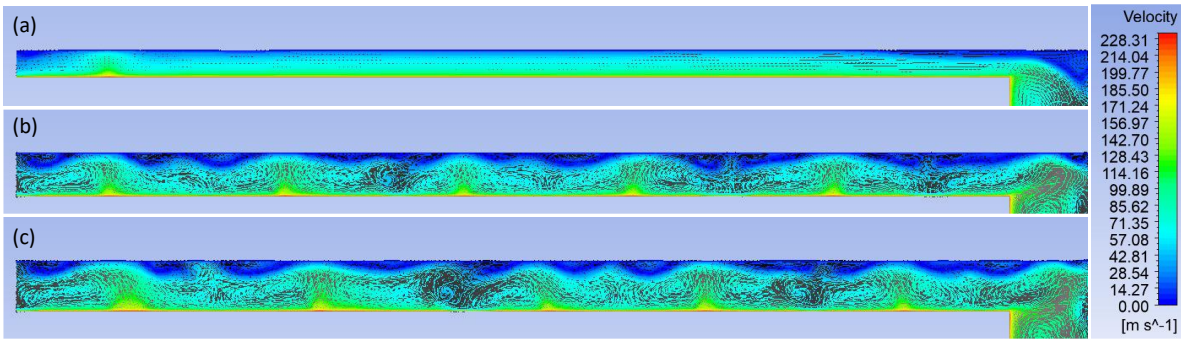

Fig. 6-30 Velocity contour of the FESS in Y-Z plane for reversed trapezoid shape under 1 bar pressure and rotational velocity of 1600 rad/s as a function of B/C ratio where: (a) 0.5, (b) 1, and (c) 1.5

The half-ellipse shape exhibits a superior Nusselt number relative to the other shapes assessed in each specific configuration, as evidenced in Fig. 6-31. The impact of the B/C ratio is most pronounced with this shape; an increase in the ratio correspondingly amplifies the Nusselt number more significantly than with other shapes under consideration. Fig. 6-32 portrays that as the fluid navigates the annular gap, it encounters the slit walls. This interaction, influenced by inertial forces and boundary layer separation, instigates the development of small-scale vortex structures. Upon analysing the streamline patterns of the four models within the slit region, it becomes clear that these vortex structures centralise within the slit area across all models. Specifically for the half-ellipse shape, a vortex envelops the entire grooved slit, in contrast to the other shapes where "flow dead zones" are identified. These zones are indicative of diminished heat transfer capabilities, thus resulting in significantly lower Nusselt numbers. Flow dead zones are characterised by relatively isolated low-speed vortices that hinder mass exchange with the main flow in the slit, fostering the formation of a thin boundary layer.

As delineated in Fig. 6-33, the mainstream fluid's collision with the wall on the slit's left side generates a region of high velocity, fostering enhanced mixing and heat exchange between the differing temperature fluids. Within the slit, the fluid's velocity progressively declines along the vortex's rotational direction due to the viscous and friction forces exerted by the wall. Consequently, this creates a low-velocity region along the right wall of the slit where the mixing effect is diminished, leading to the formation of a cooler temperature zone. The extent of the high-velocity region is notably larger in the half-ellipse model than in others. This observation can be ascribed to the model's unique geometrical characteristics, which facilitate greater fluid-wall interaction, thus bolstering the mixing and heat transfer processes between the fluids.

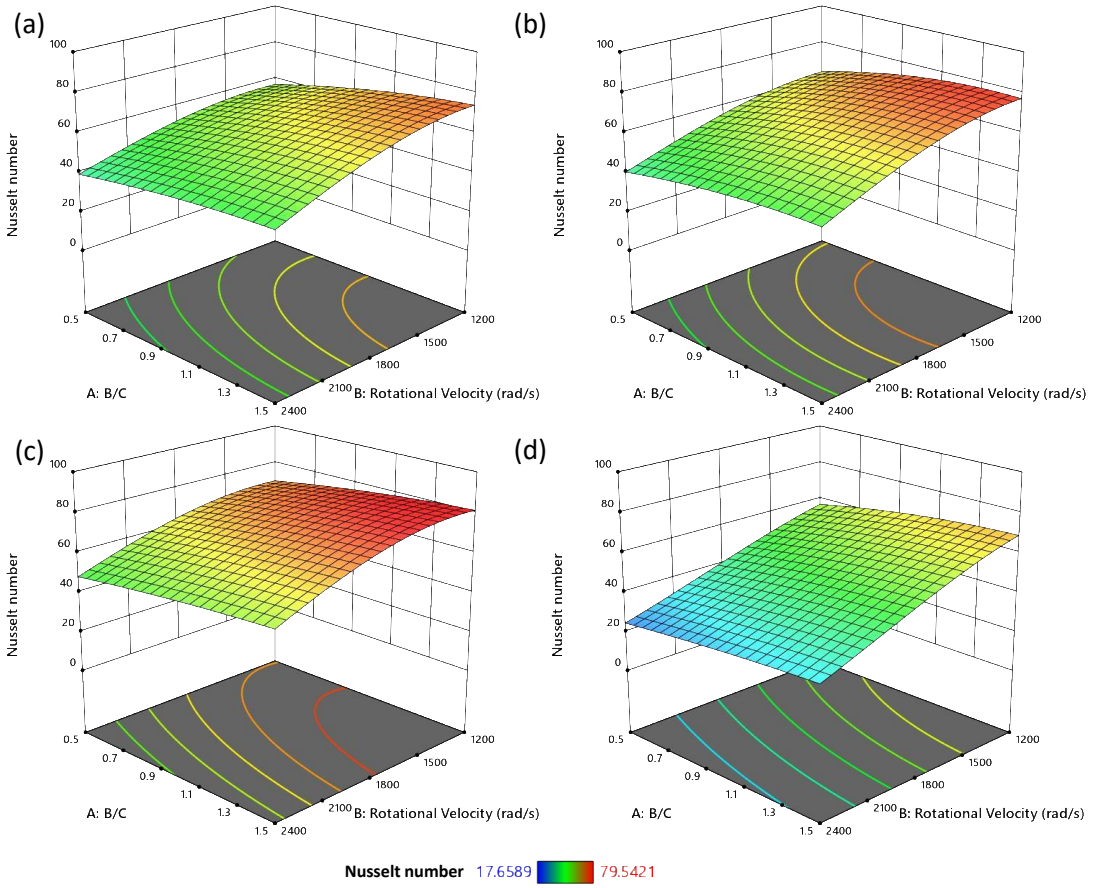

Fig. 6-31 3D plot of Nusselt number for a half-ellipse shape as a function of factors D and E where: (a) radial/grooved, (b) radial/inserted, (c) axial/grooved, and (d) axial/inserted

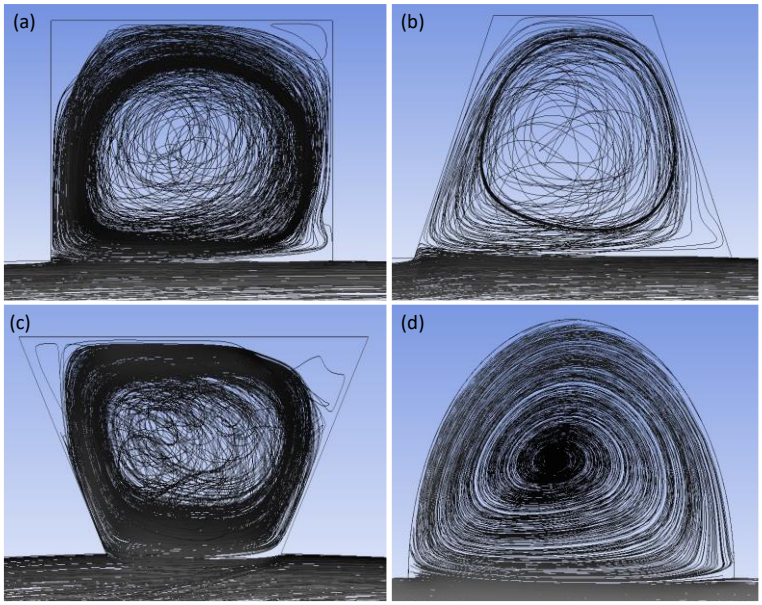

Fig. 6-32 The streamlines distribution of the FESS in the X-Y plane for the axial/grooved configuration under 1 bar pressure and rotational velocity of 1600 rad/s for: (a) rectangle, (b) trapezoid, (c) reversed trapezoid, and (d) half-ellipse

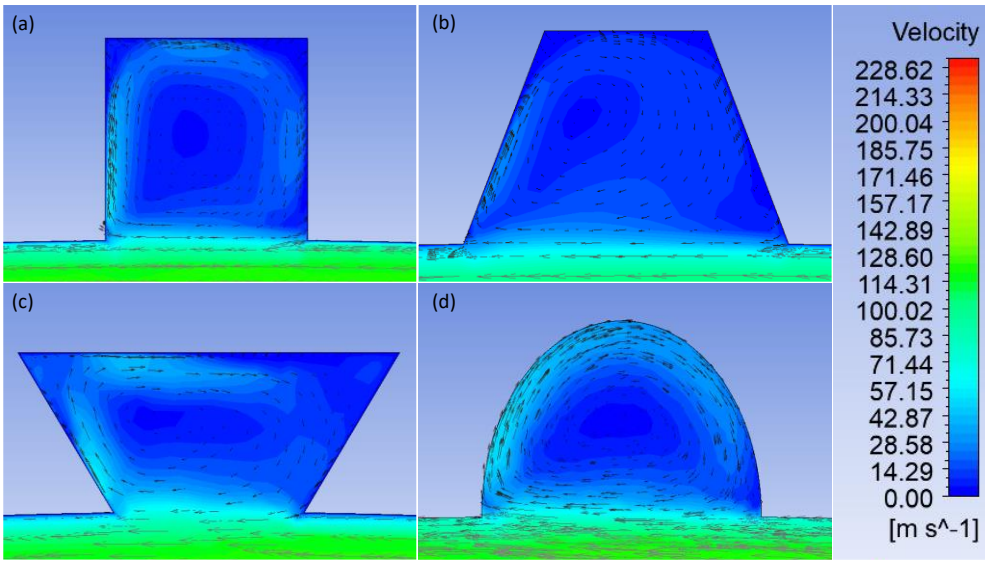

Fig. 6-33 Velocity contour of the FESS in X-Y plane for the axial/grooved configuration under 1 bar pressure and rotational velocity of 1600 rad/s for: (a) rectangle, (b) trapezoid, (c) reversed trapezoid, and (d) half-ellipse

Fig. 6-34 depicts the velocity contour within the air gap that lies between the rotor and the housing along the Y-Z plane, characterised by a half-ellipse geometric configuration. The illustration indicates a progressive decrease in the number of Taylor vortices with the transition through various configurations: from (a) radial/grooved to (b) radial/inserted, followed by (c) axial/grooved, and ending in (d) axial/inserted. In the axial/inserted configuration, the formation of Taylor vortices is notably absent. This absence is attributed to the disruptive influence of the slit, which induces a backflow effect,

effectively hindering the creation of Taylor vortices. Contrastingly, within the radial/inserted configuration, the presence and quantity of slits play a significant role in determining the number of Taylor vortices. These vortices are confined to the regions between slits, with the slits effectively acting as barriers that prevent the formation of secondary vortices in the spaces immediately adjacent to the rotor. This phenomenon underscores the intricate relationship between structural features and the fluid dynamics within the system.

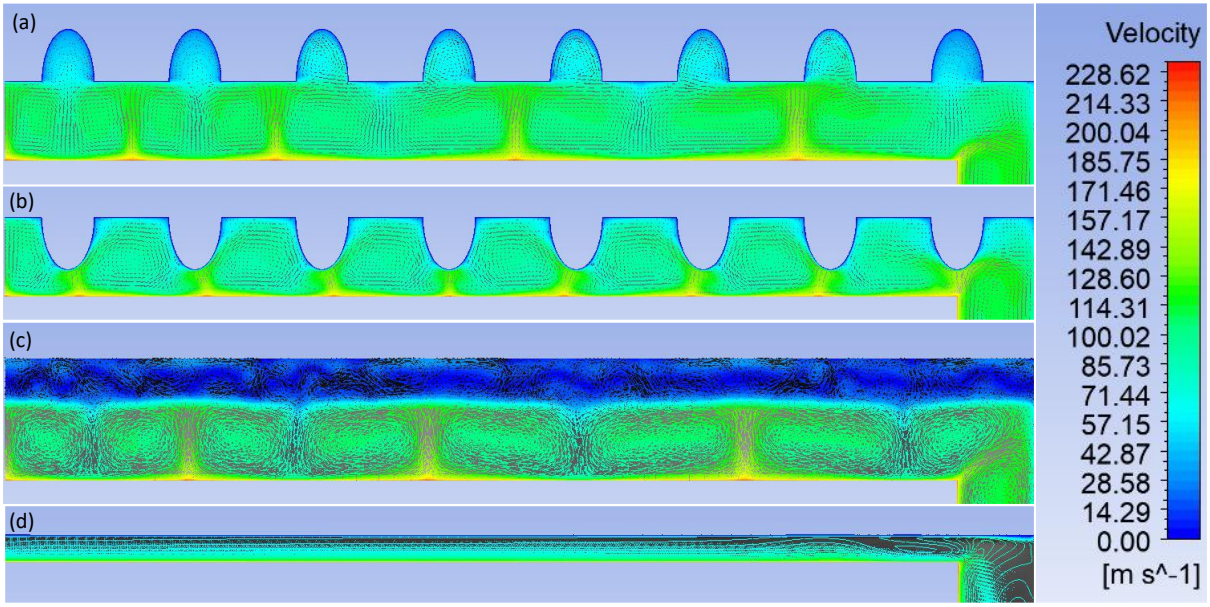

Fig. 6-34 Velocity contour of the FESS in Y-Z plane for half-ellipse shape under 1 bar pressure and rotational velocity of 1600 rad/s as a function of factors D and E where: (a) radial/grooved, (b) radial/inserted, (c) axial/grooved, and (d) axial/inserted

Fig. 6-35 presents the velocity contours for the radial grooved configuration across all studied geometries. It is observed that each slit shape fosters the formation of either secondary vortices within it or permits a segment of the primary vortices to penetrate the slit. This interaction promotes enhanced mixing of hot and cold air streams, which is critical for efficient thermal management. In Fig. 6-36, the velocity vectors are delineated in correspondence with the slit positions as established in Fig. 6-35. It is evident that a slit may contain a single secondary vortex, which circulates within it. However, this can lead to the formation of flow dead zones, as previously mentioned. Alternatively, if a slit harbours two vortices that are extensions of the primary vortices, these dead zones are mitigated, resulting in superior fluid mixing. The incidence of secondary vortices within the slits is generally commensurate with that of the primary vortices for all configurations, with the notable exception of the half-ellipse shape. In the case of the half-ellipse, there is a disproportionately higher occurrence of secondary vortices, as depicted in Fig. 6-35. This difference highlights the unique fluid dynamic characteristics imparted by the half-ellipse geometry on the system's mixing efficiency.

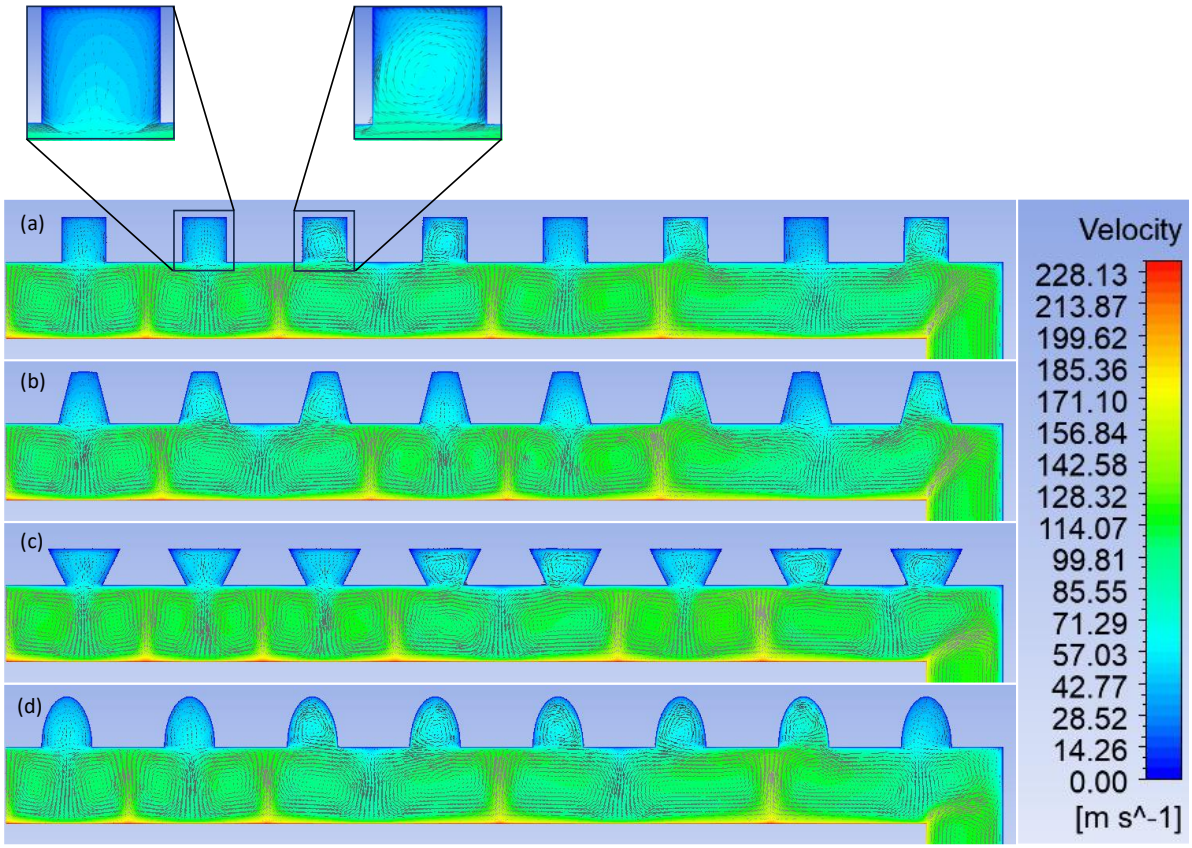

Fig. 6-35 Velocity contour of the FESS in Y-Z plane for the radial/grooved configuration under 1 bar pressure and rotational velocity of 1600 rad/s for: (a) rectangle, (b) trapezoid, (c) reversed trapezoid, and (d) half-ellipse

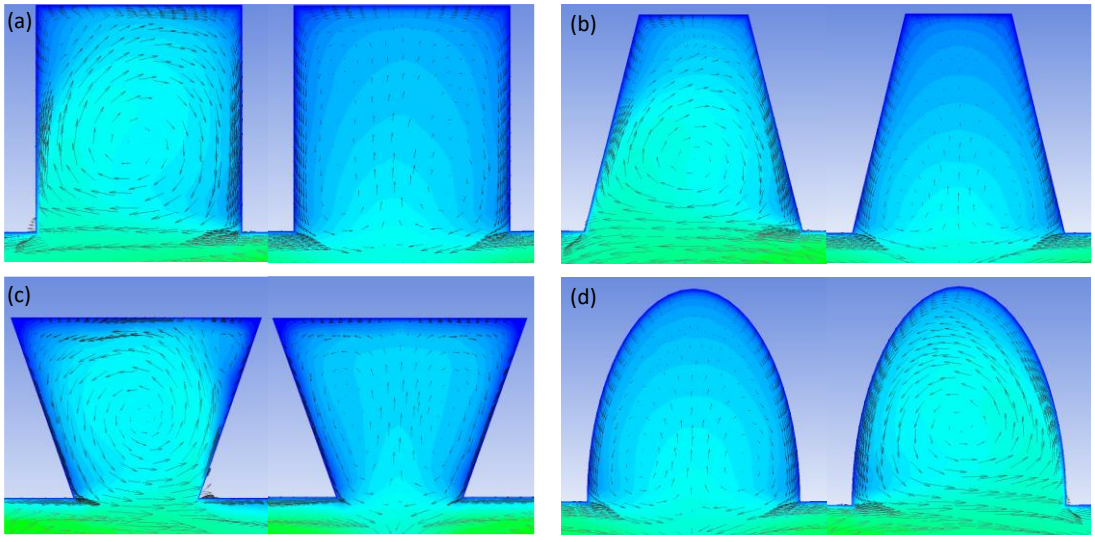

Fig. 6-36 Velocity contour of the slit in Y-Z plane for the radial/grooved configuration under 1 bar pressure and rotational velocity of 1600 rad/s for: (a) rectangle, (b) trapezoid, (c) reversed trapezoid, and (d) half-ellipse

In the pursuit of maximising the Nusselt number to enhance convective heat transfer between the rotor and the casing, a comprehensive investigation utilising RSM focused on six influential factors. The enhancement of the Nusselt number can be strategically achieved through several design and operational modifications. Increasing the B/C ratio has been identified as beneficial. Having a rotational velocity within 1200 to 1600 rad/s contributes positively, likely by allowing for more stable and coherent heat transfer surfaces. Elevating the pressure within the cavity is another method that intensifies the heat transfer coefficient, contributing to an increased Nusselt number. The use of slits oriented in the axial direction aligns with the thermal gradient, thereby promoting more effective convection. Employing a grooved configuration further augments the surface area and turbulent flow, both conducive to heat transfer enhancement. Lastly, adopting a half-ellipse shape for the components has been shown to be particularly effective in improving the Nusselt number.

6.2.7. Optimisation

For multiple-response optimisation, Myers and Montgomery [383] introduced "desirability". Desirability is the multi-criterion decision-making goal. The function gives each response a value between zero and one, with one indicating the highest desirability and zero conditions outside the desirable range. The objective function represents overall desirability as the geometric mean of transformed responses. It increases linearly from zero outside limits to one at the target point. Weighting each objective's importance maximises this desirability function using numerical optimisation. This optimisation framework uses a single desirability function with multiple responses and variables. The optimisation aimed to minimise windage losses while simultaneously maximising the Nusselt number, thereby achieving an ideal balance between fluid dynamics and heat transfer performance.

The anticipated windage losses and Nusselt number for the suggested design were validated against CFD simulations for each scenario to corroborate the accuracy of the predictions. The comparison reveals a close correlation between the numerical simulations and the forecasted data, with a marginal discrepancy of 3% in windage losses and 4% in the Nusselt number. These comparisons were made under the condition that the rotational velocity was maintained at 2400 rad/s, which is the maximum rotational velocity of the rotor meaning the flywheel is fully charged.

Considering the dual objectives of minimising windage losses while simultaneously maximising the Nusselt number, the most desirable scenario was identified with a B/C ratio of 1.2, pressure at 0.47 bar, axial direction for the slit, a grooved configuration, and a trapezoid-shaped slit. This configuration yielded windage losses of 1467 W and a Nusselt number of 42. In contrast, when the focus is solely on reducing windage losses, the optimal design shifts towards a B/C ratio of 1, a reduced pressure of 0.2 bar, radial slit orientation, grooved surface, and a reversed trapezoid slit shape, achieving significantly lower windage losses of 738 W but with a reduced Nusselt number of 19. Conversely, to prioritise the maximisation of the Nusselt number exclusively, the design parameters would adjust to a B/C ratio of

0.5, an elevated pressure of 1 bar, axial slit orientation, grooved configuration, and a trapezoid slit shape, resulting in higher windage losses of 2147 W but an improved Nusselt number of 59.

6.3. The Effect of Slits

This research delved into the role of slits in enhancing the efficiency of FESS, with a focus on reducing windage losses and increasing Nusselt number. Utilising RSM, the study identified the most effective combinations of design variables (including shapes, orientations, configurations, pressure levels, rotational velocities, and B/C ratios) to pinpoint an optimal solution. To evaluate the effectiveness of the optimised design, comparisons were made against a base model, which mirrored the optimised design in all aspects except for the inclusion of slits in the casing. This comparative approach was essential to isolate and understand the effects of slits on system performance. The outcomes of this comparison were revealing.

In the first scenario, aiming to optimise both windage losses and the Nusselt number, the slit-enhanced design yielded an 8% reduction in windage losses and an 11% increase in the Nusselt number compared to the base model at the same pressure level. When the optimisation was geared solely towards windage losses, the advanced design achieved a 9% decrease in windage losses, and unexpectedly, a 14% increase in the Nusselt number compared to the base model at the same pressure level. In the third scenario, with a focus on the Nusselt number, the optimised design still managed to offer a 3% reduction in windage losses while significantly boosting the Nusselt number by 18% compared to the base model at the same pressure level. These findings indicate that strategic slit incorporation in the design not only meets the intended optimisation goals but also consistently delivers dual benefits in terms of reducing windage losses and improving heat transfer, as quantified by the Nusselt number.

6.4. Summary

This research has investigated the effects of slit geometries on the performance of FESS through a comprehensive numerical study utilising RSM. To determine the validity of the CFD results, model validation was performed, which revealed a good agreement between the numerical and experimental data. Reducing windage losses in FESS can be achieved by optimising slit dimensions, decreasing rotational velocity, lowering cavity pressure, aligning slits radially, adopting a grooved configuration, and utilising a reversed trapezoid geometry to minimise skin friction coefficient. To achieve the highest Nusselt number within the FESS, a combination of factors, including increasing the base-to-height length ratio, maintaining rotational velocity within 1200 to 1600 rad/s, raising cavity pressure, orienting slits axially, implementing a grooved configuration, and adopting a half-ellipse component shape. The findings have revealed that slit inclusion can effectively minimise windage losses and enhance heat

transfer rates, simultaneously optimising both key performance indicators. Comparative evaluations against a base model revealed that the slit-enhanced design consistently outperformed the conventional design in all scenarios. For instance, the optimised design achieved an 8% reduction in windage losses and an 11% increase in the Nusselt number compared to the base model when both parameters were optimised simultaneously. The optimisation was performed, with numerical values in good agreement with the model predictions. The critical contribution of this work is studying the relationships and effects of various parameters on the performance of flywheel energy storage, which offer valuable insights for improving FESS efficiency, reliability, and longevity, while also contributing to broader sustainable energy goals. A portion of the numerical findings detailed in this chapter has been published in [405].

Chapter 7. Contribution of FESS Aerodynamic Performance Optimisation on Transport Decarbonisation

Chapter 7 investigates the significant role of FESS in advancing the decarbonisation of transportation. Through detailed vehicle simulation studies, including the integration of optimised FESS designs into a lightweight vehicle model, this chapter demonstrates the potential for substantial improvements in fuel efficiency and CO_2 emissions reduction. Utilising MATLAB/Simulink for modelling, it showcases how innovative FESS configurations can lead to enhanced storage system performance, highlighting the technology's potential to make transportation more sustainable.

7.1. The Optimised Designs of FESS for Vehicle Integration

The FESS used in the simulations is based on a foundational design with radial and axial radius ratios of 0.99. This model functions at standard atmospheric pressure, utilising air as the gas medium within the system. The baseline acts as a crucial benchmark for evaluating the effectiveness of subsequent optimisations. Chapter 5's comprehensive analysis revealed crucial modifications that can optimise system performance by reducing windage losses. The optimised design suggests radial and axial radius ratios of 0.96. In addition, the rotor's surface roughness has been developed to 4.6×10^{-7}m, while the housing's surface roughness has been refined to 6.9×10^{-7}m. These modifications are crucial for improving the aerodynamic efficiency of the FESS. Additional optimisation was determined in Chapter 6, where the incorporation of a reversed trapezoidal slit shape was implemented within the housing. This design is innovative in its approach, as it incorporates a radial slit orientation and a base length to height ratio of 1. Moreover, the system's ideal pressure level for enhancing performance is established at a reduced pressure level of 200mbar.

To improve performance, four additional models were created, all of which were adaptations of the final optimised model with slit walls. The second model operates under atmospheric pressure and uses air as the gas, similar to the baseline model, but incorporates slit walls, which lowers windage losses to 2002 watts. Models 3 and 5 highlight the considerable benefits of working at a reduced pressure of 200 mbar, with windage losses declining to 784 watts with air and 285 watts with helium, respectively. The fourth model examines the impact of replacing air with helium while maintaining standard atmospheric pressure and records windage losses at 641 watts. When compared to using air at partial vacuum pressure, using helium as the gas medium at atmospheric pressure can further reduce windage losses.

A fundamental assumption guiding these optimisations (model 3-5), whether using Helium as the gas medium or operating the system under partial vacuum pressure, is the integration of efficient seals for the FESS. This assumption opens the possibility of using gases other than air. Helium emerged as the

best choice for the gas medium within the FESS due to its favourable properties that match the system's operational requirements. The result of these optimisations led to a comprehensive comparison between the final optimised systems and the baseline model. This comparative analysis is crucial in demonstrating the improvements in efficiency and performance brought about by the series of aerodynamic and design enhancements. The integration of these optimisations represents a significant step forward in the development of more efficient and effective FESS.

Table 7-1 presents a comparative analysis between the baseline model and the final optimised models of the FESS. This comparison highlights the effectiveness of the optimisation strategies implemented in the final models, particularly the integration of slit walls.

Model 5 demonstrates a remarkable reduction in windage losses, achieving approximately an 88% decrease compared to the baseline model. This substantial reduction indicates that the optimisation techniques have been highly effective in minimising aerodynamic friction losses within the system. As a direct consequence of the reduced windage losses, the standby time for the FESS in the optimised model is significantly enhanced.

Table 7-1 The comparison of the baseline and final optimised models

#	Specifications	Radial radius ratio	Axial radius ratio	Pressure	Gas	Total Windage losses (W)
1	Baseline model	0.99	0.99	1000	Air	2407
2	Final optimised model + Silt walls	0.96	0.96	1000	Air	2002
3	Final optimised model + Silt walls	0.96	0.96	200	Air	784
4	Final optimised model + Silt walls	0.96	0.96	1000	He	641
5	Final optimised model+ slit walls	0.96	0.96	200	He	285

Reducing windage losses significantly affects the standby losses, thereby influencing the self-discharge rate of the system. At a maximum rotational velocity of 2400 rad/s, the flywheel achieves a full State of Charge (SOC), while a minimum velocity of 600 rad/s corresponds to a SOC of zero. Setting the SOC to zero at 600 rad/s, rather than when the flywheel is completely stopped, facilitates easier recharging of the flywheel and reduces mechanical stresses associated with starting from rest, thereby improving the overall efficiency and longevity of the system. Fig. 7-1 delineates the SOC over time for the baseline model compared to the four optimised models. The baseline model undergoes complete discharge due to mechanical losses (windage and bearing losses) within 43 minutes when fully charged.

Conversely, Model 2, incorporating the final optimised model with slit walls at atmospheric pressure using air, extends this period by 35% relative to the baseline model. Model 3 exhibits a 200% increase in discharge time compared to the baseline, while Model 4 shows a 245% increase. Model 5 demonstrates the most substantial enhancement, prolonging the duration by 580% compared to the baseline, thereby extending the operational period to approximately six times that of the base model. This advancement enables the FESS to serve as a medium-duration storage solution, transcending its previous limitation to short-duration storage, and offering improved efficacy for both long and short vehicular journeys.

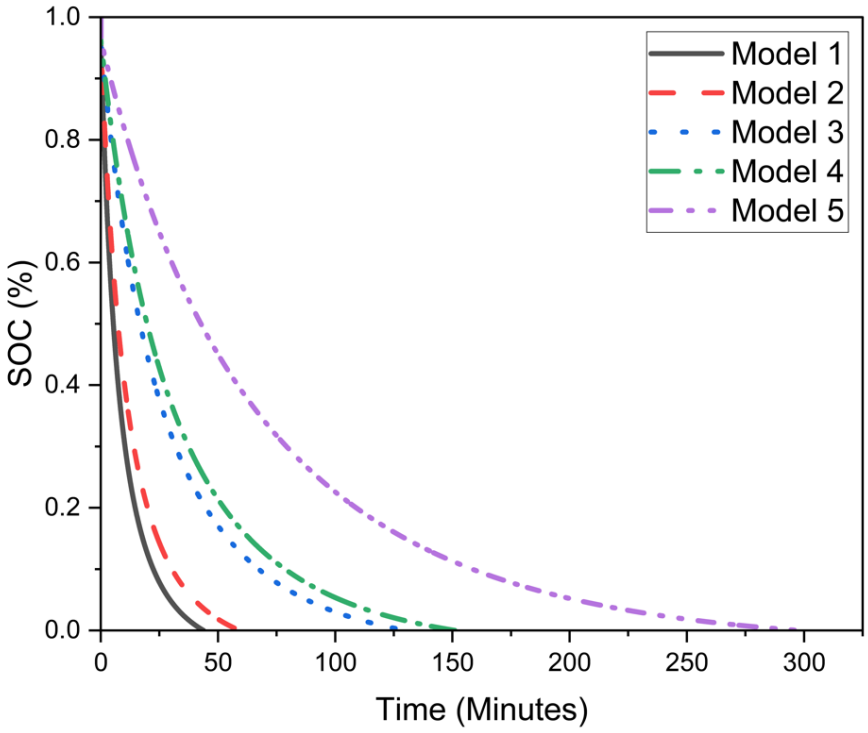

Fig. 7-1 The FESS's state of charge over time for the base model and the four optimised models

7.2. Vehicle Simulation

The development of Computer Aided Engineering (CAE) has become a pivotal factor in the vehicle design process, significantly improving its efficiency and precision. This is largely due to the advancements in computing power, which allow manufacturers to entirely design, simulate, and fine-tune vehicles through computer simulations prior to production [406]. Such progress reflects wider developments within automotive research, including vehicle dynamics, where a multitude of software tools have been developed to evaluate the energy efficiency of vehicle powertrains [407].

Among these tools, MATLAB/Simulink emerges as the preferred choice for its comprehensive toolkit that supports detailed modelling, simulation, and analysis of complex systems. The widespread

adoption of MATLAB/Simulink by engineers and researchers is due to its robustness, adaptability, and the extensive availability of libraries and pre-built models [408]. This software is instrumental in investigating how energy storage solutions, like FESS, can be integrated into vehicles. It enables the simulation of various scenarios to evaluate potential enhancements in energy efficiency and reduction of environmental impact [409]. The presence of open-source vehicle models in MATLAB/Simulink's environment is especially advantageous, as these models are thoroughly developed, tested, and validated, offering a solid basis for further exploration. They also significantly reduce the time needed for research by eliminating the necessity to create new vehicle models[409].

Using a computational model in MATLAB/Simulink, it is possible to simulate a vehicle navigating through a specific driving cycle in order to investigate the impact of incorporating a FESS into the vehicle powertrain on performance.

7.3. Vehicle Model Selection

The primary aim of choosing a particular vehicle for the simulation model lies in obtaining the precise design and accurate specifications of its powertrain. The objective is to select a vehicle that is widely used in the UK, thereby facilitating an understanding of the potential fuel savings achievable by integrating a FESS into the powertrain of an existing vehicle. Ford and Vauxhall vehicles, comprising about 25% of all cars on the road, are the most prevalent brands in the UK. They are followed in popularity by Volkswagen, BMW, Audi, and Mercedes. The Ford Fiesta, with 1.47 million units, the Ford Focus, with 1.08 million units, and the Vauxhall Corsa, with 1.02 million units, rank as the most common car models, according to DVLA 2020 data [410].

The Vauxhall Corsa has been especially notable, earning the title of best-selling car in 2021 and 2022 [410]. This hatchback car is widely popular in the UK. The Vauxhall Corsa was selected for the simulation because it is available in conventional ICE, hybrid, and fully electric powertrain configurations [411]. Table 7-2 contains detailed specifications for the Vauxhall Corsa used in the simulation.

Hybrid vehicles offer enhanced energy efficiency and reduced emissions compared to traditional vehicles by utilising a dual propulsion system that mitigates the range constraints of fully electric vehicles [412]. These vehicles employ both petroleum fuel and an electrical storage device, like a battery pack, to store energy. This energy is then converted into mechanical energy through the use of an ICE and an electric motor. The electric motor plays a key role in decreasing energy consumption and emissions, while the ICE extends the vehicle's range. HEVs are primarily available in two configurations: series and parallel hybrids [413].

HEVs are categorised into three drivetrain types: series hybrid, parallel hybrid, and series-parallel hybrid. The series hybrid represents the most straightforward configuration, wherein power is supplied directly to the electric motor. This motor receives its power from a generator, which in turn is powered

by either a diesel or petrol engine or from a battery. The parallel drivetrain setup allows both the ICE and the electric motor to contribute power directly to the vehicle's propulsion. Meanwhile, the series-parallel hybrid drivetrain merges the features and advantages of both the series and parallel configurations, offering a blend of their complexity and benefits [414].

Table 7-2 Model parameters of 2024 Vauxhall Corsa [411][411], [415]

Vehicle	HEV
Vehicle mass	1267 kg
Frontal area	2.13 m^2
Aerodynamic drag coefficient	0.29
Tyre radius	0.3015 m
Rolling resistance coefficient	0.011
Internal combustion engine	74 kW@5500 rpm
Cylinder capacity	1199 cm^3
Motor/Generator	21 kW
Engine Type	Spark-ignition

7.3.1. Hybrid Vehicle Model

The HEV model was constructed using MATLAB version 2023b. Fig. 7-2 illustrates the system's primary components in a simplified form, encompassing vehicle dynamics, a power splitter, an engine, a motor, and a battery. MATLAB/Simulink's open-source hybrid vehicle model uses the series-parallel hybrid vehicle powertrain model, which was used in this work [416]. Fig. 7-3 displays the comprehensive HEV model within MATLAB/Simulink, where the engine, motor, and vehicle dynamics are interconnected through a power splitting device. The control input for the vehicle's speed reflects the desired speed levels. Each simulation's outcomes, covering aspects like vehicle speeds, fuel usage, gear shifts, and battery status are documented and evaluated.

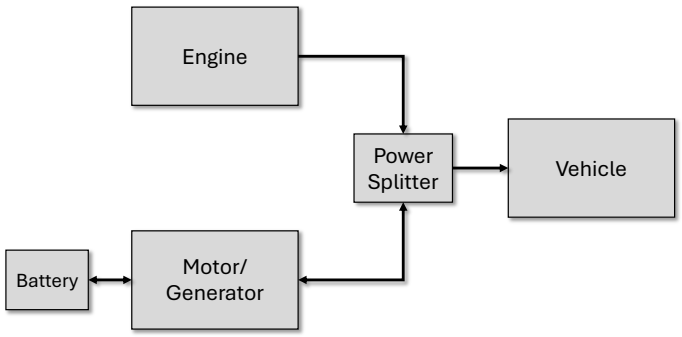

Fig. 7-2 Schematic diagram of the HEV main blocks

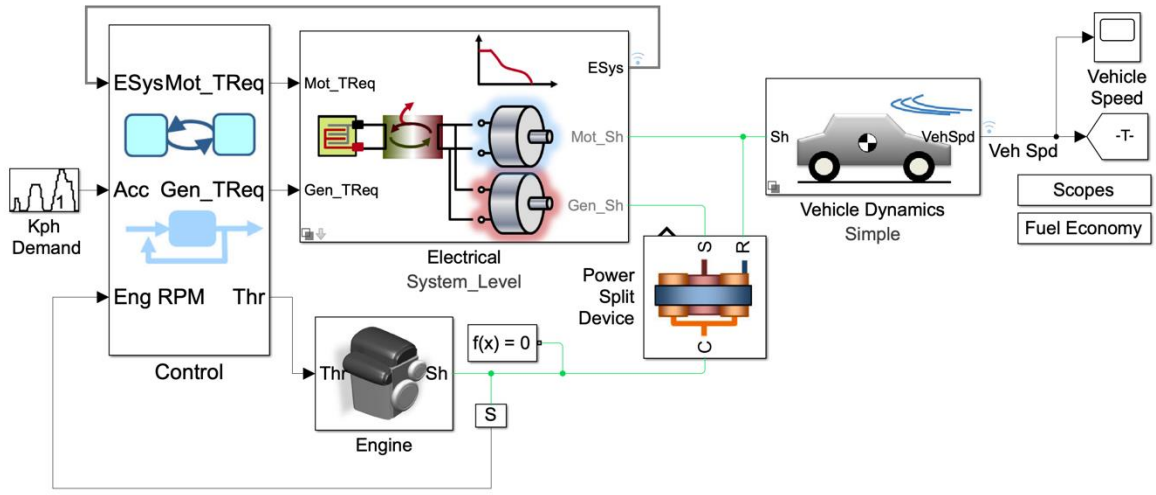

Fig. 7-3 Detailed MATLAB/Simulink open-source hybrid vehicle series-parallel model [416]

The power split device is the control centre of a hybrid vehicle, managing the interaction between the ICE, generator, and electric motor. It enables the car to work in two ways: either the electric motor and the ICE operate separately or together to power the vehicle.

The controller is designed to gather critical data from the vehicle's dynamics, including the speeds of both the motor and the generator, as well as information relating to braking and acceleration activities [416]. This set of inputs allows the controller to effectively run the vehicle, ensuring it performs well and efficiently. In the Simulink model, there's a control section that handles the vehicle's power. It checks vehicle speed and gives updates on speed, braking, and when to charge the battery. A special part of the model, called Mode Logic, decides if the vehicle should use the electric motor, the ICE, or both. It also turns the driver's acceleration into engine and motor speeds. This helps the controller adjust the engine and motor settings to suit the driving conditions [417].

The electrical block in the model controls how the vehicle manages electrical energy. It receives torque requests for both the motor and the generator from the vehicle's controller. The system includes a synchronous motor and drive, which uses the torque request to drive the vehicle, and a synchronous generator and drive, which recharges the battery. The DC-DC converter regulates the power flow to maintain optimal battery charge levels, managing the energy exchange between the battery bank and the rest of the system [416]. This ensures that the battery is charged efficiently during periods of low power demand and discharged when more power is needed. The electrical measurements are made to monitor the system's performance, including the battery system, the motor and generator RPM systems, and the DC-DC converter system [418].

The ICE block diagram represents the ICE's operational flow in the hybrid vehicle model. The engine receives the throttle position from the controller, which adjusts the amount of fuel and air entering the engine for combustion. The throttle's input directly influences the engine's power output. The engine shaft is connected to a switch 'S' that allows the engine to be engaged or disengaged from the drivetrain.

This enables the transition between the ICE and electric motors in the hybrid system, effectively managing the vehicle's propulsion [419].

The vehicle dynamics block diagram visualises how various forces interact to determine a vehicle's speed. The Torque Source is connected to a switch 'S' and symbolises the vehicle's propulsion, generated by either the ICE or the electric motor. The input brake pedal signals that braking force can be applied, which affects the vehicle's motion. This torque interacts with the Load Torque, which takes into account the vehicle's inertia and the road load. The Vehicle Speed and Power block computes the vehicle's speed using the propulsion torque and the load torque. External factors such as Aerodynamic Drag and Gravity also impact the vehicle's dynamics. Aerodynamic drag is influenced by the vehicle's speed and affects its ability to accelerate, while gravity's effect is dependent on the road's inclination, exerting additional load that can either slow down the vehicle when going uphill or accelerate it when going downhill [420].

7.3.2. Driving Cycle

The United Nations Economic Commission for Europe (UNECE), through its world forum for the harmonisation of vehicle regulations, established a group focused on pollution and energy. This group was tasked with creating a roadmap for the development of the Worldwide Harmonised Light Vehicle Test Procedure (WLTP). In 2009, this initiative led to the proposal of a Global Technical Regulation (GTR) specifically for light-duty vehicles. As part of the vehicle type approval testing process, the WLTP was introduced to replace the New European Driving Cycle (NEDC). The WLTP was designed based on two principal elements: the development of a standardised driving cycle that accurately represents global driving conditions, and the establishment of a uniform testing procedure that sets out the conditions, tolerances, requirements, and other parameters for emissions testing [421].

The accurate measurement of emissions and fuel consumption necessitates the use of well-defined driving cycles. To cater to different vehicle characteristics, three distinct driving cycles were developed, each representing a specific vehicle class. These classes were determined based on the Power-to-Mass Ratio (PMR) of vehicles, which is the ratio of rated power (W) to vehicle weight (kg). The WLTP classified vehicles into three categories, as detailed in Table 7-3. The respective driving cycles for these vehicle classes are depicted in Fig. 7-4. Additionally, selected data from these driving cycles are presented in Table 7-4, with comprehensive details available in Appendix C [422].

Table 7-3 WLTP vehicle categories [422]

Category	Speed phases	Power to mass ratio (PMR)
Class 1	Low, medium	≤ 22
Class 2	Low, medium, high	34 ≥ PMR > 22
Class 3	Low, medium, high, extra-high	> 34

Table 7-4 WLTP driving cycles data [422]

	Class 1	Class 2	Class 3
Distance (m)	8091	14664	23266
Duration (s)	1022	1477	1801
Average speed (km/h)	36.1	42.6	55.9
Maximum speed (km/h)	64.4	85.2	131.3
Idle time (s)	203	233	227

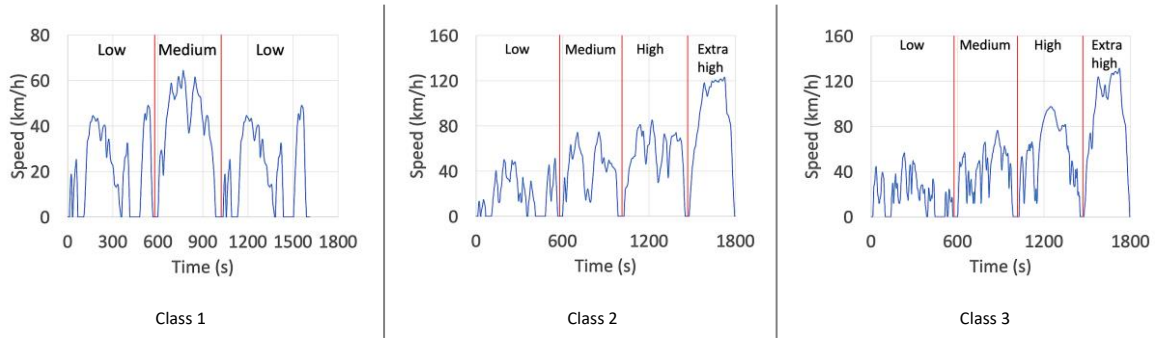

Fig. 7-4 The driving cycles of the WLTP test classes [422]

The three driving cycles mentioned earlier were used to assess the feasibility of integrating the FESS into light-duty vehicles and to determine the speed demand for the HEV model. This investigation aims to determine the potential fuel and emission savings that FESS can offer. A crucial step in this assessment is calculating the amount of energy that can be stored in an average light-duty vehicle. This calculation is based on the vehicle's kinetic energy at a given speed before braking, which is expressed by the following equation:

$$Kinetic\ Energy = \frac{1}{2}mv^2 \quad (7\text{-}1)$$

Where *m* is the mass of the vehicle and *v* is the speed of the vehicle before braking. According to data, the average mass of a light-duty vehicle in the UK is approximately 1,800 kg. The typical vehicle speed under free-flow conditions ranges between 50 and 110 kph (equivalent to 14-30.5 m/s) for urban driving

and motorways, respectively [423]. Therefore, the available kinetic energy in these vehicles can vary from 176 to 840 kJ.

Using the WLTP driving cycle in simulation can have a significant impact on the results when comparing a vehicle with and without the FESS. The WLTP, which is a more rigorous and realistic measure of vehicle performance, can help better understand how FESS affects energy efficiency and emissions. The detailed driving conditions outlined in the WLTP cycle allow for a thorough assessment of the benefits of incorporating FESS into vehicle design.

7.4. Integration of FESS into the Hybrid Vehicle Model

7.4.1. Powertrain Structure

Representation of the FESS configuration in the powertrain of a hybrid vehicle is provided in Fig. 7-5. The central element of the powertrain is the power splitter device, particularly a planetary gear set, which creates links among the different power sources. The main power source for the vehicle is an ICE, where its crankshaft output directly interacts with the planet carrier's input. To manage the flywheel's velocity, the FESS is linked to a CVT, which is further connected to the ring gear through a gear set. Furthermore, a motor/generator is connected to the sun gear via another gear set, transitioning between motor and generator modes as per the operational necessities of the vehicle.

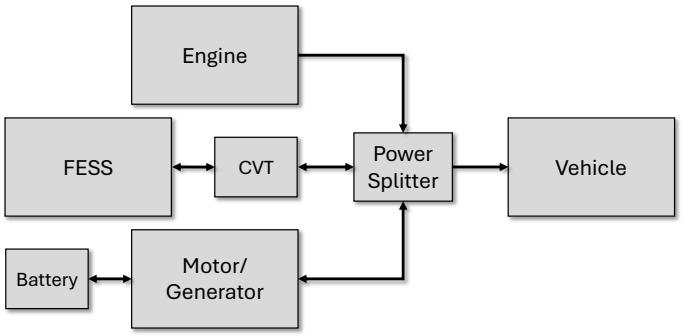

Fig. 7-5 Schematic diagram of the integrated hybrid vehicle main blocks

7.4.2. Operating Modes

The process of driving includes three main operational stages: driving, braking, and parking [424]. The features of the proposed powertrain system are divided into a total of six distinct modes, each outlined by the driving conditions and the driver's preferences. These modes include pure electric driving, fuel-powered driving, full-power driving, on-the-go charging, braking, and parking.

7.4.2.1. Pure Electric Driving Mode

This method utilises the electric motor's great effectiveness and torque at low velocities to propel the vehicle exclusively using electrical power at the beginning. If the flywheel has a high initial velocity from previous regenerative braking, it propels the vehicle at the start to improve energy efficiency. At the same time, the electric motor functions as a generator, converting some of the flywheel's energy into electrical energy to charge the battery. This method is also chosen when the vehicle operates under light loads or when the ICE's velocity for a specific vehicle speed is lower than idle, turning off the ICE to decrease unnecessary fuel usage and emissions.

7.4.2.2. Fuel-Powered Driving Mode

When the vehicle speeds up to a specific velocity and the load is reasonable, the ICE functions independently to move the vehicle, operating within its effective span. The electric engine does not add rotational force and stays inactive, aligning with the velocity of the vehicle.

7.4.2.3. Full-Power Driving Mode

When the driver attempts to accelerate, such as for overtaking, the vehicle enters a full power driving mode. In this scenario, the ICE follows its optimal or peak torque curve, resulting in high thermal efficiency. If the ICE's torque is insufficient to meet the vehicle's torque requirements, the electric motor steps in to compensate. Furthermore, if the FESS is charged, its kinetic energy is released and transferred to the planetary gear set's carrier gear of the power splitter device. As a result, the power splitter harnesses the combined forces of the ICE, electric motor, and FESS to propel the vehicle.

7.4.2.4. On-the-go Charging Mode

This mode is activated when the battery's SOC falls below the minimum threshold during operation, requiring recharging. The control unit then selects the on-the-go charging mode. In this mode, depending on the driving conditions, the ICE operates at its optimal or maximum torque curve to maintain normal vehicle functionality. The MG converts the surplus power generated by the ICE into electrical energy, which is used to recharge the battery.

7.4.2.5. Braking Mode

As part of the flywheel configuration with the vehicular drivetrain, the regenerative braking modes are an essential part of the amount of recovered energy. Regulation No. 13 of the Economic Commission for Europe of the United Nations (UN/ECE) stated that a regenerative braking system could be categorised into two main categories, which are: Category A: The regenerative braking system only

works when the throttle is depressed and is not part of the primary braking system. Category B: the primary braking system is regenerative braking, which makes the amount of recovered energy higher, but it will be more involved in terms of control and safety. The regulations also stated that the anti-locking braking system (ABS) must have control over the regenerative braking system at any given time for both categories. Regenerative braking can be combined with regular friction braking by two strategies. The first one is called the "parallel braking strategy," where regenerative braking works in parallel with friction braking [425].

As shown in Fig. 7-6 (a), the required power needed to decelerate the vehicle is divided between friction braking and regenerative braking, making it a low-energy recovery technique. The other strategy is called the series braking strategy, where the regenerative braking works first and then the friction braking. The fictional brake can only operate under certain conditions, such as when the regenerative brake cannot deliver the requested braking power. The efficiency of series regenerative braking is greater than that of parallel regenerative braking. The serial braking strategy, therefore, improves more compared to the parallel braking strategy. The regenerative power is insufficiently large to cover the necessary braking power. The regenerative braking system usually works in conjunction with the conventional brake, as shown in Fig. 7-6 (b) [425] [162].

This method employs a series regenerative braking technique, in which the vehicle's recuperable kinetic energy is routed directly into the FESS via the power splitter device. If the braking force generated by the FESS is insufficient to meet the braking demand, both regenerative and friction braking modes must be used simultaneously. Friction braking is used during emergency braking or when the FESS has reached its full charge capacity. Importantly, the ICE remains inactive during the braking phase, preventing unnecessary fuel consumption and emissions.

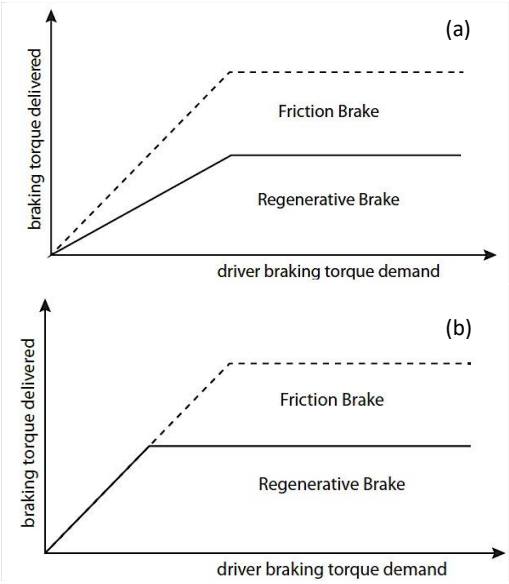

Fig. 7-6 (a) Parallel Regenerative braking strategy, (b) Series Regenerative braking strategy [425]

7.4.2.6. Parking Mode

When the vehicle comes to a stop after driving, the FESS and the MG have a reverse speed relationship. In this state, the MG generates positive torque and operates as a generator. The kinetic energy stored in the FESS during operation can then be transferred back to the battery via the MG.

7.4.3. FESS Modelling

The FESS incorporated into the powertrain operates at high speeds, enabling it to capture the vehicle's kinetic energy during braking phases and enhance the vehicle's dynamics while driving. The flywheel's rotor, a rotating mass m (in kg) with a moment of inertia J (in kg·m^2), spins at an angular velocity ω (in rad/s), storing kinetic energy E (in joules) as follows:

$$E = \frac{1}{2} J \omega^2 \tag{7-2}$$

The kinetic energy available from a flywheel operating between its minimum and maximum angular velocities can be expressed as:

$$E_{max} = \frac{1}{2} J ({\omega_{max}}^2 - {\omega_{min}}^2) \tag{7-3}$$

Where ω_{max} and ω_{min} represent the flywheel's maximum and minimum permissible angular velocities, respectively. Given that the moment of inertia J depends on the flywheel's geometry and mass, the expression for stored energy can be reformulated as:

$$E_{max} = \frac{1}{4} m r^2 ({\omega_{max}}^2 - {\omega_{min}}^2) \tag{7-4}$$

Where m is the mass of the flywheel and r is the flywheel radius. Furthermore, the SOC of the flywheel can be determined by:

$$\text{State of charge (SOC)} = \lambda(t) = \frac{\omega(t)^2 - {\omega_{min}}^2}{{\omega_{max}}^2 - {\omega_{min}}^2} \tag{7-5}$$

Where $\omega(t)$ is the flywheel's instantaneous angular velocity. Initially, at the start of the simulation, the SOC is zero, remaining so after the FESS reaches its minimum rotational speed, indicating it cannot yet contribute to vehicle acceleration. If $\omega(t) = \omega_{min}$, then the SOC is zero; if $\omega(t) = \omega_{max}$, then the SOC is one. Table 7-5 lists the physical parameters of the FESS system.

Table 7-5 FESS physical system parameters

Parameter	Value
Mass	53 kg
Flywheel radius	0.13 m
Flywheel length	0.13 m
Maximum rotational velocity	2400 rad/s
Minimum rotational velocity	600 rad/s

7.4.4. FESS Mechanical Losses

During the operation of the FESS, there are inevitable power losses attributed to windage and bearing friction. Therefore, the rotational speed of the FESS decreases when the vehicle is stationary or when the FESS is not actively powering the vehicle. To account for windage losses, mathematical expressions have been developed for each of the five models under examination, with their respective equations detailed in Table 7-6.

Table 7-6 the mathematical expression for windage losses for the five studied models

Model #	**Windage losses mathematical expression**
Model 1	$P_{windage} = 2 \times 10^{-7}\omega(t)^3 + 7 \times 10^{-8}\omega(t)^2 - 3 \times 10^{-8}\omega(t) + 3 \times 10^{-9}$
Model 2	$P_{windage} = 1.45 \times 10^{-7}\omega(t)^3 + 6 \times 10^{-8}\omega(t)^2 - 2 \times 10^{-8}\omega(t) + 3 \times 10^{-9}$
Model 3	$P_{windage} = 6 \times 10^{-8}\omega(t)^3 + 2 \times 10^{-8}\omega(t)^2 - 9 \times 10^{-9}\omega(t) + 1 \times 10^{-9}$
Model 4	$P_{windage} = 5 \times 10^{-8}\omega(t)^3 + 2 \times 10^{-8}\omega(t)^2 - 7 \times 10^{-9}\omega(t) + 9 \times 10^{-10}$
Model 5	$P_{windage} = 2 \times 10^{-8}\omega(t)^3 + 8 \times 10^{-9}\omega(t)^2 - 3 \times 10^{-9}\omega(t) + 4 \times 10^{-10}$

The other mechanical loss is the bearing loss, which can be calculated using a mathematical expression based on the analytical data from the experimental studies. This expression reflects the correlation between the bearing losses and the flywheel's rotational velocity, as the rotational velocity is the only parameter affecting the bearing losses. The bearing losses can be calculated by:

$$P_{bearing} = 9 \times 10^{-7}\omega(t)^2 + 3 \times 10^{-2}\omega(t) - 16.9 \quad (7\text{-}6)$$

The equation for the power balance of the FESS is:

$$P_{out} = P_{in} - P_{windage} - P_{bearing} \quad (7\text{-}7)$$

Where P_{in} is the initial power stored in the FESS, P_{out} is available output power after the mechanical losses, $P_{windage}$ and $P_{bearing}$ are windage and bearing losses of FESS.

7.4.5. Rule-Based Control Strategy

The rule-based method is the most widely used control strategy for HEVs, encompassing both deterministic and fuzzy logic-based approaches [426], [427]. As a result, this section introduces a rule-based control strategy that uses critical thresholds such as vehicle speed, battery SOC, torque difference, and flywheel rotational speed. This strategy adjusts each component's operational state based on real-time data and predefined rules, increasing the vehicle's overall efficiency.

Traditional ICEs in conventional vehicles frequently operate under suboptimal conditions to maintain driving force balance, resulting in higher fuel consumption. This control strategy aims to improve

engine performance by utilising an auxiliary motor and a FESS, allowing the engine to operate within its most efficient range whenever possible. It also establishes upper and lower limits for the battery's SOC to prevent overcharging or deep discharge.

Vehicle operational states are switched based on vehicle speed and driver inputs, such as acceleration and brake pedal signals, which indicate the torque required at the wheels. A positive torque demand with no acceleration input indicates a driving state, whereas a non-activated brake during driving causes a transition to the braking state. In the driving mode, the control algorithm determines the best operational mode by comparing the demanded torque to the engine torque delivered to the wheels at the current speed. The simulation model of the FESS is integrated into an open-source HEV model, as shown in the powertrain schematic in Fig. 7-7.

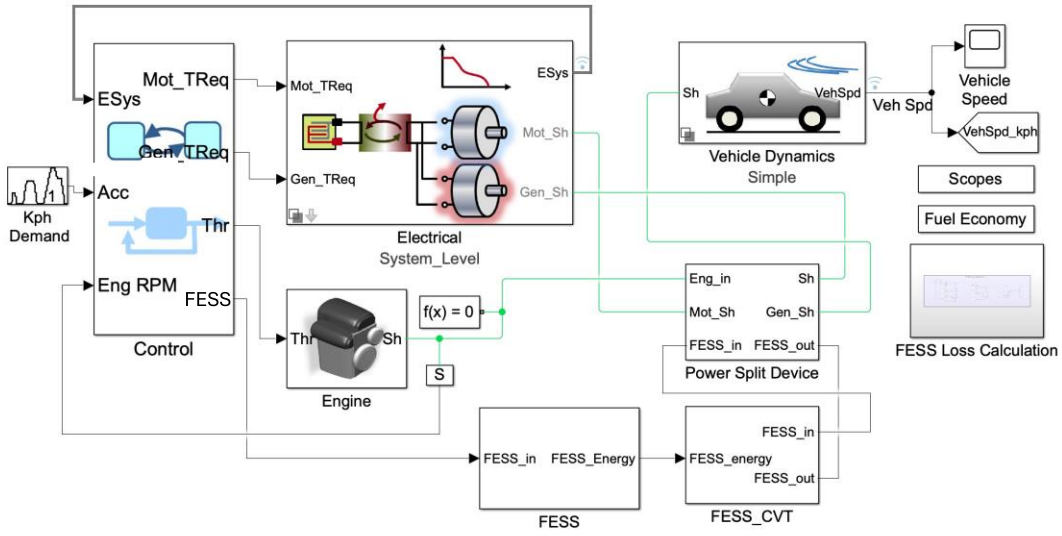

Fig. 7-7 Detailed MATLAB/Simulink open-source hybrid vehicle series-parallel model with FESS

7.5. FESS Impact on Vehicle Performance

7.5.1. Model Verification

The data relevant to the selected vehicle is available and has been disclosed in accordance with the WLTP driving cycles [428]. Consequently, to assess the model's accuracy before incorporating the FESS, the WLTP conditions were selected as the benchmark. The available fuel consumption figures for the vehicle, alongside the corresponding data generated by the model, are presented in Table 7-7. The comparison reveals that the model's fuel consumption estimates closely align with the actual values provided by the vehicle's manufacturer. This close correlation indicates that the model serves as an accurate representation of the real vehicle's performance. It proves to be a reliable tool for comparative analysis, with the variance between the model's simulations and the actual data being approximately 1%. This minimal discrepancy underscores the model's effectiveness in mirroring the vehicle's fuel consumption characteristics under WLTP conditions.

The analysis was carried out across three different WLTP driving cycle classes. In the first WLTP cycle, the simulation reported fuel consumption of 3.903 litres per 100 kilometres, which was slightly lower than the manufacturer's reference value of 4.1 litres per 100 kilometres. The second WLTP cycle followed a similar pattern, with the simulated value at 4.014 litres per 100 kilometres versus the reference value of 4.1 litres per 100 kilometres. During the third WLTP cycle, the simulation produced a value of 5.32 litres per 100 kilometres, compared to the reference value of 5.5 litres per 100 kilometres. Despite this, the difference remains small, demonstrating the model's ability to accurately reflect the vehicle's fuel consumption under a variety of driving conditions.

Table 7-7 Fuel consumption values for simulation and reference values based on the driving cycle

Driving cycle	**Simulation fuel consumption (L/100 km)**	**Reference fuel consumption (L/km)**
WLTP Class 1	3.903	4.1
WLTP Class 2	4.014	4.1
WLTP Class 3	5.32	5.5

7.5.2. Analysis of The FESS Models

The evaluation of vehicle fuel consumption and CO_2 emissions was carried out across the same WLTP driving cycle classes for five distinct models of FESS. These models included one baseline model and four optimised versions, each successive model showcasing incremental improvements over its predecessor. This iterative optimisation resulted in Model 5, which showed a significant reduction in windage losses, with an 88% decrease compared to the baseline model.

The incorporation of FESS into HEV demonstrates a progressive improvement in both fuel consumption and emissions reduction. Starting with the baseline model (Model 1) and progressing through Models 2–5, each iteration of FESS has been modified for greater performance in terms of reducing windage losses, allowing the system to function better for longer periods. The results of these optimisations are evident when comparing the fuel consumption and CO_2 emissions across the WLTP Class 1, 2, and 3 driving cycles, as shown in Table 7-8.

For WLTP Class 1, the HEV model without the FESS showed a fuel consumption of 3.903 L/100 km and CO_2 emissions of 92.70 g/km. The introduction of Model 1 FESS reduced these figures to 3.676 L/100 km and 87.31 g/km, respectively, indicating a notable improvement in vehicle efficiency. This trend continued with each subsequent model, culminating in Model 5, which reduced fuel consumption to 3.4463 L/100 km and CO_2 emissions to 81.85 g/km, marking a substantial improvement over the HEV without having FESS. A similar pattern of efficiency gains was observed in WLTP Class 2, with the HEV without the FESS fuel consumption of 4.014 L/100 km and CO_2 emissions of 95.33 g/km

being progressively reduced by each FESS model. Model 5 achieved the lowest fuel consumption and CO_2 emissions in this class at 3.1873 L/100 km and 75.70 g/km, respectively.

WLTP Class 3, which represents more demanding driving conditions, also showed significant improvements. From the HEV's fuel consumption of 5.32 L/100 km and CO_2 emissions of 126.35 g/km, the optimised Model 5 managed to reduce these figures to 4.5796 L/100 km and 108.77 g/km, respectively.

Fig. 7-8 shows the percentage reduction in fuel consumption for an HEV equipped with the five different models of the FESS, as compared to an HEV without a FESS. Each line represents one of the five FESS models. Model 1 establishes the baseline for fuel reduction efficiency. Models 2 through 5 show progressive reductions in fuel consumption. Model 5 achieves the highest percentage of fuel reduction across all WLTP classes, with a peak in WLTP Class 2. The figure indicates that the percentage reduction in fuel consumption is highest for all FESS models during the WLTP Class 2 driving cycle. This peak efficiency reflects the optimal potential for recovering lost kinetic energy in this specific driving scenario. The nature of WLTP Class 2, which includes a balance of stop-start traffic and steady-speed driving, presents the most opportunities for the FESS to recuperate and store kinetic energy during deceleration phases. This energy can then be efficiently reused, leading to a more pronounced reduction in fuel consumption compared to WLTP Classes 1 and 3. Such a pattern suggests that FESS technology is particularly advantageous in driving cycles that mirror urban commuting, where frequent braking and acceleration are common.

On average, the HEV without the FESS had a fuel consumption of 4.412 L/100 km and CO_2 emissions of 104.79 g/km. The sequential improvements brought by each FESS model led to Model 5, which exhibited the most substantial efficiency gains, with average fuel consumption and CO_2 emissions reduced to 3.7377 L/100 km and 88.77 g/km, respectively. By integrating the baseline FESS model, fuel consumption can be reduced by an average of 13%, and CO_2 emissions by 10%. Furthermore, implementing Model 5 of the FESS achieves even greater efficiencies, reducing fuel consumption by 18% and CO_2 emissions by 15%. These reductions are significant, particularly for a HEV of such a lightweight design. This suggests that heavier vehicles, which possess greater kinetic energy that can be captured and stored, could see even more substantial decreases in both fuel consumption and CO_2 emissions upon incorporating FESS.

Additionally, the benefits of FESS are not limited to HEVs alone. Conventional ICE vehicles could also experience marked improvements in fuel efficiency and emissions reductions with the adoption of FESS. The inherent capacity of FESS to efficiently store and release kinetic energy makes it a potent tool for enhancing vehicle performance across a wide spectrum of vehicle types and weights, leading to significant environmental benefits.

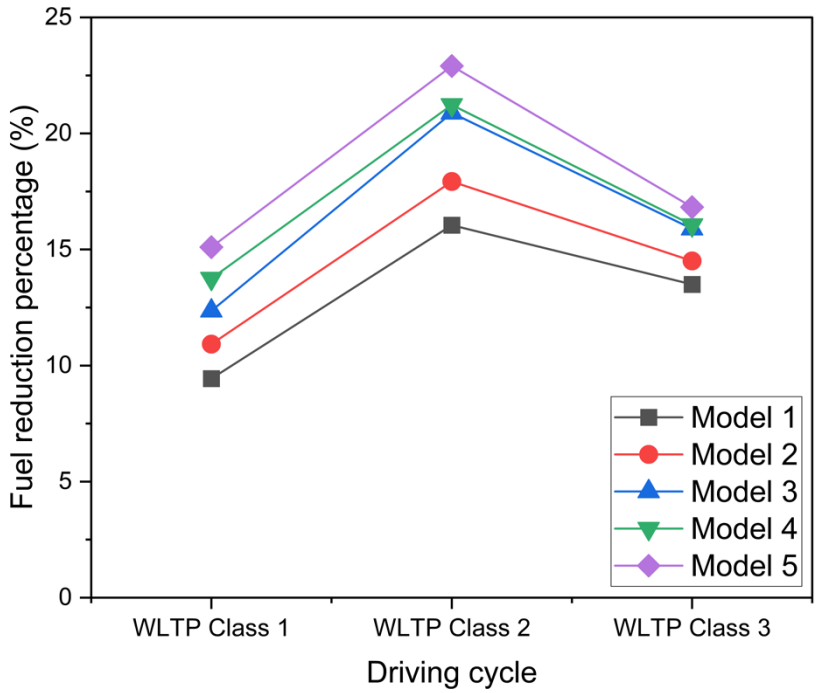

Fig. 7-8 Percentage reduction in fuel consumption for an HEV equipped with various FESS models across three WLTP driving cycle classes

Table 7-8 Fuel consumption and CO_2 emission values for HEV without and with FESS for the five examined models based on the driving cycle

Driving cycle	**HEV**		**Model 1**		**Model 2**		**Model 3**		**Model 4**		**Model 5**	
	Fuel consumption (L/100 km)	CO_2 emissions (g/km)	Fuel consumption (L/100 km)	CO_2 emissions (g/km)	Fuel consumption (L/100 km)	CO_2 emissions (g/km)	Fuel consumption (L/100 km)	CO_2 emissions (g/km)	Fuel consumption (L/100 km)	CO_2 emissions (g/km)	Fuel consumption (L/100 km)	CO_2 emissions (g/km)
WLTP Class 1	3.903	92.70	3.676	87.31	3.6157	85.87	3.5574	84.49	3.5010	83.15	3.4463	81.85
WLTP Class 2	4.014	95.33	3.471	82.44	3.3931	80.59	3.2709	77.68	3.2566	77.34	3.1873	75.70
WLTP Class 3	5.32	126.35	4.763	113.12	4.7074	111.80	4.6311	109.99	4.6220	109.77	4.5796	108.77
Average	4.412	104.79	3.97	94.29	3.9054	92.75	3.8198	90.72	3.7932	90.09	3.7377	88.77

7.6. Summary

This chapter details the optimisation of FESS designs for vehicle integration, demonstrating significant reductions in windage losses through novel design modifications such as the implementation of slit shapes and adjustments in radial and axial radius ratios. These enhancements, combined with the use of helium as a gas medium and operating at reduced pressure levels, markedly improve the aerodynamic efficiency of FESS, leading to considerable reductions in standby losses and extended operational periods for the storage system. The chapter also explores vehicle simulation with MATLAB/Simulink. Using the 2024 Vauxhall Corsa, which is available in hybrid versions, the study investigates how incorporating FESS could reduce fuel consumption and emissions. The integration of FESS into the hybrid vehicle model is examined through various operational modes, including pure electric driving, fuel-powered driving, and regenerative braking, highlighting the potential of FESS to enhance vehicle performance by efficiently capturing and storing kinetic energy during braking phases. Significant findings from simulations demonstrate that FESS integration can lead to substantial improvements in fuel consumption and CO_2 emissions across various driving cycles. The analysis shows that optimised FESS models, particularly the final model, significantly reduce windage losses, translating to enhanced vehicle efficiency and lower environmental impact. These improvements are quantified through comparative analyses of fuel consumption and CO_2 emissions between a hybrid electric vehicle with and without FESS integration across different WLTP classes. This chapter presents a comprehensive study on the benefits of incorporating optimised FESS into vehicle powertrains, demonstrating significant progress in transport decarbonisation through improved vehicle efficiency and lower environmental impact.

Chapter 8. Conclusion and Future Work

Exploring advanced energy recovery solutions emerges as a critical focus in addressing the rising urgency of limiting emissions and combating climate change. The transport sector, which contributes significantly to global CO_2 emissions, requires the development and implementation of innovative technologies to facilitate transition to sustainability. Among these, the use of FESS presents a promising opportunity for improving vehicle efficiency and environmental performance. FESS technology, known for its durability, efficiency, and eco-friendliness, introduces a feasible option to conventional battery storage systems, which frequently face environmental and recycling obstacles. The capability of FESS to enhance vehicle fuel efficiency while simultaneously decreasing CO_2 emissions is in line with the UK government's emissions reduction targets, highlighting its importance and significance in the realm of sustainable transportation endeavours.

This thesis presents a novel aerodynamic design for FESS that aims to maximise energy recovery while minimising losses through the use of advanced computational fluid dynamics (CFD) simulations. The study evaluates the aerodynamic performance of FESS under various conditions, with a focus on reducing aerodynamic losses and increasing system efficiency. The study aims to establish a direct correlation between aerodynamic efficiency and system design parameters by investigating the impact of geometric configurations and operating conditions. Furthermore, the study investigates the effects of introducing slit walls into the FESS casing, specifically their impact on the system's aerodynamic efficiency. The study uses a comprehensive analysis to identify optimal configurations that yield maximum energy storage efficiency while minimising losses, thereby contributing to the development of a sustainable and low-carbon powertrain.

This thesis explores the design of an optimal FESS to ensure reliable operation in vehicular applications. The proposed design incorporates novel operational concepts and design elements, including a novel casing design shape. This thesis not only emphasises the vital role of FESS in progressing low-emission transportation solutions but also outlines a comprehensive route for refining FESS design. The insights gained from this work are positioned to significantly contribute to the larger goals of clean energy storage solutions, providing a strategic path towards achieving a more sustainable and effective storage solutions.

8.1. Research Questions

The thesis was divided into seven distinct segments, with each segment addressed in a separate chapter. Concluding remarks for each segment are presented at the conclusion of their respective chapters. This summary will primarily concentrate on the collective response of the study to the research questions posed initially.

8.1.1. How do energy recovery systems enhance transportation energy efficiency and emissions reduction?

Chapter 2 critically explored the energy recovery systems landscape, focusing on FESS and its potential to improve transportation energy efficiency. This review lays the groundwork for the evaluation of current energy storage technologies, highlighting their limitations, and identifying areas for improvement. Key findings include:

1. The review evaluates existing energy recovery solutions, highlighting FESS as an under-optimised but promising technology for energy efficiency and integration in vehicles despite notable advancements.
2. It identifies barriers to FESS adoption in transportation, particularly emphasising the lack of research on aerodynamic design optimisation for minimising energy losses.
3. A significant research gap in the aerodynamic performance optimisation of FESS is revealed, marking a lack of focus on this crucial aspect despite the extensive exploration of mechanical and electrical dimensions.
4. FESS is recognised for its unique advantages over alternative energy storage solutions, especially regarding reliability and environmental impact, while also noting the necessity for technological advancements to address current limitations.
5. Lastly, the chapter establishes a solid basis for the objectives set out in this thesis, emphasising the critical need for focused research into aerodynamic optimisation and energy efficiency to advance FESS technology.

8.1.2. How do CFD and DoE enhance FESS optimisation precision and reliability for low-carbon solutions?

Chapter 3 of the thesis presents a hybrid design approach combining theoretical analysis with CFD simulations to explore the performance of the studied FESS, setting the stage for further optimisation focused on energy efficiency and sustainability. Key findings include:

1. Utilising CFD allows for rapid evaluation of design variations, providing flexibility to modify studied parameters without substantial additional costs, thereby facilitating more informed design decisions early in the design process.

2. The integration of DoE with CFD simulation provides a structured method to systematically understand the interplay between design and operational variables, enabling efficient exploration of the design space and identification of optimum design parameters for FESS.
3. CFD simulations are validated against experimental data to ensure accuracy, leveraging various turbulence models to analyse the operation of FESS in different environmental conditions, including partial vacuum settings.
4. This structured approach, combining the precision of CFD modelling with the systematic exploration provided by DoE, significantly enhances the reliability and precision of FESS optimisation.

8.1.3. How do FESS design parameters impact its windage losses and heat transfer, and what are the optimal conditions for energy efficiency and thermal management?

Chapter 4 provides an in-depth examination of the CFD simulations, which explain the complex dynamics inherent to the FESS flow dynamics. This chapter is critical for understanding the factors that affect energy efficiency and thermal management. Key findings include:

1. Windage losses in FESS are significantly influenced by the airgap size and rotational speed. Smaller airgaps and higher rotational speeds lead to increased windage losses.
2. The optimal radius ratio for minimising windage losses while ensuring efficient kinetic energy storage is identified as 0.95, balancing the benefits of reduced air resistance with the need for effective energy storage capacity.
3. Heat transfer efficiency, as indicated by the Nusselt number, improves with increasing rotational speeds up to a certain point, beyond which it begins to decline. This suggests the existence of an optimal speed range for thermal management of FESS.
4. Enhanced convective heat transfer is achieved through the formation of Taylor-Couette flow within the airgap, with the number of Taylor vortices increasing with rotational speed. This flow improves the mixing of air, enhancing heat dissipation from the rotor to the working fluid.
5. The analysis concludes that the design and operating conditions of FESS have a profound impact on its aerodynamic performance and thermal management capabilities. Optimising these parameters is crucial for enhancing the system's energy efficiency and operational effectiveness.

8.1.4. How do geometric and operating conditions in FESS affect its aerodynamic performance, and what configurations yield maximum energy storage efficiency with minimal losses?

Chapter 5 combines statistical methods with CFD simulations to optimise the FESS's geometric and operating parameters, resulting in improved performance and efficiency. Key findings include:

1. Modifications in the airgap size and surface roughness significantly impact windage losses, with larger airgaps and smoother surfaces leading to lower windage losses, thus enhancing system efficiency.
2. Optimal FESS configurations are identified with a balance between the airgap size, operational speed, and surface roughness, showcasing the importance of a holistic approach to FESS design for maximising energy storage efficiency with minimal losses.
3. The introduction of a partial vacuum within the FESS casing emerges as a pivotal factor in reducing windage losses, illustrating the critical role of operating conditions in optimising the aerodynamic performance of the system.
4. The use of helium as an alternative medium within the FESS casing substantially improves aerodynamic efficiency by reducing windage losses, underpinning the potential of operational modifications in enhancing the system performance.
5. The findings underscore the combined effects of geometric and operational modifications in FESS on improving aerodynamic efficiency, paving the way for advanced FESS designs with optimised energy storage and minimal losses.

8.1.5. How do slit walls in FESS casing affect aerodynamic efficiency and what are the optimal characteristics for system efficiency?

Chapter 6 investigates the effects of innovative casing design on FESS performance, demonstrating how structural modifications can have a significant impact on efficiency and operational effectiveness. Key findings include:

1. Incorporating slit walls, particularly in trapezoidal and rectangular configurations, optimally reduces windage losses, with the rectangular geometry showing the lowest windage losses at maximum rotational velocity.
2. The presence of slit walls notably enhances the Nusselt number, indicating improved convective heat transfer, with the half-ellipse shape yielding the highest Nusselt numbers across all configurations.
3. The optimal number of slit walls is identified as 16, balancing the reduction in windage losses with the enhancement in heat transfer efficiency.
4. The axial orientation and grooved configuration of slit walls are determined to be most effective in reducing windage losses and enhancing the Nusselt number, suggesting strategic design directions for FESS efficiency improvements.
5. The study confirms that strategic slit incorporation not only meets intended optimisation goals but also consistently delivers dual benefits in terms of reducing windage losses and improving

heat transfer, showcasing the effectiveness of design optimisations in FESS performance enhancement.

8.1.6. How does integrating optimised FESS into light-duty vehicles affect fuel efficiency and emissions reduction?

Chapter 7 investigates the integration of optimised FESS models into light-duty vehicles, evaluating the impact on fuel efficiency and emissions reduction. Key findings include:

1. Integrating optimised FESS into light-duty vehicles significantly enhances fuel efficiency, with up to 18% reduction in fuel consumption across various WLTP classes.
2. FESS incorporation leads to notable emissions reduction, achieving up to 15% reduction in CO_2 emissions, supporting global sustainability goals.
3. Extended standby times of FESS enhance vehicle operational duration and efficiency, supporting longer vehicular journeys with minimal energy losses.
4. Optimisations in FESS design, such as slit walls and the use of helium at reduced pressure, considerably reduce windage losses, improving fuel efficiency and emissions.

8.2. Contributions to Knowledge

This thesis has made several significant contributions to the field of energy storage and recovery systems, particularly in the context of optimising FESS for improved energy efficiency in light-duty vehicles. The research findings not only advance the understanding of FESS design and integration but also offer valuable insights for the broader pursuit of sustainable transportation solutions. The contributions to knowledge encompass:

1. Through a detailed investigation of aerodynamic performance and design parameters, this thesis has identified key factors that significantly influence FESS efficiency. The development of an optimised design that minimises windage losses and enhances thermal management represents a substantial contribution to the field of energy storage systems.
2. The adoption of a hybrid design approach, combining CFD simulations with statistical optimisation tools, sets a standard for the investigation of energy storage systems. This methodological approach has proven successful in bridging the gap between theoretical predictions and practical applications, providing a solid foundation for future research in this area.
3. By demonstrating the potential of optimised FESS to significantly improve fuel efficiency and reduce carbon emissions in light-duty vehicles, this thesis contributes to the global efforts to decarbonise transportation. The findings provide a compelling case for the integration of FESS in the automotive industry, highlighting its role in advancing sustainable mobility.

4. The comprehensive analysis of design, performance, and integration challenges associated with FESS has laid a solid foundation for further investigation. The identification of future research directions, including the exploration of hybrid energy systems and large-scale experimental validations, offers a clear roadmap for advancing this promising technology.
5. Beyond its academic contributions, this thesis offers practical insights for policymakers and industry stakeholders. The recommendations for FESS adoption and the cost-benefit analysis provided here can inform policy decisions and strategic planning, facilitating the broader implementation of energy recovery systems in transportation.

8.3. Implications for Practice

The findings of this thesis on optimising FESS for light-duty vehicles hold profound implications for practice, particularly within the automotive industry and sustainable transportation development. By showcasing the enhanced energy efficiency and emissions reduction capabilities of the optimised FESS, this research offers a noticeable solution to some of the most pressing challenges facing the sector today. For automotive manufacturers, the integration of an optimised FESS represents an opportunity to advance current energy recovery technologies, enabling the production of vehicles that are not only more fuel-efficient but also have a lower environmental impact. Such advancements could play a pivotal role in meeting increasing emissions regulations and consumer demands for greener transportation options. Moreover, the detailed design and operational insights provided by this study serve as a valuable resource for engineers and designers seeking to incorporate FESS into vehicles. The optimisation strategies identified, including aerodynamic improvements and thermal management techniques, offer practical guidance that can be directly applied to the development of next-generation energy storage solutions.

For policymakers and regulatory bodies, the evidence presented in support of FESS as a viable technology for reducing vehicle emissions underscores the importance of supportive frameworks and incentives to encourage the adoption of such technologies. Investment in research and development, coupled with policies that favour the use of energy-efficient technologies, could significantly enhance the automotive industry's contribution to achieving carbon reduction targets. In the broader context of sustainable transportation, the successful deployment of optimised FESS technologies could inspire further exploration of hybrid energy systems and alternative energy recovery solutions. As such, the implications of this thesis extend beyond the immediate benefits of improved FESS performance, pointing the way towards a more sustainable and efficient transportation future.

8.4. Limitations of the Study

While this thesis provides significant insights into the optimisation of FESS for light-duty vehicles, it is important to acknowledge the limitations encountered during the research process. One of the primary limitations arises from the reliance on CFD simulations to predict the aerodynamic performance of the FESS. Despite the high degree of accuracy and reliability of these simulations, as confirmed by experimental validations, they inherently involve certain assumptions and simplifications that may not fully capture the complexities of real-world operating conditions.

Another limitation pertains to the scope of the experimental validations conducted. The experiments were designed to test specific aspects of the FESS performance, particularly in relation to aerodynamic and thermal efficiency. However, these tests were conducted under controlled conditions that may not perfectly emulate the variable and unpredictable nature of actual automotive environments.

Furthermore, the economic analysis of the optimised FESS integration into light-duty vehicles was based on current market conditions and pricing. Changes in economic factors, material costs, or manufacturing technologies could affect the cost-benefit analysis presented, impacting the feasibility and attractiveness of FESS adoption from a commercial perspective. Finally, the focus on light-duty vehicles as the primary application for the optimised FESS, while justified by the significant potential for impact in this segment, means that the findings may not be directly applicable to other vehicle types or transportation modes. Additional research would be required to adapt and validate the optimised FESS for use in heavy-duty vehicles or public transportation systems.

8.5. Recommendations for Future Work

Building upon the foundation established by this thesis in optimising FESS for light-duty vehicles, several avenues for future research emerge. These recommendations aim to address the limitations identified in the study, explore new dimensions of FESS application, and further contribute to the field of sustainable transportation.

1. Future studies should aim to conduct extensive experimental validations of the optimised FESS under a wider array of real-world operating conditions. This includes testing the system in diverse environmental conditions, under variable loads, and over extended periods to better understand its performance and durability in actual automotive applications.
2. Continuous advancements in materials science and engineering present opportunities to further enhance FESS efficiency and sustainability. Future research could explore the use of novel materials with superior mechanical, thermal, and aerodynamic properties, as well as innovative manufacturing techniques that could reduce costs and improve system performance.
3. While this thesis focuses on light-duty vehicles, the potential benefits of optimised FESS could extend to heavy-duty vehicles, public transportation systems, and even stationary energy

storage applications. Future research should investigate the adaptation and optimisation of FESS for these diverse applications, evaluating performance, efficiency, and environmental impacts across different transportation modes.

4. It is recommended that future studies conduct a techno-economic assessment to validate the design choices made in this research for the proposed FESS models, ensuring their feasibility and economic viability.
5. Further research should investigate the effectiveness of active cooling systems in improving the performance of FESS models. This study only considered passive cooling effects.

8.6. Concluding Remarks

This thesis has advanced the understanding and development of optimised FESS for light-duty vehicles, marking a significant step toward more efficient and sustainable transportation solutions. Through careful research, innovative design optimisation, and comprehensive analysis, the study has demonstrated the potential of FESS to enhance energy recovery, improve vehicle performance, and reduce environmental impact. While acknowledging the limitations of the current study, the recommendations for future work set forth a roadmap for addressing these challenges, exploring new opportunities, and continuing the pursuit of sustainable energy storage technologies. The implications of this research for practice underscore the pivotal role of FESS in the automotive industry's transition to sustainability, offering valuable insights for manufacturers, policymakers, and researchers alike.

References

[1] B. Gills and J. Morgan, ‘Global climate emergency: After COP24, climate science, urgency, and the threat to humanity’, in *Economics and Climate Emergency*, Routledge, 2022, pp. 253–270.

[2] M. Anwar *et al.*, ‘Sources of carbon dioxide and environmental Issues’, *Sustainable Agriculture Reviews 37: Carbon Sequestration Vol. 1 Introduction and Biochemical Methods*, pp. 13–36, 2019.

[3] C. T. Lee, H. Hashim, C. S. Ho, Y. Van Fan, and J. J. Klemeš, ‘Sustaining the low-carbon emission development in Asia and beyond: Sustainable energy, water, transportation and low-carbon emission technology’, *Journal of Cleaner Production*, vol. 146, pp. 1–13, 2017.

[4] H. Ritchie, ‘Cars, planes, trains: where do CO2 emissions from transport come from?’, Oct. 2020. Accessed: Mar. 09, 2023. [Online]. Available: https://ourworldindata.org/co2-emissions-from-transport

[5] M. R. Cruz, D. Z. Fitiwi, S. F. Santos, and J. P. Catalão, ‘A comprehensive survey of flexibility options for supporting the low-carbon energy future’, *Renewable and Sustainable Energy Reviews*, vol. 97, pp. 338–353, 2018.

[6] S. Gössling, J. Kees, and T. Litman, ‘The lifetime cost of driving a car’, *Ecological Economics*, vol. 194, p. 107335, 2022.

[7] H. AYDIN and C. İLKILIÇ, ‘Air pollution, pollutant emissions and harmfull effects’, *Journal of Engineering and Technology*, vol. 1, no. 1, pp. 8–15, 2017.

[8] M. Ehsani, A. Ahmadi, and D. Fadai, ‘Modeling of vehicle fuel consumption and carbon dioxide emission in road transport’, *Renewable and sustainable energy reviews*, vol. 53, pp. 1638–1648, 2016.

[9] N. Kronberg, ‘Transport Statistics Great Britain: 2022 Domestic Travel’, National statistics. Accessed: Nov. 03, 2023. [Online]. Available: https://www.gov.uk/government/statistics/transport-statistics-great-britain-2022/transport-statistics-great-britain-2022-domestic-travel

[10] J. Liu, A. Khattak, and X. Wang, ‘A comparative study of driving performance in metropolitan regions using large-scale vehicle trajectory data: Implications for sustainable cities’, *International Journal of Sustainable Transportation*, vol. 11, no. 3, pp. 170–185, 2017.

[11] D. Transport, ‘A Better, Greener Britain’, *Department for Transport*, 2021.

[12] S. Goss, ‘A zero emission vehicle (ZEV) mandate and CO emissions regulation’, 2023.

[13] C. Brand, J. Anable, I. Ketsopoulou, and J. Watson, ‘Road to zero or road to nowhere? Disrupting transport and energy in a zero carbon world’, *Energy Policy*, vol. 139, p. 111334, 2020.

[14] P. Aguilar and B. Groß, ‘Battery electric vehicles and fuel cell electric vehicles, an analysis of alternative powertrains as a mean to decarbonise the transport sector’, *Sustainable Energy Technologies and Assessments*, vol. 53, p. 102624, 2022.

[15] D. F. Dominković, I. Bačeković, A. S. Pedersen, and G. Krajačić, ‘The future of transportation in sustainable energy systems: Opportunities and barriers in a clean energy transition’, *Renewable and Sustainable Energy Reviews*, vol. 82, pp. 1823–1838, 2018.

[16] T. R. Hawkins, O. M. Gausen, and A. H. Strømman, ‘Environmental impacts of hybrid and electric vehicles—a review’, *The International Journal of Life Cycle Assessment*, vol. 17, pp. 997–1014, 2012.

[17] R. Macário, H. Meersman, and E. van de Voorde, ‘European Union and United Kingdom: Research roadmap for transport policy’, *A Research Agenda for Transport Policy*, p. 126, 2019.

[18] Automotive Council UK, ‘Light Duty Vehicle <3.5t Roadmap 2020’, Advanced Propulsion Centre Uk, Narrative Report, Feb. 2021.

[19] M. Juhala, ‘Improving vehicle rolling resistance and aerodynamics’, in *Alternative fuels and advanced vehicle technologies for improved environmental performance*, Elsevier, 2014, pp. 462–475.

[20] M. N. Sudin, M. A. Abdullah, S. A. Shamsuddin, F. R. Ramli, and M. M. Tahir, 'Review of research on vehicles aerodynamic drag reduction methods', *International Journal of Mechanical and Mechatronics Engineering*, vol. 14, no. 02, pp. 37–47, 2014.
[21] J. C. Kelly, J. L. Sullivan, A. Burnham, and A. Elgowainy, 'Impacts of vehicle weight reduction via material substitution on life-cycle greenhouse gas emissions', *Environmental science & technology*, vol. 49, no. 20, pp. 12535–12542, 2015.
[22] G. Conway, A. Joshi, F. Leach, A. García, and P. K. Senecal, 'A review of current and future powertrain technologies and trends in 2020', *Transportation Engineering*, vol. 5, p. 100080, 2021.
[23] Y. Al-Wreikat, C. Serrano, and J. R. Sodré, 'Driving behaviour and trip condition effects on the energy consumption of an electric vehicle under real-world driving', *Applied Energy*, vol. 297, p. 117096, 2021.
[24] M. S. Koroma *et al.*, 'Life cycle assessment of battery electric vehicles: Implications of future electricity mix and different battery end-of-life management', *Science of the Total Environment*, vol. 831, p. 154859, 2022.
[25] J. Lepitzki and J. Axsen, 'The role of a low carbon fuel standard in achieving long-term GHG reduction targets', *Energy Policy*, vol. 119, pp. 423–440, 2018.
[26] K. De Brucker, A. Verbeke, and C. Macharis, 'The applicability of multicriteria-analysis to the evaluation of intelligent transport systems (ITS)', *Research in Transportation Economics*, vol. 8, pp. 151–179, 2004.
[27] A. Gabriel-Buenaventura and B. Azzopardi, 'Energy recovery systems for retrofitting in internal combustion engine vehicles: A review of techniques', *Renewable and Sustainable Energy Reviews*, vol. 41, pp. 955–964, 2015.
[28] L. Rodgers, S. Zoepf, and J. Prenninger, 'Analysing the energy consumption of the BMW ActiveE field trial vehicles with application to distance to empty algorithms', *Transportation Research Procedia*, vol. 4, pp. 42–54, 2014.
[29] W. Zhao, T. Zhang, H. Kildahl, and Y. Ding, 'Mobile energy recovery and storage: Multiple energy-powered EVs and refuelling stations', *Energy*, vol. 257, p. 124697, 2022.
[30] B. Qawasmeh, A. Al-Salaymeh, A. Swaity, A. Mosleh, and S. Boshmaf, 'Investigation of performance characteristics of hybrid cars', *Environmental Engineering*, vol. 14, pp. 59–69, 2017.
[31] M. Tahani, S. Javan, and M. Biglari, 'A comprehensive study on waste heat recovery from internal combustion engines using organic Rankine cycle', *Thermal Science*, vol. 17, no. 2, pp. 611–624, 2013.
[32] N. V. Burnete, F. Mariasiu, D. Moldovanu, and C. Depcik, 'Simulink model of a thermoelectric generator for vehicle waste heat recovery', *Applied Sciences*, vol. 11, no. 3, p. 1340, 2021.
[33] S. Lion, C. N. Michos, I. Vlaskos, C. Rouaud, and R. Taccani, 'A review of waste heat recovery and Organic Rankine Cycles (ORC) in on-off highway vehicle Heavy Duty Diesel Engine applications', *Renewable and Sustainable Energy Reviews*, vol. 79, pp. 691–708, 2017.
[34] E. Alwi, B. Amin, and W. Afnison, 'Electric turbo compounding (ETC) as exhaust energy recovery system on vehicle', *GEOMATE Journal*, vol. 19, no. 71, pp. 228–234, 2020.
[35] M. A. Abdelkareem *et al.*, 'Vibration energy harvesting in automotive suspension system: A detailed review', *Applied energy*, vol. 229, pp. 672–699, 2018.
[36] L. Yu, S. Huo, W. Xuan, and L. Zuo, 'Assessment of ride comfort and braking performance using energy-harvesting shock absorber', *SAE International Journal of Passenger Cars-Mechanical Systems*, vol. 8, no. 2015-01–0649, pp. 482–491, 2015.
[37] C. Śliwiński, 'Kinetic energy recovery systems in motor vehicles', presented at the IOP Conference Series: Materials Science and Engineering, IOP Publishing, 2016, p. 012056.
[38] K. Erhan and E. Özdemir, 'Prototype production and comparative analysis of high-speed flywheel energy storage systems during regenerative braking in hybrid and electric vehicles', *Journal of Energy Storage*, vol. 43, p. 103237, 2021.
[39] C. Armenta-Déu and H. Cortés, 'Analysis of Kinetic Energy Recovery Systems in Electric Vehicles', *Vehicles*, vol. 5, no. 2, pp. 387–403, 2023.

[40] R. T. Doucette and M. D. McCulloch, ‘A comparison of high-speed flywheels, batteries, and ultracapacitors on the bases of cost and fuel economy as the energy storage system in a fuel cell based hybrid electric vehicle’, *Journal of Power Sources*, vol. 196, no. 3, pp. 1163–1170, Feb. 2011, doi: 10.1016/j.jpowsour.2010.08.100.
[41] X. Luo, J. Wang, M. Dooner, and J. Clarke, ‘Overview of current development in electrical energy storage technologies and the application potential in power system operation’, *Applied energy*, vol. 137, pp. 511–536, 2015.
[42] D. Majumdar, M. Mandal, and S. K. Bhattacharya, ‘Journey from supercapacitors to supercapatteries: recent advancements in electrochemical energy storage systems’, *Emergent Materials*, vol. 3, pp. 347–367, 2020.
[43] D. Deng, ‘Li-ion batteries: basics, progress, and challenges’, *Energy Science & Engineering*, vol. 3, no. 5, pp. 385–418, 2015.
[44] H. Chen, T. N. Cong, W. Yang, C. Tan, Y. Li, and Y. Ding, ‘Progress in electrical energy storage system: A critical review’, *Progress in natural science*, vol. 19, no. 3, pp. 291–312, 2009.
[45] International Electrotechnical Commission, ‘Electrical energy storage: white paper’, *Geneva, Switzerland: International Electrotechnical Commission*, pp. 1–78, 2011.
[46] I. Hadjipaschalis, A. Poullikkas, and V. Efthimiou, ‘Overview of current and future energy storage technologies for electric power applications’, *Renewable and sustainable energy reviews*, vol. 13, no. 6–7, pp. 1513–1522, 2009.
[47] G. Ries and H.-W. Neumueller, ‘Comparison of energy storage in flywheels and SMES’, *Physica C: Superconductivity*, vol. 357, pp. 1306–1310, 2001.
[48] F. A. Farret and M. G. Simoes, *Integration of alternative sources of energy*. John Wiley & Sons, 2006.
[49] J. Kondoh *et al.*, ‘Electrical energy storage systems for energy networks’, *Energy conversion and management*, vol. 41, no. 17, pp. 1863–1874, 2000.
[50] S. M. Schoenung, ‘Characteristics and technologies for long-vs. short-term energy storage: a study by the DOE energy storage systems program’, Sandia National Lab.(SNL-NM), Albuquerque, NM (United States); Sandia …, 2001.
[51] A. Du Pasquier, I. Plitz, S. Menocal, and G. Amatucci, ‘A comparative study of Li-ion battery, supercapacitor and nonaqueous asymmetric hybrid devices for automotive applications’, *Journal of power sources*, vol. 115, no. 1, pp. 171–178, 2003.
[52] K. Tweed, ‘UK launches Europe’s largest energy storage trial’, *IEEE Spectrum. Published 1st August*, 2013.
[53] N. Author, ‘Review of electrical energy storage technologies and systems and of their potential for the UK’, *EA Technology*, vol. 1, p. 34, 2004.
[54] M. Beaudin, H. Zareipour, A. Schellenberglabe, and W. Rosehart, ‘Energy storage for mitigating the variability of renewable electricity sources: An updated review’, *Energy for sustainable development*, vol. 14, no. 4, pp. 302–314, 2010.
[55] F. Díaz-González, A. Sumper, O. Gomis-Bellmunt, and F. D. Bianchi, ‘Energy management of flywheel-based energy storage device for wind power smoothing’, *Applied energy*, vol. 110, pp. 207–219, 2013.
[56] C. J. Rydh and B. A. Sandén, ‘Energy analysis of batteries in photovoltaic systems. Part II: Energy return factors and overall battery efficiencies’, *Energy conversion and management*, vol. 46, no. 11–12, pp. 1980–2000, 2005.
[57] M. Winter and R. J. Brodd, ‘What are batteries, fuel cells, and supercapacitors?’, *Chemical reviews*, vol. 104, no. 10, pp. 4245–4270, 2004.
[58] J. R. Miller, ‘Capacitors for Power Grid Storage’, presented at the Trans-Atlantic Workshop on Storage Technologies for Power Grids Washington DC Convention Center, 2010, pp. 19–20.
[59] E. N. Power, ‘Capacitors age and capacitors have an end of life’, *White paper*, 2008.
[60] S. C. Smith, P. Sen, and B. Kroposki, ‘Advancement of energy storage devices and applications in electrical power system’, presented at the 2008 IEEE Power and Energy Society General Meeting-Conversion and Delivery of Electrical Energy in the 21st Century, IEEE, 2008, pp. 1–8.

[61] H. Ibrahim, A. Ilinca, and J. Perron, ‘Energy storage systems—Characteristics and comparisons’, *Renewable and sustainable energy reviews*, vol. 12, no. 5, pp. 1221–1250, 2008.
[62] W. F. Pickard, A. Q. Shen, and N. J. Hansing, ‘Parking the power: Strategies and physical limitations for bulk energy storage in supply–demand matching on a grid whose input power is provided by intermittent sources’, *Renewable and Sustainable Energy Reviews*, vol. 13, no. 8, pp. 1934–1945, 2009.
[63] W. Smith, ‘The role of fuel cells in energy storage’, *Journal of Power Sources*, vol. 86, no. 1–2, pp. 74–83, 2000.
[64] J. P. Barton and D. G. Infield, ‘Energy storage and its use with intermittent renewable energy’, *IEEE transactions on energy conversion*, vol. 19, no. 2, pp. 441–448, 2004.
[65] C. Schaber, P. Mazza, and R. Hammerschlag, ‘Utility-scale storage of renewable energy’, *The Electricity Journal*, vol. 17, no. 6, pp. 21–29, 2004.
[66] R. Baxter, *Energy storage: a nontechnical guide*. PennWell Books, 2006.
[67] A. Brito, *Dynamic Modelling*. BoD–Books on Demand, 2010.
[68] P. Taylor, R. Bolton, D. Stone, X.-P. Zhang, C. Martin, and P. Upham, ‘Pathways for energy storage in the UK’, *Report for the centre for low carbon futures, York*, 2012.
[69] P. De Boer and J. Raadschelders, ‘Flow Batteries: Briefing Paper’, *Leonardo Energy,[Online]. Available: http://www. leonardoenergy. org/drupal/files/2007/Briefing% 20paper*, 2007.
[70] D. Rastler, ‘Overview of electric energy storage options for the electric enterprise’, presented at the Electric Power Research Institute, Presentation at the CEC Staff Workshop on Energy Storage Technologies, 2009.
[71] S. Mekhilef, R. Saidur, and A. Safari, ‘Comparative study of different fuel cell technologies’, *Renewable and Sustainable Energy Reviews*, vol. 16, no. 1, pp. 981–989, 2012.
[72] E. Pipitone, G. Vitale, R. Lanzafame, S. Brusca, S. Mauro, and S. Beccari, ‘A Feasibility Analysis of an Electric KERS for Internal Combustion Engine Vehicles’, SAE Technical Paper, 0148–7191, 2019.
[73] A. T. Hamada and M. F. Orhan, ‘An overview of regenerative braking systems’, *Journal of Energy Storage*, vol. 52, p. 105033, 2022.
[74] Y. Wang *et al.*, ‘A comprehensive review of battery modeling and state estimation approaches for advanced battery management systems’, *Renewable and Sustainable Energy Reviews*, vol. 131, p. 110015, 2020.
[75] H. Budde-Meiwes *et al.*, ‘A review of current automotive battery technology and future prospects’, *Proceedings of the Institution of Mechanical Engineers, Part D: Journal of Automobile Engineering*, vol. 227, no. 5, pp. 761–776, 2013.
[76] S. Shah, ‘The design and development of a high speed composite flywheel for hybrid vehicles’, 2007.
[77] M. Morris and S. Tosunoglu, ‘Comparison of rechargeable battery technologies’, presented at the ASME Early Career Technical Conference, Atlanta, Georgia, 2012, pp. 2–12.
[78] A. Burke, ‘Ultracapacitor technologies and application in hybrid and electric vehicles’, *International Journal of Energy Research*, vol. 34, no. 2, pp. 133–151, 2010.
[79] L. Pugi, M. Pagliai, A. Nocentini, G. Lutzemberger, and A. Pretto, ‘Design of a hydraulic servo-actuation fed by a regenerative braking system’, *Applied Energy*, vol. 187, pp. 96–115, 2017.
[80] X. Li and A. Palazzolo, ‘A review of flywheel energy storage systems: state of the art and opportunities’, *Journal of Energy Storage*, vol. 46, p. 103576, 2022.
[81] J. Van Mierlo, P. Van den Bossche, and G. Maggetto, ‘Models of energy sources for EV and HEV: fuel cells, batteries, ultracapacitors, flywheels and engine-generators’, *Journal of power sources*, vol. 128, no. 1, pp. 76–89, 2004.
[82] M. Krack, M. Secanell, and P. Mertiny, ‘Rotor design for high-speed flywheel energy storage systems’, *Energy Storage in the Emerging Era of Smart Grids; IntechOpen: London, UK*, pp. 41–68, 2011.
[83] S. M. Lukic, J. Cao, R. C. Bansal, F. Rodriguez, and A. Emadi, ‘Energy storage systems for automotive applications’, *IEEE Transactions on industrial electronics*, vol. 55, no. 6, pp. 2258–2267, 2008.

[84] M. E. Amiryar and K. R. Pullen, ‘A review of flywheel energy storage system technologies and their applications’, *Applied Sciences*, vol. 7, no. 3, p. 286, 2017.
[85] M. Hedlund, J. Lundin, J. De Santiago, J. Abrahamsson, and H. Bernhoff, ‘Flywheel energy storage for automotive applications’, *Energies*, vol. 8, no. 10, pp. 10636–10663, 2015.
[86] G. Berdichevsky, K. Kelty, J. Straubel, and E. Toomre, ‘The tesla roadster battery system’, *Tesla Motors*, vol. 1, no. 5, pp. 1–5, 2006.
[87] L. Lu, X. Han, J. Li, J. Hua, and M. Ouyang, ‘A review on the key issues for lithium-ion battery management in electric vehicles’, *Journal of power sources*, vol. 226, pp. 272–288, 2013.
[88] D. Xingjian, W. Kunpeng, Z. Xiaozhang, J. Xinjian, and Z. Kai, ‘A review on flywheel energy storage technology in fifty years’, *Energy Storage Science and Technology*, vol. 7, no. 5, p. 765, 2018.
[89] S. Bhardwaj *et al.*, ‘Problems Faced by Automobile Industries: Case Study on Tesla’, *International journal of Tourism and hospitality in Asia Pasific (IJTHAP)*, vol. 3, no. 2, pp. 78–88, 2020.
[90] F. Faraji, A. Majazi, and K. Al-Haddad, ‘A comprehensive review of flywheel energy storage system technology’, *Renewable and Sustainable Energy Reviews*, vol. 67, pp. 477–490, 2017.
[91] J. M. Madura and D. Lieu, ‘Analysis of an electromechanical flywheel for use as a dedicated high-power device in a hybrid electric vehicle’, *Power*, vol. 2, no. 1.815, pp. 49–8, 2019.
[92] J. Hilton, ‘Flybrid systems—Mechanical hybrid systems’, *Proceedings of the Engine Expo*, 2008.
[93] I. Foley, ‘Williams Hybrid Power—Flywheel energy storage’, *Engine Expo*, 2013.
[94] G. Genta, *Kinetic energy storage: theory and practice of advanced flywheel systems*. Butterworth-Heinemann, 1985.
[95] R. C. Clerk, ‘The utilization of flywheel energy’, *SAE Transactions*, pp. 508–543, 1964.
[96] D. Rabenhorst, ‘PRIMARY ENERGY STORAGE AND THE SUPER FLYWHEEL.’, JOHNS HOPKINS UNIV SILVER SPRING MD APPLIED PHYSICS LAB, 1969.
[97] A. Buchroithner, *Flywheel Energy Storage: In Automotive Engineering*. Springer Nature, 2023.
[98] R. F. Post, ‘A new look at an old idea-The electromechanical battery’, *Science and Technology Review*, 1996.
[99] F. J. Thoolen, ‘Development of an advanced high speed flywheel energy storage system’, 1993.
[100] A. G. Olabi, T. Wilberforce, M. A. Abdelkareem, and M. Ramadan, ‘Critical review of flywheel energy storage system’, *Energies*, vol. 14, no. 8, p. 2159, 2021.
[101] M. E. Amiryar and K. R. Pullen, ‘Analysis of standby losses and charging cycles in flywheel energy storage systems’, *Energies*, vol. 13, no. 17, p. 4441, 2020.
[102] R. Hebner, J. Beno, and A. Walls, ‘Flywheel batteries come around again’, *IEEE spectrum*, vol. 39, no. 4, pp. 46–51, 2002.
[103] H. Liu and J. Jiang, ‘Flywheel energy storage—An upswing technology for energy sustainability’, *Energy and Buildings*, vol. 39, no. 5, pp. 599–604, May 2007, doi: 10.1016/j.enbuild.2006.10.001.
[104] R. Sebastián and R. P. Alzola, ‘Flywheel energy storage systems: Review and simulation for an isolated wind power system’, *Renewable and Sustainable Energy Reviews*, vol. 16, no. 9, pp. 6803–6813, 2012.
[105] M. Read, R. Smith, and K. Pullen, ‘Optimisation of flywheel energy storage systems with geared transmission for hybrid vehicles’, *Mechanism and Machine Theory*, vol. 87, pp. 191–209, 2015.
[106] Sam, ‘Flywheel hybrid systems (KERS)’, Racecar Engineering. Accessed: Dec. 29, 2023. [Online]. Available: https://www.racecar-engineering.com/articles/f1/flywheel-hybrid-systems-kers/
[107] ‘Punch Flybrid history’, Punch Flybrid. Accessed: Dec. 29, 2023. [Online]. Available: https://punchflybrid.com/our-roots-2/

[108] S. Miladinović, L. Ivanović, M. Blagojević, and B. Stojanović, ‘The development of magnetic gears for transportation applications’, *Mobility and Vehicle Mechanics*, vol. 43, no. 1, pp. 39–55, 2017.
[109] J. Li, J. Zhao, and X. Zhang, ‘A novel energy recovery system integrating flywheel and flow regeneration for a hydraulic excavator boom system’, *Energies*, vol. 13, no. 2, p. 315, 2020.
[110] S. Wicki and E. G. Hansen, ‘Clean energy storage technology in the making: An innovation systems perspective on flywheel energy storage’, *Journal of cleaner production*, vol. 162, pp. 1118–1134, 2017.
[111] L. Hua, Z. Jian, X. Da, and M. Xiaojun, ‘Design for hybrid electric drive system of armored vehicle with two energy storage devices’, presented at the 2009 International Conference on Sustainable Power Generation and Supply, IEEE, 2009, pp. 1–5.
[112] D. Cross and J. Hilton, ‘High speed flywheel based hybrid systems for low carbon vehicles’, presented at the IET HEVC 2008-Hybrid and Eco-Friendly Vehicle Conference, IET, 2008, pp. 1–5.
[113] A. Boretti, ‘Comparison of fuel economies of high efficiency diesel and hydrogen engines powering a compact car with a flywheel based kinetic energy recovery systems’, *International Journal of Hydrogen Energy*, vol. 35, no. 16, pp. 8417–8424, 2010.
[114] J. G. Hansen, ‘An assessment of flywheel high power energy storage technology for hybrid vehicles’, Oak Ridge National Lab.(ORNL), Oak Ridge, TN (United States), 2012.
[115] R. Hayes, J. Kajs, R. Thompson, and J. Beno, ‘Design and testing of a flywheel battery for a transit bus’, *SAE transactions*, pp. 2199–2207, 1999.
[116] C. Hearn, M. Flynn, M. Lewis, R. Thompson, B. Murphy, and R. Longoria, ‘Low cost flywheel energy storage for a fuel cell powered transit bus’, presented at the 2007 IEEE Vehicle Power and Propulsion Conference, IEEE, 2007, pp. 829–836.
[117] L. Hickman, ‘F1 fuel-saving flywheel to be fitted to London’s buses’, *The Guardian*, Apr. 18, 2012. Accessed: Feb. 28, 2022. [Online]. Available: https://www.theguardian.com/environment/2012/apr/18/f1-fuel-saving-flywheel-buses
[118] T. for L. | E. J. Matters, ‘Bus fleet data & audits’, Transport for London. Accessed: Nov. 07, 2023. [Online]. Available: https://www.tfl.gov.uk/corporate/publications-and-reports/bus-fleet-data-and-audits
[119] ‘Flybus to start testing first flywheel hybrid bus - The Commercial Vehicle Show’. Accessed: Nov. 02, 2023. [Online]. Available: https://cvshow.com/flybus-to-start-testing-first-flywheel-hybrid-bus/
[120] ‘GKN - Gyrodrive - Advanced Propulsion Centre’. Accessed: Feb. 28, 2022. [Online]. Available: https://www.apcuk.co.uk/case-studies/gkn-gyrodrive/
[121] M. Meinert, P. Prenleloup, S. Schmid, and R. Palacin, ‘Energy storage technologies and hybrid architectures for specific diesel-driven rail duty cycles: Design and system integration aspects’, *Applied Energy*, vol. 157, pp. 619–629, 2015.
[122] O. Solis *et al.*, ‘LA metro red line wayside energy storage substation revenue service regenerative energy saving results’, presented at the ASME/IEEE Joint Rail Conference, American Society of Mechanical Engineers, 2014, p. V001T07A003.
[123] R. Thelen, J. Herbst, and M. Caprio, ‘A 2 MW flywheel for hybrid locomotive power’, presented at the 2003 IEEE 58th Vehicular Technology Conference. VTC 2003-Fall (IEEE Cat. No. 03CH37484), IEEE, 2003, pp. 3231–3235.
[124] J. P. Torreglosa, P. Garcia, L. M. Fernández, and F. Jurado, ‘Predictive control for the energy management of a fuel-cell–battery–supercapacitor tramway’, *IEEE Transactions on Industrial Informatics*, vol. 10, no. 1, pp. 276–285, 2013.
[125] F. Lacôte, ‘Alstom-Future trends in railway transportation’, *Japan Railway and Transport Review*, vol. 42, pp. 4–9, 2005.
[126] T. Ratniyomchai, S. Hillmansen, and P. Tricoli, ‘Recent developments and applications of energy storage devices in electrified railways’, *IET Electrical Systems in Transportation*, vol. 4, no. 1, pp. 9–20, 2014.
[127] M. M. Flynn, P. McMullen, and O. Solis, ‘Saving energy using flywheels’, *IEEE Industry applications magazine*, vol. 14, no. 6, pp. 69–76, 2008.

[128] ‘PUNCH Power 200’, Punch Flybrid. Accessed: Nov. 07, 2023. [Online]. Available: https://punchflybrid.com/punch-power-200/
[129] B. Bolund, H. Bernhoff, and M. Leijon, ‘Flywheel energy and power storage systems’, *Renewable and Sustainable Energy Reviews*, vol. 11, no. 2, pp. 235–258, 2007.
[130] T. M. Letcher, R. Law, and D. Reay, *Storing energy: with special reference to renewable energy sources*, vol. 86. Elsevier Amsterdam, 2016.
[131] P. Komor and J. Glassmire, ‘Electricity Storage and Renewables for Island Power. A Guide for Decision Makers’, 2012.
[132] S. EirGrid, ‘All--Island Generation Capacity Statement 2012--2021, SONI & EirGrid’, *EirGrid & SONI*, 2011.
[133] V. Gevorgian and D. Corbus, ‘Ramping performance analysis of the Kahuku wind-energy battery storage system’, National Renewable Energy Lab.(NREL), Golden, CO (United States), 2013.
[134] M. P. Schroeder, J. Yu, and D. Teumim, *Guiding the selection and application of wayside energy storage technologies for rail transit and electric utilities*, no. TCRP Project J-6/Task 75. 2010.
[135] ‘Alaskan microgrid to pair battery, flywheel storage systems for Anchorage area’, Utility Dive. Accessed: Nov. 04, 2023. [Online]. Available: https://www.utilitydive.com/news/alaskan-microgrid-to-pair-battery-flywheel-storage-systems-for-anchorage-a/435609/
[136] ‘Electromagnetic Aircraft Launch System - EMALS’. Accessed: Nov. 04, 2023. [Online]. Available: https://www.globalsecurity.org/military/systems/ship/systems/emals.htm
[137] ‘Aircraft Launch and Recovery Systems’, General Atomics. Accessed: Nov. 04, 2023. [Online]. Available: https://www.ga.com/alre
[138] W. Gengji and W. Ping, ‘Rotor loss analysis of PMSM in flywheel energy storage system as uninterruptable power supply’, *IEEE Transactions on Applied Superconductivity*, vol. 26, no. 7, pp. 1–5, 2016.
[139] A. Frank and N. Beachley, ‘Improved fuel economy in automobiles by use of a flywheel energy management system’, presented at the Flywheel Technology Symposium, 1975, p. 76.
[140] U. Diego-Ayala, P. Martinez-Gonzalez, N. McGlashan, and K. Pullen, ‘The mechanical hybrid vehicle: an investigation of a flywheel-based vehicular regenerative energy capture system’, *Proceedings of the Institution of Mechanical Engineers, Part D: Journal of Automobile Engineering*, vol. 222, no. 11, pp. 2087–2101, 2008.
[141] D. B. Kok, ‘Design optimisation of a flywheel hybrid vehicle’, 1999.
[142] W. V. Loscutoff, ‘Flywheel-heat engine power for an energy-economic personal vehicle’, Battelle Pacific Northwest Labs., Richland, Wash.(USA), 1976.
[143] C. Wang, X. Liang, C. Chapelsky, D. Koval, and A. Knight, ‘Application of flywheel system in series hybrid transit bus’, presented at the 2009 IEEE Vehicle Power and Propulsion Conference, IEEE, 2009, pp. 1529–1534.
[144] P. Dietrich, M. K. Eberle, and H. U. Hörler, ‘Results of the ETH-hybrid III-vehicle project and outlook’, SAE Technical Paper, 0148–7191, 1999.
[145] J. Lundin, ‘Flywheel in an all-electric propulsion system’, 2011.
[146] P. D. Agarwal, ‘Energy Utilization of electric and hybrid vehicles and their impact on US national energy consumption’, *International Journal of Vehicle Design*, vol. 3, no. 4, pp. 436–449, 1982.
[147] L. Lawson, ‘Applications of kinetic energy storage to transportation systems’, *High Speed Ground Transportation Journal*, vol. 12, no. 3, 1978.
[148] A. V. Filatov and E. H. Maslen, ‘Passive magnetic bearing for flywheel energy storage systems’, *IEEE Transactions on Magnetics*, vol. 37, no. 6, pp. 3913–3924, 2001.
[149] C. Sami, L. Luc, R. Gunther, and T. A. M. Tolio, ‘CIRP Encyclopedia of Production Engineering’, 2019.
[150] V. Arora, P. Van der Hoogt, R. Aarts, and A. de Boer, ‘Identification of dynamic properties of radial air-foil bearings’, *International journal of mechanics and materials in design*, vol. 6, no. 4, pp. 305–318, 2010.
[151] M. Michalec, P. Svoboda, I. Křupka, and M. Hartl, ‘A review of the design and optimization of large-scale hydrostatic bearing systems’, *Engineering Science and Technology, an*

International Journal, vol. 24, no. 4, pp. 936–958, Aug. 2021, doi: 10.1016/j.jestch.2021.01.010.
[152] T. Inoue, H. Niimi, and Y. Ishida, 'Vibration suppression of the rotor system using both a ball balancer and axial control of the repulsive magnetic bearing', *Journal of Vibration and Control*, vol. 18, no. 4, pp. 484–498, 2012.
[153] C. A. Fonseca, I. Santos, and H. I. Weber, 'An experimental and theoretical approach of a pinned and a conventional ball bearing for active magnetic bearings', *Mechanical Systems and Signal Processing*, vol. 138, p. 106541, 2020.
[154] L. Ai, G. Zhang, W. Li, G. Liu, and Q. Liu, 'Optimization of radial-type superconducting magnetic bearing using the Taguchi method', *Physica C: Superconductivity and its Applications*, vol. 550, pp. 57–64, Jul. 2018, doi: 10.1016/j.physc.2018.03.013.
[155] R. K. Upadhyay and L. A. Kumaraswamidhas, 'Bearing failure issues and corrective measures through surface engineering', in *Handbook of Materials Failure Analysis*, Elsevier, 2018, pp. 209–233.
[156] G. Bischof, K. Reisinger, T. Singraber, and A. Summer, 'Gyroscopic Bearing Loads in Vehicular Flywheel-Based KERS', *SAE International Journal of Passenger Cars-Mechanical Systems*, vol. 7, no. 2014-01–0839, pp. 196–210, 2014.
[157] M. Isono, K. Yoshii, M. Hirose, T. Maeda, N. Sugitani, and K. Kurihara, 'Operation tests of 10 kWh-class flywheel energy storage system with radial-type superconducting magnetic bearings', *J Cryogenic Soc Jpn*, vol. 40, no. 12, pp. 578–584, 2005.
[158] K. Murakami, M. Komori, H. Mitsuda, and A. Inoue, 'Design of an energy storage flywheel system using permanent magnet bearing (PMB) and superconducting magnetic bearing (SMB)', *Cryogenics*, vol. 47, no. 4, pp. 272–277, 2007.
[159] D. Cross and C. Brockbank, 'Mechanical hybrid system comprising a flywheel and CVT for motorsport and mainstream automotive applications', presented at the SAE World Congress & Exhibition, 2006.
[160] K. Ghedamsi, D. Aouzellag, and E. Berkouk, 'Control of wind generator associated to a flywheel energy storage system', *Renewable Energy*, vol. 33, no. 9, pp. 2145–2156, 2008.
[161] M. Ye, S. Jiao, and B. Cao, 'Energy recovery for the main and auxiliary sources of electric vehicles', *Energies*, vol. 3, no. 10, pp. 1673–1690, 2010.
[162] C.-H. Cheng and J.-X. Ye, 'GA-based neural network for energy recovery system of the electric motorcycle', *Expert Systems with Applications*, vol. 38, no. 4, pp. 3034–3039, 2011.
[163] D. E. Kirk, *Optimal control theory: an introduction*. Courier Corporation, 2004.
[164] S. R. Cikanek and K. E. Bailey, 'Regenerative braking system for a hybrid electric vehicle', presented at the Proceedings of the 2002 American Control Conference (IEEE Cat. No. CH37301), IEEE, 2002, pp. 3129–3134.
[165] K. Inoue, K. Ogata, and T. Kato, 'Efficient power regeneration and drive of an induction motor by means of optimal torque derived by the variational method', *Electrical Engineering in Japan*, vol. 173, no. 1, pp. 41–50, 2010.
[166] J. Cao, B. Cao, W. Chen, and P. Xu, 'Neural network self-adaptive PID control for driving and regenerative braking of electric vehicle', presented at the 2007 IEEE international conference on automation and logistics, IEEE, 2007, pp. 2029–2034.
[167] Y. Xiao, X. Ge, and Z. Zheng, 'Analysis and Control of Flywheel Energy Storage Systems', *Energy Storage-Technologies and Applications*, 2013.
[168] M. Ghanaatian and S. Lotfifard, 'Control of flywheel energy storage systems in the presence of uncertainties', *IEEE Transactions on Sustainable Energy*, vol. 10, no. 1, pp. 36–45, 2018.
[169] Y. Zhou, Y. Li, Q. Lv, D. Lv, Y. Yang, and J. Zheng, 'Investigation of a high speed permanent magnet synchronous machine for magnetic suspended flywheel energy storage system', presented at the 2020 IEEE 4th Conference on Energy Internet and Energy System Integration (EI2), IEEE, 2020, pp. 2733–2737.
[170] V. M. Jape, H. M. Suryawanshi, and J. P. Modak, 'An efficient grasshopper optimization with recurrent neural network controller-based induction motor to replace flywheel of the process machine', *Transactions of the Institute of Measurement and Control*, vol. 43, no. 1, pp. 151–166, 2021.

[171] A. Khodadoost Arani, B. Zaker, and G. Gharehpetian, ‘A control strategy for flywheel energy storage system for frequency stability improvement in islanded microgrid’, *Iranian Journal of Electrical and Electronic Engineering*, vol. 13, no. 1, pp. 10–21, 2017.
[172] T. Wen, B. Xiang, and S. Zhang, ‘Optimal control for hybrid magnetically suspended flywheel rotor based on state feedback exact linearization model’, *Science Progress*, vol. 103, no. 3, p. 0036850420951389, 2020.
[173] W. Wang, Y. Li, M. Shi, and Y. Song, ‘Optimization and control of battery-flywheel compound energy storage system during an electric vehicle braking’, *Energy*, vol. 226, p. 120404, Jul. 2021, doi: 10.1016/j.energy.2021.120404.
[174] M. Mansour, S. Bendoukha, N. Barhoumi, and M. F. Mimouni, ‘A comparative study of the speed control of an IM–based flywheel energy storage system using PI–DTC and RFOC strategies’, *International Journal of Emerging Electric Power Systems*, vol. 22, no. 1, pp. 73–83, 2021.
[175] A. Buchroithner, H. Wegleiter, and B. Schweighofer, ‘Flywheel energy storage systems compared to competing technologies for grid load mitigation in EV fast-charging applications’, presented at the 2018 IEEE 27th International Symposium on Industrial Electronics (ISIE), IEEE, 2018, pp. 508–514.
[176] T. Ayodele, A. Ogunjuyigbe, and N. Oyelowo, ‘Hybridisation of battery/flywheel energy storage system to improve ageing of lead-acid batteries in PV-powered applications’, *International Journal of Sustainable Engineering*, vol. 13, no. 5, pp. 337–359, 2020.
[177] J. L. Strubhar, R. C. Thompson, T. T. Pak, J. J. Zierer, J. H. Beno, and R. J. Hayes, ‘Lightweight containment for high-energy rotating machines’, *IEEE transactions on magnetics*, vol. 39, no. 1, pp. 378–383, 2003.
[178] D. Bender, ‘Recommended practices for the safe design and operation of flywheels’, *US Department of Energy: Oak Ridge, TN, USA*, 2015.
[179] H. Naunheimer, B. Bertsche, J. Ryborz, and W. Novak, *Automotive transmissions: fundamentals, selection, design and application*. Springer Science & Business Media, 2010.
[180] G. Lechner and H. Naunheimer, *Automotive transmissions: fundamentals, selection, design and application*. Springer Science & Business Media, 1999.
[181] N. H. Beachley and A. A. Frank, ‘Continuously variable transmissions: Theory and practice’, Lawrence Livermore National Lab.(LLNL), Livermore, CA (United States), 1979.
[182] C. Brockbank and C. Greenwood, ‘Fuel economy benefits of a flywheel & CVT based mechanical hybrid for city bus and commercial vehicle applications’, *SAE International Journal of Commercial Vehicles*, vol. 2, no. 2009-01–2868, 2009.
[183] S. Akehurst, C. Brace, N. Vaughan, P. Milner, and Y. Hosoi, ‘Performance investigations of a novel rolling traction CVT’, *SAE transactions*, pp. 979–986, 2001.
[184] B. Bonsen, R. Pulles, S. Simons, M. Steinbuch, and P. Veenhuizen, ‘Implementation of a slip controlled CVT in a production vehicle’, presented at the Proceedings of 2005 IEEE Conference on Control Applications, 2005. CCA 2005., IEEE, 2005, pp. 1212–1217.
[185] L. Bertini, L. Carmignani, and F. Frendo, ‘Analytical model for the power losses in rubber V-belt continuously variable transmission (CVT)’, *Mechanism and Machine Theory*, vol. 78, pp. 289–306, 2014.
[186] E. L. Kumm, ‘Design study of flat belt CVT for electric vehicles’, 1980.
[187] M. Read, ‘Flywheel energy storage systems for rail’, 2010.
[188] K. van Berkel, L. Römers, T. Hofman, B. Vroemen, and M. Steinbuch, ‘Design of a low-cost hybrid powertrain with large fuel savings’, presented at the Proceedings of the 25th World Battery, Hybrid and Fuel Cell Electric Vehicle Symposium & Exhibition, Shenzhen, China, 2010.
[189] T. van Keulen, D. van Mullem, B. de Jager, J. T. Kessels, and M. Steinbuch, ‘Design, implementation, and experimental validation of optimal power split control for hybrid electric trucks’, *Control Engineering Practice*, vol. 20, no. 5, pp. 547–558, 2012.
[190] S. J. Amodeo, H. G. Chiacchiarini, and A. R. Oliva, ‘High-performance control of a DC–DC Z-source converter used for an excitation field driver’, *IEEE transactions on power electronics*, vol. 27, no. 6, pp. 2947–2957, 2011.

[191] A. S. Abdel-Khalik, A. A. Elserougi, A. M. Massoud, and S. Ahmed, ‘Fault current contribution of medium voltage inverter and doubly-fed induction-machine-based flywheel energy storage system’, *IEEE Transactions on Sustainable Energy*, vol. 4, no. 1, pp. 58–67, 2012.
[192] S.-M. Jang, D.-J. You, K.-J. Ko, and S.-K. Choi, ‘Design and experimental evaluation of synchronous machine without iron loss using double-sided Halbach magnetized PM rotor in high power FESS’, *IEEE transactions on magnetics*, vol. 44, no. 11, pp. 4337–4340, 2008.
[193] G. Liu and C. Zhang, ‘Sliding mode control of reaction flywheel-based brushless DC motor with buck converter’, *Chinese Journal of Aeronautics*, vol. 26, no. 4, pp. 967–975, 2013.
[194] J.-D. Park, C. Kalev, and H. F. Hofmann, ‘Control of high-speed solid-rotor synchronous reluctance motor/generator for flywheel-based uninterruptible power supplies’, *IEEE Transactions on Industrial Electronics*, vol. 55, no. 8, pp. 3038–3046, 2008.
[195] E. Severson, R. Nilssen, T. Undeland, and N. Mohan, ‘Magnetic equivalent circuit modeling of the AC homopolar machine for flywheel energy storage’, *IEEE Transactions on Energy Conversion*, vol. 30, no. 4, pp. 1670–1678, 2015.
[196] X.-L. Wang, Q.-C. Zhong, Z.-Q. Deng, and S.-Z. Yue, ‘Current-controlled multiphase slice permanent magnetic bearingless motors with open-circuited phases: Fault-tolerant controllability and its verification’, *IEEE Transactions on Industrial Electronics*, vol. 59, no. 5, pp. 2059–2072, 2011.
[197] L. Chang, ‘Comparison of AC drives for electric vehicles-a report on experts’ opinion survey’, *IEEE Aerospace and Electronic Systems Magazine*, vol. 9, no. 8, pp. 7–11, 1994.
[198] M. Ehsani, Y. Gao, and S. Gay, ‘Characterization of electric motor drives for traction applications’, presented at the IECON’03. 29th Annual Conference of the IEEE Industrial Electronics Society (IEEE Cat. No. 03CH37468), IEEE, 2003, pp. 891–896.
[199] A. Dhand and K. Pullen, ‘Review of battery electric vehicle propulsion systems incorporating flywheel energy storage’, *International Journal of Automotive Technology*, vol. 16, no. 3, pp. 487–500, 2015.
[200] S. Arnold, A. Saleeb, and N. Al-Zoubi, ‘Deformation and life analysis of composite flywheel disk systems’, *Composites part B: engineering*, vol. 33, no. 6, pp. 433–459, 2002.
[201] T. J. Pieronek, D. K. Decker, and V. A. Spector, ‘Spacecraft flywheel systems-benefits, and issues’, presented at the Proceedings of the IEEE 1997 National Aerospace and Electronics Conference. NAECON 1997, IEEE, 1997, pp. 589–593.
[202] H. Nakai, A. Matsuda, and M. Suzuki, ‘Development and testing of the suspension system for a flywheel battery’, *Control Engineering Practice*, vol. 9, no. 10, pp. 1039–1046, 2001.
[203] Z. Haitao and L. Xin, ‘Certification considerations for minimizing hazards caused by uncontained turbine engine and auxiliary power unit rotor failure’, *Procedia Engineering*, vol. 17, pp. 521–528, 2011.
[204] G. Fischer, R. Grothaus, and W. Hufenbach, ‘Experimental Failure Effect Analysis of Composite High-Speed Flywheel Rotors’, in *Composite Materials: Testing and Design, Fourteenth Volume*, ASTM International, 2003.
[205] A. Buchroithner, A. Brandstatter, and M. Recheis, ‘Mobile flywheel energy storage systems: determining rolling element bearing loads to expand possibilities’, *IEEE Vehicular Technology Magazine*, vol. 12, no. 3, pp. 83–94, 2017.
[206] A. T. McDonald, ‘Simplified gyrodynamics of road vehicles with high-energy flywheels’, presented at the 1980 Flywheel Technology Symposium, US Department of Energy, 1980, pp. 240–258.
[207] H. Otaki, ‘Some analysis of gyroidal effect and the development of a flywheel powered vehicle’, *SAE Transactions*, pp. 2503–2518, 1980.
[208] E. Butikov, ‘Precession and nutation of a gyroscope’, *EUROPEAN JOURNAL OF PHYSICS Eur. J. Phys*, vol. 27, pp. 1071–1081, Sep. 2006, doi: 10.1088/0143-0807/27/5/006.
[209] M. Kissai, ‘Optimal Coordination of Chassis Systems for Vehicle Motion Control’, 2019.
[210] T. M. Gür, ‘Review of electrical energy storage technologies, materials and systems: challenges and prospects for large-scale grid storage’, *Energy & Environmental Science*, vol. 11, no. 10, pp. 2696–2767, 2018.

[211] K. Pullen and C. Ellis, ‘Kinetic energy storage for vehicles’, presented at the IET-The Institution of Engineering and Technolgy Hybrid Vehicle Conference 2006, IET, 2006, pp. 91–108.
[212] P. Martinez-Gonzalez, ‘A study on the integration of a high-speed flywheel as an energy storage device in hybrid vehicles’, 2010.
[213] K. R. Pullen and A. Dhand, ‘15 - Mechanical and electrical flywheel hybrid technology to store energy in vehicles’, in *Alternative Fuels and Advanced Vehicle Technologies for Improved Environmental Performance*, R. Folkson, Ed., Woodhead Publishing, 2014, pp. 476–504. doi: 10.1533/9780857097422.2.476.
[214] S. Gurumurthy, A. Sharma, S. Sarkar, and V. Agarwal, ‘Apportioning and mitigation of losses in a Flywheel Energy Storage system’, presented at the 2013 4th IEEE international symposium on power electronics for distributed generation systems (PEDG), IEEE, 2013, pp. 1–6.
[215] A. Nachouane, A. Abdelli, G. Friedrich, and S. Vivier, ‘Estimation of windage losses inside very narrow air gaps of high speed electrical machines without an internal ventilation using CFD methods’, presented at the 2016 XXII International Conference on Electrical Machines (ICEM), IEEE, 2016, pp. 2704–2710.
[216] K. R. Anderson, J. Lin, and A. Wong, ‘Experimental and Numerical Study of Windage Losses in the Narrow Gap Region of a High-Speed Electric Motor’, *Fluids*, vol. 3, no. 1, p. 22, 2018.
[217] Y. Okada, T. Kosaka, and N. Matsui, ‘Windage loss reduction for hybrid excitation flux switching motors based on rotor structure design’, presented at the 2017 IEEE International Electric Machines and Drives Conference (IEMDC), IEEE, 2017, pp. 1–8.
[218] M. L. Hosain, R. B. Fdhila, and K. Rönnberg, ‘Air-gap flow and thermal analysis of rotating machines using CFD’, *Energy Procedia*, vol. 105, pp. 5153–5159, 2017.
[219] K. R. Anderson, J. Lin, C. McNamara, and V. Magri, ‘CFD study of forced air cooling and windage losses in a high speed electric motor’, *Journal of Electronics Cooling and Thermal Control*, vol. 5, no. 02, p. 27, 2015.
[220] A. Rasekh, P. Sergeant, and J. Vierendeels, ‘Development of correlations for windage power losses modeling in an axial flux permanent magnet synchronous machine with geometrical features of the magnets’, *Energies*, vol. 9, no. 12, p. 1009, 2016.
[221] M. L. Hosain and R. B. Fdhila, ‘Air-gap heat transfer in rotating electrical machines: a parametric study’, *Energy Procedia*, vol. 142, pp. 4176–4181, 2017.
[222] M. L. Hosain, R. B. Fdhila, and K. Rönnberg, ‘Taylor-Couette flow and transient heat transfer inside the annulus air-gap of rotating electrical machines’, *Applied Energy*, vol. 207, pp. 624–633, 2017.
[223] E. E. Swanson, P. S. O’Meara, and H.-H. Tsuei, ‘Annular Gap Windage Loss Measurements for High Speed Electrical Machinery’, presented at the Turbo Expo: Power for Land, Sea, and Air, American Society of Mechanical Engineers, 2017, p. V05BT15A005.
[224] E. E. Swanson, H.-H. Tsuei, and P. S. O’Meara, ‘The Effect of Axial Flow Velocity on Annular Gap Windage Power Loss’, presented at the Turbo Expo: Power for Land, Sea, and Air, American Society of Mechanical Engineers, 2017, p. V02BT42A002.
[225] J. F. Walton, H. Heshmat, and M. Tomaszewski, ‘Power Loss in High-Speed Micro Turbomachinery: An Experimental Study’, presented at the Turbo Expo: Power for Land, Sea, and Air, American Society of Mechanical Engineers, 2012, pp. 871–880.
[226] S. B. Pawar and B. Thorat, ‘CFD simulation of Taylor–Couette flow in scraped surface heat exchanger’, *Chemical Engineering Research and Design*, vol. 90, no. 3, pp. 313–322, 2012.
[227] V. Kale, M. Thomas, and M. Secanell, ‘On determining the optimal shape, speed, and size of metal flywheel rotors with maximum kinetic energy’, *Structural and Multidisciplinary Optimization*, vol. 64, no. 3, pp. 1481–1499, 2021.
[228] D.-D. Dang, X.-T. Pham, P. Labbe, F. Torriano, J.-F. Morissette, and C. Hudon, ‘CFD analysis of turbulent convective heat transfer in a hydro-generator rotor-stator system’, *Applied Thermal Engineering*, vol. 130, pp. 17–28, 2018.
[229] I. Chirită, N. Tănase, S. E. Apostol, C. Ilie, and M. Popa, ‘Design optimization of a flywheel using solidworks modeling and simulation capabilities’, presented at the 2017 International Conference on ENERGY and ENVIRONMENT (CIEM), IEEE, 2017, pp. 344–348.

[230] H. Nakane, Y. Okada, T. Kosaka, and N. Matsui, ‘Experimental study on windage loss reduction using two types of rotor for hybrid excitation flux switching motor’, presented at the 2016 XXII International Conference on Electrical Machines (ICEM), IEEE, 2016, pp. 1707–1713.
[231] P.-D. Pfister and Y. Perriard, ‘A 200 000 rpm, 2 kW slotless permanent magnet motor’, presented at the 2008 International Conference on Electrical Machines and Systems, IEEE, 2008, pp. 3054–3059.
[232] C. Wei *et al.*, ‘Research on windage losses of smooth rotor supported by active magnetic bearings in a vacuum chamber’, *Vacuum*, vol. 159, pp. 76–81, 2019.
[233] M. Awad and W. Martin, ‘Windage loss reduction study for TFTR pulse generator’, presented at the 17th IEEE/NPSS Symposium Fusion Engineering (Cat. No. 97CH36131), IEEE, 1997, pp. 1125–1128.
[234] C. Gazley Jr, ‘Heat-transfer characteristics of the rotational and axial flow between concentric cylinders’, *Transactions of the American Society of Mechanical Engineers*, vol. 80, no. 1, pp. 79–89, 1958.
[235] K. M. Becker and J. Kaye, ‘Measurements of diabatic flow in an annulus with an inner rotating cylinder’, 1962.
[236] F. Tachibana and S. Fukui, ‘Convective heat transfer of the rotational and axial flow between two concentric cylinders’, *Bulletin of JSME*, vol. 7, no. 26, pp. 385–391, 1964.
[237] D. A. Howey, P. R. Childs, and A. S. Holmes, ‘Air-gap convection in rotating electrical machines’, *IEEE transactions on industrial electronics*, vol. 59, no. 3, pp. 1367–1375, 2010.
[238] F. Asami, M. Miyatake, S. Yoshimoto, E. Tanaka, and T. Yamauchi, ‘A method of reducing windage power loss of a high-Speed motor using a viscous vacuum pump’, *Precision Engineering*, vol. 48, pp. 60–66, 2017.
[239] T. Engel and D. Braid, ‘High-speed motor for use in an ultrahigh-vacuum environment’, *Review of scientific instruments*, vol. 56, no. 8, pp. 1668–1669, 1985.
[240] M. E. Amiryar, K. R. Pullen, and D. Nankoo, ‘Development of a high-fidelity model for an electrically driven energy storage flywheel suitable for small scale residential applications’, *Applied Sciences*, vol. 8, no. 3, p. 453, 2018.
[241] H.-P. Liu, M. Werst, J. J. Hahne, and D. Bogard, ‘Prediction of windage losses of an enclosed high speed composite rotor in low air pressure environments’, presented at the Heat Transfer Summer Conference, 2003, pp. 15–23.
[242] Y. Suzuki, A. Koyanagi, M. Kobayashi, and R. Shimada, ‘Novel applications of the flywheel energy storage system’, *Energy*, vol. 30, no. 11–12, pp. 2128–2143, 2005.
[243] M. A. Skinner, ‘Characterization of passive discharge losses in a flywheel energy storage system’, 2017.
[244] L. Matuszewski, ‘New designs of centrifugal magnetic fluid seals for rotating shafts in marine technology’, *Polish Maritime Research*, vol. 26, no. 2, pp. 33–46, 2019.
[245] K. M. Katcher, T. Revak, A. Rimpel, J. Ratay, and K. Brun, ‘Abradable Seal Test Rig for Quantifying Abradable Material Performance During Labyrinth Seal Rubs in Centrifugal Compressors: Design and Test Results’, presented at the Turbo Expo: Power for Land, Sea, and Air, American Society of Mechanical Engineers, 2022, p. V007T19A005.
[246] K. Kalista, J. Liska, and J. Jakl, ‘A vibration sensor-based method for generating the precise rotor orbit shape with general notch filter method for new rotor seal design testing and diagnostics’, *Sensors*, vol. 21, no. 15, p. 5249, 2021.
[247] T. M. Adams and R. A. Layton, ‘Introductory Mems’, *Fabrication and*, 2010.
[248] M. Strasik *et al.*, ‘An overview of Boeing flywheel energy storage systems with high-temperature superconducting bearings’, *Superconductor science and technology*, vol. 23, no. 3, p. 034021, 2010.
[249] X. Li, N. Erd, and A. Binder, ‘Evaluation of flywheel energy storage systems for residential photovoltaic installations’, presented at the 2016 International symposium on power electronics, electrical drives, automation and motion (SPEEDAM), IEEE, 2016, pp. 255–260.
[250] H. Wang, Z. Wu, K. Liu, J. Wei, and H. Hu, ‘Modeling and control strategies of a novel axial hybrid magnetic bearing for flywheel energy storage system’, *IEEE/ASME Transactions on Mechatronics*, vol. 27, no. 5, pp. 3819–3829, 2022.

[251] T. S. Slininger, W. Chan, E. L. Severson, and B. Jawdat, ‘An overview on passive magnetic bearings’, presented at the 2021 IEEE International Electric Machines & Drives Conference (IEMDC), IEEE, 2021, pp. 1–8.
[252] J. Lenz, B. Blackman, A. Taylor, R. Morgan, and C. Crua, ‘Selection of test methods to examine the fracture mechanics of carbon fibre composite flywheels’, presented at the 16th European Conference on Composite Materials, 2014, pp. 22–26.
[253] J. Hahne, M. Werst, C. Penney, H.-P. Liu, J. O’Rarden, and D. Bogard, ‘Measurement of windage losses and temperature distribution for a high speed composite rotor in a stator assembly at low air pressures’, presented at the Heat Transfer Summer Conference, 2003, pp. 7–14.
[254] S. Sun, D. Liu, Y.-Z. Wang, S. M. R. S. Naqvi, and H.-B. Kim, ‘Heat transfer characteristics of Taylor–Couette flow with axially distributed slits using field synergy principle and entropy generation analysis’, *International Communications in Heat and Mass Transfer*, vol. 129, p. 105699, 2021.
[255] S. Sun, D. Liu, W.-D. Shi, Y.-Z. Wang, and H.-B. Kim, ‘Numerical Simulations of Heat Transfer Performance of Taylor–Couette Flow in Slit Model’, *Arabian Journal for Science and Engineering*, vol. 46, pp. 7153–7170, 2021.
[256] T. Tsukahara, M. Ishikawa, and Y. Kawaguchi, ‘DNS study of the turbulent Taylor-Vortex flow on a ribbed inner cylinder’, *Advances in Mechanical Engineering*, vol. 5, p. 628490, 2013.
[257] E. S. Karakas, ‘Computational investigation of cavitation performance and heat transfer in cryogenic centrifugal pumps with helical inducers’, 2019.
[258] T. Hayase, J. Humphrey, and R. Greif, ‘Numerical calculation of convective heat transfer between rotating coaxial cylinders with periodically embedded cavities’, 1992.
[259] S. Gokul and M. Deepu, ‘Fluid Flow and Heat Transfer in an Annulus With Ribs on the Rotating Inner Cylinder Surface’, *Journal of Thermal Science and Engineering Applications*, vol. 12, no. 4, p. 041026, 2020.
[260] S.-C. Tzeng, W.-P. Ma, C.-W. Lin, W.-Y. Jywe, C.-H. Liu, and Y.-C. Wang, ‘Experimental investigation of lubrication and cooling effects of high-speed rotating machines’, *The International Journal of Advanced Manufacturing Technology*, vol. 35, pp. 394–399, 2007.
[261] C. Kim, K.-S. Lee, and S.-J. Yook, ‘Effect of air-gap fans on cooling of windings in a large-capacity, high-speed induction motor’, *Applied Thermal Engineering*, vol. 100, pp. 658–667, 2016.
[262] D. Liu, S. Ding, W. Zhou, S. Sun, and H. Kim, ‘Turbulent Taylor–Couette flow and its heat transfer characteristic based on PANS model’, *Journal of Drainage and Irrigation Machinery Engineering*, vol. 37, no. 10, pp. 889–894, 2019.
[263] D. Liu, M. I. A. Mohammedsalih, A.-G. N. Kofi, N. K. Amponsah-Gyenin, S. Ding, and S. Sun, ‘Numerical study of heat flow characteristics of turbulent Taylor-Couette flow in slit wall model.’, *Journal of Engineering Research*, vol. 10, no. 1B, pp. 312–331, 2022.
[264] D. Liu, C. Chao, Y. Wang, F. Zhu, and H.-B. Kim, ‘Axial slit wall effect on the flow instability and heat transfer in rotating concentric cylinders’, *Journal of Mechanical Science and Technology*, vol. 30, pp. 5513–5519, 2016.
[265] Y. Sommerer and G. Lauriat, ‘Numerical study of steady forced convection in a grooved annulus using a design of experiments’, *J. Heat Transfer*, vol. 123, no. 5, pp. 837–848, 2001.
[266] X. Zhu, R. Ostilla-Mónico, R. Verzicco, and D. Lohse, ‘Direct numerical simulation of Taylor–Couette flow with grooved walls: torque scaling and flow structure’, *Journal of fluid mechanics*, vol. 794, pp. 746–774, 2016.
[267] D. Liu, Y. Qi, S. Sun, and Y.-Z. Wang, ‘Numerical investigation of flow and heat transfer between concentric cylinders with slit wall’, *Case Studies in Thermal Engineering*, vol. 22, p. 100783, 2020.
[268] K. Bilen, M. Cetin, H. Gul, and T. Balta, ‘The investigation of groove geometry effect on heat transfer for internally grooved tubes’, *Applied Thermal Engineering*, vol. 29, no. 4, pp. 753–761, 2009.

[269] D. Lorenzini-Gutierrez, A. Hernandez-Guerrero, J. L. Luviano-Ortiz, and J. C. Leon-Conejo, 'Numerical and experimental analysis of heat transfer enhancement in a grooved channel with curved flow deflectors', *Applied Thermal Engineering*, vol. 75, pp. 800–808, 2015.
[270] J. Liu, G. Xie, and T. W. Simon, 'Turbulent flow and heat transfer enhancement in rectangular channels with novel cylindrical grooves', *International Journal of Heat and Mass Transfer*, vol. 81, pp. 563–577, 2015.
[271] Y. Joo and S. J. Kim, 'Thermal optimization of vertically oriented, internally finned tubes in natural convection', *International Journal of Heat and Mass Transfer*, vol. 93, pp. 991–999, 2016.
[272] S. Eiamsa-ard and P. Promvonge, 'Thermal characteristics of turbulent rib-grooved channel flows', *International Communications in Heat and Mass Transfer*, vol. 36, no. 7, pp. 705–711, Aug. 2009, doi: 10.1016/j.icheatmasstransfer.2009.03.025.
[273] A. Nouri-Borujerdi and M. Nakhchi, 'Heat transfer enhancement in annular flow with outer grooved cylinder and rotating inner cylinder: Review and experiments', *Applied Thermal Engineering*, vol. 120, pp. 257–268, 2017.
[274] A. Nouri-Borujerdi and M. Nakhchi, 'Optimization of the heat transfer coefficient and pressure drop of Taylor-Couette-Poiseuille flows between an inner rotating cylinder and an outer grooved stationary cylinder', *International Journal of Heat and Mass Transfer*, vol. 108, pp. 1449–1459, 2017.
[275] D. Liu, S. Sun, S. Ding, N. K. Amponsah-Gyenin, and H.-B. Kim, 'Slit aspect ratio effect on flow instability and heat transfer characteristics of wavy vortex flow', *Arabian Journal for Science and Engineering*, vol. 44, no. 9, pp. 7767–7777, 2019.
[276] D. Henderson, H. Junaidi, T. Muneer, T. Grassie, and J. Currie, 'Experimental and CFD investigation of an ICSSWH at various inclinations', *Renewable and Sustainable Energy Reviews*, vol. 11, no. 6, pp. 1087–1116, Aug. 2007, doi: 10.1016/j.rser.2005.11.003.
[277] S. R. Shabanian, M. Rahimi, M. Shahhosseini, and A. A. Alsairafi, 'CFD and experimental studies on heat transfer enhancement in an air cooler equipped with different tube inserts', *International Communications in Heat and Mass Transfer*, vol. 38, no. 3, pp. 383–390, Mar. 2011, doi: 10.1016/j.icheatmasstransfer.2010.12.015.
[278] B. L. Smith, 'The difference between traditional experiments and CFD validation benchmark experiments', *Nuclear Engineering and Design*, vol. 312, pp. 42–47, Feb. 2017, doi: 10.1016/j.nucengdes.2016.10.007.
[279] J. H. Ferziger and M. PERIĆ, 'Further discussion of numerical errors in CFD', *International Journal for Numerical Methods in Fluids*, vol. 23, no. 12, pp. 1263–1274, 1996.
[280] G. A. Narsilio, O. Buzzi, S. Fityus, T. S. Yun, and D. W. Smith, 'Upscaling of Navier–Stokes equations in porous media: Theoretical, numerical and experimental approach', *Computers and Geotechnics*, vol. 36, no. 7, pp. 1200–1206, Sep. 2009, doi: 10.1016/j.compgeo.2009.05.006.
[281] C. Y. Wu, Y. M. Ferng, C. C. Chieng, and C. C. Liu, 'Investigating the advantages and disadvantages of realistic approach and porous approach for closely packed pebbles in CFD simulation', *Nuclear Engineering and Design*, vol. 240, no. 5, pp. 1151–1159, May 2010, doi: 10.1016/j.nucengdes.2010.01.015.
[282] H. Khoshdast, V. Shojaei, and H. Khoshdast, 'Combined application of computational fluid dynamics (CFD) and design of experiments (DOE) to hydrodynamic simulation of a coal classifier', *International Journal of Mining and Geo-Engineering*, vol. 51, no. 1, pp. 9–24, 2017.
[283] J. O. B. Lira, H. G. Riella, N. Padoin, and C. Soares, 'CFD + DoE optimization of a flat plate photocatalytic reactor applied to NOx abatement', *Chemical Engineering and Processing - Process Intensification*, vol. 154, p. 107998, Aug. 2020, doi: 10.1016/j.cep.2020.107998.
[284] M. Uy and J. K. Telford, 'Optimization by design of experiment techniques', presented at the 2009 IEEE Aerospace conference, IEEE, 2009, pp. 1–10.
[285] G.-J. Park, 'Design of experiments', *Analytic methods for design practice*, pp. 309–391, 2007.
[286] S. S. Garud, I. A. Karimi, and M. Kraft, 'Design of computer experiments: A review', *Computers & Chemical Engineering*, vol. 106, pp. 71–95, 2017.
[287] H. Guo and A. Mettas, 'Design of experiments and data analysis', presented at the 2012 Annual Reliability and Maintainability Symposium, 2010.

[288] B. Durakovic, ‘Design of experiments application, concepts, examples: State of the art’, *Periodicals of Engineering and Natural Sciences*, vol. 5, no. 3, 2017.
[289] J. Blazek, *Computational fluid dynamics: principles and applications*. Butterworth-Heinemann, 2015.
[290] Z. Ali, J. Tyacke, R. Watson, P. G. Tucker, and S. Shahpar, ‘Efficient preprocessing of complex geometries for CFD simulations’, *International Journal of Computational Fluid Dynamics*, vol. 33, no. 3, pp. 98–114, 2019.
[291] D. J. Mavriplis, ‘Progress in CFD discretizations, algorithms and solvers for aerodynamic flows’, presented at the AIAA Aviation 2019 Forum, 2019, p. 2944.
[292] J. E. Matsson, *An Introduction to Ansys Fluent 2023*. Sdc Publications, 2023.
[293] B. Andersson, R. Andersson, L. Håkansson, M. Mortensen, R. Sudiyo, and B. Van Wachem, *Computational fluid dynamics for engineers*. Cambridge university press, 2011.
[294] J. Tu, G. H. Yeoh, and C. Liu, ‘Chapter 3 - Governing Equations for CFD—Fundamentals’, in *Computational Fluid Dynamics*, J. Tu, G. H. Yeoh, and C. Liu, Eds., Burlington: Butterworth-Heinemann, 2008, pp. 65–125. doi: 10.1016/B978-075068563-4.50005-7.
[295] J. D. Anderson and J. Wendt, *Computational fluid dynamics*, vol. 206. Springer, 1995.
[296] C. Lin, M. H. Tawhai, G. Mclennan, and E. A. Hoffman, ‘Computational fluid dynamics’, *IEEE Engineering in Medicine and Biology Magazine*, vol. 28, no. 3, pp. 25–33, 2009.
[297] J.-D. Müller, *Essentials of computational fluid dynamics*. CRC Press, 2015.
[298] G. Chen, Q. Xiong, P. J. Morris, E. G. Paterson, A. Sergeev, and Y. Wang, ‘OpenFOAM for computational fluid dynamics’, *Notices of the AMS*, vol. 61, no. 4, pp. 354–363, 2014.
[299] J. E. Matsson, *An Introduction to ANSYS Fluent 2022*. Sdc Publications, 2022.
[300] H. Versteeg and W. Malalasekera, ‘Computational fluid dynamics’, *The finite volume method*, pp. 1–26, 1995.
[301] M. Keating and A. Principal Engineer, ‘Accelerating CFD solutions’, *advantage*, vol. 1, p. 48, 2011.
[302] M. Tabib, M. S. Siddiqui, A. Rasheed, and T. Kvamsdal, ‘Industrial scale turbine and associated wake development-comparison of RANS based Actuator Line Vs Sliding Mesh Interface Vs Multiple Reference Frame method.’, *Energy Procedia*, vol. 137, pp. 487–496, 2017.
[303] P. Romanazzi and D. A. Howey, ‘Air-gap convection in a switched reluctance machine’, presented at the 2015 Tenth International Conference on Ecological Vehicles and Renewable Energies (EVER), IEEE, 2015, pp. 1–7.
[304] D. S. Adebayo and A. Rona, ‘The three-dimensional velocity distribution of wide gap Taylor-Couette flow modelled by CFD’, *International Journal of Rotating Machinery*, vol. 2016, 2016.
[305] D. A. Howey, A. S. Holmes, and K. R. Pullen, ‘Measurement and CFD prediction of heat transfer in air-cooled disc-type electrical machines’, *IEEE Transactions on Industry Applications*, vol. 47, no. 4, pp. 1716–1723, 2011.
[306] C. Jungreuthmayer *et al.*, ‘A detailed heat and fluid flow analysis of an internal permanent magnet synchronous machine by means of computational fluid dynamics’, *IEEE Transactions on Industrial Electronics*, vol. 59, no. 12, pp. 4568–4578, 2011.
[307] K. M. Tenny and J. S. Cooper, ‘Ideal Gas Behavior’, 2017.
[308] R. Kuhne and P. Michalopoulos, ‘Continuum flow models’, *Traffic flow theory: A state of the art reportrevised monograph on traffic flow theory*, vol. 18, 1997.
[309] A. S. Balankin and B. E. Elizarraraz, ‘Map of fluid flow in fractal porous medium into fractal continuum flow’, *Physical Review E*, vol. 85, no. 5, p. 056314, 2012.
[310] B. Ma, V. Ruwet, P. Corieri, R. Theunissen, M. Riethmuller, and C. Darquenne, ‘CFD simulation and experimental validation of fluid flow and particle transport in a model of alveolated airways’, *Journal of aerosol science*, vol. 40, no. 5, pp. 403–414, 2009.
[311] M. Heggemann, S. Hirschberg, L. Spiegel, and C. Bachmann, ‘CFD simulation and experimental validation of fluid flow in liquid distributors’, *Chemical Engineering Research and Design*, vol. 85, no. 1, pp. 59–64, 2007.

[312] M. Khoshvaght-Aliabadi, S. Zangouei, and F. Hormozi, ‘Performance of a plate-fin heat exchanger with vortex-generator channels: 3D-CFD simulation and experimental validation’, *International Journal of Thermal Sciences*, vol. 88, pp. 180–192, 2015.
[313] ‘F-Boost products page’, Punch Flybrid. Accessed: Nov. 12, 2023. [Online]. Available: https://punchflybrid.com/f-boost-products-page/
[314] R. Donnelly, ‘Experiments on the stability of viscous flow between rotating cylinders I. Torque measurements’, *Proceedings of the Royal Society of London. Series A. Mathematical and Physical Sciences*, vol. 246, no. 1246, pp. 312–325, 1958.
[315] R. Donnelly and N. Simon, ‘An empirical torque relation for supercritical flow between rotating cylinders’, *Journal of Fluid Mechanics*, vol. 7, no. 3, pp. 401–418, 1960.
[316] H. Reichardt, ‘Über die Geschwindigkeitsverteilung in einer geradlinigen turbulenten Couetteströmung’, *ZAMM-Journal of Applied Mathematics and Mechanics/Zeitschrift für Angewandte Mathematik und Mechanik*, vol. 36, no. S1, pp. S26–S29, 1956.
[317] T. Tatsumi, ‘Turbulence as a complex mechanical-system’, *Applied energy*, vol. 67, no. 1–2, pp. 91–116, 2000.
[318] H. Aoki, H. Nohira, and H. Arai, ‘Convective heat transfer in an annulus with an inner rotating cylinder’, *Bulletin of JSME*, vol. 10, no. 39, pp. 523–532, 1967.
[319] R. Pena-Alzola, R. Sebastián, J. Quesada, and A. Colmenar, ‘Review of flywheel based energy storage systems’, presented at the 2011 International Conference on Power Engineering, Energy and Electrical Drives, IEEE, 2011, pp. 1–6.
[320] F. Wardle, *Ultra-precision bearings*. Elsevier, 2015.
[321] A. Palmgren, ‘Ball and roller bearing engineering’, *Philadelphia: SKF Industries Inc*, 1959.
[322] S. Rastegarzadeh, M. Mahzoon, and H. Mohammadi, ‘A novel modular designing for multi-ring flywheel rotor to optimize energy consumption in light metro trains’, *Energy*, vol. 206, p. 118092, 2020.
[323] J. W. Daily and R. E. Nece, ‘Chamber dimension effects on induced flow and frictional resistance of enclosed rotating disks’, 1960.
[324] W. M. Rohsenow, J. P. Hartnett, and E. N. Ganic, ‘Handbook of heat transfer fundamentals’, 1985.
[325] H.-P. Liu, M. Werst, J. Hahne, and D. Bogard, ‘Investigation of windage splits in an enclosed test fixture having a high speed composite rotor in low air pressure environments’, presented at the 2004 12th Symposium on Electromagnetic Launch Technology, IEEE, 2004, pp. 223–228.
[326] J. W. Beck, ‘Bimodal two-stream distribution and compressible Couette flow’, *Rarefied Gas Dynamics, Volume 1*, vol. 1, p. 354, 1965.
[327] L. Lees, ‘A kinetic theory description of rarefied gas flows’, 1959.
[328] A. Kuhlthau, ‘Air friction on rapidly moving surfaces’, *Journal of Applied Physics*, vol. 20, no. 2, pp. 217–223, 1949.
[329] D. J. Alofs and G. S. Springer, ‘Rotating cylinder apparatus for rarefied gas flow studies’, *Review of Scientific Instruments*, vol. 41, no. 8, pp. 1161–1163, 1970.
[330] E. H. Kennard, *Kinetic theory of gases*, vol. 483. McGraw-hill New York, 1938.
[331] J. Bowyer and L. Talbot, ‘Engineering Projects Research Report HE-150-199’, *University of California: Berkeley, CA, USA*, 1956.
[332] U. Diego-Ayala, *An investigation into hybrid power trains for vehicles with regenerative braking*. bramona, 2007.
[333] T. Jokinen, V. Hrabovcova, and J. Pyrhonen, *Design of rotating electrical machines*. John Wiley & Sons, 2013.
[334] P. R. Childs, *Rotating flow*. Elsevier, 2010.
[335] T. v Kármán, ‘Über laminare und turbulente Reibung’, *ZAMM-Journal of Applied Mathematics and Mechanics/Zeitschrift für Angewandte Mathematik und Mechanik*, vol. 1, no. 4, pp. 233–252, 1921.
[336] L. Dorfman, ‘Resistance of a rotating rough disc’, *Tech. phys. Zhurnal Tekhnicheskoi Fiziki*, vol. 28, pp. 353–367, 1958.
[337] F. Bayley and J. Owen, ‘Flow between a rotating and a stationary disc’, *Aeronautical Quarterly*, vol. 20, no. 4, pp. 333–354, 1969.

[338] D. H. Sharp, ‘An overview of Rayleigh-Taylor instability’, *Physica D: Nonlinear Phenomena*, vol. 12, no. 1–3, pp. 3–18, 1984.
[339] S. S. Deshmukh, S. Vedantam, J. B. Joshi, and S. B. Koganti, ‘Computational flow modeling and visualization in the annular region of annular centrifugal extractor’, *Industrial & engineering chemistry research*, vol. 46, no. 25, pp. 8343–8354, 2007.
[340] K. W. Moser *et al.*, ‘Visualization of Taylor–Couette and spiral Poiseuille flows using a snapshot FLASH spatial tagging sequence’, *Magnetic resonance imaging*, vol. 18, no. 2, pp. 199–207, 2000.
[341] C. D. Andereck, S. Liu, and H. L. Swinney, ‘Flow regimes in a circular Couette system with independently rotating cylinders’, *Journal of fluid mechanics*, vol. 164, pp. 155–183, 1986.
[342] C.-J. Wu, L. Wang, and J.-Z. Wu, ‘Suppression of the von Kármán vortex street behind a circular cylinder by a travelling wave generated by a flexible surface’, *Journal of Fluid Mechanics*, vol. 574, pp. 365–391, 2007.
[343] P. Acarnley, B. Mecrow, J. Burdess, J. Fawcett, P. Dickinson, and J. Kelly, ‘An integrated flywheel/machine energy store for road vehicles’, presented at the IEE Colloquium on New Topologies for Permanent Magnet Machines (Digest No: 1997/090), IET, 1997, pp. 9–1.
[344] P. Reinke, M. Schmidt, and T. Beckmann, ‘The cavitating Taylor-Couette flow’, *Physics of Fluids*, vol. 30, no. 10, p. 104101, 2018.
[345] J. E. Vrancik, *Prediction of windage power loss in alternators*, vol. 4849. National Aeronautics and Space Administration, 1968.
[346] C. S. Hearn, ‘Design methodologies for advanced flywheel energy storage’, 2013.
[347] P. Tsilingiris, ‘Thermal flywheel effects on the time varying conduction heat transfer through structural walls’, *Energy and Buildings*, vol. 35, no. 10, pp. 1037–1047, 2003.
[348] A. S. Nagorny, N. V. Dravid, R. H. Jansen, and B. H. Kenny, ‘Design aspects of a high speed permanent magnet synchronous motor/generator for flywheel applications’, presented at the IEEE International Conference on Electric Machines and Drives, 2005., IEEE, 2005, pp. 635–641.
[349] C. Huynh, P. McMullen, A. Filatov, S. Imani, H. A. Toliyat, and S. Talebi, ‘Flywheel energy storage system for naval applications’, presented at the Turbo Expo: Power for Land, Sea, and Air, 2006, pp. 25–33.
[350] M. A. Sokolov *et al.*, ‘Analytical method for design and thermal evaluation of a long-term flywheel energy storage system’, presented at the 2016 International Symposium on Power Electronics, Electrical Drives, Automation and Motion (SPEEDAM), IEEE, 2016, pp. 270–275.
[351] A. Feliciano de Oliveira, ‘Thermal analysis of a vacuum sealed flywheel’, 2021.
[352] S. Choudhury, ‘Flywheel energy storage systems: A critical review on technologies, applications, and future prospects’, *International Transactions on Electrical Energy Systems*, vol. 31, no. 9, p. e13024, 2021.
[353] R. Tamrakar and N. D. Mittal, *Design and Static Stress Analysis of Single Cylinder Crankshaft*. LAP LAMBERT Academic Publishing, 2019.
[354] H. J. Petroski and R. P. Ojdrovic, ‘The concrete cylinder: stress analysis and failure modes’, *International journal of fracture*, vol. 34, no. 4, pp. 263–279, 1987.
[355] M. Bayat, M. Saleem, B. Sahari, A. Hamouda, and E. Mahdi, ‘Mechanical and thermal stresses in a functionally graded rotating disk with variable thickness due to radially symmetry loads’, *International Journal of Pressure Vessels and Piping*, vol. 86, no. 6, pp. 357–372, 2009.
[356] D. R. Talancon, *Design, Fabrication, and Testing of the INSTAR [INertial STorage And Recovery] System A Flywheel-Based, High Power Energy Storage System for Improved Hybrid Vehicle Fuel Efficiency*. University of California, Berkeley, 2015.
[357] S. R. Holm, ‘Modelling and optimization of a permanent-magnet machine in a flywheel’, 2003.
[358] P. F. Ribeiro, B. K. Johnson, M. L. Crow, A. Arsoy, and Y. Liu, ‘Energy storage systems for advanced power applications’, *Proceedings of the IEEE*, vol. 89, no. 12, pp. 1744–1756, 2001.
[359] P. Singh and H. Chaudhary, ‘Optimal design of the flywheel using nature inspired optimization algorithms’, *Open Agriculture*, vol. 3, no. 1, pp. 490–499, 2018.

[360] H. Asodariya, H. V. Patel, D. Babariya, and K. Maniya, ‘Application of multi criteria decision making method to select and validate the material of a flywheel design’, *Materials Today: Proceedings*, vol. 5, no. 9, pp. 17147–17155, 2018.
[361] P. Purohit and M. Ramachandran, ‘Selection of flywheel material using multicriteria decision making fuzzy TOPSIS’, *Indian Journal of Science and Technology*, vol. 8, no. 33, pp. 1–5, 2015.
[362] A. P. Punde and G. Gattani, ‘Analysis of flywheel’, *International Journal of Modern Engineering Research (IJMER)*, vol. 3, no. 2, pp. 1097–9, 2013.
[363] Y. Han, Z. Ren, and Y. Tong, ‘General Design Method of Flywheel Rotor for Energy Storage System’, *Energy Procedia*, vol. 16, pp. 359–364, Jan. 2012, doi: 10.1016/j.egypro.2012.01.059.
[364] K. van Berkel, S. Rullens, T. Hofman, B. Vroemen, and M. Steinbuch, ‘Topology and flywheel size optimization for mechanical hybrid powertrains’, *IEEE Transactions on Vehicular Technology*, vol. 63, no. 9, pp. 4192–4205, 2014.
[365] S. Motaman, M. Eltaweel, M. R. Herfatmanesh, T. Knichel, and A. Deakin, ‘Numerical analysis of a flywheel energy storage system for low carbon powertrain applications’, *Journal of Energy Storage*, vol. 61, p. 106808, May 2023, doi: 10.1016/j.est.2023.106808.
[366] P. K. Kundu, I. M. Cohen, and D. R. Dowling, ‘Chapter 11 - Instability’, in *Fluid Mechanics (Sixth Edition)*, P. K. Kundu, I. M. Cohen, and D. R. Dowling, Eds., Boston: Academic Press, 2016, pp. 533–602. doi: 10.1016/B978-0-12-405935-1.00011-3.
[367] R. Deng, D. Y. Arifin, Y. C. Mak, and C. Wang, ‘Characterization of Taylor vortex flow in a short liquid column’, *AIChE journal*, vol. 55, no. 12, pp. 3056–3065, 2009.
[368] D. S. Adebayo, ‘Annular flows and their interaction with a cylindrical probe’, 2012.
[369] M. Eltaweel, C. Kalyvas, Y. Chen, and M. R. Herfatmanesh, ‘Development of a CFD Model for the Estimation of Windage Losses Inside the Narrow Air Gap of an Enclosed High-Speed Flywheel’, presented at the International Conference on Energy and Sustainable Futures, Springer Nature Switzerland Cham, 2022, pp. 157–167.
[370] H. Scheffe, *The analysis of variance*, vol. 72. John Wiley & Sons, 1999.
[371] M. Kadivar, D. Tormey, and G. McGranaghan, ‘A review on turbulent flow over rough surfaces: Fundamentals and theories’, *International Journal of Thermofluids*, vol. 10, p. 100077, May 2021, doi: 10.1016/j.ijft.2021.100077.
[372] A. T. Abbas, A. A. Al-Abduljabbar, I. A. Alnaser, M. F. Aly, I. H. Abdelgaliel, and A. Elkaseer, ‘A Closer Look at Precision Hard Turning of AISI4340: Multi-Objective Optimization for Simultaneous Low Surface Roughness and High Productivity’, *Materials*, vol. 15, no. 6, p. 2106, 2022.
[373] C.-D. Wen and I. Mudawar, ‘Modeling the effects of surface roughness on the emissivity of aluminum alloys’, *International journal of heat and mass transfer*, vol. 49, no. 23–24, pp. 4279–4289, 2006.
[374] M. Tabatabaei, A. Lovison, M. Tan, M. Hartikainen, and K. Miettinen, ‘ANOVA-MOP: ANOVA decomposition for multiobjective optimization’, *SIAM Journal on Optimization*, vol. 28, no. 4, pp. 3260–3289, 2018.
[375] M. G. Larson, ‘Analysis of variance’, *Circulation*, vol. 117, no. 1, pp. 115–121, 2008.
[376] A. C. Atkinson, M. Riani, and A. Corbellini, ‘The box–cox transformation: Review and extensions’, 2021.
[377] M. Fénot, Y. Bertin, E. Dorignac, and G. Lalizel, ‘A review of heat transfer between concentric rotating cylinders with or without axial flow’, *International journal of thermal sciences*, vol. 50, no. 7, pp. 1138–1155, 2011.
[378] R. A. Verschoof *et al.*, ‘Rough-wall turbulent Taylor-Couette flow: The effect of the rib height’, *The European Physical Journal E*, vol. 41, no. 10, pp. 1–9, 2018.
[379] L. Hu, Q. Deng, Z. Liu, J. Li, and Z. Feng, ‘Effects of Surface Roughness on Windage Loss and Flow Characteristics in Shaft-Type Gap with Critical CO2’, *Applied Sciences*, vol. 12, no. 24, p. 12631, 2022.
[380] L. Pokorny, N. J. Saikia, Y. Takeda, and E. J. Windhab, ‘Influence of surface roughness on the flow behavior in TVF and WVF’, presented at the Proceedings of the 10th International Symposium on Ultrasonic Doppler Methods for Fluid Mechanics and Fluid Engineering (ISUD

10), 10th International Symposium on Ultrasonic Doppler Methods for Fluid …, 2016, pp. 13–16.
[381] L. Gaied, E. Berrich, M. Bigerelle, and F. Aloui, ‘Experimental study of the wall surfaces’ roughness influence on the hydrodynamics’ instabilities in a Couette-Taylor flow’, presented at the 23èmeCongrès Français de Mécanique, 2018.
[382] P. Berghout, X. Zhu, D. Chung, R. Verzicco, R. J. Stevens, and D. Lohse, ‘Direct numerical simulations of Taylor–Couette turbulence: the effects of sand grain roughness’, *Journal of fluid mechanics*, vol. 873, pp. 260–286, 2019.
[383] R. H. Myers, D. C. Montgomery, and C. M. Anderson-Cook, *Response surface methodology: process and product optimization using designed experiments*. John Wiley & Sons, 2016.
[384] ‘Standard | Pfeiffer Vacuum’. Accessed: Feb. 27, 2023. [Online]. Available: https://www.pfeiffer-vacuum.com/en/products/vacuum-generation/rotary-vane-pumps/two-stage/standard/16158/duo-3-dc-24-v-dc-dn-16-iso-kf
[385] ‘vacuum pump selection and calculation- Vacuum Pump - EVP Vacuum Solution!’ Accessed: Feb. 27, 2023. [Online]. Available: https://www.evpvacuum.com/vacuum-pump-selection-and-calculation.html
[386] W.-H. Chen *et al.*, ‘A comprehensive review of thermoelectric generation optimization by statistical approach: Taguchi method, analysis of variance (ANOVA), and response surface methodology (RSM)’, *Renewable and Sustainable Energy Reviews*, vol. 169, p. 112917, 2022.
[387] W.-H. Chen, C.-Y. Chen, C.-Y. Huang, and C.-J. Hwang, ‘Power output analysis and optimization of two straight-bladed vertical-axis wind turbines’, *Applied energy*, vol. 185, pp. 223–232, 2017.
[388] Z. Bao, F. Yang, Z. Wu, S. N. Nyamsi, and Z. Zhang, ‘Optimal design of metal hydride reactors based on CFD–Taguchi combined method’, *Energy Conversion and Management*, vol. 65, pp. 322–330, 2013.
[389] H. A. Petit, C. I. Paulo, O. A. Cabrera, and E. F. Irassar, ‘Modelling and optimization of an inclined plane classifier using CFD-DPM and the Taguchi method’, *Applied Mathematical Modelling*, vol. 77, pp. 617–634, 2020.
[390] N. Mandal, B. Doloi, B. Mondal, and R. Das, ‘Optimization of flank wear using Zirconia Toughened Alumina (ZTA) cutting tool: Taguchi method and Regression analysis’, *Measurement*, vol. 44, no. 10, pp. 2149–2155, 2011.
[391] M. H. Khanjanpour and A. A. Javadi, ‘Optimization of the hydrodynamic performance of a vertical Axis tidal (VAT) turbine using CFD-Taguchi approach’, *Energy Conversion and Management*, vol. 222, p. 113235, 2020.
[392] K. Yamagata, J. Kobuchi, and R. Shimada, ‘Study of cooling gases for windage loss reduction’, *IEEJ Transactions on Power and Energy*, vol. 120, no. 3, pp. 478–483, 2000.
[393] J. Kobuchi, K. Oobayashi, and R. Shimada, ‘Windage loss reduction of flywheel/generator system using He and SF/sub 6/gas mixtures’, presented at the IECEC-97 Proceedings of the Thirty-Second Intersociety Energy Conversion Engineering Conference (Cat. No. 97CH6203), IEEE, 1997, pp. 1754–1757.
[394] L. Hu, Q. Deng, J. Li, and Z. Feng, ‘Model improvement for shaft-type windage loss with CO2’, *The Journal of Supercritical Fluids*, vol. 190, p. 105747, 2022.
[395] V. Reidenbach, P. Harris, Y. Lee, and D. Lord, ‘Rheological study of foam fracturing fluids using nitrogen and carbon dioxide’, *SPE Production Engineering*, vol. 1, no. 04, pp. 245–254, 1986.
[396] A. Hasçalık and U. Çaydaş, ‘Optimization of turning parameters for surface roughness and tool life based on the Taguchi method’, *The International Journal of Advanced Manufacturing Technology*, vol. 38, no. 9, pp. 896–903, 2008.
[397] Z. Wang, Y. Wang, and M. Zhuang, ‘Improvement of the aerodynamic performance of vertical axis wind turbines with leading-edge serrations and helical blades using CFD and Taguchi method’, *Energy conversion and management*, vol. 177, pp. 107–121, 2018.
[398] R. K. Roy, *A primer on the Taguchi method*. Society of Manufacturing Engineers, 2010.
[399] A. B. Naik and A. C. Reddy, ‘Optimization of tensile strength in TIG welding using the Taguchi method and analysis of variance (ANOVA)’, *Thermal Science and Engineering Progress*, vol. 8, pp. 327–339, 2018.

[400] R. L. Ott and M. T. Longnecker, *An introduction to statistical methods and data analysis*. Cengage Learning, 2015.
[401] M. S. Phadke, *Quality engineering using robust design*. Prentice Hall PTR, 1995.
[402] M. Eltaweel and M. R. Herfatmanesh, 'Analysis of Standby Power in an Enclosed High-Speed Flywheel Energy Storage System Using the CFD-ANOVA Approach', SAE Technical Paper, 2023.
[403] K. Ryu and K.-S. Lee, 'Generalized heat-transfer and fluid-flow correlations for corrugated louvered fins', *International Journal of Heat and Mass Transfer*, vol. 83, pp. 604–612, 2015.
[404] A. Nouri-Borujerdi, M. Bovand, S. Rashidi, and K. Dincer, 'Geometric parameters and response surface methodology on cooling performance of vortex tubes', *International Journal of Sustainable Energy*, vol. 36, no. 9, pp. 872–886, Oct. 2017, doi: 10.1080/14786451.2015.1127233.
[405] M. Eltaweel and M. R. Herfatmanesh, 'Numerical Investigation of Windage Loss and Heat Transfer in a High-Speed Flywheel Energy Storage System With Slit Wall', presented at the Turbo Expo: Power for Land, Sea, and Air, American Society of Mechanical Engineers, 2023, p. V006T09A013.
[406] Z. Pan, X. Wang, R. Teng, and X. Cao, 'Computer-aided design-while-engineering technology in top-down modeling of mechanical product', *Computers in industry*, vol. 75, pp. 151–161, 2016.
[407] K. Tammi, T. Minav, and J. Kortelainen, 'Thirty years of electro-hybrid powertrain simulation', *IEEE access*, vol. 6, pp. 35250–35259, 2018.
[408] C. S. Chin, *Computer-Aided Control Systems Design: Practical Applications Using MATLAB® and Simulink®*. CRC Press, 2012.
[409] A. Szántó and G. Á. Szíki, 'Review of modern vehicle powertrains and their modelling and simulation in MATLAB/Simulink', *International Journal of Engineering and Management Sciences*, vol. 5, no. 2, pp. 232–250, 2020.
[410] 'Vehicle licensing statistics: April to June 2022', GOV.UK. Accessed: Mar. 26, 2024. [Online]. Available: https://www.gov.uk/government/statistics/vehicle-licensing-statistics-april-to-june-2022/vehicle-licensing-statistics-april-to-june-2022
[411] 'Vauxhall Corsa | Small Cars | Vauxhall'. Accessed: Mar. 26, 2024. [Online]. Available: https://www.vauxhall.co.uk/cars/new-corsa/overview.html
[412] F. Sher *et al.*, 'Novel strategies to reduce engine emissions and improve energy efficiency in hybrid vehicles', *Cleaner Engineering and Technology*, vol. 2, p. 100074, 2021.
[413] V. Krithika and C. Subramani, 'A comprehensive review on choice of hybrid vehicles and power converters, control strategies for hybrid electric vehicles', *International journal of energy research*, vol. 42, no. 5, pp. 1789–1812, 2018.
[414] N. N. Mustafi, 'An overview of hybrid electric vehicle technology', *Engines and Fuels for Future Transport*, pp. 73–102, 2022.
[415] '**New Corsa Top For Aerodynamics**
'. Accessed: Mar. 26, 2024. [Online]. Available: https://www.vauxhall.co.uk/experience/vauxhall-news/2019/08/new-corsa-top-for-aerodynamics.html
[416] S. Miller, 'Hybrid-electric vehicle model in simulink', *https//www. mathworks. com/matlabcentral/fileexchange/28441). MATLAB Cent. File Exch*, 2024.
[417] K. Koprubasi *et al.*, 'Application of model-based design techniques for the control development and optimization of a hybrid-electric vehicle', SAE Technical Paper, 0148–7191, 2009.
[418] F. Mohammadi, G.-A. Nazri, and M. Saif, 'Modeling, Simulation, and analysis of hybrid electric vehicle using MATLAB/simulink', presented at the 2019 International Conference on Power Generation Systems and Renewable Energy Technologies (PGSRET), IEEE, 2019, pp. 1–5.
[419] 'Generic internal combustion engine - MATLAB - MathWorks United Kingdom'. Accessed: Mar. 27, 2024. [Online]. Available: https://uk.mathworks.com/help/sdl/ref/genericengine.html
[420] 'Vehicle Dynamics Blockset Documentation - MathWorks United Kingdom'. Accessed: Mar. 27, 2024. [Online]. Available: https://uk.mathworks.com/help/vdynblks/

[421] ‘Vehicle Certification Agency’, Vehicle Certification Agency. Accessed: Nov. 10, 2023. [Online]. Available: https://www.vehicle-certification-agency.gov.uk/
[422] ‘International: Light-duty: Worldwide Harmonized Light Vehicles Test Procedure (WLTP) | Transport Policy’. Accessed: Nov. 10, 2023. [Online]. Available: https://www.transportpolicy.net/standard/international-light-duty-worldwide-harmonized-light-vehicles-test-procedure-wltp/
[423] P. Balendra, ‘Vehicle Speed Compliance Statistics, Great Britain: January–June 2020’, *Technical Report September, Department for Transport*, 2020.
[424] D. Shi, S. Wang, P. Pisu, L. Chen, R. Wang, and R. Wang, ‘Modeling and optimal energy management of a power split hybrid electric vehicle’, *Science China Technological Sciences*, vol. 60, pp. 713–725, 2017.
[425] R. No, ‘of the Economic Commission for Europe of the United Nations (UN/ECE)—Uniform provisions concerning the approval of vehicles of categories M’, *N and O with regard to braking [2016/194]*, vol. 10, 13.
[426] E. Vinot and R. Trigui, ‘Optimal energy management of HEVs with hybrid storage system’, *Energy Conversion and Management*, vol. 76, pp. 437–452, 2013.
[427] S. Sarvaiya, S. Ganesh, and B. Xu, ‘Comparative analysis of hybrid vehicle energy management strategies with optimization of fuel economy and battery life’, *Energy*, vol. 228, p. 120604, 2021.
[428] ‘Vauxhall | Order your Vauxhall New Corsa 5 Door Hatchback GS Hybrid 1.2 100PS e-DCT6 Dual Clutch 6-speed online’. Accessed: Mar. 31, 2024. [Online]. Available: https://store.vauxhall.co.uk/selector/configurable/new-corsa-5-door-hatchback/gs/hybrid-1-2-100ps-e-dct6-dual-clutch-6-speed-hybrid/arctic-white-brilliant/cloth-banda-white-marvel-black?_gl=1*1oxbtj9*_ga*MjEzOTI3NTI0Ni4xNzA1MDc0NDQ1*_ga_DS96737T2L*MTcxMTgwODg2Mi41LjEuMTcxMTgwODg5Mi4wLjAuMA..
[429] ‘Super Precision Bearings | Products | NSK Global’. Accessed: Mar. 12, 2022. [Online]. Available: https://www.nsk.com/products/spb/

Appendix A

Table A-1 Values of permissible static load factor [320] [429]

Operation conditions	**Lower limits of $f_s = C_s/F_s$**	
	Ball bearings	Roller bearings
Low noise applications	2	3
Bearings subjected to vibration and shock loads	1.5	2
Standard operating conditions	1	1.5

Table A-2 values of load, torque and lubrication factors [320] [429]

	Equivalent load factors		**Load torque factors**		**Lubrication factor f_o**		
Bearing type	*Xs*	*Ys*	*z*	*y*	Oil mist/ injection	Oil bath/grease	Oil bath/jet
Single row radial	0.6	0.5	0.0007	0.55	0.7-1	1.5-2	3-4
Angular contact ($\alpha = 15°$)	0.5	0.47	0.001	0.33	1	3	6
($\alpha = 20°$)	0.5	0.42	0.001	0.33	1	3	6
($\alpha = 25°$)	0.5	0.38	0.001	0.33	1	3	6
($\alpha = 30°$)	0.5	0.33	0.001	0.33	1	3	6
($\alpha = 35°$)	0.5	0.29	0.001	0.33	1	3	6
($\alpha = 40°$)	0.5	0.26	0.001	0.33	1	3	6
Angular contact double row	-	-	-	-	2	6	9

Table A-3 Values of load factors X and Y for angular bearings [320] [429]

Nominal contact angle	$\frac{F_a}{C_s}$	**e**	$\frac{F_a}{F_r} \leq e$		$\frac{F_a}{F_r} > e$	
			X	Y	X	Y
15	0.178	0.38	1	0	0.44	1.47
	0.357	0.40				1.40
	0.714	0.43				1.30
	1.070	0.46				1.23
	1.430	0.47				1.19
	2.140	0.50				1.12
	3.570	0.55				1.02
	5.350	0.56				1.00
18	-	0.57	1	0	0.43	1.00
25	-	0.68	1	0	0.41	0.87
30	-	0.80	1	0	0.39	0.76
40	-	1.14	1	0	0.35	0.57
50	-	1.49	-	-	0.73	1
55	-	1.79	-	-	0.81	1
60	-	2.17	-	-	0.92	1

Appendix B

Table B-1 The rotor mass, material cost, and kinetic energy of each flywheel configuration calculation

Material	Radius (m)	Max rotational speed @ 2 factor of safety	Mass (kg)	Kinetic Energy (KJ)	Rotor Cost (£)
Steel 4340	0.06	5372	5.2	136	12.5
	0.07	4605	8.3	215	19.9
	0.08	4029	12.4	322	29.7
	0.09	3581	17.6	458	42.3
	0.1	3223	24.2	628	58.0
	0.11	2930	32.2	836	77.2
	0.12	2686	41.8	1085	100.3
	0.13	2479	53.1	1380	127.5
Aluminium 7075	0.08	3981	4.5	115	18.1
	0.09	3539	6.4	163	25.7
	0.1	3185	8.8	224	35.3
	0.11	2895	11.7	298	47.0
	0.12	2654	15.2	387	61.0
	0.13	2450	19.4	492	77.5
	0.14	2275	24.2	614	96.8
	0.15	2123	29.8	755	119.1
17-7 PH Stainless steel	0.06	5420	5.3	140	25.4
	0.07	4646	8.4	222	40.3
	0.08	4065	12.5	332	60.2
	0.09	3614	17.9	472	85.7
	0.1	3252	24.5	648	117.6
	0.11	2957	32.6	862	156.5
	0.12	2710	42.3	1119	203.1
	0.13	2502	53.8	1423	258.3
Alloy steel 30CrNiMo8	0.07	3626	8.4	135	53.5
	0.08	3173	12.5	201	79.8
	0.09	2820	17.8	286	113.7
	0.1	2538	24.4	393	155.9
	0.11	2308	32.4	522	207.6
	0.12	2115	42.1	678	269.5
	0.13	1953	53.5	862	342.6
Maraging steel 18Ni250	0.06	5683	5.4	158	195.3
	0.07	4871	8.6	250	310.2

Titanium Ti-15V-3Cr-3Al-3Sn ST 790 °C	0.06	6253	3.2	114	64.6
	0.07	5360	5.1	180	102.5
	0.08	4690	7.7	269	153.1
	0.09	4169	10.9	383	217.9
	0.1	3752	14.9	526	298.9
	0.11	3411	19.9	700	397.9
Kevlar	0.06	15180	0.9	126	27.5
	0.07	13011	1.4	200	43.7
	0.08	11385	2.1	299	65.2
	0.09	10120	3.0	426	92.9
	0.1	9108	4.1	584	127.4
	0.11	8280	5.4	778	169.6
Toray T1000G composite	0.06	12273	1.1	102	88.5
	0.07	10520	1.7	163	140.5
	0.08	9205	2.6	243	209.7
	0.09	8182	3.7	346	298.6
	0.1	7364	5.1	474	409.6
Carbon fibre reinforced +epoxy resin	0.07	10172	1.5	131	77.9
	0.08	8900	2.2	195	116.2
	0.09	7911	3.2	278	165.5
	0.1	7120	4.4	382	227.0
	0.11	6473	5.8	508	302.2
S Glass	0.08	6154	2.8	116	55.4
	0.09	5470	3.9	165	78.8
	0.1	4923	5.4	226	108.2
	0.11	4475	7.2	301	144.0

Appendix C

Table C-1 Parameter details for the WLTP class 1 cycle

Phase	Duration	Stop duration	Distance	Stop percentage	Max. velocity	Avg. Velocity w/o stops	Avg. Velocity w/ stops	Min. acceleration	Max. acceleration
	s	s	m		km/h	km/h	km/h	m/s²	m/s²
Low	589	155	3324	26.3%	49.1	27.6	20.3	-1.00	0.76
Middle	433	48	4767	11.1%	64.4	44.6	39.6	-0.57	0.63
Total	**1022**	**203**	**8091**						

Table C-2 Parameter details for the WLTP class 2 cycle

Phase	Duration	Stop duration	Distance	Stop percentage	Max. velocity	Avg. Velocity w/o stops	Avg. Velocity w/ stops	Min. acceleration	Max. acceleration
	s	s	m		km/h	km/h	km/h	m/s²	m/s²
Low	589	155	3132	26.3%	51.4	26.0	19.1	-1.07	0.92
Middle	433	48	4712	11.1%	74.7	44.1	39.2	-0.99	0.96
High	455	30	6820	6.6%	85.2	57.8	54.0	-1.11	0.85
Total	**1477**	**233**	**14664**						

Table C-3 Parameter details for the WLTP class 3 cycle

Phase	Duration	Stop duration	Distance	Stop percentage	Max. velocity	Avg. Velocity w/o stops	Avg. Velocity w/ stops	Min. acceleration	Max. acceleration
	s	s	m		km/h	km/h	km/h	m/s²	m/s²
Low	590	145	3095	24.6%	56.5	25.0	18.9	-1.47	1.47
Middle	433	47	4756	10.9%	76.6	44.4	39.5	-1.49	1.57
High	455	29	7162	6.4%	97.4	60.5	56.7	-1.49	1.58
Extra-High	323	6	8254	1.9%	131.3	93.7	92.0	-1.21	1.03
Total	**1801**	**227**	**23266**						